

THESIS

*Experimental and Mathematical
Investigation of the Chaotic Dripping Mode*

By **Jevgenijs TRUNINS**

A THESIS SUBMITTED TO KINGSTON UNIVERSITY OF LONDON

FOR THE DEGREE OF DOCTOR OF PHILOSOPHY

DEPARTMENT OF MECHANICAL ENGINEERING

JUNE 2018

© Jevgenijs Trunins, 2018

AUTHOR'S DECLARATION

I declare that this thesis material contains my own original work, with all references to other sources clearly identified in this work. I confirm that this thesis presented for the degree of Doctor of Philosophy is composed entirely by myself and solely results from my own work. I declare that no material contained here has been used in any other academic award submission. I do confirm that while registered for a research degree at Kingston University, I have not been a registered candidate or enrolled student at any other academic or professional institution.

ACKNOWLEDGEMENTS

I would like to thank my mentor Prof Andy Augousti, for all the hard work and his patience, interesting discussions and valuable lessons, limitless support and encouragement throughout my studies. I'm extremely lucky that random occasion provided me with an opportunity to follow guidelines of such a brilliant teacher. I also would like to thank Dr Barnaby Osborne for giving me an opportunity to start this research and pursue my life interests. I would like to thank all the members of staff at Kingston University who helped me a lot in research and laboratory work. Special gratitude should be given to Prof Barbara Pierscionek for her support in hard times.

I must thank Kimia Salehzadeh for the support and encouragement she gave me. Her spirit really helped me out in hard times. Importantly, I would like to say thank you to my family who always have been by my side. Completing my work would have been much tougher if it were not for the support of my friends.

Finally, I would like to thank Kingston University research committee for funding othis research.

ABSTRACT

The dynamics of fluid flow unveils complicated dynamical behaviour. Systems such as a dripping tap are no exception. Flow through a nozzle produces three different modes: periodic dripping, chaotic dripping and jetting streams. This research concentrates on a study of the chaotic behaviour of a dripping tap. This involves both mathematical model studies and experimental studies. In addition, the work involves the development of an experimental facility to allow future study of the system in microgravity conditions.

The facility to achieve microgravity conditions is a Drop Tower type, which uses a novel approach to achieve these conditions. The novelty is in the use of linear electromagnetic motors. The facility was built and is in the final stage of the commissioning process, and when it is ready it will allow up to 2.12 s of test time.

The mathematical model uses an existing Mass-Spring-Damper model, with Reynolds numbers between 4 to 175, and a step size of 0.4. The results showed multiple bifurcation regions appearing before chaotic regions. Similarly, experimental results showed that some instabilities exist in this region. The model also explained and showed multiple bifurcations and an increase in dripping time due to instabilities, and has identified that those processes are due either to perturbations of the system or due to initial instabilities of the system. These results were confirmed by experiment.

To achieve the required experimental goals a test module was developed whose requirements were set to fulfil the microgravity experiment conditions, in case future

research is required. The experimental results showed some similarities with the mathematical model. At the same time, there was found to be quite a lot of disagreement. Results identified two different limit cycle attractors in periodic dripping mode: strong single-point attractors and regional attractors. Also, limit cycle attractors and strange attractors in chaotic mode were identified. More importantly, it has been identified that the chaotic region consists of areas where the system is stable (and produces a single region attractor), and others where the system is not (and this produces strange attractors), and there are points where, depending on the disturbances to the system, both types can be observed.

The work done has led to several discoveries and achievements. Although the Drop Tower project could not be completed it may nonetheless be considered as a success. The facility has been fully assembled and calibrated to meet the set of design requirements, and to some extent was commissioned allowing future progress to discover modification requirements.

The study of the Mass-Spring-Damper model led to the conclusion that the model is oversimplified and in its current state should be used only for descriptive purposes, when illustrating chaotic behaviour. Additionally, it was found that the model predicts bifurcations outside the experimentally determined chaotic region. Nevertheless, the work identified some possible improvements to the model.

Experimentally it was found that the region of chaotic behaviour is located around a Reynolds number of 43 in contrast to what was previously reported. The study of the periodic dripping region showed that the system, if disturbed, can develop history dependent phenomena (where the subsequent drop periods follow a well identified sequence). Satellite drops were discovered to exist beyond the previously predicted value of flow rate. It was discovered that the fluid supply system can have a major effect on the drop dynamics (different types of post-detachment developments were found - termed here

regular residual mass and wetted mass - along with the discovery of different types of drop detachment (regular mass, mid-size drops and jets) coexisting within the chaotic region. The drop horizontal disturbance study led to the unconfirmed discovery of two modes of vibrations, where the system response follows a standard damped response and an amplitude modulated damped response.

LIST OF CONTENTS

AUTHOR’S DECLARATION	III
ACKNOWLEDGEMENTS	IV
ABSTRACT.....	V
LIST OF CONTENTS.....	VIII
LIST OF TABLES.....	XV
LIST OF FIGURES.....	XVII
LIST OF ABBREVIATIONS	XXVI
NOMENCLATURE	XXVII
INTRODUCTION	1
1.1 Research problem identification.....	3
1.2 Research methodology.....	4
1.3 Thesis structure.....	6
1.4 Changes to the original research proposal	8

LITERATURE REVIEW.....	9
2.1 Jetting tap dynamics	10
2.2 Dripping tap dynamics	14
2.3 Studies of chaotic dripping mode.....	18
2.4 Investigation into the experimental methodology	25
2.5 Video processing techniques for edge detection	27
2.6 Microgravity research facility.....	30
DROP TOWER.....	34
3.1 Drop Tower design	34
3.1.1 Design aim	35
3.1.2 Design requirements	36
3.1.3 Design main elements.....	36
3.1.4 Operational description.....	39
3.1.5 Operational procedure	40
3.1.6 Final Drop Tower characteristics.....	43
3.1.7 Microgravity test cycle calculations	44
3.1.8 Emergency cycle description.....	51
3.1.9 Additional design characteristics	51
3.2 Drop Tower work management	53
3.2.1 Work assignment statement.....	54
3.2.2 Work Planning	55
3.2.3 Work Budget.....	56
3.3 Drop Tower assembly work	58

3.3.1	Magnetic track installation	58
3.3.2	Installation of the guide rails	60
3.3.3	Trolley and motor assembly, installation and testing.....	63
3.3.4	Drag shield assembly and installation	65
3.3.5	Surrounding installation	67
3.3.6	Electrical system installation.....	70
3.3.7	Positioning sensor installation.....	77
3.3.8	Safety system installation.....	78
3.3.9	Damper mounts anchor bolts calculations.....	81
3.3.10	Damper bracket design and FEA	84
3.4	Drop Tower calibration.....	86
3.4.1	Magnetic track alignment procedure	87
3.4.2	Guide rail alignment procedure	87
3.4.3	Measurement noise error identification.....	89
3.4.4	Fixed position testing	91
3.4.5	Dynamic position testing.....	92
3.4.6	Motor alignment procedure	95
3.4.7	Microgravity test calibration	96
3.5	Risk assessment and operational assessment documents.....	98
3.6	Future suggestions	104
MATHEMATICAL MODELLING.....		106
4.1	The 1-D Mass-Spring-Damper model formulation.....	107
4.2	The 1-D MSD model computational code.....	109
4.2.1	Power law investigation of the bifurcation plot results.....	116

4.3	One-dimensional MSD model results	119
4.3.1	Confirmation of results	120
4.3.2	Analysis of results.....	121
EXPERIMENTAL MODULE		134
5.1	Experimental module operational targets.....	135
5.1.1	Experimental constraints and requirements.....	137
5.1.2	Result in reliability constraints and requirements	141
5.1.3	Drop Tower constraints	142
5.2	Experimental module requirements summary	142
5.3	Experimental module design and assembly	143
5.3.1	Fluid system.....	146
5.3.2	Structural design	152
5.3.3	Data collection and data processing	156
5.3.4	Camera system.....	161
5.3.5	Electronics system	164
5.3.6	Test module budget.....	167
5.4	Module calibration	167
5.4.1	Syringe pump calibration.....	168
5.4.2	Camera calibration.....	170
5.4.3	Temperature sensor calibration.....	172
5.5	Experimental procedure	173
EXPERIMENTAL CAMPAIGN.....		179
6.1	Summary of the assumptions and experimental variables.....	180

6.2	Experimental variables measurement summary	193
6.3	Video processing software.....	195
6.3.1	Edge detection methods comparison.....	197
6.3.2	Video processing pseudo code	199
6.3.3	Video results post-processing.....	205
6.4	Confirmation of the processing and post-processing codes operation.....	209
6.4.1	Video synchronisation and detachment identification process	213
6.4.2	Bifurcation plot adaptation.....	216
6.5	Experiment processing & post-processing code analysis	224
6.5.1	Confirmation of cameras operation.....	225
6.5.2	Discussion of anomalous results	229
EXPERIMENTAL RESULTS DISCUSSION		244
7.1	Investigation of the constants in the Mass-Spring-Damper model	245
7.1.1	Critical mass and critical distance	246
7.1.2	Damper and spring constants	248
7.1.3	Residual mass/volume and restoring distance.....	254
7.1.4	Horizontal behaviour.....	258
7.2	Discussion of experimental results	262
7.2.1	Periodic dripping	268
7.2.2	Chaotic dripping.....	271
7.2.3	Summary of experimental results.....	283
7.3	Future models.....	289
CONCLUSION		294

8.1	Drop Tower work	294
8.2	Mathematical modelling results	297
8.3	Experimental results	299
REFERENCES		302
APPENDICES		311
Appendix A.	Learjet laboratory floor plan	311
Appendix B.	Drop Tower experiment procedure checklist	312
Appendix C.	Operational profile calculations “MATLAB®” code	313
Appendix D.	Drop Tower project Gantt chart (extended)	315
Appendix E.	Drop Tower work budget (extended)	316
Appendix F.	Circuit diagram (by “Micromech Systems Ltd”)	320
Appendix G.	Drop Tower manufacturing components (CAD files)	326
Appendix H.	MSD model “MATLAB®” codes	333
	Appendix H.A. 1-D model simulation running code	333
	Appendix H.B. 1-D dripping dynamics modelling	334
	Appendix H.C. ODE45 MS solver	336
	Appendix H.D. Power law investigation code	336
	Appendix H.E. Results presentation code	339
Appendix I.	1-D model results	342
Appendix J.	Experimental module technical drawings	349

Appendix K. Raspberry PI software installation	363
Appendix L. Experimental module operational code	367
Appendix L.A. ADXL345.py – Accelerometer code	367
Appendix L.B. MAX31855.py – Temperature sensor code	368
Appendix L.C. Test_1.py – Main test code	370
Appendix M. Experimental module circuit diagram	374
Appendix N. Camera distortion and pixel seizing results	375
Appendix O. Experimental error calculations.....	377
Appendix P. Experimental variable recorded data	381
Appendix Q. Video processing “MATLAB® code	384
Appendix Q.A. Run video processing.....	384
Appendix Q.B. Nozzle identification code	397
Appendix Q.C. Drop identification code	398
Appendix Q.D. Spring & damper constants investigation.....	403

LIST OF TABLES

Chapter 2

Table 2.6.1: Summary of recently operational microgravity facilities	31
--	----

Chapter 3

Table 3.1.1: Drop Tower operational phases	40
--	----

Table 3.1.2: Operational procedure cycles.....	41
--	----

Table 3.1.3: Commissioned Drop Tower characteristics	44
--	----

Table 3.2.1: Assembly works budget breakdown	57
--	----

Table 3.3.1: Rail joint measurements.....	62
---	----

Table 3.3.2: Motion controller input functions	76
--	----

Table 3.4.1: Static position measurements.....	91
--	----

Table 3.4.2 Measurements of motor alignments.....	96
---	----

Table 3.5.1: Risk assessment weighting table.....	98
---	----

Table 3.5.2: Drop Tower risk assessment	100
---	-----

Table 3.5.3: Operational assessment.....	103
--	-----

Chapter 5

Table 5.1.1: Air density at different temperatures	138
--	-----

Table 5.1.2: Experimental variable specification.....	140
---	-----

Table 5.2.1: Experimental module requirements.....	143
Table 5.3.1: Pump trade-off analysis.....	147
Table 5.3.2: Nozzle inner diameter error studies.....	150
Table 5.3.3: The budget of the experimental module memory storage.....	161
Table 5.3.4: Raspberry Pis GPIO pins connection summary.....	165
Table 5.3.5: Experimental module cost budget.....	167
Table 5.4.1: Temperature sensor calibration readings.....	173

Chapter 6

Table 6.1.1: Experimental uncertainty/correction value table.....	181
Table 6.1.2: Water density measurements.....	183
Table 6.1.3: Water kinematic viscosity measurements.....	184
Table 6.2.1: Pressure records during the test campaign.....	194
Table 6.4.1: The selected flow rate influence propagation map.....	219
Table 6.4.2: The influence region identification map.....	219

LIST OF FIGURES

Chapter 2

Figure 2.1.1: The stability regimes (parabolic profile)	12
Figure 2.2.1: Liquid thread formation.....	16
Figure 2.3.1: Bifurcation diagram.....	19
Figure 2.3.2: The composite plot of approximate areas of investigation.....	24

Chapter 3

Figure 3.1.1: Kingston University Microgravity Drop Tower.....	35
Figure 3.1.2: Design main elements.....	37
Figure 3.1.3: Drive system elements - plan view.....	38
Figure 3.1.4: Electronics cabinet and Control unit	38
Figure 3.1.5: Drop Tower operational phases for microgravity test	39
Figure 3.1.6: Drop Tower operational sequence diagram.....	42
Figure 3.1.7: Drop Tower log file example.....	43
Figure 3.1.8: Drag shield sizing description	46
Figure 3.1.9: Low gravity test velocity and acceleration diagram.....	47
Figure 3.1.10: Drop Tower test profile calculation pseudo code.....	49
Figure 3.1.11: Drop Tower profile “MATLAB®” calculation code output.....	50

Figure 3.1.12: Test time and mass dependence (for zero gravity test)	52
Figure 3.1.13: Payload mass, micro-gravity quality and test time dependence	53
Figure 3.2.1: Drop Tower work project milestones (updated 2014)	55
Figure 3.3.1: CAD drawing of the main support structure (Isometric view)	58
Figure 3.3.2: Magnet track specifications.....	59
Figure 3.3.3: CAD of the magnets base plate (Isometric view)	60
Figure 3.3.4: Guide rails with guide rollers (LLEHS 25 Speedi-Roll).....	60
Figure 3.3.5: Rail joint connection and measurements.....	61
Figure 3.3.6: CAD of the rail joint (Top view).....	62
Figure 3.3.7: L-bracket with adjusting screws.....	62
Figure 3.3.8: Trolley with the motors attached to the rails.....	63
Figure 3.3.9: "Bosh Rexroth" 30x30-aluminium profile [49]	65
Figure 3.3.10: Payload advisable sizing calculation.....	65
Figure 3.3.11: Drag shield attached to the trolley	66
Figure 3.3.12: Ground level section assembled.....	68
Figure 3.3.13: Back support structure.....	68
Figure 3.3.14: Third level section CAD (Isometric view).....	69
Figure 3.3.15: Thermocouple attached to a motor.....	71
Figure 3.3.16: Drop Tower ground level	71
Figure 3.3.17: Drag shield wiring.....	73
Figure 3.3.18: Drop Tower cable trunking sizing.....	73
Figure 3.3.19: Drop Tower control panel	74
Figure 3.3.20: Installed position system	77

Figure 3.3.21: Magnetic position sensor strip scale.....	77
Figure 3.3.22: Damper brackets installed	79
Figure 3.3.23: Damper brackets installed on the drag shield and placed on the damper.....	80
Figure 3.3.24: Anchor bolts calculation force diagram.....	82
Figure 3.3.25: The damper bracket CAD model (Isometric view)	84
Figure 3.3.26: Bracket loading torque calculations	85
Figure 3.3.27: Damper bracket simulation (Top view).....	85
Figure 3.3.28: Damper bracket angle bracket simulation (Isometric view).....	86
Figure 3.4.1: Guide rail alignment gauge.....	87
Figure 3.4.2: Baumer laser digital sensor installed	88
Figure 3.4.3: Electromagnetic noise measurements.....	90
Figure 3.4.4: Initial signal readings	93
Figure 3.4.5: Dynamic testing results; maximum offset and maximum possible error	93
Figure 3.4.6: Static and dynamic tests comparison.....	94
Figure 3.4.7: Motor alignments measurements description (schematics).....	95
Figure 3.4.8 Position calibration of the trolley guide rollers	95
 Chapter 4	
Figure 4.2.1: Simulation running pseudo code	110
Figure 4.2.2: 1-D dripping dynamics simulation pseudo code	111
Figure 4.2.3: Power law investigation pseudo code.....	117
Figure 4.2.4: The bifurcation start-end and period jump identified;.....	118
Figure 4.3.1: 1-D MSD model performance validation	120
Figure 4.3.2: 1-D MSD Centre of Mass location results (Period 1)	121

Figure 4.3.3: 1-D MSD model Centre of Mass location.....	122
Figure 4.3.4: 1-D MSD model bifurcation results	123
Figure 4.3.5: 1-D MSD results in the experimental investigation region.....	124
Figure 4.3.6: Power law investigation results.....	125
Figure 4.3.7: Bifurcation regions power law investigation scaling factor results	127
Figure 4.3.8: Bifurcation process investigation region.....	128
Figure 4.3.9: Bifurcation process (1).....	130
Figure 4.3.10: Bifurcation process (2).....	131
Figure 4.3.11: Fully developed chaotic region	132
Figure 4.3.12: Clustering	133
 Chapter 5	
Figure 5.1.1: Research target interlinks and procedure	136
Figure 5.1.2: Water dynamic and kinematic viscosities vs temperature	138
Figure 5.1.3: Water density and surface tension vs temperature.....	138
Figure 5.3.1: Assembled experimental module	144
Figure 5.3.2: Isometric view of the experimental module design	144
Figure 5.3.3: Fluid system components.....	145
Figure 5.3.4: Structure components.....	145
Figure 5.3.5: Data processing, cameras and electronics components.....	146
Figure 5.3.6: Manufactured nozzle	148
Figure 5.3.7: Droplet at the nozzle tip	149
Figure 5.3.8: The nozzle inner diameter error studies	149
Figure 5.3.9: Tee-connector fixed on the test chamber top plate	150

Figure 5.3.10: Backlit panels	151
Figure 5.3.11: Test chamber water collection pot.....	152
Figure 5.3.12: ADXL335 accelerometer sensor	152
Figure 5.3.13: Vibration damping mats between the structure components.....	153
Figure 5.3.14: Test chamber support front schematics	154
Figure 5.3.15: Test chamber support struts FEA simulation	155
Figure 5.3.16: Syringe pump bracket set-up CAD model rendering	155
Figure 5.3.17: Syringe fixing bracket FEA simulation.....	156
Figure 5.3.18: Raspberry Pi 2B.....	157
Figure 5.3.19: Raspberry PI computer enclosure.....	158
Figure 5.3.20: Raspberry Pi camera enclosed in a case	162
Figure 5.3.21: Video enhancement steps	163
Figure 5.3.22: Front panel component	164
Figure 5.4.1: Pump calibration results	169
Figure 5.4.2: Nozzle with attached mesh.....	170
Figure 5.4.3: Camera pixel sizing and distortion study	171
Figure 5.5.1: Experimental procedure outline.....	174
Figure 5.5.2: Example of the experimental log file	175
Figure 5.5.3: Example of communication window for experimental module	176
 Chapter 6	
Figure 6.1.1: Weber number uncertainty range	192
Figure 6.1.2: Reynolds number uncertainty	193
Figure 6.2.1: Temperature variation during test campaign	195

Figure 6.3.1: “MATLAB®” edge detection methods comparison.....	197
Figure 6.3.2: Drop after post-processing	199
Figure 6.3.3: Drop shape identification pseudo code	200
Figure 6.3.4: Nozzle identification pseudo code	201
Figure 6.3.5: Nozzle identification processing steps	202
Figure 6.3.6: Drop shape identification pseudo code	204
Figure 6.3.7: Drop identification processing steps	205
Figure 6.3.8: Video results post-processing pseudo code.....	206
Figure 6.3.9: X and Y coordinate results rotation	208
Figure 6.4.1: Video post-processing code communication messages (Part 2)	211
Figure 6.4.2: Synchronisation plot.....	212
Figure 6.4.3: Video manual synchronisation, camera view.....	212
Figure 6.4.4: Detachment identification procedure	214
Figure 6.4.5: Bifurcation results plot before processing.....	217
Figure 6.4.6: The influence map development example.....	220
Figure 6.4.7: Bifurcation plot results adaptation	222
Figure 6.4.8: Drop type by its quantity (as identified by the applied procedure).....	222
Figure 6.4.9: Mid drops at flow rate of 120 ml/hr as a cause of low acceptable data points.....	223
Figure 6.5.1: Drop stable state CoM variation readings.....	225
Figure 6.5.2: Drop stable state mass variation readings	227
Figure 6.5.3: Error in camera edge detection due shutter time.....	228
Figure 6.5.4: Drop interaction with a surface	230

Figure 6.5.5: Drop before detachment	231
Figure 6.5.6: System surface tension investigation.....	232
Figure 6.5.7: Drop detachment investigation at low flow rate.....	233
Figure 6.5.8: The recorded detachment process (No.1)	234
Figure 6.5.9: Post-detachment development types	234
Figure 6.5.10: Readings of volume after detachment	235
Figure 6.5.11: The results of the investigation of the volume after detachment.....	236
Figure 6.5.12: Liquid formation at the nozzle surface	237
Figure 6.5.13: Drop attachment shifted due to liquid formation at the nozzle surface.....	237
Figure 6.5.14: Air bubble in a pendant drop	238
Figure 6.5.15: Jetting stream formation after drop detachment	239
Figure 6.5.16: Jet development volume plot ^(*) at a flow rate of 275.8 ml/hr.....	239
Figure 6.5.17: Comparison of the Z-CoM behaviour of the jet stream and regular dripping.....	241
Figure 6.5.18: Mid drop development	242
 Chapter 7	
Figure 7.1.1: Drop critical volume investigation	247
Figure 7.1.2 The recorded detachment process (No.2)	248
Figure 7.1.3: Induced vibrations video recording	249
Figure 7.1.4: Spring and damping constants investigation	249
Figure 7.1.5: Spring constant results.....	251
Figure 7.1.6: Visual observation of unstable behaviour of the drop above the threshold value.....	252

Figure 7.1.7: Damping coefficient results	253
Figure 7.1.8: Spring and damper determination pseudo code	253
Figure 7.1.9: Normal residual volume and wetting volume separation region	255
Figure 7.1.10: Residue volume study	255
Figure 7.1.11: Normal residual mass flow rate linear dependency	256
Figure 7.1.12: Drop z-coordinate mass dependence investigation	257
Figure 7.1.13: Horizontal vibration test.....	258
Figure 7.1.14: X and Y coordinate vibration test combined plot	259
Figure 7.1.15: Amplitude modulated horizontal vibrations.....	261
Figure 7.1.16: Standard damped vibrations in the vertical axis	262
Figure 7.2.1: Period versus flow rate 3-D plot	265
Figure 7.2.2: Period versus flow rate plot – plan view of Figure 7.2.1 for ease of viewing.....	266
Figure 7.2.3: Transition from periodic dripping to chaotic dripping.....	267
Figure 7.2.4: Quasi-periodic dripping period versus flow rate plot	268
Figure 7.2.5: Single period strong attractor	269
Figure 7.2.6: Sequence map of 70.2 ml/hr.....	270
Figure 7.2.7: Single period region attractor.....	270
Figure 7.2.8: Chaotic dripping bifurcation plot No.1	272
Figure 7.2.9: Chaotic dripping bifurcation plot No.2	274
Figure 7.2.10: Single region attractor	275
Figure 7.2.11: Single region attractor with high disturbances.....	276
Figure 7.2.12: Unstable single region attractor	277

Figure 7.2.13: Weak single region attractor.....	277
Figure 7.2.14: Sequence map of 323.7 ml/hr.....	278
Figure 7.2.15: Return maps a flow rate of 323.7 ml/hr.....	279
Figure 7.2.16: Period jumps.....	280
Figure 7.2.17: Period jump development.....	281
Figure 7.2.18: Limit cycle attractors – periodic attractors.....	282
Figure 7.2.19: Strange attractors.....	283
Figure 7.2.20: Strange satellite drop detachment.....	288

LIST OF ABBREVIATIONS

AC – Alternating Current	HV – High Voltage
CAD – Computational-aided Design	I/O – Input/Output
CNC – Computer Numerical Control	I ² C – Inter-Integrated Circuit
CoM – Centre of Mass	LED – Light Emitting Diode
DAc – Digital Acquisition	LV – Low Voltage (24 V DC)
DC – Direct Current	microSD – Micro Solid Drive
DoF – Degree of Freedom	MSD – Mass-Spring-Damper
EMC – Electromagnetic Compatibility	PC – Personal Computer
FEA – Finite Element Analysis	PTFE – Polytetrafluoroethylene
FoS – Factor of Safety	SPI – Serial Peripheral Interface
fps – frames-per-second	UPS – Uninterrupted Power Supply
GND – Ground (electrics)	USB – Universal Serial Bus
GPIO – General-Purpose Input/Output	VGA – Video Graphics Adaptor
HDMI – High Definition Multimedia Interface	

NOMENCLATURE

- Drop tower related nomenclature

a	$\frac{m}{s^2}$	drag shield acceleration	E_d	Nm	damper stroke energy absorbed
$a_{a(max)}$	$\frac{m}{s^2}$	acceleration limited by allowable acceleration	E_{d-c}	Nm	damper stroke energy ratio
a_{dec}	$\frac{m}{s^2}$	maximum deceleration	E_p	Nm	damper potential energy
$a_{F(max)}$	$\frac{m}{s^2}$	acceleration limited by motor force	$Error$	mm	sensor total error
a_{max}	$\frac{m}{s^2}$	payload maximal allowable acceleration	$Error_{DAq}$	μm	data acquisition error
$a_{v(max)}$	$\frac{m}{s^2}$	acceleration limited by allowable velocity	$Error_{sen}$	mm	sensor distance error
B	m	size of the payload	$Error_{sig}$	μm	distance error due to signal
b	m	payload height	F_d	N	damping force
D	mm	measurements distance	$F_{d,max}$	N	damper maximal counterforce
D_b	m	manufacturing diameter	F_{max}	N	motor maximum force
D_{dr}	m	manufacturing diameter	F_{Sd}	N	concrete design force
D_{Gr}	m	manufacturing diameter	FoS	–	factor of safety
D_I, D_f	mm	measurements range	H	m	drag shield movement height
dx	m	sensor step size	H_{pay}	m	maximal payload side dimension
			h_{acc}	m	acceleration / deceleration height

h_d	m	drag shield height	v	$\frac{m}{s}$	velocity increase during acceleration / deceleration
h_{damp}	m	damper mount height	v_f	$\frac{m}{s}$	final velocity after payload detachment
h_s	m	vertical sensor displacement	v_{max}	$\frac{m}{s}$	maximal allowable velocity
$h_{s,act}$	m	damper actual stroke length	v_{sens}	m	maximal allowable velocity at upper limit
$h_{s,max}$	m	damper maximal stroke length	W_{dry}	m	drag shield outer width
h_{sens}	m	sensor position height	x_{bolts}	m	distance between midpoint and bolt
l	m	payload movement distance	γ_{con}	–	concrete strength reduction factor
M	kg	payload mass	γ_C	–	safety factor
M_{dry}	kg	drag shield and motor mass	γ_f	–	partial safety factor
M_{full}	kg	drag shield mass with payload	γ_M	–	concrete partial strength reduction factor
Md	mm	measurements distance	γ_2	–	reduction factor for the system with low to acceptable level of installation
N	–	number of motors	ζ	deg	maximal tilt angle for damper installation
N_a, N_b	N	normal forces	η	–	motors efficiency
N_{bolts}	–	number of anchor bolts	η_e	–	edge reduction factor
N_{Rd}	N	concrete design reaction	η_s	–	spacing reduction factor
n	–	simulation step number	ξ	$\frac{m}{s^2}$	required gravitational acceleration
O	m	manufacturing offset value	ξ_{max}	$\frac{m}{s^2}$	maximal allowable gravitational acceleration
P_{dp}	Pa	load pressure	σ_{con}	MPa	concrete strength
RES_I	mm	sensor resolution	ς	deg	sensor angular position
RES_F	mm	sensor resolution			
r_{damp}	m	damper contact radius			
S	mV	analogue signal voltage			
S_a, S_b	N	shear forces			
T_{ab}	Nm	load torque			

- Experimental nomenclature

A	–	original image matrix	K	–	constant
A	–	bifurcation region area	K_c	–	viscometer constant
m		amplitude of disturbance	k	$\frac{N}{m}$	spring constant
a	–	output image matrix	k_y	$\frac{N}{m}$	spring constant in y-direction
a	–	dimensions unit	k_z	$\frac{N}{m}$	spring constant in z-direction
a_{dist}	m	radius of a disturbance	l_o	m	unit length
Bo_c	–	critical Bond number	m	kg	drop mass
Bo_o	–	Bond value for outer nozzle diameter	ṁ	kg/s	mass flow rate
Bo	–	Bond number	m_c	kg	drop critical mass
c	$\frac{N \cdot s}{m}$	damping constant	m_i	kg	drop initial mass
c_y	$\frac{N \cdot s}{m}$	damping variable in y-direction	m_o	kg	unit mass
c_z	$\frac{N \cdot s}{m}$	damping variable in z-direction	m_r	kg	drop residual mass
d	m	diameter of a nozzle	n	–	simulation step number
d_o	m	outer diameter of a nozzle	n_{total}	–	total simulation steps
dt	s	simulation time increment	N	–	period number
dm	kg	simulation mass increment	P₁	–	constant
dv	$\frac{\mu m}{s}$	pump linear velocity fluctuation	P₂	–	constant
G	–	edge change magnitude	P_{horiz}	–	pixel x-coordinate
G_X	–	horizontal edge change	P_{vert}	–	pixel y-coordinate
G_Y	–	vertical edge change	p	Pa	fluid pressure
g	$\frac{m}{s^2}$	acceleration due to gravity	PXL	$\frac{\mu m}{pixel}$	pixel size
I_c	–	influence value	r	m	nozzle radius
			r_{wet}	m	wetted nozzle radius
			Re	–	Reynolds number

rot_{xz}	–	rotation matrix	\dot{V}_{err}	$\frac{ml}{hr}$	flow rate calibration factor
rot_{yz}	–	rotation matrix	\dot{V}_{max}	$\frac{ml}{hr}$	maximal flow rate
S	–	threshold value	\dot{V}_{min}	$\frac{ml}{hr}$	minimal flow rate
s	–	standard deviation of Gaussian distribution	v_f	–	simulation final velocity
T	s	period of vibration	v_i	–	simulation initial velocity
$T_{i,max}$	s	maximum dripping period	v_o	$\frac{m}{s}$	flow velocity
$T_{i,min}$	s	minimum dripping period	v_r	$\frac{m}{s}$	radial velocity component
T_{mes}	$^{\circ}C$	measured temperature of the liquid	v_z	$\frac{m}{s}$	vertical velocity component
T_n	s	drop period	v_{∞}	$\frac{m}{s}$	flow velocity disturbance
T_o	$^{\circ}C$	temperature	We	–	Weber number We_c – critical Weber number
t	s	time	X	$pixel$	image lateral distance
t_o	s	unit time	\mathbf{X}	–	image processing operator
t_{cam}	s	frames recording period	x	m	CoM lateral coordinate
t_{det}	s	time of the drop detachment	x_{syr}	m	syringe extension distance
t_{exp}	s	exposure time	\bar{x}	m	centroid coordinate
t_f	s	final time	Y	$pixel$	image vertical distance
t_i	s	time at the specific step	\mathbf{Y}	–	image processing operator
t_n	s	final test time	y	m	CoM lateral coordinate
V	m^3	drop volume	y_{crit}	m	CoM critical lateral distance
V_{crit}	m^3	drop critical volume	y_{AM}	m	disturbance modulated amplitude
V_i	m^3	volume of section	\bar{y}	m	centroid coordinate
V_{res}	m^3	residual volume	z	m	CoM vertical coordinate
V_{syr}	m^3	syringe volume	z_o	m	CoM reset distance
\dot{V}	$\frac{ml}{hr}$	flow rate	z_{crit}	m	CoM critical vertical distance
\dot{V}_{calib}	$\frac{ml}{hr}$	pump actual flow rate			

z_i	m	CoM initial vertical distance	ρ^*	$\frac{kg}{m^3}$	calculated density of water
z_n	m	CoM final vertical distance	$(\rho)^*$	$\frac{kg}{m^3}$	calculated density of air
\dot{z}	$\frac{m}{s}$	drop vertical velocity	σ	$\frac{N}{m}$	surface tension
\bar{z}	m	centroid coordinate	σ^*	$\frac{N}{m}$	calculated surface tension
α_{xz}	rad	axis rotation	ζ	–	power law constant
α_{yz}	rad	axis rotation	τ	–	power law constant
δ	–	logarithmic decrement	φ	rad	phase shift
ε	–	threshold value	Ψ_c	–	number of repeats for a given period
ζ	–	damping coefficient	Ψ_{max}	–	maximal number of repeats
Θ	–	edge change direction	ψ	m^3	Harkins-Brown correction factor
θ	rad	surface contact angle	Ω	–	Strouhal number
λ	m	wavelength	ω	Hz	wave frequency
μ	$Pa \cdot s$	dynamic viscosity	$\nabla^2 G$	–	Laplacian of Gaussian operator
$\Delta\mu_{err}$	$Pa \cdot s$	dynamic viscosity correction factor	Δd	mm	nozzle diameter error
μ^*	$Pa \cdot s$	calculated dynamic viscosity	Δh	m	step height
ν	$\frac{m^2}{s}$	kinematic viscosity	Δm	g	total drop mass uncertainty
ν_{err}	$\frac{m^2}{s}$	kinematic viscosity correction factor	Δm_{time}	kg	mass uncertainty due to camera shutter time
ν^*	$\frac{m^2}{s}$	calculated kinematic viscosity	ΔT_o	$^{\circ}C$	thermocouple reading mean divergence
ξ	$\frac{m}{s^2}$	acceleration constant	ΔV	m^3	total drop volume uncertainty
ρ	$\frac{kg}{m^3}$	fluid density	ΔV_{time}	m^3	volume uncertainty due to camera shutter time
ρ_{err}	$\frac{kg}{m^3}$	density correction factor	$\Delta \dot{V}_{err}$	$\frac{ml}{hr}$	flow rate uncertainty due to pump calibration
ρ_{out}	$\frac{kg}{m^3}$	density of the external medium			

$\Delta\dot{V}_{fluct}$	$\frac{ml}{hr}$	flow rate uncertainty due to pump drive fluctuation	$\Delta\nu^*$	$\frac{m^2}{s}$	calculated kinematic viscosity uncertainty
Δv_{fluct}	$\frac{m}{s}$	pump linear velocity fluctuation	$\Delta\rho$	$\frac{kg}{m^3}$	total density uncertainty
Δv_o	$\frac{m}{s}$	flow velocity increment	$\Delta\rho^*$	$\frac{kg}{m^3}$	calculated density uncertainty of water
Δx	m	CoM coordinate uncertainty	$(\Delta\rho)^*$	$\frac{kg}{m^3}$	calculated density uncertainty of air
Δx_{fluct}	m	pump drive fluctuation	$\Delta\sigma^*$	$\frac{N}{m}$	calculated surface tension uncertainty
Δy	m	CoM coordinate uncertainty			
Δz	m	CoM coordinate uncertainty			
$\Delta\mu^*$	$Pa \cdot s$	calculated dynamic viscosity uncertainty			

[This page is intended to be blank]

CHAPTER 1

INTRODUCTION

Fluid flow exhibits complicated physical dynamical behaviour. The study of this behaviour has a long history beginning in ancient civilisations. Archimedes outlined the first known fluid dynamic and fluid static fundamental principles in his work *On Floating Bodies* [1]. Time passed and many other theories were developed, leading eventually to the formulation of the Navier-Stokes equations in the 19th century. The Navier-Stokes set of equations assume that the fluid is continuous in the area of interest, and they are derived from the mass continuity equation, conservation of linear and angular momentum and conservation of energy. This set of equations can, in principle, predict fluid behaviour at any instant in time if only the initial conditions are known. Unfortunately, even though the equations can predict the future of fluid systems, the full solution to these equations has still not been found¹. At the same time, a numerical approach allows one to find solutions to the Navier-Stokes equation but this is limited by the precision of the solution and the computational power required. In addition, in some cases the flow becomes highly dependent on the initial parameters, which in the case of slight variations could lead to marginal errors in the results.

¹ At the time of writing this Thesis there was a claim of finding the solution to Navier-Stokes equation (“Existence of the strong solution to Navier-Stokes equation” by Mukhtarbay Otelbaev [Authors translation]), unfortunately the scientific community has not yet confirmed the solution to be correct.

The investigation of fluid jets and drop formation started in 19th century with the work of Félix Savart, Joseph Plateau and Thomas Tate. In 1879, Lord Rayleigh did extensive studies on the jet breakup [2]. Later his work was advanced by many other authors to include multiple other parameters, such as but is not limited to, the viscosity and the density of the surrounding fluid, and the drop detachment mass correction factor.

The 20th century saw the development of more sophisticated photographic technology and the introduction of computers, which allowed for fast advances in the studies of drop dynamics. With the help of the computational fluid dynamics, more precise and refined models could be simulated. The advances in photography brought video recording with high resolution, so that experiments could be recorded and post-processed. Both technological advances allowed the experimental confirmation of increasingly sophisticated models.

The mathematical models and the experimental results showed that at the transition between slow dripping (steady dripping) and fluid jetting (where a single unbroken column of the fluid can be observed) there is a specific region of uncertainty. The revelation of chaos theory and its implementation into drop stability studies by Robert Shaw [3] brought a new approach to solving the problem of drop behaviour. Shaw proposed that the drop could be represented as an oscillating mass on a spring. His model results were confirmed by experimental data. The model was later refined [4] by introducing a damping component into the equation, leading to a more sophisticated but at the same time much more descriptive model of this behaviour. This mathematical model (as far as the literature review was able to show) remains the closest approximation of the phenomenon.

This research studies the behaviour of dripping water, where the behaviour is of a chaotic nature. The research provides an extensive study of a pre-existing one-dimensional Mass-Spring-Damper (MSD) model based on a model developed by Kiyono and Fuchikami [4], which models the drop as a damped mass on a spring. In addition to that, a new model

outline will be proposed which can predict 3-dimensional behaviour. The mathematical model was compared to experimental results obtained under normal gravitational conditions.

The research topic initially proposed an additional study of the same flow region under microgravity conditions. For this reason, this work includes a discussion of the development of a dedicated experimental facility. The work done on the Drop Tower was justified, as it will allow for future investigation and research in the area of droplet behaviour under microgravity conditions. The experimental module, which was developed to confirm the theoretical results, allows one to control the required flow rate and has the ability to video record from two perpendicular directions the dripping water. By doing so, the post-processing analysis code developed here allows one to acquire the properties to describe the drop 3-dimensionally at any specific time.

The experimental facility is a drop tower, using electromagnetic linear motors to catapult a payload in a parabolic trajectory, which should allow around 2.1 seconds of microgravity. Unfortunately due to unforeseen circumstances the work was not completed, which led to a change in the topic deliverables.

1.1 Research problem identification

The topic described above has a range of studies already accomplished. It is logical, therefore, to ask what else is required to describe the system.

Firstly, it is required still to characterise more fully the nature of the system. In the transition from stable dripping to jetting the system starts to behave non-periodically, but to date there is only a vague description of this process. Even more, the shapes of the jet and the drop are quite distinctive under observation, so it is expected that the fluid will go through a complex transition, which also has not been fully described. The only valid

mathematical representation given to date is the Mass-Spring-Damper (MSD) model, but even so this model is over simplified. The implications of this model for chaotic behaviour required exploration. Several studies have been conducted to confirm that the MSD model is a correct representation of dripping dynamics; unfortunately, there is still not enough experimental evidence that the model does correctly confirm the experimental behaviour in the chaotic regions. In addition, even though the horizontal oscillations of the dripping drop in normal gravity can be neglected compared to the vertical, in the chaotic region these oscillations should affect the results by introducing slight deviations in the results, which in the region of chaos become crucial. The current 1-dimensional model does not include this and will lead to slight differences in the results, which leads to another important reason of this investigation – to provide some insight into drop behaviour in the horizontal direction when the drop is excited.

Therefore, the first research target was to study the non-periodic behaviour of the dripping tap based on experimental and mathematical results.

Secondly, it was required to scrutinise the MSD model and report all discrepancies, and provide an extensive analysis of this.

Thirdly, it was proposed to investigate the possibility of advancing the mathematical model by incorporating lateral movement.

1.2 Research methodology

This research aims to investigate water-dripping dynamics with a special interest in chaotic mode behaviour under normal gravitational conditions.

To proceed with the research problems outlined above an experimental module was developed. Experimentally it was required to identify the dripping periods at a range of flow rates of between typically 60 – 330 ml/hr. The experiment nozzle opening was set to

be ≈ 1 mm in diameter, with the outer diameter equal to ≈ 2 mm (the nozzle outer diameter, mentioned here, can affect the drop attachment surface tension forces – e.g. solid to liquid interaction). These flow rates, which correspond to Reynolds numbers between approximately 20 – 100 that were identified as the most appropriate regions to seek chaotic behaviour [5]. The experiments were required to be conducted under normal gravitational conditions, with the variables affecting the system to be monitored and recorded. To identify the dripping period and record the Centre of Mass (CoM) location two cameras were used recording at 30 frames-per-second (fps). To acquire correct 3-dimensional pictures of the dripping nozzle the cameras were located in a horizontal plane (with the nozzle directed vertically downwards in a direction normal to this plane) with an angle of 90° between them. To identify the CoM position and dripping time the recorded video files were post-processed, using an edge detection method. The following paragraph summarises the methodology employed to address the research objectives outlined in the previous section.

The post-processed data was used to evaluate how chaotic or deterministic a system is. In addition, drop periodicity data was used to construct a bifurcation diagram – describing the drop formation process as a function of the flow velocity. The bifurcation diagram shows the areas of chaotic formation as well as the zones of deterministic behaviour. The CoM location is mapped with respect to time, and the experimental data of the temporal position of the CoM of the attached drop is recorded for a series of experiments. The results of this work led to answering the first identified objective of this research, as well as to formulate a more advanced mathematical model as identified in third research objective. In addition, the fixed drop mass was subjected to induced damped vibrations, and the CoM location recorded. This data was utilised in providing spring and damping constants for the proposed Mass-Spring-Damper (MSD) model. To achieve the second research objective, an extensive analysis of the existing mathematical model [6] was undertaken (with the input parameters matching the original model). The results also allowed for a detailed

explanation of the bifurcation process, providing additional information to answer the first research objective.

A relatively high volume of test data was compared to the modelled data identifying that the MSD model can indeed predict chaotic behaviour, but should be used with caution, as it is more of a descriptive than predictive model.

Part of the work for this research concentrated on the development of a large dedicated experimental facility. The Drop Tower facility was constructed specifically for microgravity research. The facility operates on a novel approach using the electromagnetic linear motors as a drive system and operates using a parabolic motion principle. To achieve the required result, which was identified as the development of the facility for microgravity experiments, additional targets were set: to construct the facility based on the predefined design, calibrate the facility for future operation, and to commission the facility along with the development of operational documentation.

1.3 Thesis structure

This thesis is organised in alignment with previously outlined methodology to address the research objectives identified above. In simple terms, it is separated into the following areas:

1. Review of the relevant literature
2. Design and development of the microgravity Drop Tower
3. Mathematical modelling
4. Experimental work

The thesis consists of eight separate chapters (1 – 8). Following this introduction is the literature review. This review is presented in six subsections covering different aspects of the research topic. This includes the dynamics of fluid behaviour (sections 2.1 – 2.3), the

experimental set-up design (section 0) and video processing literature (section 2.5), as well a discussion of the current facilities available for microgravity research (section 2.6).

The third chapter outlines the development process of the microgravity Drop Tower facility with an explanation of the management of this project, its commissioning process and a description of the operating procedure.

Chapter 4 discusses the mathematical model of the dynamics of the dripping tap. In the first part (section 4.1) the reader is introduced to mathematical formulation of the Mass-Spring-Damper (MSD) model, followed by presentation of the outline of the developed code in section 4.2 and section 4.3 concerns the analysis of the results: firstly confirming the operation of the developed code (which is referenced to Kiyono and Fuchikami, 1999 [4]), while the second part provides an analysis of the results.

Chapters 5 to 7 deal with the experimental work. The details of the design of the experimental module are given in chapter 5, where firstly the module parameters, constraints and requirements are set (sections 5.1 and 5.2). Secondly (section 5.3 and 5.4), the module design, assembly and calibration is presented. Section 5.5 details the experimental procedure. Chapter 6 describes the preparatory work for the experimental campaign, as well as the experimental campaign itself. The preparatory work included measurements of the experimental variables (sections 6.1 – 6.2), and video processing, post-processing code development, and analysis (section 6.3 – 6.4). It is important to mention here that the results of section 6.5 provides some insight into the complexity of the dynamic system, commenting on the problems that arose during the experiments as well-unexpected findings. The summary of experimental results comprises chapter 7. The values for advanced mathematical model are reported in section 7.1. While the rest of the chapter deals with periodic dripping and the chaotic behaviour that was identified.

The conclusion (chapter 8) summarises all the findings of the investigation and comments on the objectives achieved and questions raised in this research.

In addition, this thesis contains a glossary of abbreviations used (consistent throughout the thesis), nomenclature, and additional useful information is contained in the Appendix.

1.4 Changes to the original research proposal

It was mentioned before that the initial idea was to investigate drop behaviour not only in normal gravity but also under microgravity conditions. Unfortunately, due to multiple circumstances the Drop Tower project did not complete. The reasons for this decision are quite complex – mostly associated with the complexity of the project (the Drop Tower as proposed was unique and is based on a novel design) as well as due to financial limitations. Nevertheless, this work includes a full acknowledgment of the development process in the hope of shedding some light on the future development of the same kind of facility. Currently, the Drop Tower is fully assembled with the confirmed required alignment of the motors to the magnetic track. The motor operation was also confirmed in a low-velocity test, as well as its ability to operate along the whole track length. Section 3.6 concludes the development of the current project with some suggestions for the future.

CHAPTER 2

LITERATURE REVIEW

The literature review chapter consists of an analysis of the available information on the subject related to this research. The chapter structure follows the investigative procedures required to undertake research on this topic. As described in the introduction the research concentrates on fluid flow through a nozzle with a narrow opening (e.g. a capillary-like system), more specifically looking at a dripping system. The main interest is in describing the chaotic behaviour of dripping through a mathematical model and by conducting experimental investigations. The experiments require the development of the experimental module. And finally, an original objective involved development of a test facility for microgravity research. This is the flow of background research, which will be presented in this chapter.

It begins with the investigation of jetting tap dynamics (section 1), where the crucial idea of flow instability (the flow of the jet becoming unstable) is defined. The first section leads on to dripping tap dynamics (section 2.2), which explains the physics behind drop formation and detachment. Following section 2.3, that discusses in more details the chaos behind the dripping tap dynamics. The following two sections – 0 and 2.5 – of this chapter are devoted to the summary of the experimental investigative technique and video processing technique for drop dynamics.

The last section 2.6 is an outline of the available facilities for microgravity research.

2.1 Jetting tap dynamics

The dripping dynamics of a fluid show various types of behaviour. Three different areas that can be identified are a periodic mode, a chaotic dripping mode and liquid jetting. This section concentrates specifically on the liquid jetting mode.

The main parameters that affect the system are flow inertia, gravitational acceleration, surface tension and viscosity. The flow velocity and gravity tend to extend the fluid jet while the surface tension continuously tends to minimise the drop surface area. Stream flow, as theorised by Lord Rayleigh [2] and Joseph Plateau [7], will always contain instabilities (flow oscillations). The jet instability causes the drop shape to develop a thinner cross-sectional area in a specific region (necking).

Rayleigh [2] proposed that jet instability has two causes. The first is due to capillary forces when the density difference between fluids (the flowing fluid and the fluid which it is projected into) is high [2], [7]. The second has a dynamic nature and arises when the density difference is small [2]. The topic of this research concentrates on the former cause.

Rayleigh argues with Plateau here, showing that the dynamic growth of the disturbance is dominated by the fastest growing disturbance, which is not dependent on the initial size of the disturbance (assuming that all disturbances start with extremely small values if the time period is taken to be long enough).

Rayleigh in his calculations makes several important assumptions [5]. The fluid is:

- Irrotational
- Non-viscous
- Incompressible
- Unaffected by surface tension

He then calculates the relationship between the wavelength (λ) and diameter of the disturbance ($2a_{dist}$) which will lead most rapidly to breakdown:

$$\lambda = 4.508 \times 2a_{dist} \quad \Bigg| \quad 2.1.1$$

The corresponding number that was obtained by Plateau was $\lambda = 4.38 \times 2a_{dist}$.

Later, Susumu Tomotika [8] investigated the behaviour of jet flow, which included viscosity. This study enhanced Rayleigh theory, by arguing that his studies provided no definitive evidence of the size of drops that could form due to viscous liquid issued in a vacuum. Tomotika's studies were based on the experiments carried out by Geoffrey Taylor (in unpublished work [8]), which concluded that the wavelength of the fluid disturbance is dependent on the viscosity ratio between the cylindrical column of the fluid and the surrounding fluid. In addition, when the viscosity ratio becomes finite (in Rayleigh's work it was assumed to be infinite) there will be a wave that always has a maximum value of the wavelength, which is proportional to the degree of instability. The wave with the maximum wavelength would lead to the fluid column breaking at a certain size [8].

The studies of Plateau, Rayleigh, Tomotika and others concluded that the fluid column would break at some time with the formation of drops of similar size. The jetting stream was imposed by the harmonic disturbances at a specific frequency in their experiment. The breakup occurs due to capillary instabilities, which can be external or internal in nature [2], [5] – [8].

Later in 1985, Sherry Leib and Raymond Goldstein [9] demonstrated in their studies that the instability could be related to the Weber number (Equation 2.1.2). Their work found that at specific Weber numbers (the relative influence of flow inertia to surface tension – see Equation 2.1.2) there will be instability in the drop size at the end of the fluid column. Meaning that, at certain disturbance frequencies with known Weber number (We), there might be absolute instability. Absolute instability can be explained as the instability that amplifies itself within the same distance region [5].

$$We = \frac{\rho d}{\sigma} v_o^2$$

2.1.2

where: ρ – density of the liquid

d – characteristic length (diameter)

σ – surface tension

v_o – flow velocity

In their investigation, they considered the fluid to be:

- Non-viscous
- Incompressible
- Irrotational

Assuming that the flow velocity is of small amplitude and there exist uniform axial disturbances:

$$v_{\infty} e^{-i\Omega t}$$

2.1.3

$$\Omega = \omega a_{dist} / v_o$$

2.1.4

where: v_{∞} – amplitude of the flow velocity disturbance

Ω – Strouhal number (describes the oscillation of the flow with the respect to its inertia)

t – time (dimensionless – here only)

ω – frequency

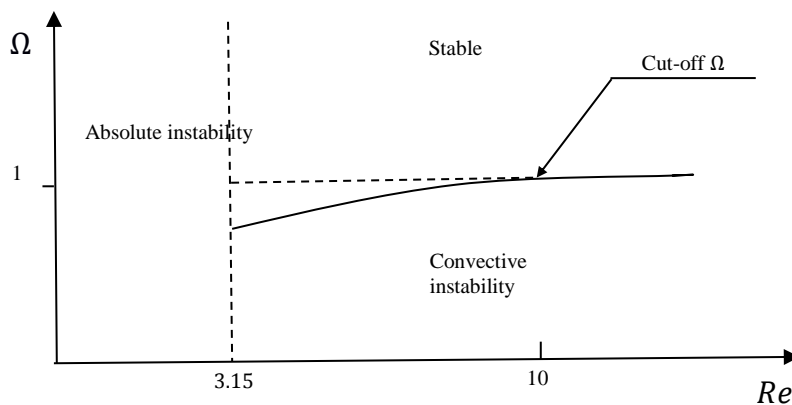


Figure 2.1.1: The stability regimes (parabolic profile)

(Reproduced from [9])

Moreover, assuming that the flow profile exiting the capillary is not of a plug profile (velocity across the tube is constant) but is of parabolic profile (Hagen-Poiseuille profile) they came up with results describing the stability regimes in the Reynolds number (Equation 2.1.5) and Strouhal number plane (Figure 2.1.1) [9].

$$Re = \frac{\rho v_o d}{\mu} \quad \left| \quad 2.1.5 \right.$$

where: ρ – density

v_o – velocity

d – fluid flow diameter

μ – dynamic viscosity

When the Reynolds number is decreased the instability starts to develop (Rayleigh instability), leading to two solutions (spatial instability – instability which develops in three spatial dimensions, and temporal instability – instability which develops with time). Lieb and Goldstein speculated that in fact, the instability starts to develop not only downstream but also up the jet stream [5]. Lieb and Goldstein found that below the critical Reynolds number there persists absolute instability [9], while above this value the flows can be either convective unstable (meaning that the stability amplifies and drifts away from its origin), or stable (the perturbation dies off after some time), depending on the Strouhal number. The cut-off Strouhal number is shown in Figure 2.1.1 as a solid black line. In addition, Lieb and Goldstein found that if the jet stream changes from a Hagen-Poiseuille profile to a plug profile the Reynolds number for the absolute instability increases.

Similarly, to Lieb and Goldstein’s speculation on the propagation of the perturbing wave in both directions, Lin and Lian [10] came up with a similar idea. Their study investigated convective and absolute instabilities as a function of the Reynolds number, which followed the same outcome as proposed by Lieb and Goldstein. Later, the experimental investigation performed by Cordero et al. confirmed that the jetting instability is due to a convective instability [11].

Another tempting speculation raised by Lin and Lian is that the jet absolute instability can correspond to a dripping mode (the region where the Weber number is small) [10].

To take instabilities into account Funada and Joseph [12] (later refined further by Funada, Joseph and Yamashita [13]) tried to improve Tomotika's work. Their results concluded that the capillary instability can occur in a vacuum, and that the critical wavelength for the instability is independent of the Reynolds number, but that the Reynolds number does affect the maximum growth rate and the wavelength of the maximum growth.

2.2 Dripping tap dynamics

After the speculation by Lin and Lian [10] on the relationship between drop formation and the onset of dripping at a specific Weber number, Christopher Clanet and Juan Lasheras [14] extended the work of Taylor [15] and found out experimentally that the critical Weber (We_c) number that represents this transition can be estimated as:

$$We_c = 4 \frac{Bo_o}{Bo} \left[1 + KBo_oBo - \left((1 + KBo_oBo)^2 - 1 \right)^{\frac{1}{2}} \right]^2 \quad \left| \quad 2.2.1 \right.$$

where: Bo_o , Bo – Bond number for outside and inside of nozzle respectively

K – is constant value (for water in air equal to 0.37)

Their experiment involved identification of the transition velocity between dripping and jetting using a high-speed camera. Their results were in good agreement with the experimental data [14]. In their calculations, they approximated the Bond number to be:

$$Bo \equiv \sqrt{\frac{\rho g d^2}{2\sigma}} \quad \left| \quad 2.2.2 \right.$$

where: ρ – fluid density

g – acceleration due to gravity

d – diameter of the nozzle (inner or outer corresponding to Bo and Bo_o)

σ – surface tension

Their work also identifies that there are two regions in dripping dynamics: one is periodic dripping and the other is the dripping faucet region (chaotic region). The critical Weber number, that they calculated corresponds to the region where the quasi-periodic regime stops and jetting starts.

Actually, later it will be shown that the dynamics of dripping exhibits three regions. The first is associated with periodic dripping, the second with quasi-periodic and finally there is chaotic dripping [4], [5]. Periodic dripping is the development of drops, which detach with the same period. Quasi-periodic dripping is periodic dripping where detachment does vary but follows a sequence in the repetition of periods. Chaotic dripping is where the time of detachment varies with no identifiable repetition pattern. The cause of the period variation is due to instabilities in the drop growth. The instabilities appear after the drop necking process, which is followed by detachment, which introduces an unbalanced capillary force acting in the opposite direction to the flow and the inability of the drop to stabilise the vibration that this causes.

While continuously increasing the flow velocity at some point it will bring an end to periodic dripping and with period doubling will move to quasi-periodic (multiple period repetition), followed by the chaotic region. The chaotic region instabilities will continue to grow which were identified as Rayleigh instabilities [5], [14] (similar to those in jetting dynamics), leading to the development of a jet at a specific (critical) Weber number. The actual cause of the Rayleigh instability is because air starts to enter the capillary and changes the flow profile [14].

Separately, Jens Eggers and Todd Dupont in 1994 published their mathematical model that describes drop formation [16]. Their calculations are based on the Navier-Stokes equation in one-dimensional cylindrical coordinate system (Equation 2.2.3 – modified Navier-Stokes equation and Equation 2.2.4 – modified continuity equation), with the fluid flow considered to be viscous, axisymmetric and incompressible. Their solution predicted drop

shape formation well, but could not solve the singularity of detachment (the point where the radius of the column tends to zero – prior to detachment). They defined the singularity as a necking radius, which tends to zero (the process by which drop detachment happens). Later, Eggers refined the model [17] by introducing the notion of the adaptive grid, which allows one to go beyond the singularity and increases the resolution.

$$\begin{aligned} \partial_t v_r + v_r \partial_r v_r + v_z \partial_z v_r &= -\frac{\partial_r p}{\rho} + \nu \left(\partial_r^2 v_r + \partial_z^2 v_r + \frac{\partial_r v_r}{r} - \frac{v_r}{r^2} \right) \\ \partial_t v_z + v_r \partial_r v_z + v_z \partial_z v_z &= -\frac{\partial_z p}{\rho} + \nu \left(\partial_r^2 v_z + \partial_z^2 v_z + \frac{\partial_r v_z}{r} \right) - g \end{aligned} \quad \left. \vphantom{\begin{aligned} \partial_t v_r + v_r \partial_r v_r + v_z \partial_z v_r &= -\frac{\partial_r p}{\rho} + \nu \left(\partial_r^2 v_r + \partial_z^2 v_r + \frac{\partial_r v_r}{r} - \frac{v_r}{r^2} \right) \\ \partial_t v_z + v_r \partial_r v_z + v_z \partial_z v_z &= -\frac{\partial_z p}{\rho} + \nu \left(\partial_r^2 v_z + \partial_z^2 v_z + \frac{\partial_r v_z}{r} \right) - g \right.} 2.2.3$$

$$\partial_r v_r + \partial_z v_z + \frac{v_r}{r} = 0 \quad 2.2.4$$

where: v_r and v_z – velocity components along the r-axis and z-axis respectively

p – pressure

ρ – density

ν – kinematic viscosity ($\nu = \mu/\rho$)

Xiaoguang Zhang also tried to solve the problem of drop dynamic behaviour using the Navier-Stokes equation, but the solution is limited to specific Reynolds numbers and cannot incorporate the instability after detachment [18]. However, importantly his work identified that the flow instability at detachment leads to the formation of the liquid thread [18].

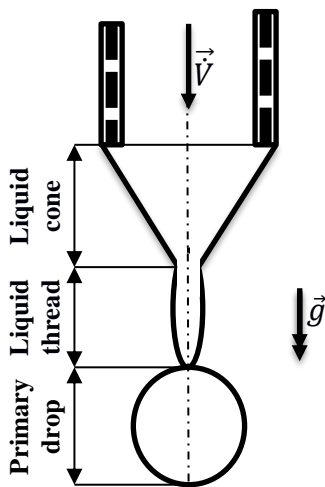


Figure 2.2.1: Liquid thread formation
(reproduced from [18])

The formation of the liquid thread and subsequent detachment of the ‘primary’ drop leads to the formation of small satellite drops (drop rupture) [18], [19], (Figure 2.2.1). When the primary drop detaches under the unbalanced capillary force the thread whirls back and breaks again at low to moderate flow rates.

For higher flow rates, the inertia of the thread is high enough to push it into the liquid cone [18].

Based on experimental results Zhang found that the formation of the satellite drop depends on inertia, capillary forces and gravity. The resulting relationship gives a threshold value (S) as:

$$S = We \cdot Bo^{0.3921} \quad | \quad 2.2.5$$

The satellite drops will be formed only if the threshold value (S) is less than 0.0125.

D. Harkins and F.E. Brown introduced the formulation of maximum drop volume that detaches from the nozzle in 1919. The maximal drop volume (V_{crit}) that can be sustained can be expressed by Tate's law [19], [20]:

$$V_{crit}(\rho - \rho_{out})g = \pi d \sigma \sin \theta \quad | \quad 2.2.6$$

where: ρ and ρ_{out} – are the density of the liquid and the surrounding medium

θ – is surface contact angle

Zhang and Mori experimentally determined and approximated the correction factor (ψ) which depends on the mass of the drop and the surface tension [19], [20] can be expressed as:

$$V = \frac{\psi 2\pi r_{wet} \sigma}{(\rho - \rho_{out})g} \quad | \quad 2.2.7$$

where: ψ – Harkins-Brown correction factor

r_{wet} – is the radius of the outer edge of nozzle tip (wetting radius)

V – is the detached volume

The experimental assumption was made by Zhang and Mori that drop at detachment is assumed to be stable (no fluctuation of the Centre of Mass – CoM), the flow velocity prior to detachment is zero, and the nozzle tip is fully wetted. The correction factor is included to account for the satellite drops. The most common way of expressing the correction factor as a function of the maximal volume and the wetted tip radius is [20]:

$$\psi = 0.6 + 0.4 \left[1 - \frac{r_{wet}}{0.73} \left(\frac{\psi}{V} \right)^{1/3} \right]^{2.3} \quad | \quad 2.2.8$$

$$\psi = 0.6 + 0.4 \left[1 - \frac{r_{wet}}{V^{1/3}} \right]^3 \quad | \quad 2.2.9$$

Where Equation 2.2.8 is used when the drop volume is known and is applicable to the range that satisfies $0 \leq r/V^{1/3} \leq 0.95$, and Equation 2.2.9 when the surface tension is well known with the ratio satisfying $0 \leq r(\psi/V)^{1/3} \leq 0.73$. The correlations gave no bias deviation exceeding $\pm 1\%$ with respect to the experimental data.

2.3 Studies of chaotic dripping mode

In the case when the vibration of the system is not fully damped and the surface instability has reached, a critical point the subsequent drop mass will be different compared to the previous drop mass. This leads to quasi-periodic dripping. In this case, the periods continue to repeat themselves, and follow the same periodic function [5]. This process is called bifurcation, which can be identified as a dynamic system with a multi-period response. If the flow velocity is increased even more, the bifurcation will continue, creating more dripping periods. If we continue to increase the flow, the number of the periods will increase until it becomes impossible to determine the number of periods. The problem arises due to measurement sensitivity or computational rounding errors, which render it impossible to resolve the difference in periods. This area is known as the deterministically chaotic or chaotic dripping mode.

The regions described above are identified in Figure 2.3.1. The attractor is defined as the set of periods towards which the disturbed systems progress in development. The point attractor is the single period to which the disturbed perturbed state will converge toward over time. The limit cycle attractor is a system, which in the case of any perturbation will tend to diverge to a specific path and later should converge to repeating periods.

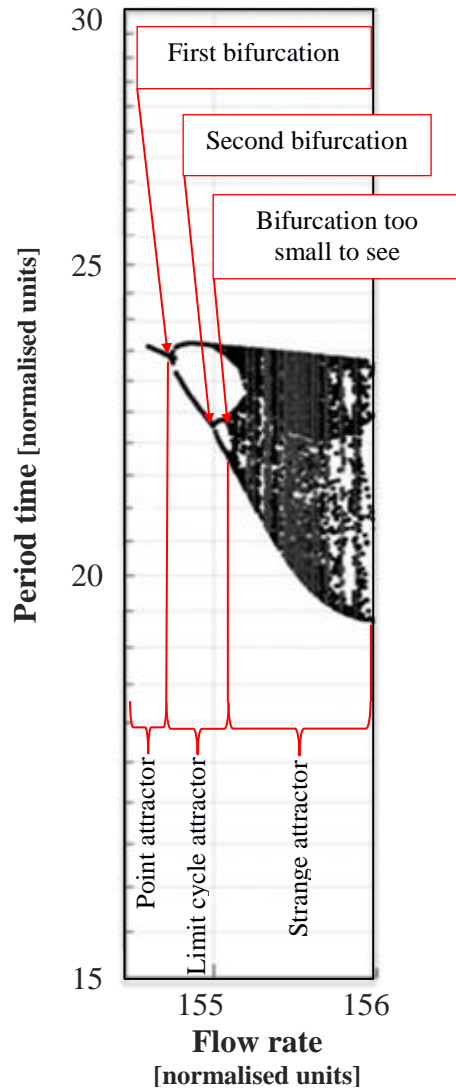


Figure 2.3.1: Bifurcation diagram

Unfortunately, he concluded that there is no answer on “how long” the quasi-periodic system can result in its repetition [21].

Robert Shaw was the first to study the dripping faucet as a chaotic system [3]. His system was a simple approximation to the drop motion represented by a mass – spring model, governed by the following Equations 2.3.1. In his work, the mass was constantly increasing and the detachment mass was linearly proportional to the constant value [3].

$$\begin{aligned} \frac{\partial z}{\partial t} &= v_o \\ \frac{\partial z}{\partial t} \left[m \frac{\partial z}{\partial t} \right] &= -mg - kz - cv_o \end{aligned} \quad \left. \vphantom{\begin{aligned} \frac{\partial z}{\partial t} &= v_o \\ \frac{\partial z}{\partial t} \left[m \frac{\partial z}{\partial t} \right] &= -mg - kz - cv_o \end{aligned}} \right| 2.3.1$$

where: z – axial position of Centre of Mass (CoM)

Strange attractors form a multi-periodic system where the path of future development is dependent on even slight perturbations [21]. One of the people who first started to study deterministic chaotic systems in fluid flow was Edward Lorenz [21]. He used deterministic ordinary nonlinear differential equations to represent hydrodynamic flows.

Lorenz found that the solutions to those equations result in instabilities, which in most cases are non-periodic (chaotic). He argued that any closed system with finite dimensions requires its future state to be randomly close to its past history.

v_o – flow velocity

g – acceleration due to gravity

k – spring constant

t – time

m – mass of the drop at an instant of time

c – is a damping constant value

Later Kiyono and Fuchikami refined the mass – spring model, experimentally defining the spring and damping coefficients [4], [6]. Their model was governed by:

$$\frac{d(mv_o)}{dt} = -kz - c \frac{dz}{dt} + mg \quad | \quad 2.3.2$$

$$\frac{d(mv_o)}{dt} = m \frac{d^2z}{dt^2} + \left(\frac{dz}{dt} - v_o \right) \frac{dm}{dt} \quad | \quad 2.3.3$$

where: $d(mv_o)/dt$ – change of momentum

v_o – flow velocity

They also assumed that the flow rate is constant and the value $v_o \cdot dm/dt$ was negligible.

The units were normalised to set the gravitational acceleration to be equal to one. The value of the spring constant (k) is dependent on the mass value [4]:

$$k(m) = \begin{cases} -11.4m + 52.5 & (m < 4.61) \\ 0 & (m \geq 4.61) \end{cases} \quad | \quad 2.3.4$$

The residual mass after drop detachment was calculated as [4]:

$$m_r = 0.2m + 0.3, \quad \text{when } z = z_{crit} = 5.5 \quad | \quad 2.3.5$$

In addition, when detachment happened the following assumption was made for the reset conditions [4]:

$$\left\{ \begin{array}{l} z = 2.0 = const \\ \dot{z} = 0 \end{array} \right\}, \quad \text{when } z = z_{crit} = 5.5 \quad | \quad 2.3.6$$

The model proved to be of a similar nature to the experimental results. It confirmed bifurcation and quasi-periodic dripping.

Kiyono and Fuchikami also maintained the model as one dimensional, but later Barnaby Osborne and Chris Welch [22] introduced a second dimension to the system (incorporating both lateral and axial movement of the drop), which was not done before. They also included inertia as the calculations involved a consideration of microgravity. The set of Equations 2.3.7 – 2.3.8 were solved using a Runge-Kutta algorithm.

$$\frac{\partial}{\partial t} \left[m \frac{\partial z}{\partial t} \right] + k_z z + \frac{c_z \partial z}{\partial t} = \left(v_o - \frac{\partial z}{\partial t} \right) \frac{\partial m}{\partial t} \quad | \quad 2.3.7$$

$$\frac{\partial}{\partial t} \left[m \frac{\partial y}{\partial t} \right] + k_y y + c_y \frac{\partial y}{\partial t} = 0 \quad | \quad 2.3.8$$

where: y – lateral position CoM

z – vertical position of the CoM

The spring and damper constants were given by [22]:

$$k_z(m) = \begin{cases} 44.71 - 16.3m & (m < 4.61) \\ 0 & (m \geq 4.61) \end{cases} \quad | \quad 2.3.9$$

$$k_y(m) = \begin{cases} 57.1 - 12.1m & (m < 4.61) \\ 0 & (m \geq 4.61) \end{cases} \quad | \quad 2.3.10$$

$$c_z = 0.0409 \text{ (Ns/m)} \quad | \quad 2.3.11$$

$$c_y = 0.0551 \text{ (Ns/m)} \quad | \quad 2.3.12$$

The assumption was made that detachment happens when the CoM reaches a critical value in either direction. The value of the residual mass and the z-direction and z-velocity was reset based on the Kiyono and Fuchikami approximation (Equations 2.3.5 – 2.3.6). The reset conditions for the lateral position and velocity were chosen to be [22]:

$$\begin{cases} y = y_{t-1}/2 \\ \dot{y} = -3\dot{y}_{t-1} \end{cases}, \quad \text{when } y = y_{crit} \quad | \quad 2.3.13$$

Unfortunately, in their publication, they have not reported on the value of the critical lateral position, stating that it was acquired empirically.

Their results showed that there is a deviation from the experimental results, and proposed that the 2 Degree of Freedom (DoF) Mass-Spring-Damper (MSD) model should look like a model that is based on a standard mass – spring model with a pendulum-type motion instead. In their proposed approach, the pendulum is required to have spring and damping constants, which depend on the angular position of the CoM.

The work of Kiyono and Fuchikami, and Osborne and Welch both extensively used nondimensional units. The following fundamental units (or conversion factors) were introduced:

$$\begin{aligned} l_o &\equiv \sqrt{(\sigma/\rho g)} = 0.27 \text{ cm} \\ t_o &\equiv (\sigma/(\rho g^3))^{1/4} = 0.017 \text{ s} \\ m_o &\equiv \rho l_o^3 = 0.020 \text{ g} \end{aligned} \quad \left. \vphantom{\begin{aligned} l_o &\equiv \sqrt{(\sigma/\rho g)} = 0.27 \text{ cm} \\ t_o &\equiv (\sigma/(\rho g^3))^{1/4} = 0.017 \text{ s} \\ m_o &\equiv \rho l_o^3 = 0.020 \text{ g} \end{aligned}} \right| 2.3.14$$

where: l_o , t_o and m_o – conversion factors

σ – surface tension

ρ – density

To understand their selection of those values, additional explanation is needed. The use of dimensionless variables allows simplification of the mathematical problem and provides independence of scale. Dimensional analysis is a method to convert one type of unit (used in the equation) to another [23]. By doing so, a numerical quantity is introduced, known as a conversion factor. The key theorem to perform dimensional analyses is the Buckingham Π theorem. This theorem provides a procedure to nondimensionalization (partial or full removal of the units) of the equation, or in other words, the theorem provides dimensionless groups (identified by the base quantities - e.g. length, mass, time) from the initial variables.

To complete the dimensional transformation, the following variables were assumed to be equal to unity: surface tension ($\sigma=72.8$ mN/m) [24], density ($\rho=998.19$ kg/m³) [24] and acceleration due to gravity ($g=9.81$ m/s²). All values correspond to water parameters at

normal pressure (101 kPa) and temperature (20 °C). The following set of equations provides the transformation which takes initial units of the surface tension, density and acceleration due to gravity and transforms them to unity by multiplying with the conversion factors (l_o , m_o and t_o).

$$\begin{aligned} \sigma \cdot [m]^0 \cdot [kg]^1 \cdot [s]^{-2} &= 1 \cdot (l_o)^0 \cdot (m_o)^1 \cdot (t_o)^{-2} \\ \rho \cdot [m]^{-3} \cdot [kg]^1 \cdot [s]^0 &= 1 \cdot (l_o)^{-3} \cdot (m_o)^1 \cdot (t_o)^0 \\ g \cdot [m]^1 \cdot [kg]^0 \cdot [s]^{-2} &= 1 \cdot (l_o)^1 \cdot (m_o)^0 \cdot (t_o)^{-2} \end{aligned} \quad \left| \quad 2.3.15 \right.$$

where: $[m]$, $[kg]$ and $[s]$ – base quantities for length, mass and time respectively

Now the set of equations 2.3.15 can be rearranged as follows:

$$\begin{aligned} \sigma &= \left(\frac{l_o}{[m]}\right)^0 \cdot \left(\frac{m_o}{[kg]}\right)^1 \cdot \left(\frac{t_o}{[s]}\right)^{-2} = \left(\frac{m_o}{[kg]}\right)^1 \cdot \left(\frac{t_o}{[s]}\right)^{-2} \\ \rho &= \left(\frac{l_o}{[m]}\right)^{-3} \cdot \left(\frac{m_o}{[kg]}\right)^1 \cdot \left(\frac{t_o}{[s]}\right)^0 = \left(\frac{l_o}{[m]}\right)^{-3} \cdot \left(\frac{m_o}{[kg]}\right)^1 \\ g &= \left(\frac{l_o}{[m]}\right)^1 \cdot \left(\frac{m_o}{[kg]}\right)^0 \cdot \left(\frac{t_o}{[s]}\right)^{-2} = \left(\frac{l_o}{[m]}\right)^1 \cdot \left(\frac{t_o}{[s]}\right)^{-2} \end{aligned} \quad \left| \quad 2.3.16 \right.$$

By taking the natural logarithm of both sides, the set of equations will take the following form:

$$\begin{aligned} \ln \sigma &= \ln \frac{m_o}{[kg]} - 2 \ln \frac{t_o}{[s]} \\ \ln \rho &= -3 \ln \frac{l_o}{[m]} + \ln \frac{m_o}{[kg]} \\ \ln g &= \ln \frac{l_o}{[m]} - 2 \ln \frac{t_o}{[s]} \end{aligned} \quad \left| \quad 2.3.17 \right.$$

Alternatively, in a matrix form, the Equation 2.3.17 can be represented as:

$$\begin{bmatrix} \ln \sigma \\ \ln \rho \\ \ln g \end{bmatrix} = \begin{bmatrix} 0 & 1 & -2 \\ -3 & 1 & 0 \\ 1 & 0 & -2 \end{bmatrix} \cdot \begin{bmatrix} \ln(l_o/[m]) \\ \ln(m_o/[kg]) \\ \ln(t_o/[s]) \end{bmatrix} \quad \left| \quad 2.3.18 \right.$$

To find the values of the conversion factors Equation 2.3.17 is rearranged, with the logarithms of the surface tension, density and acceleration due to gravity calculated.

$$\begin{bmatrix} \ln(l_o/[m]) \\ \ln(m_o/[kg]) \\ \ln(t_o/[s]) \end{bmatrix} = \begin{bmatrix} 0 & 1 & -2 \\ -3 & 1 & 0 \\ 1 & 0 & -2 \end{bmatrix}^{-1} \cdot \begin{bmatrix} \ln \sigma \\ \ln \rho \\ \ln g \end{bmatrix} \quad 2.3.19$$

$$\begin{bmatrix} \ln(l_o/[m]) \\ \ln(m_o/[kg]) \\ \ln(t_o/[s]) \end{bmatrix} = \begin{bmatrix} 0.5 & -0.5 & -0.5 \\ 1.5 & -0.5 & -1.5 \\ 0.25 & -0.25 & -0.75 \end{bmatrix} \cdot \begin{bmatrix} -2.62004 \\ 6.90594 \\ 2.28340 \end{bmatrix} = \begin{bmatrix} -5.90469 \\ -10.80813 \\ -4.09405 \end{bmatrix} \quad 2.3.20$$

$$\begin{aligned} l_o/[m] &= e^{-5.90469} \approx 0.002727 \\ m_o/[kg] &= e^{-10.80813} \approx 2.023 \cdot 10^{-5} \\ t_o/[s] &= e^{-4.09405} \approx 0.01667 \end{aligned} \quad 2.3.21$$

The calculated values of the conversion factors following the transformation are: unity length $l_o = 0.002727[m] \cong 0.27 \text{ cm}$, unity mass $m_o = 2.023 \cdot 10^{-5}[kg] \cong 0.020 \text{ g}$ and unity time $t_o = 0.01667[s] \cong 0.017 \text{ s}$. The conversion ratios presented in Equation 2.3.14 can be obtained from the inverse matrix of the initial constants of Equation 2.3.18.

$$\begin{aligned} l_o &= \sigma^{0.5} \rho^{-0.5} g^{-0.5} = \sqrt{\sigma/(\rho g)} \\ m_o &= \sigma^{1.5} \rho^{-0.5} g^{-1.5} = \sigma^{1.5} \rho^{-1.5} g^{-1.5} \rho = l_o^3 \rho \\ t_o &= \sigma^{0.25} \rho^{-0.25} g^{-0.75} = (\sigma/(\rho g^3))^{0.25} \end{aligned} \quad 2.3.22$$

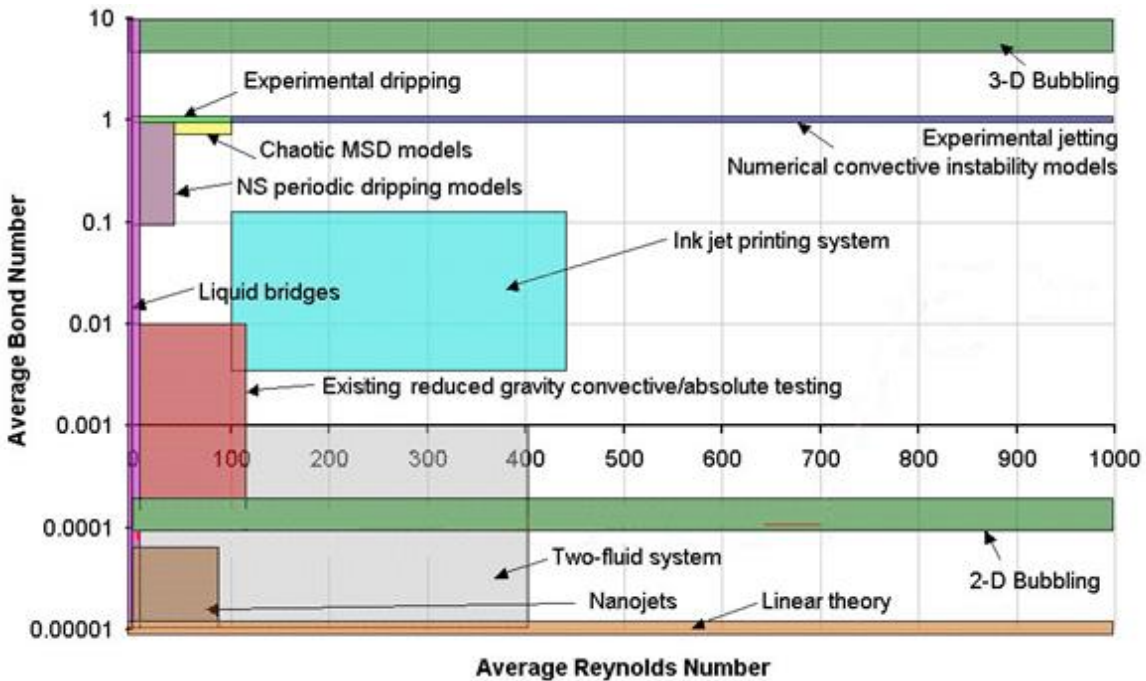


Figure 2.3.2: The composite plot of approximate areas of investigation
Copied from Osborne B. (2008) [5]; **Yellow** region – chaotic region

To characterise the approximate area of the chaotic region it is possible to use Osborne's research thesis [5], where he has identified and summarised in an elegant graph (Figure 2.3.2) different types of the fluid behaviour at low Reynolds and Bond number conditions. In this research, the Bond number is approximated to be just below one (it can be calculated using Equation 2.2.2). Figure 2.3.2 suggests that the approximate value of the transition between periodic dripping and chaotic dripping should occur at a Reynolds number of 50.

Similarly, the end of the chaotic region can be calculated using the approximation given by Clanet and Lasheras [14] in Equation 2.2.1. Later, in (section 5.1.1), it will be shown that the corresponding value is equal to $Re \approx 540$.

2.4 Investigation into the experimental methodology

For an investigation of drop dynamics, the main required areas of interest are:

- Generate appropriate fluid flow
- Set an appropriate experimental environment
- Record the results

Those areas of interest were chosen to achieve the aims of the research. It is needed to limit the investigation area by correctly identifying and setting the input parameters, and record with well-identified uncertainty the experimental outcomes. To generate fluid flow several approaches can be used, using pumps or the capillary effect. In normal gravity, the gravitational force limits the use of capillary flow, leaving experiments to rely on the pump approach. The pump is a mechanical device that creates a pressure difference to move the fluid. The system usually consists of a fluid container (syringe), motor and a container compression mechanism [19]. The choice of the motor depends on the flow velocity and the required flow precision. Gunde et al. [19], and Clanet and Lasheras [14] use gear motors with a tachometer that moves the syringe piston via spindles. Another approach is

to use syringe pumps, which already provide constant flow rates with minimum distortions [11]. When accounting for the flow rates it is important to note that flow within the pipe should be fully developed and if the flow rate's Reynolds number is below 600, the flow should be considered to have the form of a Hagen-Poiseuille profile [14].

The dispensed liquid requires to be fully characterised, which includes the density of the liquid, temperature, surface tension and viscosity. The density can be measured using a densitometer [19] or it is otherwise determined using mass and volume measurements. The density of deionized water for example at 22°C is 1000 kg/m³, its dynamic viscosity is 10⁻⁶ m²/s, and its surface tension is 0.073 kg/s² [14], and these variables are affected by temperature changes.

The syringe is usually enclosed within a thermostatic cell [19]. To prevent liquid contamination in the flow system, which might affect density and surface tension, the syringe and capillaries should be cleaned [19].

The detached drop volume also depends on the surrounding fluid density and pressure. To maintain the surrounding fluid density and pressure at a constant level the test area should be enclosed [11], [19], which will limit the fluid flow within the test area.

The fluid system, especially in the drop dynamics study, is dependent on the stability of the flow and the attached drop. This requires that any external vibrations are minimised by using either a vibration isolation plate [19] or anti-vibration mats.

The aforementioned flow and external parameters should be recorded. This can be done either by manually recording the readings or by using sensors and recording their output digitally. Digital recording can be done via a connection to a personal computer (PC) [19] or by using a Data Acquisition (DAc) platform [14]. For the fluid flow velocity, monitoring is usually performed using a motor encoder [19], which mathematically relates the angular velocity of the motor to the volume extracted per time step. The temperature is recorded via thermocouples directly submerged in the liquid [5]. Depending on the need of

the experiment, either an optical source with a detector can be used [11], [19] or a video camera [11], [14]. The optical source with the detector only provides a reference value of the object's presence, but requires less time to post-process the results [19]. The video camera, on the other hand, can provide a cross-sectional view of the drop shape, but requires additional post-processing (such as edge detection techniques). Depending on the flow velocity and drop study area, different frame rates for the camera can be acceptable. Clanet and Lesharas [14] used 1000 frames-per-second (fps) and 6000 fps (with a resolution of 192-by-240 and 32-by-240 respectively).

2.5 Video processing techniques for edge detection

Video cameras were used in this research to study drop behaviour. As mentioned in the previous section the camera is useful to fully identify the drop shape but requires additional post-processing. The focus of the video processing is to identify the shape of the drop using the edge detection method.

The edge can be defined as an abrupt change in the image colour [25]. The techniques for edge detection can be separated into three groups, gradient based, Laplacian based and non-derivative based [25].

The gradient-based method finds the maximum value of the derivative of the image gradient (the direction of the change in the colour intensity) and compares this to a threshold value. The edge is identified when the threshold value is exceeded. Well-known examples of adaptations of this method are described by Lawrence Roberts [26], Judith Prewitt [27] and Irwin Sobel [28].

The Roberts operator also known as the Roberts cross uses two 2-by-2 matrixes (\mathbf{X} and \mathbf{Y} , Equations 2.5.1 and 2.5.2), which allows one to identify the gradient using discrete differentiation by finding the sum of neighbouring diagonal pixels [26].

$$\mathbf{X} = \begin{bmatrix} +1 & 0 \\ 0 & -1 \end{bmatrix} \quad | \quad 2.5.1$$

$$\mathbf{Y} = \begin{bmatrix} 0 & +1 \\ -1 & 0 \end{bmatrix} \quad | \quad 2.5.2$$

These matrices (masks) are overlapped with the original image (\mathbf{A}) (Equation 2.5.3) to find the gradient of the original picture (Equation 2.5.4) [26].

$$\mathbf{G}_X = \mathbf{X} * \mathbf{A} \text{ and } \mathbf{G}_Y = \mathbf{Y} * \mathbf{A} \quad | \quad 2.5.3$$

$$\nabla A(x, y) = \sqrt{\mathbf{G}_X^2 + \mathbf{G}_Y^2} \quad | \quad 2.5.4$$

The Prewitt operator uses two 3-by-3 matrices (Equation 2.5.5 – 2.5.6) which contain data on the direction of the edges [25], but in comparison to Roberts cross, the Prewitt operator looks in the horizontal and vertical directions, not in the diagonal directions. These masks are used separately to derive the horizontal edge change and the vertical edge change (\mathbf{G}_X and \mathbf{G}_Y respectively; Equation 2.5.3).

$$\mathbf{X} = \begin{bmatrix} -1 & -1 & -1 \\ 0 & 0 & 0 \\ +1 & +1 & +1 \end{bmatrix} \quad | \quad 2.5.5$$

$$\mathbf{Y} = \begin{bmatrix} -1 & 0 & +1 \\ -1 & 0 & +1 \\ -1 & 0 & +1 \end{bmatrix} \quad | \quad 2.5.6$$

After this, the direction and magnitude can be calculated using equations:

$$\mathbf{G} = \sqrt{\mathbf{G}_X^2 + \mathbf{G}_Y^2} \quad | \quad 2.5.7$$

$$\Theta = \text{atan}^2(\mathbf{G}_Y, \mathbf{G}_X) \quad | \quad 2.5.8$$

The Sobel operator is similar to the Prewitt operator with the introduction of slightly different masks [27], which actually improve edge identification if the image noise level is high [25]. Similarly, the Prewitt approach then finds the horizontal and vertical derivatives (Equation 2.5.3), and then finds the direction and magnitude using Equations 2.5.7 and 2.5.8 The Prewitt kernel masks are:

$$\mathbf{X} = \begin{bmatrix} -1 & -2 & -1 \\ 0 & 0 & 0 \\ +1 & +2 & +1 \end{bmatrix} \quad \left| \quad 2.5.9 \right.$$

$$\mathbf{Y} = \begin{bmatrix} -1 & 0 & +1 \\ -2 & 0 & +2 \\ -1 & 0 & +1 \end{bmatrix} \quad \left| \quad 2.5.10 \right.$$

Laplacian based edge detection is identified by the maximum value of the derivative of the image gradient and has a zero value of the second derivative of the image gradient [25].

The examples of this approach are so called Laplacian of Gaussian operator class [25] and one specific example is the John Canny algorithm [29].

The Laplacian of Gaussian operator applies a Gaussian distribution [29] of standard deviation ($G(x, y)$) to smooth and filter the image.

$$\mathbf{G}(x, y) = \frac{1}{2\pi\sigma^2} e^{-(x^2+y^2)/2s^2} \quad \left| \quad 2.5.11 \right.$$

where: X and Y – distance from the origin

s – standard deviation of the Gaussian distribution

The Laplacian of Gaussian operator can be found using:

$$\nabla^2 \mathbf{G}(x, y) = \left[\frac{x^2 + y^2 - 2\sigma^2}{\sigma^4} \right] e^{-(x^2+y^2)/2\sigma^2} \quad \left| \quad 2.5.12 \right.$$

The output image ($\mathbf{a}(x, y)$) is found when the operator is convolved with an input image:

$$\mathbf{a}(x, y) = \mathbf{A}(x, y) * \nabla^2 \mathbf{G}(x, y) \quad \left| \quad 2.5.13 \right.$$

To restrict unnecessary zero crossings in the output image, a logical threshold value is applied.

Similar, the Canny approach applies the smoothing and filtering of the image first using the Gaussian filter. Then, Canny uses Equations 2.5.7 and 2.5.8 to find the gradient and direction. Further, Canny introduces a suppression technique to eliminate multiple responses to the edge and using connectivity analysis joins the edges. The suppression is done by introducing a noise maximum criterion, which defines the size of the noise and

introduces minimum and maximum threshold values to limit false positive and false negative responses. The edges are joined together using a feature synthesis method [29].

2.6 Microgravity research facility

Microgravity facilities are divided into six types [30], [31], summarised in Table 2.6.1:

- Drop towers
- Parabolic flights
- Balloon drops
- Sounding rockets
- International space station
- Spacecraft

There are two different approaches to using a drop tower: use of a vertical drop [31], [32], [33], and using a parabolic fall profile [34]. The main difference between these two approaches is the way they are actioned. The vertical drop is a simple free fall of the experiment, which is decelerated at the bottom, while a parabolic fall incorporates a catapult effect where the payload is first accelerated and is then allowed to freely fall back until it is decelerated [34] at the starting location.

Both types of drop towers use a similar principle of operation. A drop tower consists of a shaft, drop capsule and damping system. The payload is positioned within the drop capsule, which is usually referred to as the drag shield. In the free-fall drop tower types, an important part is the release mechanism. The release wire is usually connected to the payload and drag shield separately. The drag shield and the payload inside start to free fall when the wire is released. There is a requirement to allow for extra travel distance within the drag shield. This is because the drag shield will be affected by the drag force from the surrounding air while the payload is protected from it inside the drag shield [31], [35]. To increase the microgravity quality the air from the shaft may be removed or it is forced in

the direction of movement of the drop capsule [30], [32], [33]. This reduces the air drag force applied on the drop capsule while in fall. The deceleration usually is carried out using either friction dampers [32] or an air bag [36].

Type	Name	Duration max (s)	Accuracy (g)	Reference
Drop Tower	Micro-Gravity Laboratory of Japan	4.5	10^{-5}	[32]
	ZARM Drop Tower	9.3	10^{-6}	[34]
	ZERO-G research facility NASA	5.18	10^{-6}	[33]
	National Microgravity Laboratory, China	3.6	10^{-5}	[35]
	Dryden drop tower	2.1	10^{-3}	[35]
	Queensland 2.0 Drop tower	1.95	10^{-5}	[36]
	IDR/UPM Universidad Politécnica de Madrid	1.6	10^{-3}	[35]
	National Industrial Science and Technology	1.4	10^{-3}	[35]
Parabolic flights	CSA Falcon-20	20	0.02	[37]
	NASA KC-135	25	0.02	[37]
	Novespace A300	20	0.02	[37]
	ESA Airbus A310 Zero-G	20	0.01	[38]
Balloon drops	MIKROBA Germany	55	10^{-3}	[39]
	ESA BEXUS	360	10^{-4}	[40]
Rocket drops	ESA REXUS	360	10^{-4}	[41]
Space station	ISS	$\approx 23.5 \cdot 10^6$	10^{-5}	[31]

Table 2.6.1: Summary of recently operational microgravity facilities

Parabolic flights usually use aircraft that perform parabolic flight trajectories, where the aircraft first changes its inclination to approximately 45° and then is left in a controllable free fall [30]. Parabolic flight allows for slightly longer microgravity durations but provides lower levels of microgravity quality. The quality of microgravity for parabolic

flights is limited due to safety issues, as the payload is required to be fixed², and the working environment is very noisy due to external airflow and engine noise [30].

With the increase in height, our atmosphere becomes less dense. This provides lower air drag free fall conditions that are good enough for microgravity experiments. For the balloon drop, stratospheric balloons reach altitudes of around 40 km [30], where the experiment is dropped off and is later recovered by a parachute system. A similar approach uses sounding rockets, which reach altitudes of 400 km [30] and can provide test durations of several minutes, with a high level of microgravity quality. Unfortunately, the quality of the microgravity reduces during the test period.

Spacecraft and the International Space Station are used for longer microgravity experiments [31]. The latter provides a constant high-quality microgravity environment and for a longer time (more than 3 months) [30]. Space experiments are usually required for experiments that require long durations, such as biological or material science investigations. In the case of biological studies, the time requirements might be 30 days or more, and for material studies, processing times might reach several hours.

The choice of the facility depends on the test time required, the microgravity quality, the cost of the experiment and availability [31]. For any experiment, the minimal experimental time is determined as the time required for the system under investigation to stabilise. To achieve the required results in microgravity experiment the quality level of the microgravity is crucial. Cost and availability are important factor as there are a limited number of facilities and the prices range from £100 to £10,000 per test per kilogramme [31], [30] to run the experiment. The cost of the experiment can be reduced with the availability of research programs provided by European Space Agency [41], [40] and other space agencies, but places are limited and competition becomes extremely high.

² In some cases, the payload can be released but only for a limited time, and it should be fixed before the parabolic flight is finished and deceleration begun

Another side of microgravity research is research into human biology. The main problems for space exploration affecting a human body are muscle atrophy, leading to a loss of muscle function, and accelerated ageing due to a deconditioning syndrome of physiological systems [42]. For this purpose on Earth, a bed rest technique is used [43] that allows simulating some of the conditions related to the microgravity environment.

CHAPTER 3

DROP TOWER

This chapter will describe the building and commissioning of the Drop Tower facility at Kingston University. The chapter is divided into two parts. The first part (section 3.1) outlines the project aims and requirements, describes general design elements, followed by a description of the normal operational procedure and emergency procedure, summarising the Drop Tower characteristics, and finally describes design changes that were implemented after assembly and preliminary commissioning work was completed.

The second parts (sections 3.2 – 3.6) describe the assembly and commissioning work. First, it provides detailed information about the work management plan (work statement, planning and budget). Secondly, it explains the assembly work carried out for each system and the calibration of the crucial elements. Finally, it outlines possible future design improvements.

3.1 Drop Tower design

The microgravity Drop Tower developed at Kingston University is of a novel design (Figure 3.1.1). It is located in the Roehampton Vale campus in the Lear Jet laboratory (Appendix A). The Drop Tower initial design idea belongs to former Kingston University

London academics Dr Barnaby Osborne and Prof Chris Welch. It uses a catapult principle driven by electromagnetic linear actuators.



Figure 3.1.1: Kingston University Microgravity Drop Tower

3.1.1 Design aim

The aim of the project was to develop the microgravity research facility in Kingston University London for research and educational purpose. The design needed to incorporate a novel approach for acquiring microgravity conditions by using electromagnetic linear actuators to control the movement of the payload, instead of using a free-fall approach. In addition, it was required to target a wide range of users: researchers, students and to contribute to university outreach activity. The use of linear actuators should also allow the use of different and programmable test profiles (such as a microgravity environment, a Moon or Mars gravity environment, or acceleration and deceleration tests, etc.).

3.1.2 Design requirements

The Drop Tower original design characteristics are based on calculated values and the anticipated performance proposed by B. Osborne and C. Welch [31]. The Drop Tower needs to be around 8 meters high and to use the catapult capabilities to achieve up to 2.2 seconds of a microgravity environment. Microgravity environment quality needs to be in the range of 10^{-3} to 10^{-5} of the Earth's gravitational acceleration. The allowable mass of a payload should not exceed 20 kg and the mass of the moving enclosure (including drag shield) should not exceed 70 kg.

The experimental payload should be surrounded by an enclosure (drag shield) to eliminate air pressure loading while experiments are running. Payload size is limited by drag shield dimensions, which were set to be at least 418.6 mm cubed. To reduce the structural vibration in the experimental payload during operation of the facility, it was advised to limit contact with the drag shield by suspending the payload in mid-air. This should be incorporated into the test velocity profile to allow the payload to freely float in the air.

The design should be targeted to a wide range of users and more importantly, should contribute to the university outreach programme. From this, the following requirements have been proposed. The design should also incorporate a transparent enclosure allowing operators to witness the experimental process while operating the Drop Tower. High safety standards must be met. Finally, test recording instrumentation (video recording) should be installed.

3.1.3 Design main elements

The Drop Tower design consists of seven main elements (Figure 3.1.2):

1. Main support structure
2. Linear guide rails
3. Electromagnetic linear actuators
4. Drag shield

5. Tower enclosure
6. Electrical and control system
7. Safety system

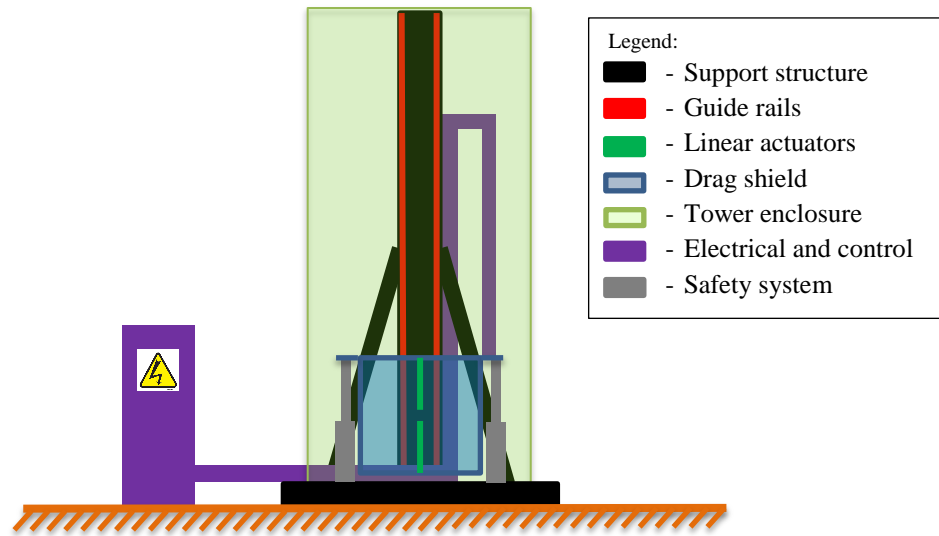


Figure 3.1.2: Design main elements

The main support structure incorporates the installation of a levelled base support, as well as an 8.4 m tall I-beam and its support. The components were manufactured and installed by an outside contractor (prior to the author's involvement). The L-brackets were Computer Numerical Control (CNC) machined for future guide systems and magnetic track installation.

Linear guide rails were installed from both sides of the magnetic track using L-shape brackets – L-brackets (Figure 3.1.3). L-brackets were CNC pre-manufactured by Kingston University technical staff.

The required rail alignment tolerance (driven by the operational requirements of the linear motors) is kept within 0.254 mm. In addition, the guide rails come in one-meter sections and are joined together with rail joints, manufactured on site.

The electromagnetic linear actuator system consists of two ironless I-Force 310 series motors [44], magnetic track sections, a trolley for motor installation, guide rail rollers and base plates for magnetic track installation (Figure 3.1.3). The base plates and trolley were

pre-manufactured on site. The motors were aligned with rail rollers, and the magnetic tracks were aligned with guide rails before system installation.

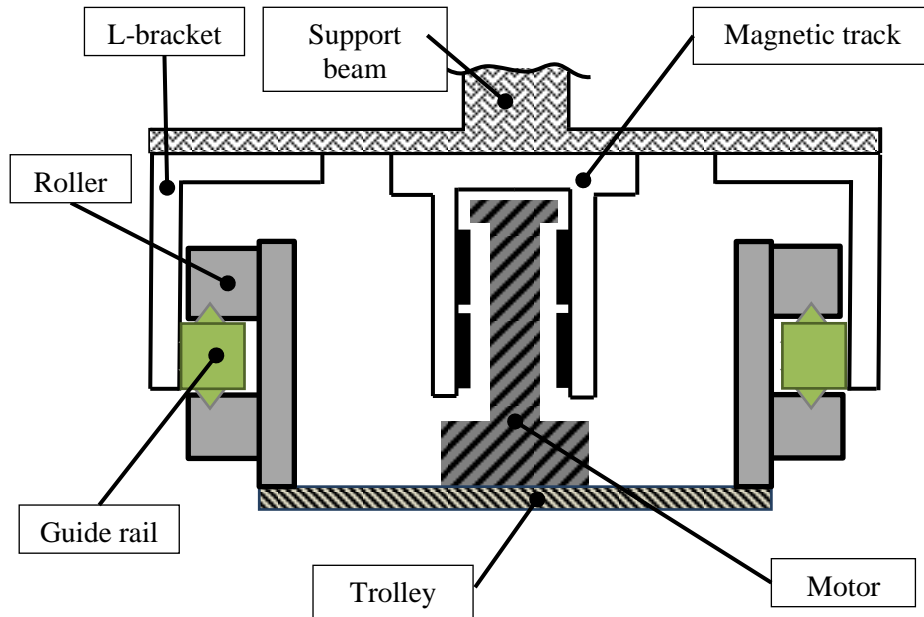


Figure 3.1.3: Drive system elements - plan view

The drag shield attaches to a trolley. It has a profile made of aluminium and enclosed by clear acrylic sheets. The access door is installed on the front.

The tower enclosure consists of four sections, made of aluminium profiles and clear acrylic sheets.



Figure 3.1.4: Electronics cabinet and Control unit

The electrical and control system main components include a three-phase power transformer, a high voltage to low voltage converter and a Parker Compax3 servo drive

[45]. The system is wired out from drag shield using a cable snake and is installed outside the Drop Tower in separate power cabinet (Figure 3.1.4 – left picture). In addition, a separate control unit is hard wired outside the power cabinet and is mounted on a wall next to the operator desk (Figure 3.1.4 – right picture).

The safety system includes both mechanical and electromechanical components. The mechanical system includes guide rails with end-brackets (positioned at the bottom and top of each guide rail) as well as an inertial damper in the case of uncontrolled fall of the drag shield. The electromechanical system includes the door limit switches, the drag shield position limit switches, a normally closed locking switch and an Uninterruptable Power Supply (UPS) unit for logic circuitry.

3.1.4 Operational description

The catapult principle uses an initial velocity directed upwards to deliver the payload to the required height followed by descent under the Earth's gravity (Figure 3.1.5). The catapult method allows a reduction of the height of the Drop Tower by a factor of nearly four by using both ascending and descending free fall paths.

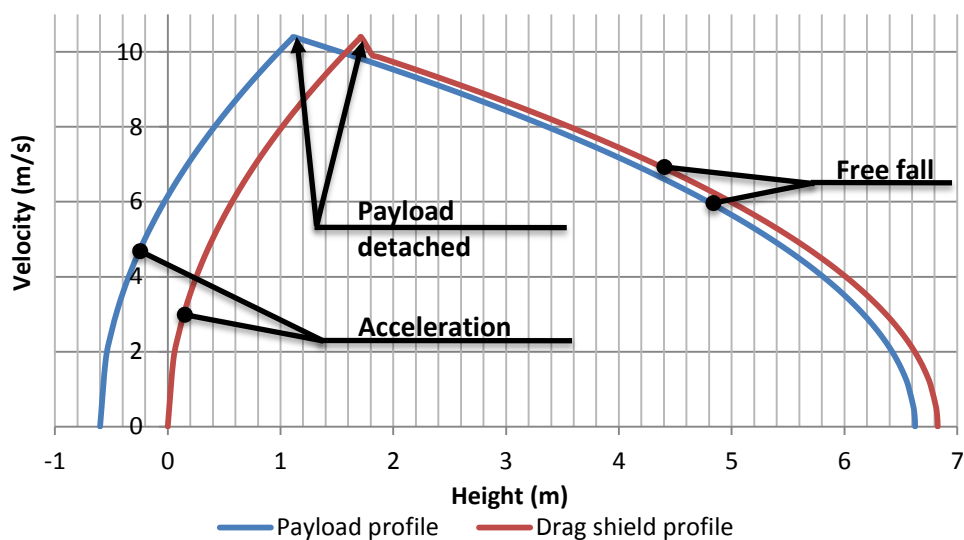


Figure 3.1.5: Drop Tower operational phases for microgravity test

The test is started using the control unit and consists of four elements described in the table below (Table 3.1.1, [31]).

The use of linear actuators allows the variation of the gravity level from nearly zero to Earth gravity, meaning that it is possible to achieve gravity conditions similar to Mars or the Moon etc. Such conditions will require changes in the test movement profile. In addition, anything other than microgravity testing will require full contact of the payload with the drag shield base. This will cause vibration transfer and will induce noise in the gravity level.

Phase name	Description
Acceleration	First, the drag shield is accelerated at 5g reaching initial velocity. The payload is allowed to detach from the drag shield base by slightly reducing the velocity of the drag shield
Parabolic travel	After the payload starts to float, the drag shield speed is returned to a free fall path profile, to match the payload speed profile. Drag shield air resistance is counteracted by the controlled motor operation.
Deceleration	Just before the drag shield is required to decelerate the speed profile of the drag shield is slightly misaligned with the payload speed allowing for smooth contact with the base of the drag shield. After this, a deceleration of 5g is initiated.
Rest time	The system is stopped and is required to remain at rest to cool the motors down until a threshold lower temperature is reached.

Table 3.1.1: Drop Tower operational phases

3.1.5 Operational procedure

In the operational procedure, three different cycles are identified (Table 3.1.2):

- Experimental cycle
- Test cycle
- Emergency cycle

All of them are different in nature and purpose. The test cycle is less complicated and is usually done before the start of the experimental campaign, and is repeated on a daily basis. The nature of the cycle allows for checking all of the components at a safe speed, causing less disruption in the case of a major emergency. The programming of the cycle was done by an external company – Micromech Systems Limited – as part of their commissioning undertaking.

Cycle type	Used for:
Experimental cycle	The experimental test cycle is the normal test procedure with a parabolic displacement profile (shown in Figure 3.1.5 and explained in Table 3.1.1 and in Part 3.1.7)
Test cycle	<p>The test cycle is a system check procedure. It is done at much lower velocities and acceleration values. It confirms the position sensor readiness and general alignment of the guide rails.</p> <p style="text-align: center;">This should be done in the first place prior to a test day campaign</p>
Emergency cycle	The emergency cycle is the stop and recovery procedure in case of abnormal operation. Can be activated manually or/and is activated automatically through software prescribed code (Part 3.1.8).

Table 3.1.2: Operational procedure cycles

The Figure 3.1.6 shows the flow of actions required based on test procedure and was developed specifically as part of the Drop Tower Safety Documentation. Here grey colour blocks are associated with the operational checklist. Red and blue highlight fault and normal flow, respectively.

In general terms, the test procedure starts with checking the electrical cabinet door is locked and switching on the personal computer (PC) to start the software programmes (the required software is usually launched automatically).

With the start-up of the PC and the initiation of the software, a digital log file is created. After a check on the electronics and control system is completed the High Voltage (HV)

power can be switched on (identified by the Light Emitting Diode (LED) light on the cabinet door). Power for the controller can now be switched on. This will be identified with a LED light on the control panel (Figure 3.1.4). The payload can now be positioned within the drag shield.

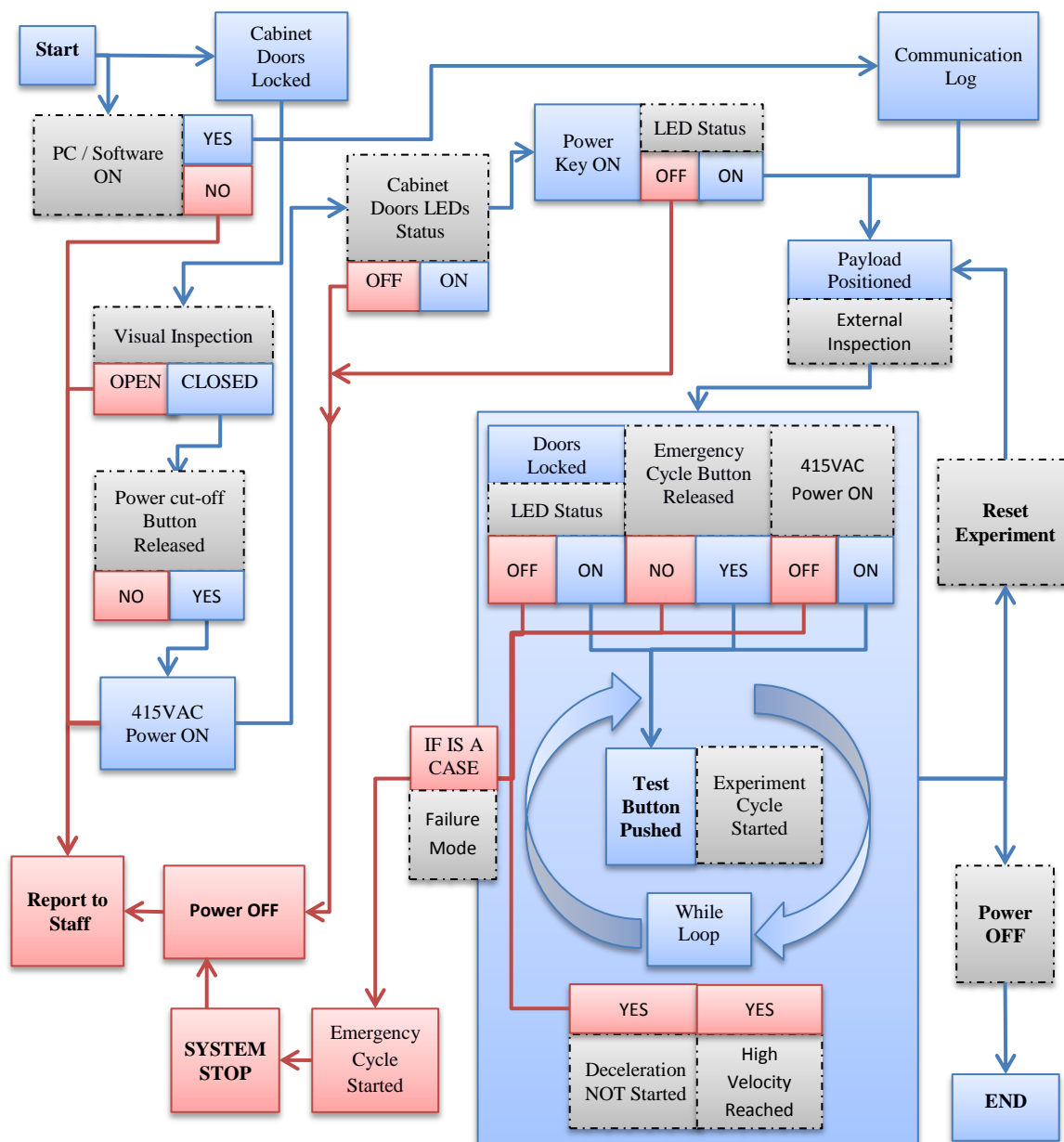


Figure 3.1.6: Drop Tower operational sequence diagram

(GREY – procedure check questions; RED – fault procedure flow; BLUE – normal operational flow)

To start a test cycle or experimental cycle, the drag shield door should be locked as well as the Drop Tower door. The status of the emergency shutdown switches is then checked to ensure that they are in the 'released' position. The experiment can now be started by pressing the "test start button" located on the control panel. The system checks if all safety

systems are locked, using safety relays and starts the experiment. While the experiment is in process the system monitors the safety relays and if any of them fails, it will direct the experiment to the emergency cycle. After the experiment is completed, it is possible to access the payload and reset it if needed.

In the case of failure during the experimental cycle and after the emergency cycle is finished the HV power should be switched off. It should be reported immediately to a staff member in the case of any failure.

```

                                Untitled
Microgravity research facility is ready for the use
Please enter today's day

DAY      03
MONH     10
YEAR     2013
HOURS    17
MINUTES  17

Total tests done #13
Time of drop tower used      0.0    s

-----
Select the test type
1 - Test Run, 2 - Microgravity Run, 0 - Close
Test selected #1
Test Run is awaiting a signal
Time      17      :      17

Ready to GO
Test started at      17      :      17
Test #      14      finished

Select the test type
1 - Test Run, 2 - Microgravity Run, 0 - Close
Test selected #0
Microgravity facility is stopped
Time      17      :      18

ANYTHING TO REPORT:  N/A

```

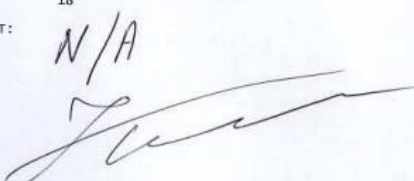


Figure 3.1.7: Drop Tower log file example

In addition to Figure 3.1.6, the Safety Operation Document includes the procedure checklist (Appendix B) and operational log files (Figure 3.1.7).

3.1.6 Final Drop Tower characteristics

The values summarised in Table 3.1.3 correspond to Drop Tower final measurements. The table is separated into four parameter groups: mechanical, performance, electrical and thermal.

Name of parameter	Value	Units	Comments
Mechanical			
Facility height	8.120 ± 0.01	m	
Mass of moving part	46.5 ± 0.5	kg	
Mass of payload	≤20	kg	
Performance			
Operational distance	6.83 ± 0.01	m	
Performance continue			
Maximum allowable speed	10.396	m/s	[46]
Test time ³	2.74	s	Calculated value only
Microgravity test ³	2.12	s	Calculated value only
Maximum allowable payload size	418.6	mm	
Selected maximum acceleration	5	g's	
Gravity quality	N/A		Was not checked
Electrical			
Supply voltage	215 ± 10%	V	Three phase with Earth
Supply frequency	50 ± 1%	Hz	
Digital Input/Output (I/O) voltage	24	V	Direct Current (DC)
Maximal force per motor	1170.0 ± 0.1	N	Two motors are used
Thermal			
Maximal operational temperature	70	°C	

Table 3.1.3: Commissioned Drop Tower characteristics

3.1.7 Microgravity test cycle calculations

The procedure for normal Drop Tower operation was outlined in previous subsections (3.1.4 and 3.1.5). The test profile is calculated based on three main inputs:

- Payload mass – M
- Size of the payload – B
- Gravitational acceleration required – ξ

³ Calculated for microgravity test conditions for 20 kg and maximal size payload

In addition to the main inputs the calculation considers separately the number of motors in operation ($N = 2$) and their efficiency ($\eta = 0.95$), and position sensor movement height ($H = 6.827$ m).

Due to performance limitations (maximum force per motor – $F_{max} = 1170$ N [44], maximum allowed acceleration – $a_{max} = 5g$ (49.05 m/s² and maximum allowable velocity – $v_{max} = 10.4$ m/s [46] the first step is to identify the acceleration required. The relationship between F_{max} and a_{max} and acceleration is:

$$a_{F(max)} = \frac{F_{max}N\eta}{M + M_{dry}} - g \quad | \quad 3.1.1$$

$$a_{a(max)} = a_{max} - g \quad | \quad 3.1.2$$

where: $a_{F(max)}$ – acceleration based on force limitation due to motors

$a_{a(max)}$ – acceleration based on maximum allowable acceleration due to payload constrain

M_{dry} – total mass of drag shield and trolley (46.5 kg)

g – Earth surface gravitational acceleration (9.81 m/s²)

The velocity gained is related to the acceleration distance (h_{acc}) by:

$$v^2 = 2ah_{acc} \quad | \quad 3.1.3$$

There will be same velocity change during the deceleration distance ($H + l - h_{acc}$) and they are related by:

$$v^2 = 2g(H + l - h_{acc}) \quad | \quad 3.1.4$$

where: $l = \frac{1}{2}(h_d - b)$ – additional payload movement for microgravity test (Figure 3.1.8)

Rearranging Equation 3.1.3 to find h_{acc} and substituting it into Equation 3.1.4 provides a relationship between velocity and acceleration:

$$v^2 = 2g(H + l - v^2/(2a)) \quad | \quad 3.1.5$$

In the case where limitations are caused due to the maximum allowable velocity, Equation 3.1.5 can be rearranged to find the acceleration value ($a_{v(max)}$) substituting v with v_{max} :

$$a_{v(max)} = \frac{v_{max}^2}{2\left(H + l - \frac{v_{max}^2}{2g}\right)} \quad \left| \quad 3.1.6 \right.$$

The acceleration that will be required to produce the required test profile is chosen based on a minimum value:

$$a = \min\left[a_F; a_{a(max)}; a_{v(max)} \right] \quad \left| \quad 3.1.7 \right.$$

The coordinate system is chosen such that the direction of positive motion is upwards and the zero is the sensor position (Figure 3.1.8). The following values were measured to be:

- $h_d = 0.97$ m – height of the drag shield
- $h_s = 0.365$ m – vertical displacement of the sensor read point from the centre of the drag shield

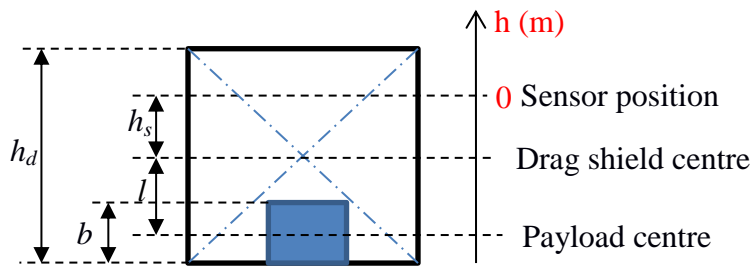


Figure 3.1.8: Drag shield sizing description

Rearranging Equations 3.1.5 and 3.1.3 to find the maximum velocity of the test (v) and height at which free fall starts (h_{acc}) gives:

$$v = \sqrt{(H + l) \frac{2ag}{a + g}} \quad \left| \quad 3.1.8 \right.$$

$$h_{acc} = v^2/2a \quad \left| \quad 3.1.9 \right.$$

In the case of low gravity tests, Equations 3.1.4 and 3.1.8 will change to:

$$a_{v(max)} = \frac{v_{max}^2}{2 \left(H - \frac{v_{max}^2}{2(g - \xi)} \right)} \quad 3.1.10$$

$$v = \sqrt{H \frac{2a(g - \xi)}{a + g - \xi}} \quad 3.1.11$$

The term $(g - \xi)$ incorporates the reduction from the normal earth surface acceleration due to gravity. In microgravity, this value is equal to zero.

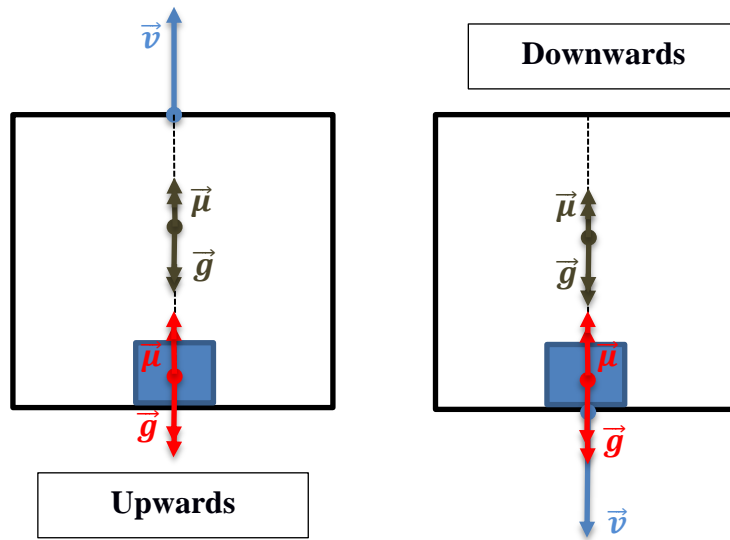


Figure 3.1.9: Low gravity test velocity and acceleration diagram

The reason for ignoring the payload movement in Equations 3.1.10 – 3.1.11 is that the test procedure requires the payload to be in contact with the drag shield. Figure 3.1.9 shows a velocity and acceleration diagram. The reason that the low gravity environment is created is that the payload always remains in contact with the bottom surface of the drag shield. In the upwards direction the drag shield is accelerated but making the velocity a bit slower than if it were in free fall, so it applies a force on the payload. At the same time in the downwards direction, the drag shield is accelerated by the Earth's gravity a bit less than the payload, so the payload is pushing on the lower surface of the drag shield.

The total test time can be found for the free-fall test and the low gravity test (respectively) using equations:

$$t = 2 \sqrt{2 \left(\frac{h_{acc}}{a} + \frac{H + l - h_{acc}}{g} \right)} \quad 3.1.12$$

$$t = 2 \sqrt{2 \left(\frac{h_{acc}}{a} + \frac{H - h_{acc}}{g - \xi} \right)} \quad 3.1.13$$

For the purposes of simulation, only some adaptations were required. These include the initial position of the payload and a slight deceleration of the drag shield to allow a non-contact free fall test. The payload initial position is set to be equal to $(-l - h_s)$, and after the acceleration is completed is equal to $(h_{acc} - l - h_s)$. At the same time just after the acceleration is completed the drag shield is decelerated to allow the payload to freely float in the centre of the drag shield. The drag shield is decelerated with maximum possible deceleration, which is selected based on the minimum value arising from the choice of maximum force (Equation 3.1.15) or maximum deceleration (a_{dec}):

$$a_{dec} = \min[a_{F(max)}; a_{a(max)}] \quad 3.1.14$$

$$a_{F(max)} = \frac{F_{max} N \eta}{M} + g \quad 3.1.15$$

The $a_{F(max)}$ has changed due to detachment of the payload and the deceleration direction is in the same direction as the gravitational acceleration. The distance travelled while the drag shield decelerates (h_{dec}) can be found based on the distance the payload has travelled and the velocity change (which is the same for both).

$$\begin{aligned} 2g(l + h_{dec}) &= v_f^2 - v^2 = 2a_{dec}h_{dec} \\ h_{dec} &= \frac{gl}{a_{dec} - g} \end{aligned} \quad 3.1.16$$

where: v_f – final velocity after payload detachment

The motor controller and servo drive are coded so that the acceleration is set depending on the velocity in the initial location and the future step velocity. The height changes with a

position sensor step size of $dx = 0.02$ mm [46]. To generate the required profile the system of dynamic equations of motion will be solved numerically:

$$\begin{aligned} h_n &= h_{n-1} + dx \\ v_n &= \sqrt{v_{n-1}^2 + 2a dx} \\ t_n &= t_{n-1} + \frac{v_n - v_{n-1}}{a} \end{aligned} \quad \left. \vphantom{\begin{aligned} h_n &= h_{n-1} + dx \\ v_n &= \sqrt{v_{n-1}^2 + 2a dx} \\ t_n &= t_{n-1} + \frac{v_n - v_{n-1}}{a} \end{aligned}} \right| 3.1.17$$

where: n – simulation step number

The code starts (Figure 3.1.10 and Appendix C) with setting up default constraints such as: $F_{max}, N, M, v_{max}, h_s, h_d, H$ and dx . The default constraints are defined as constraints, which are hard to change without mechanical design changes. The next step is to set adjustable or assumed constraints, such as: η, g and a_{max} , following input of parameters from the user such as: M, b and ξ .

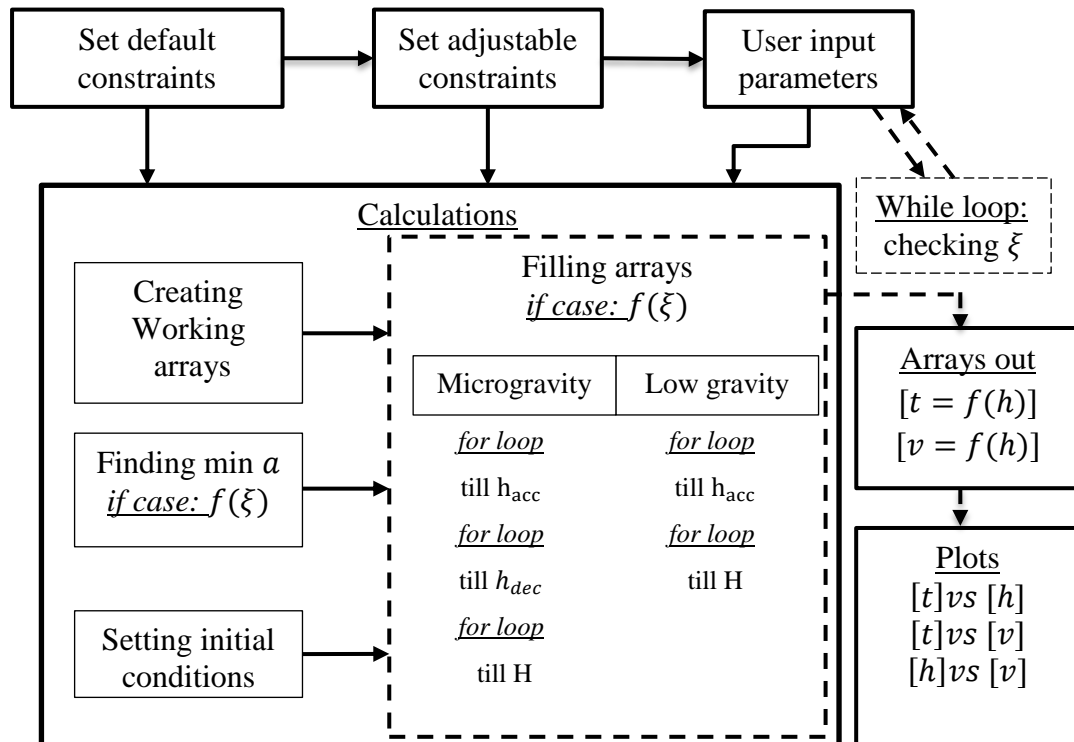


Figure 3.1.10: Drop Tower test profile calculation pseudo code

The value of the gravitational acceleration required must be checked to see if it exceeds constraints. The test profiles are limited by the value of the accelerating distance becoming

equal to zero ($h_{acc} = 0$). Using Equation 3.1.9 and substituting v^2 with the value from Equation 3.1.11, and rearranging gives the value of

$$\xi_{max} = g - \frac{a}{H - 1} \quad \left| \quad 3.1.18 \right.$$

When the default and adjustable constraints are confirmed, the calculation procedure can be started by entering the initial conditions. The minimal acceleration value is found using Equation 3.1.7 or 3.1.14. At this point, the data arrays for the drag shield and for the payload are created.

The position, velocity and time arrays are filled depending on the ξ value and the “for loops” are followed until a specific height is reached (h_{acc}). When the arrays are filled the results produced and plots are displayed (Figure 3.1.11).

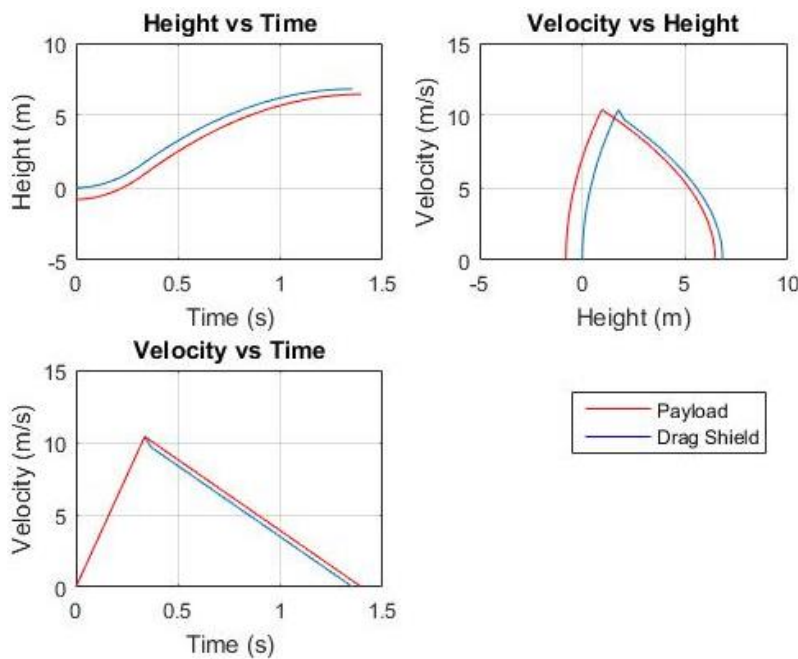


Figure 3.1.11: Drop Tower profile “MATLAB®” calculation code output

It is important to note that the simulation in Figure 3.1.11 was done for zero gravity, and for a payload of mass 20 kg and size 100 mm in height. The simulation shows only one-half of the test, the upwards direction, but it is understood that the graphs for both drag shield and payload will follow a similar profile in the reverse direction. The total test duration is 2.704 seconds, and microgravity conditions should last for 2.031 seconds.

3.1.8 Emergency cycle description

The emergency cycle was developed in the case of an error in the normal operational cycle. This can happen due to a performance error in either the control system or the motors (e.g. errors in a signal timing, high temperature of the motors, fault in door locks, fault in limit switches, etc.), or human error (the simulation code was set wrongly), or if any emergency shutdown buttons were activated. The emergency cycle allows the safe return of the drag shield and the payload to the initial location.

The motor controller monitors three inputs:

- A temperature error signal
- The top position limit switch
- The emergency shutdown relay

In the case when abnormal operation is detected, the system recalculates the motion profile. The emergency cycle does not depend on the direction of the motion. In both directions, the drag shield is first decelerated at the maximal allowable rate (using Equations 3.1.2, 3.1.14 – 3.1.15) and then slowly returned down. This is done by the motor controller and in the case of failure, using the equations just mentioned it recalculates the profile and adjusts the velocity profile to meet the required values.

3.1.9 Additional design characteristics

The payload mass, size of the experiment and test time (Figure 3.1.13), as described in subsection 3.1.7 are limited by the position sensor speed constraints, which is 10.4 m/s [46], the maximal force of the motors, 1170.0 N [44], and by design constraints on the maximal allowable acceleration or deceleration.

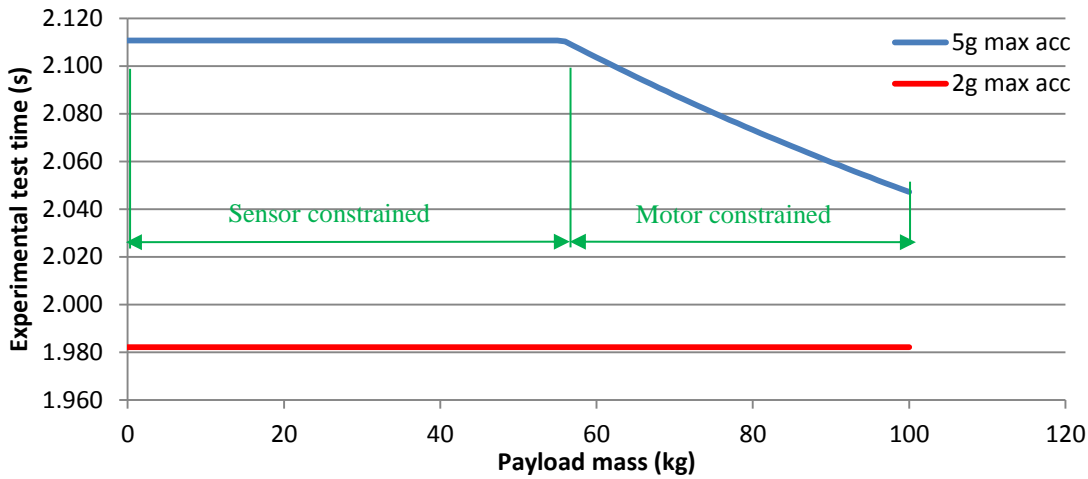


Figure 3.1.12: Test time and mass dependence (for zero gravity test)

Figure 3.1.13 illustrates that the experimental time does not depend on the mass of a payload until a threshold value is reached (Figure 3.1.12 – blue line). In this region, the constraint is due to the allowable sensor speed. For example, for a free fall environment the allowable mass of the payload with no effect on test time is around 55 kg. After this point, the experimental duration starts to reduce due to limitations on the maximal catapult velocity achieved due to the maximal allowable motor force. The acceleration or deceleration can be adjusted for payloads that are more sensitive. When reducing the maximal allowable acceleration/deceleration this will reduce the test time (Figure 3.1.12 – red line). As a matter of fact, the limitation on the test time arises only due to the implied acceleration limit. On the other hand, with a reduced maximal acceleration this allows for a bigger variety of experiments on board.

In low gravity experiments, the test time can be increased (Figure 3.1.13). It does not mean it will increase for all potential payload masses. For example, the 0.030g low gravity test shows that at payload masses higher than ≈ 47 kg the test time will be lower than in the free fall test. This is due to the additional time acquired by the free fall test when the payload is allowed to separate from the drag shield. The test time increases with an increase of the required gravity level.

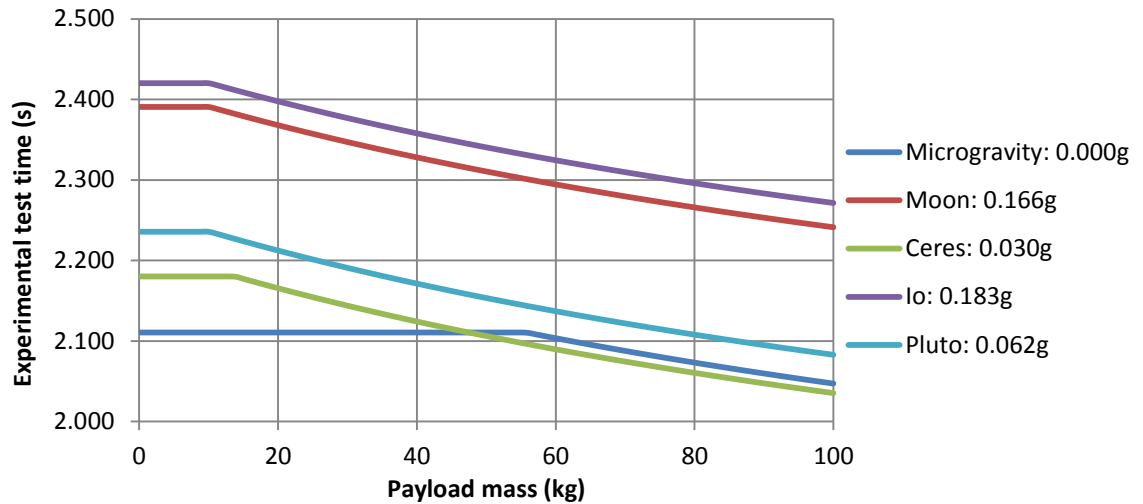


Figure 3.1.13: Payload mass, micro-gravity quality and test time dependence
(Height of the payload was taken as 100 mm for all cases)

Due to the use of the catapult principle, the experimental payload is accessed in the same area, minimising the test reset time. The use of the linear actuators to drive the experiment increases the available test time. If there is no requirement to reset the payload, (the experimental payload is self-contained) the test can be repeated with no waiting time. The only limitation here is the motor temperature. Allowing a little time for air-cooling of the motors the Drop Tower is expected to run up to 4600 tests a day and reach approximately 2 hours and 48 minutes of total microgravity test time.

3.2 Drop Tower work management

The Drop Tower work included several interlinked aspects. First, it was required to understand the initial design. Secondly, to assemble the structure and, if required, to design and manufacture missing components. Thirdly, to calibrate the system for operation. Finally, full commissioning of the facility.

The size of the development and complexity of the system required the use of management procedures to make sure the workflow occurs in the right order. The project required an additional budget for the purchase of missing components, and due to the scale of the

project budget monitoring was important as well. It required constant communication between the supervisory team, suppliers and the finance department.

The work did face several delays due to unforeseen reasons and was required to adopt a constantly changing support level. This required continuous communication with all interested parties, to allow the project to continue.

The following subsections will discuss the overall work, which was undertaken to make sure that the Kingston University Drop Tower was ready for operation. Unfortunately, the drop tower was still not completed and the project has now been closed.

3.2.1 Work assignment statement

It was required to fully build, test and commission a microgravity research facility at the Kingston University Roehampton Vale campus. Unfortunately, the commissioning was not completed, but some of information on possible future steps will be summarised in section 3.6. The work included the assembly of hardware components using tools fit for purpose to allow for high strength and durability for a long duration of use. In addition, several procedures were developed and implemented to calibrate the drive system and to achieve the required microgravity performance. The commissioned Drop Tower should be targeted at a wide range of audiences, which implies that the developed facility should have safety systems in place to minimise the risk to anyone (including staff, students and visitors).

Project pack documentation was developed, which included a health and safety assessment, a project outline with a time frame, a laboratory time sheet and a risk assessment. The job required work at heights, so all-necessary training was completed prior to the start of the work assignment. In addition, several hardware components required designing and manufacturing in the workshops.

The work time management was self-arranged but within the deadlines outlined by the supervisory team. Stock orders, tool hiring and off-site contractors were self-arranged and confirmed with the supervisory team.

After the work completion, user documentation was developed, indicating the operational procedure, maintenance procedure, risk assessment, failure mode analysis and bill of materials.

3.2.2 Work Planning

The work was divided into eight parts (Figure 3.2.1, a full version of work plan is available in Appendix D) which followed one from another. The steps presented were considered important milestones. The first target was to achieve an understanding of the project to be carried out. This included the study of the proposed Drop Tower design, developing a project plan and revising the existing stock list. At the same time, it was required to prepare project pack documentation and attend training sessions for the cherry picker and scissor lift operation.

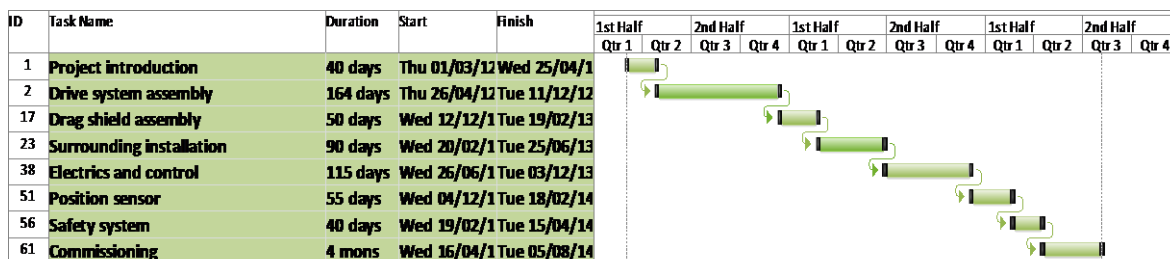


Figure 3.2.1: Drop Tower work project milestones (updated 2014)

Drive system assembly work (discussed later in subsections 3.3.1 – 3.3.3) included the development of the alignment procedure (subsections 3.4.1 – 3.4.6). This was done to confirm the operational plan for the installation of the magnetic track, followed by guide rail installation. Additional component manufacturing was required. In addition, a scissor lift was required for assembly purposes.

After the drive system was completed work followed by assembling and installing the drag shield (subsection 3.3.4). The drag shield was hooked up to the trolley attached to the guide system. The following step was to assemble the surrounding structure (subsection 3.3.5). Installation was carried out in four sections and for this purpose, the cherry picker was required. Additional components purchases were made (such as aluminium profiles, connectors and “Lexan” polycarbonate sheets).

The electronic system assembly (subsection 3.3.6) was done by a contracted company – “Micromech Systems Limited”, who determined the initial selection of components. The installation of electronic components includes drag shield components, surrounding safety systems and the control panel. The wiring was enclosed in cable trunking and the connection between the drag shield and the surroundings were made via flexible snake trunking.

Position system installation included the development of the sensor attachment bracket, followed by installing the sensor and testing sensor operation (subsection 1.1.1).

Finally, the safety system was installed, which included soft flooring and a damper system (subsections 3.3.8 – 3.3.10).

After the assembly of all systems was, completed work needed to proceed to final commissioning. The initial control system was developed by Micromech. They also approved the electronic safety system. Documentation for the operation, maintenance and safety were produced.

3.2.3 Work Budget

The overall Drop Tower budget can be separated into two different sections. The first is the purchase of initially planned components and the second is the budget expenditure on assembly and commissioning work. The first phase includes the greater part of the budget and included pre-manufacturing of the main structure and purchase of the drive system

components. The second phase budget (Table 3.2.1 and Appendix E) was part of the work carried out by the author and described here. This included the expenditures required to fully assemble and commission the Drop Tower.

The second phase budget is divided into five main categories. Other expenses included the purchase of tools or hire and delivery payments. The main expenses were part of the electronics, control and structure categories totalling approximately 70% of the total budget spend.

No.	System element	Supplier	Cost (£)	VAT
1	Control	Magnetic Shielding	2,539.30	507.86
		Micromech	1,134.11	226.82
		National Instruments	223.74	44.75
		RS	311.83	62.37
2	Electronics	Amethyst Design	216.00	43.20
		KUSCO	984.22	196.84
		Micromech	8,562.00	1,712.40
		RS	339.58	67.92
3	Structure	Direct Plastic	184.36	36.87
		RS	964.03	192.81
4	Safety	RS	11.82	2.36
		AnyFoam	35.56	7.11
		Simple Foam Products	218.96	43.79
5	Other	Already Hire	1,280.00	256.00
		RS	32.20	6.44
		Micromech	30.00	6.00
		Magnetic Shielding	40.00	8.00
Sub-total (£)			17,107.71	3,421.54
Grand total (£)			20,529.25	

Table 3.2.1: Assembly works budget breakdown

3.3 Drop Tower assembly work

Drop Tower assembly work planning was described in subsection 3.2.2. The following section will provide detailed information on all actions taken to fully construct the facility.

A list of the actions associated with the assembly work can be separated into eight systems:

- Magnetic track installation (subsection 3.1.1)
- Guide rail installation (subsection 3.1.2)
- Trolley and motor installation and testing (subsection 3.1.3)
- Drag shield installation (subsection 3.1.4)
- Surrounding installation (subsection 3.1.5)
- Electronics installation (subsection 3.1.6)
- Position sensor installation (subsection 3.1.7)
- Safety system installation (subsections 3.1.8 – 3.1.9)



*Figure 3.3.1: CAD drawing of the main support structure (Isometric view)
[by permission of B. Osborne]*

The initial manufacturing work and main support structure were completed before the start of this project. This included the Computer Numerical Control (CNC) manufacturing of the main support structure (Figure 3.3.1), CNC manufacturing of the magnet base plates, manufacturing of the L-brackets and cutting to size of the ground level surrounding support structure with its acrylic safety sheets.

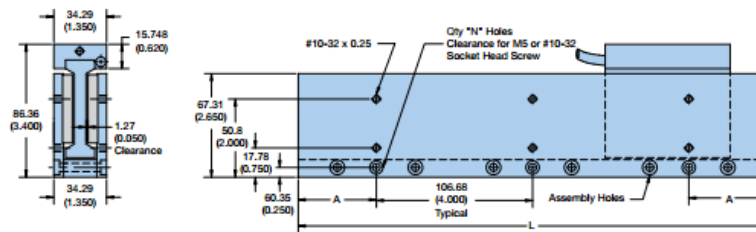
3.3.1 Magnetic track installation

The magnetic track installation required inspection of the attachment surface for any roughness on the surface of the main support beam and smoothing this to increase the

alignment precision, followed by attachment of the magnets to the base support and then attaching these and aligning them to the main support structure along the driveway.

Magnets were purchased from “Parker Hannifin Corporation” (Figure 3.3.2). The track (31009M-N) length is 243.84 mm, which required 33 tracks to be installed in order to cover the whole track. The fixing points were located at the bottom of the track. The clearance was 1.27 mm (or 0.05 inch), and it is important to note for future alignment procedures that the minimum offset was chosen to be 0.01 inch or 0.254 mm. The safety margin was chosen to minimise damage in case of an accident.

310xxS Single Piece – mm (in)



	310xxM Modular	310xxM1 Modular	310xxS Single Piece
Incremental Length – mm (in)	60.96 (2.4)	60.96 (2.4)	30.48 (1.2)
Minimum Length – mm (in)	121.92 (4.8)	121.92 (4.8)	213.4 (8.4)
Maximum Length – mm (in) (for single piece)	1584.96 (62.4)	1584.96 (62.4)	1615.4 (63.6)
Weight – kg/m (lbs/ft)	12.7 (8.50)	12.7 (8.50)	12.7 (8.50)

Figure 3.3.2: Magnet track specifications

(L=243.84mm) [44]

The magnets are attached to the base plate (Figure 3.3.3) via four fixing screws synced inside the plate. A scissor lift was ordered to proceed with the installation. The alignment procedure is explained in the subsection 3.4.1. Nylon nuts were used for fixing the plates to prevent them from unfastening due to vibration when the Drop Tower becomes operational. A gap of approximately 1.5 m was left at the bottom of the Drop Tower to allow for future integration of the trolley with the motors.

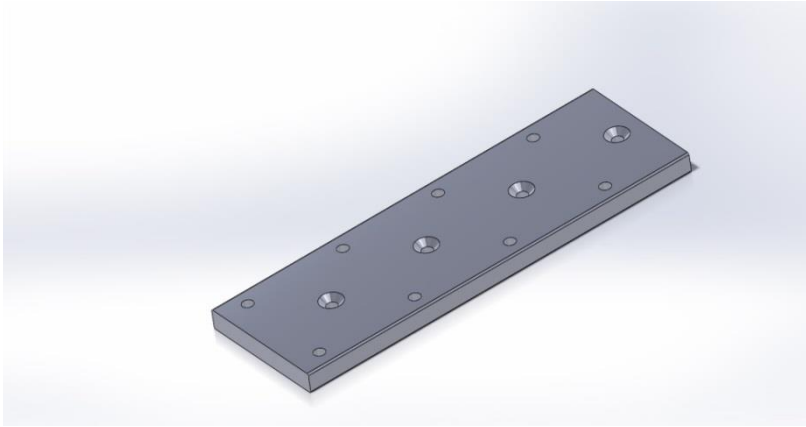


Figure 3.3.3: CAD of the magnets base plate (Isometric view)
[by permission of B. Osborne]

3.3.2 Installation of the guide rails

Installation of the guide rails was a major part of the construction process and took most of the time due to alignment requirements. The guide system consists of 124 L-brackets, 16 guide rails and 14 rail joints installed on the both sides of the magnetic tracks.



Figure 3.3.4: Guide rails with guide rollers
(LLEHS 25 Speedi-Roll)

The guide rails used are “SKF Group” LLEHS 25 Speedi-Roll (Figure 3.3.4, [47]). Each rail is 1 m in length. They are fixed to the L-brackets by eight fixing points.

The guide rails are joined by guide rail joints manufactured in house using mild steel. The requirements for the rail joint were:

- It should make a solid and smooth connection between the rails
- The joint should fit inside the rail, so there will be no obstruction to sliding components

The rail joint is made to fit snugly inside the guide rail, which does not allow for lateral movements. At the same time, the fastening holes in the rail joints are offset (Figure 3.3.5, Left) in a way that allows for constant compression between the guide rails and tension in the rail joint.

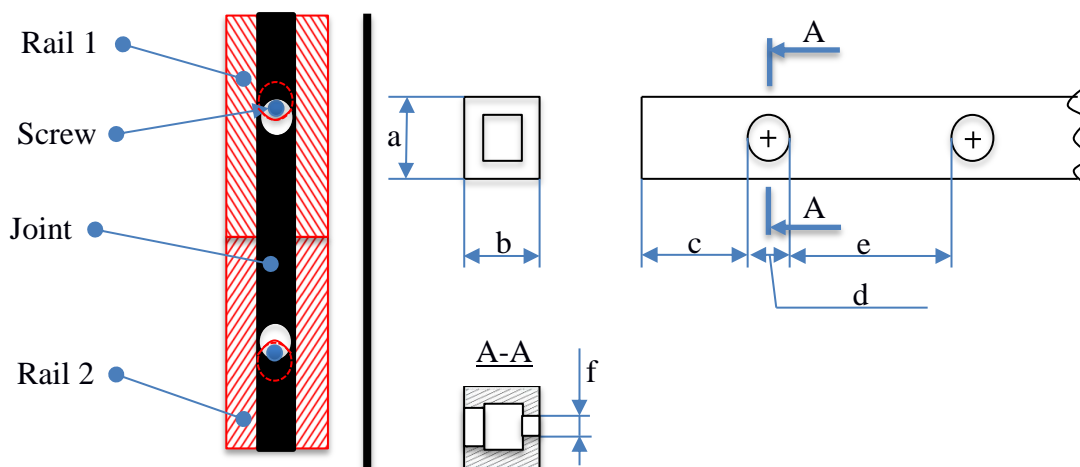


Figure 3.3.5: Rail joint connection and measurements
 Connection schematics (Left); Measurements schematics (Right);

Several measurements were made to confirm the actual sizes of the guide rails (Figure 3.3.5 – Right and Table 3.3.1). The measurements were taken using a digital Vernier calliper using different guide rails for measurement. In the final design of the rail joint (Figure 3.3.6) the required dimensions were averaged. The joint consists of four holes (two per guide rail), allowing for additional fixtures and limiting the rotation of the joint in case of a fault in manufacturing. The offset of the holes was calculated based on the M6 bolt major diameter of 5.978 mm (maximum value, fine thread series [48]) the offset was calculated to be 0.269 mm:

$$O = \frac{D_{dr}}{2} + \frac{D_{GR}}{2} - D_b \quad \left| \quad 3.3.1 \right.$$

where: D_{dr} – diameter of the drill bit (selected as 6.2 mm)

D_{GR} – average diameter of the guide rail hole (6.294 mm)

D_b – M6 bolt maximal major diameter

Measurement	No.1	No. 2	No. 3	No. 4	No. 5	Average
	±0.001	±0.001	±0.001	±0.001	±0.001	±0.001
	(mm)	(mm)	(mm)	(mm)	(mm)	(mm)
a	10.998	10.947	10.922	N/A	N/A	10.956
b	12.929	12.827	12.954	N/A	N/A	12.903
c	56.998	57.379	56.921	57.074	N/A	57.093
d	10.947	10.871	10.922	10.871	N/A	10.903
e	113.919	114.198	113.970	113.970	N/A	114.014
f	6.248	6.223	6.350	6.198	6.452	6.294

Table 3.3.1: Rail joint measurements

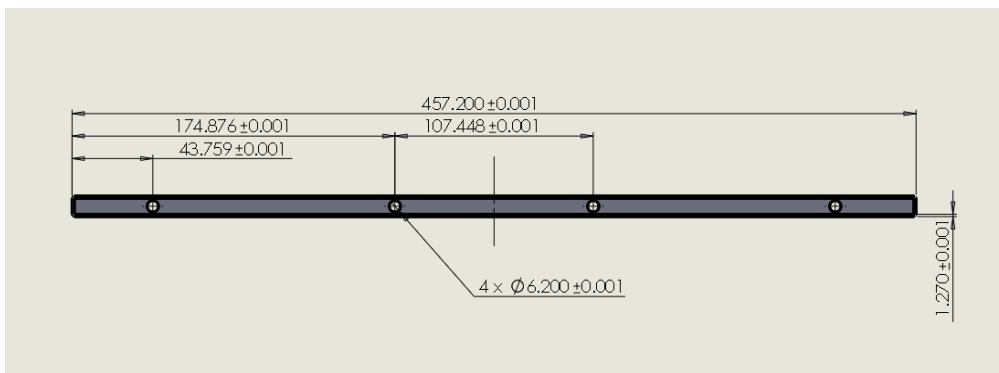


Figure 3.3.6: CAD of the rail joint (Top view)

The L-brackets (Figure 3.3.7) were made from a solid L-shape mild steel profile and holes were made using a CNC machine. The L-bracket was fixed to the main support structure using two bolts with nylon nuts (to prevent loosening due to vibration), and then the guide rail was fixed to the L-brackets.



Figure 3.3.7: L-bracket with adjusting screws

The positioning of the L-brackets is calibrated using four base screws. The transition between the rails was checked visually with the aid of spare guide rollers, which needed to slide with no obstruction at the transition point.

Similarly, to the magnetic track the bottom guide rails were not installed until the trolley with motors was put up. For safety reasons both rails have the end brackets fixed at each end, to prevent the trolley sliding out in case of an emergency. The alignment process of the guide rails will be discussed separately (subsections 3.4.2 – 3.4.5). The alignment calibration (subsections 3.4.4 and 3.4.5) will later verify that the installation meets the design requirements. The connection between the rails produces no obstruction to the trolley movement and there is a limited amount of the movement at intersections that can be ignored.

3.3.3 Trolley and motor assembly, installation and testing

The trolley is part of the drive system and is the attachment point for the motors and drag shield (Figure 3.3.8).



Figure 3.3.8: Trolley with the motors attached to the rails

The purpose of the trolley is to slide up and down following the guide rails. The trolley design and Finite Element Analyses (FEA) were conducted prior to the start of this project. The mass of the trolley was measured as 5.5 ± 0.5 kg. It is CNC machined aluminium plate of 10 mm thickness.

It was designed to allow three motors to be installed, but based on the selected drop tower performance characteristics only two were needed at the moment.

The trolley is mounted onto the guide rails using five sets of guide rollers per side. The rollers and motors were aligned and correctly spaced to meet alignment constraints (a detailed explanation of the alignment will be given in subsection 3.4.6).

The motors used are “Parker Hannifin Corporation” 310-6M-NC-WD7T [44] with a six pole coil size, no cooling and triple winding specifications. The peak force of the motor is rated at 1170.0 N.

The trolley with the motors already aligned was installed from the bottom of the guide system. The motors were required to be slid into the magnetic track. For this specific reason, the first 1.5 m of the magnetic track and guide rails were not installed, as mentioned previously. After the trolley was installed, the last magnetic tracks and guide rails were installed and aligned.

The motor and trolley checking procedure included the visual inspection of free (non-contact) sliding over the whole track length, as well as checks of the correct motor spacing. The last was done to make sure that the coils of the motors are not misaligned (which will mean that the motors act one against another thereby reducing the total performance capability). The procedure for the test was the following:

- First, the trolley was raised and fixed at 200 mm above its ground level
- Both ground (GND) wires of the motors were grounded.
- One phase wire of a single motor was connected to the power source positive terminal (the terminal was required to be able to supply 24 V Direct Current (DC) which is able to provide at least 2 A of current)
- The trolley was detached and was left to hang using only coil traction
- The same phase wire of the second motor was connected to the positive terminal
- Any change in the trolley position was checked and noted
- The first motor was disconnected from the power source
- Any change in the trolley position was checked and noted

When one of the phases of the first motor is energised, the trolley aligns with the magnetic track magnets. If the motor spacing is incorrect, the energising of the same coil of the

second motor will lead to movement of the trolley. Similarly, de-energising one of the motors in the case of incorrect motor spacing will lead to trolley movement. All three phases were checked, and the position of the motors was adjusted to align the coils. For the test, two power supply units were used, both capable of delivering 30 V at 3 A current.

3.3.4 Drag shield assembly and installation

The drag shield is made of pre-cut “Bosh Rexroth” 30 mm square aluminium profiles (Figure 3.3.9, [49]). “Bosh Rexroth” aluminium profiles allow for easy assembly using a slotted structure. The connection of the structure was made using right angle and 45-degree angle die-cast aluminium connectors from the same company.

Clear “Lexan” polycarbonate sheets [50] are used as a cover material, due to their good impact resistance. The sheets are fixed directly onto the drag shield structure from outside. To restrict any airflow as well as to identify the moving hazard black and yellow tape with adhesive backing is applied to the edges of the drag shield.

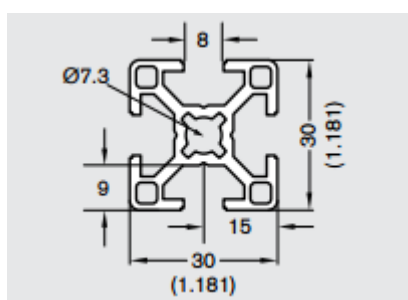


Figure 3.3.9: “Bosh Rexroth” 30x30-aluminium profile [49]

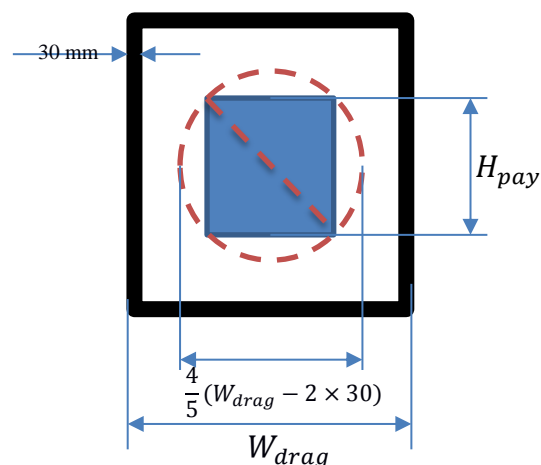


Figure 3.3.10: Payload advisable sizing calculation

The outer size of the drag shield is 970×800×800 mm (Height × Depth × Width). The advisable payload size was set to be 418.6 mm cubed. This is assuming that the payload is allowed to freely rotate inside the drag shield (Figure 3.3.10), as per the test description in

subsection 3.1.4 and the free space distance margin of 1/5 of the inside distance is included.

$$H_{pay} = \sqrt{\frac{1}{2} \left[\frac{4}{5} (W_{drag} - 2 \times 30) \right]^2} = 418.6 \text{ mm} \quad \left. \vphantom{H_{pay}} \right| \quad 3.3.2$$

where: H_{pay} – payload maximal length (height, width and depth)

W_{drag} – outer width of the drag shield (measured in mm)

The design FEA considered a minimum factor of safety of 1.5 when loaded in the worst-case scenario is when the drag shield and payload mass is represented as a point load of This occurs 70 kg at the extreme front end location and is accelerated at 5g. The actual mass of the drag shield is 41 ± 0.5 kg (front and back mass distribution is 17.5 ± 0.5 and 23.5 ± 0.5 kg accordingly) and at the moment the centre of mass is located at 341.4 ± 15.4 mm from the outer front. The mass of the payload was selected to be 20 kg bringing the total mass of the moving part including the payload to 66.5 kg (the mass of the trolley is 6.5 kg – subsection 3.3.3). The difference here was set for additional safety.

The drag shield door is front facing and opens outwards. A key lock was installed for safety reasons.



Figure 3.3.11: Drag shield attached to the trolley

The drag shield is fixed to the trolley with four M8 bolts and two M6 threaded rods. The threaded rods are fixed to the trolley under the motors and are used as positioning fixtures. The drag shield is first hooked up onto the threaded rods. Then it is brought to the correct position by tightening the nuts on those rods. Finally, when the drag shield is in the correct position, it is fixed with the main holding bolts (Figure 3.3.11).

3.3.5 Surrounding installation

The purpose of the surrounding is to enclose the test area for safety reasons. The enclosure requirements are:

- To limit access to people while the test is running
- To protect people outside from hazardous particles in case of Drop Tower failure

The surrounding structure uses similar components to the drag shield from the “Bosch Rexroth” range [49], namely aluminium profiles of 90 and 45 mm square sections. It also incorporates various connectors depending on the profile size. Due to its easy construction and limitations on the length of the aluminium profiles available, the drop tower surrounding is built in four sections. Before assembly was started, all the required parts apart from the top section (level three sections) were pre-cut. Level three sizing was done after the three other levels were installed due to the surrounding constraints from the roof of the laboratory (structural beams, pipe work, etc.).

The ground level section is made with a mix of 45 and 90 mm square profiles and with the “Lexan” polycarbonate sheets fitted in the middle of the structure (Figure 3.3.12). A polycarbonate cover was installed at the back of the tower only at ground level to limit accidental access. It was not necessary to install it at any other level, as it did not raise any hazard. A lockable door is installed at front and it opens outward. This section is fixed to ground support beams at four points with bolts. The lockable door and use of polycarbonate sheets fulfil the requirements for the surrounding.



Figure 3.3.12: Ground level section assembled

A rear support structure (Figure 3.3.13) is used to isolate the surrounding from horizontal movements, and in simple terms acts as a leash.



Figure 3.3.13: Back support structure

Level one and two follow a similar structural arrangement as the first one but use only 45 mm square profiles with 90° connectors. The structure of levels one and two can be represented as a rectangular frame where the bottom strut is a bit offset from the edge, leaving a space for airflow. The polycarbonate sheets are attached on the outer surface, also leaving a small gap at the bottom (Figure 3.1.1).

The design of the third level is similar to the previous two. It uses “Bosch Rexroth” 45 mm square profiles with 90° and 45° connectors. The maximal allowable height was found to be 1500 mm and for the purpose of stiffening the structure, a top diagonal crossbar was added.



Figure 3.3.14: Third level section CAD (Isometric view)

The assembly of the surrounding required the use of a cherry picker. The cherry picker location was limited and it could not be directly positioned facing backwards or on the left side of the structure. The cherry picker was positioned directly facing the right side of the Drop Tower, and for that reason, a specific assembly approach was used. The approach for the assembly was as follows:

- Install the back structure
- Install the back support structure (which is already assembled prior to this on the ground)
- Install the structure on the left side (the full side was already assembled on the ground with the “Lexan” sheet attached)
- Install the front structure
- Install the right structure
- Install “Lexan” sheets on the right and front sides

3.3.6 Electrical system installation

Most of the electrical system for the Drop Tower was developed by Micromech, who also certified the safety of the electronics system safety. The list of deliverables, which was required from them, included:

- Control panel development, with fan, filter, housing servo drive, 24 V DC Uninterruptable Power Supply (UPS), controller, emergency stopping relays and control gears
- Existing control unit rewired with a 4-meter cable
- Emergency stop pod (to be mounted by the Drop Tower door) with a 9.5 m cable
- High-flex motor power cable, 15 m long
- Junction box for joining two motor cables into one high-flex cable
- Electrical drawings (Appendix F)

All electronic components can be separated into five groups:

- Drag shield components
- Drop tower components
- Electronics cabinet
- Control unit
- Wiring

Drag shield components include a drag shield door limit switch, a video camera, a 3-axis accelerometer and two thermocouples. All of these components can be disconnected just outside the drag shield if maintenance is required.

The temperature of the motors is checked by the servo drive. Unfortunately, due to limited port availability in the servo drive, it is possible to monitor only one motor temperature. In the case of a motor overheating the servo-drive shuts down the power to the motors, which will lead to an uncontrolled fall of the drag shield. For this reason, additional K-type thermocouples were installed to continuously monitor the temperature (Figure 3.3.15).



Figure 3.3.15: Thermocouple attached to a motor

The thermocouples are directly attached to the motors and the signals are processed by the “National Instruments” NI USB-6210 Data Acquisition (DAc) [51]. The sensing is done continuously at 2.4 Hz (allowing for around five sample readings per test).

In the case of overheating (selected as any temperature exceeding 70 °C – which is below the servo drive limitation of 100 °C), a red Light Emitting Diode (LED) activates on the control unit. There are two LEDs, one for each motor (Figure 3.1.4).

The limit switch in the drag shield monitors whether the door is closed and sends the signal to the controller if it is not. Before the start of the experiment the drag shield door should be closed, otherwise, the controller will not allow the tower to operate. The system enters the emergency cycle if the switch becomes open during a test.

In addition, a camera and 3-axis accelerometer is installed for information and outreach purposes. As an accelerometer is attached to the drag shield the value of microgravity is somewhat compromised due to vibration of the system.



Figure 3.3.16: Drop Tower ground level

Drop tower components include a door guard lock, top and bottom position limit switches, a position sensor and an emergency stop pod. An emergency stop pod (Figure 3.3.16) is installed just outside the surrounding doors. In an emergency when the emergency button is activated the drive control reverts to the emergency cycle and returns the drag shield to ground level.

A surrounding Allen-Bradley guard lock TLS-GD2 [52] is used to lock the door. It is normally closed when not powered. In addition, when the test is in operation the door is locked automatically. This prevents accidental access to the facility. In the case of emergency or power cut off the door lock is connected to a time relay, which is set for 10 seconds, and it will unlock the door only when this duration has passed. Another safety feature includes an incorporated limit switch, which does not allow the test to proceed if the door is not closed.

There are two limit switches installed. One indicates ground level and it is normally closed when the drag shield is at ground level. In the case when the limit switch signal setting is low, the operation of the Drop Tower cannot be started. In addition, when the test cycle is finished and the sensor reads a 'closed' signal but the motors are still in operation, the motor controller will cut the power from the motors. Another limit switch is installed at a height of 5.283 ± 0.001 m above the position sensor. It sends a signal to the motor controller at a height of 5.312 ± 0.001 m when the drag shield is moving upwards, to check the running velocity. Another signal is sent when the drag shield is moving downwards at a height of 5.254 ± 0.001 m. These signals are used to check if the drag shield velocity is not exceeding dangerous limits, which might result in an overshoot of the final position and damage to the facility. In the upwards direction the drag shield might end up hitting the top brackets and in the downwards direction hitting the dampers. To confirm that the drag shield velocity is not beyond dangerous limits the threshold velocity value (v_{sens}) can be found using the following equation:

$$v_{sens} = \sqrt{2(g - \xi)(H - h_{sens})} \pm 0.004$$

where: g – acceleration due to gravity

ξ – required gravitational acceleration

H – drag shield movement height

h_{sens} – sensor position height ($h_{sens} = 5.312\text{ m}$ in the upwards direction and $h_{sens} = 5.254\text{ m}$ in the downwards direction)

Using a zero gravity level the approximate error value based on a measured height error was calculated to be $\pm 0.004\text{ m/s}$. If it is assumed that, the velocity will continue to increase in a parabolic manner the final value before deceleration will be over by 0.046 m/s . The position sensor dictates that the maximal velocity is limited to be 10.4 m/s , for this reason, it is advised to decrease the maximal allowable velocity from 10.4 to 10.396 m/s .

The wiring used is standardised and clearly numbered (based on the circuit diagram in Appendix F). The following wire colour code was used:

- Alternating Current (AC) power– Brown, Black and Grey – supply lines, Light Blue – neutral
- DC control circuit and Input/Output (I/O) – Dark Blue
- Earth – Green/Yellow

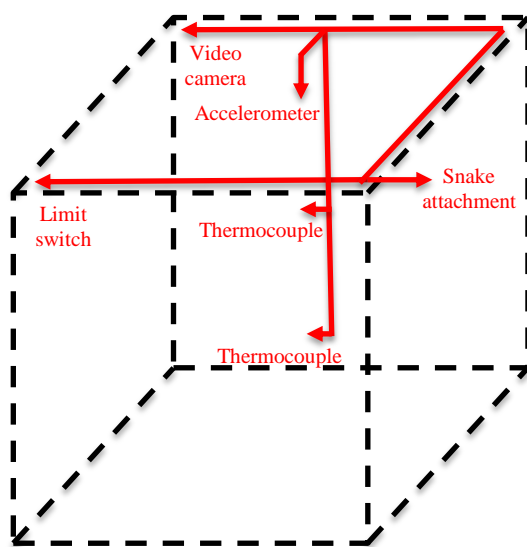


Figure 3.3.17: Drag shield wiring

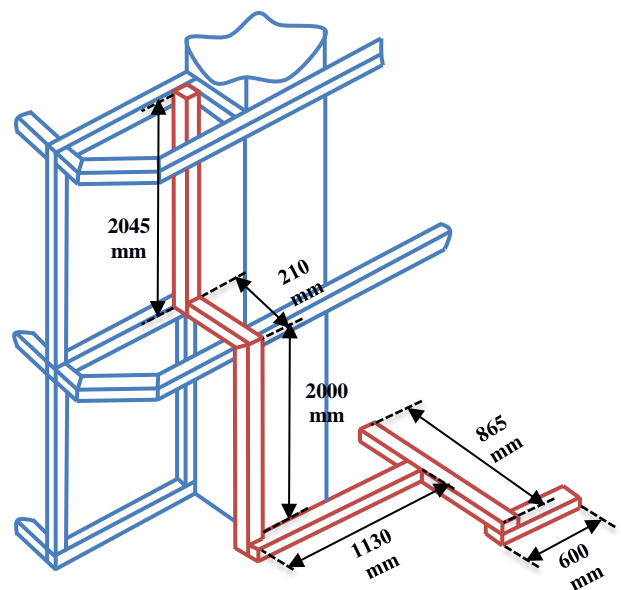


Figure 3.3.18: Drop Tower cable trunking sizing

The wiring was done in two separate sections. This was done to allow the drag shield to be easily detached for maintenance. The drag shield wiring electronics lines are shown in Figure 3.3.17. The wiring is enclosed under a plastic cover to reduce possible obstruction.

Just outside the drag shield, the cables are enclosed in flexible cable snake trunking, which allows keeping the cables safely connected to a moving drag shield. The cable snake is attached to the top of the first level (Figure 3.1.1), where the cable enclosure starts. Cables are fully enclosed and follow around 7 meters of trunking (Figure 3.3.18).

The control panel (Figure 3.3.19) consist of a key switch, illuminated push button, green status LED, test start button, emergency shutdown button and six red status LEDs. A key switch and illuminated push button wired in series activate the control panel (the push button is illuminated green when 'ON'). The green LED shows for easy reference that the 24 V DC UPS supply is active. The test start button is enclosed under a protective cover to protect it from accidental activation and allows activation of a test procedure. It is directly wired into the motor controller input.



Figure 3.3.19: Drop Tower control panel

The emergency shutdown button activates the emergency cycle and is wired into the emergency stop relay. Two red LEDs indicate that the drag shield and surrounding door are closed. Two others are used as overheating indicators in the motors. Two other LEDs were left as spares.

The main control panel is a “Rittal” AE1260.500 wall mounted panel, with dimensions of 600mm x 1200mm x 300mm (Width x Height x Depth). The wiring enters through cable glands and an RS-232 connector. The control panel is located in a corner with the door hinged on the left-hand side. The cable glands and the RS-232 connector are fitted on the right-hand side. The cooling fan is installed at the bottom of the right-hand side, with an air outlet on the top right-hand side. The cabinet main components include:

- Main power isolator
- “Crouzet” MWUA 3-phase monitoring relay
- “Phoenix Contact” 24 V DC UPS with battery module
- 415-230 V AC 3-phase power transformer
- “Parker Hannifin Corporation” ElectroMagnetic Compatibility (EMC) filter
- “Parker Hannifin Corporation” brakes resistor
- “Allen Bradley” MSR138.1DP emergency-stop safety relay with time delayed output and manual reset

All electrical components are powered externally from a 415 V AC 3-phase power source. This source is constantly monitored by a “Crouzet” 84873025 MWUA 3-phase monitoring relay [53]. The main input power line is separated and feeds into a 24 V DC “Phoenix Contact” UPS with battery module [54], transformer TTP3 7.5kVA 3-phase transformer (to reduce the drive voltage to 230 V AC 3-phase), air cooling system, and cabinet LED indicator (to identify the presence of High Voltage – HV). The transformer power lines are then filtered using a “Parker Hannifin Corporation” EMC filter and connected to a “Parker Hannifin Corporation” Compax3 servo drive model number C3S300V4F12I10T10M00. From the servo drive, the power line is connected to the motors in parallel. A “Parker Hannifin Corporation” brake resistor is connected to the servo drive and is used to de-energize the HV circuit after switching off the servo drive to the motors, and is installed outside the cabinet.

A UPS 24 V DC line is connected in parallel with a “Trio” MC302X motion controller, servo drive and to power relays and the shutdown circuit. The shutdown circuit is

monitored by a time relay, so in the case of the power being cut off the Low Voltage (LV) lines remain powered for 10 seconds. The shutdown circuit consists of components connected in series, which includes: shutdown buttons, a door limit switch, a guard lock, and followed by the control panel key switch and push button. The shutdown circuit components were wired into the emergency time-delayed relay. In the case of activation of the shutdown circuit, it will isolate the servo drive HV power to allow a controlled stop to be performed before switching off. The locking guard switch will be released only when the time delay has elapsed and the lower surrounding limit switch signals that the drag shield is in the ground position. The “Trio” motion controller has an input signal (Table 3.3.2), allowing to it communicate an activation signal (WDOG), emergency status (IN(0) – IN(2), and logic signals (IN(3) – IN/OP(9)).

Address	Function
WDOG	Enable Drive
IN(0)	Emergency circuit healthy status
IN(1)	Drive fault
IN(2)	3-phase power fault
IN(3)	Signal of upper limit switch
IN/OP (8)	Signal of lower limit switch
IN/OP(9)	Test cycle START button
IN/OP(10)	Spare
IN/OP(11)	Spare

Table 3.3.2: Motion controller input functions

The motion controller is connected to a personal computer (PC). The connection is made via RS-232 connector with the following set up:

- Stop Bits =1
- Flow control = NONE
- Port = COM3
- BpS = 38400
- Data = 8 bits
- Parity = Even
- Received buffer = 1
- Transmit buffer = 1

3.3.7 Positioning sensor installation

The position sensor allows the motion controller to set the required speed and acceleration of the drag shield depending on its position. The positioning system itself includes a magnetic position sensor, magnetic strip and sensor bracket. The position sensor bracket is attached to a trolley with two M4 screws with nylon nuts. The sensor is fixed to a bracket with three M3 fixing screws with nylon nuts. The sensor is allowed to move around slightly to find exactly the right place (according to the specifications [46]) before it is fixed in place. The positioning bracket was manufactured in-house from a solid piece of aluminium (Figure 3.3.20 and Appendix G).



Figure 3.3.20: Installed position system

The position strip is attached using adhesive to the magnetic tracks on the right-hand side. The strip was attached from top to bottom of the magnetic tracks with the help of a premanufactured gauge for correct positioning. The magnetic strip itself consist of a continuous repetition of magnetised and non-magnetised areas (Figure 3.3.21)

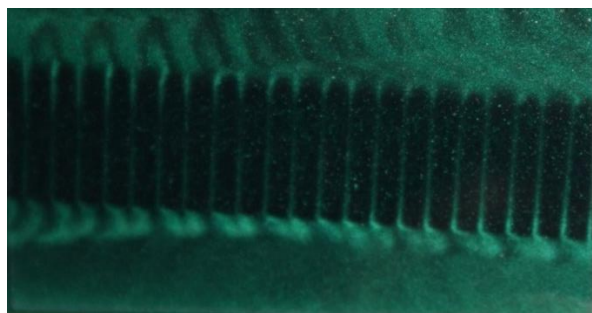


Figure 3.3.21: Magnetic position sensor strip scale

The position sensor is an “RLS” LM10IC020BA10A00 linear encoder [46], with a 20 μm resolution and it is limited to 10.4 m/s maximal velocity. The position sensor required to be installed with a tolerance of 0.1 – 1.5 mm height, $\pm 3^\circ$ pitch, $\pm 1^\circ$ yaw, $\pm 3^\circ$ lateral roll and ± 1 mm lateral offset. The sensor is limited to a maximal shock acceleration/deceleration of 300 m/s^2 (which correspond to $30.58g$ at $g = 9.81 \text{ m/s}^2$).

After installation was completed, a test reading was done to confirm that the sensor is operational and to find the error level. The electronic systems of the Drop Tower were switched on, with the computer software communicating to the motor controller. The sensor position was zeroed. The sensor, attached to the trolley, was raised to a maximal height and then lowered down to the initial position. The average error was found to be 85 μm over the total movement distance of 13.654 m.

3.3.8 Safety system installation

The safety system includes components that will reduce the damage to hardware in case of failure of the Drop Tower motors or test procedure failure. This includes the rail end brackets, damper system, soft flooring, top-level limit switch, low voltage UPS and the operational principle itself.

The servo drives operational principle and our operational procedure allows for a fail-safe in the case of HV failure. In the case of HV failure, the motors start to decelerate, which will generate a back current flowing to the servo drive. It does not matter if the motors are accelerating or decelerating or going up or down, due to gravity the drag shield will always end up at the bottom of the Drop Tower and will always decelerating. Still, it is important to note that in the case of HV failure deceleration is not so effective, which might result in high velocities reached at the bottom.

In the case of HV failure, it was important to make sure that the LV UPS provides continuous power to the control system for the time the emergency cycle is in place. The

UPS used is a “Phoenix Contact” TRIO-UPS/1AC/24VDC/5 - 2866611 [54] with an input voltage from 100 V AC to 240 V AC, and an output current limited by a fuse to 5 A. The power storage used has a capacity of 1.3 Ah, which will provide an uninterrupted power supply for at least 15.6 minutes in the case of HV failure. The UPS with its storage unit is installed in the electrical cabinet.

The top limit switch, a “Honeywell” PK 81116 [55] is installed as a preventative measure to limit the possibility of derailing the trolley from the top and hitting the dampers at the bottom. It was installed at a height of 5.283 ± 0.001 m from the position sensor initial position. When the trolley passes it, the controller receives the signal and compares the velocity of the drag shield with the threshold value. If the value is exceeded the emergency cycle should be started (subsection 3.1.8.)

In the case of uncontrolled descent of the drag shield, a damper system was installed. It consists of two dampers raised above ground level on damper mounts (Figure 3.3.22), and damper brackets attached to a drag shield. FEA of the damper mounts was conducted prior to the project. The damper mount is fixed to the ground with eight M10 ground anchor bolts. The bolts ground fixture was strengthened by applying masonry resin prior to fixing.



Figure 3.3.22: Damper brackets installed

The dampers used are “Weforma” heavy-duty shock absorbers LDS-32-250 [56]. They provide a 250 mm stroke length with energy per stroke ratio of 10 kN·m, a maximal

counterforce of 50 kN and a maximal angular tolerance in an emergency of 2.5° . The dampers are fixed to the damper mounts via four M12 screws.

The damper mounts positions were chosen so that the damper will touch the centre of the damper bracket. The damper bracket top surface should align with the top surface of the drag shield, and the far side of the brackets should be aligned with the back of the drag shield (Figure 3.3.23). At the same time, the width of the damper bracket should not obstruct the movement of the drag shield.

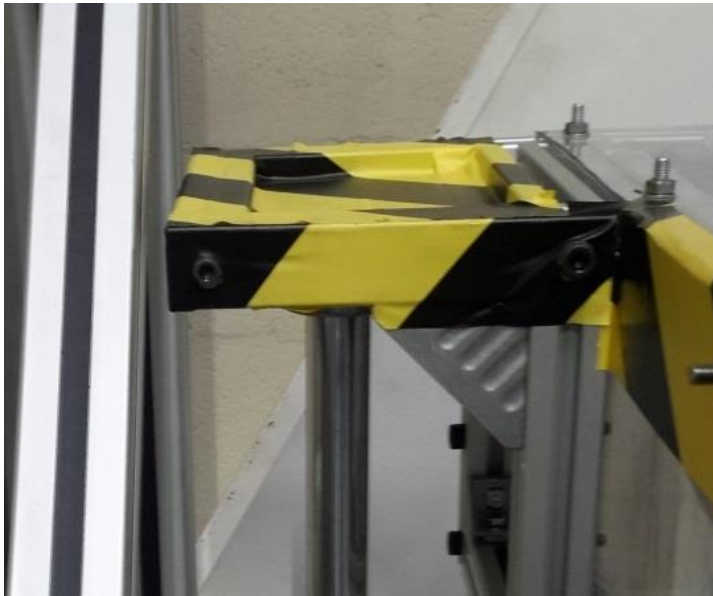


Figure 3.3.23: Damper brackets installed on the drag shield and placed on the damper

The damper brackets are mounted using six M5 bolts with nylon nuts and are fixed directly to the frame of the drag shield. The design and FEA of the brackets are discussed in subsection 3.3.10.

Additionally, the end-brackets were installed at each end of the guide rails. The brackets are screw clamp type and should provide an additional obstruction in case of emergency.

As a last safety precaution, a soft flooring “Any Foam” closed cell was used under the drag shield. It is used as damping flooring for the drag shield when the dampers were pushed down. The only purpose is to safeguard the integrity of the drag shield in case of an emergency stop, so as to minimise the damage to payload.

3.3.9 Damper mounts anchor bolts calculations

Calculations were carried out to make sure that the chosen bolts would hold the load. The stroke energy ratio of the damper is $E_{d-c} = 10 \text{ kN}\cdot\text{m}$, with a maximal stroke of $h_{s,max} = 0.25 \text{ meters}$ and a maximal damper counterforce $F_{d,max} = 50 \text{ kN}$ [56]. The damper operational principle provides that the damper speed proportionally decreases with the displacement [56].

The following assumptions were made to account for the worst-case scenario:

- Only one damper will take the load
- The drag shield falling from a height of $H = 8 \text{ m}$ with no resistive force
- The initial velocity of the drag shield is zero
- The height of the damper on the damper mount is $h_{damp} = 1.25 \text{ m}$
- The drag shield mass with a payload is $M_{full} = 100 \text{ kg}$
- At the time of contact, the force applied to the damper is not vertical but is tilted at $\zeta = 2.5^\circ$ (maximal for the damper in emergency [56])
- Gravitational acceleration constant is $g = 9.81 \text{ m/s}^2$
- Assuming that the energy absorbed by the damper is proportional to the stroke depth

The total energy of the fall is:

$$E = \frac{1}{2} M_{full} v^2 = m = M_{full} g (H - h_{damp}) \quad \left| \quad 3.3.4 \right.$$

The damper stroke energy absorbed can be calculated as:

$$E_d = E_{d-c} \frac{h_{s,act}}{h_{s,max}} \quad \left| \quad 3.3.5 \right.$$

where: $h_{s,act}$ – actual stroke distance

The stroke also changes the potential energy, which should also be absorbed and is represented as:

$$E_p = M_{full}g h_{s,act} \quad \left| \quad 3.3.6 \right.$$

The energy of the system can be represented as $E + E_p - E_d = 0$, or combining 3.3.4 - 3.3.6 together and rearranging for h_s :

$$h_{s,act} = \frac{M_{full}g(H - h_{damp})}{\frac{E_{d-c}}{h_{s,max}} - M_{full}g} \quad \left| \quad 3.3.7 \right.$$

The damping force F_d is constant as the damper speed is proportional to the stroke distance travelled, and is equal to:

$$F_d = \frac{M_{full}g(H - h_{damp} + h_{s,act})}{h_{s,act}} \quad \left| \quad 3.3.8 \right.$$

Using Equations 3.3.7 and 3.3.8 values of were calculated as $h_{s,act} = 0.170$ m and $F_d = 40001.33$ N. The force equilibrium equations for the anchor bolts (Figure 3.3.24) are:

$$\begin{aligned} F_d/N_{bolts} \cos \zeta &= N_a + N_b \\ F_d/N_{bolts} \sin \zeta &= S_a + S_b \\ F_d/N_{bolts}(x_{bolts} \cos \zeta - h_{damp} \sin \zeta) &= 2x_{bolts}N_b \end{aligned} \quad \left| \quad 3.3.9 \right.$$

where: $x_{bolts} = 0.04$ m – distance between midpoint and bolts
 $N_{bolts} = 4$ – number of anchor bolt pairs

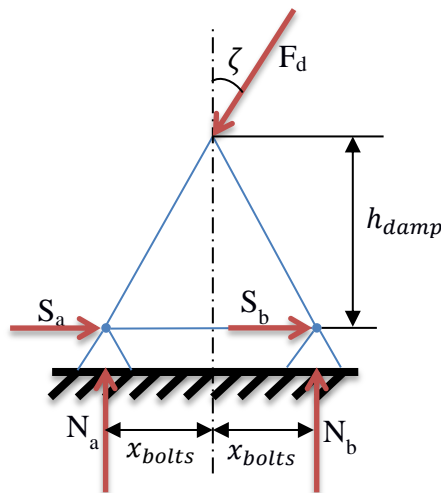


Figure 3.3.24: Anchor bolts calculation force diagram

Considering that the applied load is within 10^0 [57] “Rawlplug Ltd” advised considering only the tensile load of the anchor. Solving the set of Equations 3.3.9 only $N_b = 895.042$ N is in tension.

The selected bolts are “Rawlplug Ltd” M10 loose bolt with a characteristic resistance of $N_{Rk} = 16.7$ kN in tension [57]. A partial safety factor concept was used to confirm that the load on the concrete does not exceed the allowable force. The partial safety method includes that the design reaction – N_{Rd} should be greater than the design action – F_{Sd} [58].

$$F_{Sd} \leq N_{Rd} \quad \Bigg| \quad 3.3.10$$

Design reaction includes a partial safety factor for the material, concrete strength reduction factor, edge reduction factor and spacing reduction factor.

The following assumptions and constants were used:

- Partial safety factor for variable action $\gamma_f = 1.5$ [58]
- Concrete strength $\sigma_{con} = 20$ MPa [57]
- Concrete strength reduction factor can be calculated as [57]:

$$\gamma_{con} = \frac{1}{\sqrt{\frac{\sigma_{con}}{30}}} = 1.22$$

- The partial strength reduction factor for the material can be calculated as [58]:

$$\gamma_M = \gamma_C \cdot \gamma_2 = 2.1$$

where: $\gamma_C = 1.5$

$\gamma_2 = 1.4$ – specific for systems with a low, but still acceptable level of installation safety

- The edge reduction factor for the selected bolt and the spacing of 80 mm is $\eta_e = 0.8$ [57]
- The spacing reduction factor for the selected bolt and the spacing of 80 mm is $\eta_s = 0.7$ [57]

The design action can be calculated as:

$$F_{Sd} = N_b \gamma_f \quad \Bigg| \quad 3.3.11$$

Moreover, the design resistance as:

$$N_{Rd} = \frac{N_{Rk}}{\gamma_{con}\gamma_M} \eta_e \eta_s \quad \left| \quad 3.3.12 \right.$$

Calculating and comparing $F_{Sd} = 1342 \text{ N}$ and $N_{Rd} = 3650 \text{ N}$, shows that the design reaction is well above the design action value.

3.3.10 Damper bracket design and FEA

The damper brackets structure consists of “Bosh Rexroth” 30 mm x 30 mm aluminium profiles, a cast aluminium angle bracket and steel plate 10 mm thick. The plate is enclosed within the aluminium structure. The damper bracket is attached to a drag shield using six M5 bolts. The top structure is held together with bolt inserts. The side structure is fixed using angle brackets.

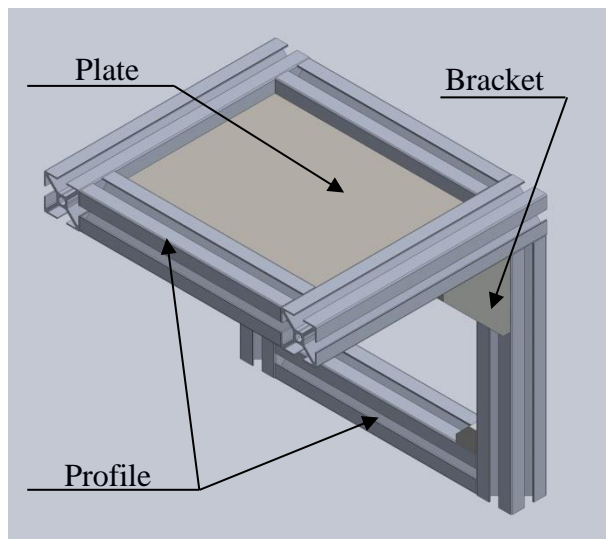


Figure 3.3.25: The damper bracket CAD model (Isometric view)

For the FEA simulation the following assumptions were made:

- The only load bearing components are: top plate and angle bracket
- The load is normal to the plate
- The load is constant and is equal to the maximum load from damper calculations ($F_d = 40001.33 \text{ N}$ – subsection 3.3.9)
- The load is evenly taken by the surface within a radius of the damper bracket ($r_{damp} = 45 \text{ mm}$)
- The damper bracket plate is firmly fixed around its edge of 10.5 mm

- Both brackets are loaded evenly
- The distance between the bracket edge and the centre of the pressure is equal to 70 mm

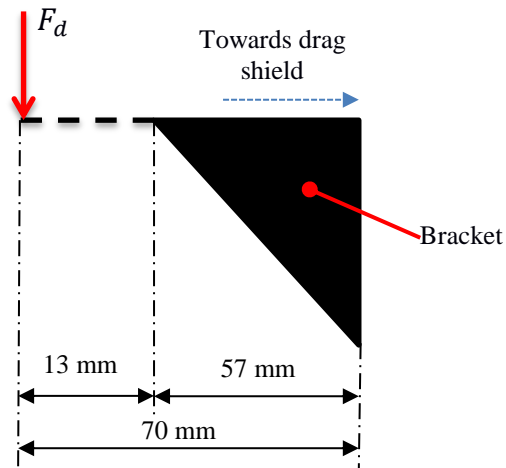


Figure 3.3.26: Bracket loading torque calculations

For the simulation Solidworks, software was used with a high mesh quality (21278 nodes and an element size of 4.44174 mm). The loading case included a Factor of Safety (FoS) of 1.5. The pressure required for the plate to withstand becomes equal to:

$$P_{dp} = \frac{4F_d}{\pi r_{damp}^2} FoS = 37.746 \text{ MPa} \quad \left. \vphantom{\frac{4F_d}{\pi r_{damp}^2} FoS} \right| 3.3.13$$

where: P_{dp} – pressure load for damper plate

F_d – maximal damper load

r_{damp} – contact surface radius

FoS – Factor of Safety

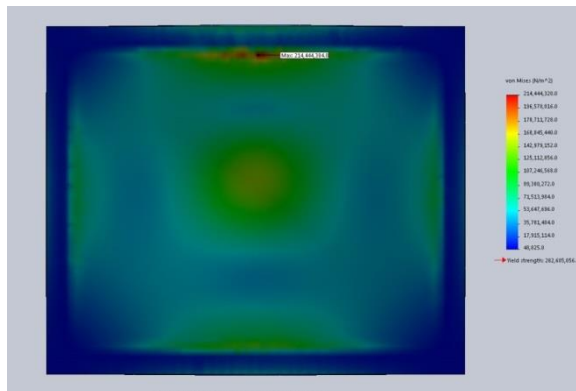


Figure 3.3.27: Damper bracket simulation (Top view)

The maximum stress was found to be 214.444 MPa (Figure 3.3.27) which is 24% below the yield strength, which did include the FoS.

The loaded torque on the bracket was calculated to be:

$$T_{db} = \frac{F_d}{2} 0.07 = 1.4 \text{ kNm} \quad \left| \quad 3.3.14 \right.$$

The maximal von Mises stress was found to be 24.953 MPa (Figure 3.3.28), which is 8.76% of the yield strength. The mesh was set to have 561735 nodes with an element size of 1.421 mm.

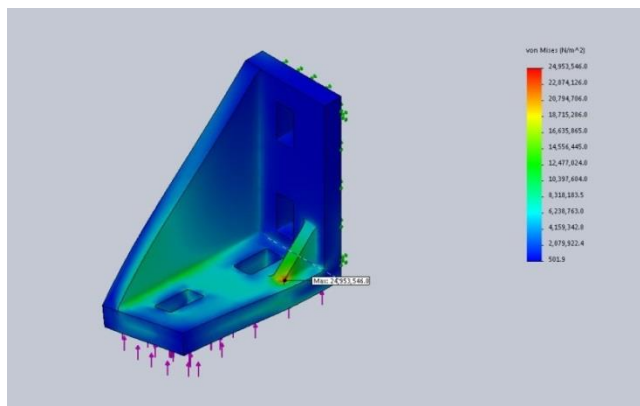


Figure 3.3.28: Damper bracket angle bracket simulation (Isometric view)

3.4 Drop Tower calibration

Calibration of the Drop Tower had several major milestones:

- Magnetic track alignment
- Guide rail alignment
- Motor alignment
- Microgravity test calibration

Not all of the above milestones have been achieved due to problems discussed in section 3.6. The following subsections will provide detailed information on the work carried out.

3.4.1 Magnetic track alignment procedure

The magnetic tracks were first attached to the main I-beam with loose bolts to allow for movement. The long line gauge and brackets were used to align the tracks. An aluminium line gauge was used, as it is a non-ferrous material and can be used in the proximity of the magnets. When the gauge was fixed, the fixing bolts were tightened. The gauge used was 2m long to allow coverage of at least five already fixed tracks and to align a further three track sections.

The system is only dependent on the horizontal distance to the guide rails due to the mechanical constraints of the system. At the trolley, the motors are fixed relative to the guide rail rollers, and the guide rails are fixed relative to the magnetic tracks on the I-beam leaving only 1-Degree of Freedom (DoF) in the system. Due to this, there was no need to have a perfect alignment normal to the ground with the only constraint being the tolerance on the pre-manufactured holes on the main I-beam. To allow for the installation of the motors (the motors are required to be slid in), the bottom tracks (approximately 1.5 m from ground level) were installed later when the alignment checks were completed and the motors were installed.

3.4.2 Guide rail alignment procedure

The guide rails were initially positioned using the pre-manufactured aluminium gauge on the guide rail rollers (Figure 3.4.1).



Figure 3.4.1: Guide rail alignment gauge

After approximate installation of the guide rails, the digital Vernier calliper was used to finalise the position and fix the guide rails in place. The twist and the distance were regulated by four point adjusting screws (Figure 3.3.7).

The tolerance on the position precision was selected to be 0.01 ± 0.005 mm (well below the required 0.254 mm, set by the linear motor lateral movement limitations [44]) from an initial measuring point of 80.50 ± 0.02 mm.

After mechanical alignment was completed, a digital check was conducted using a laser distance sensor. A “Baumer” laser digital sensor (OADM 20i4460/S14C) was used as the measuring device along with a “National Instruments” NI USB-6210 Data Acquisition (DAc) unit. The DAc was connected to the computer via a Universal Serial Bus (USB) interface and “NI LabView Signal Express” software was used to process the data.

The laser digital sensor [59] has a measurement range of 30 to 130 mm with a linear resolution of 0.005 to 0.007 mm respectively. The sensor was powered by a Direct Current (DC) power supply (“TTi” EL303R [60]) at 12.00 ± 0.01 V. The signal was acquired continuously at a frequency of 50 Hz.

The sensor was positioned at 45 degrees to the surface as the size and measuring distance requirements did not permit the installation of the sensor directly perpendicular to the magnetic track (Figure 3.4.2).



*Figure 3.4.2: Baumer laser digital sensor installed
(Left – independent rail; Right – trolley attached)*

Various tests were performed with the investigation of different sensor attachments. First were independent rail and fixed position tests (Figure 3.4.2, left), and secondly, tests were

carried out while the sensor was attached to the trolley (Figure 3.4.2, right). Tests were performed on both guide rails.

DAC [51] is a 16 analogue input (single-ended) and eight analogue input (differential) digital acquisition card of 16-bit resolution. The signal input range is ± 10 V with an accuracy of ± 2.69 mV. The DAC maximum signal acquisition frequency is 80 MHz. The signal input range and maximum frequency allowed by the DAC perfectly fit the test requirements.

The DAC was enclosed in a steel casing due to the high level of electromagnetic noise from the magnetic tracks as well as due to the length of the signal wire (10 m).

3.4.3 Measurement noise error identification

The first stage of data acquisition was to investigate the electromagnetic noise level of the system. Single point static measurements were taken (Figure 3.4.3). The test data starting time depends on initial stabilisation of the signal, which in fact depends on the acquisition response time and computer performance at the time when the test was taken.

Three different signals were acquired giving similar average values of 4.9766 ± 10^{-4} V (corresponding to 79.766 mm). After performing the test, the maximum signal deviation from the average was found to be 3.3 μ V and 3.8 μ V.

Assuming the maximum signal noise and knowing the analogue signal to distance ratio to be 0.1 V/mm [59], the maximal distance error from the signal losses is:

$$Error_{signal} = \pm 3.888 \cdot 10^{-6} / 0.1 = \pm 38.88 \mu m \quad | \quad 3.4.1$$

The sensor resolution was considered to be linearly proportional to the measuring distance (Md) measured in millimetres, based on the user guidelines [59].

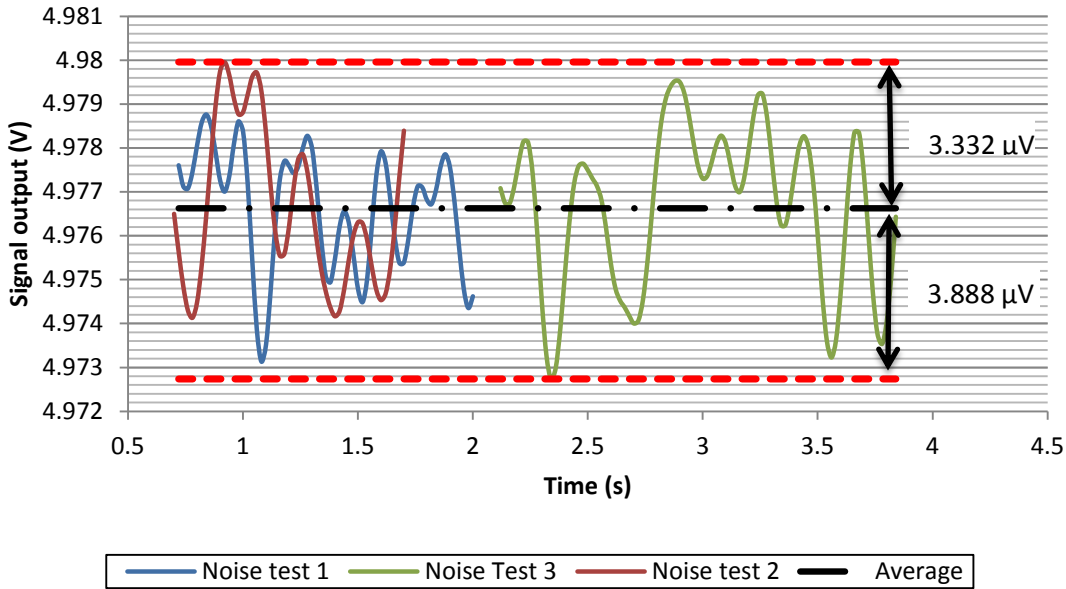


Figure 3.4.3: Electromagnetic noise measurements

So at the lower end of the measurement range (D_I), namely 30 mm, the resolution is 0.05 mm (RES_I) and at 130 mm (D_F) the corresponding resolution is 0.07 mm (RES_F) [59]. The sensor uncertainty is:

$$Error_{sensor} = \pm \left[RES_I + (Md - D_I) \frac{\Delta RES}{\Delta D} \right] \quad 3.4.2$$

$$Error_{sensor} = \pm \left[0.05 + (Md - 30) \frac{0.07 - 0.05}{130 - 30} \right]$$

$$Error_{sensor} = \pm (44 + 0.2 \cdot X) \cdot 10^{-3} \text{ mm} \quad 3.4.3$$

where: X – mean reading distance (mm)

The DAC signal error as mentioned in subsection 3.4.2 is ± 2.69 mV, corresponding to a DAC error of:

$$Error_{DAq} = \pm 2.69 \cdot 10^{-3} / 0.1 = \pm 26.9 \mu m \quad 3.4.4$$

The total possible error in the readings is found to be:

$$Error = \pm [Error_{signal} + Error_{sensor} + Error_{DAq}] \quad 3.4.5$$

$$Error \pm (109.78 + 0.2 \cdot X) \cdot 10^{-3} \text{ mm}$$

This calculated error will be used in the following subsections where the actual test of the guide rail alignment will be discussed.

3.4.4 Fixed position testing

The fixed position test involved attachment of the sensor to one of the guide rails at a specific height and recording of static measurements. The procedure used was similar to what was used in the line noise investigation in subsection 3.4.3. The sensor was positioned at 45° to the surface and angled at 45° to the ground (Figure 3.4.2) at an approximate total distance of 80 mm (40 mm normal to the surface distance). This was done to allow for sensor operation due to the restricted access area (Figure 3.4.2) and sensor measurement limitations (the minimal measuring distance of the sensor is 30 mm) [59].

Several steady state readings were taken at a specific height and the average value was calculated (Table 3.4.1). The reading location was measured from the ground, and the average was calculated for the measurements taken continuously between 2 to 5 seconds (at a frequency of 50 Hz this corresponds to 100 to 250 readings).

Reading posit (m) ± 0.1	Average reading (mm), Left ± 0.11	Average reading (mm), Right ± 0.11
1	80.50	80.55
3	80.51	80.54
5	80.50	80.55
7	80.52	80.53
8	80.48	80.57

Table 3.4.1: Static position measurements

The analogue signal initially received (S) was first converted to a distance measurement ($S/0.1$). After this the result was updated based on the sensor angular position ($\cos \zeta \cdot \cos \zeta$, where $\zeta = 45^\circ$ – angular inclination of the sensor in the horizontal plane and the vertical plane). The distance to the surface can now be calculated as:

$$D = D_I + \frac{S \cdot \cos^2 \zeta}{0.1} \pm Error \quad \left| \quad 3.4.6 \right.$$

Finally, a boxcar averaging method using 50 values was used to minimise noise from the signal.

3.4.5 Dynamic position testing

Dynamic testing was carried out to confirm the static measurements. A dynamic test includes measurements along the whole length of the rail.

Similarly, to static position testing the dynamic tests used the laser distance-measuring sensor (subsection 3.4.4) installed at 45° to the vertical axis and 45° to the horizontal axis. At the same time, the sensor was installed on the trolley. By doing this it was expected to reduce mechanical vibrations as well as to allow checking of the performance closer to a real life situation (since the trolley is always in contact with both rails). The motors and the drag shield were not installed for the test for safety reasons and as it was too heavy to operate manually with these attached. In real life operation the results will continue to hold true. The factor that will change is the torque applied on the guide rails through the trolleys due to the extra weight added with a drag shield. This will provide a bending moment on the guide rails, but it won't be enough to marginally offset the guide rails position. The sensor was moved manually at a uniform rate. The test time on average was 10 seconds with a height of 8 meters this corresponds to a velocity of 0.8 m/s.

Initial test data (Figure 3.4.4) for a typical run shows spikes, which arise when the signal beam is lost. When the laser beam passes through the space between magnets it is trapped and returns no reading. Such values were substituted with previous non-corrupted values. With an acquisition rate of 50 Hz and a sensor, speed of approximately 8 m/s the corrupted data set consisted typically of 1 – 2 readings.

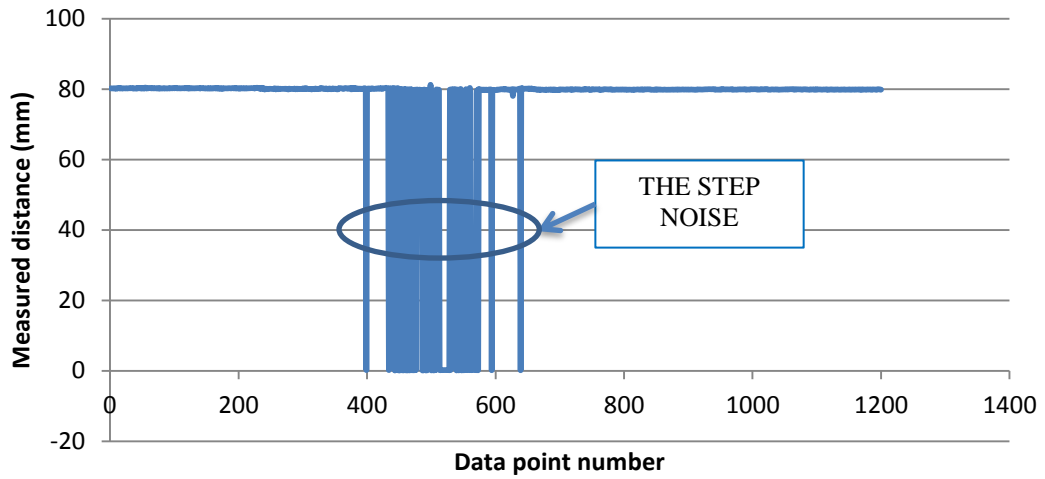


Figure 3.4.4: Initial signal readings
(An arrow indicates the location of corrupted data)

The sensor operational frequency was checked to allow for the correct number of measurements. With a guide rail brackets spacing of 125 mm and assuming that the guide brackets do not buckle it is important to have at least two readings to characterise this spacing. With our measurement rate and velocity, approximately 5 – 9 measurements were taken.

The distance to the surface was calculated using Equation 3.4.6. The initial position value was deducted to compare the offset from the centre line. Figure 3.4.5 shows four alignment results.

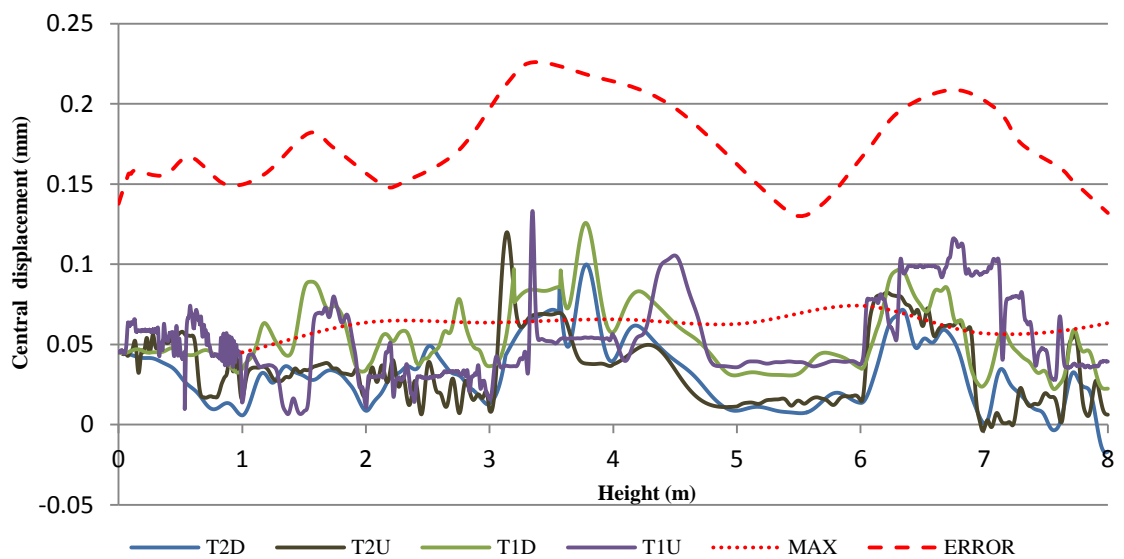


Figure 3.4.5: Dynamic testing results; maximum offset and maximum possible error
(T2D – Test 2 down, T2U – Test 2 up, T1D – Test 1 down, T1U – Test 1 up)

The tests included an alignment check in both directions: upwards and downwards. The initial offset position (at zero height) was set based on the static tests. Post processing included finding the maximum offset value (red dotted line, Figure 3.4.5) based on the available tests. Using Equation 3.4.5 the maximum displacement including the reading error was found (red dashed line, Figure 3.4.5) to be 0.226 mm, which is well below the required 0.254 mm.

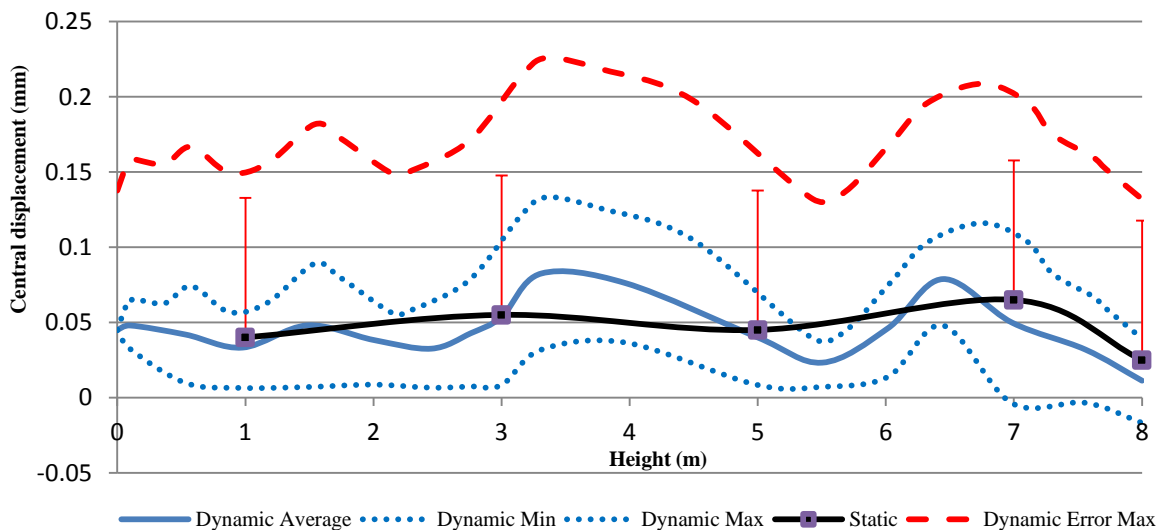


Figure 3.4.6: Static and dynamic tests comparison

Figure 3.4.6 shows the final results of position testing. The dynamic maximum values are the values of the maximum divergence from all experiments, while the dynamic error maximum curve adds an additional error of the maximum divergence based on Equation 3.4.5. Both dynamic and static tests are well within the required motor constraints. The dynamic test average using the trolley showed an advantage as it provided an additional alignment as it is connected to both rails. The dynamic tests showed also disturbances due to mechanical vibrations, which were expected. Both results are well within the limits of the requirements (which are constrained by the motor-magnets requirements to be less than 0.254 mm).

Similar dynamic testing was carried out one year after initial alignment. This was done to see if the alignment had drifted over the time period (the Drop Tower was not operational during this time). The results confirmed no change in the alignment.

3.4.6 Motor alignment procedure

The next step after the guide rails and the motors were aligned was to install the motors onto the trolley. The alignment of the components was performed in two stages. The first was to align the guide rollers on the trolley and secondly to align the motors with the guide rollers.

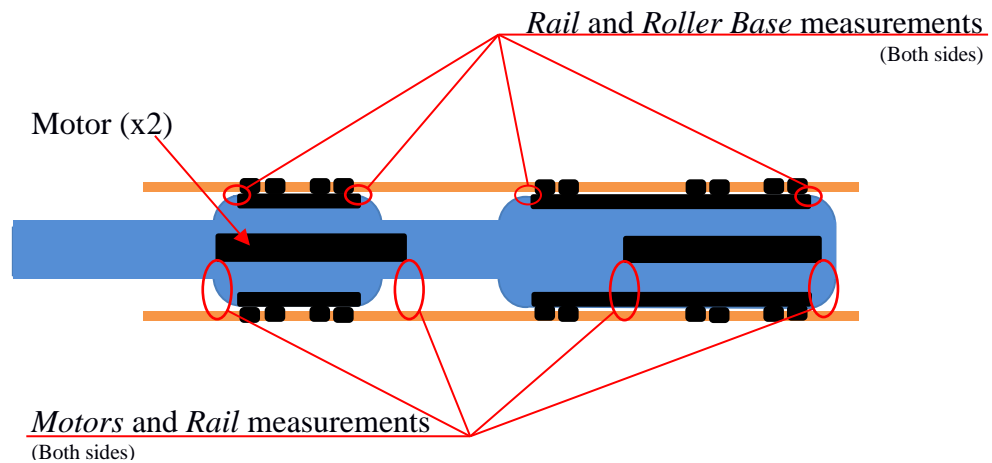


Figure 3.4.7: Motor alignments measurements description (schematics)

The alignment of the rollers was done using the spare guide rails (Figure 3.4.7 and Figure 3.4.8). First, the guide rails were slide into the rollers and the spacing between the rail and roller base was set to around 3 mm.

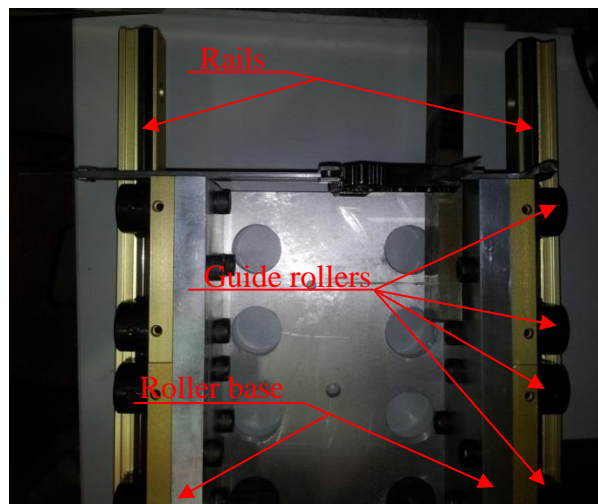


Figure 3.4.8 Position calibration of the trolley guide rollers

After the guide rollers and motors were installed, the motor positions were set and fixed. The target was to set the spacing between the motor and rollers to 93.555 ± 0.005 mm with

the maximum misalignment to be less than 0.025 mm. The decision for this tolerance was made based on previous dynamic guide rail alignment tests (subsection 3.4.5), where the maximum position variation should not exceed 0.254 mm and the maximum guide rail alignment offset with the error was found to be 0.226 mm, giving a maximum allowable variation in the motor position to be 0.028 mm. The measurements were taken in eight places. As the guide rollers were fixed in four separate sections on the roller base plates it was assumed that the guide rollers within the section should remain aligned. The final measurements are summarised in Table 3.4.2.

Measurement position	Left (mm) ±0.005 mm	Right (mm) ±0.005 mm	Difference (mm) ±0.005 mm
A	93.560	93.550	0.010
B	93.540	93.565	-0.025
C	93.555	93.560	-0.005
D	93.575	93.550	0.025

Table 3.4.2 Measurements of motor alignments

The maximum displacement in motor alignment is 0.025 ± 0.005 mm, which adds to the maximum measured displacement to become 0.251 mm, which is less than the allowable (set to be 0.254 mm).

3.4.7 Microgravity test calibration

The calibration of the microgravity test was expected to be completed when the electronics and control system are fully operational. Unfortunately, this milestone in the project was never achieved. The following steps were proposed:

1. Run the Drop Tower at a low speed (100 mm/s) with the acceleration not exceeding 12 m/s^2 . The moving trolley should not be loaded (operate with the drag shield detached). Those values were proposed by the commissioning company. Limit the movement to 2 m height.

2. Check the operation of the emergency switches. When switch is pressed, the trolley is returned at safe speed (set to be 100 mm/s) to ground level, followed by switching off the power supply.
3. Check the High Voltage (HV) power cut-off procedure.
4. Perform a run over the whole travel distance confirming the acknowledgment of the top and bottom limit switches. Confirm the readings error of the position sensor is within acceptable limits.
5. Increase the velocity with steps of 100 mm/s, reaching the maximal required velocity of 10.396 m/s. Tests to be done within 2 m height.
6. Increase the acceleration in steps of 0.1 m/s^2 , reaching the maximal required acceleration of 49.05 m/s^2 . At this stage the maximal velocity should be limited to 100 mm/s. The height is limited to 2 m.
7. Increase the speed keeping the maximal acceleration in steps of 100 mm/s, reaching the maximal required velocity.
8. Repeat procedure with the drag shield attached (from step 1 to 7)
15. Increase the payload in steps of 0.5 kg, reaching the maximal required payload mass 20 kg at maximal velocity and acceleration.

The calibration steps were developed in such a way as to find the actual (operational) limits of drop tower operation, but still taking precautions to rule out failure. It is possible to use safety regulation EN81-20/80, which emphasis the commissioning requirements for the commercial lifts.

Before the project was stopped, five steps from the list above were completed. It can be confirmed that the trolley without the drag shield attached can move up and down over the whole travel distance, is able to detect the limit switches, and responds to the emergency shutdown procedure. Finally, development of the software for the microgravity test was not started.

3.5 Risk assessment and operational assessment documents

This section provides a risk assessment and operational assessment for the microgravity Drop Tower. The assessment presented here has not been checked and certified due to the Drop Tower not achieving operational status, but the risk assessment is based on the form provided by Micromech Ltd, who were responsible for commissioning the electrical system.

Likelihood of Occurrence (LO)		Frequency of exposure (FE)		Degree of possible Harm (DH)		Number of Persons at risk (NP)	
0.03	Almost impossible	0.5	Annually	0.1	Scratch or bruise	1	1-2 persons
1	Highly unlikely	1	Monthly	0.5	Mild ill-effect	2	3-7 persons
1.5	Unlikely	1.5	Weekly	2	Break of minor bone or minor illness	4	8-15 persons
2	Possible	2.5	Daily	4	Break of major bone or major illness	8	16-50 persons
5	Even chance	4	Hourly	10	Loss of limb, eye etc. (permanent)	12	50+ persons
8	Probable	5	Constantly	15	Fatality		
10	Likely						
15	Certain						
Hazard Rating Number (HRN)=LO•FE•DH•NP							
0 – 5	Negligible						
5 – 50	Low						
50 -500	High						
>500	Unacceptable						

Table 3.5.1: Risk assessment weighting table

Identified Hazards	Initial Risk Assessment					Risk Reduction Measures	Residual Risk				
	LO	FE	DH	NP	HRN		LO	FE	DH	NP	HRN
Cables being damaged	2	5	15	1	150	The cables are enclosed in the cable trunkings and cable chain	0.03	5	15	1	2.25
Unexpected failure in drag shield movement	1.5	5	0.1	1	0.75	Three emergency switches are installed. Only qualified personnel are to use the equipment	0.03	5	0.1	1	0.015
Electric shock from control system during maintenance	2	5	15	1	150	Only qualified personnel to use the equipment. Power must be isolated before carrying out any modifications	1.5	5	15	1	112.5
Electric shock from control system during normal operation	1.5	5	15	1	112.5	All the control units are mounted within the enclosures. Power supply commons wires are linked to ground. The equipment is tested.	0.03	5	15	1	2.25
Electric shock due to access to electrics cabinet due to doors being left open	2	5	15	1	150	Emergency switch cuts off the power supply to system when the cabinet door is open	1	5	15	1	75
Risk of unexpected movement or failure due to power supply interruption	1.5	2.5	0.1	1	0.375	If power fails the emergency stop circuit will latch off, requires manual reset	0.03	2.5	0.1	1	0.0075
Risk of an unauthorised access to drop tower area while the test is running	2	2.5	15	1	75	The doors are equipped with guard switch, which is normally locked when test is running	0.03	2.5	15	1	1.125
Risk of an unauthorised access to electric cabinet	2	2.5	15	1	75	Doors are locked by key. Only qualified personnel to have access to key. Emergency switch cuts off the power supply when the cabinet door is open	0.03	2.5	15	1	1.125
Risk of an unauthorised access to the Drop Tower due to door been left open	2	2.5	15	1	75	The limit switch is installed to continuously check the door status. System does not allow to run test if the door is open	0.03	2.5	15	1	1.125

Identified Hazards	Initial Risk Assessment					Risk Reduction Measures	Residual Risk				
	LO	FE	DH	NP	HRN		LO	FE	DH	NP	HRN
Test initiated with the drag shield door been left open	2	2.5	6	1	30	Same as above	0.03	2.5	6	1	0.45
Person locked out in safety shroud	2	5	15	1	150	The operation of the Drop Tower is done under constant supervision	1	5	15	1	75
Fragments falling from drag shield	1	5	15	1	75	The Drop Tower is enclosed by Perspex from all accessible sides	0.03	5	15	1	2.25

Table 3.5.2: Drop Tower risk assessment

1. Check if the cabinet doors are locked and the cabinet switch is ON			
	<u>What are the hazards?</u>	<u>Mitigation</u>	
Possible hazards:	3-phase, 415 V AC power supplied	Cabinet door should be key locked	
	<u>What happened?</u>	<u>What to do?</u>	<u>Who is responsible?</u>
Possible issues:	Doors were left open (accidentally)	Contact staff. Staff to check if the power is switched off. Contact facility supervisor to lock the doors	Done by staff
	Doors were left open (maintenance)	Cabinet area should be isolated. Signs should be displayed	Done by supervisor
2. Check if the emergency power cut-off button is released (both: control panel and drop tower)			
	<u>What happened?</u>	<u>What to do?</u>	<u>Who is responsible?</u>
Possible issues:	No power supplied to servo drive	Contact facility supervisor to confirm facility readiness	Done by supervisor
3. Switch on 3-phase power supply (switch on Mains)			
	<u>What happened?</u>	<u>What to do?</u>	<u>Who is responsible?</u>
Possible issues:	Power cable is disconnected	Contact staff. Connect power cable to power supply	Done by staff

4. Cabinet Light Emitting Diode (LED) should be ON			
	<u>What happened?</u>	<u>What to do?</u>	<u>Who is responsible?</u>
Possible issues:	Doors are open	Switch off power supply. Contact staff. Check the doors locked	Done by staff
	LEDs are down	Switch off power supply. Contact facility supervisor	Done by supervisor
	Emergency power cut-off button is pressed down	Switch off power supply. Contact facility supervisor to confirm facility readiness	Done by staff
5. Enable power key switch			
	<u>What are the hazards?</u>	<u>Mitigation</u>	
Possible hazards:	Possible unauthorised operation	Only authorised personnel have key access	
	<u>What happened?</u>	<u>What to do?</u>	<u>Who is responsible?</u>
Possible issues:	No power supplied to servo drive	Contact facility supervisor to confirm facility readiness	Done by supervisor
Power LED on control panel should be ON			
	<u>What happened?</u>	<u>What to do?</u>	<u>Who is responsible?</u>
Possible issues:	Emergency power cut-off button is pushed down	Contact facility supervisor to confirm facility readiness	Done by supervisor
	LED is down	Switch off power supply. Contact facility supervisor	Done by supervisor
6. Switch on personal computer (PC) and wait till “Motion Perfect” and “LabView Signal Express” software is launched			
	<u>What are the hazards?</u>	<u>Mitigation</u>	
Possible hazards:	Possible override of software program	Motion controller is password locked	
	No motor temperature monitoring	Test will not run if the logic signal from Data Acquisition (DAC) is not received	
	Motion controller memory is lost	Additional copy is saved on PC	
	<u>What happened?</u>	<u>What to do?</u>	<u>Who is responsible?</u>
Possible issues:	PC is password protected	Contact staff	Done under supervision
	Temperature LEDs are ON	Contact facility supervisor	Done by supervisor

7. Payload is placed into drag shield			
	<u>What are the hazards?</u>	<u>Mitigation</u>	
Possible hazards:	Person locked in safety shroud	The test should be done under supervision. Key access to facility	
	Payload is positioned incorrectly	The test should be done under supervision. Key access to facility	
	Wrong payload property	Payload should be inspected	
	<u>What happened?</u>	<u>What to do?</u>	<u>Who is responsible?</u>
Possible issues:	No key access to facility	Contact staff	Done under supervision
8. Lock drag-shield door / Lock safety shroud door			
	<u>What are the hazards?</u>	<u>Mitigation</u>	
Possible hazards:	Start of a test while doors is open	Safety limit switches installed. Doors should be key locked	
Doors LEDs should be on			
	<u>What happened?</u>	<u>What to do?</u>	<u>Who is responsible?</u>
Possible issues:	Doors are open	Contact staff. Check the doors locked	Done by staff
	LEDs are down	Switch off power supply. Contact facility supervisor	Done by supervisor
9. Start of the test			
	<u>What are the hazards?</u>	<u>Mitigation</u>	
Possible hazards:	Accidentally start button was pressed	Button has a safety cover. Emergency cycle push button is installed	
	High terminal velocity reached	Limit switch is installed at 3/4 of total travel length to identify if velocity is exceeded nominal	
	Accidentally power cut-off button is pressed	Time relay is installed allowing for power to be supplied twice longer than is a test time	
	Motors power cut-off	The emergency cycle starts. Servo drive dumps energy received from deceleration of the motors; 25g deceleration dampers are installed	
	Bottom limit is reached	<i>Limit switch is installed to identify the emergency stop</i>	
	Drag shield limit switch fails	<i>Test will be changed to emergency cycle</i>	




Start of the test (continue)			
	<u>What are the hazards?</u>	<u>Mitigation</u>	
Possible hazards:	Safety shroud door is opened	Safety electrical key switch is installed. No power is supplied to door while test is running	
	Temperature of the motors exceeds maximum level	The safety margin is included to allow proceed with the test. The identification LED will light up; Temperature is also controlled by servo drive	
	<u>What happened?</u>	<u>What to do?</u>	<u>Who is responsible?</u>
Possible issues:	Test will not be started if emergency push button is pressed down	Contact facility supervisor to confirm facility readiness	Done by supervisor
	Test will be terminated if emergency button is pressed	Contact facility supervisor to confirm facility readiness	Done by supervisor
Other			
	<u>What happened?</u>	<u>What to do?</u>	<u>Who is responsible?</u>
Possible issues:	Bad cable connection	Disconnect power supply immediately. Wait 5 minutes before unlocking cabinet doors (based on servo drive ops. manual). Contact facility supervisor	Done by supervisor

Table 3.5.3: Operational assessment

3.6 Future suggestions

The Drop Tower project was a large undertaking for the university. First of all, the design used a novel approach in seeking to achieve microgravity conditions. The use of electromagnetic motors to propel the payload had never been used before. Secondly, drop tower facilities are not available in UK. Thirdly, this project was expensive and did require a lot of investment. All of this did affect progress. In this section, information on the final status of the drop tower and some notes for the future will be provided in case the project is ever restarted.

In the last commissioning attempt, it was found that there is a high level of noise in the signal lines of the motors. The noise appears to be generated by the motor power cables, which are enclosed in the same cable trunkings and cable snake as the signal lines. This fault was identified when checking the movement of the trolley at a velocity of 1.7 m/s. By setting the velocity to this level, an increase in the power output from the servo drives to the motors is required and at this stage, the signal lines (which control the change in the magnetic coils) become jammed. These speculations were confirmed when readings for the signal lines return value was checked on the oscilloscope, showing a high noise level. Further investigation revealed that the power cables selected by Micromech were not fit for purpose as they had a low level of electromagnetic insulation. In addition, the insulation layer that was present was not grounded.

The following was proposed: firstly new power cables should be installed with much higher electromagnetic insulation; secondly, the system requires to be rewired and the insulation should be grounded; thirdly, the connectors should be independently insulated (this includes the signal lines); lastly, the power lines should be moved to separate the

trunking and cable snake, and they should be positioned as far as possible from the signal lines.

The tests showed that the motors operating at a velocity of 1.5 m/s and an acceleration of 0.1 m/s^2 with only the trolley attached are using only 10% of the maximum available power. It is hard to predict if the motors can reach the required design velocity and acceleration with the drag shield and maximal payload mass when operating at 100% of the total power. However, there is still the possibility of installing additional motors. Unfortunately, this will require a change in the servo drive and transformer. Moreover, the installation of the additional motor will require disassembly of the lower parts of the magnetic track and guide rails to gain access to the trolley for installation of the motors.

CHAPTER 4

MATHEMATICAL MODELLING

This chapter is devoted to the formulation of the Mass-Spring-Damper (MSD) model and analysis of the results of this model. The mathematical modelling is carried out based on a model that first was proposed by Shawn [3] (section 2.3). Later developments were made by Kiyono and Fuchikami [4] and Osborne [22]. The former research has experimentally determined the coefficients for the spring and damper, while subsequent research tried to formulate a model, which can include a 2nd Degree of Freedom (DoF). The work presented here is based on the MSD model proposed by Kiyono and Fuchikami.

The current investigation novelty is an in-depth study of the MSD one dimensional model (which is currently the only mathematical model that promises to show chaotic behaviour in drop dripping dynamics), as well as a future comparison of the model to experimental results. The model results study should provide behaviour discrepancies when one compares with experimental results, as well as analysing the behaviour patterns of the model.

This chapter is structured in the following way: firstly (section 4.1), the model is formulated and the range of the investigation is set. Secondly (section 4.2), the mathematical model is developed using “MATLAB®” software. In addition, the code to investigate the fractal nature of the results is presented in subsection 4.2.1 (the shape of the

bifurcation region size changes with power law while keeping its shape largely the same). Thirdly, the results are presented in the section 4.3. The section is divided into two subsections. The first provides confirmation of the model operation, while the second section is devoted to analysis of the results. In addition, extra results are presented in Appendix I.

4.1 The 1-D Mass-Spring-Damper model formulation

To analyse the drop dynamics the Mass-Spring-Damper (MSD) model was used (section 2.3). Kiyono and Fuchikami (1999) provided the initial formulation [4], which included the experimentally determined spring coefficient (k):

$$\frac{d}{dt} \left(m \frac{dz}{dt} \right) = -kz - c \frac{dz}{dt} + mg \quad \left| \quad 4.1.1 \right.$$

where: m – mass of the drop

z – is the vertical component of the Centre of Mass (CoM) location

g – gravitational acceleration

c – damping coefficient (chosen to be: $c = 0.008$ [4])

$(-kz)$ – restoring force due to surface tension term

The spring coefficient was defined to be mass dependent and can be found using the following equation:

$$k(m) = \begin{cases} -11.4m + 52.5 & (m < 4.61) \\ 0 & (m \geq 4.61) \end{cases} \quad \left| \quad 4.1.2 \right.$$

where: m – mass of the attached drop measured in normalised mass units (Equation 4.1.3)

This means that the spring component of the drop becomes negligible when the critical mass is reached ($m_{crit} = 4.61$). Normalised (or dimensionless) units for length, time and mass with unit sizes are given by:

$$\begin{aligned}
l_o &\equiv 0.27 \text{ cm} \\
t_o &\equiv 0.017 \text{ s} \\
m_o &\equiv 0.020 \text{ g}
\end{aligned}
\quad \left| \quad 4.1.3
\right.$$

These normalised units are used henceforth in this section.

Using available experimental data they assumed that detachment of the drop should occur when the CoM location reaches a critical value ($z_{crit} = 4$, measured in normalised length units). The residual drop mass (m_r), the CoM vertical coordinate (z_o – measured in length units) and the velocity component (dz_o/dt) after detachment are updated using:

$$\begin{aligned}
m_r &= 0.068m - 0.053 \\
z_o &= 0.15 \\
\frac{dz_o}{dt} &= 0
\end{aligned}
\quad \left| \quad 4.1.4
\right.$$

With additional experimental data, Kiyono and Fuchikami later improved their model [6], by introducing the relative velocity of the drop, which obeys the following equation:

$$\frac{d}{dt} \left(m \left(\frac{dz}{dt} - v_o \right) \right) = -kz - c \frac{dz}{dt} + mg
\quad \left| \quad 4.1.5
\right.$$

where: v_o – flow velocity

$c = 0.05$ – damping parameter

The spring constant (k) was left to have same dependence as before (Equation 4.1.2). The values of the drop CoM critical value, the drop residual mass, the renewed CoM and velocity were set to:

$$\begin{aligned}
z_{crit} &= 5.5 \\
m_r &= 0.2m + 0.3 \\
z_o &= 2.0 \\
\frac{dz_o}{dt} &= 0
\end{aligned}
\quad \left| \quad 4.1.6
\right.$$

Equation 4.1.5 with the spring constant defined using Equation 4.1.2, and the simulation parameters set in Equation 4.1.6, can be used in simulation code to produce a 1-

dimensional MSD model of the drop dripping dynamics. The unit values of the variables are set using the values in Equation 4.1.3. The critical CoM location as well as the starting location for the drop was chosen based on the experimental data provided by Kiyono and Fuchikami [4].

The required starting and end velocity for the investigation can be calculated using Equation 2.1.5 which, when rearranged, gives:

$$v_o = \frac{Re\mu}{\rho d} \quad \left| \quad 4.1.7 \right.$$

where: Re – Reynolds number (for the chaotic region starting point $Re = 50$ and end point $Re=561$ – section 2.3, [5] and [14])

μ – dynamic viscosity

ρ – density

d – inner diameter of the nozzle

The chaotic region ends when the Weber number have reached critical value given by Clanet and Lasheras [14] (Equation 2.2.1, section 2.2). Due to experimental set-up limitation (explained in section 5.3.4) the maximal Reynolds number can be limited to 175.

4.2 The 1-D MSD model computational code

The dripping dynamics mathematical model in 1-dimensional space was simulated using code developed in “MATLAB®” software (Appendix H). The simulation code consists of three parts:

- Simulation running code
- Dripping dynamics modelling code – “MS_model_Kiyono”
- Differential equation solver – “MS_solver”

“Simulation running” code was developed to allow for continuous calculation of different flow rate regions, while displaying the information on the simulation progress as a percentage while recording the data into separate data files (Figure 4.2.1, Figure 4.2.2 and Appendix H.A).

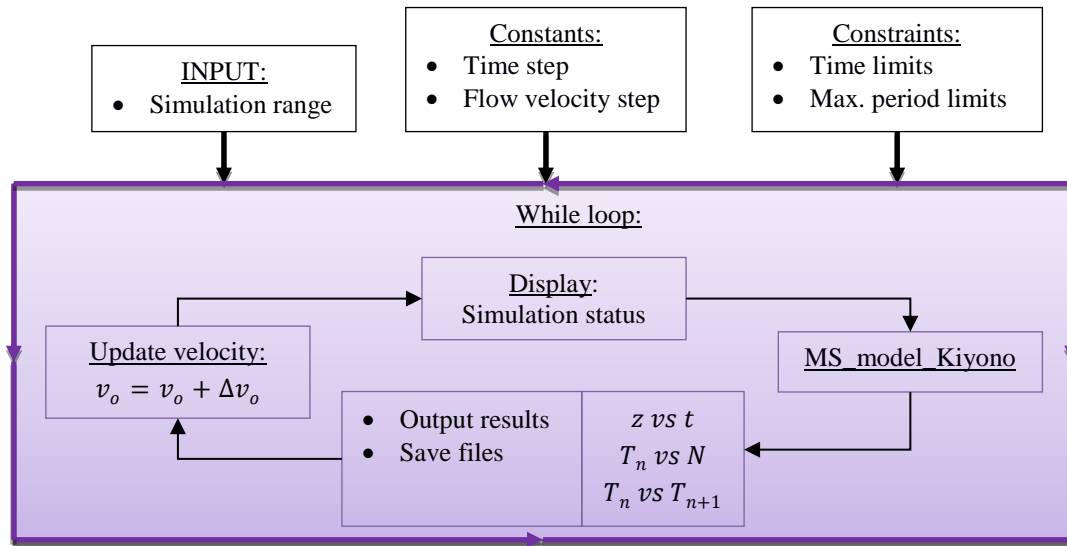


Figure 4.2.1: Simulation running pseudo code

The required inputs include the starting and finishing flow velocity under investigation. The velocity was calculated based on Equation 4.1.7 with input parameters of: $Re = 4$ as a starting point and $Re = 175$ as the end point, the inner diameter of the nozzle as 5 mm (chosen to match the diameter of the reference source [6]) density $\rho = 1001.6 \text{ kg/m}^3$ and dynamic viscosity of $\mu = 0.998 \text{ mPa}\cdot\text{s}$ at a temperature of $20 \text{ }^\circ\text{C}$ and pressure 101 kPa. The calculated velocity is equal to 0.79 mm/s and 19.933 mm/s. The simulation was decided to be limited to flow velocities of 0.005 to 0.22 in normalised units, just to cover the majority of the experimental area. The constants used in the simulation are the time step ($dt = 0.001$ of unit time, where the unit time is taken as 0.017 s – Equation 4.1.3), the flow rate step (0.00005 where the flow rate normalised unit value is taken as $\approx 0.0016 \text{ m/s}$). The expected simulation results dictates that in some cases it would be impossible to identify periodic repetition, due to the chaotic nature of the system. This led to limiting the

simulation time to 51 seconds (or 3000 time normalised units) and the maximum allowable detachment count to 100.

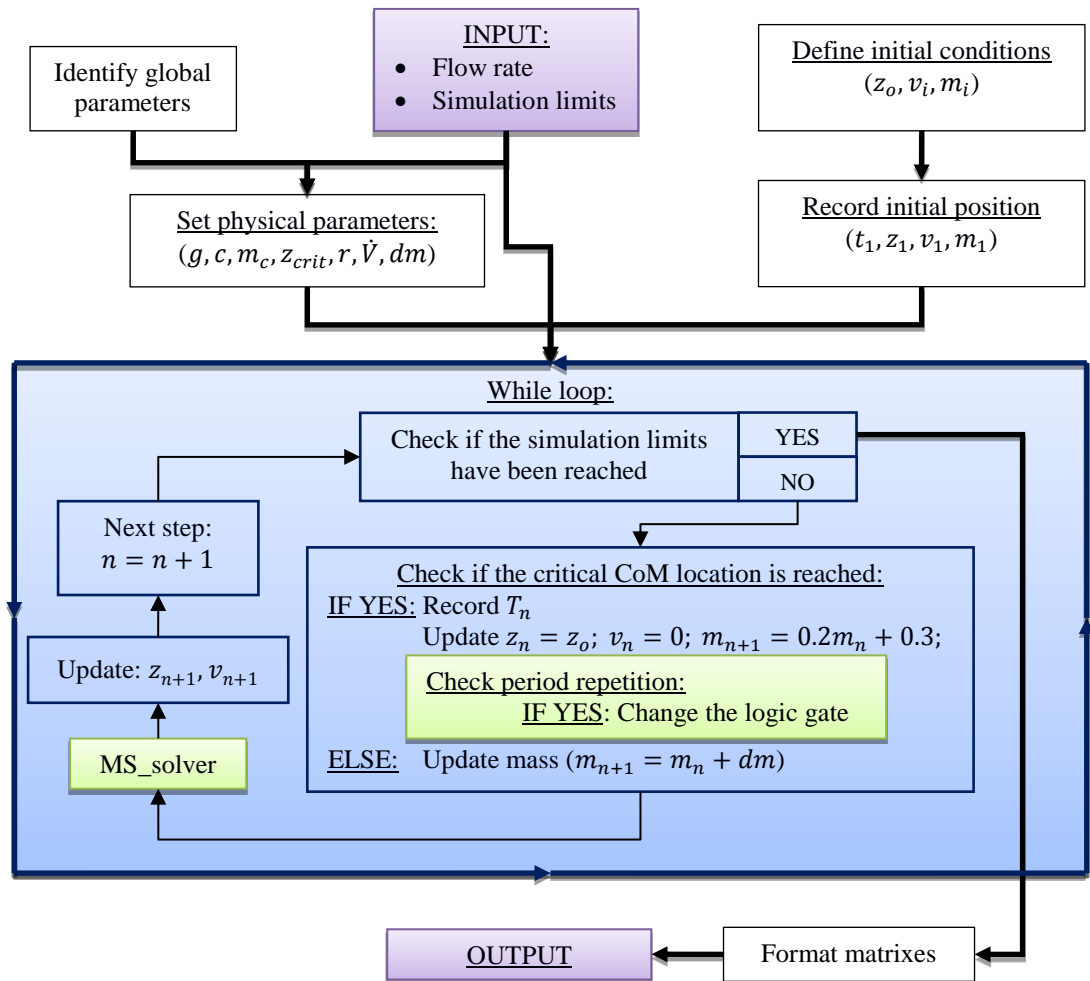


Figure 4.2.2: 1-D dripping dynamics simulation pseudo code

After all constants and constraints are set the simulation proceeds into a *while* loop where for each flow rate under investigation the repeating dripping periodicity is found, or the simulation maximum time is reached, or the maximum allowed number of dripping events has occurred. The process of identifying one of those three events is part of the subroutine code named here as “MS_model_Kiyono” (Appendix H.B). The *while* loop calculates and displays a message regarding the progress of the simulation, followed by entry into the calculation subroutine “MS_model_Kiyono” to start the calculations on drop formation. When the subroutine is completed, the results are saved in the form of a text file, which includes the Centre of Mass (CoM) position as a function of time and the dripping period. In addition, plots for the CoM vs time, dripping period vs period count and dripping period

return map are saved as ‘jpeg’ files. When the results are saved the next step in the simulation starts with an updated flow velocity, and the process continues until the full range of set velocities has been completed.

The dripping dynamics are based on the system of equations derived by Kiyono and Fuchikami [6] (Equations 4.1.1 from section 2.3). The code developed by the author initially requires some parameters mentioned previously (the flow velocity under investigation, the time step, simulation time limits and maximum allowable period count). The simulation outlines the “global” parameters (parameters that are used by the other sub-procedures). These include the following: gravitational acceleration, surface tension, flow rate, initial drop mass, critical drop mass (at which point the surface tension fails to hold the attached drop mass, which leads to necking and detachment) and the time after the last simulation step.

The initial conditions and physical parameters are set based on the normalised unit values shown in Equation 4.1.3 and are as follows:

- Gravitational constant $g = 1 \text{ ----- } 9.34 \quad m/s^2$
- Surface tension constant $c = 0.05 \text{ ----- } 0.0588 \quad mN \cdot s/m$
- Simulation starting mass $m_i = 0.02 \text{ ----- } 0.4 \quad mg$
- Drop critical mass $m_c = 4.61 \text{ ----- } 92.2 \quad mg$
- Drop CoM starting location $z_o = 2 \text{ ----- } 5.4 \quad mm$
- Drop CoM critical location $z_{crit} = 5.5 \text{ ----- } 14.85 \quad mm$
- Initial CoM velocity $v_i = 0$
- Density $\rho = 1 \text{ ----- } 1001.6 \quad kg/m^3$

The initial drop mass was chosen to be 0.02 with the CoM location chosen to be 2 (both values are unit values). Through simulations, it was found that approximation of the initial conditions has a minor impact on the system as the system stabilises within the first four detachments (section 4.3). A set of equations were used to calculate the flow rate and the mass increment for each time step.

$$\dot{V} = \pi r^2 v_o$$

$$dm = \rho \dot{V} dt$$

4.2.1

where: ρ – fluid density

\dot{V} – volumetric flow rate

r – nozzle radius (2.5 mm or 0.916 in normalised units)

v_o – flow velocity

dm – mass increment

dt – time increment

The following step of the code sets the size of the results matrices (time matrix, CoM position matrix and the detached drop mass matrix, with the exception of the dripping period matrix which is left unknown) and fills those matrices with the initial condition values. The next step is a logical *while* loop where two conditions must be satisfied in order to proceed with the simulation. Those conditions were set in “Simulation running code” and limit the simulation running time to 100 drops or by identifying repetition in the dripping periods.

Each loop starts with a check of the CoM location and if it exceeds the critical value, the code resets physical parameters (the drop mass, CoM location and speed as shown in Equation 4.1.6 – the values are assumed based on experimental results [6]). It also calculates the value of the dripping period and records it in the results matrix. The next step of the loop is only initiated when five dripping periods have been identified. The number of periods was selected based on results obtained from the first simulations, and subject to confirmation that for the single period dripping behaviour the system stabilizes within the first four drops. To identify repetition two consecutive periods should reoccur in the same order.

After all checks have been completed, the next step for the CoM location and the CoM velocity is calculated using ‘ODE45’ “MATLAB®” built in sub-code (Appendix H.C).

When the *while* loop is completed zero lines from the period, mass and CoM matrices are deleted to reduce the size of the matrix for saving.

The Equation 4.1.1 first need to be adapted by rearranging and introducing some assumptions. After rearranging:

$$\frac{dm}{dt} \frac{dz}{dt} - \frac{dm}{dt} v_o + m \frac{d^2z}{dt^2} - \frac{dv_o}{dt} = -kz - c \frac{dz}{dt} + mg \quad \left| \quad 4.2.2 \right.$$

where: $dm/dt = \dot{m}$ – mass flow rate

$v_o dm/dt \equiv 0$ – was the assumption made by Kiyono and Fuchikami as being negligible (of order v_o^2)

$dv_o/dt = 0$ – as v_o is a constant value

Dividing the whole equation by mass (m) and separating the second order component Equation 4.2.2 takes the form:

$$\frac{d^2z}{dt^2} = - \left(\frac{\dot{m} + c}{m} \right) \frac{dz}{dt} - \frac{k}{m} z + g \quad \left| \quad 4.2.3 \right.$$

Based on the time the drop mass (m) can be calculated based on the residual mass (Equation 4.1.6) and mass increase due to the constant flow rate (\dot{m}). The spring constant (k) is mass dependent (Equation 4.1.2), which requires consideration of both cases depending on the mass of the attached drop. The drop mass (m_i) can be calculated as:

$$m_i = m_r + \dot{m}(t_i - t_{det}) \quad \left| \quad 4.2.4 \right.$$

where: m_r – residual mass after last detachment

t_i – time at the i 'th step

t_{det} – time at the last drop detachment

Equation 4.2.3 depending on the value of $m_r + \dot{m}(t_i - t_{det})$ will take the form:

$$\frac{d^2z}{dt^2} = - \left(\frac{\dot{m} + c}{m_r + \dot{m}(t_i - t_{det})} \right) \frac{dz}{dt} - \frac{-11.4(m_r + \dot{m}(t_i - t_{det})) + 52.5}{m_r + \dot{m}(t_i - t_{det})} z + g \quad \left| \quad 4.2.5 \right.$$

for $m_r + \dot{m}(t_i - t_{det}) < 4.61$, and:

$$\frac{d^2z}{dt^2} = - \left(\frac{\dot{m} + c}{m_r + \dot{m}(t_i - t_{det})} \right) \frac{dz}{dt} + g \quad \left| \quad 4.2.6 \right.$$

for $m_r + \dot{m}(t_i - t_{det}) \geq 4.61$

To solve the differential Equations 4.2.5 and 4.2.6 with two unknowns (CoM location and CoM velocity) were used ‘ODE45’ “MATLAB®” built in solver. The solver as constrained by the ‘ODE45’ package requires the introduction of two first order differential equations. Begin by defining:

$$\begin{cases} x_1 = x \\ x_2 = \frac{dx}{dt} \end{cases} \quad \left| \quad 4.2.7 \right.$$

After taking the derivatives and replacing dx/dt with x_2 this provides two new first order differential equations:

$$\begin{cases} \frac{dx_1}{dt} = x_2 \\ \frac{dx_2}{dt} = \frac{d^2x_1}{dt^2} \end{cases} \quad \left| \quad 4.2.8 \right.$$

Which now can be substituted in Equations 4.2.5 and 4.2.6 leading to two first order systems of equations depending on the value of $m_r + \dot{m}(t_i - t_{det})$. Equation 4.2.5 will take the form:

$$\begin{cases} \frac{dz_1}{dt} = z_2 \\ \frac{dz_2}{dt} = - \left(\frac{\dot{m} + c}{m_r + \dot{m}(t_i - t_{det})} \right) \frac{dz}{dt} - \frac{-11.4(m_r + \dot{m}(t_i - t_{det})) + 52.5}{m_r + \dot{m}(t_i - t_{det})} z + g \end{cases} \quad \left| \quad 4.2.9 \right.$$

Moreover, the Equation 4.2.6 will take the form:

$$\begin{cases} \frac{dz_1}{dt} = z_2 \\ \frac{dz_2}{dt} = - \left(\frac{\dot{m} + c}{m_r + \dot{m}(t_i - t_{det})} \right) \frac{dz}{dt} + g \end{cases} \quad \left| \quad 4.2.10 \right.$$

The produced model required some post processing codes, which included an investigation of the bifurcation plot results (subsection 4.2.1 and Appendix H.D) and the visualisation code (Appendix H.E) for presentation of the results.

4.2.1 Power law investigation of the bifurcation plot results

The results of the 1-D Mass-Spring-Damper (MSD) model showed that there is some similarity in the bifurcation plot (Figure 4.3.5 – flow velocity versus dripping period). To investigate the possibility of the existence of a scaling factor (or power law) for the repetitive bifurcation areas, mathematical code (Figure 4.2.3) was developed using “MATLAB®” software. The code starts with the introduction of the simulation limits, constants and setting the results arrays, followed by a set of *for loops*, outlined below and explained in more detail in the following paragraphs:

- Process results *for loop*: read the results files, find the repeated sequence of length n , where $n < 100$ (if possible), plot bifurcation diagram
- Calculate enclosed areas *for loop*: find the bifurcation, calculate the area between minimum and maximum values of the period, delete false areas
- Finding the period jump *for loop*
- Finding the bifurcation start and end *for loop*
- Calculating the power values *for loop*

The initial simulation results are processed using a *for loop* in the range of the flow velocities associated with the experimental results (0.0225 – 0.130 in normalised units) and the loop step size is 0.00005. Periodic repetition is confirmed only when two consecutive periods reoccur in the same order. If repetition was not found the output results are the input file data less the first value (the first number was input as the starting point and does not arise from the simulation and for this reason is ignored). Otherwise, as a result, only the set of repetitive values is used.

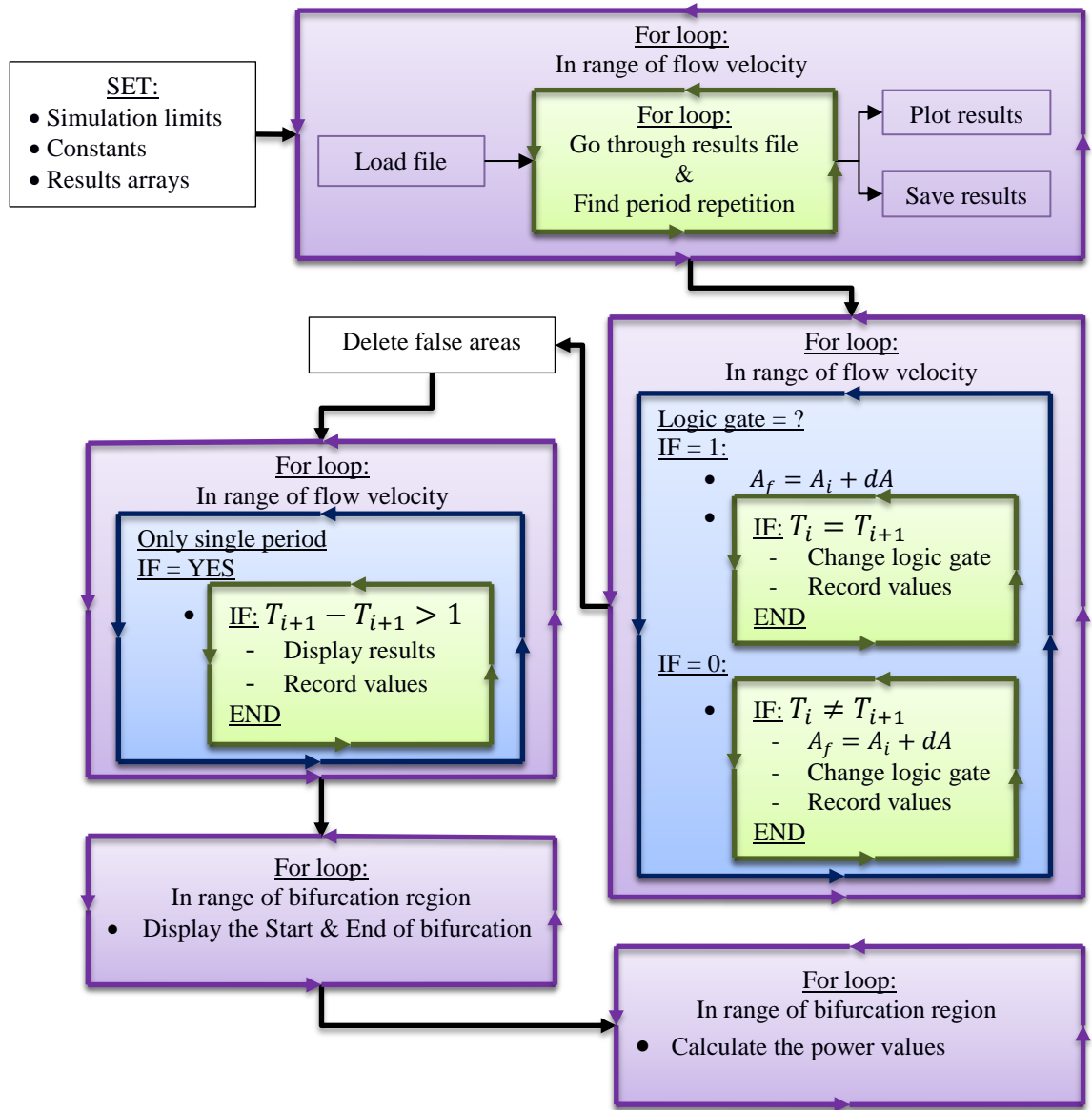


Figure 4.2.3: Power law investigation pseudo code

The area enclosed by the minimum and maximum was calculated using a trapezium area equation:

$$A = \sum_{i=v_m}^{v_n-1} \left(\frac{1}{2} dv (T_{i+1,max} + T_{i,max} - (T_{i+1,min} + T_{i,min})) \right) \quad \left| \quad 4.2.11 \right.$$

where: v_m and v_n are the values of the bifurcation region flow velocity at the start and end respectively

$T_{i,max}$ and $T_{i,min}$ are the maximum and minimum values of the dripping interval

Equation 4.2.11 assumes that between the two flow velocities (initial and final – v_i, v_f) there is a linear change in the dripping intervals (T_i and T_{i+1}).

The logic gate (see Figure 4.2.3, which checks if bifurcation exists and the enclosed area should be added – Equation 4.2.11) was used to reduce the calculation time as well as to be able to record each bifurcation region separately. The logical gate value identifies whether bifurcation was started or not. In the case when bifurcation was not yet detected the current flow velocity minimum and maximum values of the period time are checked, and if those values are not the same the area calculation is started, the logical gate value is changed and the starting velocity is recorded. In the case when bifurcation was detected the current flow velocity period is still compared, but if it is found that they are of the same value the logical value is changed, the sum of the areas and the end flow velocity are recorded. Otherwise, the summation of the areas continues.

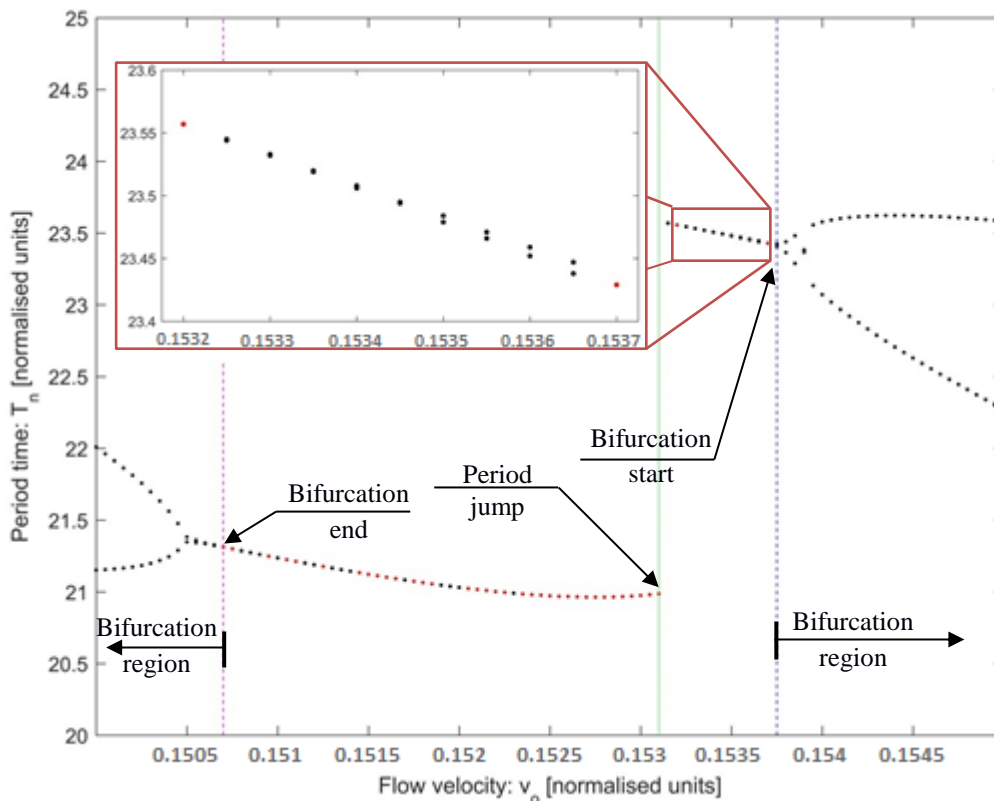


Figure 4.2.4: The bifurcation start-end and period jump identified; Area error identification; (Colour notation: **Black** – not a single period, **Red** – single period)

After all regions are identified, false areas are deleted. False areas are those that formed in a region of a single period and are usually characterised with a hundred times smaller area size than the main bifurcation regions. Figure 4.2.4 shows an enlarged view (red square) just after the period jump point one of the examples of a so-called ‘false area’, which is characterised by a single period at the beginning and at the end (**Red** dots – $v = 0.1532$ and $v = 0.1537$ respectively) and double period values in between (**Black** dots). As seen from Figure 4.2.4 the ‘false area’ is much smaller than the actual bifurcation region area (see ‘Bifurcation starts’ in Figure 4.2.4).

To identify the point of the period jump the period values are scanned for a substantial value increase (which was approximated to be higher than 1 (in normalised units)). The simulation time was reduced by introduction of the *If* statement which checks if there is only a single period (as the period jump after inspection of the results appears to be only in the single period dripping region. The resulting area, major bifurcation start and end are identified with dashed lines on the results graph (examples will be given in a future subsection associated with the results processing subsection – 4.3.2). The final loop calculates the power ratio between the related values (bifurcation region size, bifurcation length and period jump periodicity. The results of the simulation will be discussed in more detail in the following section (subsection 4.3.2).

4.3 One-dimensional MSD model results

This section consists of an analysis and comparison of the theoretical and experimental results. The theoretical work included the reproduction of a pre-existing Mass-Spring-Damper (MSD) model based on initial work by Shaw [3], followed by later developments performed by Kiyono and Fuchikami [4], [6], and by Osborne [5], [22]. The mathematical model formulation was explained in section 4.1 and the simulation procedure in section 4.2. The results of the following subsections will include confirmation that the 1-D model

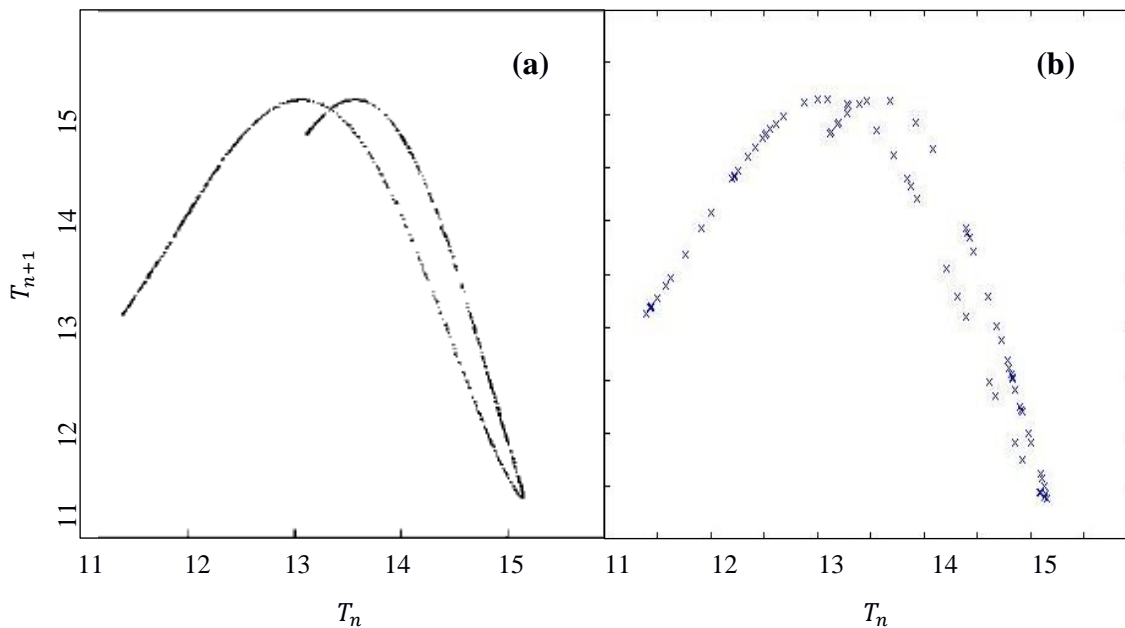
is correct, a summary of the results, the observed behaviour, chaotic development from periodic dripping through quasi-periodic dripping to chaos, and the nature of the repeatability of the system over the selected flow rate.

4.3.1 Confirmation of results

The results of the 1-D MSD model were compared to reference values [4] to confirm that the model developed is the right representation. The simulation parameters for this case were set to be exactly same as the reference values:

- Radius of the nozzle (2.5 mm, or 0.916 in normalised units)
- Flow velocity (≈ 0.0183 m/s, or 0.115 in normalised units)
- Which corresponds to a volume flow rate of ≈ 1291 ml/hr

The results confirmed that the simulation code for the 1-D model is comparable to the results of Kiyono and Fuchikami [6] and can be used for future analysis. In addition, as was expected the simulation time step (dt) has a major influence on the results. With $dt = 0.01$, the simulation produced only 11 different periods, while a time step of 0.001 has 76 periods. Unfortunately, the time required to compute increased by a factor of 14.



Periodic dripping return map. (a) – reference plot [4], (b) – simulation results plot

4.3.2 Analysis of results

The simulation results include flow velocities from 0.005 to 0.22 in normalised units (0.79 to 34.94 mm/s), which corresponds to Reynolds numbers of 4 and 175. The flow rate step was chosen to be 0.0005 ($Re = 0.4$). The simulation limits were discussed in section 4.2, where the maximum period count was set to be 100 and the time limit to 3000 (in time-normalised units).

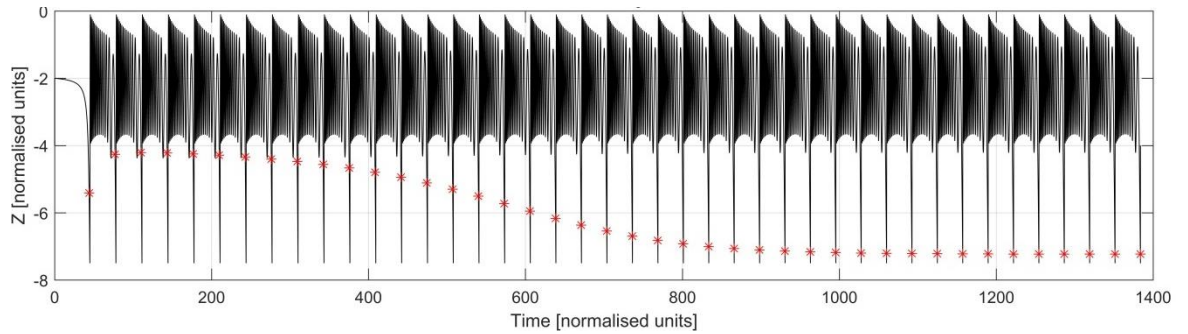


Figure 4.3.2: 1-D MSD Centre of Mass location results (Period 1)

Red – point of critical mass has been reached

The MSD operation can be visualised using a Center of Mass (CoM) location plot (Figure 4.3.2). The graph shows the results of the CoM location for a flow velocity of 0.0985, where the dripping has diverged to single period repetition ($T_n = 32.3500$).

After detachment has occurred, based on the model assumptions (section 4.1) the location of the drop updates to a value of -2 (the z-axis positive direction is assumed upwards and the top of the nozzle is zero) and the velocity of the CoM is set to zero. With this in mind to satisfy Equation 4.1.1, just after detachment of the drop the CoM is required to bounce upwards (Figure 4.3.2). The oscillation of the drop continues until the next detachment. The time and mass of the next drop detachment are based on the residual mass (described by Equation 4.1.6). In the case of single period dripping (Figure 4.3.3.a) the residual mass (or the mass at the detachment time) of the drop becomes constant, leading to repetition in the following period. The single period dripping critical mass can be achieved at any CoM velocity and is not associated with detachment location.

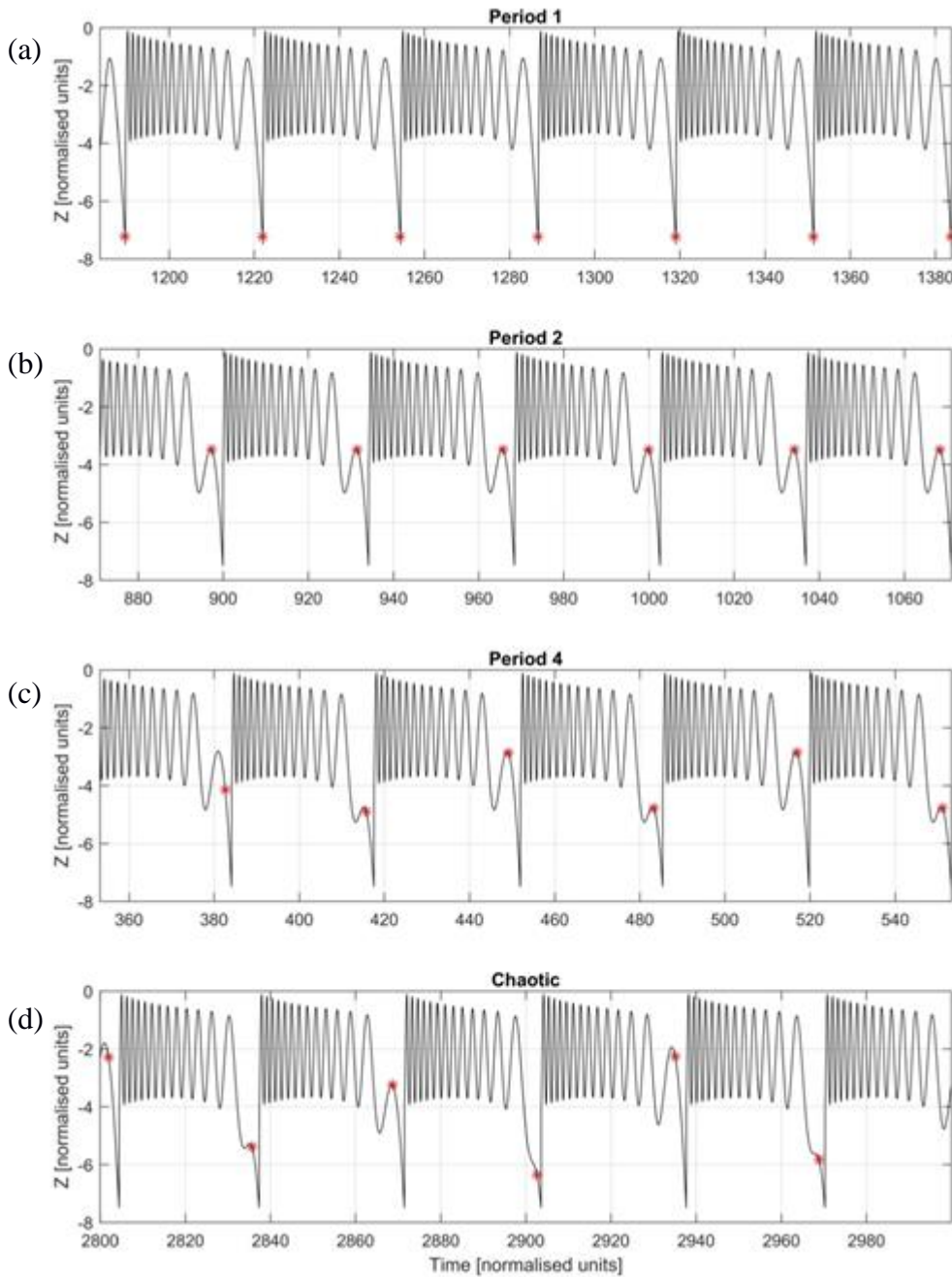


Figure 4.3.3: 1-D MSD model Centre of Mass location

(a) – single period: $v_o = 0.0985$; (b) – double periodic: $v_o = 0.0991$; (c) – quadro periodic: $v_o = 0.995$; (d) – chaotic region: $v_o = 0.10025$;

Red – point where critical mass has been reached

Quasi-periodic dripping (non-single period dripping – section 2.2) is associated with instability where the drop residual mass (section 2.2) does not remain constant so that in some cases this leads to periodic repetition (Figure 4.3.3.b – Figure 4.3.3.c).

Figure 4.3.4 is a summary of the results of the simulation, showing the period (T_n) versus the flow velocity (v_o , normalised units) and the Reynolds number. The periodic time axis

is on a logarithmic scale to aid the presentation. The red area identifies the regions where simulation did not find periodic repetition (did not converge to a solution – due to limitations applied in the code).

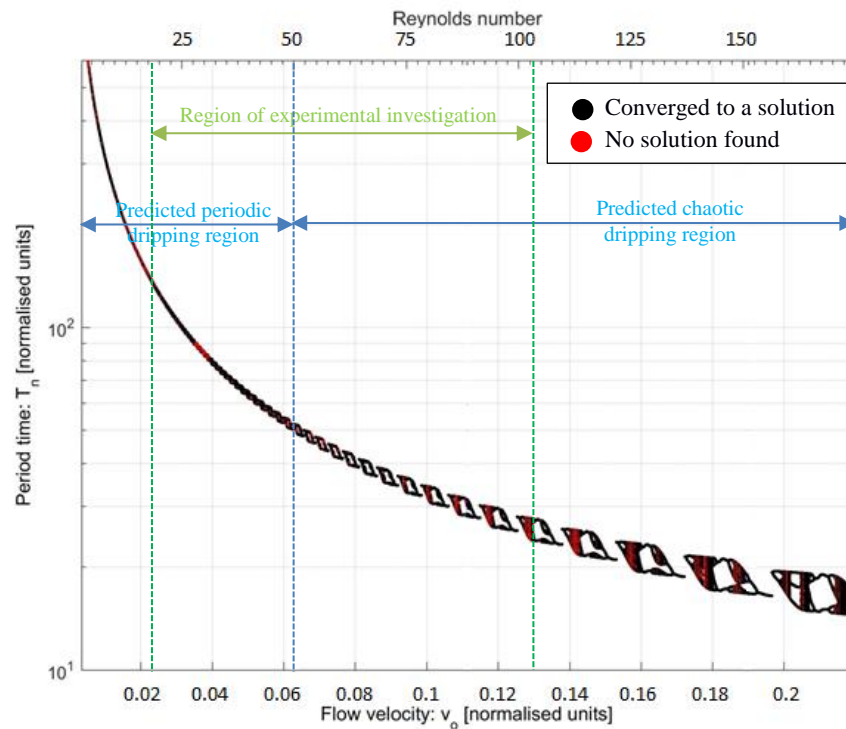


Figure 4.3.4: 1-D MSD model bifurcation results

Previously it was anticipated that the chaotic dripping region should be in the region of a Reynolds number of 50 – 562 (section 4.1). The simulation results showed that the model produces chaotic regions before the range of the predicted value (Figure 4.3.4). In the experimental results (section 7.2), it was identified that the system does exhibit some instability which one can speculative could lead to bifurcation regions, unfortunately this was not confirmed due to camera limitations. The camera is filming at a frame rate of 1/30 s, hence the time precision is limited to this value. The time step in the mathematical model is much higher (of order 10^{-4}).

Future discussions will concentrate on the region similar to experiments (Reynolds number from 50 to 100 – Figure 4.3.4). The full range of bifurcation results are provided in Appendix I. The aforementioned region shows multiple bifurcation regions (B1 – B10), separated by a period jump area.

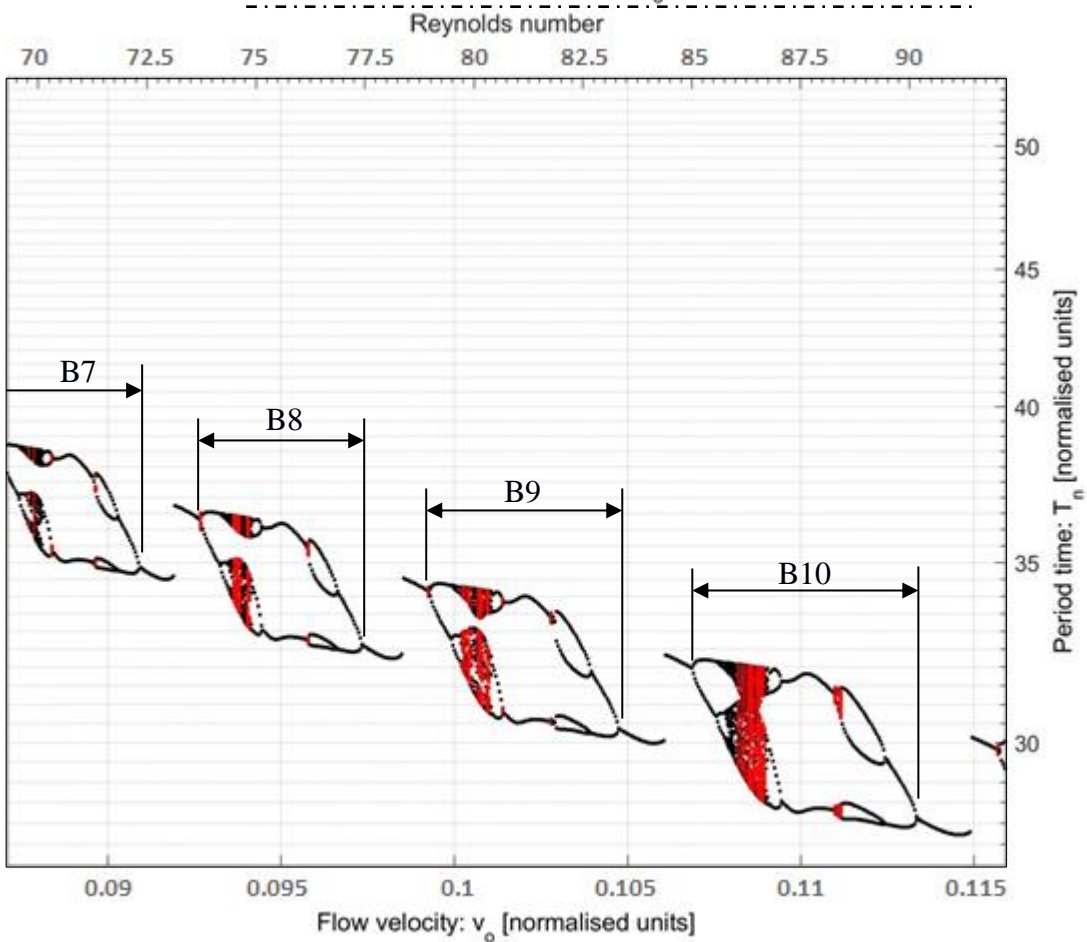
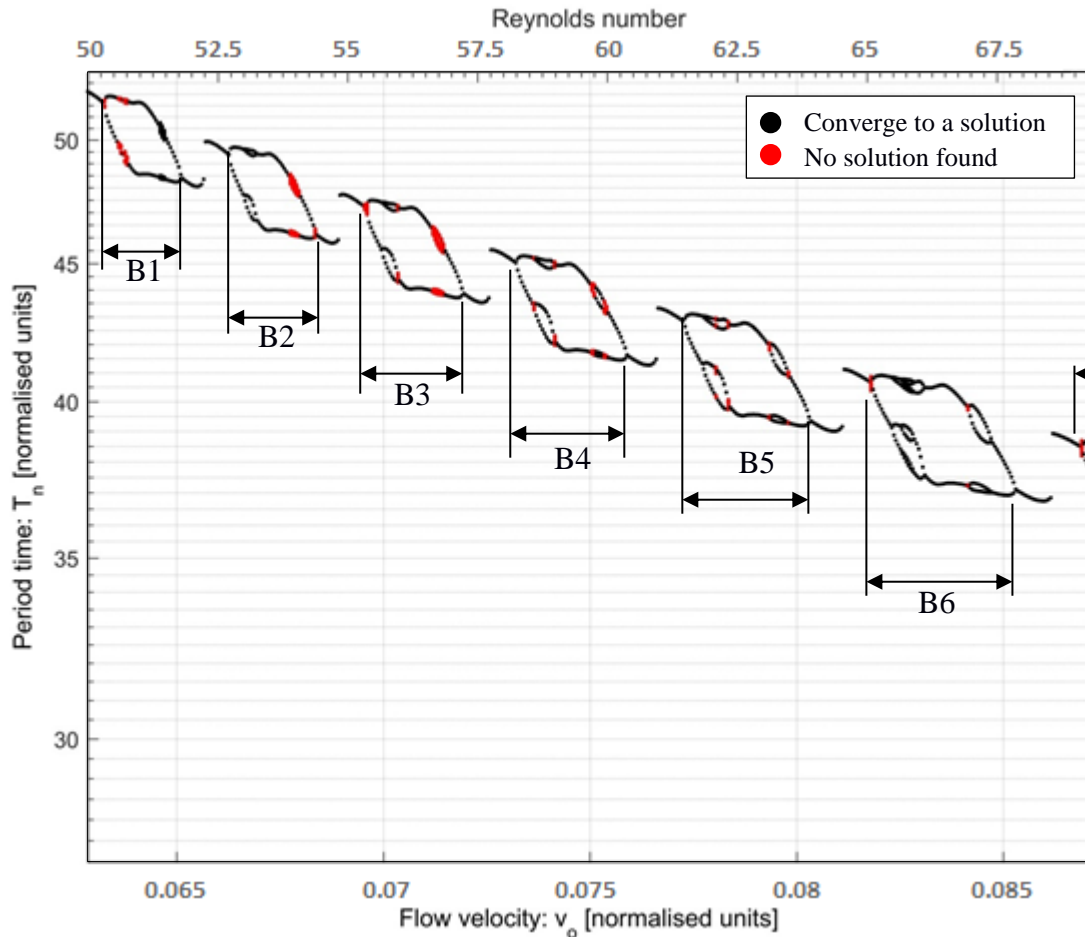


Figure 4.3.5: 1-D MSD results in the experimental investigation region

Here, the bifurcation region is defined as the area between single period solutions (where only single period dripping is occurring). The period jump region is the sudden marginal increase of the dripping period with a slight increase in the flow velocity. As the studied mathematical model does not depend on flow velocity changes (each flow velocity simulation is independent of the previous simulation). In this research, it was found that the period jump for the MSD model is associated with the initial disturbances which result in a sudden change in the attractor location, where the attractor is defined as a point on the period return map to which quasi-periodic dripping tends to converge its solution (sections 2.2 and 2.3). The bifurcation points as seen in Figure 4.3.5 are usually associated with a highly unstable dynamic system. This explains why the calculations quite often do not converge to a solution (identified in red in Figure 4.3.5). Throughout the analyses of the bifurcation map, it was noted that the bifurcation regions exhibit a repetitive pattern, with a slight change in its size. To assess this repetition the size (the area enclosed between the maximum and minimum period value) and the occurrence of the bifurcation regions were analysed. The mathematical code was developed in “MATLAB®” software (subsection 4.2.1 and Appendix H.D).

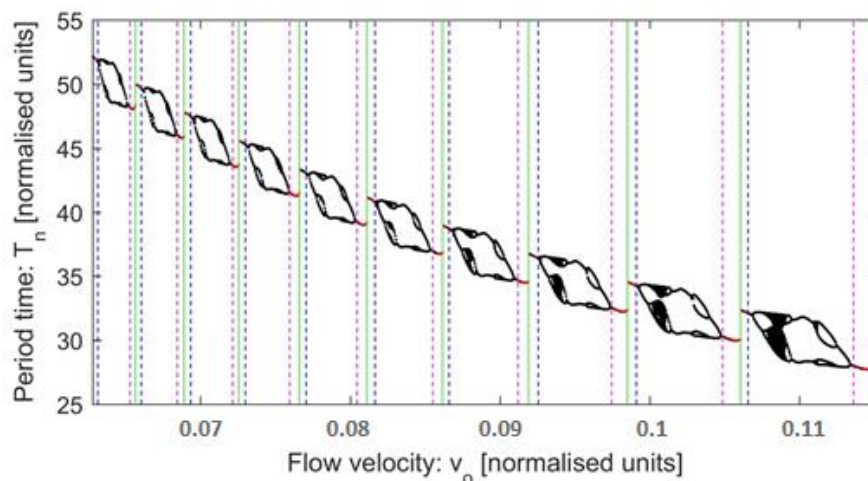


Figure 4.3.6: Power law investigation results
 (Colour notation: **Black** – not a single period, **Red** – single period, **Blue** – bifurcation start, **Magenta** – bifurcation end, **Green** – period jump)

Figure 4.3.6 shows ten bifurcation periods (B1-B10), where **Black** points are associated with multiple periods while **Red** points identify regions of a single period. Vertical lines

identify the bifurcation start, end and period jump positions are shown in **Blue**, **Magenta** and **Green** respectively.

The investigation of the power law considered the following cases:

- Bifurcation region size increase (between minimum and maximum period values)
 - Simplified case, where the bifurcation region is expected to change one-dimensionally

$$A_i = A_{i+1}^\zeta \quad | \quad 4.3.1$$

where: A_i and A_{i+1} – successive bifurcation regions

ζ – power constant

- Two-dimensional power dependence, where the bifurcation region enclosed area depends on the x and y coordinates independently

$$(a_x a_y)_i = (a_x^\zeta a_y^\tau)_{i+1} \quad | \quad 4.3.2$$

where: a_x and a_y – bifurcation area dimension change in x and y coordinates

ζ and τ – power constants

- The two-dimensional power dependence investigation was introduced, when after visual inspection of the results (as seen in Figure 4.3.6) it was found that the x -coordinate (periodic dripping time) of the bifurcation region changes at a different rate to the y -coordinate (flow velocity).
- Bifurcation start and end flow velocity (v_o) range size increase

$$(v_{bif. f.} - v_{bif. s.})_i = (v_{bif. f.} - v_{bif. s.})_{i+1}^\zeta \quad | \quad 4.3.3$$

where: $bif. f.$ and $bif. s.$ – bifurcation region (i or $i + 1$) finish and start flow velocities

Equations 4.3.1 and 4.3.2 were rearranged to calculate the power constant:

$$\zeta = \ln(A_i) / \ln(A_{i+1}) \quad | \quad 4.3.4$$

$$\zeta = \frac{\ln(v_{bif. f.} - v_{bif. s.})_i}{\ln(v_{bif. f.} - v_{bif. s.})_{i+1}} \quad | \quad 4.3.5$$

In the case of the two-dimensional power dependence, the assumption was made that

$a_x a_y = A$ hence $a_y = A/a_x$ leading to:

$$A_i = (a_x^{\zeta - \tau})_{i+1} A_{i+1}^\tau \quad | \quad 4.3.6$$

or,

$$\ln A_i = (\zeta - \tau) \ln(a_x)_{i+1} + \tau \ln A_{i+1} \quad | \quad 4.3.7$$

To solve the the equation above with two unknowns (ζ and τ) three bifurcation regions were taken into account and solved simultaneously:

$$\begin{cases} \ln A_i = (\zeta - \tau) \ln(a_x)_{i+1} + \tau \ln A_{i+1} \\ \ln A_{i+1} = (\zeta - \tau) \ln(a_x)_{i+2} + \tau \ln A_{i+2} \end{cases} \quad | \quad 4.3.8$$

or in matrix form:

$$\begin{bmatrix} \zeta - \tau \\ \tau \end{bmatrix} = \begin{bmatrix} \ln(a_x)_{i+1} & \ln A_{i+1} \\ \ln(a_x)_{i+2} & \ln A_{i+2} \end{bmatrix} / \begin{bmatrix} \ln A_i \\ \ln A_{i+1} \end{bmatrix} \quad | \quad 4.3.9$$

The solution showed no scaling law factor in any of the cases under investigation (Figure 4.3.7), resulting in the suggestion that this dynamic system is not associated with a power law dependence of the bifurcation regions for the 1-D MSD model. There was no other literature source found that can confirm this analysis, hence the results shown here should be taken with caution.

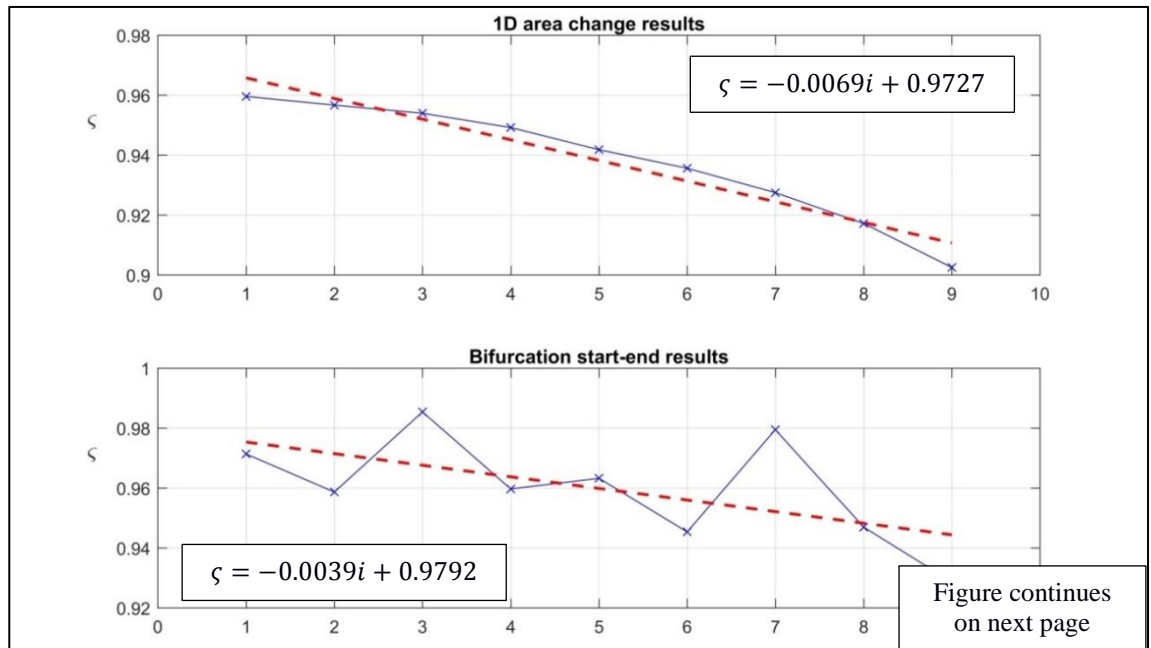


Figure 4.3.7: Bifurcation regions power law investigation scaling factor results

Blue – periodic scaling factor; *Red* – linear approximation

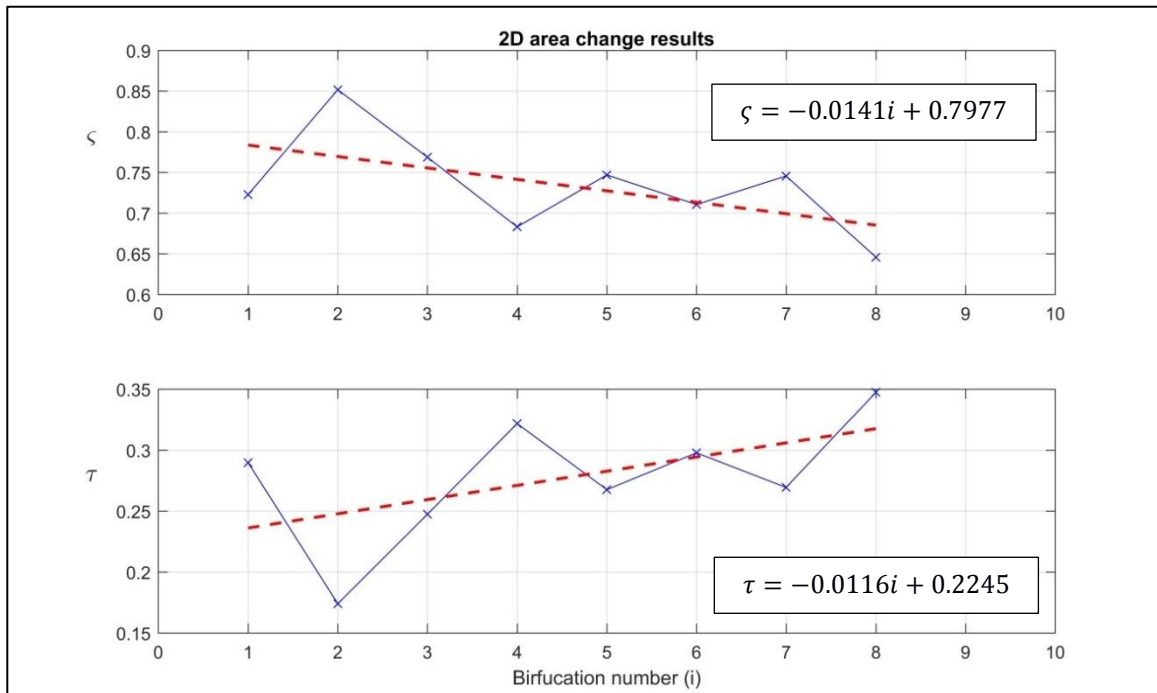


Figure 4.3.7: Bifurcation regions power law investigation scaling factor results

Blue – periodic scaling factor; *Red* – linear approximation

To investigate the bifurcation process set of periods versus period number graphs were used (Figure 4.3.8) based on the region of $v_o = [0.105, 0.1075]$.

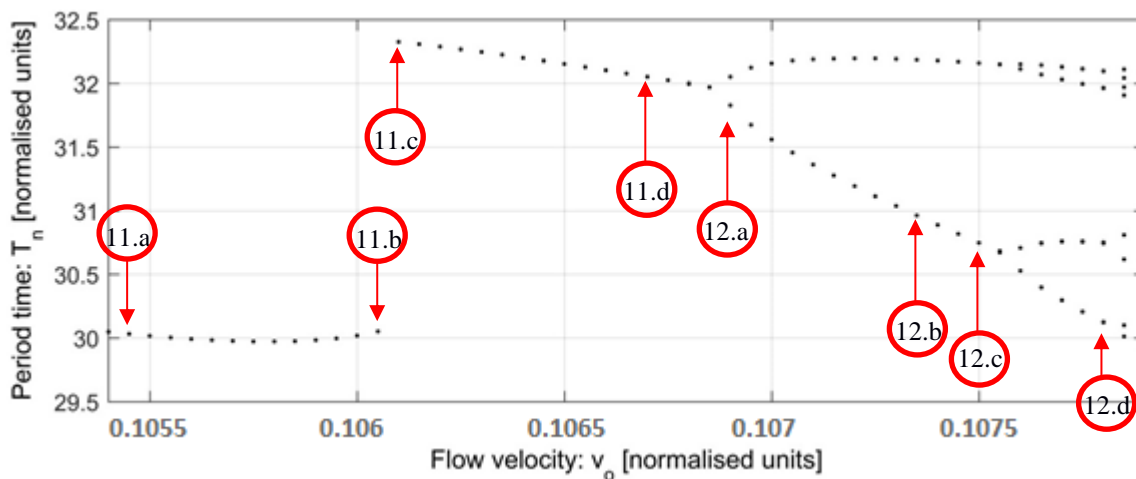


Figure 4.3.8: Bifurcation process investigation region

Prior to the discussion on the bifurcation process, it is highly important to explain the simulation starting procedure. From the MSD model Equation 4.1.1 the drop behaviour is dependent on the CoM location (z), velocity (dz/dt) and the mass (m) variables. Initial values for the drop location and its velocity are set to be equal to -2 and 0 respectively in

normalised units, similar to the simulation drop detachment reset conditions. The starting mass of the drop, on the other hand, is set to be equal to 0.02 (in normalised units) as the assumed value, and is not linked to anything. With those three variables pre-set, the drop is far from its attractor region, from which it follows that each simulation is required to adjust its dripping pattern over some time (leading to periodic or quasi-periodic dripping modes).

At the end of each bifurcation region (in the case presented in B9 – Figure 4.3.5) there is single period dripping. Convergence to the final point is achieved relatively fast, meaning that any disturbance introduced initially has a low impact on the time taken for the system to stabilise (Figure 4.3.9.a).

With an increase in the flow velocity (Figure 4.3.9.b), the stabilisation time and the initial disturbance amplitude (vibration of the drop CoM) increases, meaning that the system attractor (single point attractor) becomes less dominant. Following an additional increase in the flow rate, the system attractor will be changed in a sudden period value jump (Figure 4.3.9.c).

This leads to the statement that in the approach to the period jump point the stability of the system decreases, which leads to the conclusion that the initial conditions or disturbances in the flow will define the attractor location and the final dripping period, hence the period jump point.

The period jump marks the start of the new bifurcation region (B10 – Figure 4.3.5). The stabilisation time continues to decrease and the amplitude due to initial disturbance also reduces. In addition to that, the response of the dynamic system changes from fully damped (Figure 4.3.9.b) to slightly underdamped system (Figure 4.3.9.c). This response continues to propagate increasing the stabilisation time of the system (Figure 4.3.9.d and the amplitude of those vibrations, which still concentrates around the single point attractor.

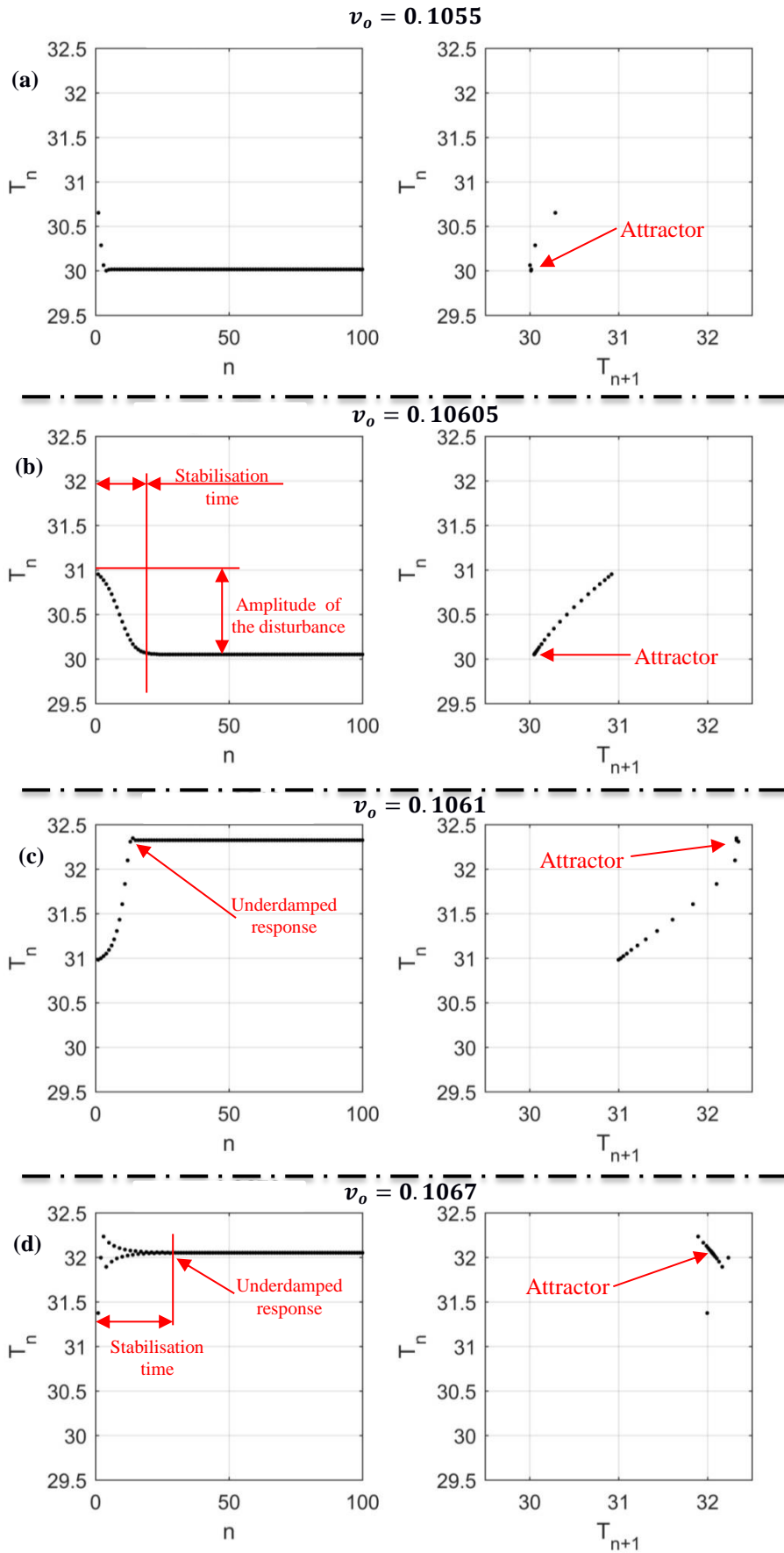


Figure 4.3.9: Bifurcation process (1)

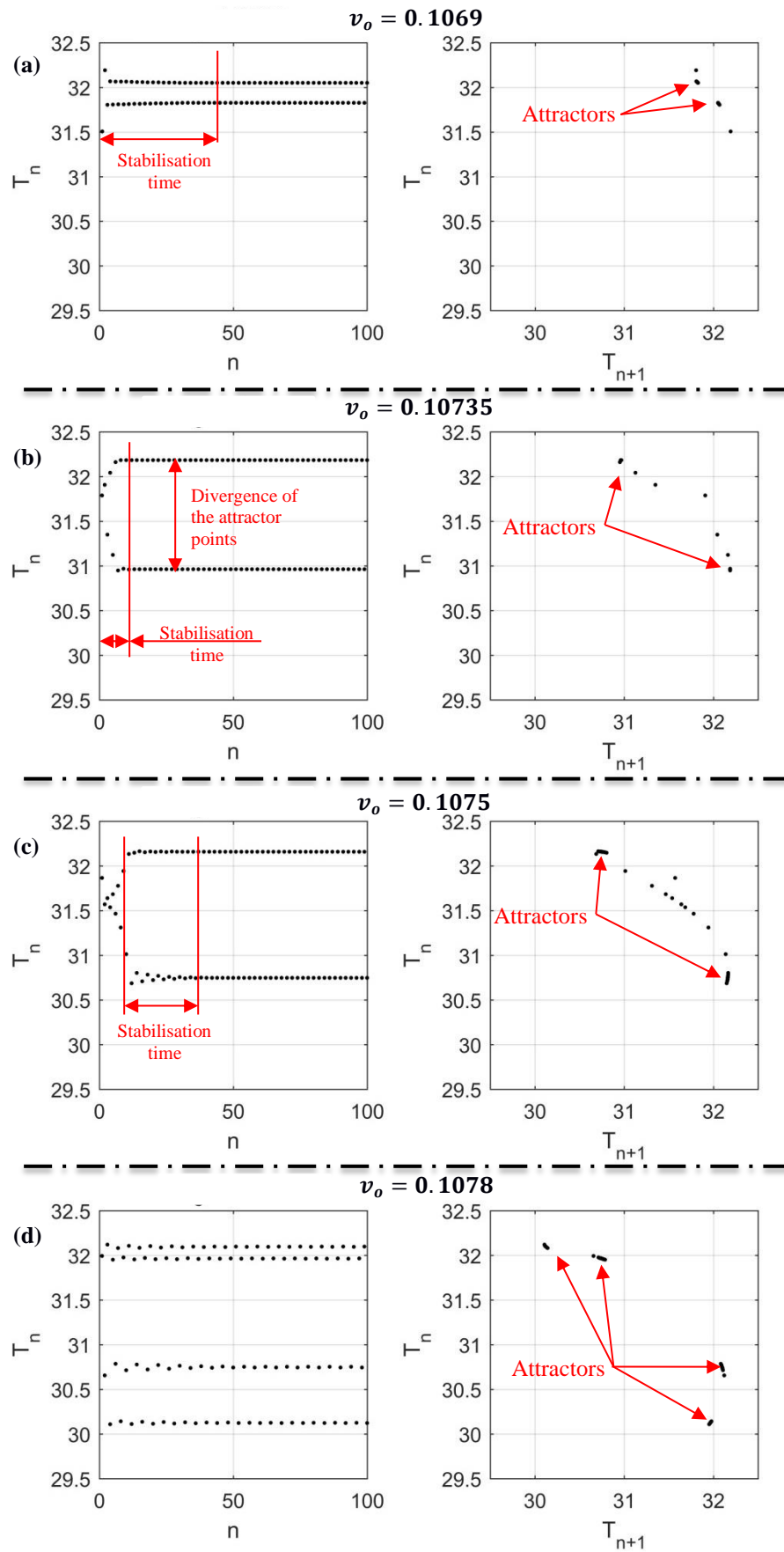


Figure 4.3.10: Bifurcation process (2)

This underdamped vibration stabilisation time with an increase in the flow rate will lead to the first bifurcation point (Figure 4.3.10.a). Based on simulation data, the point of the bifurcation is another unstable point (as mentioned above), which required additional computational time for the simulation to converge to a solution. The statement here is that in the approach to the bifurcation point the system becomes highly unstable, meaning that the bifurcation point is dependent on any disturbances to the system or on the initial conditions.

Bifurcation is identified as a quasi-periodic dripping mode where more than one attractor exists (for first level bifurcation this leads to a two-point attractor system). Following an increase in the flow velocity the system stabilisation time will be minimised (Figure 4.3.10.b). In addition, the attractor points will diverge from each other, which in the case of an additional increase in flow velocity will provide the ground for future instability (Figure 4.3.10.c). The speculated nature of the instability here is due to the same factors as before (due to flow disturbance). Similarly, both attractor points will become unstable and follow the behaviour of an underdamped system, leading to a fully developed four-point attractor system (Figure 4.3.10.d).

The simulation shows that the dynamic system should exhibit a fully developed chaotic region (Figure 4.3.11). It can be noticed (Figure 4.3.11 – T_n vs n map) that there is no correlation between previous cycles and the future periods.

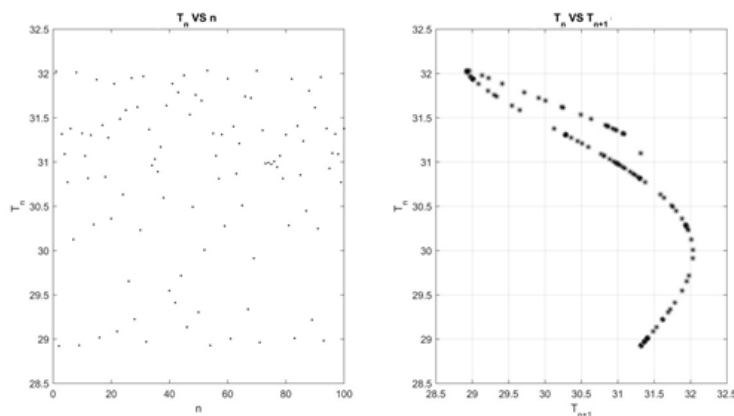


Figure 4.3.11: Fully developed chaotic region
Flow velocity of 0.1085 [Normalised units]

Away from the chaotic region clustering around the attractor points becomes well identified (Figure 4.3.12).

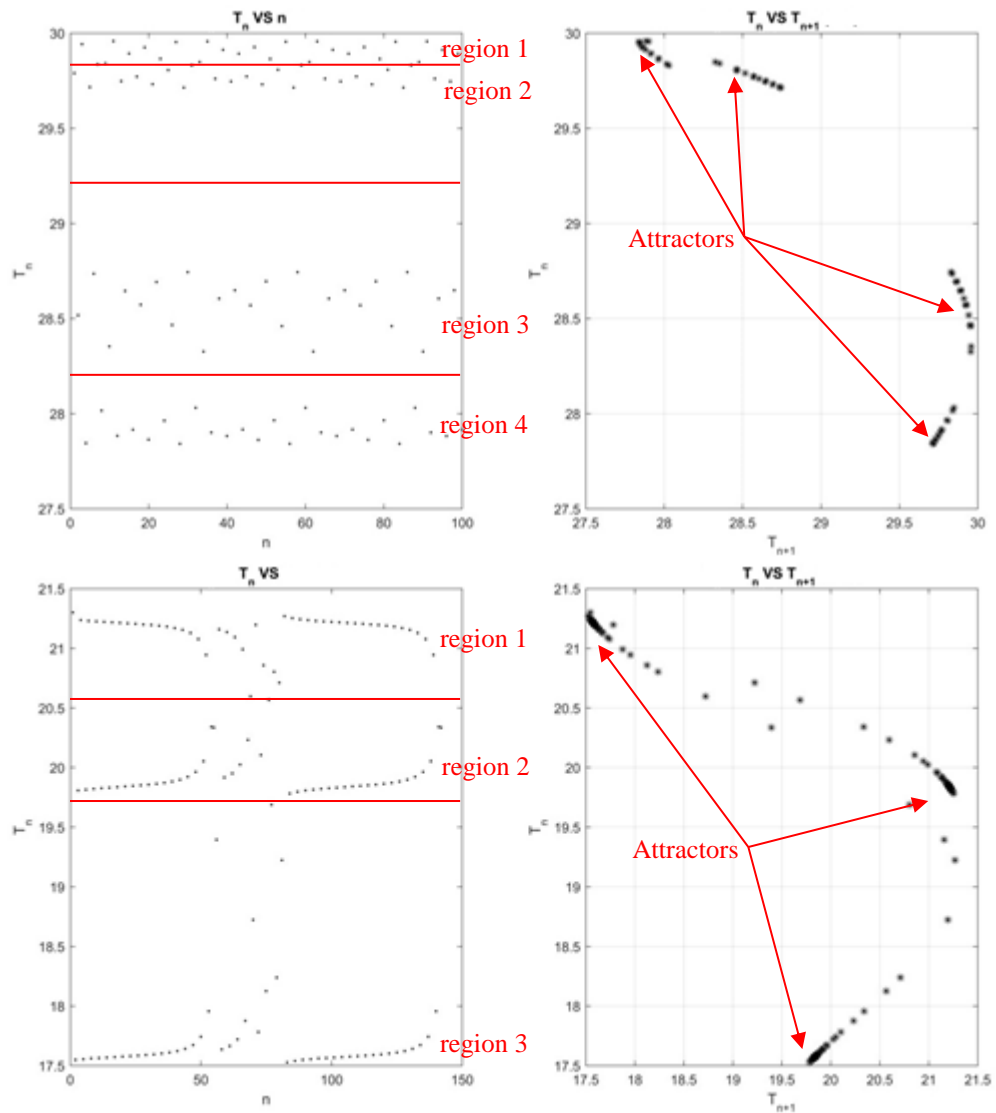


Figure 4.3.12: Clustering

a – 4-point attractor Flow rate 0.11685 [Normalised units];
b – 3-point attractor, Flow rate 0.17795 [Normalised units];

Figure 4.3.12.b displays another interesting feature of the system, where the system breaks down towards chaos but within a few drops the cycles return to the attractor region. The flow rate in Figure 4.3.12.b is close to the collapse of the attractors (leading to a two-attractor region) which, as was mentioned above, should result in a highly unstable system, which is dependent on the input conditions and other disturbances.

CHAPTER 5

EXPERIMENTAL MODULE

In previous chapters work on the mathematical model and the Drop Tower was presented. In the chapters, which will follow the third part of the work, will be presented. The experimental concept will be introduced, requiring the development of an experimental module and protocol to investigate the dynamics of fluid dripping. The initial idea was to investigate the behaviour of drops in a chaotic region in both normal and microgravity environments. The microgravity environment was to be produced using the Drop Tower (described in a previous chapter) built at Kingston University. Unfortunately, in later stages it was agreed due to circumstances beyond the control of the author to limit the experimental work to normal gravity experiments only. This chapter will discuss the experimental module that was built to achieve the required experimental results. The experimental requirements were summarised in section 1.1 and will be discussed in more detail in section 5.2.

The work described in this research is different to any other performed before in several ways. First, the amount of data that was obtained and processed is substantially larger than any before reported. One hundred and twenty tests were performed with the flow rate ranging from 60 to 332 ml/hr, with the amount of drops per test ranging from 120 to 500.

Secondly, the use of two cameras to obtain the Centre of Mass (CoM) location of the drop in three spatial dimensions, which was not performed by others. This provided insight into the drop behaviour in periodic and chaotic dripping modes, and scrutinises the existing mathematical model with some information on improving it. Thirdly, the work has shown multiple complex behaviours associated with system dynamics, such as jet formation and its collapse, mid-drops, and no-residual mass detachments (subsection 6.5.2). The design of the experimental module, its components and assembly work will be presented in the section that follows (section 5.3). This section will discuss the design consideration for experiment components and the component trade-off analysis. The design choices were made based on the requirements and similar set-ups that were overviewed in section 0 in the literature review.

The last two sections 5.4 and 5.5 will concentrate on calibration and the experimental procedure itself. To simplify the test workflow, the experimental procedure for both test types (microgravity and normal gravity) was chosen to be identical. Firstly, section 5.4 shows the calibration procedure for the installed components, which include the pump, accelerometer and thermocouple sensors. This is followed by the last section of this chapter (5.5), which discusses in detail the experiment set-up and the experimental procedure.

In addition, in the appendix sections (Appendix J – Appendix N), the experimental module technical drawings, module operational software codes, circuit diagram and camera calibration results are included.

5.1 Experimental module operational targets

The research target requires to answer the following questions (section 1.1):

1. Is the Mass-Spring-Damper (MSD) model a correct representation of dripping dynamics?

2. Identification of the parameters of the horizontal oscillations in the dripping system

To achieve those targets experimentally it is required (Figure 5.1.1) to produce water drops at a specific flow rate (chapter 1) while simultaneously recording the video from two perpendicular directions. The video data is then processed by a video processing code. This data is then used to identify the spring and damper constants (section 2.3) for the MSD model (which is considered to be a representation of the dripping dynamics), and later to be compared with a pre-existing 1-D model and outline the parameters for future MSD models. This approach should answer the first and second research questions proposed for investigation in this research.

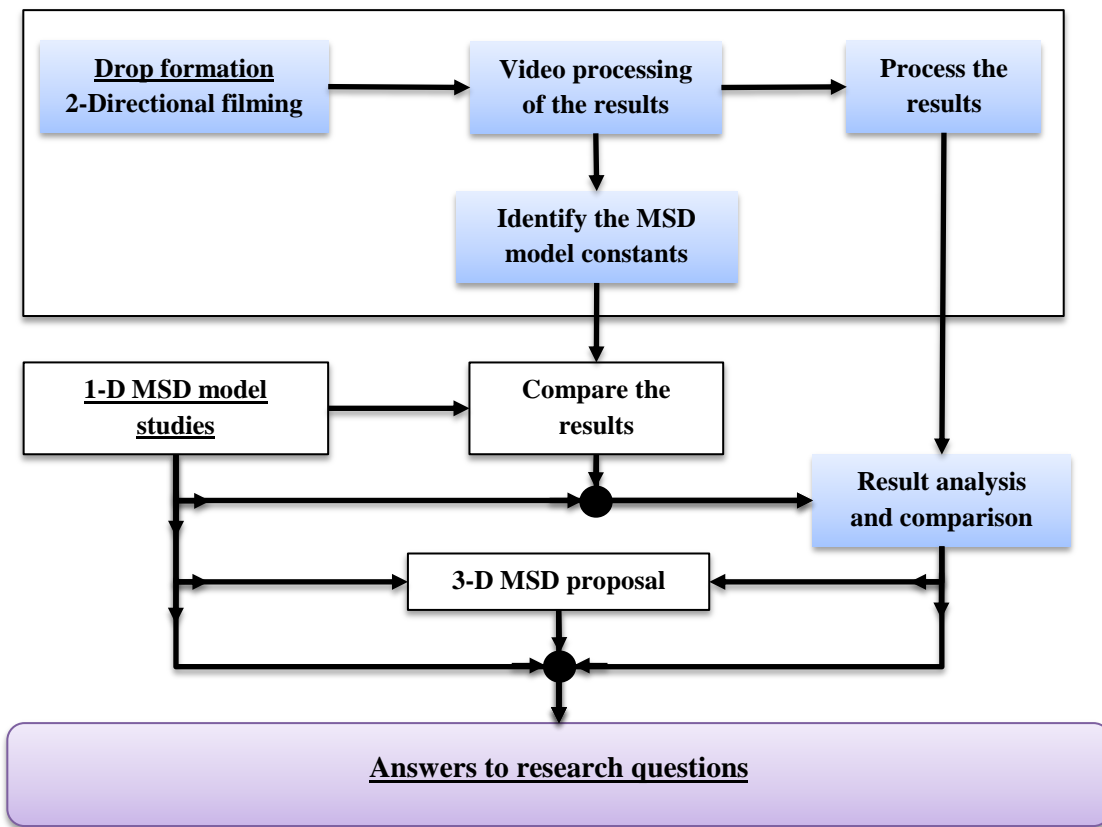


Figure 5.1.1: Research target interlinks and procedure

The experimental module should allow the tests to be carried out in a normal gravity environment. The large quantity of test data implies that the experimental reset time should be minimised. The requirements for the test module were derived from three constraints:

1. Through the test campaign, it is required to obtain the necessary experimental results, as identified by the research targets – Experimental constraints and requirements
2. The obtained results are required to be reliable with minimum errors, meaning that all dynamic system variables should be monitored – Results reliability constraints and requirements
3. The experiment module is required to operate under Drop Tower loadings – Drop Tower constraints (was not used at a later stage)

5.1.1 Experimental constraints and requirements

The experimental constraints and requirements are based mostly on previous research undertaken by Dr Barnaby Osborne [5]. For this research, the working medium was chosen to be distilled water, which is dispensed into the air. The reason for that was to have results that could be compared with previous research [4] – [5], [10], [14] – [20]. This requires the liquid under test to be fully defined.

The Navier-Stokes Equation 2.2.3 and continuity Equation 2.2.4 provide the list of the variables required to be recorded to fully define the flow. This includes the:

- Density of the liquid (ρ)
- Viscosity of the liquid (μ)
- Jet velocity (v_o)
- Pressure of the liquid (p)
- Acceleration constant (ξ)
- Time (t)
- Mass (m)
- Volume (V)

In addition, as shown by Tomotika [8], Lin and Lian [10], and Clanet and Lasheras [14] the dynamics of dripping are also specifically related to the:

- Density of the surrounding medium (ρ_{out}), and
- Fluid surface tension (σ)

The surface tension, density of the water, density of the surrounding medium and viscosity are all temperature dependent (Figure 5.1.2, Figure 5.1.3 and Table 5.1.1) [24].

Temperature (°C)	Density (g/cm ³)
15	1.225
20	1.2041
25	1.1839

Table 5.1.1: Air density at different temperatures
(at atmospheric pressure of 101 kPa; [24])

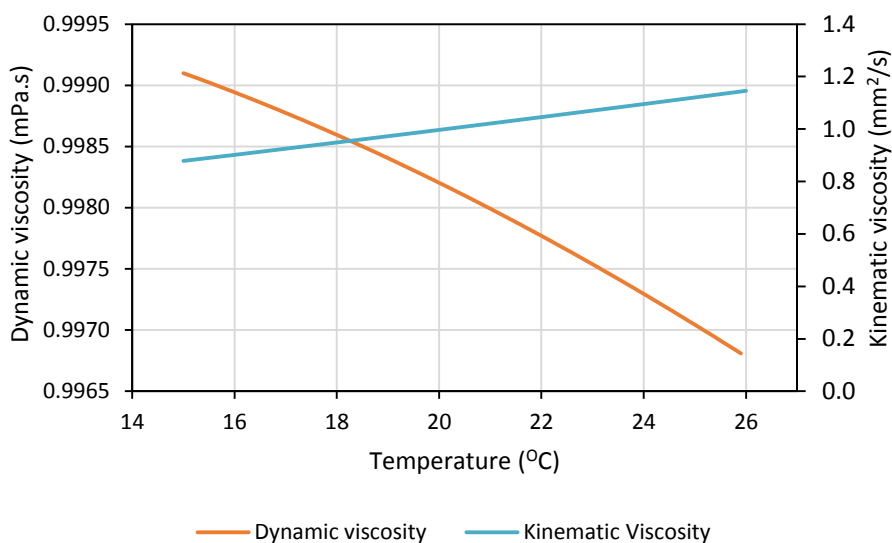


Figure 5.1.2: Water dynamic and kinematic viscosities vs temperature
(distilled water at an atmospheric pressure of 101 kPa; reproduced from [24])

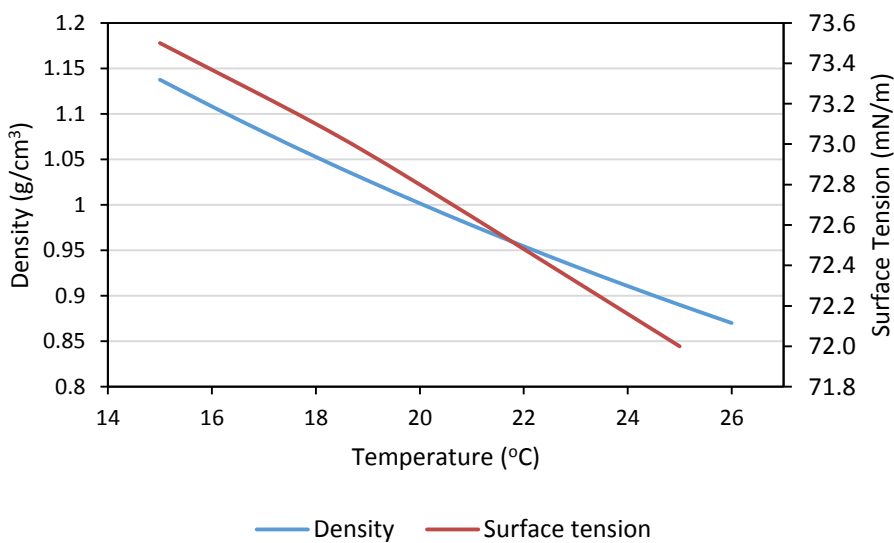


Figure 5.1.3: Water density and surface tension vs temperature
(distilled water at an atmospheric pressure of 101 kPa; reproduced from [24])

The temperature will be recorded, and using the reference values given in Figure 5.1.2, Figure 5.1.3 and Table 5.1.1 will define the values of the densities, the surface tension and the viscosity. It is assumed that the variation in the atmospheric pressure can be neglected [61], nevertheless the atmospheric pressure was monitored twice a day while the experimental campaign was undertaken (Table 6.2.1) for future reference. The reason for neglecting the pressure effects is due to the minor daily variations (within ± 3 kPa – as recorded during the test campaign – Table 6.2.1) from the selected normal pressure of 101 kPa.

The jet velocity is calculated based on Reynolds number in the region of interest. The lower limit for the Reynolds number under investigation as advised by Dr Barnaby Osborne [5] was set to be 50. The value of the top limit based on Clanet and Lasheras work [14] or Osborne [5], where the start of jetting region can be calculated using the critical Weber number (We_c) (Equation 2.2.1). The critical Weber number calculation requires knowing both the outer Bond number (Bo_o) and inner Bond number (Bo). Those values correspond to values of wetting diameter and jet stream diameter respectively. To simplify the experimental set-up non-wetting material (Polytetrafluoroethylene (PTFE) – section 5.3.1) was used as the nozzle, which leads to the assumption that the outer Bond number is equal to the inner Bond number (as it is expected there will be minimum to no contact with the nozzle tip surface). Choosing the nozzle inner diameter to be equal to 1 mm, the critical Bond number (Bo_c – Bond number when the jetting starts) using Equation 2.2.2 can be calculated to be:

$$Bo_c = 0.26 \quad \Bigg| \quad 5.1.1$$

At 20 °C temperature, 101 kPa atmospheric pressure and normal acceleration due to gravity. The value of the critical Weber number becomes equal to:

$$We_c = 4.04 \quad | \quad 5.1.2$$

Rearranging the Weber number (Equation 2.1.2) for velocity and substituting into the formula for the Reynolds number (Equation 2.1.5) gives the value of the critical Reynolds number (Re_c – Reynolds number when the jetting starts):

$$Re_c = \sqrt{We_c \frac{\sigma \rho d}{\mu^2}} = 542.64 \quad | \quad 5.1.3$$

Knowing the value of the nozzle inner diameter (d) to be 1 mm and the Reynolds number limits ($Re_{min} = 50$ and $Re_{max} = 560.86$) the minimum and maximum flow rates can be calculated using Equation 5.1.4, and these become equal to $\dot{V}_{min} \approx 141$ ml/hr $\dot{V}_{max} \approx 1534$ ml/hr.

$$\dot{V} = \pi d \frac{Re \mu}{4\rho} \quad | \quad 5.1.4$$

In summary Table 5.1.2 provides the experimental variables that are required to be monitored or controlled.

Symbol	Parameter name	Measured/controlled using
ρ	Density of the liquid	Values are set using the table relations. The value of the temperature is measured.
ρ_{out}	Density of the surrounding fluid	
μ	Viscosity of the liquid	
σ	Fluid surface tension	
p	Fluid pressure	Measured using a pressure sensor
ξ	Acceleration due to gravity	Measured using an accelerometer
v_o	Flow velocity	Controlled using a pump
ξ	Acceleration due to gravity	Controlled using the Drop Tower

Table 5.1.2: Experimental variable specification

5.1.2 Result in reliability constraints and requirements

The values being monitored or controlled were summarised in Table 5.1.2. In addition to that, to allow for future comparison to mathematical models disturbances to the experimental variables should be minimised. Section 0 provided some insight into the possibility of limiting the noise in the experimental set-up.

The fluid flow is required to have a specific flow rate, and any disturbance in the flow will affect the results, especially in the region of interest, which is the chaotic region, where the dependence of the flow velocity precision is crucial. The nature of chaos dictates that any disturbance in the system can lead to different results [5]. This leads to the fact that any fluctuations in the flow rate should be limited as much as possible and the flow should be fully developed. Another factor that affects the flow dynamics is external vibrations, which introduce additional forces and can lead to an offset of the chaotic region and corrupt the experimental data.

As was shown by Tomotika [8], the jetting system is dependent on the properties of the surrounding fluid, which means that any variation in the pressure surrounding the drop has an effect on the drop shape. To minimise this effect, the area of the experiment should be enclosed to limit those fluctuations, similarly to the experimental set-up proposed by Cordero et al. [11] and Gunde et al. [19].

Fluid properties such as density, viscosity and surface tension are also affected by the presence of contaminants.

Finally, the investigation requires that the drop surface should be fully defined in three dimensions, meaning that the recording is required to be taken from two perpendicular directions.

5.1.3 Drop Tower constraints

There are mechanical constraints associated with the operation of the Drop Tower. Normal gravity experiments are less concerned with loading constraints, which effectively requires the payload to sustain rigidity only.

Based on the Drop Tower characteristics (Table 3.1.3), the payload is required to:

- Fit into the payload maximum size constraints, which is 418.6×418.6×418.6 mm
- Sustain 5g acceleration or deceleration loadings for 0.31 seconds
- Be fully self-sustained, i.e. not connected to any external sources of power

5.2 Experimental module requirements summary

The experimental constraints outlined in the previous sections led on to the development of the experimental module requirements (Table 5.2.1). The table provides all necessary limitations for the future module design, component selection and experimental set-up. The requirements are separated into five categories based on the design system area. Additionally, the importance of the requirements is set in case the requirement is impossible to fully fulfil (1 to be of the highest importance – red, and 3 to be of the lowest importance – green).

ID	Category	Requirement	Importance
1.1	Fluid system	It is required to produce the water fluid jet	1
1.2		The flow disturbances should be minimised	1
1.3		The nozzle should be made from non-wetting material, and the external radius at the nozzle tip should be as small as possible	1
1.4		The flow temperature should be constantly monitored	1
1.5		Test cell, where the dripping is going to happen is required to be protected from external air flows	1
1.6		The external pressure should be constantly monitored	2
1.7		The fluid circuit should be well sealed	2

ID	Category	Requirement	Importance
1.8		It is required to monitor dynamic system variables: gravity, vibration	2
1.9		The fluid flow should be controlled with the flow rates to be from 141 to 1534 ml/hr	3
2.1	Structural design	The design of the module and experimental components should be able to withstand $\sim 50 \text{ m/s}^2$ acceleration/deceleration for duration of 0.31 s	1
2.2		Should operate at close to zero-g environment for duration of 2.1 s	1
2.3		Fit within the size/volume/mass of drop tower test environment	1
2.4		The structure of the test module should be designed so as to damp received external vibrations within allowed levels, within a limited time	1
3.1	Data collection	The system is required to record and store all sensor and the camera data	1
3.2		The recorded data should be easily accessible	3
3.3		The storage volume should allow for full day operation without needing uploading	3
4.1	Camera system	Record dynamic fluid system behaviour via camera use with the highest possible resolution and frame rate	1
4.2		Use of two cameras to allow for axonometric drop shape	1
4.3		It is required to use appropriate lighting to allow for the highest value in detail	2
5.1	Electronics system	The data acquisition device and the data storage device need to be included in the design	1
5.2		The experimental operation should be self-contained	1
5.3		The power system should be supplied with the design	1
5.4		The test module should be easy to reset or be able to perform several test runs without external intervention	3

Table 5.2.1: Experimental module requirements

5.3 Experimental module design and assembly

The design of the experimental module, which is based on the requirements given in the previous section, was done using Solidworks software (Figure 5.3.2). The design technical drawings are included in Appendix J.

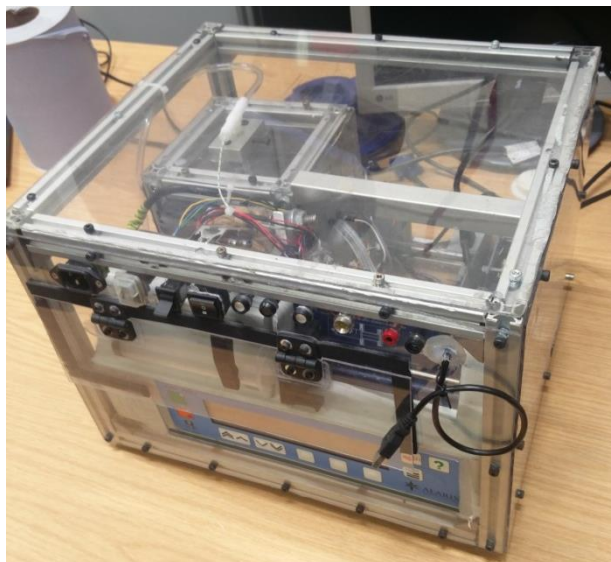


Figure 5.3.1: Assembled experimental module

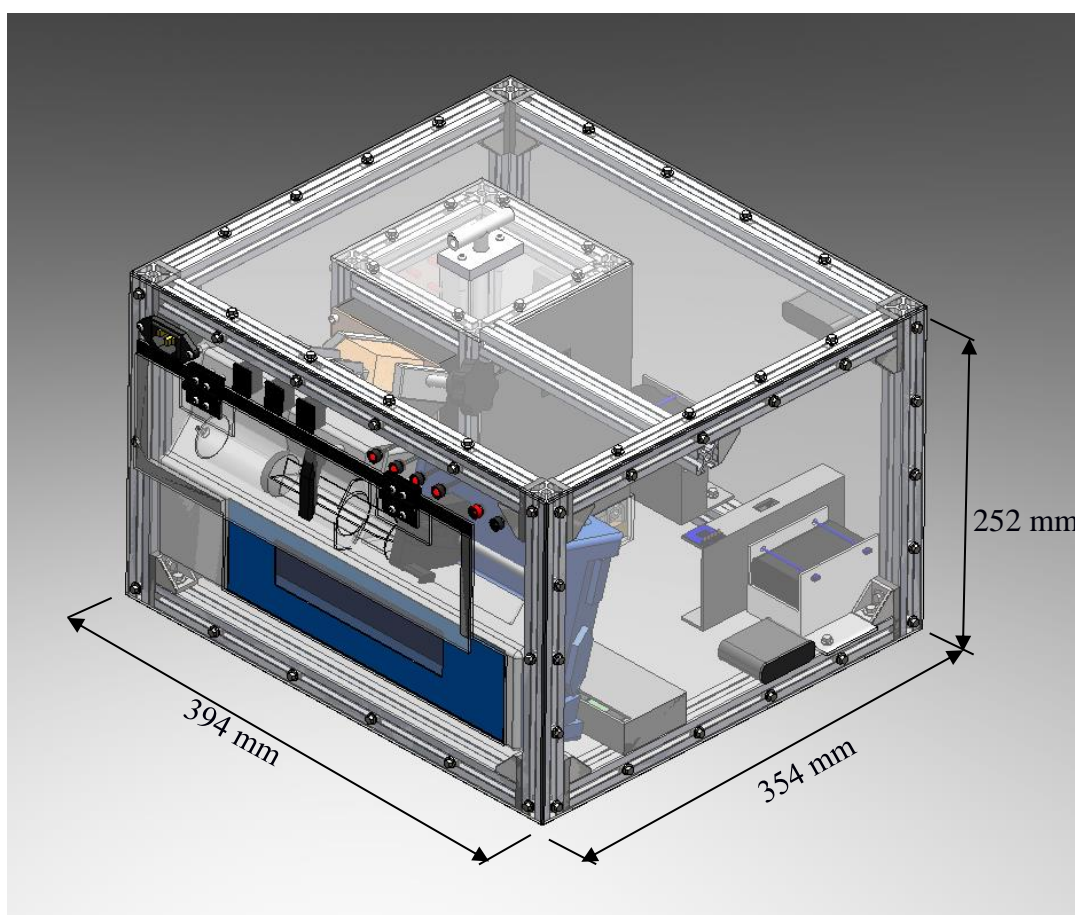


Figure 5.3.2: Isometric view of the experimental module design

The completely built module size is $394 \times 252 \times 354 \pm 0.5$ mm (Width \times Height \times Depth), with the total mass of 10.90 ± 0.05 kg (dry mass – empty mass).

The fluid system consists of (Figure 5.3.3):

- Pump

- Syringe
- Tubing and tee-connector
- Test chamber (surrounding structure, water collection pot)
- Nozzle
- Sensors (thermocouple and accelerometers)

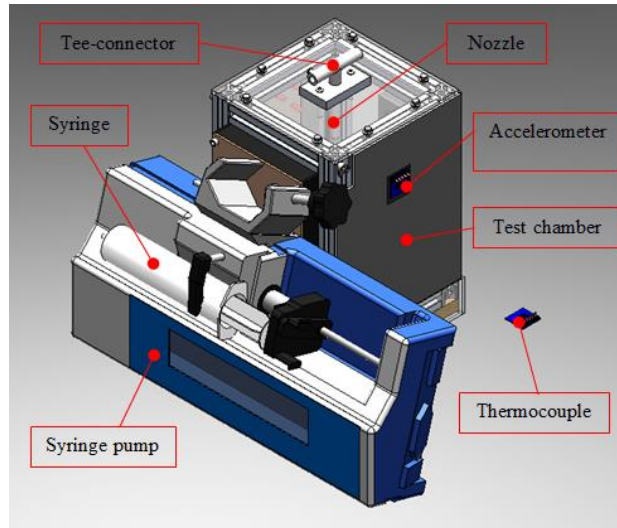


Figure 5.3.3: Fluid system components

The structure of the module consists of (Figure 5.3.4):

- Aluminium profiles with brackets
- Surrounding
- Vibration dampers

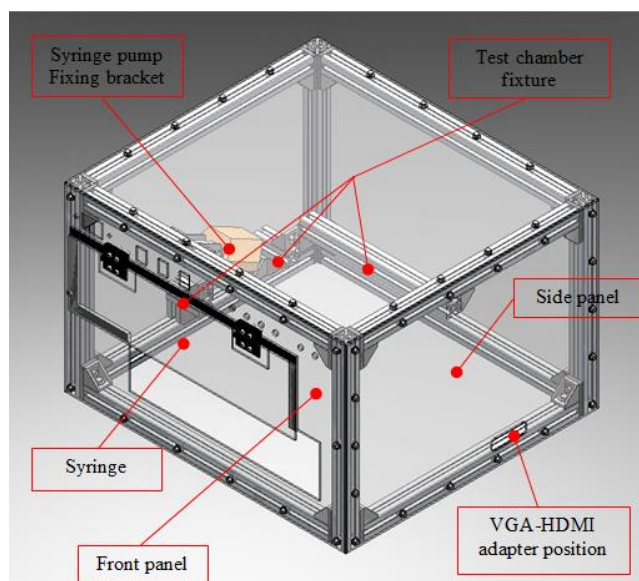


Figure 5.3.4: Structure components

The electronics, data collection and camera components consist of (Figure 5.3.5):

- Onboard computers
- Cameras
- Batteries (for onboard computer and for light panels)
- Control panel (switches, identification Light Emitting Diodes (LEDs), charging points)
- Video output cable adaptors

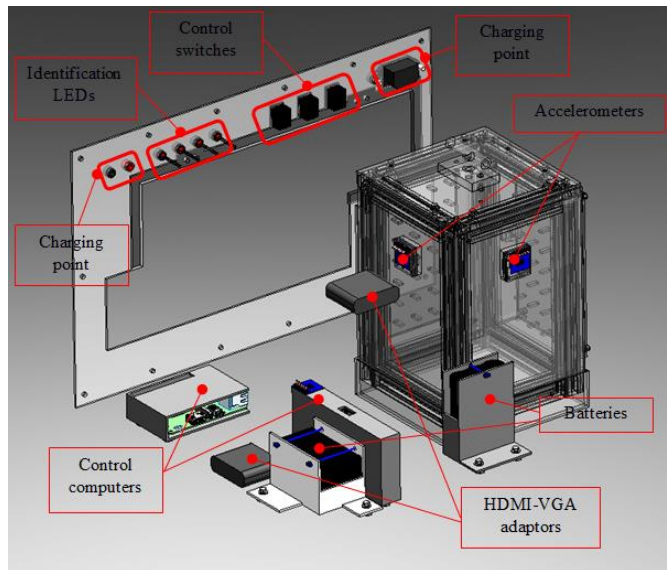


Figure 5.3.5: Data processing, cameras and electronics components

5.3.1 Fluid system

The water jet is produced using the IVAC P6000 pump [62] (Figure 5.3.3), which can provide a maximum purge rate of 500 ml/hr ($Re = 177.16$), which is below the required maximum. Nevertheless, the syringe pump allows investigation of 37% of the initially proposed flow region. At the same time, the pump provides $\pm 2\%$ volumetric flow rate error, with a flow rate step increase of 1 ml/hr (corresponding to a Reynolds number increase of 4.8×10^{-3} at 20 °C, 101 kPa). The trade-off included a comparison with a syringe pump, a peristaltic pump and a diaphragm pump. The pumps were valued under different comparison criteria (Table 5.3.1)), important to the operational and experimental constraints. Each comparison criterion has its own value of importance, on a scale from

one to three (three is the maximum and one is the minimum). The pumps were compared using the description available in a data repository [63] and online research. The performance of the pump on each comparison criterion is valued on the scale. The final choice was to use the syringe pump as it scored the highest as being the most suitable overall for experimental operation.

Comparison Criteria	Weighting	Pump Name		
		Syringe	Peristaltic	Diaphragm
High range of flow rates	3	1	3	2
Low flow induced noise	3	3	2	3
High accuracy	3	3	3	2
High volume capacity	2	2	3	3
Small size	2	2	3	2
Low mass	3	2	2	2
Small power consumption	1	2	3	3
Flow rate has high repeatability	2	3	2	3
Easy to programme	3	3	2	2
Corrosion resistance	2	3	3	3
Cost	3	3	1	1
MAX:	75	67	64	61
		Total:		

Table 5.3.1: Pump trade-off analysis

All pumps initially selected for comparison had more or less similar performances. The main drawback of the syringe pump is the allowable flow rate. For the peristaltic pump and diaphragm pump, the main drawback is the cost, which ranges from £250 to £450. In addition, the diaphragm pump has a low value of the accuracy and the limitation in allowable flow rates. At the same time, the IVAC pump was sourced for a reasonable price of £45

The syringe pump provides $\Delta x_{fluct} = \pm 1\%$ drive fluctuation which at 500 ml/hr and BD Plastic 60 syringe (which extends by $x_{syr} = 110$ mm when fully retracted at $V_{syr} = 60$ ml) corresponds to a linear velocity (Δv_{fluct}) uncertainty of:

$$\Delta v_{fluct} = \frac{\Delta x_{fluct}}{100} \cdot x_{syr} \cdot \frac{\dot{V}}{3600V_{syr}} = \pm 0.00255\dot{V} \quad \left| \quad 5.3.1 \right.$$

where: \dot{V} – volumetric flow rate (measured in ml/hr)

In addition, to minimise the disturbance the silicon-based TYGON® S3 E-3613 [64] (Figure 5.3.1) tubing is used, which can provide a 60% reduction in pulsation [65]. So that the linear velocity fluctuation now becomes equal to:

$$\Delta v_{fluct} = \pm 0.00102\dot{V} \quad \left| \quad 5.3.2 \right.$$



Figure 5.3.6: Manufactured nozzle

The nozzle (Figure 5.3.6) was made out of PolyTetraFluoroEthylene (PTFE) with the surface contact angle of 109.2° [66] and a minimum outer radius at the tip of the nozzle of $d_o = 2.00 \pm 0.05$ mm (as measured by the lathe machinery). Figure 5.3.7 shows that there is minimal contact between the drop and the nozzle. In addition, the nozzle tip was made to have the shape of a cone to reduce any accidental interference with the nozzle.

The nozzle inner diameter, as mentioned in chapter 1, was selected to be 1 mm. The bore was manufactured using a 1 mm drill bit. Due to vibration of the drill bit end the error in the inner diameter of the nozzle was estimated using the shadowgraph equipment and sample drilled specimens (Figure 5.3.8). Use of the sample units was required, as the

length of the nozzle (75 ± 0.5 mm) did not allow correct identification of the diameter with the available equipment.

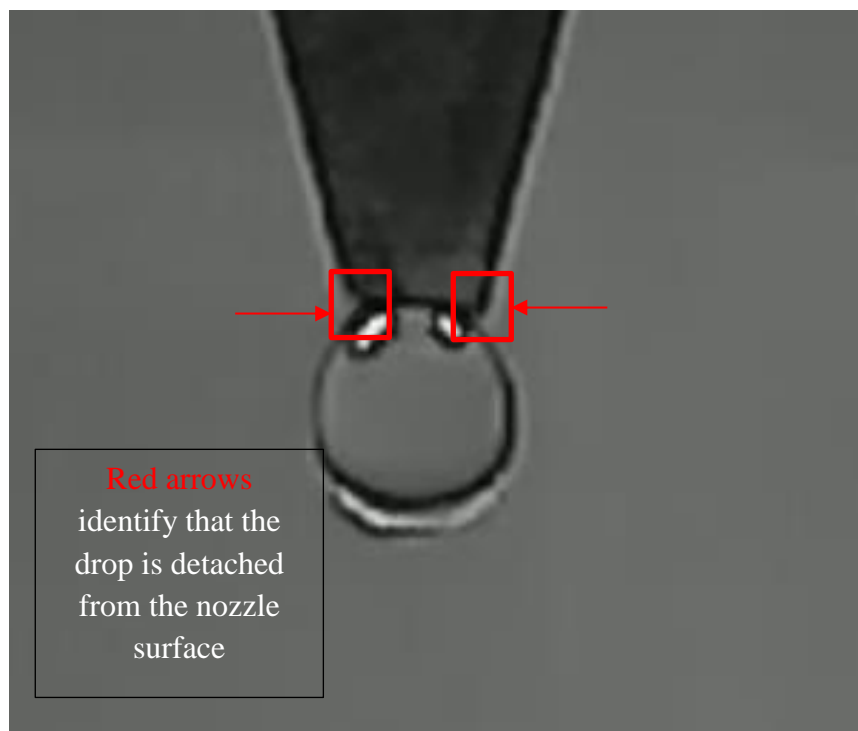


Figure 5.3.7: Droplet at the nozzle tip

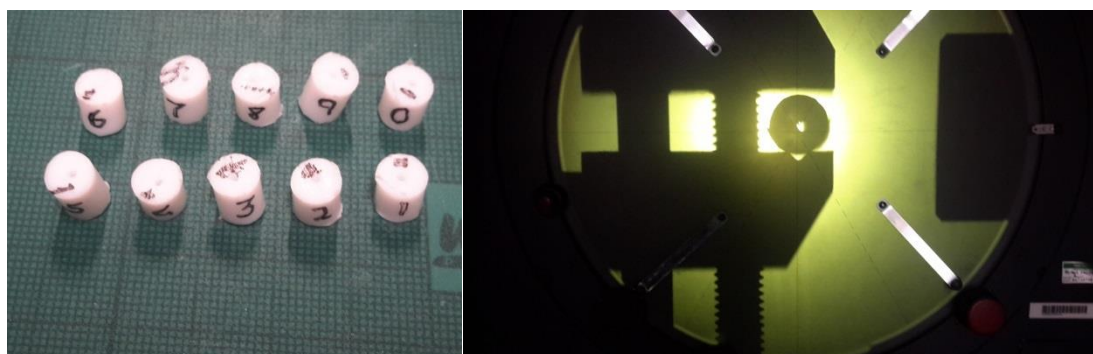


Figure 5.3.8: The nozzle inner diameter error studies

Ten samples were investigated with a total length of around 7 mm. The sample drilling side was marked, and the measurements were taken only from this side. The measurements per each sample were made in the vertical ($D1$) and horizontal ($D2$) directions (Table 5.3.2), the final result identified the nozzle to be 0.990 ± 0.0255 mm (which gives the value of the nozzle diameter most likely to be in the range of 0.9645 to 1.0155 mm). The test results also observed maximal divergence in the range of 0.915 to 1.085 mm.

Specimen #	D1, mm	D2, mm	Δ , mm
1	0.985	1.000	- 0.015
2	1.085	1.050	+0.035
3	1.015	0.940	+0.075
4	0.945	1.010	- 0.065
5	0.965	1.010	- 0.045
6	0.915	0.945	- 0.030
7	1.005	0.995	+0.010
8	0.935	1.035	- 0.100
9	0.935	1.010	- 0.075
0	0.990	1.035	- 0.045
Average:	0.9775	1.003	- 0.0255

Table 5.3.2: Nozzle inner diameter error studies

The temperature is monitored using a K-type thermocouple directly immersed into the water (Figure 5.3.3 and Figure 5.3.9). The thermocouple is positioned just before the nozzle in a fluid system and is attached using a tee-connector.

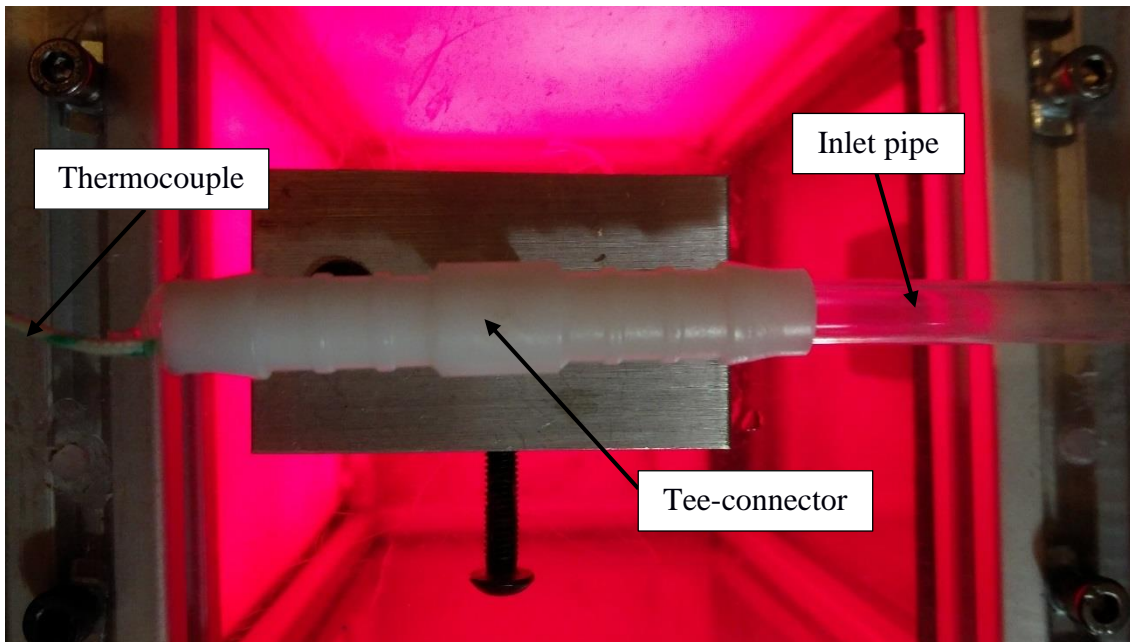


Figure 5.3.9: Tee-connector fixed on the test chamber top plate (with attached nozzle and K-type thermocouple)

The temperature sensor readings are taken using the analogue to digital converter board MAX31855K from Adafruit® [67]. The readings are done once per test with a precision of

± 0.125 °C, and it is assumed that the temperature remains constant, while the test is running. With this assumption in place, the maximal time where the temperature is assumed constant for the ground test (normal Earth acceleration due to gravity) with the lowest flow rate (taken here as 50 ml/hr) will correspond to 11 minutes. The assumption here is valid, as the temperature is not expected to change by more than 0.125 °C (which is the precision of the sensor) in 11 minutes' time.

The tests are performed in a separate enclosure (test chamber – Figure 5.3.3), which limits any accidental airflows that can affect the stability of the dripping nozzle. The enclosure is made of the Bosh Rexroth 20-by-20 mm aluminium profiles [49] and is joined together using 90-degree connectors from the same manufacturer. Two sides of the surroundings, as well as the bottom and top of the surroundings, are made of Lexan acrylic sheets 4 mm thick. Side profiles are fixed between the structural profiles, while the bottom and top are fixed on top of profiles using t-slot type M4 nuts. Backlit panels are installed on the two other sides (Figure 5.3.10).

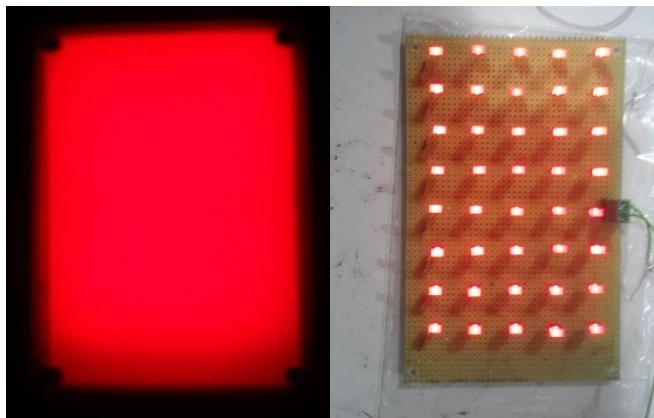


Figure 5.3.10: Backlit panels

(Left – Panel in operation under full darkness; Right – LED distribution on the panel)

The colour of the backlit panels was chosen to be monochrome red. The panel is made of 40 red LEDs, connected in eight parallel lines and five in series. The supply voltage is set to be 12 V DC (Direct Current). Each LED works at 2.4 V DC, and a current of 40.875 mA. Both panels are connected in parallel with a total power consumption of 7.848 W. The diffusion film was used to scatter the light and make the monochrome backlit panel.

At the bottom of the test chamber (Figure 5.3.3), the water collection pot (Figure 5.3.11) is installed which is made of acrylic sheets glued together using hot melt glue. The volume of the pot allows one 50 ml syringe to be dispensed before the pot is required to be emptied. The sponge is used to limit the drops bouncing up from the base. The syringe, TYGON® tubing, tee-connector, nozzle and test chamber are well sealed and do not allow the water to leak.



Figure 5.3.11: Test chamber water collection pot



Figure 5.3.12: ADXL345 accelerometer sensor
(from www.adafruit.com)

It is assumed that the pressure is always constant and set to be 101 kPa. Nevertheless, the external pressure is recorded manually twice a day using the laboratory-installed equipment (FC0510 Micromanometer from Furness Controls⁴).

Two accelerometers are fixed at two side-surrounding walls, where the cameras are mounted (Figure 5.3.3). The accelerometers used are a three-axis ADXL345 analogue sensor from Analog Devices (Figure 5.3.12) providing 0.002g sensitivity with an error of $\pm 0.3\%$ [68] and operating at 25 Hz frequency.

5.3.2 Structural design

The structure of the module is made of Bosch Rexroth 20-by-20 mm aluminium profiles [49] and is connected together using 90-degree brackets from the same provider. The

⁴ FC0510 Micromanometer was calibrated on 1st of April 2009

surrounding is made of Lexan acrylic sheets [50] 4 mm thick and fixed to the structure using M4 t-slot type nuts. To damp the induced vibrations, the rubber mats 20×40×5 mm are used between the connected components (Figure 5.3.13).

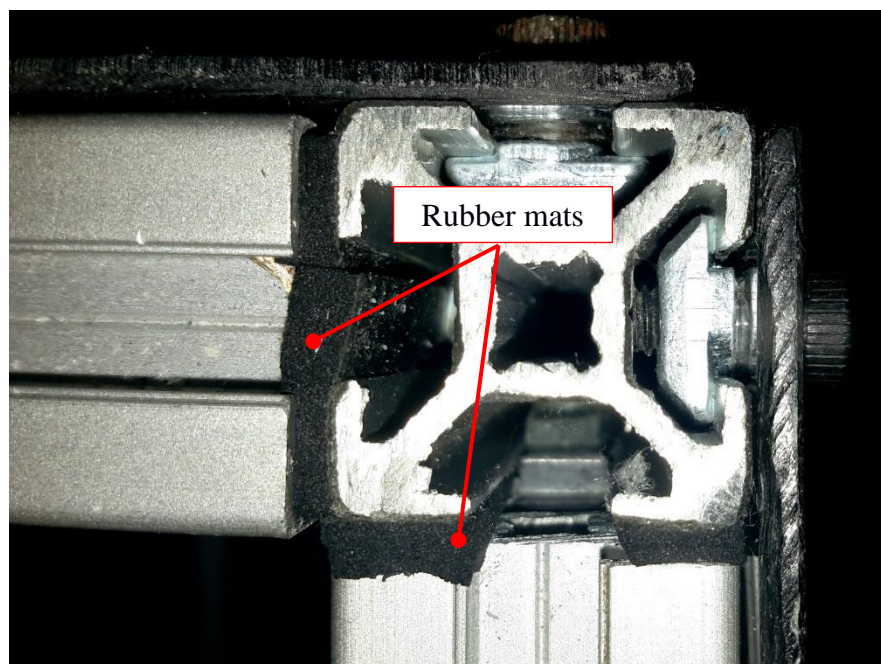


Figure 5.3.13: Vibration damping mats between the structure components

The front panel includes installation of the switches, identification LEDs, power plugs and syringe cover door (Figure 5.3.22). In addition, there is an additional cut-out to access the control panel of the syringe pump. The right and back panels have VGA-to-HDMI (Video Graphics Adaptor to High Definition Multimedia Interface) converters installed.

The test chamber is fixed to the experimental module structure via three struts: two from the left bottom side (Figure 5.3.14 – Strut A) and one right top side (Figure 5.3.14 – Strut B). The syringe is fixed from the top using the in-house manufactured bracket set-up (Figure 5.3.16). The wooden block fits into syringe pump fixture and is used as an adapter for the fixing strut (20-by-20 mm aluminium profiles [49]). The fixing strut then is fixed to the experimental module structure using two fixing brackets (made of 1060 carbon steel) and M4 t-slot screws.

The Finite Element Analyses (FEA) analysis was performed on two structural elements. One is the syringe fixing bracket and the second is the test chamber support struts, all other

components were considered to take a minimal structural load and would not be investigated, which can be expected from the considered structure (Appendix J).

The syringe pump is fixed to the front top strut via an angled bracket. The mass of the test chamber with the water filled to the maximum is 1546 ± 0.5 g.

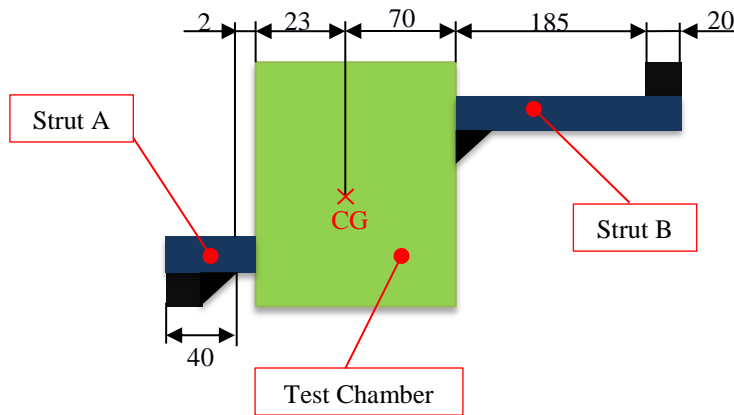


Figure 5.3.14: Test chamber support front schematics

All dimensions are in mm; black – is support area; CG – Centre of Gravity

The centre of gravity was located using Computer-aided Design (CAD) software (Solidworks) and is measured as shown in Figure 5.3.14. The considered loading case included the maximum acceleration (or deceleration) at 5g and with the assumption that the mass of the test chamber is distributed equally among the three members. The simulation was performed only for Strut B as it has the highest torque applied. The strut material is AL6060 with a yield strength of 55.15 MPa [49].

The loading case was set based on the actual location of the centre of mass of the test chamber (based on the Solidworks model – Figure 5.3.15 blue dot in left bottom corner) with the assumption that the test chamber is fully rigid. The acceleration due to gravity was set to be 9.81 m/s^2 (Figure 5.3.15 – red arrow). The mass of the test chamber under 5g acceleration was calculated to be 2.577 kg. The strut is limited to sliding on the top surface and fully fixed at the front surface (Figure 5.3.15 – green arrows). The model mesh used Jacobian 4 points with the element size of 3.14 mm. The minimum Factor of Safety (FoS) was found to be 1.1.

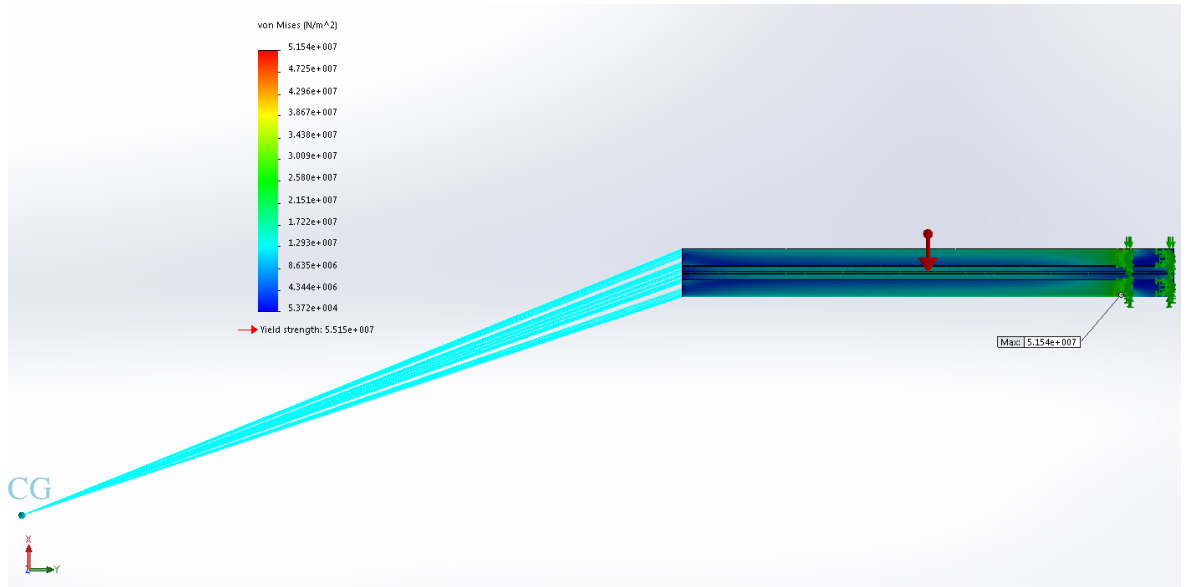


Figure 5.3.15: Test chamber support struts FEA simulation

The mass of the syringe pump was taken based on a reference from the syringe pump manual [62] and is equal to 3.5 kg. It was also assumed that both fixing brackets take equal loading (Figure 5.3.16). The bracket was fully fixed through the hole (Figure 5.3.17 – green arrows), slide fixed at two sides (sides are in contact with aluminium struts, either with the experimental module structure, or with the fixing strut). The loading area was two side holes where the fixing strut is attached, and the total loading mass was calculated to be 8.75 kg per bracket (under 5g acceleration).

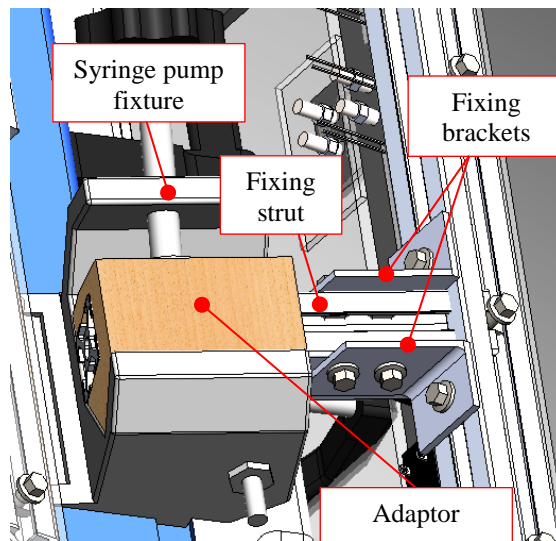


Figure 5.3.16: Syringe pump bracket set-up CAD model rendering

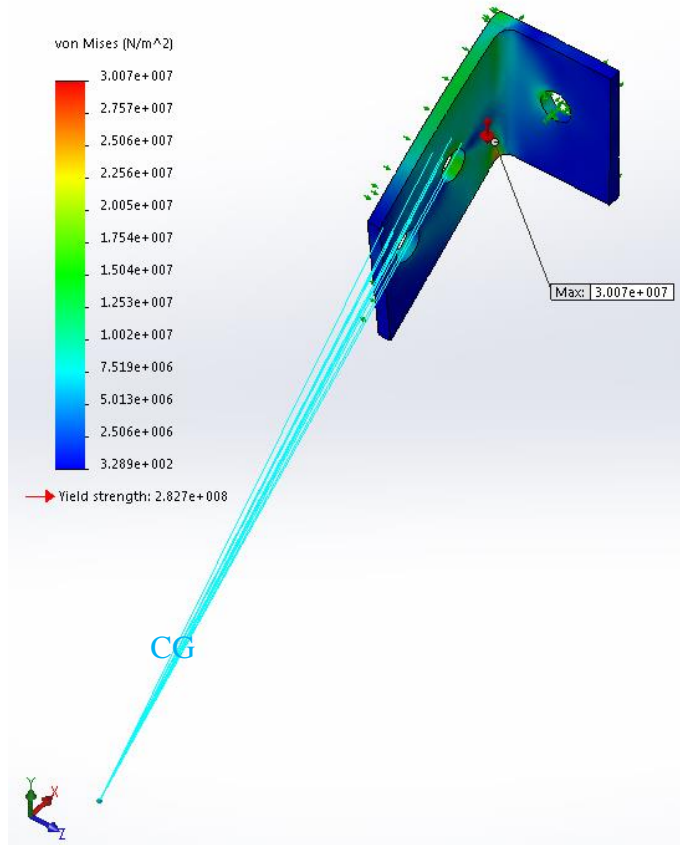


Figure 5.3.17: Syringe fixing bracket FEA simulation

The bracket yield strength is 282.7 MPa, which leads to the FoS for the bracket to be 9.4.

The model was meshed Jacobian 4 points with an element size of 1.246 mm.

5.3.3 Data collection and data processing

Based on the operational requirements (Table 5.2.1) the system is required to operate with minimal interruption from a user and record experimental video and experimental variables. The data storage should be big enough to store all received information throughout the whole day test campaign and recorded data should be easily accessible.

Two possible candidates were considered for the experimental control and data acquisition:

- NI cRIO-9014 (National Instruments) [69]
- Raspberry PI 2B (Raspberry Pi Foundation) [70]

First of all, both controllers provide a wide range of communication possibilities (via Input/Output terminals and +5V, +3.3V and ground (GND) supply lines). Secondly, the

storage memory of both controllers can be extended to values that will suit storage requirements.

The Raspberry PI computer has advantages due to its size (85×56×17 mm, compared to 172×97×88 mm), mass (45 g, compared to 488 g), Dynamic Random Access Memory (1 GB, compare to 128 MB) and Central Processing Unit (900 MHz, compared to 200 MHz). In addition, it has inputs for camera and Universal Serial Bus (USB) connectors, which simplifies the control and the communication.



Figure 5.3.18: Raspberry Pi 2B

The advantage of cRIO is that it provides high tolerance to vibration and shock loads (up to 30g), which is well above what is required. While the Raspberry PI has less tolerance to shock loads (no actual data available), but due to its mass the loading of 5g it is assumed this is harmless. In addition, the cRIO operates at 9 – 30 V DC (while the PI only at 5 V DC), which allows matching the voltage requirement to the backlit panels. The final decision was to select two Raspberry PI computers, due to the advantages mentioned above and especially its cost (£30) and possibility to connect and run the camera.

Each Raspberry Pi provides (Figure 5.3.19):

- Video camera input (using the ribbon cable)

- Four USB ports (one of which will be used for the keyboard and mouse bundle in both Pis, and for Wi-Fi bundle (internet connection) only in one Pi)
- 40 General Purpose Input/Output (GPIO) pins (providing the power supply and signal inputs or outputs)
- Power supply input (5 V DC)
- HDMI output ports (to connect to display)

In addition, there are available ports for the Local Area Network (LAN) and audio output, which would not be used in the experimental module.

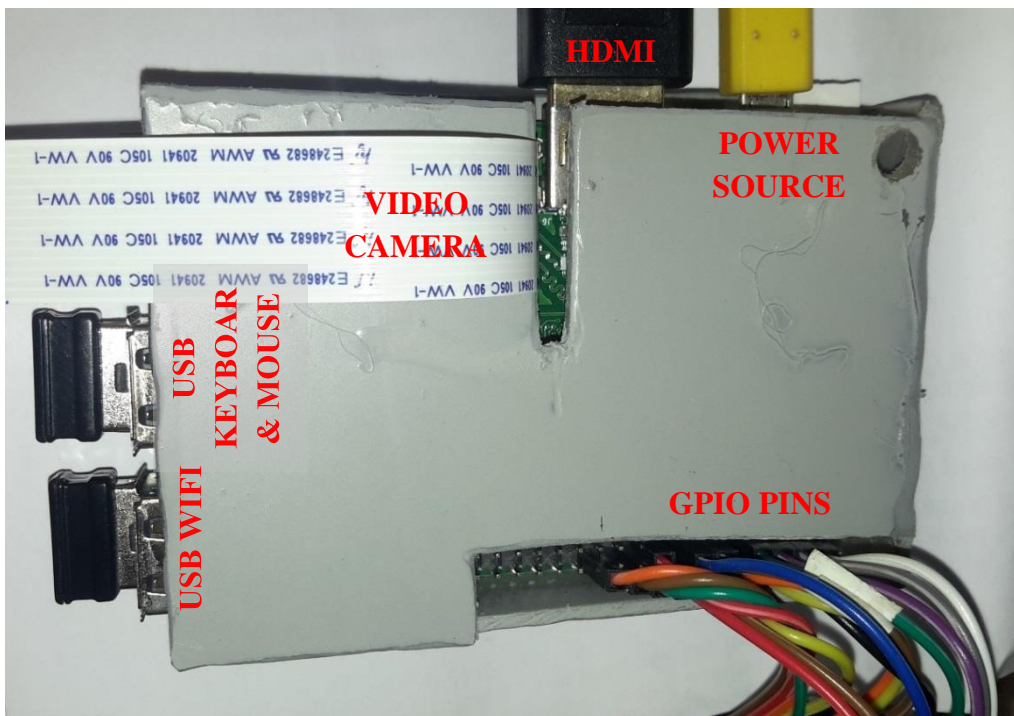


Figure 5.3.19: Raspberry Pi computer enclosure

The Raspberry Pis are enclosed in a protective cover and are fixed to the surrounding structure using the t-slot bolts-nuts.

Prior to the operation of the Raspberry Pi installations of the additional internal software were required (Appendix K), this includes the installation and activation of the Secure Shell, Inter-Integrated Circuit (I²C) and VNC Server software. VNC Server provides on start connection to Raspberry Pi via the internet, which in fact allows operating the computer without connecting to the monitor, keyboard and mouse. In addition, the installation includes writing the script programme, which will launch the operational code

at the start of the Raspberry Pi. The raspberry Pi built-in hardware protocol allows switching it ON using an external switch, via the GPIO pins. All aforementioned installations and adaptations minimise the experimental module reset time by reducing the physical contact with the computers.

The next step was to set-up the connection to the sensors. The following data is required to be recorded during the experiment:

- Video of the drop from both sides----- (continuous) ----- (internally)
- Accelerometer for both cameras----- (continuous) ----- (internally)
- Water temperature ----- (once per test) --- (internally)
- Atmospheric pressure ----- (twice a day)----- (externally)

The accelerometer and the thermocouple sensors are connected via an inter-integrated circuit (I²C with 0x53 address) bus and are powered by 3.3 V DC. The thermocouple is connected using Serial Peripheral Interface (SPI).

The code for the accelerometer operation was developed by Jonathan Williamson and is available for public use online at “www.github.com”. The following commands were used in the terminal window to install the required library on both Pi computers:

```
$ sudo apt-get update
$ sudo pip install RPi.GPIO
$ sudo pip install Adafruit_BBIO
$ cd ~
$ git clone https://github.com/adafruit/Adafruit_ADXL345.git
$ cp Adafruit_ADXL345/adxl345.py Documents
```

This allows one to upload the online code (Appendix L.A) and copying it to the required directory. Similarly, to install the thermocouple library code (written by Tony DiCola, available at “www.github.com” – Appendix L.B) the command line codes used were:

```
$ cd ~
$ git clone https://github.com/adafruit/Adafruit_Python_MAX31855.git
$ cd Adafruit_Python_MAX31855
$ sudo python setup.py install
$ cp MAX31855.py ~/home/pi/Documents
```

Each Raspberry Pi computer has only one video input (Figure 5.3.19), which results that the accelerometer and the camera on the same side are connected to the same Pi computer.

The video recording will be discussed in the following section (5.3.4). Additional information on the thermocouple and the accelerometer sensors has been provided in section 5.3.1.

To calculate the maximum required data storage the maximal test time was assumed to be eight hours per working day, with the test performed on the ground (normal gravity experiments). The decision for that because then the total reset time will be much less, as experiments can continue throughout the whole syringe volume and it is required to be reset only when the syringe is empty. While for the microgravity experiments, reset time should be done after each microgravity test (~3 seconds). To empty one syringe (50 ml) at the lowest required flow rate (experimentally set at 50 ml/hr) will take 60 minutes, and at the highest flow rate (experimentally set at 280 ml/hr) will take 11 minutes. The reset time is assumed to be 5 minutes, which in total per day will add up to an average of 11 syringes to reset, or a maximum of 420 min of test time per day.

The amount of data generated by the sensors and cameras was calculated based on the test runs. For the camera module, it was found that (with the experimental settings described in section 5.3.4) it generates 2 Mbytes/s of data. The accelerometer takes readings at 25 Hz, which corresponds to 550 Bytes/s data recording during the test time. The logging file was found to use 25.6 Bytes/test (Table 5.3.3).

The minimum amount of the memory storage required for the experimental module was found to be approximately 60 GBytes. The selected Micro Solid Drive (microSD) card was chosen to be 64 GBytes MicroSDHC card by Kingston Technology, which definitely can provide enough data storage for a working day. To upload the experimental data, the USB port is used, which is easily accessible (Figure 5.3.19).

Data source	Amount of data generated	Total data per test day (Mbytes)
Camera No.1	2 MB/s	50400
Accelerometer No.1	550 B/s	13.22
Logging file	25.6 B/test	<0.01
	Sub-Total:	50413.22
	20% Margin:	10082.64
	System Memory [70]:	496.00
	Grand Total:	60991.86

Table 5.3.3: The budget of the experimental module memory storage

5.3.4 Camera system

Two different approaches were considered to allow for video recording from two different sides. The first was to use one camera and mirror, the second was to use two cameras. The benefit to using one camera was that it was possible to use a high definition camera. To use two cameras at high definition was not possible due to the cost and experimental mass/volume restraints. At the same time, it complicated the test chamber design (which needed to incorporate a mirror) and the mirrored drop would have a different quality to non-mirrored one (complicating the post-processing of the image). However, it would benefit, as image synchronisation would not be an issue, but complicates synchronisation with the sensors.

Nevertheless, the clear benefit of selecting the Raspberry Pi computer was that it allows connecting the camera and acquiring, and storing the videos with a single system (with the sensor data). The selected camera for the operation was the Raspberry Pi camera [71], with an integrated infrared filter. It is installed on two adjacent sides of the test chamber. The camera is 20×25×10 mm and with a mass of only 3 grammes. The camera has a ¼-inch lens, which can be manually adjusted to the required focus distance (the focal distance is 65 mm). The connected camera required additional Pi computer updates, which included:


```
$ sudo raspi-config #type in command line
>> Enable camera ||>>[ENTER]
>> Finish
```

The camera is enclosed in a 3-D printed camera case (Figure 5.3.20), which fixes the camera in place and protects the electronics.

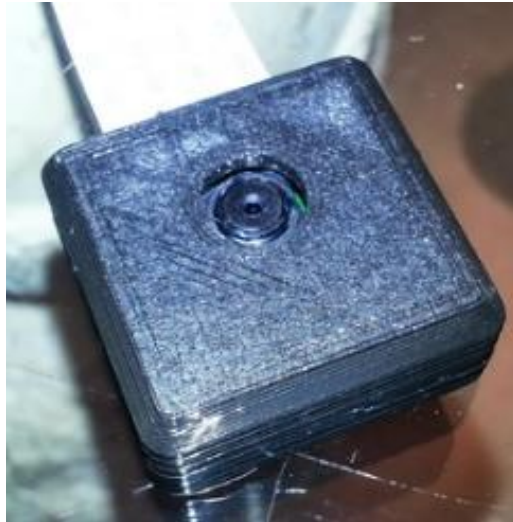


Figure 5.3.20: Raspberry Pi camera enclosed in a case
[from www.thingiverse.com/thing:92208]

The selected camera is a Raspberry PI camera working at 30 frames-per-second (fps) which allows for video to be taken at 1080p (1080 pixel lines of vertical resolution with the progressive scanning method). The frame rate was selected as the maximum available with the sharpest image quality possible by the camera specifications [71]. This filming rate now constrains the experimental range. It is important for studies to be able to observe the development of the drop, for this reason the limit of 10 – 15 frames per drop was set. The actual test flow rate range will be determined in later stages when the module operational uncertainties will be calculated (section 6.2). The picture resolution was set to be 1240 by 980 pixels. The following video picture enhancement was applied (Figure 5.3.21):

1. Metering mode (exposure zone) backlit (for back-lit object)
2. Exposure mode backlight (for back-lit object)
3. Contrast 50 (medium to high contrast)
4. Sharpness 100 (maximal)
5. Colour effect 128:128 (monochrome image)

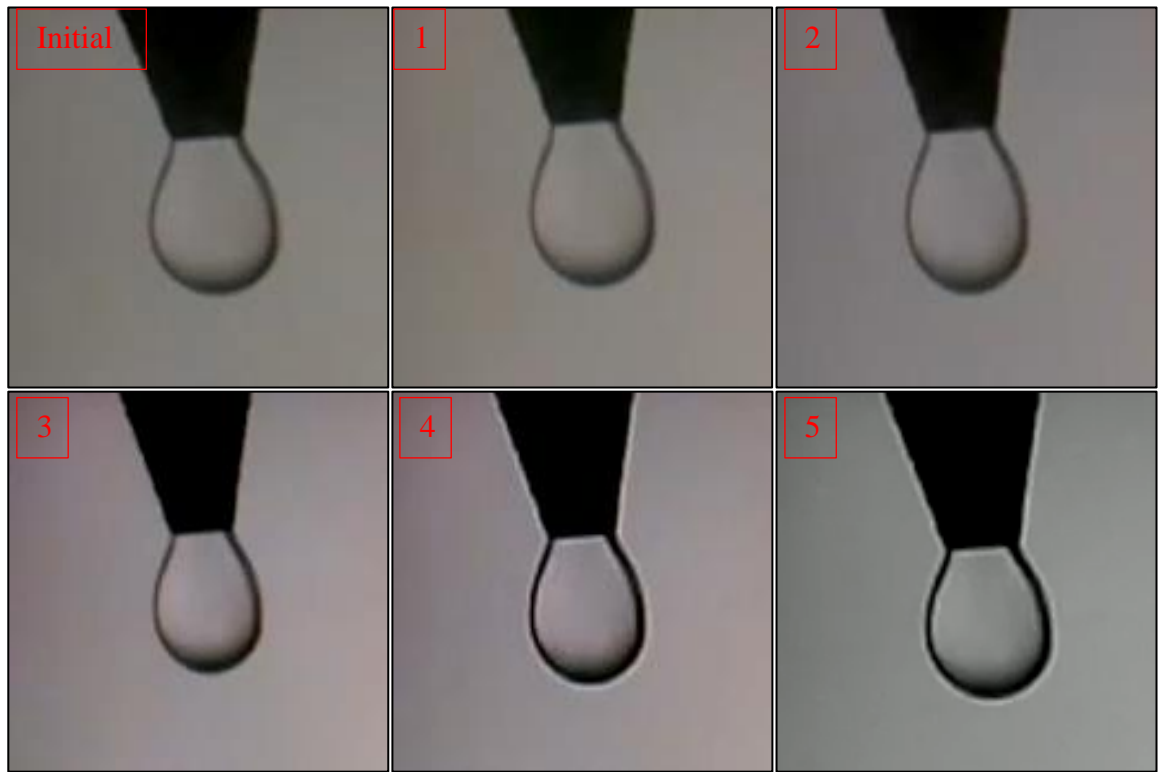


Figure 5.3.21: Video enhancement steps

The exposure mode and the exposure zone was set based on the pre-set configurations given by the camera built-in software and allowed one to concentrate light exposure only on the centre image (the nozzle and the drop). The contrast was increased to increase the visibility of the drop edge and remove the light blinks (which is created in some spots due to the roundness of the drop shape) but was not increased to the maximum as the picture will have a lot of noise. The sharpness was maximised to remove the noise from the drop edge. Finally, the monochrome colour effect was applied to stabilise the colour perception matrix from fluctuation, which occurs in a backlit illuminated picture. In addition, the exposure time was set to be 16.667 ms. The exposure time allows one to capture sharper frames when minimised but will produce a higher drop detachment time error, by not being able to identify the exact detachment time.

To run the camera module from the terminal window the following command is used:

```
$ sudo raspivid -mm backlitbacklit -ex backlight -co 50 -sh 100 -cfx
128:128 -fps 30 -w 1240 -h 980 -o {name}.h264
```

The videos from the cameras require being synchronised. This is done by sending synchronising signals from both Pis and recording the received/send time in a log file. The “Master” Pi just before it is ready to start recording, sends a signal and records the internal time. The “Slave” Pi receives the signal, records its time and starts the video recording. When the video recording is complete the procedure repeats but in the reverse direction, starting with the signal from “Slave” Pi. By following this procedure, there are two synchronisation times, one is at the beginning and another is at the end.

5.3.5 Electronics system

The electronics system consists of the system wiring, batteries and control panel. The wiring of the experimental module is shown in Appendix M.

The system is separated into two blocks based on the power supply. The first, is powered by 5 V DC and powers the Raspberry Pi computers, the second block is powered by 12 V DC and contains the light panels. The light panel power module contains a charging point (red for positive (ChP+) and black (ChP-) for negative – Figure 5.3.22). A switch (SW1) controls the charging, which is a two-position switch: 1. for charging, 2. for powering the LED panels. In the charging mode identification, LED1 is ON, and when in light panel operation LED2 is ON (Figure 5.3.22).

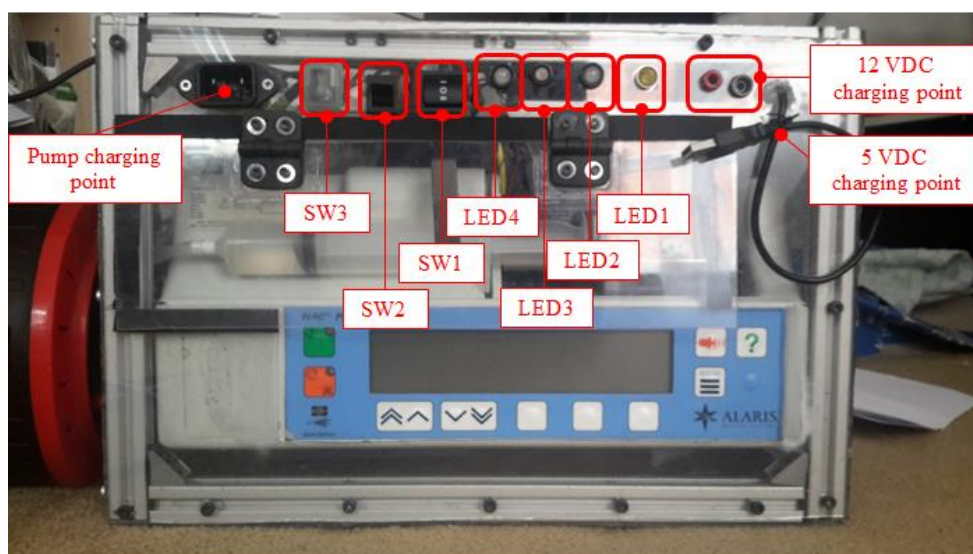


Figure 5.3.22: Front panel component

The 5 VDC battery can be charged via a USB cable (Figure 5.3.22) and has two separate outputs for each Raspberry Pi computer (in Appendix M named as “Master” and “Slave” respectively), connected via a USB-miniUSB cable. Both controllers use a similar pin connection layout for control and communication and are summarised in Table 5.3.4.

Pin No.	Name of the pin	Function	Connected to: (Master or Both)
1	3.3V	- Positive load for accelerometer	Both
2	5V	- Not Connected	Both
3	SDL – I ² C	- Serial Data Line for accelerometer	Both
4	5V	- Not Connected	Both
5	SCL- I ² C	- Serial Clock Line for accelerometer - Pi revokes signal	Both Both
6	GND	- Ground for accelerometer - Pi revokes signal	Both Slave
7	GPIO4	- Shutdown signal	Both
8	TxD	- Synchronisation signal	Both
9	GND	- Not Connected	Both
10	RxD	- Synchronisation signal	Both
11	GPIO17	- Error signal	Both
12	GPIO18	- Data Out for accelerometer	Master
13	GPIO27	- Slave Pi is ready to signal	Both
14	GND	- Test running LED ground	Both
15	GPIO22	- Test running LED 5V	Both
16	GPIO23	- Not Connected	Both
17	3V3	- Positive load for thermocouple	Master
18	GPIO24	- Chip Select pin for thermocouple	Master
19	MOSI	- Not Connected	Both
20	GND	- Ground for thermocouple	Master
21	MISO	- Not Connected	Both
22	GPIO25	- Clock signal for thermocouple	Master
23-40		- Not Connected	Both

Table 5.3.4: Raspberry Pis GPIO pins connection summary

The Raspberry Pis are inactive when the experiments are not in progress and stay in sleeping mode. The switch SW2 (Figure 5.3.22) revokes the Pis from the sleep mode (the switch grounds pin 5 – GPIO built-in activation signal). Before the experiment is started, the “Error signal” from the “Slave” Pi is checked by the “Master” Pi (which is associated with the memory issue on the “Slave” – pin 11).

When the test procedure is started (section 5.5), first the “Master” Pi awaits the initialization signal (pin 13) from the “Slave” (which means that the “Slave” Pi is also running the programme), then to synchronise the Pis a send-receive signal is used (pins 8 and 9). While the experiment is in progress identification LEDs are ON (LED3 and LED4 for “Master” and “Slave” respectively – Figure 5.3.22). When it is required to complete the experiments and put the Pis into sleep mode the “Master” first sends a signal (pin 7) to the “Slave” and then switches itself off.

Pins 1, 3, 5 and 6 on both Pis are associated with the accelerometer connection, and pins 12, 17, 18, 20 and 22 are associated with the thermocouple connection. Pins 1 and 6 (positive and ground respectively), and pins 17 and 20 (positive and ground) are supply power lines. Pins 3 and 5 are for the I²C connection, while pins 12, 18 and 22 are for the SPI connection.

Both Pis are connected to a camera and HDMI-VGA converter via video input or output ports. In addition, the “Master” Pi has a Wi-Fi bundle (to connect to the internet) connected via a USB port, and a mouse/keyboard bundle (to control the pi) also connected to the USB port.

The front panel (Figure 5.3.22) also includes a switch for the syringe pump (SW3) ON/OFF and the pump charging port.

The power budget is calculated based on the module components performance. Through tests it was found that peak power for the Raspberry Pi does not exceed 3.6 W and the power for the backlit panel does not exceed 3.924 W.

The total battery capacity required for eight hours of operation (as required by the design requirements – subsection 5.1.1) with a contingency of 15%, will be equal to:

- $\frac{3.6W \times 8h \times 2}{5V} \times 1.15 = 13.248 \text{ Ah}$ – for the 5V battery
- $\frac{3.924W \times 8h \times 2}{12V} \times 1.15 = 6.017 \text{ Ah}$ – for the 12V battery

The selected 5V battery is EC Technology USB power bank, which has a total capacity of 22.4 Ah, and the selected 12V battery is lithium-ion by Tracer, which has a total capacity of 8 Ah. Both batteries provide adequate discharge current to run the electronic components. The batteries are enclosed in plastic containers and fixed to the main structure using the t-slot bolts-nuts fixture.

5.3.6 Test module budget

The budget for the module is summarised in Table 5.3.5, which is separated into five sections based on identified sub-systems. The total cost was £950 including VAT.

System Name	Price total (£)	VAT (£)
Structure system	243.47	48.69
Fluid system	155.82	31.16
Data	121.67	24.33
Camera	77.50	15.51
Electrics	187.25	37.45
Total:	785.71	157.14
Grand total:		942.85

Table 5.3.5: Experimental module cost budget

5.4 Module calibration

Based on the test requirements the experimental variables need to be monitored (section 5.2). For that reason, additional checks for the syringe pump flow rate, thermocouple

temperature reading measurements, and camera video distortion and pixel sizing were performed. The calibration of the accelerometer was not completed as a change to this research objective occurred (section 1.4). The accelerometers were installed and connected to the on-board computers, but were not used in the experimental process. It will be assumed that the acceleration due to gravity is 9.81 m/s^2 and all vibrations can be neglected.

The following sections will summarise the calibration procedure and results of the aforementioned components.

5.4.1 Syringe pump calibration

The pump calibration was required to identify the error in the pump displayed flow rate to the actual flow rate. The idea was to set the pump to run at a specific flow rate and time the pump when it reaches the specific volume (and based on this data to then calculate the actual flow rate).

The procedure starts with filling the syringe with water and then follows:

1. Empty and dry the graduated cylinder
2. Switch on the pump and set the flow rate under investigation
3. Start the pump till it fills the tube volume
4. When the first drop comes out of the tubing start the timer
5. Stop the timer at a specific volume
6. Stop the pump
 - a. Refill the syringe if needed
7. Record the time and reset the timer
8. Repeat the procedure

To measure the dispensed volume, a 50 ml graduated cylinder was used, with a precision of $\pm 0.75 \text{ ml}$ at 20°C . Prior to dispensing water into the cylinder it was dried using cleaning tissue. The timer was stopped when a specific volume was reached (20 to 30 ml depending

on the flow rate). The visual error in reading off from the graduated cylinder is minimised by taking several measurements and averaging.

The tests were done from 50 to 300 ml/hr flow rate with the step of 5 ml/hr (Figure 5.4.1). For each flow rate, five tests were performed (Figure 5.4.1 – blue markers). The average value for each flow rate was calculated (Figure 5.4.1 – red line), and the linear trend line was calculated for all results (Figure 5.4.1 – black line).

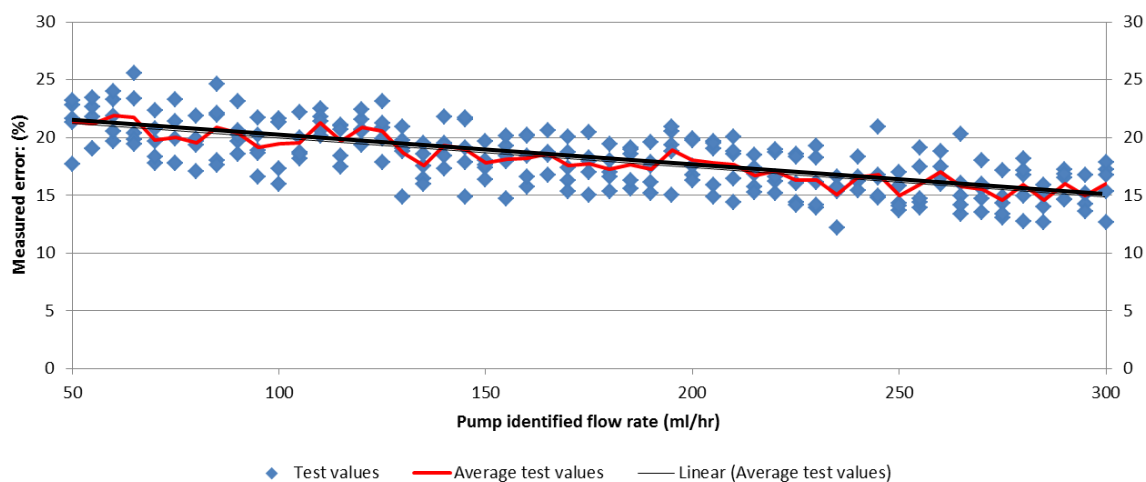


Figure 5.4.1: Pump calibration results

$$\text{Linear trend line equation: } E = -0.0253\dot{V} + 22.486$$

$$\text{Linear trend line R-squared value: } R^2 = 0.863$$

The linear trend line provides the measure of pump offset requirement when calculated for the actual flow rate. Meaning that the flow rate as set by the pump (\dot{V} – Equation 5.4.1) should be recalculated to identify the actual supply flow rate offset (\dot{V}_{calib}).

$$\dot{V}_{calib} = \frac{\dot{V}}{100} (-0.025\dot{V} + 22.5) \quad \left| \quad 5.4.1 \right.$$

The pump flow rate variation uncertainty can be assumed as the worst-case scenario variation when the offset of the average value is the highest (Figure 5.4.1 – the red line and the black line), based on the syringe pump calibration results. The value of the uncertainty is equal to $\pm 1.54\dot{V}/100$, corresponding to a flow rate of 135 ml/hr but this value will be used with all flow rates.

5.4.2 Camera calibration

The main milestones for the camera calibration were to investigate the size of the distortion across the field of view of interest and to find the size of a pixel. For this, purpose the Raspberry Pi camera with the same setting as for the experimental recording, took a video of the nozzle with a transparent mesh installed behind the nozzle (Figure 5.4.2).

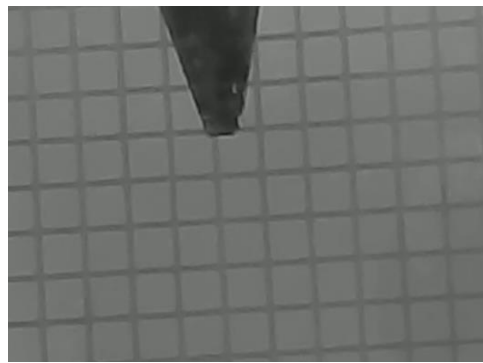


Figure 5.4.2: Nozzle with attached mesh

From the selected video, one of the frames was chosen and processed using “MATLAB®” software. Processing involved rotation of the video (by 3° anticlockwise for the “Master” Pi camera, and 4° clockwise for the “Slave” Pi camera) and applying built-in edge detection code software. The method used was the Canny method (section 2.5), with a threshold value of 0.15, 2 (Figure 5.4.3) and 0.1, 2.5 for the “Master” and “Slave” cameras respectively. In the picture, the edge is identified as white pixels. The investigation area was selected just below the nozzle tip, which is the area where the drop will be located. To produce the plot, the following code was used⁵:

```
>>-----  
1 >>S1=[400,400]; %Size of the front view region  
2 >>Front_view=zeros(S1(1,1),S1(1,2),3,'uint8'); %Set the size of the  
video matrix  
3 >>OF1=[400,675]; %Off-set frame read1  
4 >>I=VideoReader('{NAME}.mp4'); %Read video file  
5 >>nFrames=I.NumberOfFrames; %Check value of total frames
```

⁵ The code displayed here is for “Master” Pi camera. For the “Slave” camera ‘line 4’ numbers should be changed to [350,0], ‘line 13’ numbers should be changed to 0.1, 2.5, and in ‘line 14’ the number should be changed to 4.


```

6 >>Frame=read(I,50); %Set the frame to be read
7 >>for k=1:S1(1,1) %Fill the working video array
8 >>for m_l=1:S1(1,2)
9 >>Front_view(k,m_l,:)=Frame(k+OF1(1,1),m_l+OF1(1,2),:);
10>>end
11>>end
12>>Front_view=rgb2gray(Front_view); %Change colour
13>>Front_view=edge(Front_view,'Canny',0.15,2); %Identify edges
14>>Front_view=imrotate(Front_view,-3); %Rotate the video by 3deg
15>>imshow(Front_view) %Display the image
>>-----

```

where: {NAME} is the name of the video file

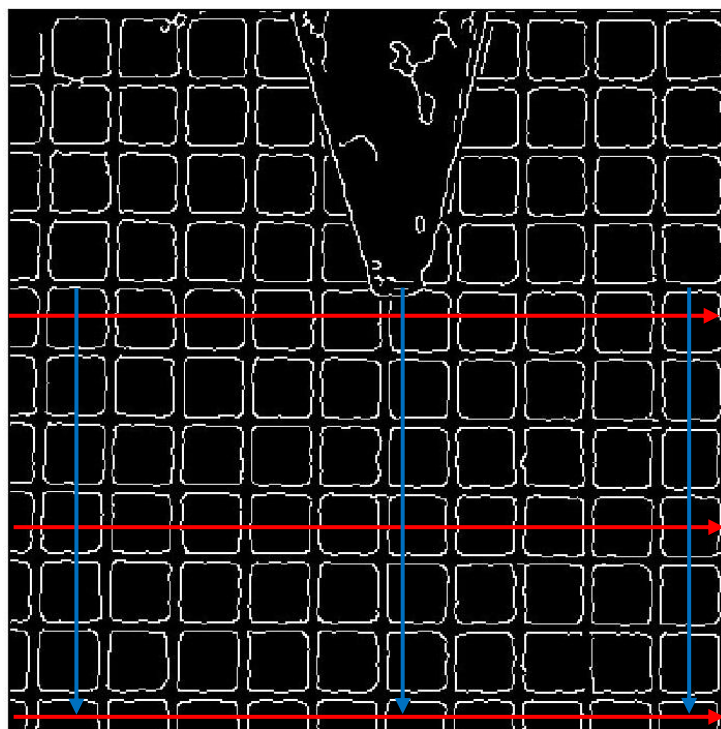


Figure 5.4.3: Camera pixel sizing and distortion study

(Camera No. 1, post processed using “MATLAB®”, edge detection method used – Canny, threshold values: 0.2, 2)

The edge locations were taken from six lines: three in the horizontal direction (Figure 5.4.3 – red) and three in the vertical direction (Figure 5.4.3 – blue). The results are recorded in Appendix N, and showed no visible distortion in the picture, apart from noise in the edge detection, which varies for both cameras within 1 pixel.

During the experimental campaign, it was found that due to picture noise the dimension of the drop edge can vary between the synchronised cameras. It was assumed that the cameras

are synchronised (the exposure timing is synchronised), meaning that cameras should acquire the same common dimensions of the drop, such as the vertical height. Following this assumption the video processing should require having a variable pixel scaling factor, which relates the best camera image to the worst one. The best camera images (from the “Slave” Pi camera) were taken to be the ones with the smallest pixel size.

To physically measure pixel size, two set of measurements were used. The first measured the width of the mesh lines, and the second measured the box between the mesh lines. Both measurements were taken using the Nikon digital microscope. The box size measurements required the use of micrometer gauge in addition, as the movement of the scope gauge lines alone did not allow full coverage of the required distance. The measurements of the mesh line gave an average value of $0.2782 \pm 5 \cdot 10^{-5}$ mm (five different measurements used), and a box size of 1.660 ± 0.005 mm (four different measurements used).

For camera 2 (the “Slave” Pi) the average box width was found to be 45.472 pixels or 36.51 ± 0.11 $\mu\text{m}/\text{pixel}$, with a mesh width of 7.273 pixels or 38.29 ± 0.01 $\mu\text{m}/\text{pixel}$. The difference in the measurements between the box and mesh size are due to the physical measuring equipment and the picture quality. The final decision for identifying the pixel size was to find average value between the minimum and maximum values that were given either by box or mesh size, which becomes equal to:

$$PXL_{c2} = 37.40 \pm 0.11 \mu\text{m}/\text{pixel} \quad \Bigg| \quad 5.4.2$$

Similarly the reference value for camera 1 (the “Master” Pi) pixel size was found to be 51.475 ± 0.445 $\mu\text{m}/\text{pixel}$. The difference in the camera readings is due to its distance to the nozzle, which is not the same.

5.4.3 Temperature sensor calibration

Three sensors were required to be calibrated: two accelerometers and one thermocouple. The temperature readings were calibrated with respect to meters available at the university

(FC0510 Micromanometer from Furness Controls⁶).

Day	Sensor reading	Calibrated sensor readings (°C) ±0.01 °C	Difference (°C)
1	21.75	21.35	-0.40
2	21.50	21.09	-0.41
3	21.25	20.82	-0.43
4	21.25	20.81	-0.44
Average:			-0.42

Table 5.4.1: Temperature sensor calibration readings

For the purpose of calibration, five readings on different days were taken (Table 5.4.1). The variation was found to be -0.42 °C, leading to an experimental thermocouple reading mean divergence of:

$$\Delta T_o = -0.42 \pm 0.125 \text{ °C}$$

5.4.3

5.5 Experimental procedure

The experimental procedure for both microgravity and normal gravity conditions are the same. As mentioned before, the control software is written in Python language and is uploaded to both Pi computers, with minor differences (Appendix L.C).

Prior to the start of the test it is important to identify the experiment time length: for the microgravity experiment, it could be 2-3 seconds, and for normal gravity conditions, it could be 6-11 minutes (under normal gravity, it is possible to run the experiment continuously until the syringe is not fully empty). This adjustment requires connection to both Pis as the value in the code needs to be changed. To do so, the monitor should be connected via VGA cable to HDMI-VGA (High Definition Multimedia Interface to Video Graphics Adaptor) adaptor. To access the code file launch terminal and enter:

⁶ FC0510 Micromanometer was calibrated on 1st of April 2009

\$ sudo nano Documents/{name}.py

where: {name}=test_1 for “Master” Pi or {name}=test_2 for “Slave” Pi

and the value of dt should be changed to the required time measured in milliseconds.

The normal operation should start with switching ON all switches on the experimental module front panel (SW1, SW2 and SW3 – Figure 5.3.22). This will switch ON: pump, light panels and both Pis. The “Slave” Pi will automatically start the code, as well as sending confirmation of the initialisation to the “Master” Pi, and will wait for the experiment start procedure (Figure 5.5.1). The next step is to set the pump flow rate, and connect to the “Master” Raspberry Pi via the VNC Viewer client.

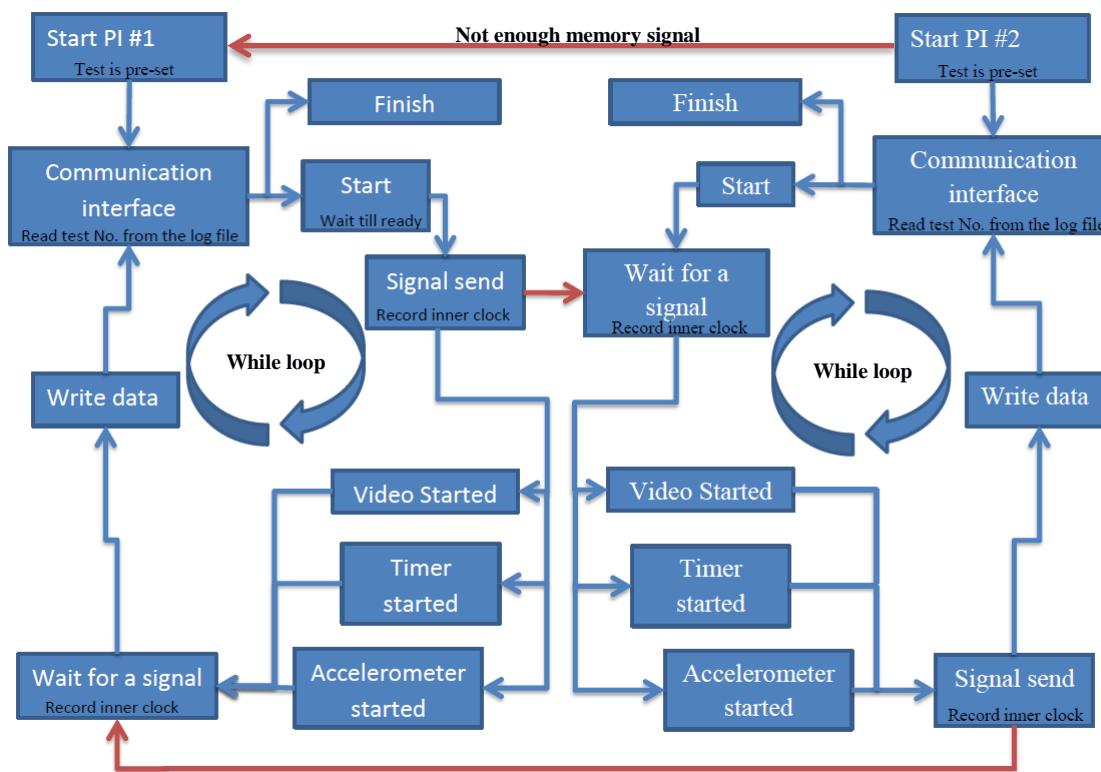


Figure 5.5.1: Experimental procedure outline

(Here Pi#1 is the “Master” Pi computer and Pi#2 is the “Slave” Pi computer)

To set up the connection between the VNC Viewer client and the “Master” Pi add a new connection and enter raspberrypi:1 in the “Name” field and 10.130.23.51:1 in the “Address” field. The password for the required connection is microgravity. When the connection with the Raspberry Pi is established, launch the terminal window and enter

```
$ sudo nano Documents /test_1.py
```

This will start the experimental procedure (Figure 5.5.1).

When the Pi computers have initialised the remaining storage memory check is performed, and the log file number is read (Figure 5.5.2). If the remaining free memory on any Pis is less than the threshold value (20% selected as a contingency), the error signal will be displayed in the communication window (Figure 5.5.3), which reads “Not enough memory”. In this case, both Pis will close the programme, but will stay online. In addition, the “Master” Pi reads the temperature.

```
0001 17:52:01 14/04/16      1.23  2.07      24.25
0002 17:54:50 14/04/16      1.36  2.2      24.25
0003 18:07:03 14/04/16      1.37  2.21      24.5
0004 18:30:39 14/04/16      1.33  2.17      24.25
0005 18:32:02 14/04/16      1.38  2.22      24.25
0006 18:32:02 14/04/16      2.23  2.96      24.25
0007 18:49:36 14/04/16      1.35  2.19      24.5
0008 21:19:11 15/04/16      1.5    2.22      24.75
0009 21:32:33 15/04/16      1.4    2.13      24.75
0010 21:37:02 15/04/16      1.38  4.18      24.75
0011 21:37:02 15/04/16      4.19  6.9      24.75
```

Figure 5.5.2: Example of the experimental log file

The log file is used to track the experiment number and record test data under a different name. The code reads the log file last test number and uses the next one as the ongoing experiment number. The log contains the information of when the test was taken (time and date), the internal clock record (test start and test end) and the temperature (only for the “Master” Pi log file).

The pump can be started when the communication message “Start a test? y/n” is received (Figure 5.5.3). This message is received only if the initialization signal from “Slave” Pi has been received, and there was no error signal received.

To proceed with the experimental procedure, enter “y” followed by the “RETURN” button, this will:

1. Read the thermocouple temperature
2. Record the internal time of the computer

3. Send the signal to start the “Slave” Pi
4. Display “Test started” message on the display
5. And it will start the test

```

File Edit Tabs Help
pi@MicroGrav ~ $ cd Documents
pi@MicroGrav ~/Documents $ sudo python test.py
Raspberry is ready in 5 seconds
Today Wed 17:13:41 11/11/15
Start a test? y/n y
Press ENTER when ready
Record Temperature of the fluid (deg C). T = 24.5
Test started
Test finished
Start a test? y/n y
Press ENTER when ready
Record Temperature of the fluid (deg C). T = 24.5
Test started
Test finished
Start a test? y/n n
pi@MicroGrav ~/Documents $

```

Figure 5.5.3: Example of communication window for experimental module

When the “Slave” Pi received the start signal, it will record the internal time and will start the experiment. In the case when “n” is entered both Pis will go on halt (or sleep mode - until the switch SW1 (Figure 5.3.22) is pressed, which will start the Pis again). In the case when any other value is entered, the same question will be repeated until either “y” or “n” is pressed. To maximise the experimental data, the procedure should only be continued when dripping has started.

The experiments on both Pis will follow the same procedure. Three different sub-programmes (threads) are started simultaneously:

- Experimental timer
- Video recording
- Accelerometer recording

The experimental timer thread counts for the duration of the experiment and terminates the two other threads when it is finished. The video thread records the video with the required parameters (section 5.3.4) and it is terminated when the timer thread is finished. Similarly,

the accelerometer thread records the gravitational acceleration values and is terminated by timer thread.

When the threads have completed the message “**Test finished**” is displayed, and the data is saved in the `~home/pi/Documents/Test` directory as the following files:

`{TETS_NO}_{PI_NO}.{EXT}`

where `{TEST_NO}` – is log file experiment number (Figure 5.5.2)

`{PI_NO}` – 1 (“Master” Pi) or 2 (“Slave” Pi)

`{EXT}` – “txt” (for accelerometer data) “h264” (for video data)

After the recording of the data is completed, the code will return to the initial message “**Start a test? y/n**” completing a single cycle of the experiment.

To minimise time consumption for the video processing a synchronisation code was implemented in both experimental computers. Still due to the volume of the experiments, it is dangerous to rely only on the cameras synchronising via running code on the computers. An additional measure was implemented to allow post-processing code to determine and correct any discrepancies. It will be shown later (subsection 6.4.1) that this measure was needed, as the synchronisation timing error was persistent across several recorded videos. Most of the time it was within a few frames (1 – 3 frames), but there were cases observed of the time error reaching up to 12 frames. It is speculated that this is due to the operation of the computers, which also explains the frequent difference in video lengths, despite the fact that based on the operational code it was expected that all video lengths should be 5 minutes.

To confirm synchronisation via post-processing code a common event was required. This event was chosen to be the first observed drop detachment. This means that each experiment should start with the drop already attached to the nozzle. To make sure that the drop edge is not confused with the nozzle edge by the video processing code the

requirements dictate that the drop maximal horizontal cross sectional diameter should be bigger than the outer nozzle diameter⁷.

Keeping the aforementioned in mind, each video recording should start with the drop attached to the nozzle, where the drop size should fit the requirements of the video processing code. The pump is started after a few seconds (2 to 3 seconds) allowing for camera recording start errors.

To remove the water from the system it is required to unscrew the wing nuts from the bottom of the experimental box, and remove the surrounding Perspex sheet. Then it is possible to access the drip tray under the test chamber.

Finally, it was found experimentally that there is the possibility of building up the air pockets in the fluid flow (while changing the syringe), which can affect the experimental results and should be removed. The best method to remove air from the fluid system is by forcing it out with a hard push on the syringe.

⁷ To identify the nozzle tip it is assumed that the nozzle edge follows a cone shape. In terms of the edge coordinate detection code it means that for the left side the edge pixel should be either one pixel below the current one or the one below and right, and for right edge either the pixel below or the pixel below and left. The nozzle bottom is identified, when there is no edge detected in either of those pixels - see section 6.3.2. As the drop grows, the contact angle between the nozzle tip and drop (contact angle here defined as the angle between the horizontal tangent line of the nozzle tip and the tangent line to the drop surface at the point of the drop-nozzle contact) passes the value of 90° . With the contact angle above 90° the edge of the drop attached to the nozzle tip will be located to the right on the left side of the nozzle and to the left on the right side. This eliminates the possibility that the nozzle edge is confused with the drop edge.

CHAPTER 6

EXPERIMENTAL CAMPAIGN

In the previous chapter, the experimental module design was discussed. The module requirements were outlined and components were selected, integrated into the module and calibrated. Here the discussion will lead on to consider the actual operation of the module. This chapter will discuss the experimental work carried out and then go on to the analysis of the experimental results. The first part of this chapter (section 6.1) will summarise the experimental assumptions and provide the error and correction factors for the experimental variables, while the second part (section 6.2) will provide the results of the recorded experimental variables. The experimental variables include the temperature readings and the pressure records for the test campaign.

The third section (6.3) explains the codes developed for video processing. Firstly, the selection of the edge detection method is explained, followed by the code for video processing and finally the post-processing code will be presented to analyse these results.

In following section (6.4), the operation of the code is confirmed. More particularly, the synchronisation of the camera (subsection 6.4.1) and the adaptation of the bifurcation plot results (subsection 6.4.2) are discussed.

Finally, section 6.5 analyses the performance of the code. Importantly, identifies the performance limits of the experimental module and describes interesting behavioural anomalies that were identified during the experimental campaign.

6.1 Summary of the assumptions and experimental variables

The experimental variables were presented in subsection 5.1.1. The following were required to be measured:

- Density of the liquid
- Viscosity of the liquid
- Fluid flow rate
- Temperature
- Fluid surface tension
- Density of the surroundings
- Atmospheric pressure
- Time step
- Drop position error
- Drop volume
- Drop mass
- Acceleration

The atmospheric pressure was considered to be constant (equal to 101 kPa) and does not affect the other variables. Nevertheless, measurements were taken for the reference purposes. With this assumption in mind, the density, viscosity, and surface tension are all assumed dependent only on temperature (Figure 5.1.2 and Figure 5.1.3). Those variables require to be confirmed and corrected for difference in properties to our experimental medium. The air density is simply set according to readings of the temperature (Table 5.1.1). Fluid flow is set by a pump, which requires to be corrected due to pump linearity error and calibration error. The uncertainty in time step, drop volume or drop mass is all-dependent on the camera performance limitation. The drop mass and drop volume are related additionally via the temperature dependent density. As the experiments were performed in normal gravity only, acceleration readings were not taken.

To align the experimental data of the density, viscosity and surface tension with their reference curves (Table 5.1.1, Figure 5.1.2 and Figure 5.1.3), the following equations were used to represent the curves:

$$\begin{aligned}
\rho^* &= 0.0005T_o^2 - 0.0437T_o + 1.686 \\
(\rho_o)^* &= -0.0041T_o + 1.2865 \\
\mu^* &= -5 \cdot 10^{-6}T_o^2 + 3 \cdot 10^{-6}T_o + 1.0002 \\
\nu^* &= 0.0001T_o^2 + 0.02T_o + 0.555 \\
\sigma^* &= -0.0021T_o^2 - 0.0648T_o + 74.953
\end{aligned}
\tag{6.1.1}$$

where: ρ^* – calculated density of water before correction (g/ml)

$(\rho_o)^*$ – calculated density of air (kg/m³)

μ^* – calculated dynamic viscosity before correction (mPa.s)

ν^* – calculated kinematic viscosity before correction (mm²/s)

σ^* – calculated surface tension before correction (mN/m)

T_o – temperature (°C)

The measurement errors and uncertainties were discussed previously in chapter 5 and are summarised in the error table (Table 6.1.1) provided below.

No.	Nature of the error	Measured/calculated value of error
1.	Temperature sensor error	$\Delta T_o = -0.42 \pm 0.125$ (°C)
2.	Exposure time	$\Delta t_{exp} = 1/60$ (s)
3.	Pump linear velocity fluctuation (including damping due to silicon-based TYGON® tubing)	$\Delta v_{lin} = \pm 0.00102\dot{V}$ (mm/s), where \dot{V} is measured in ml/hr units
4.	Nozzle inner diameter	$d = 0.990 \pm 0.0255$ (mm)
5.	Pump calibration error	$\Delta \dot{V}_{calib} = \dot{V} + \dot{V}(-0.025\dot{V} + 22.5) \pm 1.54\dot{V}/100$
6.	Nozzle outer diameter	$d_o = 2.00 \pm 0.05$ (mm)
7.	Accelerometer sensor error	$\Delta a = \pm 0.001$ (m/s ²)

Table 6.1.1: Experimental uncertainty/correction value table

First after the temperature is acquired (T_{mes}), the value is corrected to include the sensor error (Equation 5.4.3) which is given by:

$$T_o = T_{mes} + \Delta T_o = T_{mes} - 0.42 \pm 0.125$$
 (°C) 6.1.2

Now the uncertainty can be calculated using the standard error propagation method as:

$$\Delta T = \pm \sqrt{\Delta T_{sens}^2 + \Delta T_{base}^2} = \pm \sqrt{0.125^2 + 0.01^2} \cong \pm 0.125 \quad | \quad 6.1.3$$

where: ΔT – total temperature uncertainty

$\Delta T_{sens} = 0.125$ °C – sensor reading uncertainty

$\Delta T_{base} = 0.01$ °C – calibrated equipment reading uncertainty

The values of the water and air density, kinematic and dynamic viscosities and surface tension can be calculated using the following set of equations:

$$\begin{aligned} \Delta \rho^* &= \pm \sqrt{(0.0005 \cdot 2T_o \Delta T_o)^2 + (0.0437 \Delta T_o)^2} \\ \Delta(\rho_o)^* &= \pm 0.0041 \Delta T_o \\ \Delta \mu^* &= \pm \sqrt{(5 \cdot 10^{-6} \cdot 2T_o \Delta T_o)^2 + (3 \cdot 10^{-6} \Delta T_o)^2} \\ \Delta \nu^* &= \pm \sqrt{(0.0001 \cdot 2T_o \Delta T_o)^2 + (0.02 \Delta T_o)^2} \\ \Delta \sigma^* &= \pm \sqrt{(0.0021 \cdot 2T_o \Delta T_o)^2 + (0.0648 \Delta T_o)^2} \end{aligned} \quad | \quad 6.1.4$$

The temperature dependent variables uncertainty propagating error will be equal to:

$$\begin{aligned} \Delta \rho^* &= \pm 3.16 \cdot 10^{-3} \sqrt{1.563 \cdot 10^{-3} T_o^2 + 2.984} \text{ (g/ml)} \\ \Delta(\rho_o)^* &= \pm 5.125 \cdot 10^{-5} \text{ (kg/m}^3\text{)} \\ \Delta \mu^* &= \pm 1.25 \cdot 10^{-6} T_o \text{ (mPa.s)} \\ \Delta \nu^* &= \pm 2.5 \cdot 10^{-3} \text{ (mm}^2\text{/s)} \\ \Delta \sigma^* &= \pm 8.1 \cdot 10^{-3} \sqrt{4.201 \cdot 10^{-3} T_o^2 + 1} \end{aligned} \quad | \quad 6.1.5$$

Clearly $\Delta(\rho_o)^*$ – is too small to be considered and will not be considered hereafter.

Similarly for the values of $\Delta \mu^*$ and $\Delta \nu^*$.

The selected experimental liquid is distilled water. Prior to the tests, the experimental liquid was defined by the measurement of liquid density, viscosity, temperature and atmospheric pressure. The values measured are within the expected range of values (subsection 5.1.1), but with slight errors which have been included in the error Table 6.1.1.

The density was measured using laboratory weighing scales and a graduated cylinder. The measured density of the water was found to be 1.0018 ± 0.0128 g/ml based on four measurements at the temperature of 22 °C presented in Table 6.1.2 (with respect to a

reference value of 0.9978 g/ml – Figure 5.1.3). The error is within the expected limits and is equal to 4.03 mg/ml. The calculations for the reading precision ($\Delta\rho$) in this calculations and for the calculations hereafter are given in Appendix O.

Test No.	Volume (ml) ± 0.75 ml	Mass (g) ± 0.005 g	Density (g/ml)
1	20.00	20.01	1.0005
2	30.00	30.08	1.0027
3	40.00	40.12	1.0030
4	50.00	50.05	1.0010
Average:			1.0018

Table 6.1.2: Water density measurements
(At 22 °C and 101.19 kPa)

$$\rho_{err} = +0.00403 \pm 0.0128 \text{ (g/ml)}$$

6.1.6

where: ρ_{err} – correction value of density based on experimental measurements

The density uncertainty ($\Delta\rho$) can be calculated:

$$\Delta\rho = \pm\sqrt{(\Delta\rho^*)^2 + (\Delta\rho_{err})^2}$$

6.1.7

where: $\Delta\rho^*$ – density uncertainty due to temperature reading:

$$\Delta\rho_{err} = \pm\frac{1}{4}\sqrt{\sum(\Delta\rho_{ex_n}^2)}$$

$$\Delta\rho_{ex_n} = \pm\rho_{ex_n}\sqrt{\left(\frac{\Delta m_{ex_n}}{m_{ex_n}}\right)^2 + \left(\frac{\Delta V_{ex_n}}{V_{ex_n}}\right)^2}$$

$\Delta\rho_{err}$ – density measurement uncertainty

Δm_{ex_n} – mass measurement uncertainty

ΔV_{ex_n} – volume measurement uncertainty

ρ_{ex_n} – density measurement

m_{ex_n} – mass measurement

V_{ex_n} – volume measurement

ex_n – experiment number ($n = 1,2,3,4$)

The total density uncertainty now can be approximated by:

$$\Delta\rho = \pm 1.3 \cdot 10^{-2} \sqrt{8.071 \cdot 10^{-5} T_o^2 + 1} \quad | \quad 6.1.8$$

Alternatively, the term $(8.071 \cdot 10^{-5} T_o^2)$ can be neglected as relatively small for all T_o :

$$\Delta\rho = \pm 0.013 \text{ (g/ml)} \quad | \quad 6.1.9$$

The water viscosity was measured using a BS/U-tube reverse flow viscometer with nominal viscometer constant (K_C) equal to $0.0030 \pm 0.0005 \text{ mm}^2/\text{s}^2$. Four tests were performed and the average value was found to be $1.0461 \text{ mm}^2/\text{s}$ (Table 6.1.3).

Test No.	Test time (s) $\pm 0.02 \text{ s}$	Kinematic viscosity (mm^2/s)
1	348.73	1.0462
2	348.70	1.0461
3	348.63	1.0459
4	348.77	1.0463
Average:		1.0461

Table 6.1.3: Water kinematic viscosity measurements
(At 22°C and 101.19 kPa)

The expected value of the kinematic viscosity is equal to $1.0454 \text{ mm}^2/\text{s}$ (Figure 5.1.2) and the correction factor (v_{err}) due to difference in liquid property is equal to:

$$v_{err} = +0.0007 \pm 0.08718 \text{ (mm}^2/\text{s)} \quad | \quad 6.1.10$$

Where first term identifies the offset value due to liquid property and second term is the measurements uncertainty, which was calculated as:

$$\Delta v_{err} = \pm \frac{1}{4} \sqrt{\sum(\Delta v_{ex_n}^2)} \quad | \quad 6.1.11$$

$$\Delta v_{ex_n} = \pm v_{ex_n} \sqrt{\left(\frac{\Delta K_C}{K_C}\right)^2 + \left(\frac{\Delta t_{ex_n}}{t_{ex_n}}\right)^2}$$

where: K_C – viscometer constant

$$\Delta K_C = \pm 0.0005 \text{ mm}^2/\text{s}^2$$

ex_n – experiment number ($n = 1,2,3,4$)

When the kinematic viscosity value is converted to dynamic viscosity using the equation:

$$\mu^* + \mu_{err} = 10^{-3} \cdot (\rho^* + \rho_{err})(\nu^* + \nu_{err}) \quad | \quad 6.1.12$$

where: $\mu^* = \rho^* \nu^*$ – dynamic viscosity (mPa.s)

μ_{err} – dynamic viscosity correction factor (mPa.s)

ρ – density (g/mm³)

ν – kinematic viscosity (mm²/s)

The value of the dynamic viscosity correction factor can be found:

$$\mu_{err} = 10^{-3} \cdot (\rho^* \nu_{err} + \rho_{err} \nu^* + \rho_{err} \nu_{err}) \pm 0.0351 \text{ mPa/m} \quad | \quad 6.1.13$$

The uncertainty was found using the error propagation method:

$$\begin{aligned} \Delta \mu_{err}^2 &= \pm \left((\Delta(\rho^* \nu_{err}))^2 + (\Delta(\rho_{err} \nu_{err}))^2 + (\Delta(\rho_{err} \nu^*))^2 \right) \\ \Delta(\rho^* \nu_{err}) &= \pm \rho^* \nu_{err} \sqrt{\left(\frac{\Delta \rho^*}{\rho^*}\right)^2 + \left(\frac{\Delta \nu_{err}}{\nu_{err}}\right)^2} = \rho^* \nu_{err} \frac{\Delta \nu_{err}}{\nu_{err}} \\ \Delta(\rho_{err} \nu_{err}) &= \pm \rho_{err} \nu_{err} \sqrt{\left(\frac{\Delta \rho_{err}}{\rho_{err}}\right)^2 + \left(\frac{\Delta \nu_{err}}{\nu_{err}}\right)^2} = \rho_{err} \nu_{err} \frac{\Delta \nu_{err}}{\nu_{err}} \\ \Delta(\rho_{err} \nu^*) &= \pm \rho_{err} \nu^* \sqrt{\left(\frac{\Delta \rho^*}{\rho^*}\right)^2 + \left(\frac{\Delta \nu^*}{\nu^*}\right)^2} = \rho_{err} \nu^* \frac{\Delta \rho^*}{\rho^*} \end{aligned} \quad | \quad 6.1.14$$

where: $\left(\frac{\Delta \nu_{err}}{\nu_{err}}\right)^2 \gg \left(\frac{\Delta \rho_{err}}{\rho_{err}}\right)^2 \gg \left(\frac{\Delta \rho^*}{\rho^*}\right)^2$

$$\Delta \nu^* \cong 0$$

Which leads to $\Delta(\rho_{err} \nu_{err}) \gg \Delta(\rho^* \nu_{err}) \gg \Delta(\rho_{err} \nu^*)$, simplifying the first equation to:

$$\Delta \mu_{err} = \pm \rho_{err} \nu_{err} \frac{\Delta \nu_{err}}{\nu_{err}} = \pm \rho_{err} \Delta \nu_{err} = \pm 0.0351 \cdot 10^{-3} \quad | \quad 6.1.15$$

The values were recorded at a temperature of 22 °C and a pressure of 101.19 kPa. The values of the viscosity and the density as recorded are in good agreement with the reference values.

The fluid surface tension correction factor can be estimated experimentally. Unfortunately, it will require the development of the different experimental rig, which should have similar

solid to liquid contact property to fully satisfy the current experimental needs. Due to the complication it was decided to use standard values, even so that it will be shown in the future that surface tension value is slightly off (by 13% from theoretical value based on Tate's law – 6.5.2) from the expected values.

What is known about the flow rate of the pump? First, there is a fluctuation error associated with the operation of the pump and this means that the velocity of the pump motor can fluctuate ($\Delta\dot{V}_{fluct}$ – Equation 6.1.16). The pump also is required to be calibrated and has a consistent error, meaning that the flow continuously is offset from the actual value (the value which is shown on the display of the pump) – Equation 5.3.2 in subsection 5.4.1, and has an uncertainty in the reading ($\Delta\dot{V}_{calib}$).

The pump fluctuation error can be converted to a flow rate fluctuation error using the equation:

$$\Delta\dot{V}_{fluct} = \frac{\pi d^2}{4} \Delta v_{fluct} = \pm 1.456 \cdot 10^{-4} \dot{V} \text{ ml/hr} \quad \left| \quad 6.1.16 \right.$$

where: $d = 0.990 \pm 0.0255$ (mm)

\dot{V} – pump displayed flow rate, measured in ml/hr

Δv_{fluct} – pump linear velocity uncertainty (Equation 5.3.1)

Now adding the calibration factor will provide the complete correction factor including the uncertainty:

$$\dot{V}_{err} = \dot{V} + \frac{\dot{V}}{100} (-0.025\dot{V} + 22.5) \pm 1.9 \cdot 10^{-2} \dot{V} \text{ ml/hr} \quad \left| \quad 6.1.17 \right.$$

The pump flow rate, uncertainty shown in the equation above, includes the pump velocity fluctuation ($\Delta\dot{V}_{fluct} = \pm 1.456 \cdot 10^{-4} \dot{V}$) and calibration uncertainty which propagate due to pump performance error ($\Delta\dot{V}_{calib} = \pm 1.54 \cdot 10^{-2} \dot{V}$). The total uncertainty now can be calculated as:

$$\Delta\dot{V}_{err} = \pm \sqrt{\left(\frac{\partial\dot{V}_{err}}{\partial\dot{V}} \Delta\dot{V}\right)^2} = \pm(1.9 \cdot 10^{-2}\dot{V} - 7.77 \cdot 10^{-6}\dot{V}^2) \quad \left| \quad 6.1.18 \right.$$

where: $\Delta\dot{V} = \Delta\dot{V}_{fluct} + \Delta\dot{V}_{calib}$

The value $7.77 \cdot 10^{-6}\dot{V}^2$ can be neglected as being at least 10 times smaller than $1.9 \cdot 10^{-2}\dot{V}$ for all flow rates under consideration.

The uncertainty which was found ($\Delta\dot{V}_{err} = \pm 1.9 \cdot 10^{-2}\dot{V}$) gives a variation of ± 0.95 ml/hr at the set flow rate of 50 ml/hr or ± 5.32 ml/hr at a flow rate of 280 ml/hr.

The uncertainty in the volume of the drop (ΔV) due to the exposure time is found using the exposure time ($t_{exp} = 1/60$ s) and the actual flow rate. The shutter exposure time allows the capture of the volume of the drop between start (at shutter opening) and the drop end state (at shutter closing) but leads to uncertainty in the volume of the drop due to the finite shutter time during both states. The total uncertainty due to the shutter was determined to be:

$$\Delta V_{time} = \pm(\dot{V} + \dot{V}_{err})t_{exp} = \pm(5.672 \cdot 10^{-3}\dot{V} - 1.157 \cdot 10^{-6}\dot{V}^2) \text{ (mm}^3\text{)} \quad \left| \quad 6.1.19 \right.$$

where \dot{V} – is measured in ml/hr

The volume uncertainty can be simplified as the second term ($1.157 \cdot 10^{-6}\dot{V}^2$) is small compared to the first term for all flow rates, leading to:

$$\Delta V_{time} = \pm(\dot{V} + \dot{V}_{err})t_{exp} = \pm 5.672 \cdot 10^{-3}\dot{V} \text{ (mm}^3\text{)} \quad \left| \quad 6.1.20 \right.$$

where \dot{V} – is measured in ml/hr

The mass uncertainty due to the shutter exposure time in this case becomes equal to:

$$\Delta m_{time} = \pm \sqrt{(V\Delta\rho^*)^2 + (V\Delta\rho_{err})^2 + ((\rho^* + \rho_{err})\Delta V)^2} \text{ (g)} \quad \left| \quad 6.1.21 \right.$$

where: volume parameters are measured in mm^3

density parameters are measured in g/mm^3

The following assumptions were made prior to experiments:

- Density of the liquid
 - The working fluid density is assumed to be dependent on the temperature only and follow the curve shown in Figure 5.1.3 described by Equation 6.1.5 and altered by the correction factor (Equation 6.1.6) with total uncertainty based on Equation 6.1.9
- Viscosity of the liquid
 - The fluid kinematic viscosity is equal to is assumed to be dependent on the temperature only and follows the curve shown in Figure 5.1.2 described by Equation 6.1.5 and altered by the correction factor and uncertainty (Equation 6.1.10)
 - The fluid dynamic viscosity is dependent on the temperature only (Figure 5.1.2 and Equation 6.1.5) with the addition of the correction factor and uncertainty (Equation 6.1.13)
- Fluid flow rate
 - The fluid flow rate is set by the syringe pump with the calibration error and fluctuation error to be described by Table 6.1.1 and Equation 6.1.16, with an uncertainty too small to be considered
 - The fluid flow rate is set from 50 ml/hr – 288 ml/hr
- Temperature
 - The temperature of the fluid is assumed to remain constant while the experiment is running with the correction factor and uncertainty to be described by Equation 6.1.2
- Fluid surface tension
 - The fluid surface tension is assumed to be temperature dependent only and follows the curve shown in Figure 5.1.3
- Density of the surrounding
 - The density of the surroundings is taken from reference values and is temperature dependent (Equation 6.1.5) with an uncertainty value which can be neglected
- Atmospheric pressure
 - The pressure as mentioned in subsection 5.1.1 is set to be constant at 101 kPa and is assumed that any variation does not affect the variables
 - Pressure measurement were still taken twice a day for reference purposes
- Time step

- The time step is assumed to be constant with an uncertainty equal to the exposure time (Table 6.1.1)
- Drop position error
 - The pixel size can be approximated based on the nozzle outer diameter (Table 6.1.1) assumed here to be 2 mm (subsection 0) as detected in the camera picture by the edge detection code
 - The Centre of mass (CoM) location uncertainty will be determined experimentally and will be discussed in a future section (subsection 6.5.1)
- Drop volume
 - The drop volume uncertainty based on the pump error and the exposure time is set by Equation 6.1.20
 - Additionally an investigation was completed to include the drop volume variation due to camera and edge detection uncertainties (subsection 6.5.1)
- Drop mass
 - The drop mass uncertainty based on the pump error and the exposure time is set by Equation 6.1.21
 - Additionally an investigation was completed to include the drop volume variation due to camera and edge detection uncertainties (subsection 6.5.1)
- Acceleration
 - Acceleration uncertainty is presented in Table 6.1.1, but will not be considered in this study
- Other
 - Drop inner radius was assumed to be equal to 0.990 ± 0.0255 mm (Table 6.1.1)

The uncertainty calculations presented in this chapter will lead to some uncertainty in dimensionless parameters such as the Bond, Weber and Reynolds numbers, which are extensively used when comparing the theoretical results to the experimental ones.

As per Equation 2.2.2, the Bond number is equal to $\sqrt{(\rho g d^2)/2\sigma}$.

- The value of acceleration due to gravity is a constant ($g = 9.81$ m/s²)
- The surface tension was assumed to be temperature dependent ($\sigma = \sigma^* = (-2.1 \cdot 10^{-3} T_o^2 - 6.48 \cdot 10^{-2} T_o + 74.953) \cdot 10^{-3}$ N/m
- The diameter of the flow ($d = 0.99 \cdot 10^{-3}$ m), with an uncertainty equal to $\Delta d = \pm 2.55 \cdot 10^{-5}$ m

- The density is temperature dependent ($\rho^* = (5 \cdot 10^{-4}T_o^2 - 4.37 \cdot 10^{-2}T_o + 1.686) \cdot 10^3 \text{ kg/m}^3$) and should be adjusted based on the correction factor $\rho_{err} = 4.03 \text{ kg/m}^3$, with the uncertainty equal to $\Delta\rho \pm 13 \text{ kg/m}^3$.

The general form of the error propogation provides that:

$$\Delta Bo^2 = \left(\frac{\partial Bo}{\partial \rho} \Delta \rho \right)^2 + \left(\frac{\partial Bo}{\partial d} \Delta d \right)^2 \quad \left| \quad 6.1.22 \right.$$

When expanded by parts:

$$\begin{aligned} \left(\frac{\partial Bo}{\partial \rho} \Delta \rho \right)^2 &= \frac{gd^2}{8\rho\sigma} (\Delta\rho)^2 = \\ &= \frac{0.2}{(0.5T_o^2 - 43.7T_o + 1690.03) \cdot (-2.1 \cdot 10^{-3}T_o^2 - 6.48 \cdot 10^{-2}T_o + 74.953)} \end{aligned} \quad \left| \quad 6.1.23 \right.$$

and:

$$\left(\frac{\partial Bo}{\partial d} \Delta d \right)^2 = \frac{\rho g}{2\sigma} (\Delta d)^2 = \frac{31.9 \cdot (0.5T_o^2 - 43.7T_o + 1690.03) \cdot 10^{-7}}{(-2.1 \cdot 10^{-3}T_o^2 - 6.48 \cdot 10^{-2}T_o + 74.953)} \quad \left| \quad 6.1.24 \right.$$

At this stage substituting the temperature in the range of experimental interest $15 \leq T_o \leq 25 \text{ }^\circ\text{C}$, gives that $\left(\frac{\partial Bo}{\partial d} \Delta d \right)^2$ is in the order of 10^3 smaller, resulting in:

$$\begin{aligned} \Delta Bo^2 &\cong \\ &\cong \pm \frac{0.2}{-1.05 \cdot 10^{-3}T_o^4 + 5.94 \cdot 10^{-2}T_o^3 + 36.76 \cdot T_o^2 - 33.85 \cdot 10^2T_o + 12.67 \cdot 10^4} \end{aligned} \quad \left| \quad 6.1.25 \right.$$

Futher analysis showed that in the range of experimental interest (where the temperature is in the range $15 \leq T_o \leq 25 \text{ }^\circ\text{C}$) the Bond number uncertainty does not change and stays within $\Delta Bo = \pm 1.26$.

The Weber number from the Equation 2.1.2 uncertainty calculation equation will become:

$$\Delta We^2 = \left(\frac{\partial We}{\partial \rho} \Delta \rho \right)^2 + \left(\frac{\partial We}{\partial d} \Delta d \right)^2 + \left(\frac{\partial We}{\partial \dot{V}} \Delta \dot{V}_{err} \right)^2 \quad \left| \quad 6.1.26 \right.$$

Here the flow rate is the corrected value found based on the pump set flow rate (\dot{V}) as $\dot{V}_{err} = \dot{V} + \dot{V}(-0.025\dot{V} + 22.5)/100$ with the uncertainty equal to $\Delta\dot{V}_{err} = \pm 1.9 \cdot 10^{-2}\dot{V}$, and is converted into SI units. Solving by parts provides:

$$\frac{\partial We}{\partial \rho} = \frac{8\dot{V}_{err}^2}{\pi^2 \sigma d^3} = \frac{6.44 \cdot \left(\dot{V} + \frac{\dot{V}}{100}(-0.025\dot{V} + 22.5) \right)^2 \cdot 10^{-8}}{(-2.1 \cdot 10^{-3}T_o^2 - 6.48 \cdot 10^{-2}T_o + 74.953)} \quad 6.1.27$$

$$\begin{aligned} \frac{\partial We}{\partial d} &= -\frac{24\rho\dot{V}_{err}^2}{\pi^2 \sigma d^4} = \\ &= -\frac{19.53 \cdot (0.5T_o^2 - 43.7T_o + 1690.03) \cdot \left(\dot{V} + \frac{\dot{V}}{100}(-0.025\dot{V} + 22.5) \right)^2}{(-2.1 \cdot 10^{-3}T_o^2 - 6.48 \cdot 10^{-2}T_o + 74.953) \cdot 10^5} \end{aligned} \quad 6.1.28$$

$$\begin{aligned} \frac{\partial We}{\partial \dot{V}_{err}} &= \frac{16\rho\dot{V}_{err}}{\pi^2 \sigma d^3} = \\ &= \frac{4.64 \cdot (0.5T_o^2 - 43.7T_o + 1690.03) \cdot \left(\dot{V} + \frac{\dot{V}}{100}(-0.025\dot{V} + 22.5) \right) \cdot 10^5}{(-2.1 \cdot 10^{-3}T_o^2 - 6.48 \cdot 10^{-2}T_o + 74.953)} \end{aligned} \quad 6.1.29$$

When simplified the Weber number uncertainty can be presented as:

$$\Delta We^2 = \left(\frac{\left(\dot{V} + \frac{\dot{V}}{100}(-0.025\dot{V} + 22.5) \right)}{(-2.1 \cdot 10^{-3}T_o^2 - 6.48 \cdot 10^{-2}T_o + 74.953)} \right)^2 \cdot C \quad 6.1.30$$

Where C is:

$$\begin{aligned} C &= \left(83.72 \cdot \left(\dot{V} + \frac{\dot{V}}{100}(-0.025\dot{V} + 22.5) \right) \cdot 10^{-8} \right)^2 + \\ &+ \left(\frac{49.8 \cdot (0.5T_o^2 - 43.7T_o + 1690.03) \cdot \left(\dot{V} + \frac{\dot{V}}{100}(-0.025\dot{V} + 22.5) \right)}{10^{10}} \right)^2 + \\ &+ (24.5 \cdot \dot{V} \cdot (0.5T_o^2 - 43.7T_o + 1690.03) \cdot 10^{-7})^2 \end{aligned} \quad 6.1.31$$

When the experimental values of the temperature and flow rate ($50 \leq \dot{V} \leq 288$ ml/hr or $1.39 \cdot 10^{-8} \leq \dot{V} \leq 8 \cdot 10^{-8}$ m³/s) are included in the calculations Equation 6.1.31 can be simplified as the first and second terms are much smaller than the third term and can be neglected, leading to a simplified version of Weber number uncertainty:

$$\Delta We \cong \frac{24.5 \cdot \dot{V} \cdot (0.5T_o^2 - 43.7T_o + 1690.03) \cdot \left(\dot{V} + \frac{\dot{V}}{100} (-0.025\dot{V} + 22.5) \right)}{(-2.1 \cdot 10^{-3}T_o^2 - 6.48 \cdot 10^{-2}T_o + 74.953) \cdot 10^7} \quad 6.1.32$$

The value of the uncertainty can be presented in a 3D plot (Figure 6.1.1) for the range of experimental interest.

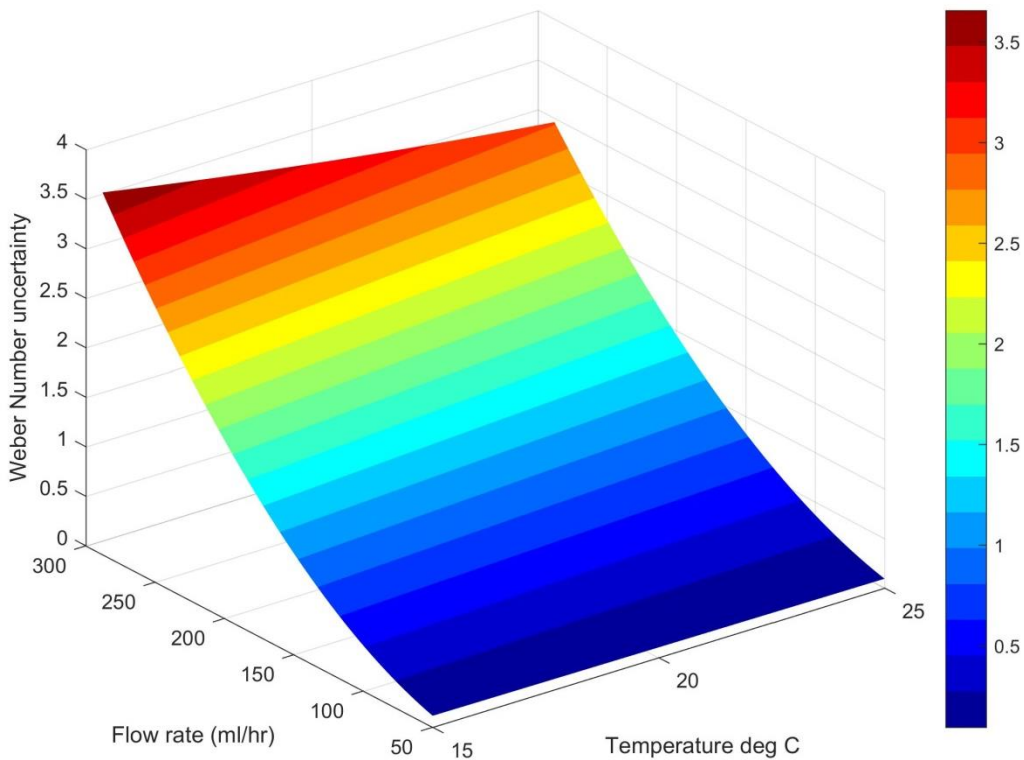


Figure 6.1.1: Weber number uncertainty range

Finally, the Reynolds number uncertainty will be:

$$\Delta Re^2 = \left(\frac{\partial Re}{\partial d} \Delta d \right)^2 + \left(\frac{\partial Re}{\partial \dot{V}} \Delta \dot{V} \right)^2 + \left(\frac{\partial Re}{\partial \nu} \Delta \nu \right)^2 \quad 6.1.33$$

Where the dynamic viscosity $\nu = \nu^* + \nu_{err}$, with the uncertainty equal to $\Delta \nu = \pm 0.087$ mm²/s. Expanding the components of Equation 6.1.33 gives:

$\frac{\partial Re}{\partial d} \Delta d = - \frac{9.28 \cdot \left(\dot{V} + \frac{\dot{V}}{100} (-0.025\dot{V} + 22.5) \right) \cdot 10^{-3}}{(0.0001T_o^2 + 0.02T_o + 0.5557)}$	6.1.34
$\frac{\partial Re}{\partial \dot{V}} \Delta \dot{V} = \frac{6.84 \cdot \dot{V} \cdot 10^{-3}}{(0.0001T_o^2 + 0.02T_o + 0.5557)}$	6.1.35
$\frac{\partial Re}{\partial v} \Delta v = - \frac{3.13 \cdot \left(\dot{V} + \frac{\dot{V}}{100} (-0.025\dot{V} + 22.5) \right) \cdot 10^{-2}}{(0.0001T_o^2 + 0.02T_o + 0.5557)^2}$	6.1.36

When calculated for the range of experimental interest the following Reynolds number uncertainty is achieved (Figure 6.1.2):

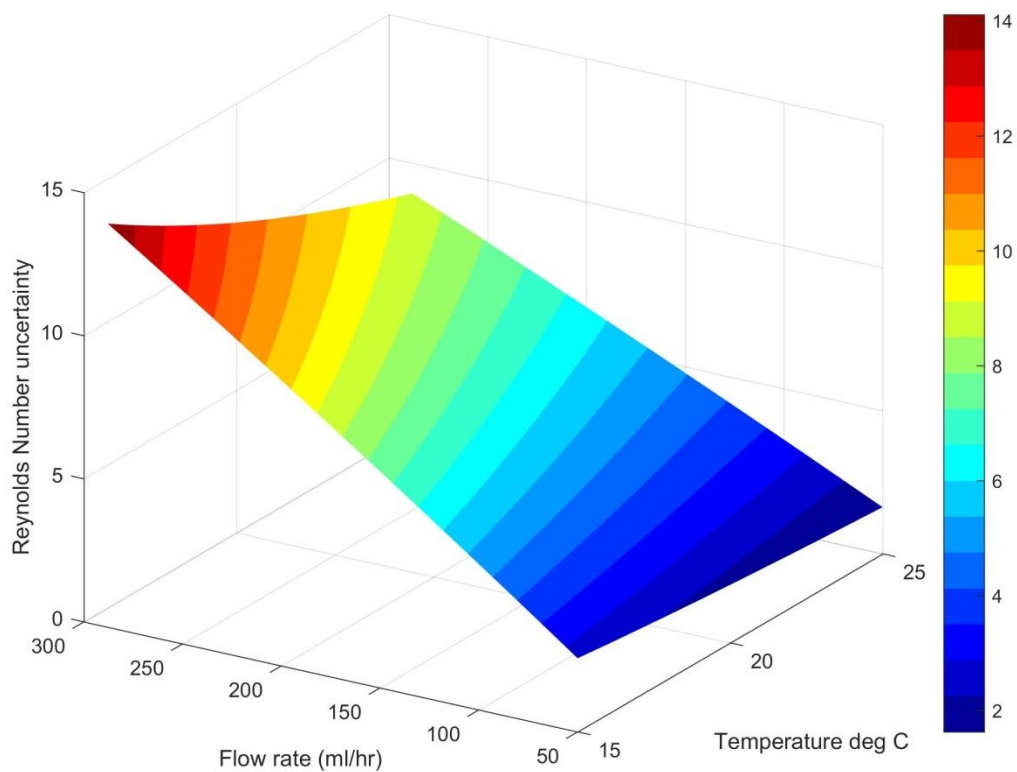


Figure 6.1.2: Reynolds number uncertainty

6.2 Experimental variables measurement summary

With the introduction of the correction factor for the flow rate it was required to check if the selected flow rate was still within the region of experimental interest. The upper flow rate is limited by the frame rate of the camera and the time it takes to fill the drop (e.g.

within 10 – 15 frames – see subsection 5.3.4). Later will be shown that the volume of the drop before detachment is around 40 mm^3 (subsection 6.5.2). with the camera limitations in mind (subsection 5.3.4 – the drop should be formed in 10 – 15 frames). The limit was set to be 288 ml/hr (section 5.2) as set by the pump, and with the correction factor, this corresponds to an actual flow rate of 332 ml/hr. This leads to the drop to be filled within 0.43 s or 13 frames, which satisfies the requirements.

It is expected that the chaotic region will start around a Reynolds number equal to 50 (subsection 5.1.1), corresponding to a flow rate of 141 ml/hr. The experimental starting flow rate was set to 50 ml/hr (set on pump), corresponding to an actual flow rate of 60.6 ml/hr, which also satisfies the requirements.

The following section provides a summary of the results for the test campaign variables that have an effect on this dynamic system. The full list of the recorded data is included in Appendix P. The tests were done with a flow rate step of 2 ml/hr (as displayed on the syringe pump) and took 5 days in total to complete. The full results provide details about the test day with corresponding test numbers, flow rates as set on the syringe pump and readjusted based on the correction factor, pressure readings at the beginning of the day and at the end, temperature readings for each test, and calculated values for the density, dynamic viscosity and surface tension.

Day	Pressure (kPa) ± 0.005 kPa	
	Beginning of the day	End of the day
1	102.44	102.28
2	102.32	101.97
3	100.23	100.16
4	99.96	100.07
5	100.12	100.77

Table 6.2.1: Pressure records during the test campaign

The temperature dependent variables with the additional correction factors (described in

previous section 6.1) taken from the analyses of the experimental results are shown in full in Appendix P.

The temperature variation during the test days is shown in Figure 6.2.1 for the reference purpose.

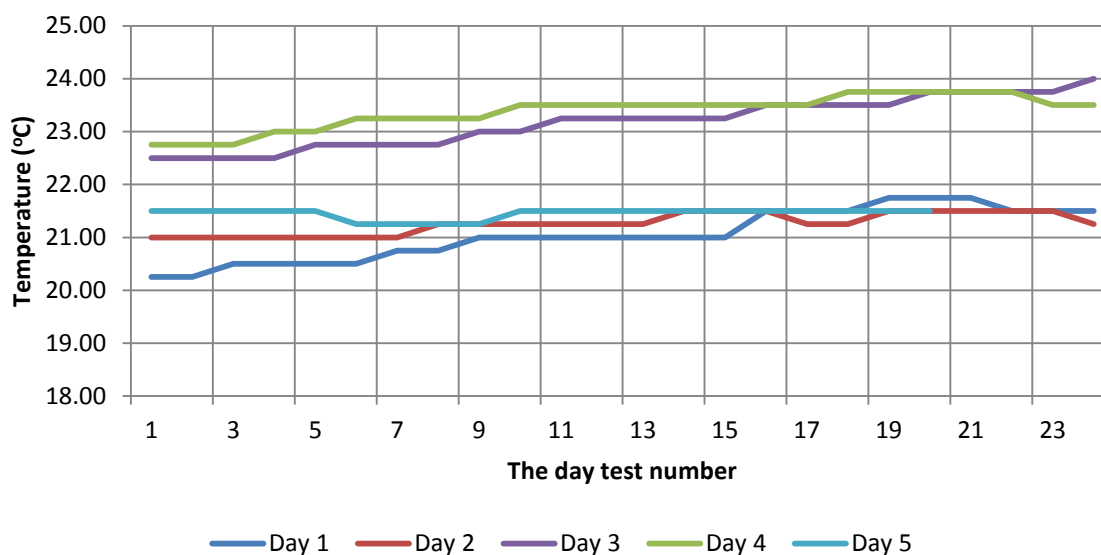


Figure 6.2.1: Temperature variation during test campaign

6.3 Video processing software

Experimental data was acquired using cameras installed at 90 degrees to each other. This positioning of the cameras allows one to fully determine the Centre of Mass (CoM) location in space (section 5.3.4). The cameras used in the experiment are Raspberry Pi cameras, which are directly connected to Raspberry Pi computers (section 5.3.5). The computers are programmed to record and synchronise videos. For video processing, which involves edge detection, “MATLAB®” software was used. The following subsection (6.3.1) will compare the different edge detection methods available in “MATLAB®”, and the sections after will discuss the code developed for video processing (subsection 6.3.2) and post-processing (subsection 6.3.3).

The output of the video processing is recorded in a set of folders, for each flow rate, containing text files of the drop edge coordinates for each frame of each camera separately.

The output of post-processing contains a summary of the experimental results.

The video processing code's first part is the main loop, and deals with file handling, running sub-codes and recording of results (Appendix Q.A). The second part identifies the nozzle shape (Appendix Q.B), and the last part (Appendix Q.C) identifies the drop shape.

The video post-processing takes the files of drop shapes from both cameras and first confirms the synchronisation, and secondly calculates the drop volume, CoM location at a specific time. Later the data is used to produce a set of results. The results include the following outputs:

- For each flow rate
 - Text files
 - Results summary file
[{flow rate}_results1.txt](#)
Includes volume (mm^3), CoM location (mm) for each time step (s)
 - Detachment summary file
[{flow rate}_results2.txt](#)
Includes volume at detachment (mm^3), CoM location at detachment (mm), time of detachment (s) and dripping period (s)
 - Detachment summary file excluding the satellite drops
[{flow rate}_results3.txt](#)
Includes same data set as the file above
 - Plots
 - Period return map – T_{n+1} vs T_n
[{flow rate}_Tn1-vs-Tn.jpeg](#)
 - Period map – T_n vs n
[{flow rate}_Tn-vs-n-all.jpeg](#)
 - Period map without satellite drops – T_n vs n
[{flow rate}_Tn-vs-n.jpeg](#)
 - Behavior plot
[{flow rate}_behaviour.jpeg](#)

Includes: mass variation: $m=f(t)$, CoM variation: $z=f(t)$, $x=f(t)$ and $y=f(t)$ for the last 10 seconds of the experiment,

- Plot of CoM horizontal coordinates at the detachment plot
[{flow rate}_detachment.jpeg](#)

- For joined results
 - Plots
 - Period versus flow rate plot: $T_n = f(\dot{V})$
[bifurcation.jpeg](#)

6.3.1 Edge detection methods comparison

For the video processing built in “MATLAB®” edge detection software was used.

Available edge detection methods are:

- Sobel
- Prewitt
- Roberts
- Laplacian of Gaussian (LoG)
- Canny

The approach to these methods and the difference between them were explained in section 2.5. To identify the most suitable candidate all methods were compared using the same video frame of the attached drop (Figure 6.3.1).

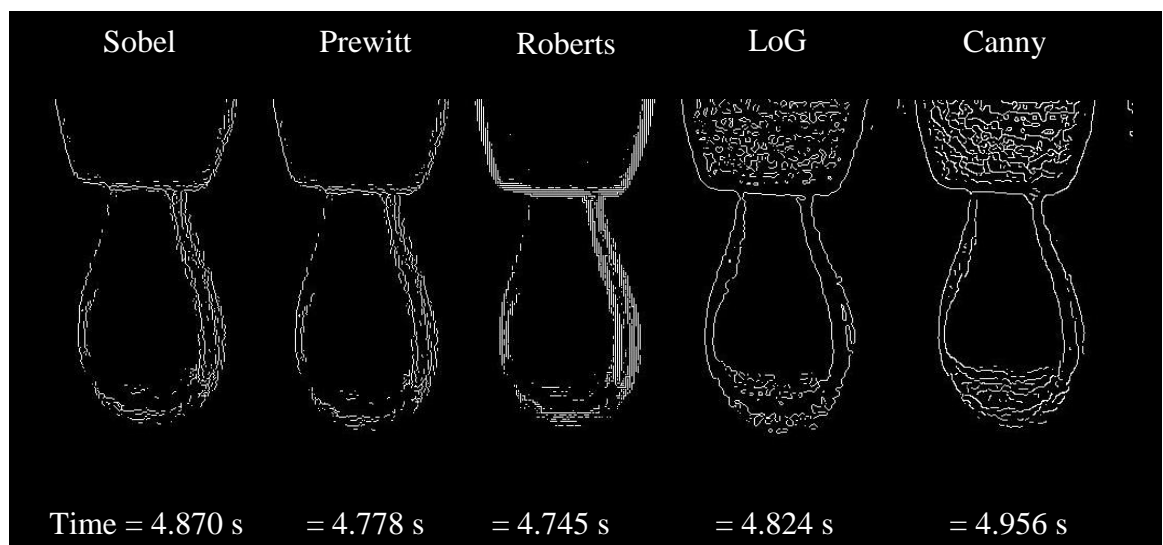


Figure 6.3.1: “MATLAB®” edge detection methods comparison

The video recording was done by the “Master” Pi camera with backlights ON. All methods were compared using the zero threshold value (default value), meaning that any identified edge will be displayed.

The main selection criteria were a fast simulation time, that the edge should be continuous and minimal noise (false edge detection) surrounding the drop. The selection was made by visual inspection of the processed frame picture.

The results gave clear identification of the positive and negative aspects of each method. As shown Sobel, Prewitt and Roberts methods use the gradient-based method, which utilises the change in the colour intensity. From Figure 6.3.1 it is observed that the left edge of the drop is badly defined, as there are side light sources (backlit panel for the second camera). In the case of the Sobel and Prewitt method, the edges are better defined (thinner) as both methods use a 3-by-3 operator to identify the edge, while the Roberts method uses a 2-by-2 operator, which makes the edge in the output image become less accurate. At the same time, the smaller the operator that is applied to the original image the less time is required for the data to be processed.

The LoG and Canny methods use a Gaussian filter first to remove unnecessary noise from the image and smooth it, and later apply the Laplacian operator to identify the edges. The Canny method, in addition, removes the weak zero crossing points and applies feature synthesis to join edges resulting in edges being longer, as seen at the bottom of the drop. The drop bottom is not well defined in all the pictures as a result of the curved shape of the drop, which does not have a change in colour intensity.

The simulation time was not considered to play a major role, nevertheless it was calculated that the Canny method requires an additional 46 hours to process data compared to the Roberts method, or 29 hours more compared to the LoG method (assuming that the average video time is 5 minutes at 30 frames per second, and the videos are processed using 8 processors).

The Canny method was therefore selected as the most suitable candidate, and additional parameters were introduced: a threshold value of 0.08 and the standard deviation of the LoG filter is set to be 2.5, resulting in a 5-by-5 filter size matrix. After post-processing of the original image, the drop has a clear edge.



*Figure 6.3.2: Drop after post-processing
(Left – original image; Right – processed image)*

The “Slave” Pi camera showed similar results with the best edge detection method being the Canny method, with the threshold value set as 0.1, and with a standard deviation of the LoG filter of 2.5.

6.3.2 Video processing pseudo code

The code for the video processing is structured in three different sections. The first part is responsible for the video files reading and saving the results. The second and third parts are responsible for identifying the nozzle and identifying the drop shape respectively.

When the code (Figure 6.3.3) is started, the values of the flow rates are required to be assigned (upper and lower limits) and the temperature too, which can be read from the test log file (Appendix P). The temperature later is used to correctly set the density and hence calculate the mass of the drop.

The main loop of the video processing starts by first reading the video file, identifying the number of frames required to process, creating the results matrix. The number of frames

will later be used as a limit for the drop shape identification loop, and the results matrix is used to record the drop shape at a specific time (frame).

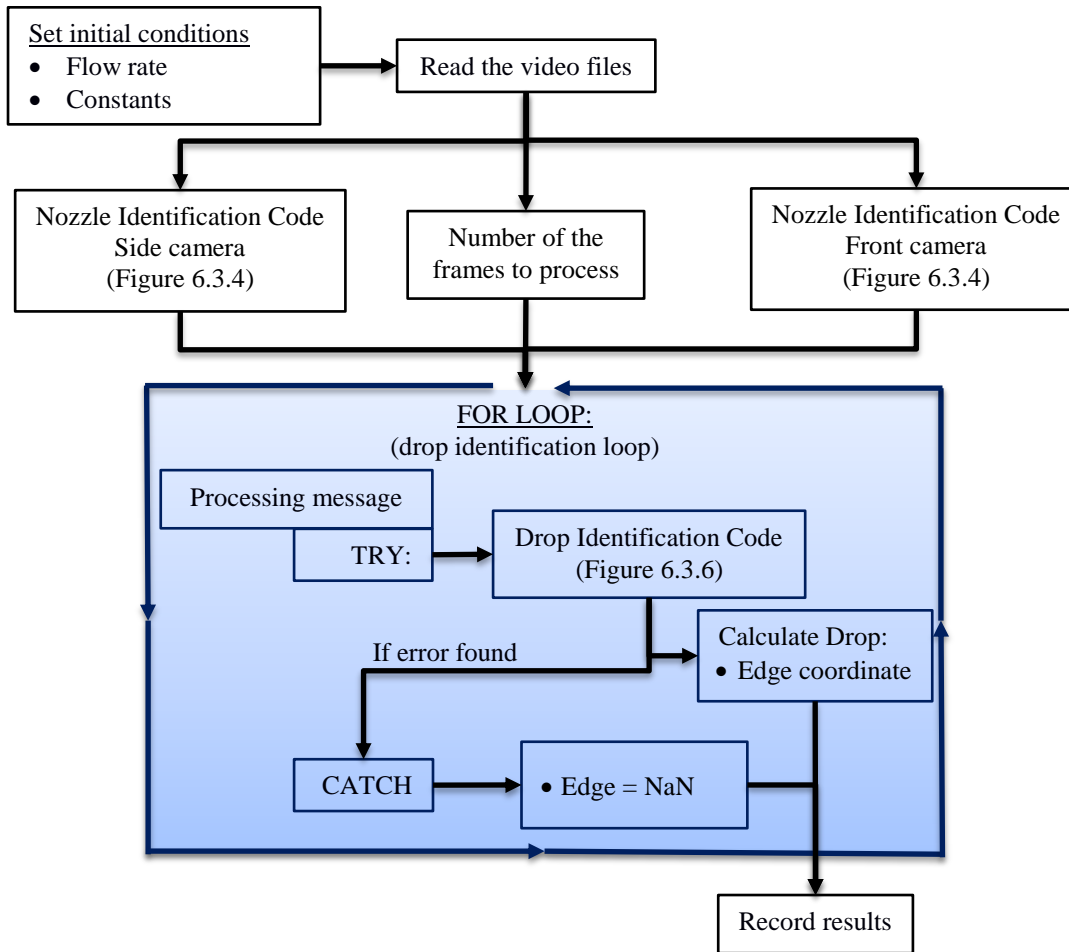


Figure 6.3.3: Drop shape identification pseudo code

The main loop then runs the nozzle identification code to identify the nozzle shape and to identify the vertical coordinate of the drop starting point. After identifying the nozzle shape, the drop shape identification loop is started, with a communication message displayed on the computer screen (showing the percentage of video frames already processed). The drop shape loop processes only if there were no errors found. If there is an error found the output for the results matrix will become “Not a Number” (NaN). In the case where there were no errors found in the drop processing loop, the output of the loop is the drop edge coordinates. This process repeats twice for each camera separately.

The nozzle identification code (Appendix Q.B, Figure 6.3.4) identifies the coordinates of the nozzle, and it was assumed that the nozzle would not move while the experiment was

running, so the programme runs once per video.

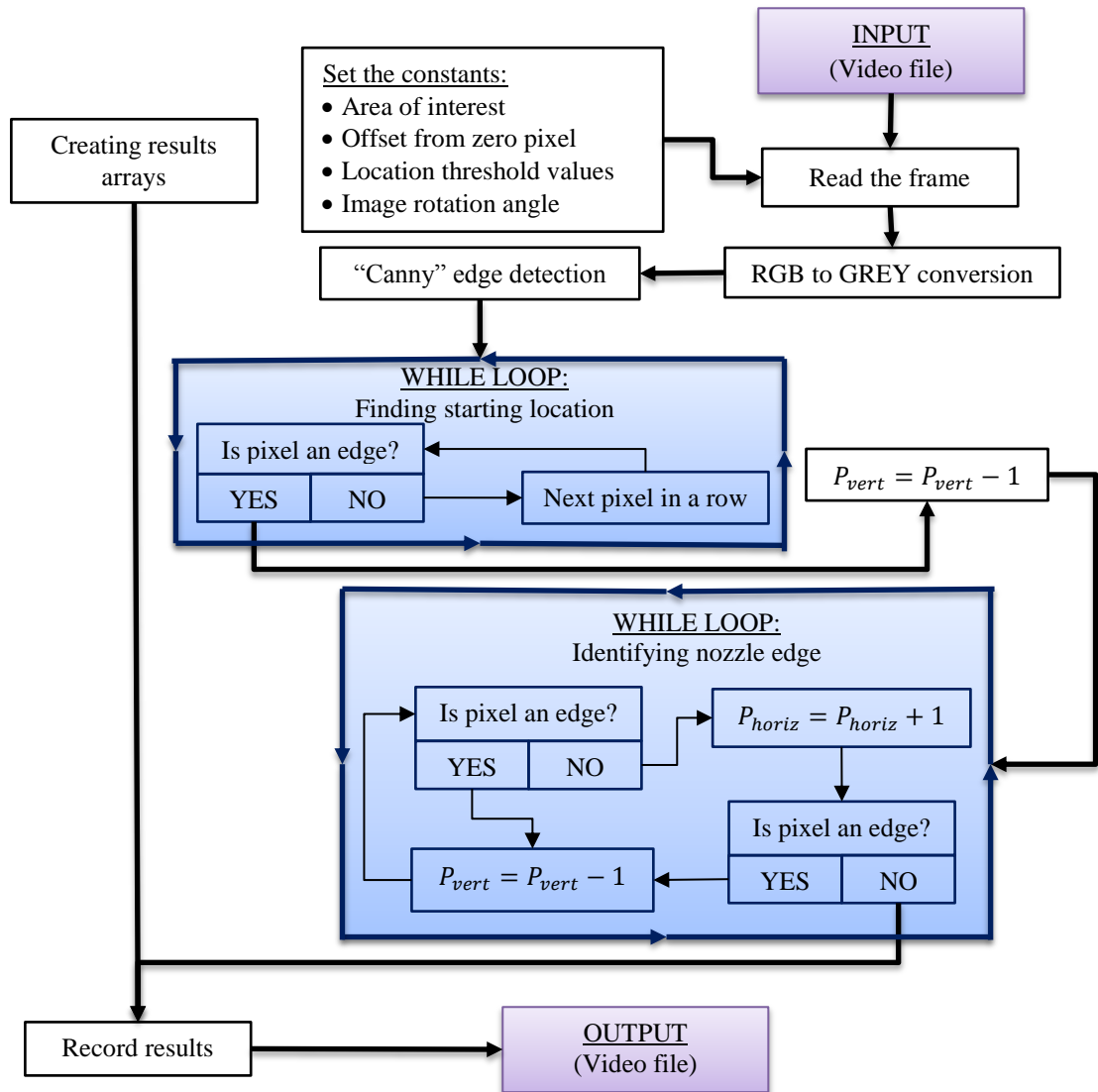
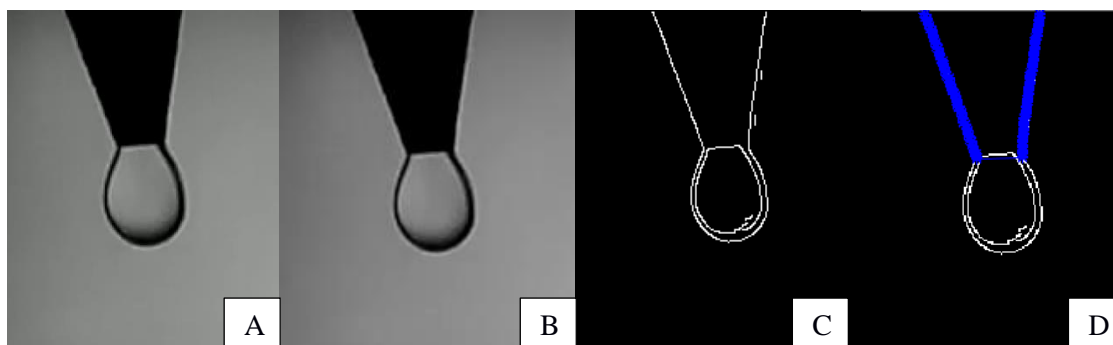


Figure 6.3.4: Nozzle identification pseudo code

The first few frames of the video are missed, as they are dim, and this is due to camera hardware limitations. The selected frame is set to be the sixth frame in the video. The limitations on the expected position of the camera are pre-set by threshold values (minimal left and maximal right coordinates: [320,800] – front video, [300,150] – side video) and are dependent on the selected camera video. Initially the area of interest is selected, followed by changing the colour of the picture from full colour to a grey scale (Figure 6.3.5), and finally applying the edge detection algorithm (using the Canny method – section 6.3.1). The selected area is set to be 400-by-400 pixels and the offset from the zero pixels was determined visually. The frames image is rotated to adjust for the camera

positioning error (-3 and +4 degrees for the “Master” Pi camera and the “Slave” camera respectively).



*Figure 6.3.5: Nozzle identification processing steps
Left to right (initial frame to processed frame)*

The nozzle identification starts at the second pixel row from the top within the selected area of interest, as the first pixel row is always black due to the nature of the “MATLAB®” software. The code then runs two loops to find the starting points of the nozzle at the left and right side, by looking at the pixel colour (one or zero). The edge is identified when a pixel is white (the value of the pixel is 1). To minimise the simulation time, the location of the nozzle edge is limited to two threshold values (left and right). When the starting points are found, an outline of the nozzle can be found. Using the assumption that the nozzle geometry always tends to go in the direction of down-right or down-left for the left and right sides respectively, and knowing the previous edge pixel, the code first checks the vertically down pixel and then the lower-right pixel for the left side of the nozzle (lower-left for the right side). The simulation ended when there were no pixels found in either of those locations.

The reasons for the code to stop identifying the nozzle edge is that experimental procedure requires to have the drop attached to the nozzle and to have a convex shape with the horizontal diameter of the nozzle bigger than the nozzle outer diameter.

The attached drop edge at the point of contact with the nozzle changes the direction of the detected edge, which with the drop starts to expand outwards (whereas the nozzle edge is

expected to tend inwards). The results are recorded in separate arrays for the left and right sides of the nozzle and are joined together at the end of the code to form a single continuous edge.

The video processing has a similar first few steps. It uses the “Canny” edge detection method with the defined region of the picture limited to a 400-by-400 pixel area and specific threshold values for edge detection based on the camera (Figure 6.3.6).

The code reads the frame, followed by choosing a specific region in a frame in which firstly the image is converted to a grey colour scale, and secondly edge detection is applied (Figure 6.3.5: A-C).

To minimise the no read errors, the area of the drop is identified by the changing colour (from black to white) of the pixels enclosed by the edge lines in two directions (left to right and bottom to top). By doing so, the error in the area of the drop is minimised, in case the edge is not correctly identified at some point of the drop. The edge in the horizontal direction is found by checking each pixel vertically starting with the threshold values. The threshold values were identified visually and were dependent on the camera. When the right and left edges were identified the pixels between those values changed in colour (Figure 6.3.7 – A). Similarly, this procedure is carried out in the vertical direction, which includes simulation limits: the drop bottom and the nozzle edge from the top.

The coordinates of the drop were identified in two parts (the left and right side of the drop). The edge is first identified by scanning each row (from the nozzle bottom edge to the drop bottom) starting from the threshold value. When the edge is identified, the filter is applied to smooth the curve. The filter used is a rational transfer function filter built into “MATLAB®” software.

Finally, the drop edge arrays are joined together to create a single edge (Figure 6.3.7 – B). The output results are saved in text files `{frame number}_cam1.txt` or `{frame number}_cam2.txt` in separate folders named by flow rate value.

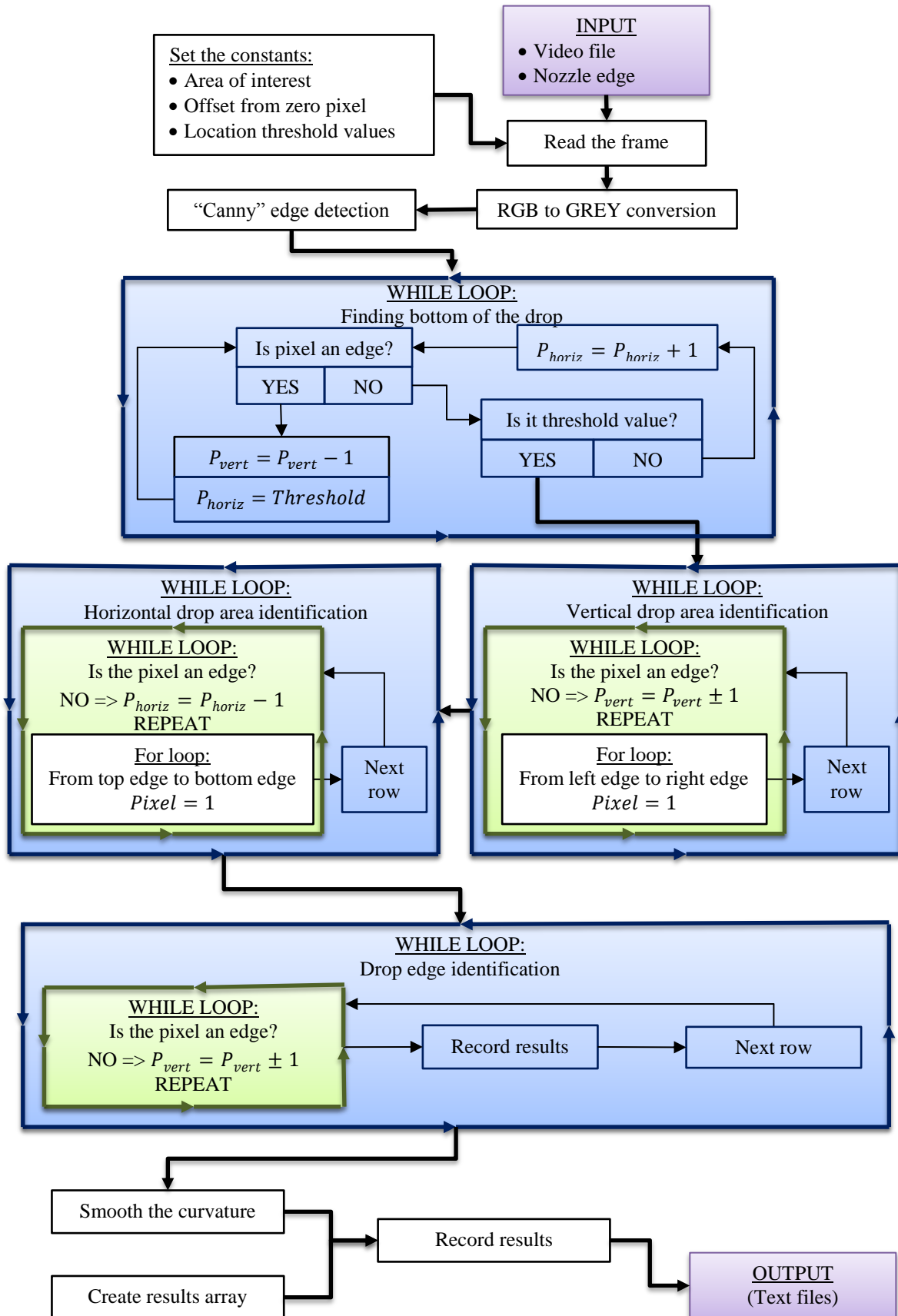


Figure 6.3.6: Drop shape identification pseudo code

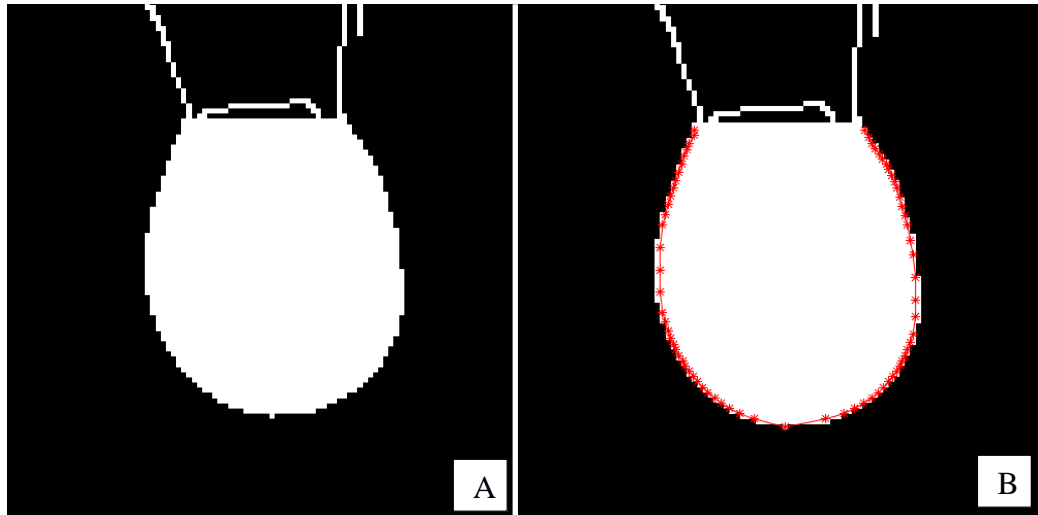


Figure 6.3.7: Drop identification processing steps

Red – smoothed curvature of the drop

6.3.3 Video results post-processing

The post-processing code is all about combining the results of the drop shape in each frame together. The code starts with reading the recently saved files from the video processing code and allocating the first detachment, with a communication message indicating that the process of synchronisation is running. After the synchronisation frames identified (the synchronisation frames here means the frames with the same event as seen on the front and side videos), the drop shape calculations are performed in a *for loop*. The loop reads the edge coordinates from the side and front cameras and in the first step sets the axis and zero point on the image. The zero point is the middle of the nozzle attachment point. With the positive vertical direction (z-coordinate) going downwards, and horizontal directions (x-coordinate and y-coordinate) going to the right. The x-coordinate is associated with the “Master” Pi camera (also referred to as the front camera), while the y-coordinate is visible from the side camera or “Slave” camera.

Now when the correct starting frame has been identified and the coordinate system has been applied the results can be combined in a common matrix for resizing. The resizing loop is a *for loop* which first identifies the scaling factor and applies it to the results to achieve similar sizing of the drop.

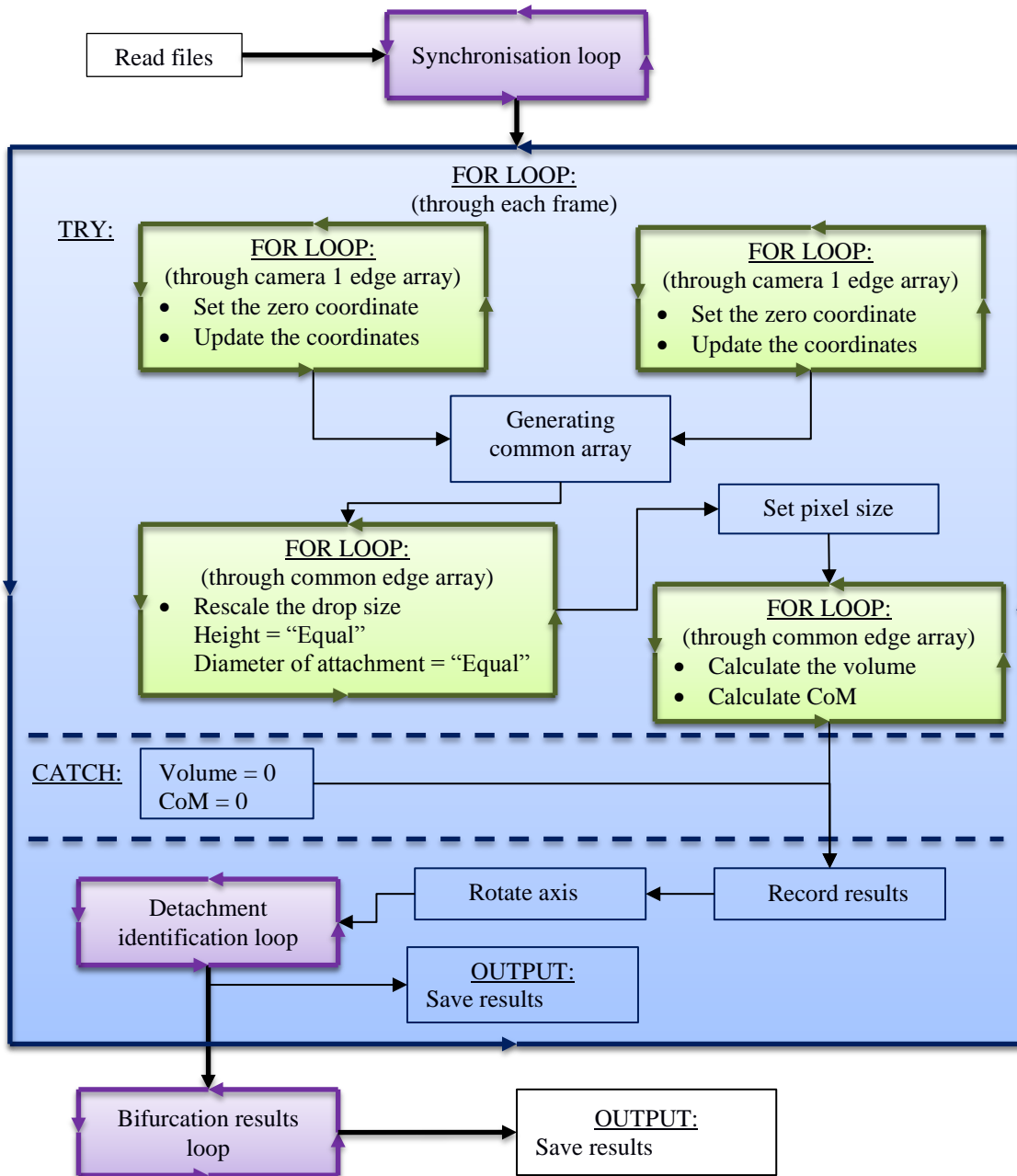


Figure 6.3.8: Video results post-processing pseudo code

Some definitions are needed here. The scaling factor is identified as a variable, which can change from one, frame to the next and is calculated as the average of two ratios: the ratio of the widths of the drop at attachment and the ratio between of drop heights. Those parameters are selected as they are expected to have the same value in both views, if the drop images are synchronised correctly. Nevertheless, it is understood that there might be some discrepancies in the drop heights especially at the point of the drop detachment (where the drop necking process is happening and the drop vertical length is increased dramatically) with the time uncertainty between the frames (section 6.1). The scaling factor

is applied to coordinates for both sides with the drop height and drop attachment width being the same for both cameras.

Now that the drop shapes in both pictures have the common parameters, the CoM and volume can be calculated. The common drop shape array is resized once more now to allow for a change in drop shape coordinates vertically in steps of one pixel. Then the coordinates are scaled to change the units to millimetres. The multiplication factor is calculated based on: the width of the drop attachment divide by 2 mm (which is the outer nozzle diameter – section 6.1). The volume and CoM calculation loop is a *for loop* which goes through each common array result and calculates the parameters as:

$$\begin{aligned}
 V &= \sum(\pi d_{1_i} d_{2_i} \Delta h) \\
 \bar{x}_c &= \sum(V_i \bar{x}_i) / \sum(V_i) \\
 \bar{y}_c &= \sum(V_i \bar{y}_i) / \sum(V_i) \\
 \bar{z}_c &= \sum(V_i \bar{z}_i) / \sum(V_i)
 \end{aligned}
 \tag{6.3.1}$$

where: V – drop volume

V_i – volume of i 'th section

d_{1_i} and d_{2_i} – diameters of the drop at the height i

Δh – height step

\bar{x}_c , \bar{y}_c and \bar{z}_c – centroid coordinates of the drop

\bar{x}_i , \bar{y}_i and \bar{z}_i – centroid coordinate of the drop slice at the height i

As is visible from Equation 6.3.1 the volume is calculated in stepwise fashion taking the cross-sectional volume of each pixel thickness and adding them together. The assumption here is that the drop edge remains constant within this step thickness

Unwanted errors are then removed from the results, which occur during the reading of the initial edge files. The code skips particular frames if the error was identified, and then the code assigns zero to the values of the volume and CoM. After this, it is possible to do final corrections to the results by slightly rotating the axes. The axes are required to be rotated when the mean value curve for the x-coordinate and/or the y-coordinate do not lies on the zero value (Figure 6.3.9 – A).

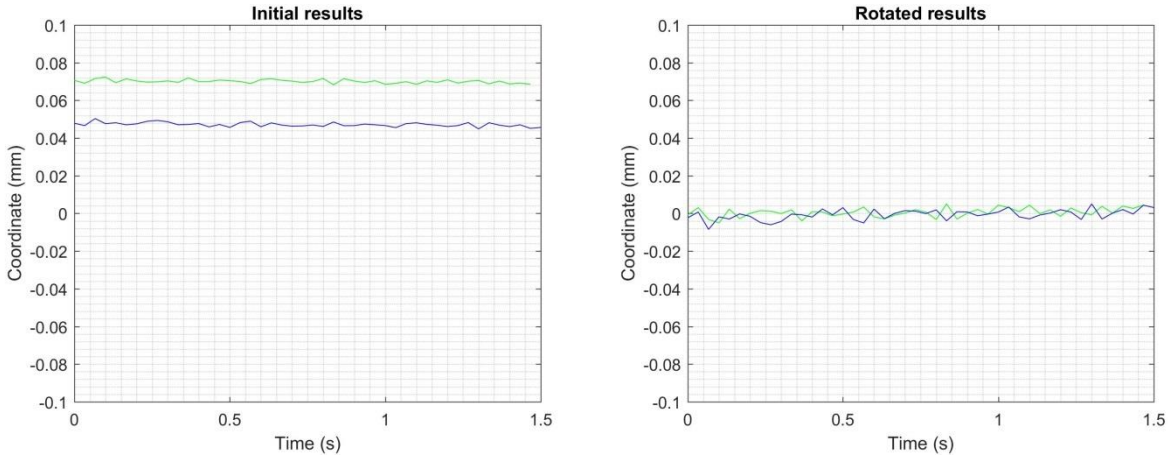


Figure 6.3.9: X and Y coordinate results rotation

Blue – front camera; Green – side camera;

The axes are rotated using two rotation matrixes and applied to the results array (Figure 6.3.9 – B):

$$\begin{aligned}
 \alpha_{xz} &= \tan^{-1} \left(\frac{\sum_{i=1}^n (x_i)}{n} / \frac{\sum_{i=1}^n (z_i)}{n} \right) \\
 \alpha_{yz} &= \tan^{-1} \left(\frac{\sum_{i=1}^n (y_i)}{n} / \frac{\sum_{i=1}^n (z_i)}{n} \right) \\
 rot_{xz} &= \begin{bmatrix} \cos \alpha_{xz} & 0 & \sin \alpha_{xz} \\ 0 & 1 & 0 \\ -\sin \alpha_{xz} & 0 & \cos \alpha_{xz} \end{bmatrix} \\
 rot_{yz} &= \begin{bmatrix} 1 & 0 & 0 \\ 0 & \cos \alpha_{yz} & \sin \alpha_{yz} \\ 0 & -\sin \alpha_{yz} & \cos \alpha_{yz} \end{bmatrix} \\
 \begin{bmatrix} x_n \\ y_n \\ z_n \end{bmatrix} &= rot_{xz} \times rot_{yz} \times \begin{bmatrix} x_i \\ y_i \\ z_i \end{bmatrix}
 \end{aligned}
 \tag{6.3.2}$$

where: α_{xz} and α_{yz} – axis rotation angles for x-z plane and y-z plane

rot_{xz} and rot_{yz} – rotation matrix

i and n – initial and final coordinates of x, y and z

The next step in the post-processing code is to identify the detachment time. The detachment loop is quite similar to the one used to identify the synchronisation frame as it works on a similar principle. The full discussion and the formulation of the process to identify the detachment and the video synchronisation will be discussed in subsection 6.4.1. In short, the process seeks to allocate a rapid decrease in the volume and vertical

distance of the drop CoM simultaneously. The drop detachment identification is the last part of the main *for loop*. At this point, the results are saved.

When all the flow rates calculations are completed there remain the last part of the code, which is the bifurcation loop calculation (explained in subsection 6.4.2).

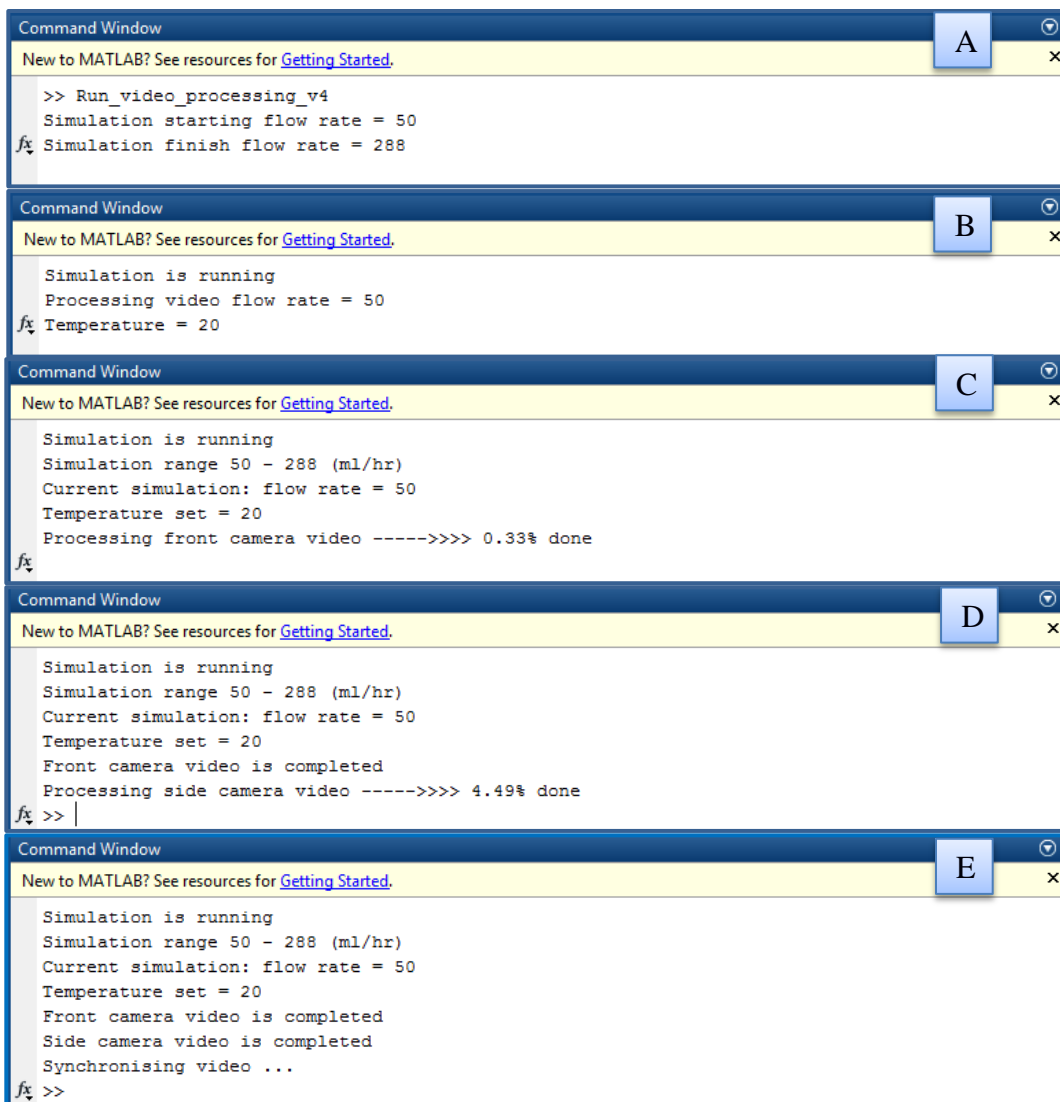
6.4 Confirmation of the processing and post-processing codes operation

As mentioned before in section 5.5 the camera operation is required to be fully synchronized and for that reason, a specific operational procedure was implemented. In short, a lot was done to synchronize the start of the video recordings, including the synchronisation of the computers (which run the cameras) as well as identification of common events in the videos in case of delays un the computer processing. Nevertheless, it was observed that the recordings may contain frame number disagreements of the common event (i.e. the frame numbers of the event do not match each other). Subsection 6.4.1 which follows discusses the outcome of the code compiled (subsection 6.3.3).

The post-processing code as presented in the subsection 6.3.3 contains several hundred lines of code. It was expected that several modifications would be required prior to the final version. This section is devoted to explaining some of the parts in the code that required the results of the video processing code. In some cases, it will provide some insight into the complexity of the processing of the experimental results. In some cases, it will explain the mitigating approach adopted to limit the uncertainties in the results.

The experiments were performed on a range of flow rates from 50 to 288 ml/hr as set on the syringe pump (or 60.6 to 332.1 ml/hr with the syringe pump correction factor) with a step size of 2 ml/hr. Two cameras were required to video record the experiments, with the “Master” computer acquiring the fluid temperature at the beginning of the experiment (Appendix P). In total, 120 experiments were done with a total of 240 videos recorded at

30 frames per second for 5 minutes each. One hour and forty-five minutes on average was required to process the results of one experiment. The code was developed to allow as little time as possible to be spent by a user. The procedure of the code has already been explained and in a set of prints (Figure 6.4.1) the code communication messages.



```
Command Window
New to MATLAB? See resources for Getting Started.
>> Run_video_processing_v4
Simulation starting flow rate = 50
fx Simulation finish flow rate = 288

Command Window
New to MATLAB? See resources for Getting Started.
Simulation is running
Processing video flow rate = 50
fx Temperature = 20

Command Window
New to MATLAB? See resources for Getting Started.
Simulation is running
Simulation range 50 - 288 (ml/hr)
Current simulation: flow rate = 50
Temperature set = 20
Processing front camera video ----->>> 0.33% done
fx

Command Window
New to MATLAB? See resources for Getting Started.
Simulation is running
Simulation range 50 - 288 (ml/hr)
Current simulation: flow rate = 50
Temperature set = 20
Front camera video is completed
Processing side camera video ----->>> 4.49% done
fx >>

Command Window
New to MATLAB? See resources for Getting Started.
Simulation is running
Simulation range 50 - 288 (ml/hr)
Current simulation: flow rate = 50
Temperature set = 20
Front camera video is completed
Side camera video is completed
Synchronising video ...
fx >>
```

Figure 6.4.1: Video post-processing code communication messages (Part 1)

First (Figure 6.4.1 – A), the code asks to set the flow rates (as is set in the syringe pump), with the starting and finishing flow rates in units of ml/hr. The second message (Figure 6.4.1 – B) asks for the temperature of the liquid to be entered (Appendix P) which is used to calculate the water density (section 6.2). The third and fourth (Figure 6.4.1 – C and D) messages are read only, displaying the percentage of processed frames for both front and side cameras. The fifth message (Figure 6.4.1 – E) displays the video synchronisation

process (subsection 6.4.1), showing the frame numbers of the first detected detached droplet for the front and side cameras, while displaying the synchronisation plot (Figure 6.4.2).

A screenshot of a MATLAB Command Window titled "Command Window" with a yellow header bar containing the text "New to MATLAB? See resources for Getting Started." and a blue button with the letter "F". The window displays the following text:

```
Simulation is running
Simulation range 50 - 288 (ml/hr)
Current simulation: flow rate = 50
Temperature set = 20
Front camera video is completed
Side camera video is completed
Synchronising video ...
frame_no_start_front =

    8

frame_no_start_side =

   91

Frame error encountered, Do you want to continue? (y/n) -> n
Do you want to keep front frame (y/n)? -> n
Do you want to keep side frame (y/n)? -> n
Set the new frame for front video = 120
Do you want to keep front frame (y/n)? -> n
Set the new frame for side video = 120
Do you want to keep side frame (y/n)? -> n
Set the new frame for front video = 140
Do you want to keep front frame (y/n)? -> n
Set the new frame for side video = 140
Do you want to keep side frame (y/n)? -> n
Set the new frame for front video = 150
Do you want to keep front frame (y/n)? -> n
Set the new frame for side video = 150
Do you want to keep side frame (y/n)? -> n
Set the new frame for front video = 160
Do you want to keep front frame (y/n)? -> n
Set the new frame for side video = 160
Do you want to keep side frame (y/n)? -> n
Set the new frame for front video = 165
Do you want to keep front frame (y/n)? -> y
Set the new frame for side video = 165
Do you want to keep side frame (y/n)? -> n
Set the new frame for side video = 164
Do you want to keep side frame (y/n)? -> y
Confirm the synchronisation (y/n)? -> y
Synchronising video is completed
Drop shape calculations ...
Drop shape calculations is completed
Saving the results ...
```

Figure 6.4.1: Video post-processing code communication messages (Part 2)

In case the difference between the frames exceeds a threshold value of three frames, the code enters ‘manual synchronisation loop’ (Figure 6.4.1 – F). First it requires the user to confirm that manual synchronisation is required by entering “y” or “n” (the logic question reads: “Frame error encountered, do you want to continue (y/n)?”; where by entering “n” it will continue with the ‘manual synchronisation loop’, and by entering “y” will proceed with the automatically selected frames).

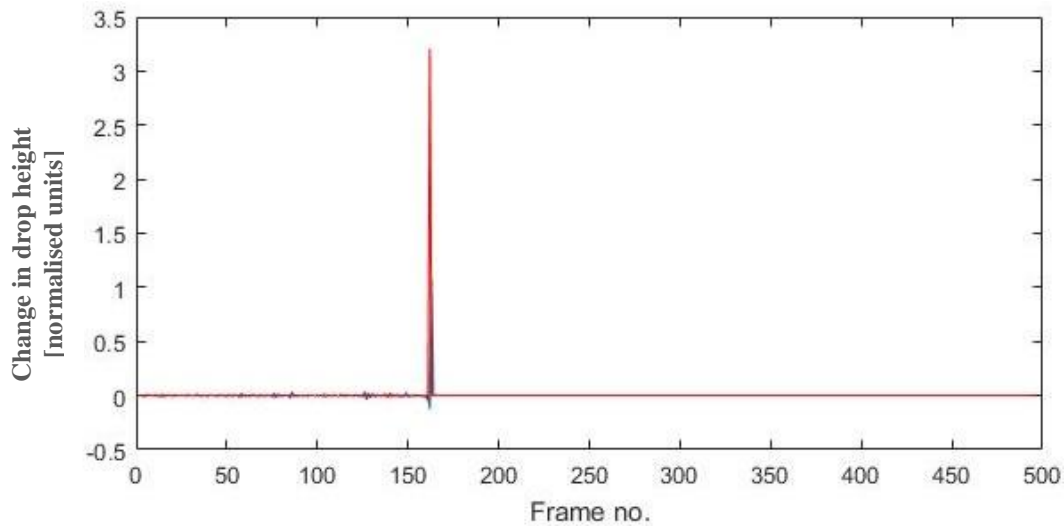


Figure 6.4.2: Synchronisation plot

Secondly, when the request to enter the manual synchronisation loop is acknowledged, the code opens an additional window with frames from the two videos displayed side by side (Figure 6.4.3).



Figure 6.4.3: Video manual synchronisation, camera view

This is followed by logic questions which allows the user to select if changes of the frames are needed for the front or side cameras (“Do you want to keep front/side frame (y/n)?”). When frames for both videos have been selected for synchronisation, the final logic question appears (“Confirm the synchronisation (y/n)?”) to confirm the selection, in case it was required to reselect an already confirmed frame number. The lines that follow communicate that the drop calculations have been started, drop calculations have been completed and finally the results are saved. The process is looped so after the results of one simulation are saved the next flow rate in the range undergoes the same process again.

The subsections that follow will explain the video synchronisation process (subsection 6.4.1) and adaptation of the bifurcation plot (subsection 6.4.2).

6.4.1 Video synchronisation and detachment identification process

For video synchronisation as previously explained, it was required to have a common event. This event was chosen to be the first drop detachment. Unfortunately, due to camera and computer a slight desynchronization appeared in some tests. Due to the large volume of recordings to be processed, it was less time consuming to develop an approach, which can automate the synchronisation. It was also considered that the process should be used to identify any detachment throughout the experimental results, not just the first one.

The detachment event can be identified by the sudden change in the drop dimensions (the length of the drop in the vertical direction). Secondly, after detachment the drop volume also decreases. Unfortunately, similar behaviour patterns can also be applied to different events. To summarise those:

- Drop length variation prior to detachment

Drop length is not a constant value throughout the experiment. Subsection 6.5.2 shows that the drop Centre of Mass (CoM) (hence length) varies due to the necking process or the development of jetting streams. In addition, there is the possibility of jetting streams⁸ and mid drop⁹ detachments (discussed later in subsection 6.5.2) having different lengths than the usual drop length.

- Drop length variation after detachment

⁸ Jetting streams are defined as columns of fluid with a length which is typically more than ten times greater than the outer diameter of the nozzle. The formation of jetting streams will be discussed later within this chapter.

⁹ A mid drop is defined as a drop with a volume which does not corresponds to the mass at detachment of the drop, nor is associated with satellite drops, but arises as the product of the chaotic region [14] (occurring during period doubling – the bifurcation process). The formation of the mid drops will be discussed later within this chapter.

The drop length after detachment is also not constant, sometimes it can have close to zero, but sometime a residual mass will exist (discussed further in subsection 6.5.2). At the same time mid drops at detachment have a tendency to leave a substantial mass behind.

- Drop vibration

Drop vibration can cause severe variation in the drop length and volume, and as it occurs mainly when the mass of the drop is more than half of the critical mass (see subsection 7.1.2), this can lead to errors in detachment detection.

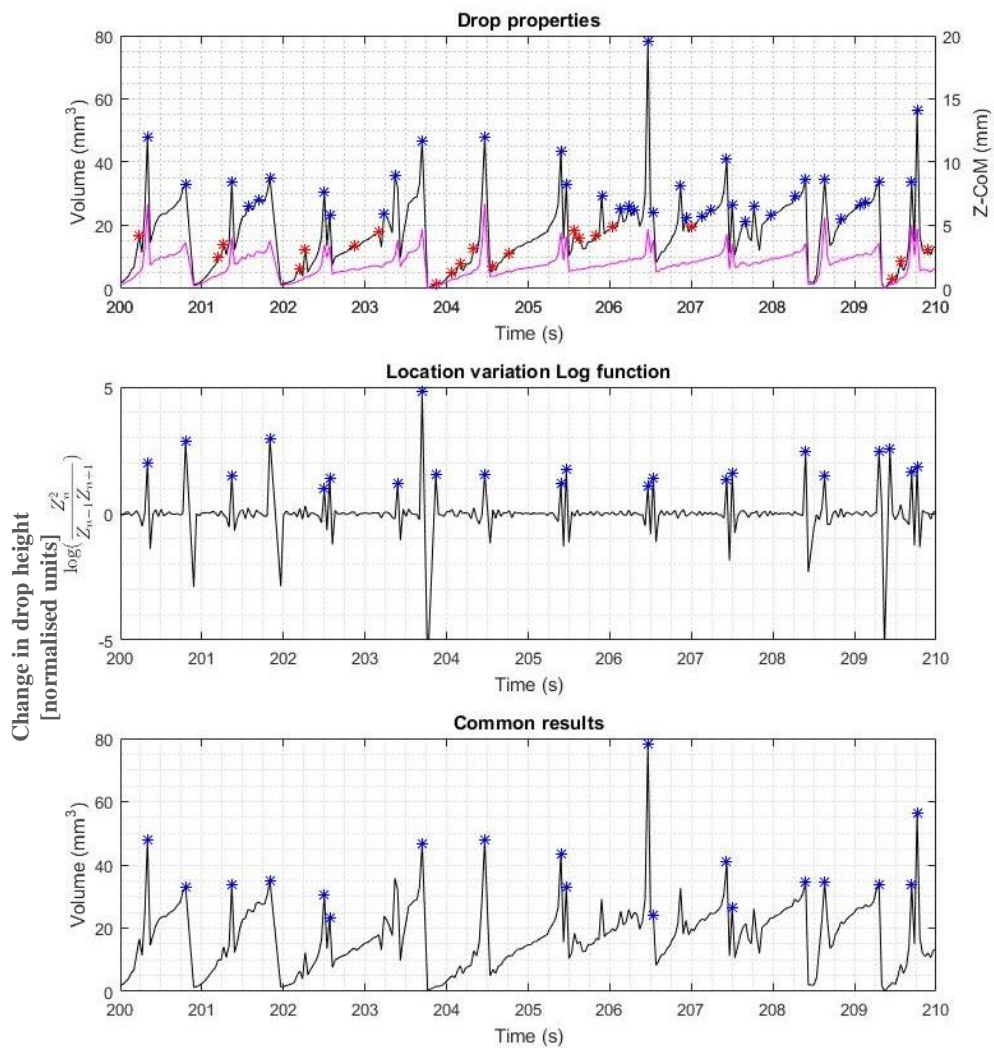


Figure 6.4.4: Detachment identification procedure

Top plot: **Black line** – drop volume plot; **Pink line** – Z-coordinate plot; **Red marker** – identified peaks on volume plot; **Blue marker** – identified peak above threshold value on volume plot.

Mid plot: **Black line** – logarithmic squared rate of change of Z-coordinate; **Blue marker** – identified peaks above threshold value.

Bottom plot: **Black line** – drop volume plot; **Blue marker** – peak joined results.

Detachment is identified as the peak value on the volume plot above the threshold value (Figure 6.4.4 – top plot, blue marker) when at the same time the logarithmic fourth order rate of change of vertical CoM location (Equation 6.4.1) is also above the threshold value (Figure 6.4.4 – mid plot, blue marker). The logarithmic rate of change is identified by Equation 6.4.1, with the threshold value to be above 2. Moreover, the threshold value of the volume is set to be equal to 20 mm³.

$$\log\left(\frac{z_n^4}{z_{n-2}z_{n-1}z_{n+1}z_{n+2}}\right) > 2 \quad \Bigg| \quad 6.4.1$$

where: z_i – are coordinates at time t_i

The logarithmic function has been developed to identify peaks in the signal given the specific characteristics of this signal. It identifies sudden decreases in the value of the following data (z_{n+1} and z_{n+2}) with respect to the current point (z_n). In the case of detachment the values of z_{n-2} and z_{n-1} are comparable to z_n whereas z_{n+1} and z_{n+2} are much lower, which will give a logarithmic ratio above 2. Inclusion of the z_{n-2} and z_{n-1} values in the equation filters out high amplitude variations (as these can cause false detachment detection). In the case of high amplitude fluctuations of the z-coordinate, which do not lead to detachment, the values of z_{n-2} and z_{n+2} will be comparable to z_n and the values of z_{n-1} and z_{n+1} will be lower (it is possible to assume these to be half of the z_n value) which will lead to a logarithmic ratio below 1. In the case where the vibrations occur just prior to detachment (i.e. z_{n+2} values are low value compared to z_n), the value of the logarithmic ratio will be around 1.5. The logarithmic function allows smoothing of the response, meaning that the smaller the ratio is the closer to zero the logarithmic value becomes. The higher the ratio is, and with the value of z_n being one of the highest, the higher logarithmic ratio is. It is worth mentioning that the function only considers positive values. In the case where any denominator z-coordinate value become equal to zero the values are substituted with minimum values from the range of (z_{n-2} , z_{n-1} , z_{n+1} and z_{n+2}

$\neq 0$). In the case where the numerator becomes equal to zero, the logarithmic function is set to be zero.

The process of acquiring results is as follows:

1. All peak values of the volume plot are identified (top plot – red and blue marker), where the peak is a sharp transition from a lower value to a higher value and back to a lower value (using the “MATLAB®” built-in function)
2. Eliminate those peaks that are below the threshold value of 20 mm^3 (top plot – blue marker)
3. Apply Equation 6.4.1 to the z-coordinate
4. Identify the peak values of the results from step three which are above the threshold value of 2
5. Consider only those results as detachment that are common between the results of steps two and four

The threshold values were chosen so as to minimise the error in the identification process. The error via visual inspection was found to be around 4%, and is more associated with the higher flow rates. Equation 6.4.1 as presented here allows for fast and simple method to identify critical rate of change in any system. The critical rate of change is set by the threshold value. The input parameters small vibrations are smoothed (in our case the vibrations frequency is less than time step - $1/30 \text{ s}$) by applying the logarithmic function.

The process described above is related to detachment identification. The synchronisation identification code operates only with Equation 6.4.1, as the volume of the drop has not yet been defined. The “MATLAB®” codes described here are presented in Appendix Q.A.

6.4.2 Bifurcation plot adaptation

Another important element of confirming the code operation was to achieve useful results from the bifurcation plots. It was discussed earlier in this chapter and will be more explicitly described in section 6.5 that the video processing can result in uncertainties. In addition, the experimental results are quite sensitive to any external disturbances (such as

pump pulsation, mechanical vibration of the experimental module, etc.). The following figure is example of data overcrowding, with multiple errors and slight variations in results due to external disturbances (Figure 6.4.5).

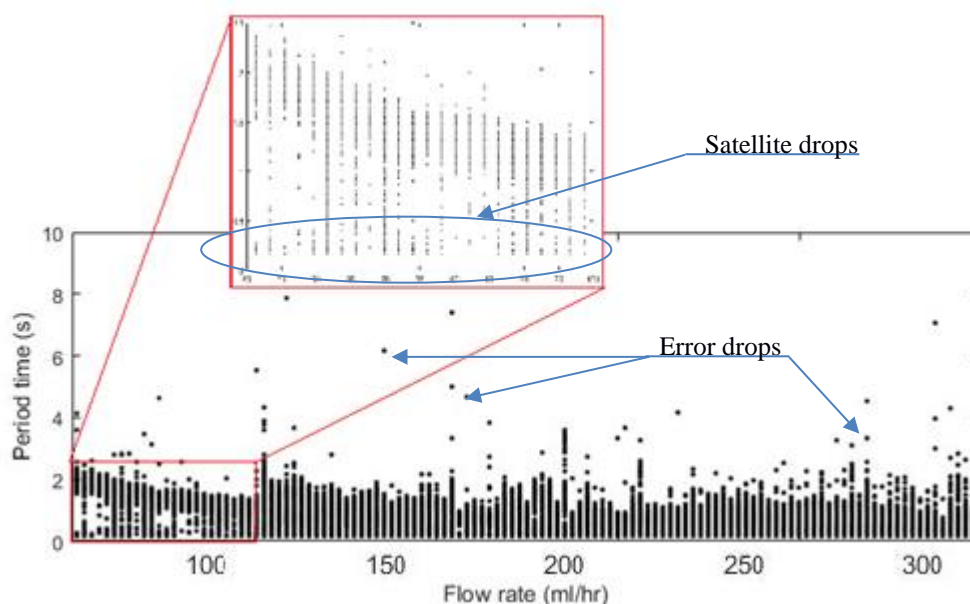


Figure 6.4.5: Bifurcation results plot before processing

The results presented in Figure 6.4.5 above by simply plotting all available points in their original form does not allow the identification of the importance of each data point. The importance here is defined as how many times the data point has been repeated (each flow rate has from ~260 to ~590 data points, for lower and higher flow rate respectively). Secondly, it can be seen that there are single points which are far away from the main group (anomalous drops), as well as points which are part of the satellite drops. The following approach was implemented to achieve readable result from the data.

1. It was required to identify the anomalous drops and remove them from consideration
2. It was required to identify the satellite drops and remove them from consideration
3. Identify the range of most probable periodic time where the main drops appear
4. By applying the range make sure not to miss sudden increase in the period
5. By the use of colour identify the importance of each point, where importance was as defined above

First three points are used to minimise the uncertainties of the experiment results. A fourth should provide some adaptation in the case of a sudden change in the expected region of periodic dripping, while the last part in this requirement list allows the repeatability of the results to be displayed. The filter that was developed is an adaptive filter (whose width varies depending on previous flow rate data point distribution) that allows, after applying it, to omit data, which is spurious.

It is clear that the values of the detached drop periods should be limited to a specific region (the area of interest). This region is initially unknown, but it is expected that at each flow rate the periodic values should be located close to the surrounding flow rate drop period values. The assumption here is that the bifurcation region is not limited to a few flow rates (the bifurcation region here is defined as the region from the point of first bifurcation up to the point where quasi-periodic behaviour ceases to exist), meaning that the region of bifurcation is large compare to the step size in the flow rate change. By applying this assumption, it is possible based on the previous known periods to select the specific region where it is expected the quasi-periodic or single periodic dripping will propagate. By doing the following, we can limit the error values (as they appear far from the bifurcation region – Figure 6.4.5) and satellite drops (as they tend to exist also far from the region of interest – Figure 6.4.5).

To define this region it was decided to use an *influence map*, which is created, based on the previous periods and the extent to which they are repeated. At each flow rate, the number of times each period repeats itself was calculated. The *influence* of each currently considered period is calculated as the ratio of this repetition rate for each period to the maximal repeating value:

$$I_c = \left\{ \begin{array}{l|l} 0 & \Psi_c/\Psi_{max} \leq 1/3 \\ 1 & 1/3 < \Psi_c/\Psi_{max} \leq 2/3 \\ 2 & 2/3 < \Psi_c/\Psi_{max} \leq 1 \end{array} \right\} \quad \left. \vphantom{I_c} \right| \quad 6.4.2$$

where: I_c – influence value of chosen period

Ψ_c – number of repeats for a given period

Ψ_{max} – maximal number of repeats for any period

The *influence* propagates in both forward and vertical directions, and the propagation region can reach as far as two flow rates ahead and two time steps lower or higher (Table 6.4.1).

t_{n+2}		0	0		0	0		1	1	
t_{n+1}		0	0		1	0		2	1	
t_n	$I_c = 0$	0	0	$I_c = 1$	1	0	$I_c = 2$	2	1	
t_{n-1}		0	0		1	0		2	1	
t_{n-2}		0	0		0	0		1	1	
		\dot{V}_n	\dot{V}_{n+1}	\dot{V}_{n+2}	\dot{V}_n	\dot{V}_{n+1}	\dot{V}_{n+2}	\dot{V}_n	\dot{V}_{n+1}	\dot{V}_{n+2}

Table 6.4.1: The selected flow rate influence propagation map

Each period of the current flow rate produces *influence maps*, which are then joined together, by adding the influence numbers for each time step (Table 6.4.2). The future region (next flow rate) of interest is identified as the region between the lower time containing a value ≥ 1 and a higher time containing a value ≥ 1 .

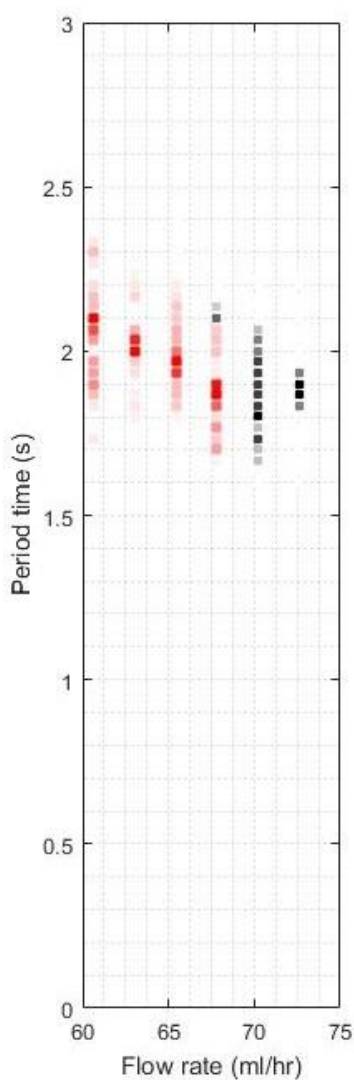
Time	Period repetition value	Influence value	Flowrate	
			\dot{V}_{n+1}	\dot{V}_{n+2}
t_{n+5}	$\Psi_c = 0$		0	0
t_{n+4}	$\Psi_c \leq 1/3$	$I_c = 0$	0	0
t_{n+3}	$\Psi_c = 0$		2	1
t_{n+2}	$1/3 \leq \Psi_c \leq 2/3$	$I_c = 1$	3	1
t_{n+1}	$2/3 \leq \Psi_c \leq 1$	$I_c = 2$	5	2
t_n	$1/3 \leq \Psi_c \leq 2/3$	$I_c = 1$	5	2
t_{n-1}	$2/3 \leq \Psi_c \leq 1$	$I_c = 2$	4	2
t_{n-2}	$\Psi_c \leq 1/3$	$I_c = 0$	3	1
t_{n-3}	$1/3 \leq \Psi_c \leq 2/3$	$I_c = 1$	2	1
t_{n-4}	$\Psi_c \leq 1/3$	$I_c = 0$	1	0
t_{n-5}	$\Psi_c \leq 1/3$	$I_c = 0$	0	0
t_{n-6}	$\Psi_c = 0$		0	0

Table 6.4.2: The influence region identification map

Dark grey – influence region; Light grey – considered region;

In addition, to lower the error rate of the described procedure, a threshold value of $2\Delta t = 2/30$ s is added to the minimum and maximum time values in the acquired periodic time range. The time limits (as identified in Table 6.4.2 in light grey colour) are now restrictions for the following flow rate drops periods. Meaning that only the periods that fall into this region will be considered. The *influence region* values of the flow rate after the next one remain and will be added to the influence map of new current flow rate.

The first flow rate region (50 ml/hr as set on the pump) was identified visually as it was noticed that it provided a good, separated region (the region of interest lies between the period values of 1.5 – 2.7 s, Figure 6.4.5).



The following figure (Figure 6.4.6) shows the example of the process of identification of the *influence map* at the current flow rate to be equal to 67.82 ml/hr (as set on the pump). The red colour shades are applied to each point, where a darker colour represents more values that repeat more and lighter shades are associated with less repeated periods. The colour is defined here using a polynomial equation of power 1.5 (the power used to increase colour intensity for more often repeated values):

$$Colour = 1 - \left(\frac{\Psi_c}{\Psi_{max}} \right)^{1.5}$$

Figure 6.4.6: The influence map development example

Red – period repetition; **Grey** – influence region

To identify the drop type quantity the following assumptions were made:

- Total number of drops recorded – this is the quantity of all recorded drops
- Main drops total number – is the quantity of all periods which are included in considered region
- Satellite drops total number – is the quantity of all periods which are below period minimal value of the considered region as well as with period smaller than $4/30$ s
- Error values total number – is the quantity of the periods which are above period maximum value of the considered region
- Mid drops total number – is the quantity whose period is between the period minimal value of the considered region and the satellite drop

So far, we have discussed how the selection of the working region is done. It is possible to summarise the overall procedure in the flow diagram shown in Figure 6.4.7.

Firstly, the file with the detachment data is read for each flow rate separately. Depending on the flow rate the *if statement* code selects the path. For the flow rate of 50 ml/hr (as set on the pump) the limits are introduced manually and the periodic map is calculated. The periodic map generates the influence region, which can expand up to two flow rates ahead. If the flow rate is not equal to 50 ml/hr, the current influence map identifies the periodic map from the initial results. Now the check for the period jump is carried out. In simple terms, this determines whether the highest period selected repeats itself more than 20% of the maximal period repetition in the selected periodic range. If so, the periodic map is updated with the initial data array by adding an extra time step. When the value of the highest period is below 20%, the influence map of the current flow rate is combined with the influence map of previous flow rate influence region over the current one. New influence regions are created for two successive periods after the one been considered just now. Prior to the start of the next flow rate calculations, the drop types are counted and the bifurcation plot is updated. When all flow rates are completed, the drop type bar plot is produced.

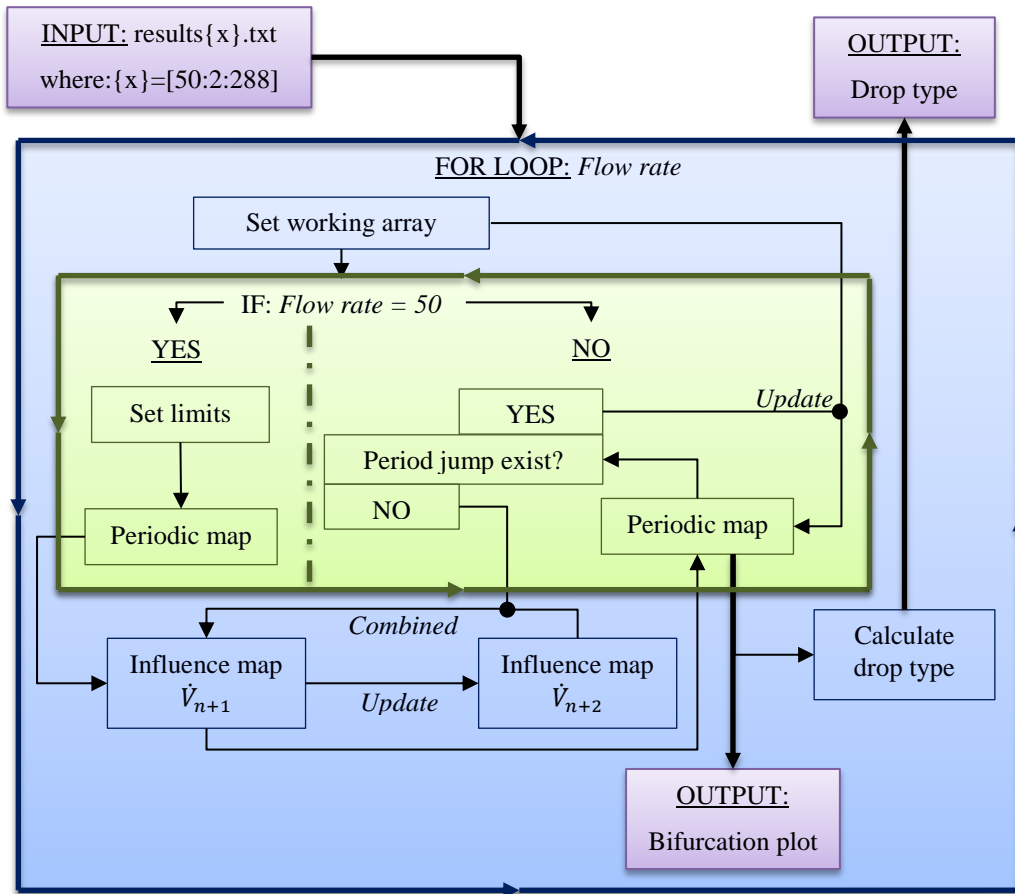


Figure 6.4.7: Bifurcation plot results adaptation

The following figure (Figure 6.4.8) shows the points have been eliminated throughout all experimental flow rates using the current method explained here.

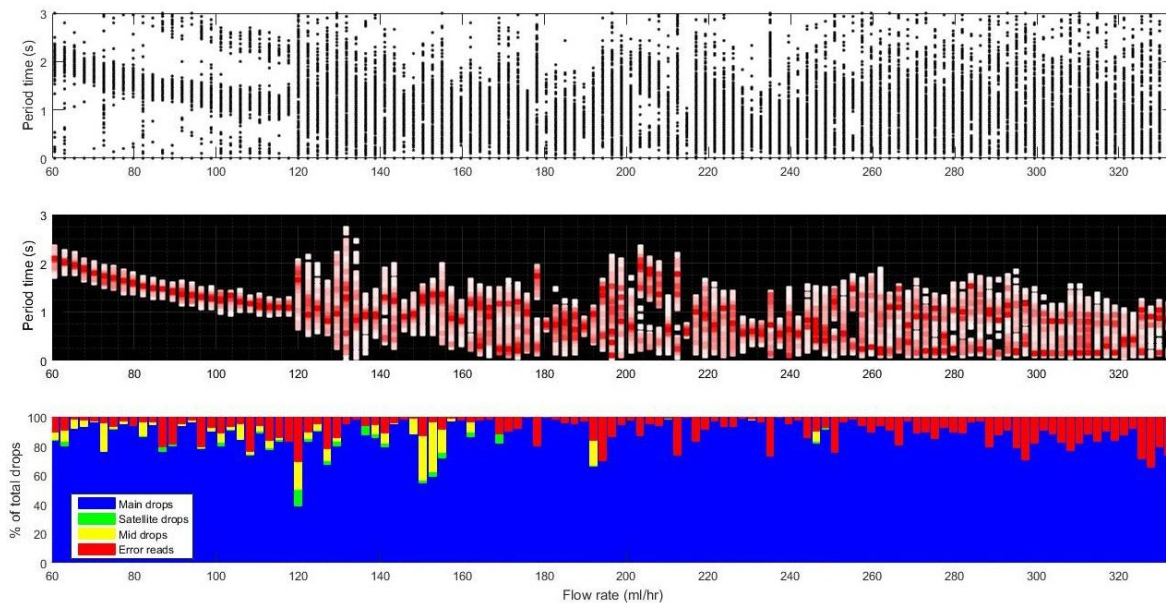


Figure 6.4.8: Drop type by its quantity (as identified by the applied procedure)

Top plot – initial periodic data; Mid plot – processed periodic data; Bottom plot – drop type in percentage

The values are distinguished as the proportion of drops (as percentages) identified as main drops, satellite drops, mid drops and error periods. The figure also shows the initial results (top graph) and updated results (mid graph).

The presented results showed that on average 87.6% of the results data were considered in the plot. At the same time in some regions ($\dot{V} = 120$ ml/hr, or $\dot{V} = 150.4$ to 152.7 ml/hr, or $\dot{V} = 191.9$ ml/hr) the usable data were below 60%. The reason for this is the flow instabilities associated with high degree of bifurcation (section 7.2) at these specific flow rates. To demonstrate this flow rates from 117.7 ml/hr to 122.4 ml/hr were considered. In Figure 6.4.8, between those flow rates (at a flow rate of 120 ml/hr) there exists a region where a low proportion of data points have been used. Figure 6.4.9 shows the difference in the drop CoM behaviour at those flow rates.

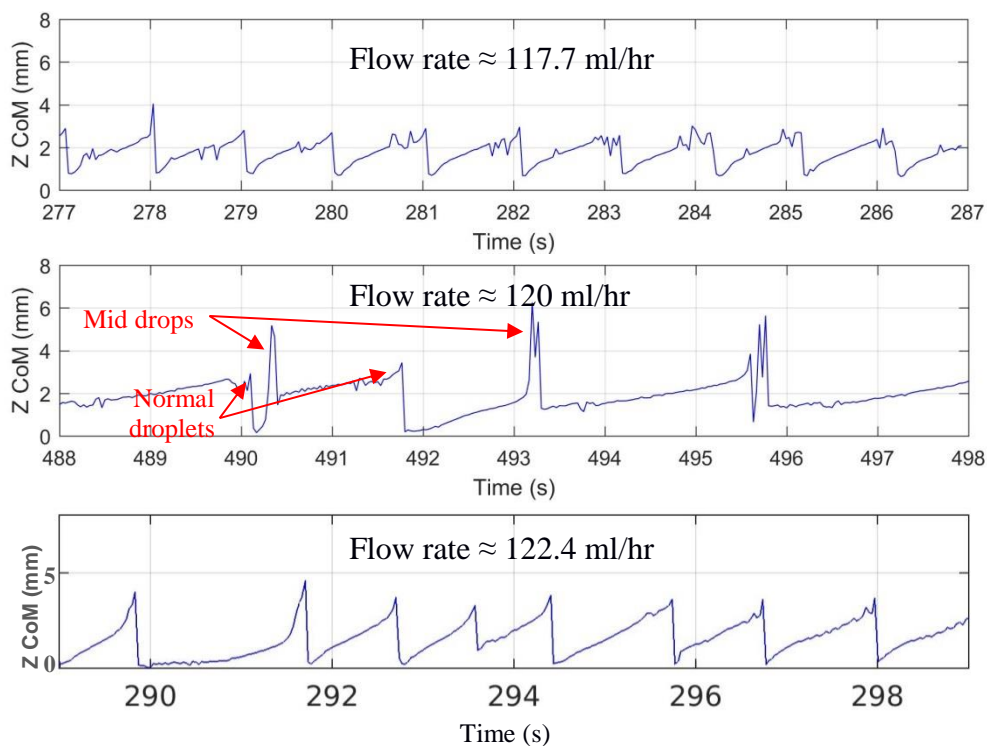


Figure 6.4.9: Mid drops at flow rate of 120 ml/hr as a cause of low acceptable data points

Specifically at a flow rate equal to 120 ml/hr the formation of mid drops becomes consistent, while at flow rates before and after only dripping is observed (based on

experiments it is expected that the critical distance¹⁰ to be equal to $t \approx 3$ mm plus necking length¹¹). Similar processes are observed at other flow rates, when low number of acceptable data points was used. The complete discussion of the results will be given in chapter 10. The results in Figure 6.4.8 show that the error values are consistent throughout the flow rates under the investigation with on average to be equal to 9.2%, which was expected.

6.5 Experiment processing & post-processing code analysis

Up to now, the video processing and post-processing code development and logic behind them have been discussed. This section will provide discuss the camera operation. The experimental work included the video recording of drop behaviour from two different directions at the flow rates under investigation. The selected volumetric flow rate range was between 50 ml/hr and 288 ml/hr as set on the pump (subsection 5.4.1), and the actual flow rate range is equal to 60.6 – 332.1 ml/hr). This section will confirm the camera operation and discuss the main difficulties encountered in the experimental work itself and data post-processing.

It was mentioned in subsection 5.4.2 that the drop Centre of Mass (CoM) position error can only be determined experimentally, as it is based on the experimental module operation (pump noise) and location (mechanical vibration of the system). In subsection 6.5.1, which follows the results of the position error will be presented.

In addition, this section will look into the anomalies that occurred during the experimental campaign. Subsection 6.5.2 will discuss their nature and how this affects the results.

¹⁰ An experimentally determined number (will be discussed in subsection 7.1.1)

¹¹ The necking process starts when the critical distance is reached. The necking process lead to detachment but prior to that the CoM an travels additional distance (first discussed in subsection 6.5.2)

6.5.1 Confirmation of cameras operation

The starting point is to confirm the camera operation. The video recording of the drop was undertaken to confirm the camera set-up, operation and post-processing code operation. The main reason for doing so was to identify if it was viable with the existing hardware setup to obtain usable results. The experimental procedure included video recording of the stable drop from two perpendicular directions. Stable drop are identified as those drops, which had enough time to settle free from any forced vibrations with no volume increase (the drop was given a few minutes before acquiring the results). The videos were synchronised by providing each camera with a reference event: detachment of a single drop, followed by the development of the drop to an arbitrary volume.

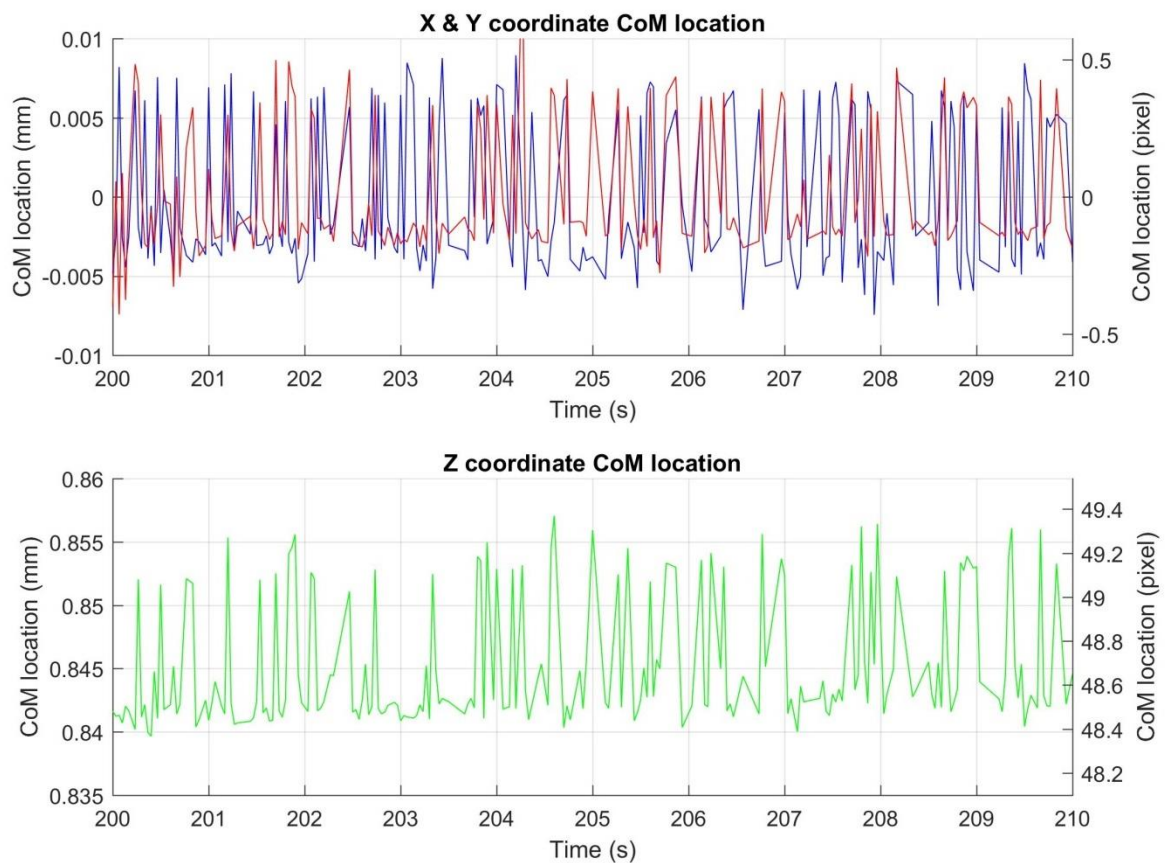


Figure 6.5.1: Drop stable state CoM variation readings

RED – Camera 2 horizontal location; **BLUE** – Camera 1 horizontal location;
GREEN – vertical location;

The resulting videos were then processed with the edge detection code (subsection 6.3.2 and Appendix Q) followed by post-processing code where the two cameras results are merged together.

The Centre of Mass (CoM) location of the drop was recorded and plotted against time (Figure 6.5.1). Satisfactory results should see a minimal disturbance in the CoM location (which should be small compared to the actual drop size).

The experiment (Figure 6.5.1 X and Y coordinates plot – top plot) produced satisfactory results with a slight reading noise. The noise errors were measured based on the sample data of 300 points (which corresponds to 10 seconds of filming) from which maximum and minimum values were extracted, and using camera pixel reading uncertainty values ($\pm 0.11 \mu\text{m}/\text{pixel}$ from Equation 5.4.2) converted into distance units.

For camera 2 (the “Slave” camera) the resulting value is equal to approximately $\pm 9.47 \mu\text{m}$ and for camera 1 (the “Master” camera) this is approximately equal to $\pm 16.20 \mu\text{m}$, both values being for horizontal directions. The vertical measurements lead to a similar error value of $\pm 17.41 \mu\text{m}$. The differences in the values are explained by the camera limitation (camera light reception fluctuates), video processing limitation (edge detection is dependent on the level of the light), and natural vibration of the drop (which in the vertical direction has a higher influence).

Nevertheless, the measured uncertainty in the horizontal direction to compare to the width of the drop is approximately 0.52%, and 0.58% for the vertical uncertainty with respect to the length of the drop.

Similarly, the stable drop volume and mass errors, based on maximal and minimal experimental values were found to be equal to: $\Delta V_{\text{video}} = \pm 0.053 \text{ mm}^3$ and $\Delta m_{\text{video}} = \pm 0.053 \text{ mg}$ (where the density of water was assumed to be 1 g/cm^3 , while the volume was calculated using the process explained in subsection 6.3.3).

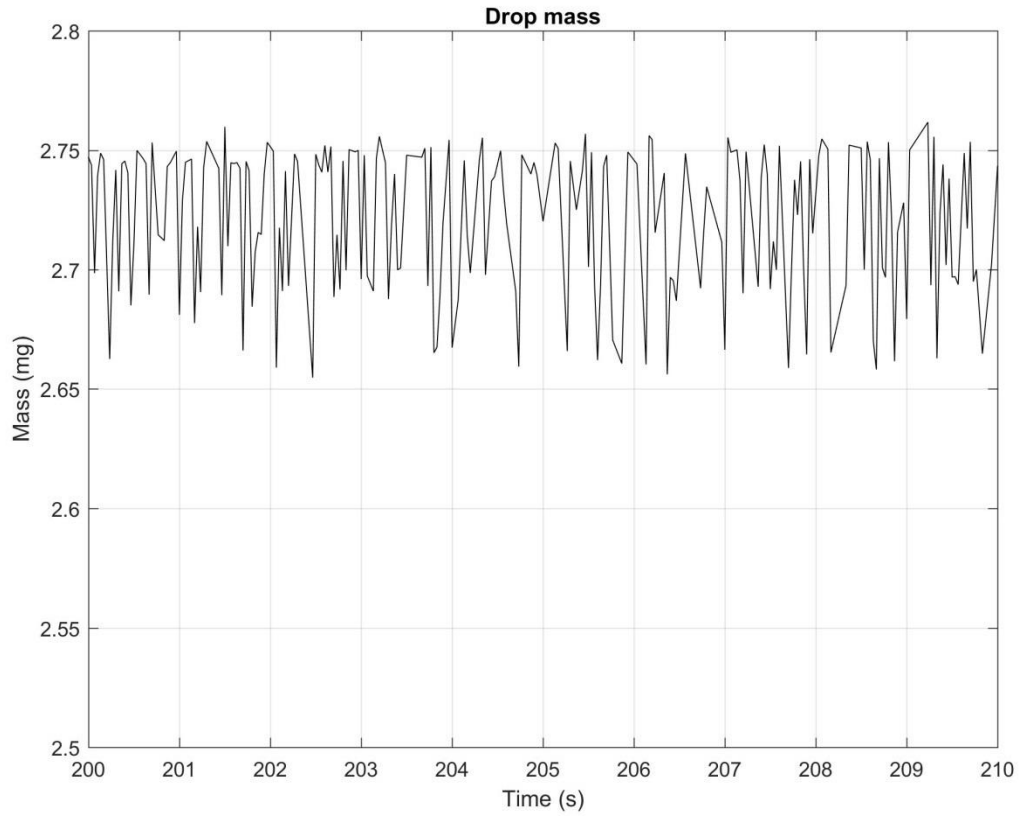


Figure 6.5.2: Drop stable state mass variation readings

Those values now can be used to complete the uncertainty list (section 6.1) in the measurement variables. The total uncertainties now become equal to:

$$\begin{aligned}
 \Delta x &= \pm 0.016 \text{ mm} \\
 \Delta y &= \pm 0.009 \text{ mm} \\
 \Delta z &= \pm 0.017 \text{ mm} \\
 \Delta V_{video} &= \pm 0.053 \text{ mm}^3 \\
 \Delta m_{video} &= \pm 0.053 \text{ mg} \\
 \Delta V &= \sqrt{\Delta V_{time}^2 + \Delta V_{video}^2} \\
 \Delta m &= \sqrt{\Delta m_{time}^2 + \Delta m_{video}^2}
 \end{aligned}
 \tag{6.5.1}$$

where: ΔV_{time} – volume uncertainty due to camera shutter time (Equation 6.1.20)

Δm_{time} – mass uncertainty due to camera shutter time (Equation 6.1.21)

ΔV – total volume uncertainty

Δm – total mass uncertainty

One of the additional problems associated with the camera operation is related to the blurring effect of the fast moving drop. The camera shutter open time is set to be 1/60 s (as explained in section 6.1). The open shutter imprints on an image each position of the drop. This produces some errors in identification of the drop edge when the drop movement is fast leading to a blurring effect. The errors can be approximated during stable drop growth (with the flow rates limited by the experimental range) and when the drop is subjected only to natural vibrations. The uncertainty values of the volume, mass, and CoM location can be assumed equal to rest uncertainty values. As the rate of change in the drop shape becomes higher, the result captured by the camera becomes more subjected to errors due to the blurring effect, which are hard to predict and measure.

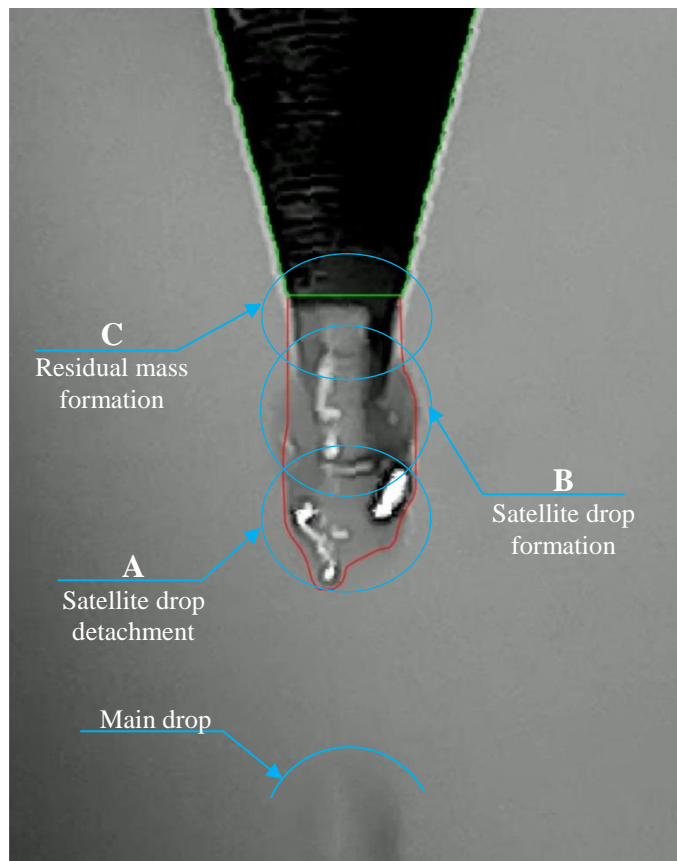


Figure 6.5.3: Error in camera edge detection due to shutter time
Green – nozzle outline; **Red** – drop edge outline;

Figure 6.5.3 is one of the examples taken at the time of detachment of the satellite drop (the main drop blurred image is also visible at the bottom of the image). It shows that the edge detection code has identified the edge, which actually corresponds to several events

combined together. The first of them is the formation of the satellite drop (Figure 6.5.3 – A), the second is the detachment (Figure 6.5.3 – B) and thirdly the formation of the residual volume (Figure 6.5.3 – C). This specific case showed the error which in this particular case results in multiple complications. Firstly, the drop size is comparable to the actual drop prior to detachment resulting in the code being unable to identify the correct frame for detachment resulting in uncertainty in the detachment period. Secondly, the CoM vertical location does not correspond to the actual detachment location. Thirdly, the volume of the drop in that frame cannot be determined correctly. The experiments showed that this flaw in the operation of the camera does not happen often (and it is usually associated with the necking process) and can be neglected in the post-processing code.

To summarise, the camera operation with the implementation of the processing code can provide data for later analysis. The post-processing code has shown that the results do contain slight reading uncertainty but in comparison to the size of the drop, they can be used usefully for analysis of the behaviour of the physical system. While the noise of the system becomes higher if the drop oscillations are fast, events of this sort can be neglected due to the fact that these events most often are associated with the necking process (which happens within a single frame capture time).

6.5.2 Discussion of anomalous results

A large number of the variables affect and complicate the analysis of fluid flow experiments. This section discusses the problems encountered in the tests, as well as giving a brief outline of the unexpected findings. Briefly, the topics discussed will include:

- Pendant drop surface tension
- Residual volume after detachment
- Water formation on the nozzle surface
- Air bubbles in the fluid supply
- Periodic jetting streams

The nozzle material (Polytetrafluoroethylene – PTFE) was chosen as a hydrophobic material in order to minimise the interaction between the liquid and the solid at the points of contact. By doing so, it was expected that the pendant drop shape will be determined only by the liquid-liquid surface tension. During tests it was found that the pendant drop still continues to have constant contact with the surface as soon as the surface of the tip came into contact with the liquid (for dry surface contact see Figure 5.3.7 or Figure 6.5.4 – A, for wetting surface contact – Figure 6.5.4 – B). The difference between two states can be identified as how the drop is attached at the nozzle. In the case of the dry contact, the drop's convex shape continues past the outer edge of the nozzle and has minimal interaction with the nozzle tip surface. While the wetting surface shows no such interaction and the drop has full contact with it. The wetting of the surface usually happens during the drop detachment process and cannot be eliminated, meaning that any future calculations of the drop constants (such as surface tension or surface contact angle) if required to be performed should take into account the contact diameter which was 2 mm (which is the outer diameter of the nozzle tip).

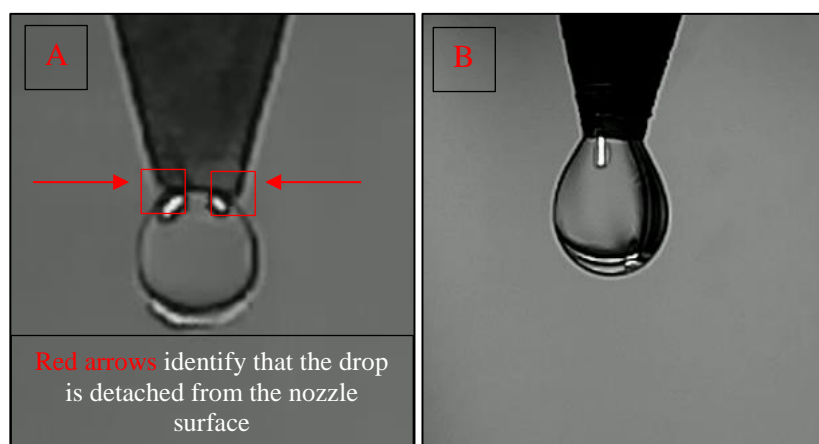


Figure 6.5.4: Drop interaction with a surface

A – drop contact with non-wetted surface; B – drop contact with fully wetted surface; Another anomaly associated with the nozzle material is the drop critical mass. The critical mass of the drop is defined as the mass at which the surface tension forces are unable to hold the drop attached to the nozzle and at which point the necking process begins. Based

on the Tate's law (Equation 2.2.6) the theoretical maximum volume that can be suspended at the nozzle is calculated as:

$$V_{crit}(\rho - \rho_{out})g = \pi d \sigma \sin \theta$$

where: V_{crit} – drop volume

ρ and ρ_{out} – density of the liquid and surrounding liquid respectively

g – acceleration due to gravity

d – nozzle diameter

σ – surface tension

θ – surface contact angle

With the following approximations: outer diameter of the nozzle $d = d_o = 2$ mm, medium density difference $\rho - \rho_{out} = 997.00$ kg/m³ (at 20 °C, 100 kPa), $g = 9.81$ m/s², $\sigma = 72.8$ mPa/m (at 20 °C, 100 kPa) and $\theta \approx 90^\circ$ (assumed as the contact angle between the nozzle and liquid – Figure 6.5.5) the total maximal volume that can be attached to the nozzle should be equal to 46.767 mm³. At the same time, the experimental investigation into the critical mass of the drop (discussed in future subsection 7.1.1) showed that the average size of the drop was around 40.450 mm³. As seen, the difference between the values is substantial and cannot be accounted by the reading errors.

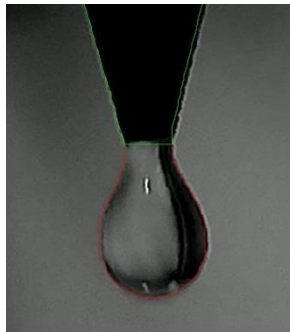


Figure 6.5.5: Drop before detachment

Analysis of the nature of the error based on Equation 2.2.6 and the visual observation showed that the only physical parameter that can affect the drop size in such a way is the surface tension.

Further investigation was performed to investigate the value of the surface tension. Additional experiments were done where the drop was left to develop and detach at a low flow rate (set to 2.449 ml/hr). The results showed (Figure 6.5.6) that the maximal drop volume is equal to 40.450 mm³ or 40.329 mg.

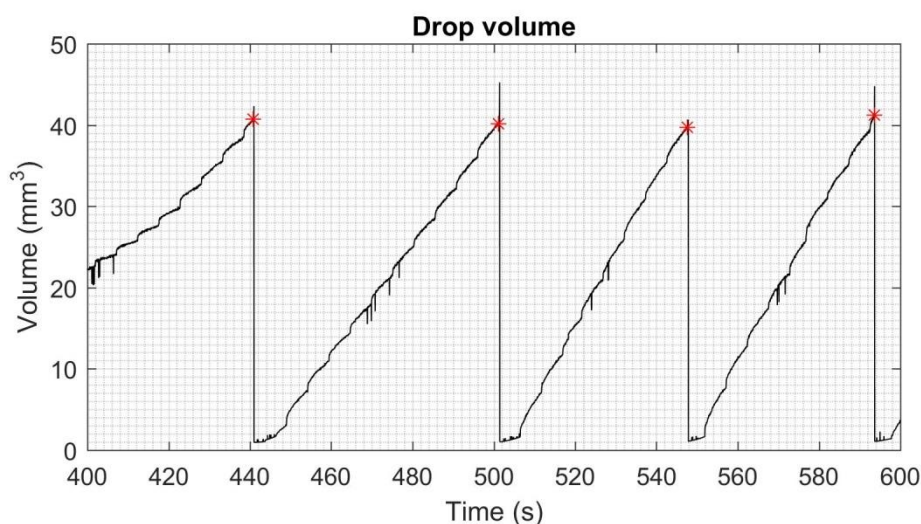


Figure 6.5.6: System surface tension investigation¹²

Red – the point where the critical mass has been reached

The difference in numbers allows one to speculate that due to the use of the PTFE as the nozzle material the effective surface tension has been changed. Any further investigations require much more complicated analysis as the contact surface tension force and the surface tension angle vary continuously with the geometry of the drop and the problem becomes dynamic in nature. The contact surface tension is the combined liquid-to-liquid, liquid to solid and liquid to air interaction. Even so, it is possible to neglect liquid-air interaction as being small when compare with the liquid-liquid interaction, but the liquid-solid interaction must still be considered. As shown in Figure 6.5.7 there is no visible volume growth after detachment (441 s) until the specific time (446.4 s) where growth starts. Using the volume growth profile and extrapolating the normal development

¹² The visible system noise is due to pump operation at low flow rates. This statement is confirmed by the consistent repetition of the sudden increase in flow rate, which was calculated to be ≈ 3.6 ml/hr (at a nominal pump flow rate of 2.5 ml/hr). The investigation showed that at the flow rates of interest (60.6 – 332.1 ml/hr) the fluctuation ceased to be detectable.

backwards (Figure 6.5.7 – green line), the missing volume has been identified as 1.880 mm³.

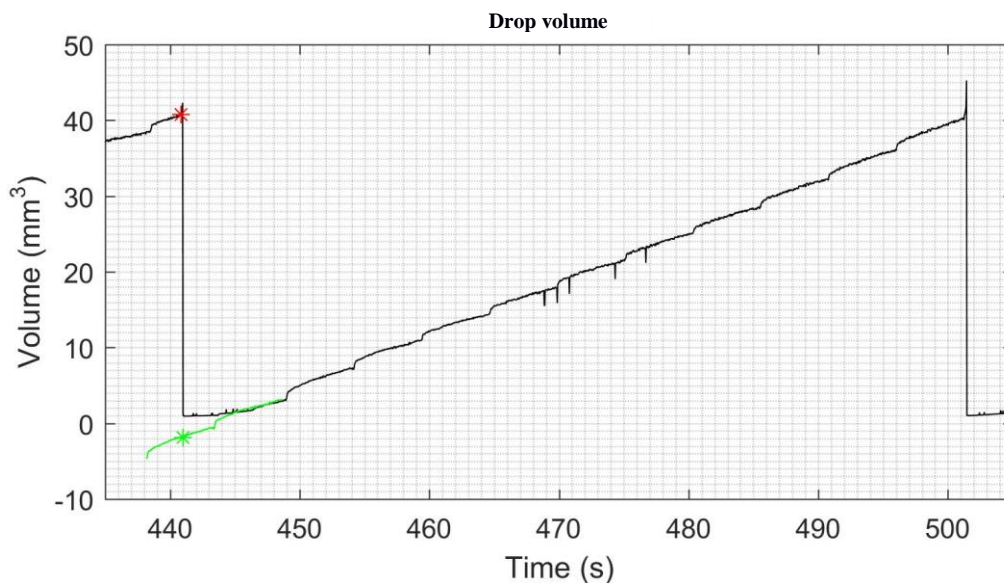


Figure 6.5.7: Drop detachment investigation at low flow rate

Green – expected growth profile; **Red** – point of critical volume reached;

This supports speculation of the importance of including the liquid-solid surface interaction as the volume has been either pushed back into the system (possibly back into the syringe) or dragged out by the detached drop. Other possibilities include detection problems, or squashing liquid into air pockets inside the fluid supply system.

The detection problem possibility is less likely as approximate calculations can show. The non-accounted liquid ($V = 1.88 \text{ mm}^3$) which is equal to $1.88/0.0374^3 \approx 35937 \text{ pixels}^3$ (Equation 5.4.2) at the nozzle tip of 2 mm in diameter (or $2/0.0374 = 53 \text{ pixels}$) should have a width approximately equal to a diameter of the nozzle. Simple assuming that the missing volume is in form of cylinder will give a height of that cylinder to be $4 \cdot 35937/(\pi \cdot 53^2) = 16 \text{ pixels}$, which understandably is a high number not to be able to detect (Figure 6.5.8).

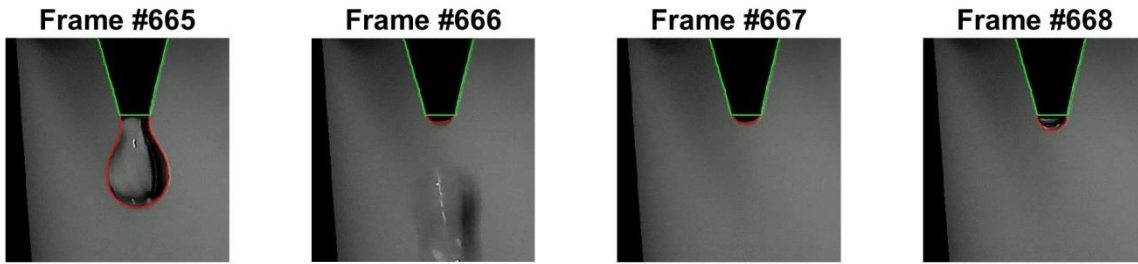


Figure 6.5.8: The recorded detachment process (No.1)

Green – nozzle outline; *Red* – drop outline;

The results showed that due to PTFE-water and water-water interaction in a capillary-like system (the nozzle inner diameter is 0.99 mm and the outer diameter is 2 mm) the detachment process (which defines the critical mass and to a lesser extent the residual mass) is dependent on the joint surface tension forces. Nevertheless, the calculation of the actual value of the surface tension is beyond the scope of the current topic.

The detachment process should lead to the development of the residual mass [4]. The following paragraphs will demonstrate that it is not often the case.

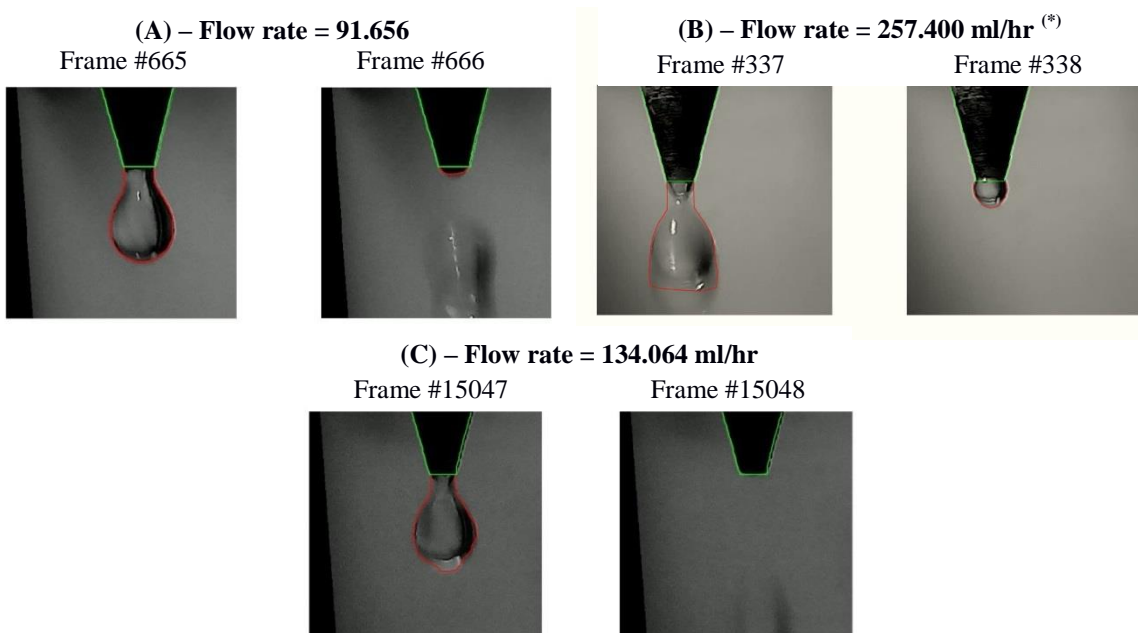


Figure 6.5.9: Post-detachment development types

A – residual volume; B – surface wetting volume; C – no residual volume

(*) – edge detection is unable to detect the edge due to blurring effect

It was found that there are two types of post-detachment developments as seen from the experimental results. The first is the standard residual volume left over by the previous

drop [4], and the second is the *surface wetting volume* (or no residual volume as variation of it) (Figure 6.5.9). No residual volume after the detachment is most likely to be an error in detection as the volume is much smaller than the pixel size, nevertheless it will be included as a separate type of post-detachment development type in the later analyses.

The normal residual volume is defined as the volume that is left after the detachment which after detachment continues it grow. The wetting volume is the volume which is left after the detachment but is delayed in its growth, with a volume typically ten times lower than the normal residual volume. The delay in the flow is due to the water being pushed back partially occupying air pockets within the fluid system. The observed '*surface wetting volume*' is due to the wetting of the material and is the remains of the drop previously attached. Similarly, when no volume is detected the volume growth is delayed after the detachment process.

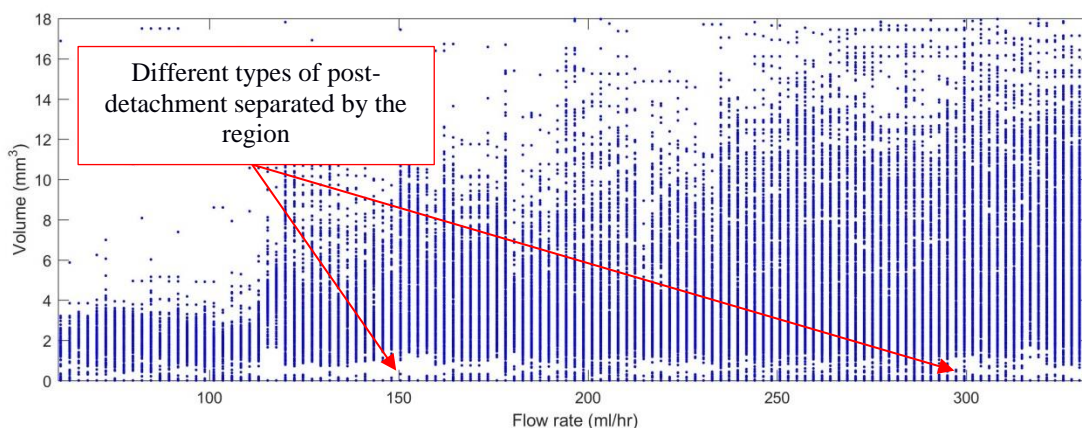


Figure 6.5.10: Readings of volume after detachment

As seen from Figure 6.5.10 the main region (the region with the denser population of data points) of the detachment mass is well below a volume of 20 mm^3 . The value of the wetting volume was taken to be around 2.5% of the critical volume ($0.025 \cdot 40.45 = 1.012 \text{ mm}^3$), which also can be identified on the graph (it is possible to see that there is a gap in the plot around this volume value). Thirdly, the no-volume type was taken as anything between an actual zero value and the camera volume uncertainty value (which is 0.053 mm^3). The

proportion of each post-detachment type was then converted and displayed as a percentage of the total data points (Figure 6.5.11).

Figure 6.5.11 summarises the proportion of each post-detachment type. The process for the identification of the residual volume was limited to a simple reading of the residual mass after the detachment. The values were separated into three categories as described above. Here certain assumptions were needed. The volume of the normal residual mass should not exceed 18 mm^3 (an arbitrary value was chosen to limit the error values from the video post-processing code)¹³. The limitation applied here constrains only few percent of the data (around 4% of the false data were eliminated), still leaving a minimum of 250 data points per test.

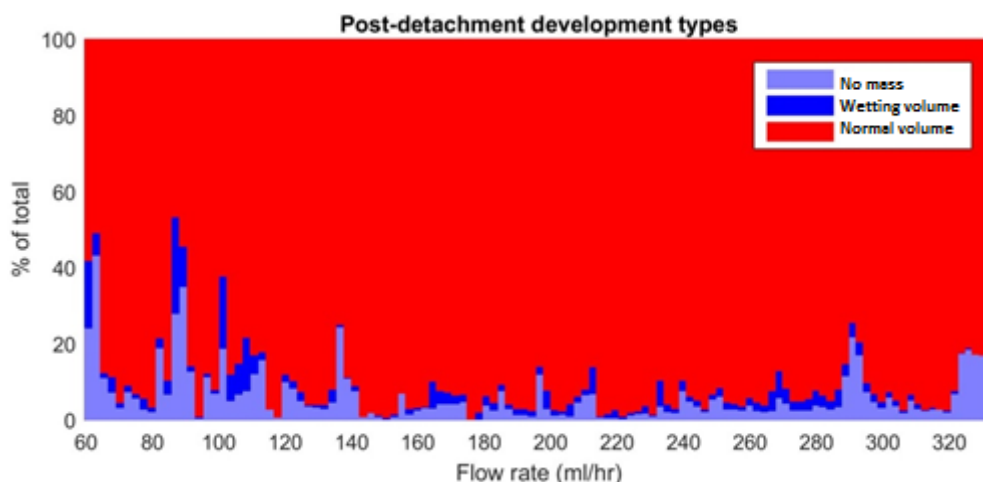


Figure 6.5.11: The results of the investigation of the volume after detachment

Figure 6.5.11 identified that the majority of detachments have a normal residual mass. There was no clear dependence found of the residual volume quantity on its type or any other parameters. Even so it is possible to speculate that after detachment there is less normal residual volume created at lower flow rates (below a flow rate of $\approx 120 \text{ ml/hr}$) and it was assumed that in the dripping period between $60.6 - 332.1 \text{ ml/hr}$, with current experimental set-up the average chance of the development of a wetting volume type is equal to 9%.

¹³ The post-processing code identifies some detachment incorrectly, which leads to a volume of the post-detachment drop being higher than it otherwise would be.

Some of the observed anomalies are associated with experimental set-up errors. In some cases, due to accidents in the tests there were found to be water formations on the side of the nozzle (Figure 6.5.12). The following can lead to errors in the determination of the nozzle, as the edge of the nozzle does not follow the cone shape (the detected edge pixel is located outside the search area – as explained in subsection 6.3.2; it is expected that the edge of the nozzle in the result presented will extend either down or down-left).

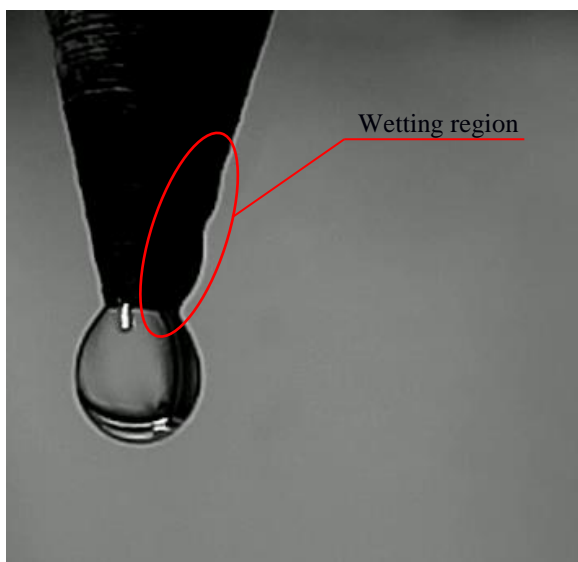


Figure 6.5.12: Liquid formation at the nozzle surface

In the worst-case scenario (Figure 6.5.13), the wetted region on the side becomes linked to the nozzle tip, which actually results in an offset of the drop CoM location (as seen from the figure below). As the area of the contact is increased, the results become unreliable and they were not used in any future analysis.



Figure 6.5.13: Drop attachment shifted due to liquid formation at the nozzle surface

Another anomaly encountered, which can potentially have an effect on the results, are entrapped air bubbles in the fluid flow (Figure 6.5.14 – left). In some cases it can lead to a catastrophic effect, when instead of the formation of pendant drop there is an air bubble, which has a much bigger size than the normal (expected) drop size (Figure 6.5.14 – right).

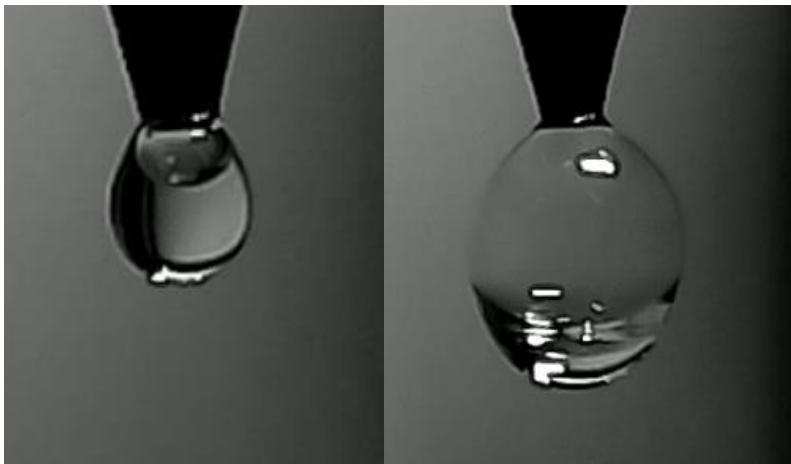


Figure 6.5.14: Air bubble in a pendant drop

The reason for this unfortunate event is that there is occasionally air trapped in the fluid supply system and it is pushed out by the fluid flow. At the same time, the fluid surface tension forms a bubble, which does not allow this air to escape. Through experimentation it was found that trapped air can remain within the system for quite some time (throughout the whole syringe volume), affecting the results of several experiments in a row. Experiments with such abnormalities were not considered as it was suspected that the drop contact force and the surface tension of the drop were affected and cannot be compared to other experiments. To remove the air from the system it was required to manually push some water out of the syringe at a high rate. By doing so, any air pockets within the system are filled with water, coming through at high speed and with some momentum, and the air is pushed out from the system through the nozzle opening.

On the other hand, the experiments also identified that in some flow rates (more often it observed at higher flow rates – and first detected at 178.1 ml/hr) that the drop detachment leads to formation of a jetting stream (Figure 6.5.15). A jetting stream is defined as a

column of a fluid with a length which typically ten times or more greater than the contact diameter of the drop [14].

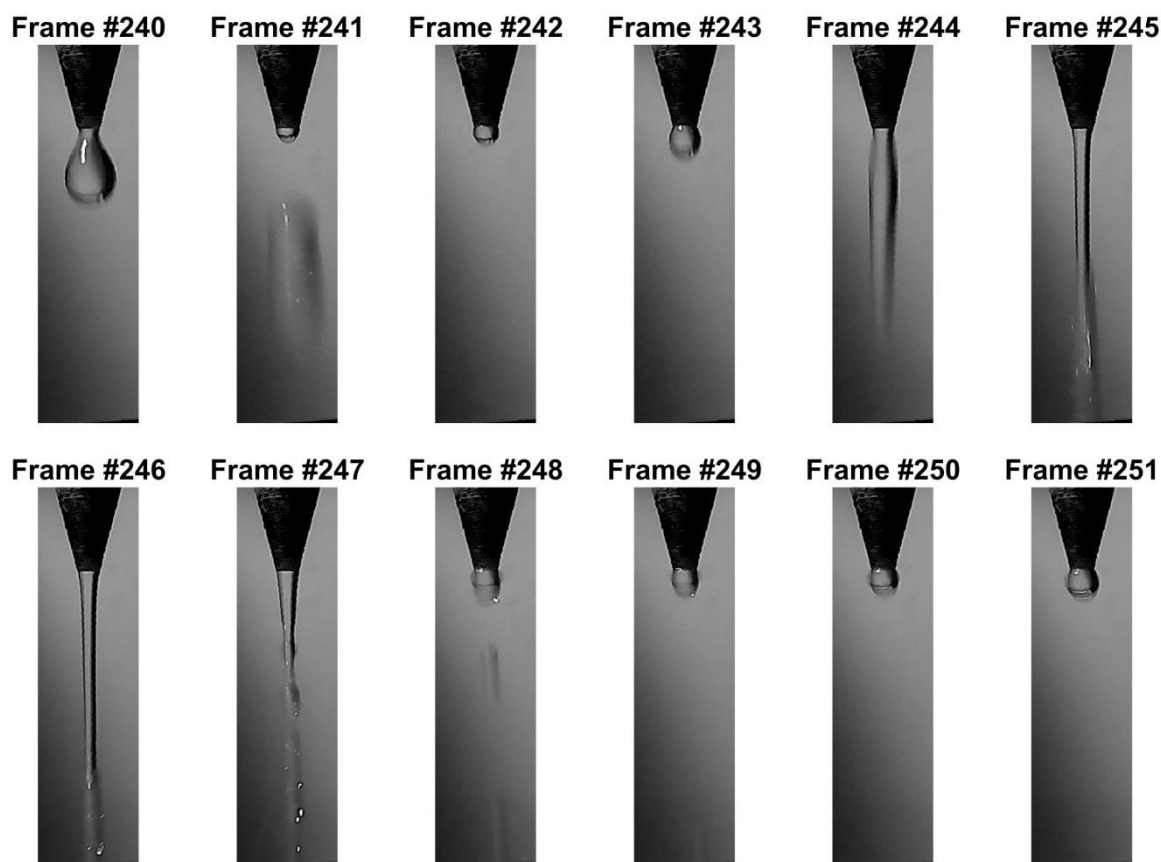


Figure 6.5.15: Jetting stream formation after drop detachment at a flow rate of 275.2 ml/hr

Analyses of these events lead to the conclusion that the jets formed are due to a sudden increase in the flow rate (Figure 6.5.16 – frames #243 – #245).

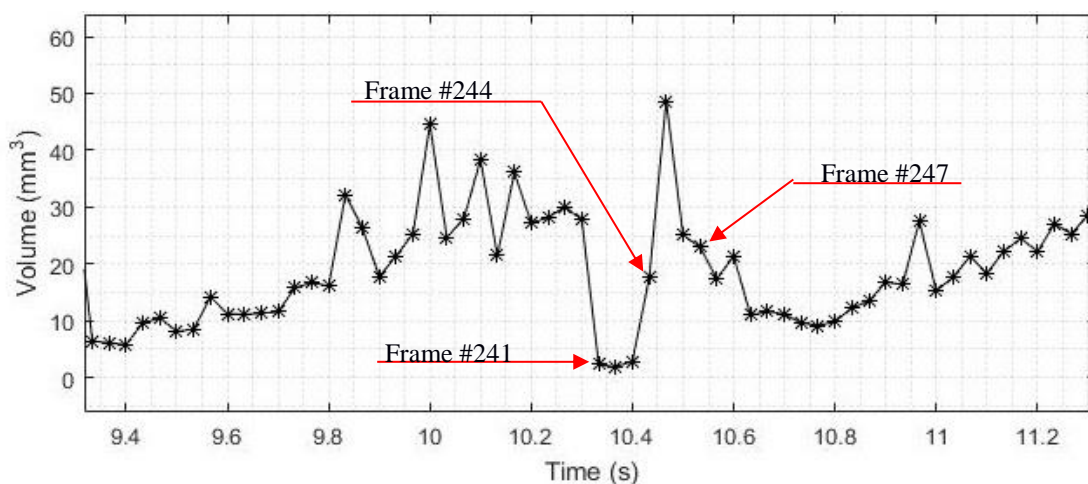


Figure 6.5.16: Jet development volume plot^(*) at a flow rate of 275.8 ml/hr

^(*) The volume variation is due to the error in edge detection due to the blurring effect (subsection 6.5.1), as well as due to some fluid being pushed back into the capillary

Between frames #243 – #245 the extracted volume grows at a much faster rate. The calculated value showed that the average flow rate in the range of those frames is equal to ≈ 2.119 l/hr with a nominal supply flow rate of only 0.276 l/hr. The reason for this increase is speculative. It is proposed that after detachment (frame #241) some of the drop residual volume collapses into the nozzle capillary. As the water is not compressible, liquid is pushed either into the air pockets within the fluid system, or it stretches the pipes of the liquid supply (which are made of flexible Tygon® tubing). The volume of the residue remains constant and with no vibration¹⁴ between frames #241 and #243 and at this low level (named earlier as the *wetting volume*), this implies that the volume level within the nozzle capillary is above the opening (leading to the delay in drop growth, similar to Figure 6.5.7). The increased air pressure or the stretched tubing, as well as capillary action add additional velocity to the fluid flow (corresponding to an increase in the flow rate between frames #243 – #245). With the additional flow velocity, the critical Weber number (section 2.2) is reached and the jet is formed. The jet develops Rayleigh instability, which leads to a change in the flow parameters as air starts to enter the capillary [14]. The increased flow velocity slowly dies down (towards the operating flow rate) and is unable to support the jet stream as the Weber number becomes lower than the critical number, so that the jet stream collapses into the pendant drop. In addition, while the flow velocity was increased it drained additional liquid from the fluid system (overshoot of the dynamic system), which then needs to be refilled, leading to slower volume growth (Figure 6.5.17) after the collapse of the jet stream.

Figure 6.5.17 compares the behaviour of the drop at three successive flow rates. The slow flow rate (212.4 ml/hr) between the jetting streams is distinctive even on the Z-CoM plot as the drops centre of mass coordinate grows more slowly than in the plots above or below.

¹⁴ The statement on the lack of observable vibration is made based on the computer analysed results, which confirms a stable CoM location in these frames. This is confirmed by visual observations. As was mentioned previously (subsection 6.5.1), it is possible to visually identify the vibration (or fast drop movement), as the drop edge becomes blurred, due to the camera's shutter opening time.

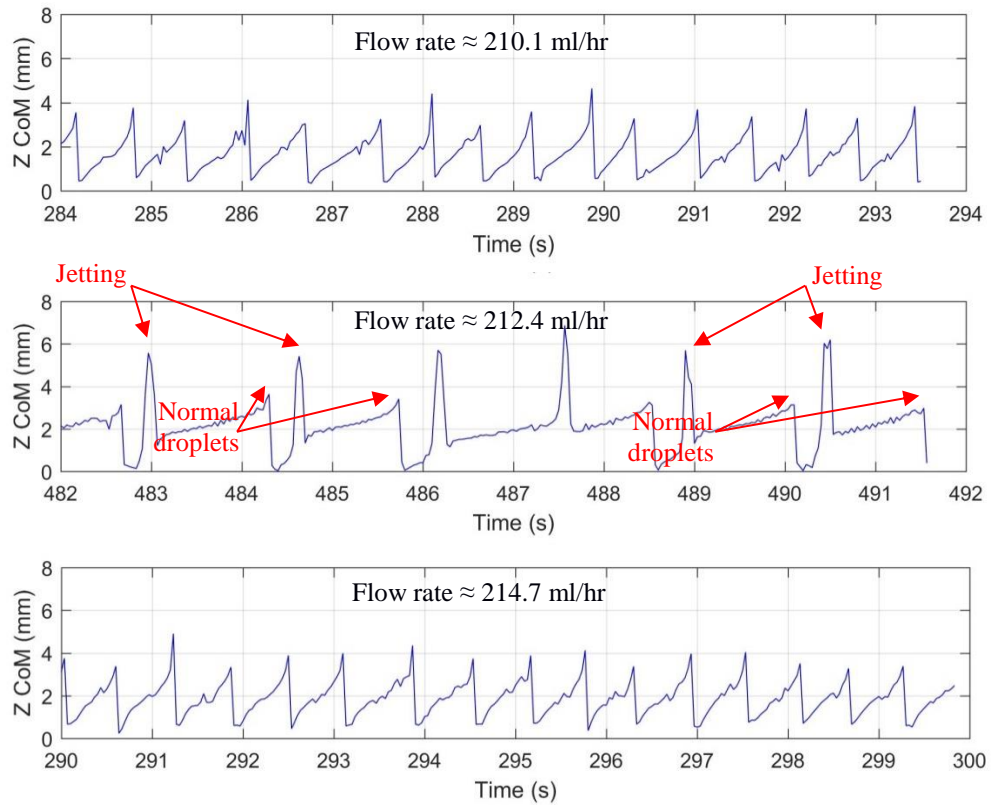


Figure 6.5.17: Comparison of the Z-CoM behaviour of the jet stream and regular dripping

Some flow rates (above 120 ml/hr) also exhibit *mid drop* detachment. The *mid drops* are defined as drops with a volume which does not correspond to either the critical mass detachment nor are associated with satellite drops, but are products of the chaotic region [14] (period doubling of the bifurcation process). Figure 6.5.18 shows the process of mid drop development and detachment. Similarly, to jetting formation this process is due to the increase in flow velocity. The recorded flow rate in this case is 895.4 ml/hr (with an actual supply flow rate equal to 275.8 ml/hr).

The above events have been described by Clanet and Lasheras [14] (section 2.2). Mid drops are formed for the first time at the point of the first bifurcation and are identifiers of the transition from periodic dripping to the chaotic region, while the jetting stream identifies the end of the chaotic region and the start of the jetting region. The values of the flow velocities based on their research and current work does not match, which is proposed here to be due to the set-up of their experiment.

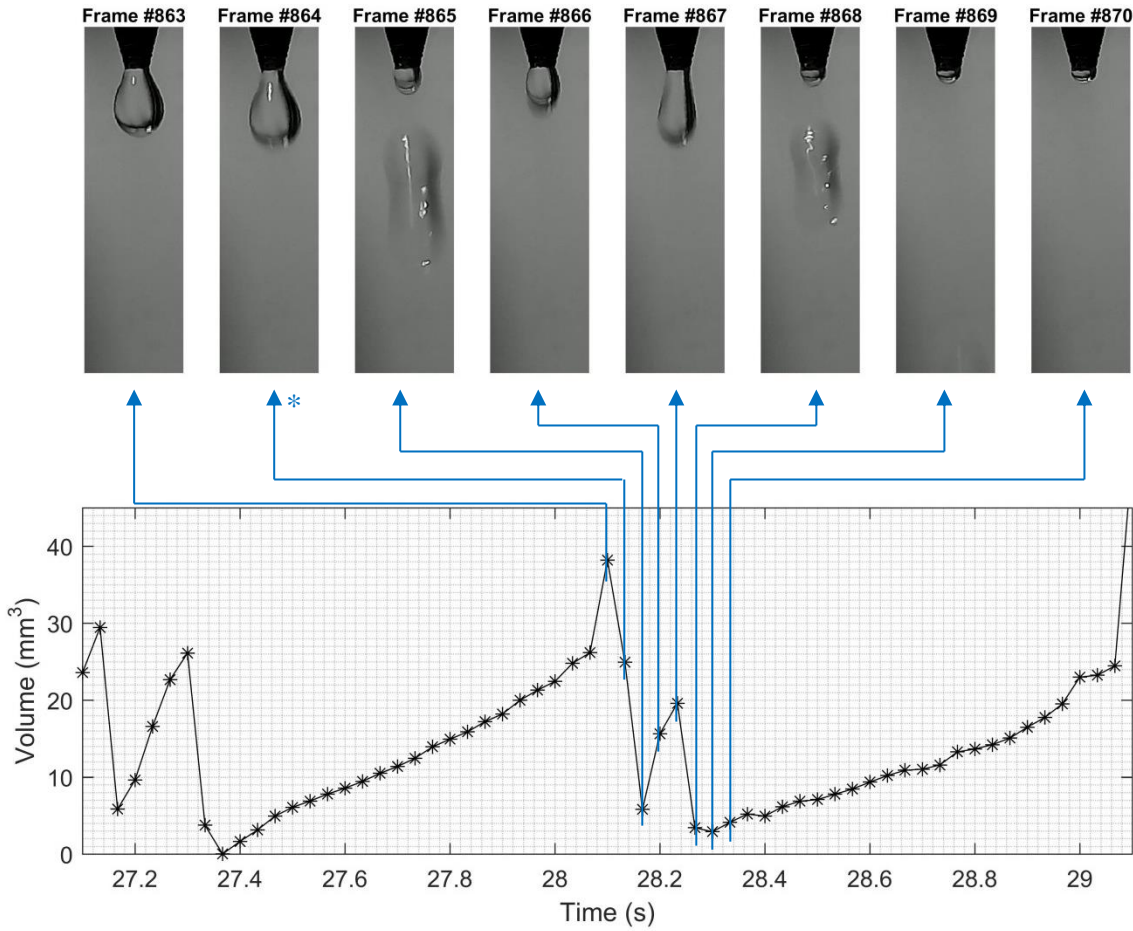


Figure 6.5.18: Mid drop development

(*) Volume error is due to synchronisation with the second camera, which identifies this drop as already detached

Based on Clanet and Lasheras calculations the jetting should start at a flow velocity described by Equation 2.2.1:

$$v_o = \sqrt{\frac{We_c}{d(\rho - \rho_{out})/(\sigma \sin \theta)}}$$

where: v_o – flow velocity

We_c – critical Weber number

$d = 0.990 \text{ mm}$ – inner diameter of the nozzle (subsection 5.3.1)

$(\rho - \rho_{out})/(\sigma \sin \theta)$ – density to surface tension effective ratio

The density to surface tension ratio can be calculated using Tate's law (Equation 2.2.6) and the values acquired from experiments described in this subsection.

$$\frac{\rho - \rho_{out}}{\sigma \sin \theta} = \frac{\pi d_o}{V_{crit}} = \frac{2 \cdot 10^{-3}}{40.45 \cdot 10^{-9}} = 155.332 \cdot 10^3 \text{ (s}^2/\text{m)}$$

where: $d_o = 2 \text{ mm}$ – outer diameter of the nozzle

$V_{crit} = 40.45 \text{ mm}^3$ – drop critical volume

The critical Weber number was calculated based on Equation 2.2.1:

$$\text{We}_c = 4 \frac{Bo_o}{Bo} \left[1 + KBo_oBo - ((1 + KBo_oBo)^2 - 1)^{\frac{1}{2}} \right]^2 = 4.32$$

Where $Bo_o = 0.5191$ and $Bo = 0.2570$ are Bond numbers for the outer and inner nozzle diameters and can be described by Equation 2.2.2:

$$Bo \equiv \sqrt{\frac{(\rho - \rho_{out})gd^2}{2\sigma \sin \theta}}$$

where: $g = 9.81 \text{ m/s}^2$ – acceleration due to gravity

The calculated values showed that the jetting regime is expected to start at a flow rate of 1.552 l/hr (where the flow rate is calculated as $\dot{V} = v_o \pi d^2 / 4$), which in our case was equal to 178.1 ml/hr following correction. The disagreement here confirms the presence of the internal force that pushes the liquid above this value to create the jetting stream. Moreover, at the same time by itself this flow rate is unable to provide enough flow velocity to continuously produce the jetting stream. The periodic jetting stream with dripping continues past the threshold flow rate and this has been explained the by reduced flow velocity beyond any drop collapse. Beyond this threshold flow rate the process of detachment continues to be complicated, where depending on the flow rate are observed: periodic jet-drop detachment, chaotic dripping (as shown in Figure 6.5.17), and periodic jets where jets are formed at the time of drop detachment, not as separate entities (observed for the first time at a flow rate equal to 212.4 ml/hr). The last process is explained due to fast and unstable drop detachment, when air enters the capillary changing the flow properties which leads to a higher Weber number than it is under.

CHAPTER 7

EXPERIMENTAL RESULTS DISCUSSION

The previous chapter described some of the results following post-processing, including an outline of the anomalies, which were observed during the experiment. Firstly in subsection 6.5.1 limitations of the experimental module were identified: Centre of Mass (CoM) coordinate reading error, volume and mass variation error. These error parameters were consistent throughout the experiments, but some limitations were noticed. The errors grew much bigger in some cases when it came to the detachment process due to limitations of the camera (as described in subsection 6.5.2). It was found that in rare cases of detachment (especially associated with the higher flow rates) the video recording produces a blurred image of the drop, as the shutter (with an opening time equal to $1/60$ s) captures several locations of the same drop in a single frame.

In same subsection a description of other experimental errors was provided, such as trapped air bubbles inside the system and wetted regions on the side of the nozzle. The experiments when such events occurred were required to be redone and were not included in the analyses. Unfortunately, it also was found that the experimental setup idea of using non-wetting material for the nozzle did not bring anticipated results. It was assumed and initially confirmed in the experiments that the pendant drop attachment diameter will be equal to the inner radius of the nozzle. By doing so, the drop surface tension variation from the standard water surface will be minimised. The experiments showed that after several

drops the surface of nozzle tip becomes wetted which leads to two consequences. Firstly, the attached drop surface tension should be recalculated. Secondly, even after detachment the observable mass growth is sometimes delayed when the surface is wetted at the nozzle tip. At the same time it was found that in some cases due to drop detachment instability the flow develops mid-size drops (which are not classified as satellite drops, nor are they actual drops), and fluid jetting streams (which after some time collapse and are followed by normal dripping). Importantly, subsection 6.5.2 showed that due to multiple anomalies, the bifurcation plot (discussed further in section 7.2) has a complex nature and it should be carefully analysed.

This chapter will discuss the results acquired during the experimental campaign. The experimental targets were set in section 1.1. The experimental flow rate range was set to be between 60.6 ml/hr and 332.1 ml/hr (the values here include the pump flow rate correction factor). The experimental results were used to confirm the results of the theoretical model, to study the non-periodic behaviour of the drop and to provide vital information for the lateral 3-dimensional mathematical model. This chapter consists of three parts and it will discuss the Mass-Spring-Damper (MSD) related constants in section 7.1. The section to follow (7.2) will comment on the nature of the chaotic behaviour observed in the experimental investigation. Finally, section 7.3 will propose advanced model parameters.

7.1 Investigation of the constants in the Mass-Spring-Damper model

This chapter concentrates on explaining the drop parameters associated with the Mass-Spring-Damper (MSD) model parameters, which also included the Centre of Mass (CoM) horizontal behaviour analysis (subsection 7.1.4).

The one-dimensional MSD model assumes the following constants, which were required to be confirmed:

- Drop critical mass (m_c) and detachment distance (z_c) – discussed in subsection 7.1.1
- Spring and damper constants for the dynamic system (k and c) – discussed in subsection 7.1.2
- Drop residual mass (m_r) and restoring distance (z_o) – discussed in subsection 7.1.3

By combining the information from chapters 4 and 6 the outline of the proposed mathematical model is presented in section 7.3, thereby addressing one of the research targets.

7.1.1 Critical mass and critical distance

To find the detachment distance and mass at detachment several preliminary investigative experiments were carried out and processed using the post-processing code (detailed in subsections 6.3.2 and 6.3.3). Detachment was identified using the procedure explained in subsection 6.4.1. The critical mass (m_c) is the mass at which necking begins and using the experimentally determined critical volume (V_{crit}) it is calculated as:

$$m_c = V_{crit}\rho$$

where: ρ – density of the liquid

The value of the critical volume was determined as the mean volume, which was recorded in multiple experiments prior to detachment at low flow rates. It can be seen from Figure 7.1.1 that after the critical volume has been reached (identified in red), the drop volume start to increase rapidly.

The actual reason for this sudden increase in volume is due to high speed movement of the drop (Figure 7.1.2) arising from the fact that supporting forces can no longer balance the weight of the drop. It is also visible that prior to detachment the volume grew linearly (Figure 7.1.1) as would be expected.

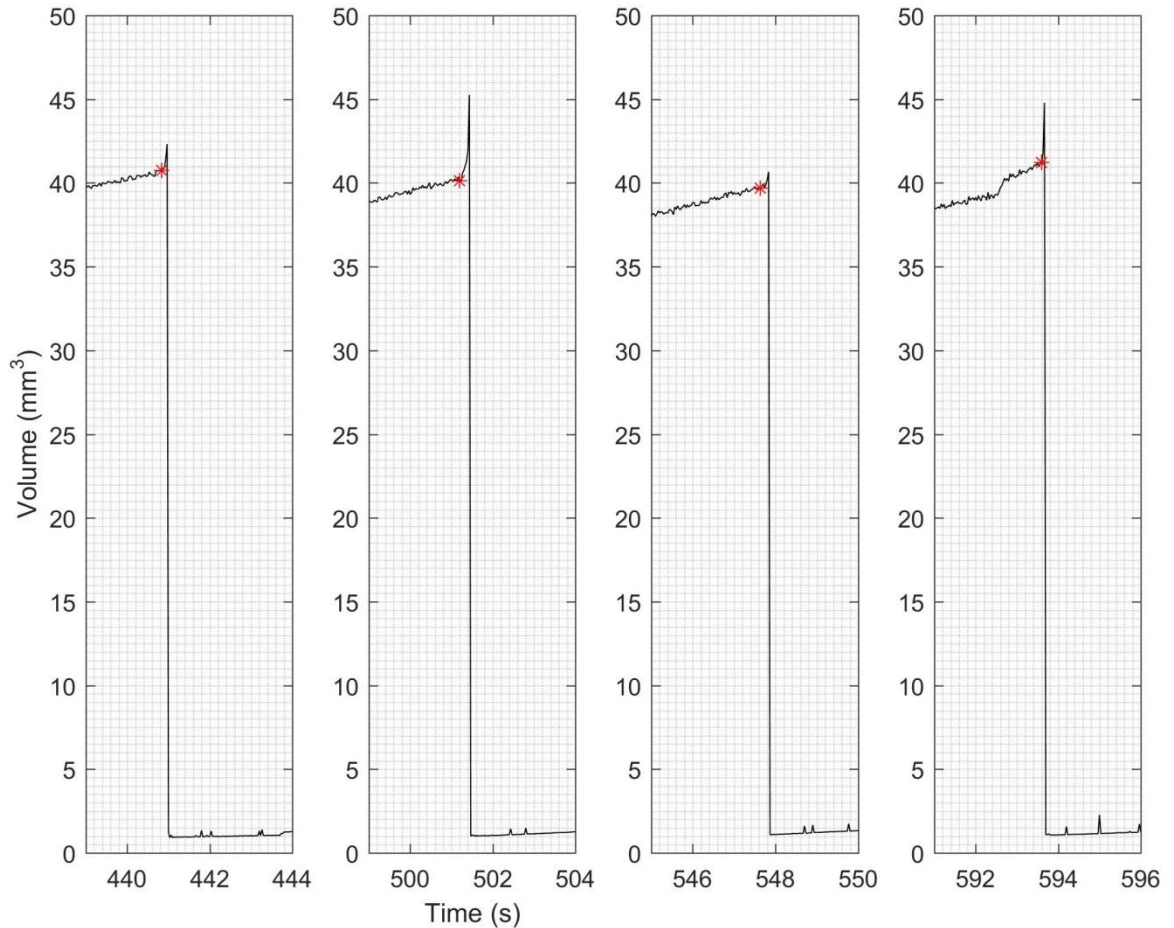


Figure 7.1.1: Drop critical volume investigation¹⁵

Red – critical mass

The mean value of the critical volume was found to be equal to¹⁶ $40.45 \pm 1.88 \text{ mm}^3$ (the uncertainty here is given for the maximal flow rate, for comparison the lowest flow rate will have an uncertainty of $\pm 0.35 \text{ mm}^3$). Assuming the fluid density to be equal to 999.099 kg/m^3 (measurements were taken at $15 \text{ }^\circ\text{C}$ – Figure 5.1.3) the critical mass of the drop is equal to $40.41 \pm 2.24 \text{ mg}$ (the uncertainty here is given for the maximal flow rate and $15 \text{ }^\circ\text{C}$, for comparison the lowest flow rate based on Equation 6.1.21 will give $\pm 0.69 \text{ mg}$, and with an increase in the temperature the uncertainty reduces to $\pm 1.84 \text{ mg}$ for the highest flow rate). Similarly, the critical distance was found to be equal to $3.05 \pm 0.02 \text{ mm}$.

¹⁵ The system noise visible is due to pump malfunction at low flow rates. This statement is confirmed by the consistent repetition of the sudden increase in flow rate, which was calculated to be $\approx 3.6 \text{ ml/hr}$ (at a pumping flow rate of 2.5 ml/hr). The investigation showed that at flow rates of interest ($60.6 - 332.1 \text{ ml/hr}$) the fluctuation ceased to be detectable.

¹⁶ The error calculations for values presented here are given in Appendix O

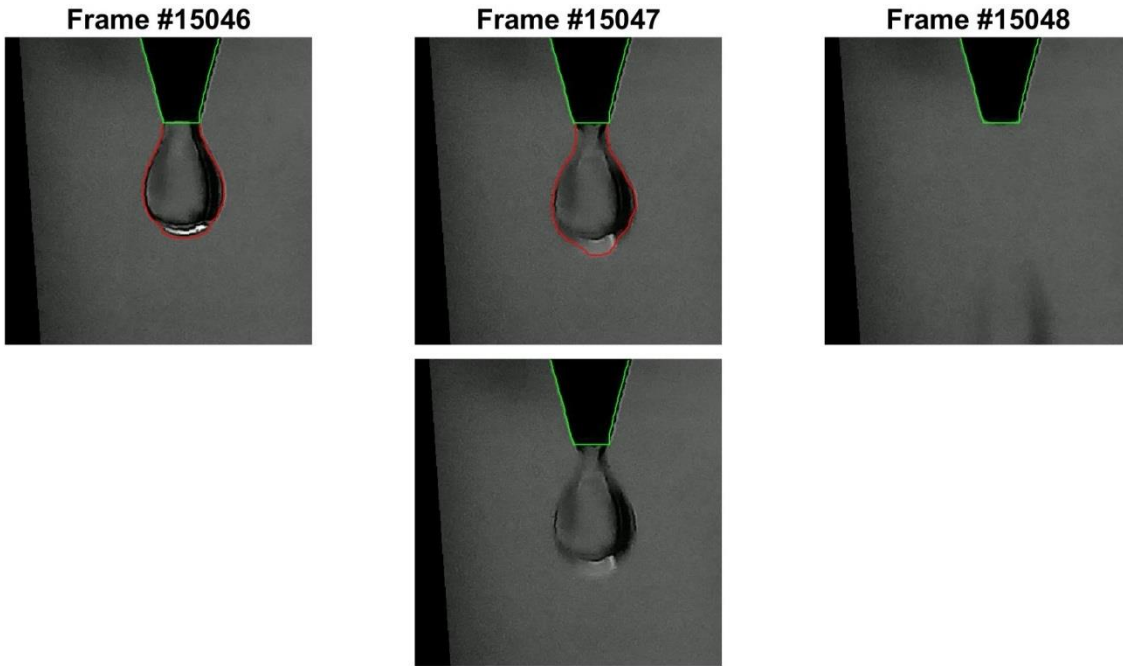


Figure 7.1.2 The recorded detachment process (No.2)

Frames are taken from Camera No.2; It corresponds to a time of 501.4 seconds in Figure 7.1.1

Green – nozzle outline; Red – drop outline;

7.1.2 Damper and spring constants

The investigation of the spring constant and the damping constants required separate experiments. A vibration test was performed on drops with different masses. The drops were stabilised by stopping the pump and allowing some time (approximately 1 minute) for the drop vibration to settle down. This was followed by applying an impulse (by tapping) to the nozzle top in order to excite the drop. The following assumptions were made at this stage:

- The nozzle vibration due to the impulse dies down much more quickly than the drop vibration. As seen from the experimental results below this was confirmed to be true (Figure 7.1.3). The example presents the nozzle behaviour just after the induced vibration (Frame #1024), which shows that there is no visible variation in the nozzle tip position, neither is there any visible vibration of it in the following frames. In addition, the drop CoM location is referenced to the centre of the nozzle tip, which allows the vibration of the drop to be observed independently of the movement of the nozzle.

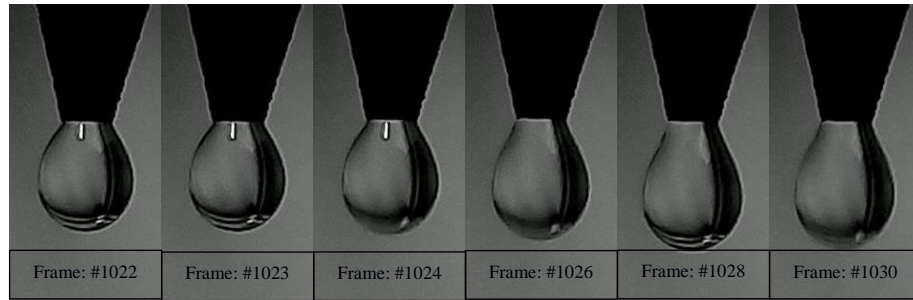


Figure 7.1.3: Induced vibrations video recording

- Any mass increase due to a shift of the liquid from the pipe to the drop is considered to introduce only a slight variation in spring and damping constants and should differ by no more than 10% from the value of the starting drop mass (Figure 7.1.4 – a).

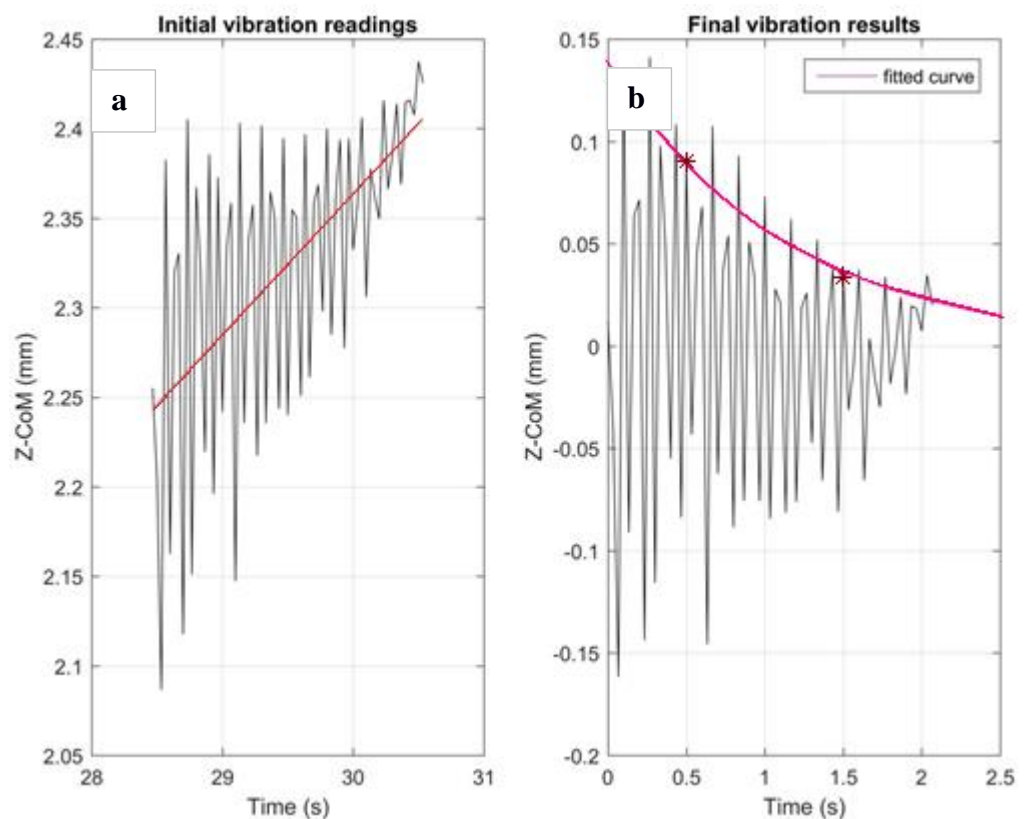


Figure 7.1.4: Spring and damping constants investigation

Red line – mean CoM location change due to additional mass; **Brown marker** – range of the vibration starting and end points; **Magenta** – mean curve of damped vibration

- The associated mass variation at the beginning and at the end of the test (Figure 7.1.4 – a) required additional adaptation of the data, where the red line is a line of best fit. The results were adjusted so that the fitted line will be level at a zero level and with no mass increase. This leads to the assumption that:
- The mass (m) of the drop undergoing the vibration test is taken as the mean value over the whole region considered ($m = \frac{1}{n} \sum m_n$).

- The data points do not provide enough information to definitely confirm the waveform with confidence, but it was assumed that the frequency of the drop vibration is approximately 30/4 Hz (where 30 is the frame rate and assuming the vibration period is close to 4 frames). It is, however, understood that the data points shown here could correspond to much higher frequencies and that the lower frequency is calculated due to sampling error (according to Nyquists Theorem). The calculation will proceed with this assumption in mind.

The results were adjusted using the following equation:

$$z_{f,n} = z_{i,n} - (P_1 t_n + P_2) \quad \left| \quad 7.1.1 \right.$$

where: $z_{f,n}$ and $z_{i,n}$ – vertical n 'th coordinates after and before adjustment

P_1 and P_2 – constants of the line of best fit

t_n – test time at n 'th step

The following step was to adjust the time values so that they began at zero (Figure 7.1.4 – b), and using the positive peak values of the curvature a first order exponential curve ($z_n = P_3 e^{\zeta \omega t_n}$) was fitted. Two peak points were selected (Figure 7.1.4 – b in red), and the values of the time (t_i and t_n), location (z_i and z_n) and number of periods (N) were recorded. The damping and spring coefficients were calculated using the dynamic relationship:

$$\begin{aligned} \delta &= \frac{1}{N} \ln \left(\frac{z_i}{z_n} \right) \\ \zeta &= \sqrt{\frac{\delta^2}{4\pi^2 + \delta^2}} \\ \omega &= \sqrt{\frac{4\pi^2 + \delta^2}{T^2}} \\ T &= \frac{t_n - t_i}{N} \\ k &= m\omega^2 \\ c &= 2\zeta\sqrt{km} \end{aligned} \quad \left| \quad 7.1.2 \right.$$

where: δ – logarithmic decrement

ζ – damping coefficient

T – vibration period (s)

ω – wave frequency (s^{-1})

k – spring constant

c – damping constant

The analysis showed that the spring constant is mass dependent and fit a linear curve

(Figure 7.1.5) described by the following equation:

$$k(m) = 10.18m - 206.35 \quad | \quad 7.1.3$$

where: k measured in mN/m

m measured in mg

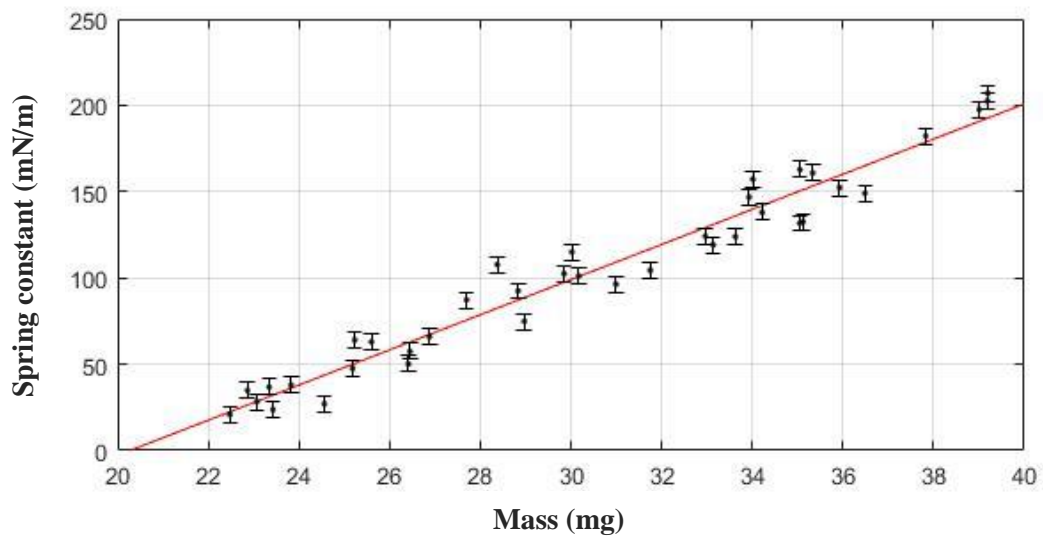


Figure 7.1.5: Spring constant results

The error calculations are presented separately in Appendix O. The results showed that the system becomes overdamped at a mass equal to ≈ 20.27 mg. This is also confirmed by visual observation (Figure 7.1.6).

The following graph shows that after detachment the vibrations do not show themselves until a mass of ≈ 20 mg is reached, and the drop growth is stable relative to drops with a mass above 20 mg.

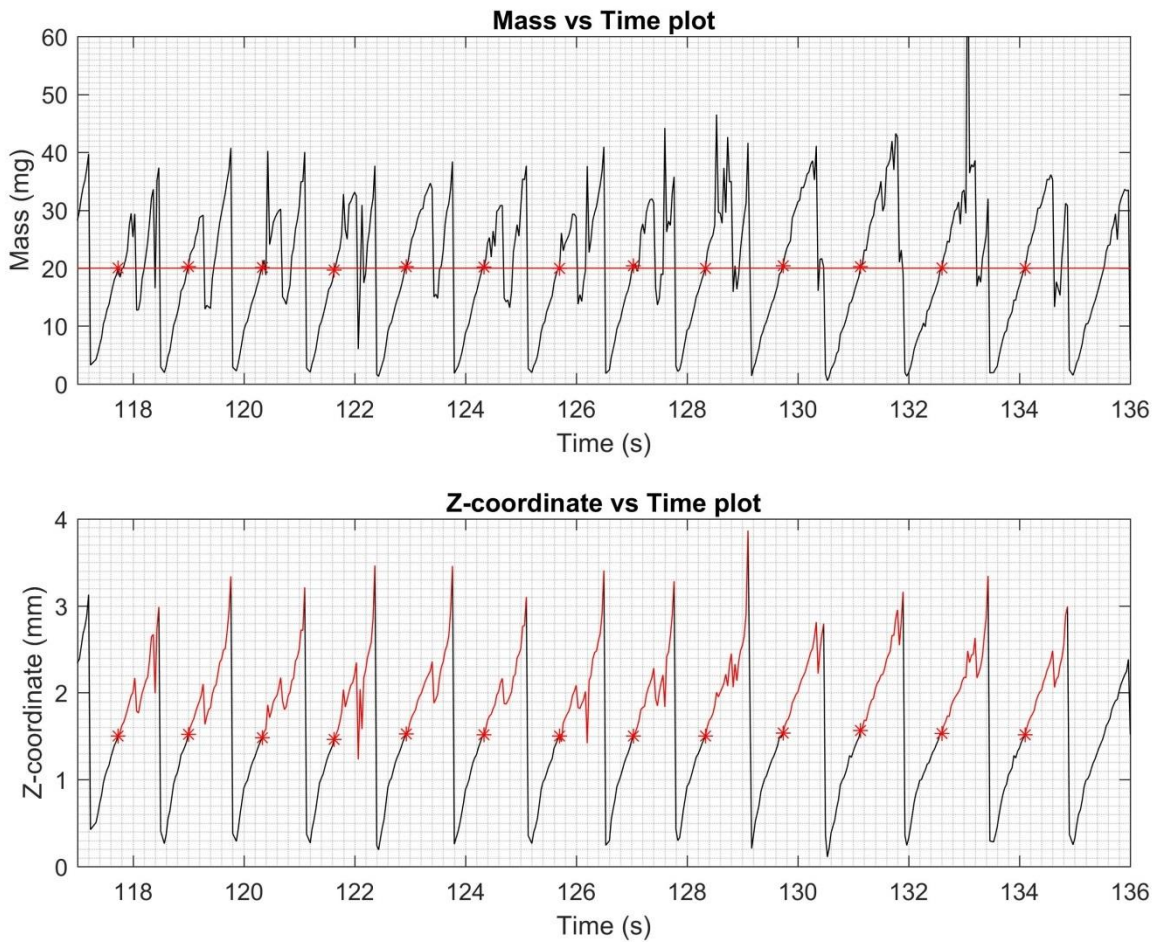


Figure 7.1.6: Visual observation of unstable behaviour of the drop above the threshold value

Red marker – identifies threshold value; **Red** top – threshold limit; **Red** bottom – behaviour above threshold value

Here it is important to note two things. First, the drop mass exhibits large variations after the threshold value. This can be explained by the presence of Rayleigh instabilities (air gets into the capillary) and error in the detection of the drop edge due to camera limitations. Secondly, the rate of change in the z-coordinate of the drop increases past $z \approx 0.9$ mm (the fact that it is not an experimental error artefact can be seen from the fact that the volume increase its rate at the same successive time instances, whereas it remains constant before and after). This is explained by the change in the shape of the drop from convex to concave.

The damping constant was produced from the same set of results using Equation 7.1.2 (Figure 7.1.7). It showed that damper constant is also mass dependent and can be described by following equation:

$$c(m) = 0.49m - 10.11$$

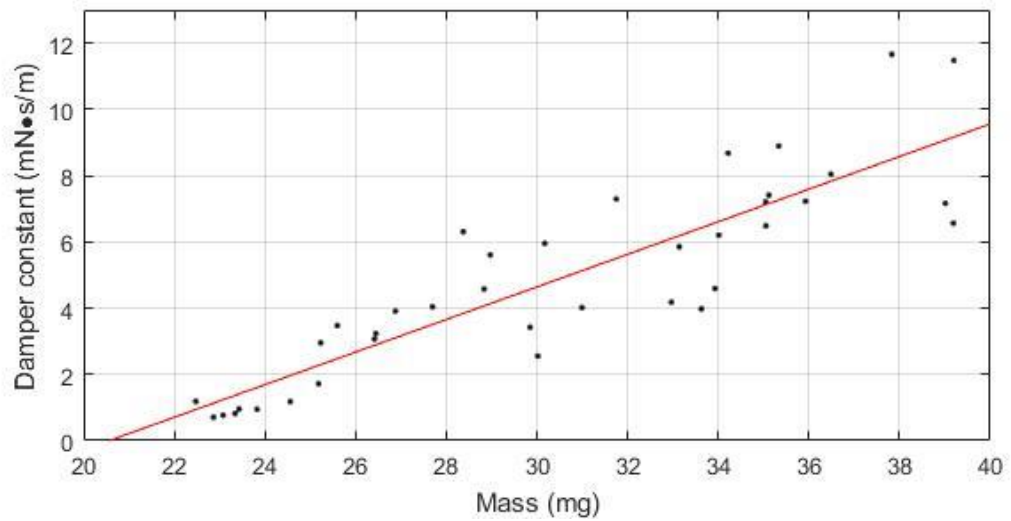


Figure 7.1.7: Damping coefficient results

Similarly, to the spring constant the damping constant becomes equal to zero at a mass of ≈ 20.63 mg. Importantly the system is undamped when the mass is under ≈ 25.25 mg.

$$4km > c^2 \text{ for } m < 25.25 \text{ mg}$$

The code (Figure 7.1.8) used to investigate the spring and damping constants is presented in Appendix Q.D. The code relies on processed data from the videos (explained in subsection 6.3.3) and a region selected visually (where the vibration test has been performed), identified as a periodic variation of the z-coordinate in the results graph (Figure 7.1.4) and this is set as the first input to the code.

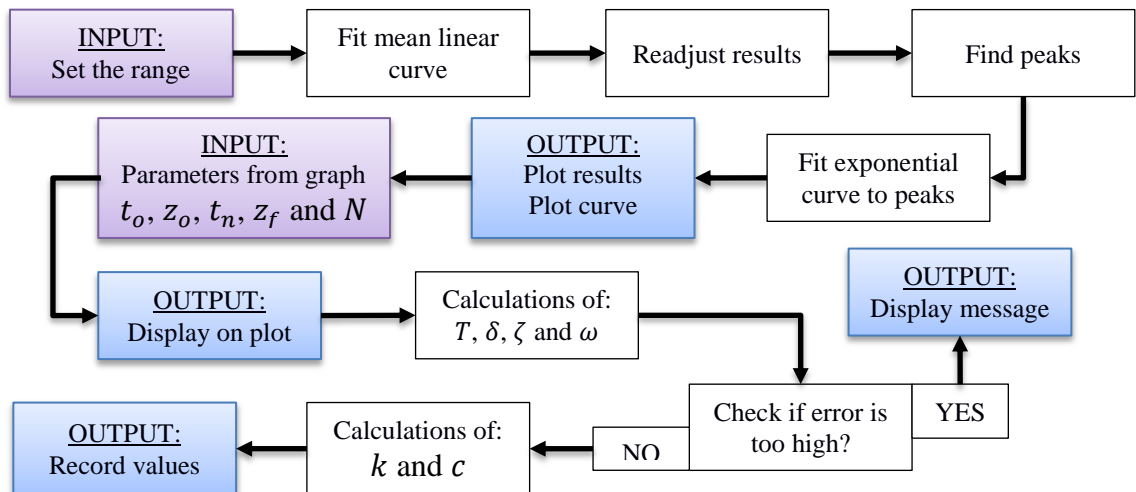


Figure 7.1.8: Spring and damper determination pseudo code

A line of best fit is fitted to the plot data, and the results are readjusted to allow for linear development around the zero value (as explained above in Figure 7.1.4). Then positive peaks are identified using “MATLAB®” software’s built-in function (`findpeaks(x,t)`) and a first order exponential curve is approximated based on those peaks. The first output in the code will plot readjusted and levelled results with the exponential curve plotted on top. Then the code requires the parameters from the graph to be entered, such as the first amplitude of the first maximum (preferably one that lies close to the exponential curve) with its corresponding time, and the final amplitude with its respective time and the total number of periods. The selected coordinates in the next step are plotted on the graph and calculations are started. The programme also checks whether the calculated exponential decay coefficients are within 5% of the fitted and if so it displays a message “[Error to high](#)”. If this is not the case the calculations continue until the spring and damper constants are calculated and recorded in the output array.

7.1.3 Residual mass/volume and restoring distance

In subsection 6.5.2 it was shown that when the drop detaches it has two options in its development. The first is that the drop will detach with little to no mass remaining at the nozzle, otherwise it will have some substantial mass left over. In terms of definitions, the wetting volume is defined as the volume that was left after detachment and it is usually below 2.5% of the drop’s critical volume (Figure 7.1.9). The residual mass is the mass that is left after detachment and it is usually well above 5% of the critical mass. It was also identified that the wetting volume is sometimes very small (lower than 0.05% of the critical volume) and can be associated with error in the video processing, where the tip of the nozzle was identified one or two pixels lower than it is actually was. This volume was considered a zero volume residue, but it was noted that it was hard to judge if this volume was actually zero or if it arose from errors in the video processing.

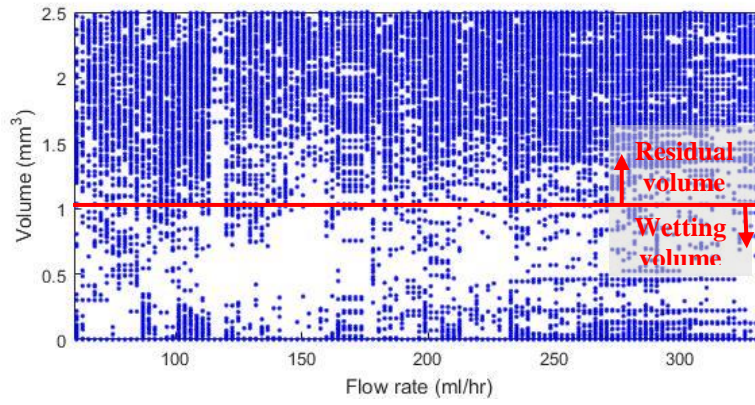


Figure 7.1.9: Normal residual volume and wetting volume separation region

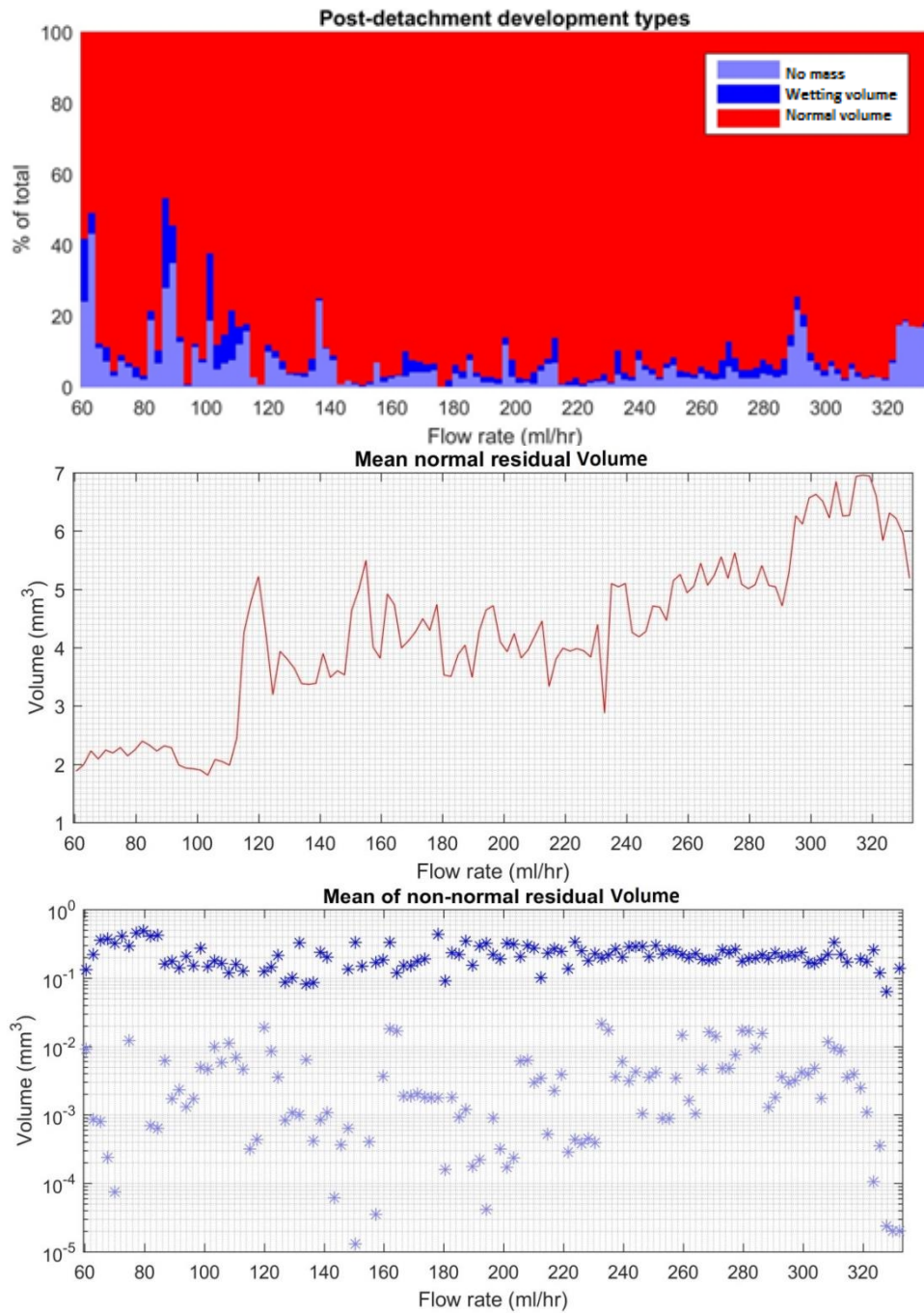


Figure 7.1.10: Residue volume study

It was stated speculatively that the zero volume and wetting volume appearance does not depend on the flow rate and the assumption was made that the appearance of those types of residue has a 9% probability at any flow rate. Figure 7.1.10 is a summary of the distribution of drop types and the mean values of the volume residues for each flow rate.

The volume of non-normal residues (which in the figure above is considered to be the wetting volume and zero volume) does not show any obvious dependence on flow rate. The visual difference between zero volume and the wetting volume is due to the threshold values applied while separating the values and calculating the mean values (artefact of classification process and averaging). On the other hand, the normal type of residue showed that with an increase in the flow rate the mean drop residue volume increases, with some exceptions (Figure 7.1.11). The region of the exceptions is identified as below 115.3 ml/hr where the mean residual volume can be approximated with a horizontal line with an average value of $2.472 \pm \Delta V \text{ mm}^3$.

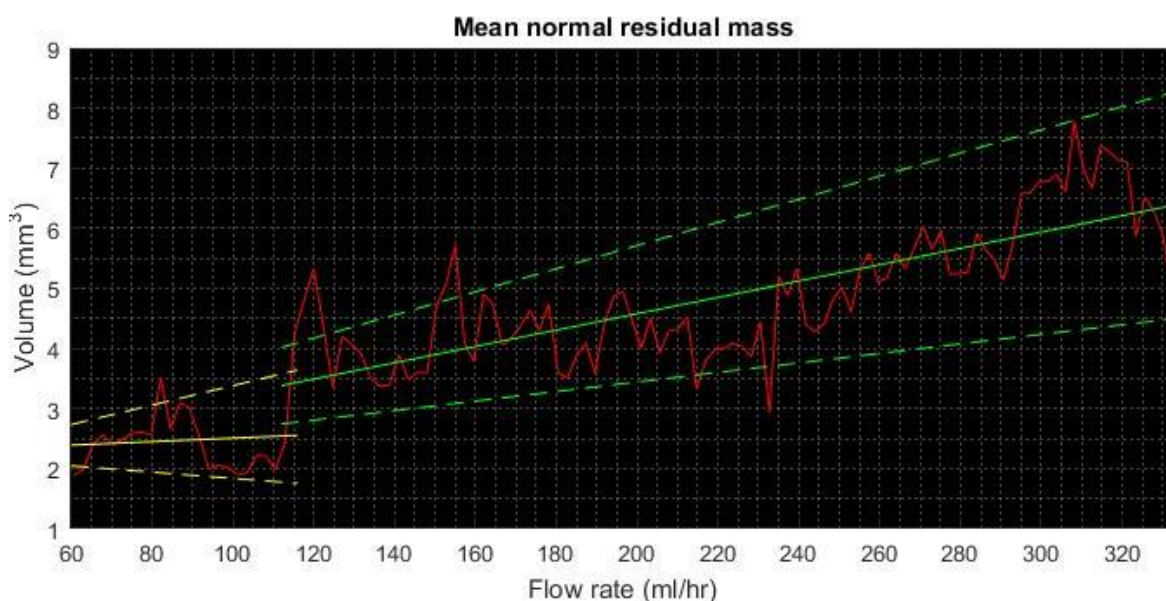


Figure 7.1.11: Normal residual mass flow rate linear dependency

Red – mean residual mass; **Blue** – linear fit curve for results below 115.3 ml/hr;
Green – linear fit curve for the results above 115.3 ml/hr; **Dashed lines** – volume uncertainty regions

Above the flow rate given above the residual volume starts to grow with a linear dependence approximated as:

$$V_{res} = 0.014\dot{V} + 1.857 \pm \Delta V$$

where: V_{res} – residual volume

\dot{V} – volumetric flow rate

ΔV – volume uncertainty

Figure 7.1.12 shows that the drop vertical CoM location grows linearly when the flow rate is constant (when variations due to drop oscillations are ignored and similarly with the necking region). Also, subsection 7.1.1 identified that the drop vertical coordinate has a threshold value that separates two types of drop shape (convex and concave).

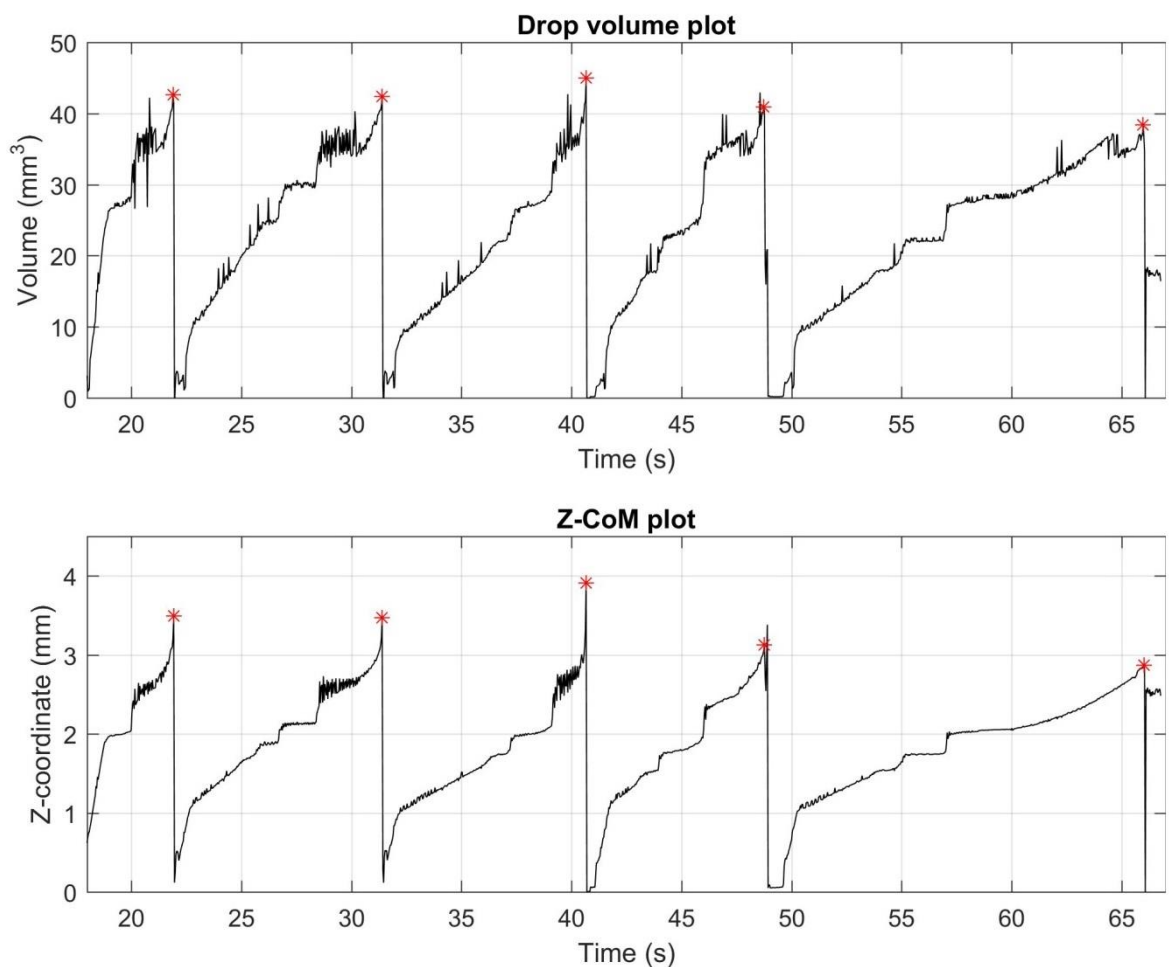


Figure 7.1.12: Drop z-coordinate mass dependence investigation¹⁷

Red – drop detachment point

When considering the restoring distance of the drop after detachment, it is possible to set two relationships that link the mass of the drop to its vertical location:

¹⁷ The disturbance in the graph is due to variation of the flow rate while recording the drop shape, and is part of the experimental regime

$$z_o = 0.133m_{res} \quad | \quad \text{for } m_{res} < 0.9 \text{ mm}$$

$$z_o = 0.1m_{res} \quad | \quad \text{for } m_{res} > 0.9 \text{ mm}$$

7.1.7

where: z_o – is the restoring vertical distance

m_{res} – residual mass

By applying one of those equations to residual mass, it is possible to identify the restoring vertical coordinate of the CoM location.

7.1.4 Horizontal behaviour

To investigate the horizontal behaviour of the drop, similarly to the investigation of the spring and damping constants, the attached drop was mechanically excited.

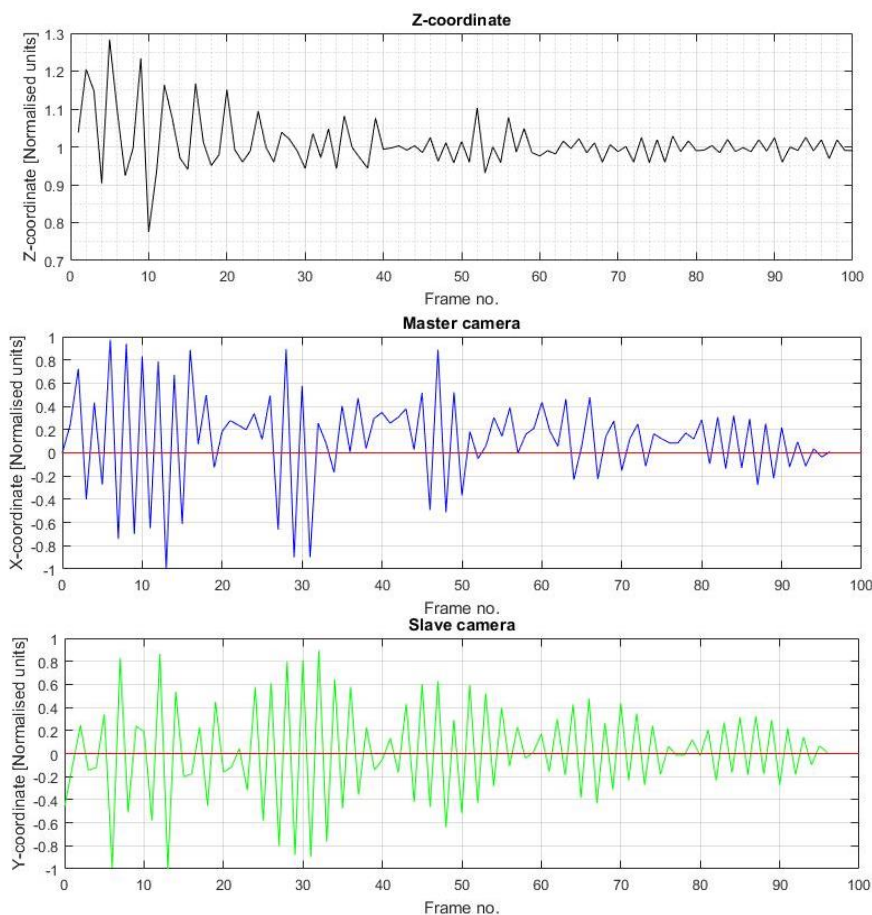


Figure 7.1.13: Horizontal vibration test

Black – vertical coordinate; **Blue** – “Master” camera horizontal coordinate; **Green** – “Slave” camera horizontal coordinate; **Red** – zero level;

Initially some time was given for a drop to settle down (around a few minutes). Then the nozzle was given a single, vertical tap, which resulted in drop excitation (Figure 7.1.13 –

Z-coordinate plot). The drop was left to settle down. The results were recorded from two sides allowing tracking the movement of the drop in 3-dimensional space.

Figure 7.1.13 shows a typical response of the drop. The units in the graph are normalised based on the mean value of the vertical CoM location for the z-coordinate and the maximum value of the amplitude offset for the x and y coordinates. The x-coordinate unit was chosen to be frame numbers (frame rate 1/30 s). The following can be identified from the graphs:

1. The excitation of the vertical coordinate provides no firm evidence of its natural frequency. As the data points are limited (due to the camera frame rate limitation), one cannot be sure about the waveform, due to sampling errors in accordance with Nyquist theorem. Similarly the horizontal vibrations, which also lack more frequent data points.
2. The “Master” camera is less sensitive, as mentioned earlier in the section, with correspondingly greater uncertainties.
3. Based on the points above it is hard to judge if the horizontal and vertical excitations are independent
4. Interestingly, even with the limited number of data points it is possible to confirm that horizontal excitations consist of two modes: the first is a pendulum-like swinging mode and the second is an amplitude modulation mode.

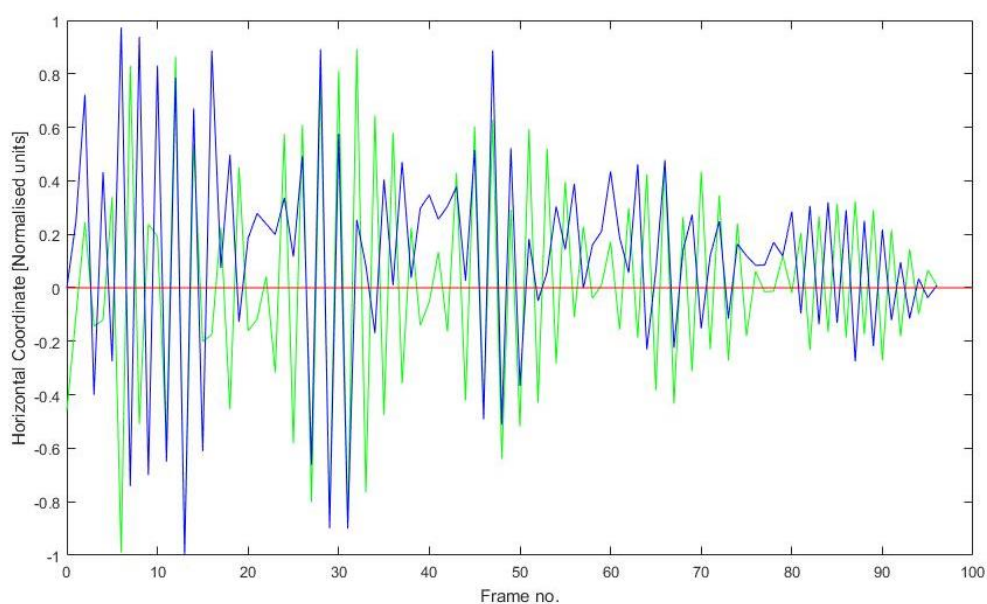


Figure 7.1.14: X and Y coordinate vibration test combined plot

Blue – “Master” camera horizontal coordinate; **Green** – “Slave” camera horizontal coordinate; **Red** – zero level;

When the results of both horizontal coordinates are overlapped and compared, there was no consistency found in the CoM swing mode (Figure 7.1.14). That again provides the evidence that it is impossible to estimate the oscillatory or behaviour pattern of the drop CoM. Nevertheless, it is clear that the drop movement is a pendulum-like swing.

On the other hand, the amplitude modulation can be investigated. It is hard to associate an amplitude modulation with the vertical motion, but it is noticeable that the swing mode persists for longer and has much higher variations (as a percentage of the initial disturbance) compared to vertical vibrations. The initial disturbance of the vertical vibration (as shown in Figure 7.1.13) disturbance was around 29% of the normalised location (the unit value for the z-coordinate is equal to ≈ 1.7 mm). After frame number 70 on the Z-coordinate plot (Figure 7.1.13), the variation is limited to 4% (corresponding to 0.068 mm). At the same time, the vibrations in the horizontal directions start with a disturbance of 0.4 mm and after the 70th frame still have roughly 50% of the initial disturbance (0.2 mm), which surpasses the amplitude of the fluctuations in the vertical direction.

The amplitude modulation was observed on several occasions, exhibiting a similar behaviour pattern (Figure 7.1.15). An analysis was attempted to characterize the modulating function; additionally, no evidence was found that the vibrations are mass dependent (similarly to the vertical oscillations). The calculated value for spring constant was equal to $1.275 \cdot 10^{-3}$ to $2.887 \cdot 10^{-3}$ mN/m for the mass range of 19.90 to 23.49 mg. The value for the damping constant for the similar mass range was calculated to be equal to $1.556 \cdot 10^{-3}$ to $2.091 \cdot 10^{-3}$ mNs/m, similarly with no dependency on the mass.

For the studies was used the sinusoidal wave of the form:

$$y_{AM}(t) = Ae^{-\gamma t} \cos(\omega t + \varphi) \quad \Bigg| \quad 7.1.8$$

where: y_{AM} – disturbance modulated amplitude

t – time

A – amplitude of disturbance

γ – damping coefficient

ω – oscillation frequency

φ – oscillation phase shift

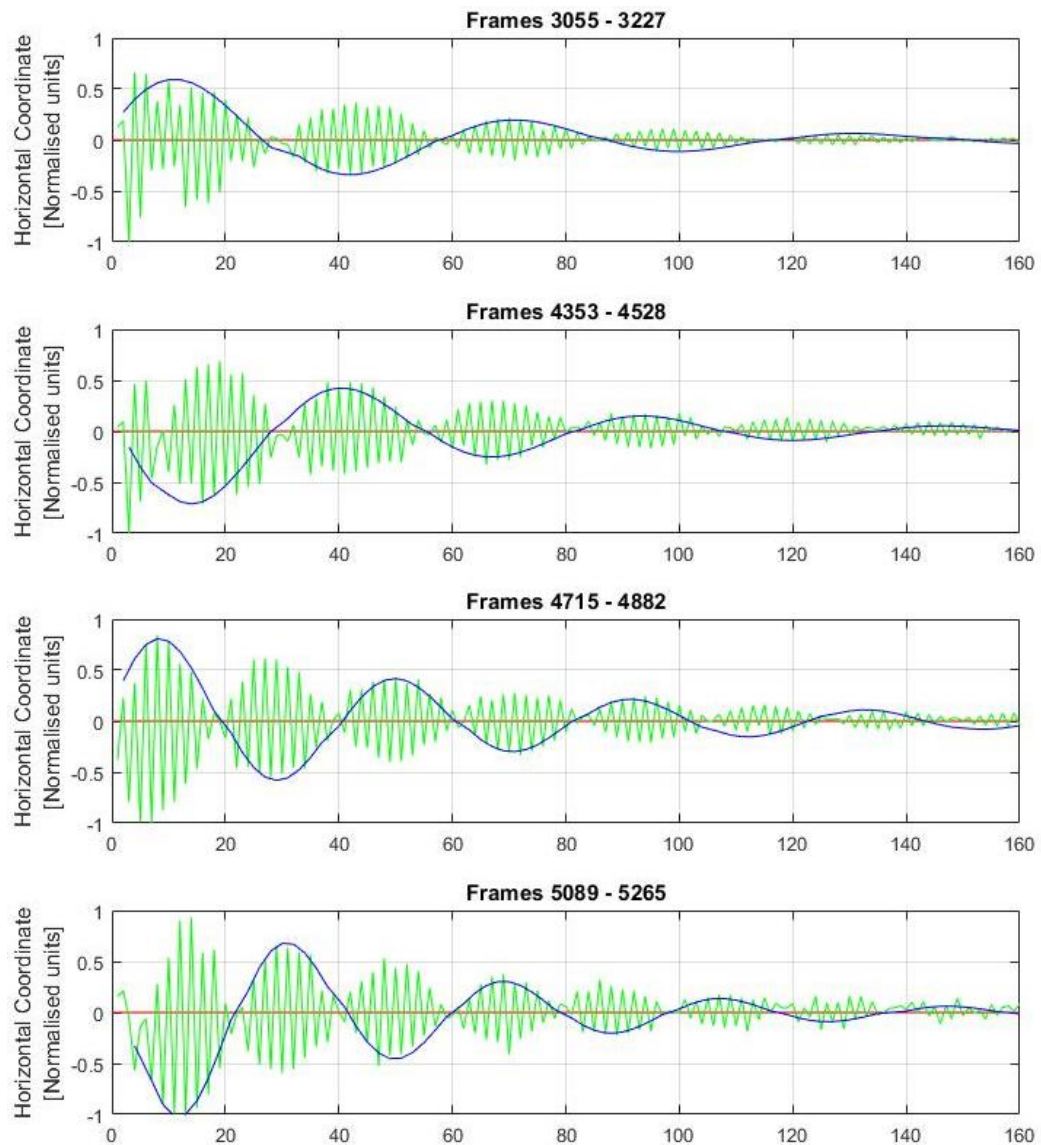


Figure 7.1.15: Amplitude modulated horizontal vibrations

Figure displaying four different tests; **Green** – “Slave” camera horizontal coordinate; **Red** – zero level; **Blue** – sinusoidal fitted curve

The sinusoidal wave was chosen to have the best fit with the peak values using “MATLAB®” basic functions. The results of the vibrations shown in the first and fourth sets of data (frames from 3055 and 5089 respectively) both show an acceptable fit. On the other hand, the results in the second and third data set produced visible errors (the second data set has errors at the beginning and the third has a mismatch in the last four

fluctuations); although it is open to interpretation. This raised another speculation that not only is the amplitude of the horizontal vibrations modulated but also the frequency of the modulation varies with the time.

To complicate the matter even more, it was observed on different occasions that in some cases there are no modulations and then the drop horizontal vibrations decay with normal exponential decay (Figure 7.1.16). It can be confirmed that this type of the oscillation exists over the similar mass ranges to modulated decay.

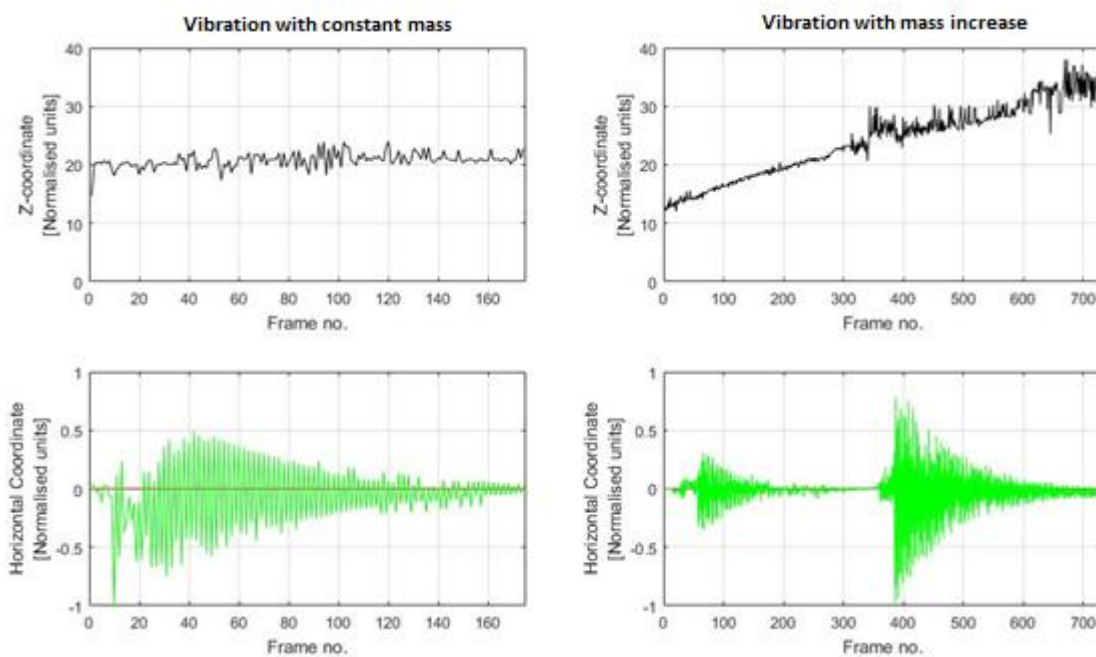


Figure 7.1.16: Standard damped vibrations in the vertical axis

Black – vertical coordinate; **Green** – “Slave” camera horizontal coordinate; **Red** – zero level;

7.2 Discussion of experimental results

To begin the analysis let us summarise what we know so far about the drop behaviour from the mathematical model and from the experimental results so far:

- Mathematical modelling
 - The mathematical model predicts that bifurcation regions will appear and collapse over all flow rates under study
 - The bifurcation region size increases in period range and flow rate range with an increase in flow rate

- In the approach to period jump the stability of the system decreases, which leads to the results that any disturbance will define an attractor point
- Similarly, in the approach to bifurcation the system is highly unstable and is heavily influenced by small disturbances in the system
- Experimental result analysis so far
 - Drop necking begins when the drop reaches a critical volume of 40.45 mm^3
 - Detachment can produce a secondary break-up where satellite drops with a mass much smaller than the critical mass and which occur within $1/10^{\text{th}}$ of a second after the main detachment
 - The residual mass can be of two types:
 - Normal residual mass, which is constant below flow rates of 115.3 ml/hr, and starts to grow after this flow rate with a dependence approximated by the linear equation: $V_{res} = 0.014\dot{V} + 1.857$
 - Wetting volume or zero volume which has a value of less than 1 mm^3 , appearing on average every 10^{th} drop (the actual likelihood was approximately 9%) over all flow rates
 - Post detachment, the following scenarios can occur:
 - Normal drops – these are drops whose development or volume increases with time and tends to follow a straight line with the slope of this line being proportional to the supply flow rate
 - Mid drops – they are drops that form at a much faster rate than the supply flow rate leading to rapid detachment. This is first encountered at flow rate of 120 ml/hr and it is consistently observed thereafter.
 - Jets – these are columns of fluid whose length exceeds the attachment diameter by a factor of 10 or more [14]. These are first formed at a flow rate of 178.1 ml/hr and then consistently observed thereafter.

This section provides an analysis of the experimental results with the help of a plot of period versus flow rate (Figure 7.2.2).

The bifurcation plot displays the time between drop detachments (i.e. drop periods) with respect to the flow rate. The development of the code was shown in subsection 6.4.2. A

different colour was introduced to allow for identification of how often each period is repeated, where darker shades represent value that repeat more often.

The first thing that stands out is the distribution of the results over the plot area. It is clear that there are two regions clearly identifiable at a flow rate of 120 ml/hr. Below this flow rate the drop periods concentrate along a single distinctive curve with the centre line identified by the concentration of darker red squares. Beyond this flow rate the drop period values becomes highly unpredictable with no well-defined real peaks in the distribution of period values.

This unpredictability is due to the chaotic nature of the flow and this specific point has been identified as the first major bifurcation point where the transition to a fully chaotic flow regime occurs. To demonstrate this process period maps are presented in Figure 7.2.1 and Figure 7.2.3 showing two flow rates prior to bifurcation. Figure 7.2.2 is a plan view of Figure 7.2.1 and is used herewith for ease of viewing. The following notation is used when referring to the plots:

- The return map is the period map where the following period is plotted against the current period
- The period sequence map is the period map where the current period is plotted against its dripping sequence

The plots before bifurcation exhibit stable dripping with minor noise in the system, which can be assumed, do not significantly affect the dripping behaviour.

For instance, a flow rate of 115 ml/hr has limited variation and the most repeated points do appear to focus close to a single line on the sequence map, concentrated near to a attractor (as seen on the return map). At the subsequent flow rate (117 ml/hr) it is possible to note similar behaviour, although the concentration of the most repeated values on the sequence map becomes a little wider, as predicted from the mathematical model as the system becomes less stable.

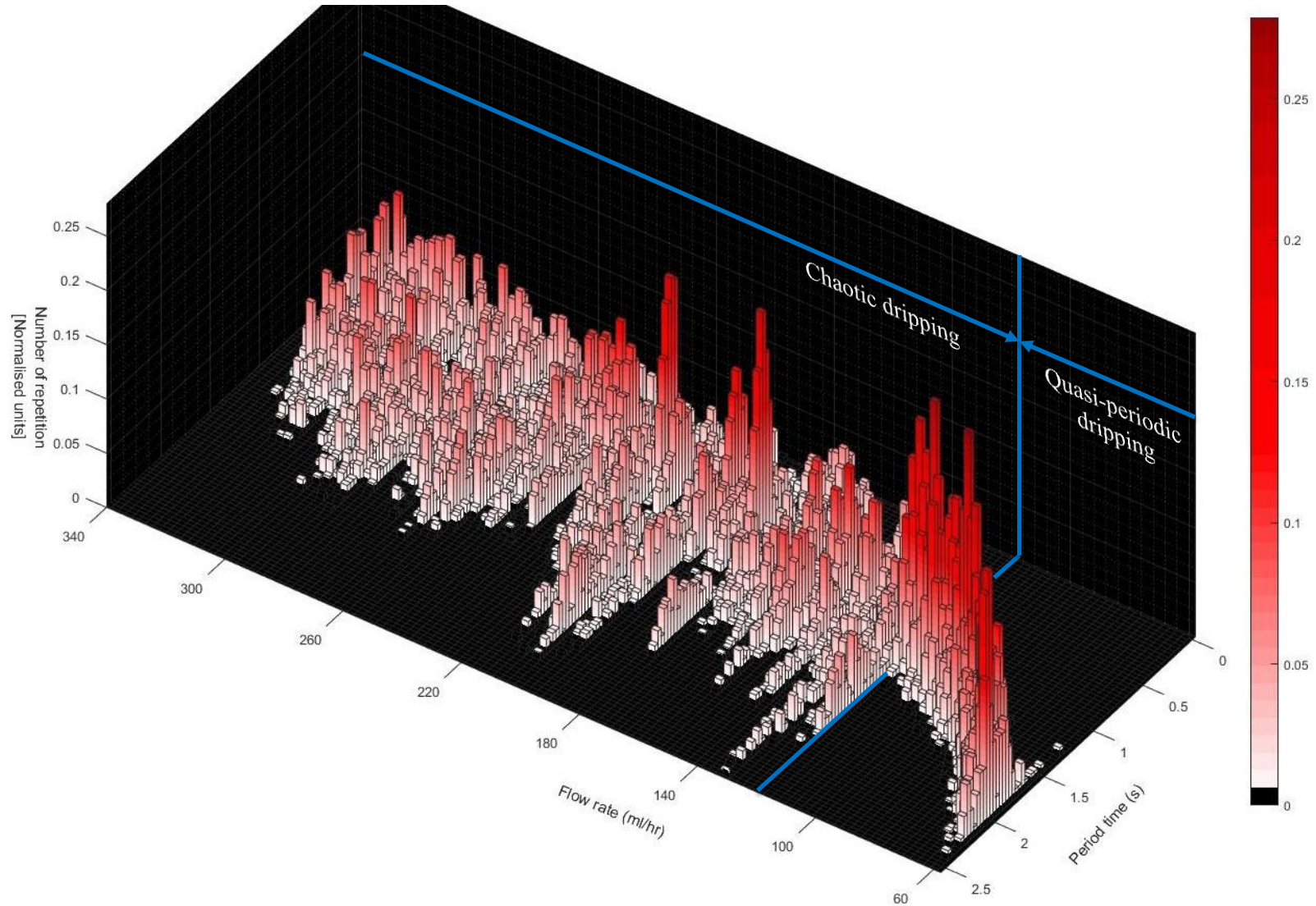


Figure 7.2.1: Period versus flow rate 3-D plot

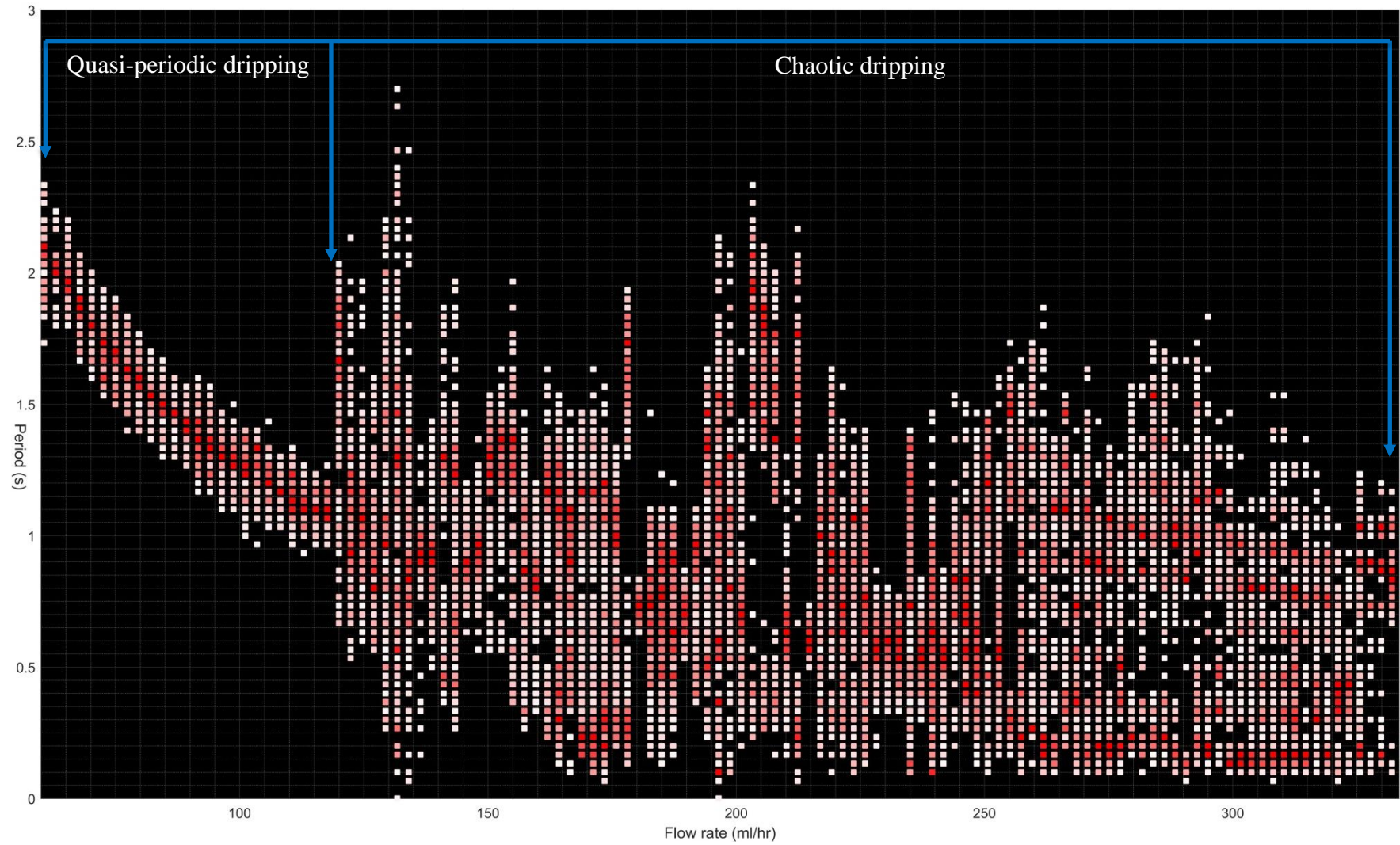


Figure 7.2.2: Period versus flow rate plot – plan view of Figure 7.2.1 for ease of viewing

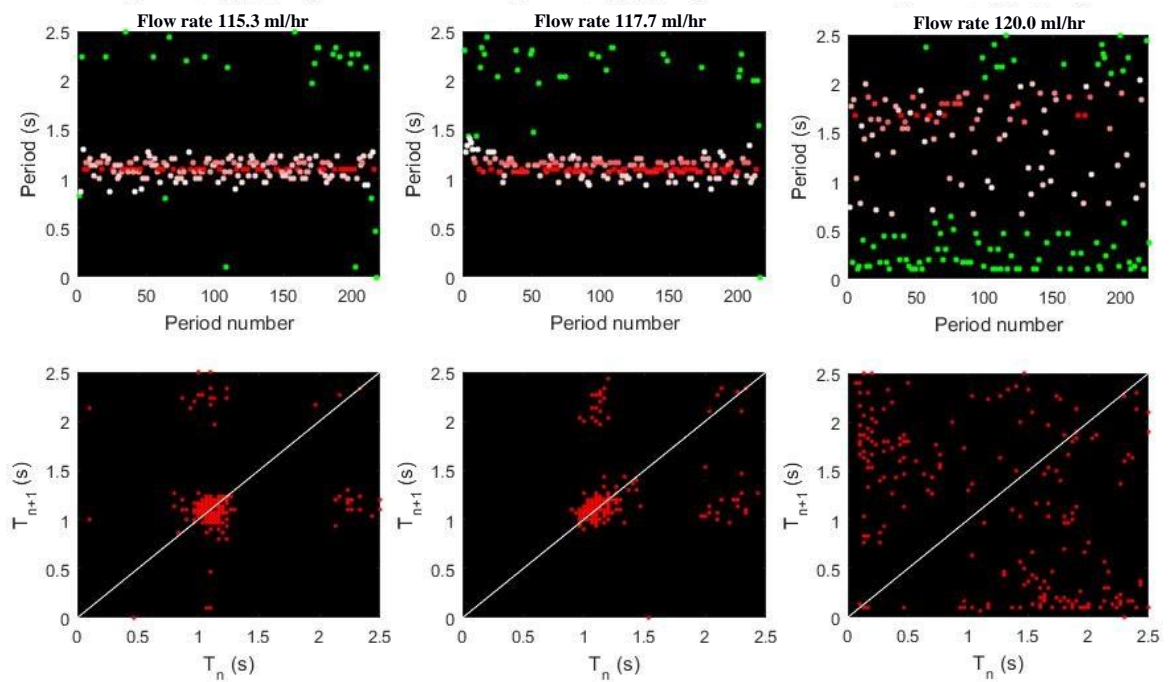


Figure 7.2.3: Transition from periodic dripping to chaotic dripping

Top plots – Sequence maps: *Shades of Red* – considered values; *Green* – other values;¹⁸

Bottom plots – Return maps: *Red* – data points; *White* – axis of symmetry

Entering bifurcation leads to a dispersion away from the line of symmetry on the return plot. It is possible to note that quite a lot of the points start to concentrate close to the axis on the return map, meaning that every second drop is a short drop. In other words it is a repetition of the major drops (albeit with a quite a large spread in period values) followed immediately by a single quick drop. In addition, the plot at 120 ml/hr shows a transition to increase in period length as seen in sequence map. The concentration of periods for the main drop has risen above 1.5 seconds (the bifurcation plot shows period values of around 1.7 – 2 s). Lower flow rates have a mean value of the detachment period of around 1.2 s. As reported earlier in subsection 6.5.2 this specific flow rate is the place of the first appearance of so-called mid-drops formation, where a drop following detachment is formed at a much faster rate (exceeding the supply flow rate), although the drop still detaches at the critical volume, then leading on to a drop to follow that will be formed at a much slower rate.

¹⁸ The values considered here are the values that fall within the influence region, as defined in subsection 6.4.2. hence other values are the values that have been left out due to lower repetition rates.

The following subsections will discuss these two regions separately (periodic dripping – subsection 7.2.1 and chaotic dripping – subsection 7.2.2). The return map displays only those data points that have repeated more than 10% of the maximally repeated data point. The colour scheme employed in the graphs is the following:

- Shades of red – less intense colour signifies less repeating values
- Green – identifies the points, which were left out of the bifurcation plot due to being outside the influence region (subsection 6.4.2).
- White line on the return maps – line of symmetry

7.2.1 Periodic dripping

Periodic dripping was identified in the region with flow rates between 60.6 – 120 ml/hr. This area consists of a distinctive profile where the most reoccurring period approximately follows, in general, a single profile.

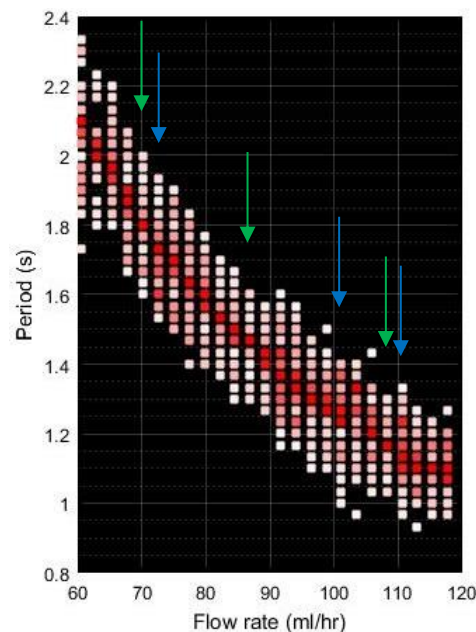


Figure 7.2.4: Quasi-periodic dripping period versus flow rate plot

Shades of Red – considered values; *Green* – strong attractor; *Blue* – weak attractors

The following flow rates will be considered as the basis for single period strong attractor dripping. The single period strong attractor is defined as the single point attractor, which with minor disturbances will always return the system back to stable dripping (at the same

point). In Figure 7.2.5 the most reoccurring period is clearly identified, with the values of other periods being much less frequent (as seen in sequence map).

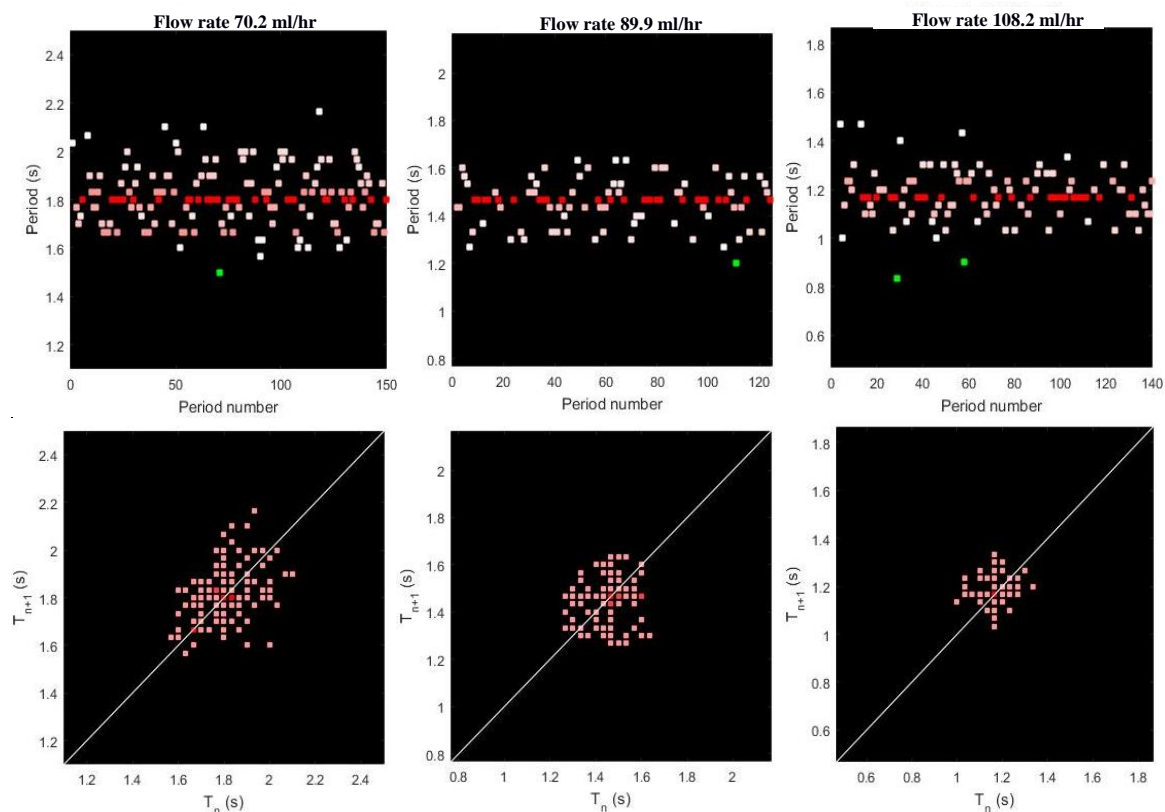


Figure 7.2.5: Single period strong attractor

Shades of Red – considered values; *Green* – other values; *White* – axis of symmetry

The return maps also identify the disturbance of the system and its response pattern. First, the wider the distribution of points the larger the disturbance of the system is. The sequence maps show that with a few anomalous values 108 ml/hr is the most stable flow rate with most periods densely concentrated around the attractor. The anomalies here are a few periods at the beginning of the experiment, which at a later stage – above a drop number of 60 – do not appear. Secondly, the extended shape of the data points along the $T_n = T_{n+1}$ line on the return maps signals that the response of the system is history dependent. Meaning that any initial distortion affects the set of following periods in like a linked chain. To explain this behaviour sequence map of the 70 ml/hr period is presented separately (Figure 7.2.6).

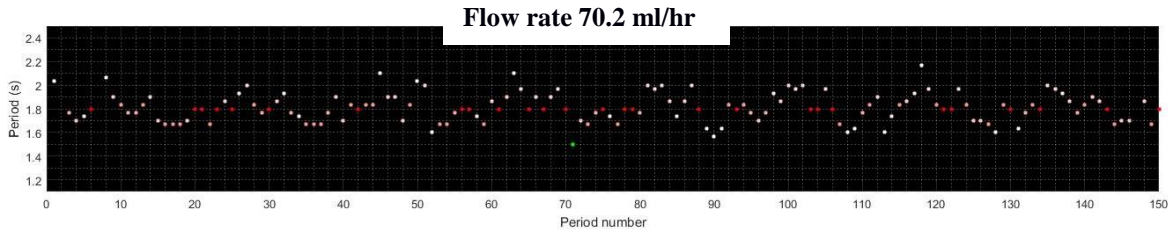


Figure 7.2.6: Sequence map of 70.2 ml/hr

Shades of Red – considered values; *Green* – other values;

In multiple instances in this plot it is visible how the period appears to follow a single curve (for example $n = 15 \rightarrow 19$ or $n = 113 \rightarrow 117$). History dependence provides here a measure of system stability. It is well understood that a disturbance in the system persists in any drop, but nevertheless those disturbances have minor effect and the dripping period continues to change along the line.

In the next figure (Figure 7.2.7) the system stability becomes weaker, leading to local bifurcation and period doubling.

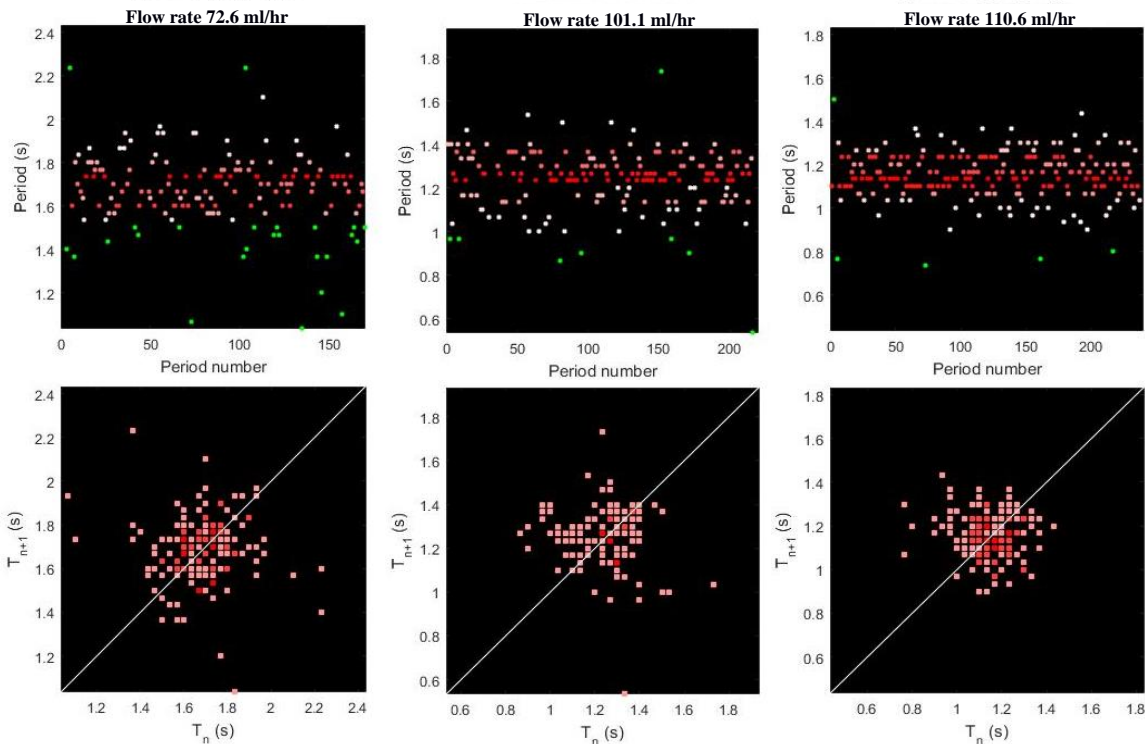


Figure 7.2.7: Single period region attractor

Shades of Red – considered values; *Green* – other values; *White* – axis of symmetry

The local bifurcation happens at the point where the attractor is weak creating a region which as an attractor rather than a single point. In the associated pattern, there is a high

disturbance in the results but the majority of the periods still belong to the attractor region, as seen on the return maps. Periodic history dependence still exists but it is much less clear. To summarise, the periodic dripping region consists of a strong single-point attractors as well attractor regions, which lie close to each other. The system is considered to be stable throughout but may present local period doubling. The scale of these bifurcations is small and lasts over approximately 4 ml/hr flow rates. There is no unit structure repetition between the strong single-point attractors and regional attractors that can be identified. The mathematical model predicts that the bifurcation regions appear below the predicted chaotic regions (Figure 4.3.4). Similarly, weak attractors, hence local bifurcation can be expected to have a similarity with the mathematical model of bifurcation in the predicted periodic region (subsection 4.3.2), but the similarity of its nature cannot be fully confirmed due to camera frame rate limitations. The frame rates limit the precision of determination of the drop detachment time. The dripping period does fluctuates for each flow rate due to the nature of the physical system, which as always is expected to have noise, but the variation is limited and it is attracted to a single region or point. In some cases, this leads to a history-dependant dripping period, where the following set of drop periods follows a periodic curve. The noise in the system does sometimes lead to the development of satellite drops, slow drop development (which then gives long periods) or detachment of the drops prior to reaching the critical mass (which also affects the period) but as shown in the previous chapter (subsection 6.4.2) these affects are limited to 20% of the detached drops across the periodic dripping region.

7.2.2 Chaotic dripping

This section now continues with an analysis of the chaotic region. The significate feature of the graph is the wide variation in the data. Nevertheless, the variation has a pattern that

will be explained. The graph exhibits a repetition of regions with stable dripping followed by chaotic dripping at each stage.

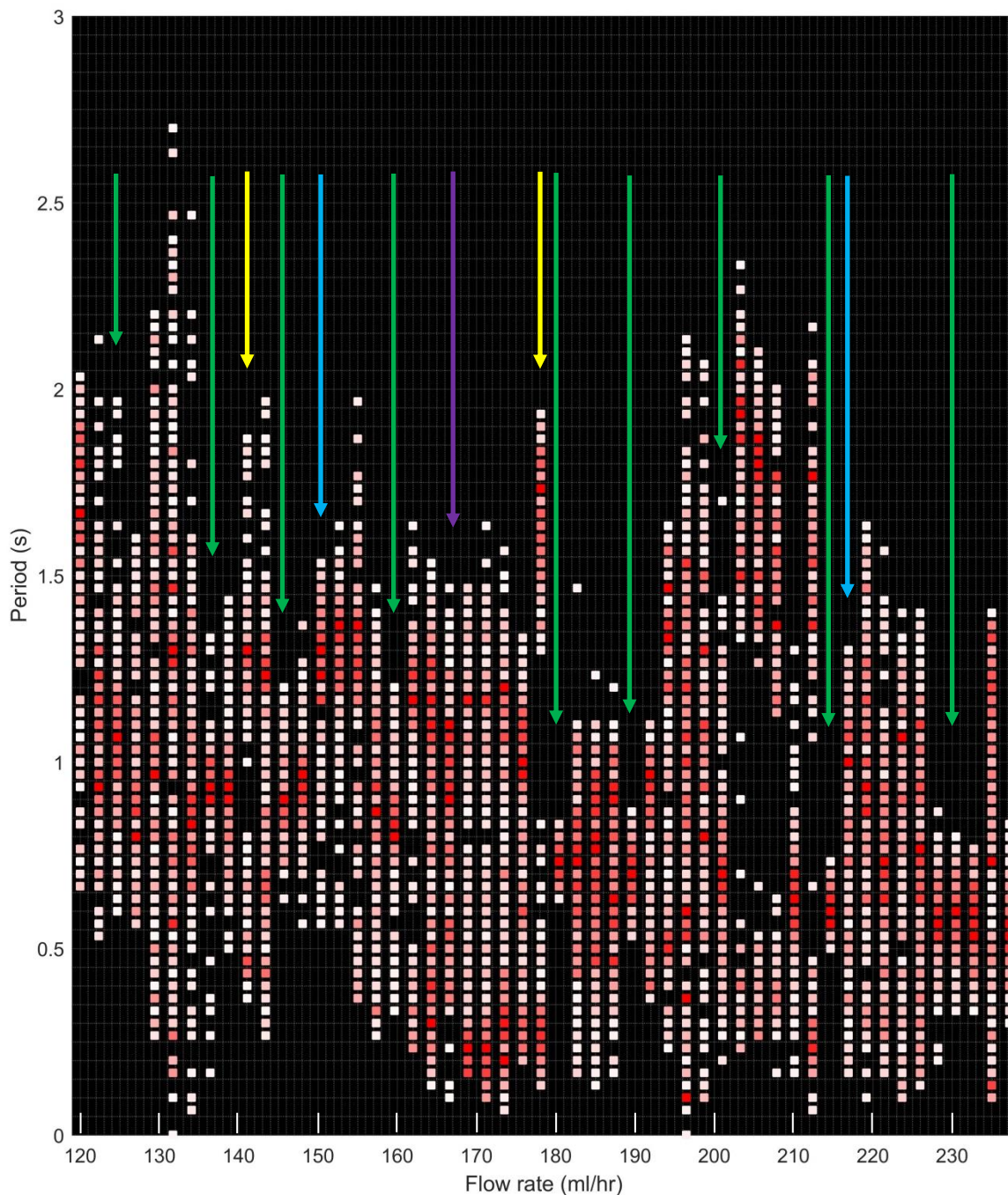


Figure 7.2.8: Chaotic dripping bifurcation plot No.1

Green – Single period weak attractor; **Blue** – Period jump; **Yellow** – Limit cycle attractor
(quasi-periodic dripping; **Purple** – strange attractor

Across the specific experimental region, it was noted that the chaotic region exist in the range of flow rates between 120 to 332.1 ml/hr. In this region, it is possible to identify: limit cycle attractors (termed here as regional attractors, unstable regional attractors and

double attractors), strange attractor, and period jumps (Figure 7.2.8 and Figure 7.2.9). The repetition of a transition from periodic to non-periodic regions was predicted by the mathematical model. Firstly, the mathematical model predicts that the bifurcation regions will repeat, with a periodic dripping region in between. Secondly, the repetition should have some sort of self-similarity in the bifurcation regions. In the experimental data this is not the case and the difference in the experimental results and the mathematical model are relatively obvious.

The bifurcation regions in the experimental data show that there is no specific pattern in either its size (the flow rate region across which the bifurcation persists) at which flow rate it occurs, nor in the amplitude of the data points in the bifurcation regions. An example of this last lack of correlation is clearly identified by comparing the bifurcation regions in the ranges 180.4 – 189.6 ml/hr and 159.7 – 180.4 ml/hr.

The points where the bifurcation plot converges toward a single attractor can be identified in the previous figures by looking for the flow rates where the most repetitive points (shaded darker red) concentrate around a single point (identified by the green lines in Figure 7.2.8 and Figure 7.2.9). The sections between these points are bifurcation regions, which repeat with no dependence on the flow rate, and they have a different development of the bifurcation regions. For example, the first bifurcation region starts at 120 ml/hr and finishes at 124.7 ml/hr, with a period jump followed by a bifurcation region with no definite attractor, collapsing into a weak attractor region. The second bifurcation region starts at 124.7 ml/hr and finishes at the flow rate of 136.4 ml/hr with complete bifurcation into multiple regions and attractors that don't have related locations (and are not located locally to each other) across the flow rates in the region. The bifurcation region that follows (with flow rates from 136.4 to 145.7 ml/hr) goes through a weakening of the single region attractor towards a more unstable flow rate, followed by a chaotic region with identifiable attractors which continues until the collapse of the bifurcation.

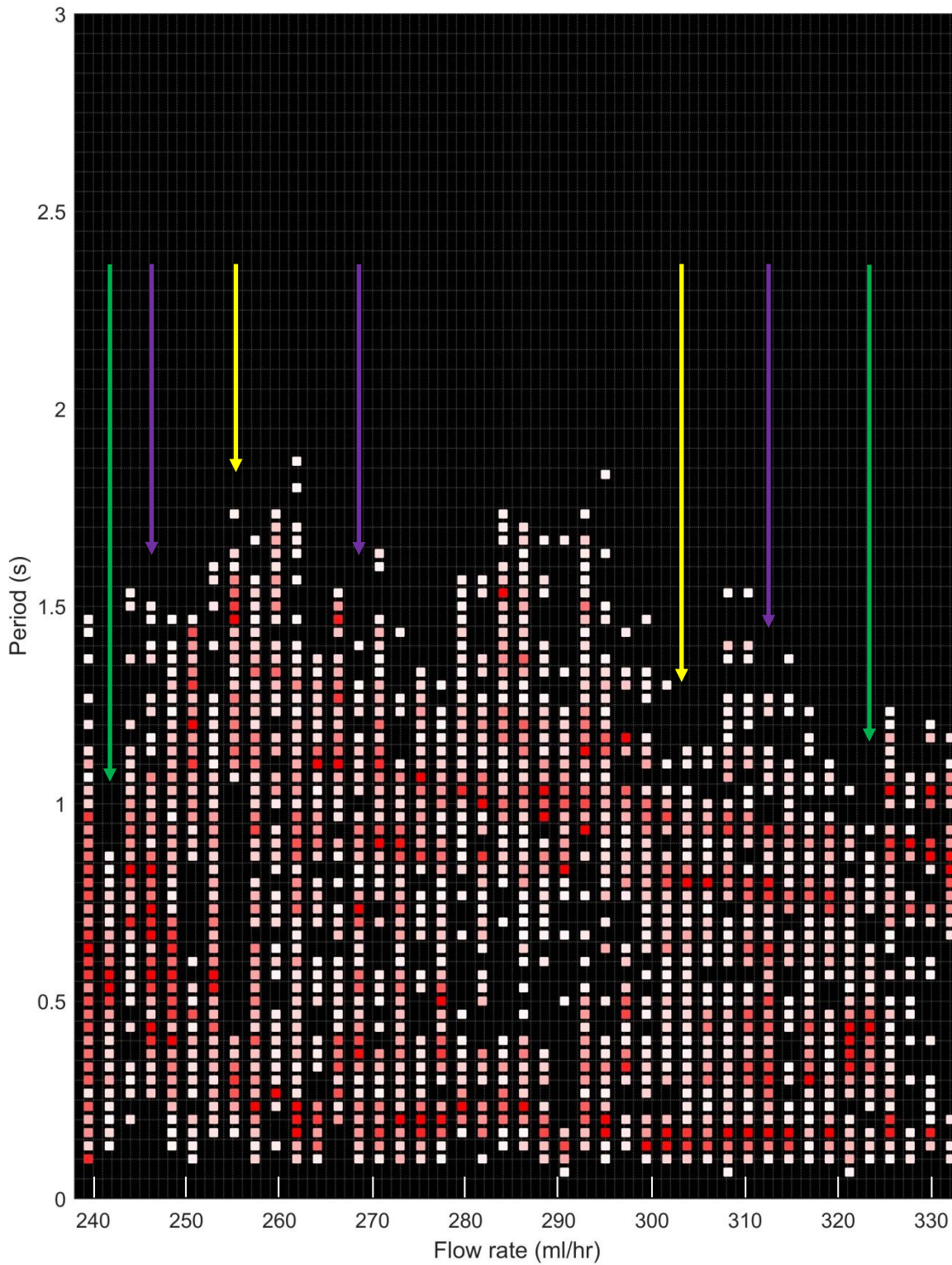


Figure 7.2.9: Chaotic dripping bifurcation plot No.2

Green – single period weak attractor; *Yellow* – Limit cycle attractor, quasi-periodic dripping;

Purple – strange attractor

One can argue that the exact value of the start (or end) of bifurcation could be missed, falling between the flow rate steps and this could lead to it not being identified in the experimental data. However, even if this is the case the localisation of the data points

should be observed, and this should allow for the identification of different bifurcation regions. Example of this can be seen at a flow rate of 252.9 ml/hr (Figure 7.2.9)

The studies here of the experimental data will begin with an analysis of the single point or area attractors. The terminology used here is significant. The single region attractor is the range of the detachment time where the drops detach most often. The detachment periods are close to each other (sequence map – Figure 7.2.10) and are concentrated in a single area around the line of symmetry on the return map. The detachment periods are clustered densely around the single region attractor, with insignificant variation (a few detachment periods are far off – Figure 7.2.10). The insignificance of these removed periods can be demonstrated by the quick return of the next dripping period back to the region of influence of the attractor.

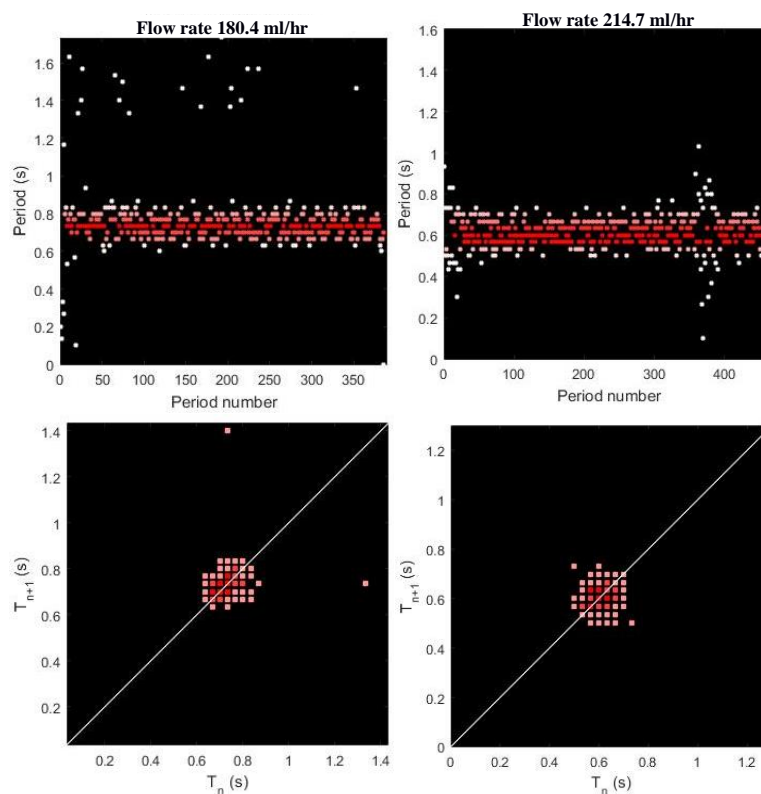


Figure 7.2.10: Single region attractor

Shades of Red – considered values; *White* – axis of symmetry

The flow rate is increased and the variations start to build up (Figure 7.2.11). The sequence map shows that the variations are now wider (for example at a flow rate of 230.5 ml/hr a variation of 0.5 s reached, based on main group of periodic data points: between 0.3 – 0.8),

but the return map continues to have a similar pattern with a concentration of the most repeated points close to the line of symmetry.

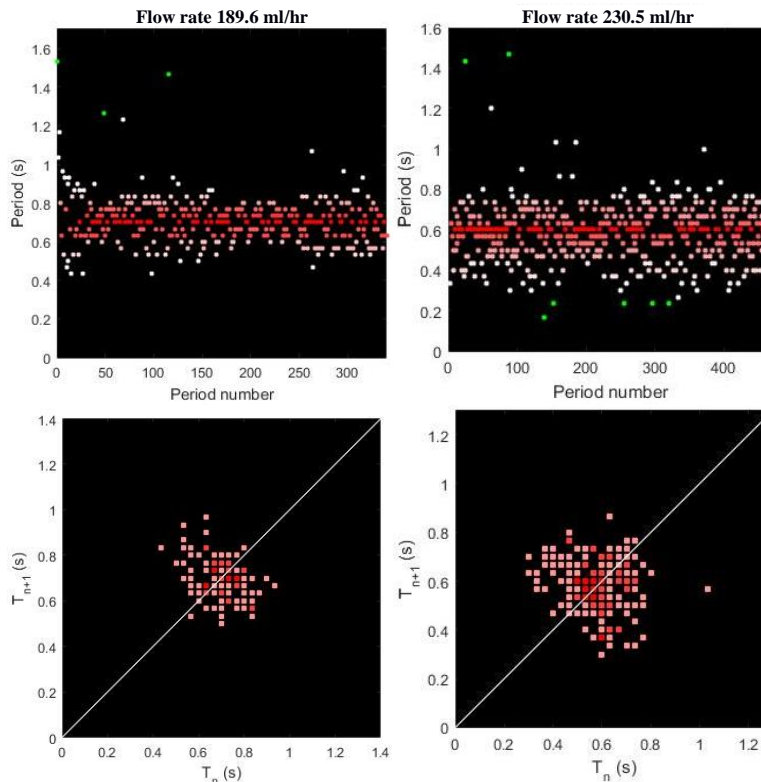


Figure 7.2.11: Single region attractor with high disturbances

Shades of Red – considered values; *Green* – other values; *White* – axis of symmetry

In the following stage, the attractor becomes unstable (Figure 7.2.12) and develops from a region attractor into unstable dripping (or unstable single region attractor). The unstable attractor appears at the flow rates in between the single region attractor and weak attractor (Figure 7.2.13), and can be characterised by dripping which starts with some stability but time develops into unstable dripping. A single region weak attractor is in some ways similar to a single region attractor, but with a much wider variation of period, yet it is still concentrated around the line of symmetry in the return map.

The sequence map in the following figure is a good example of unstable attractor type of behaviour. It is possible to notice that at the start of the experiment dripping occurring within a single region but later the detachment periods of the drops started to diverge from the attractor region, with the variation in periods growing bigger.

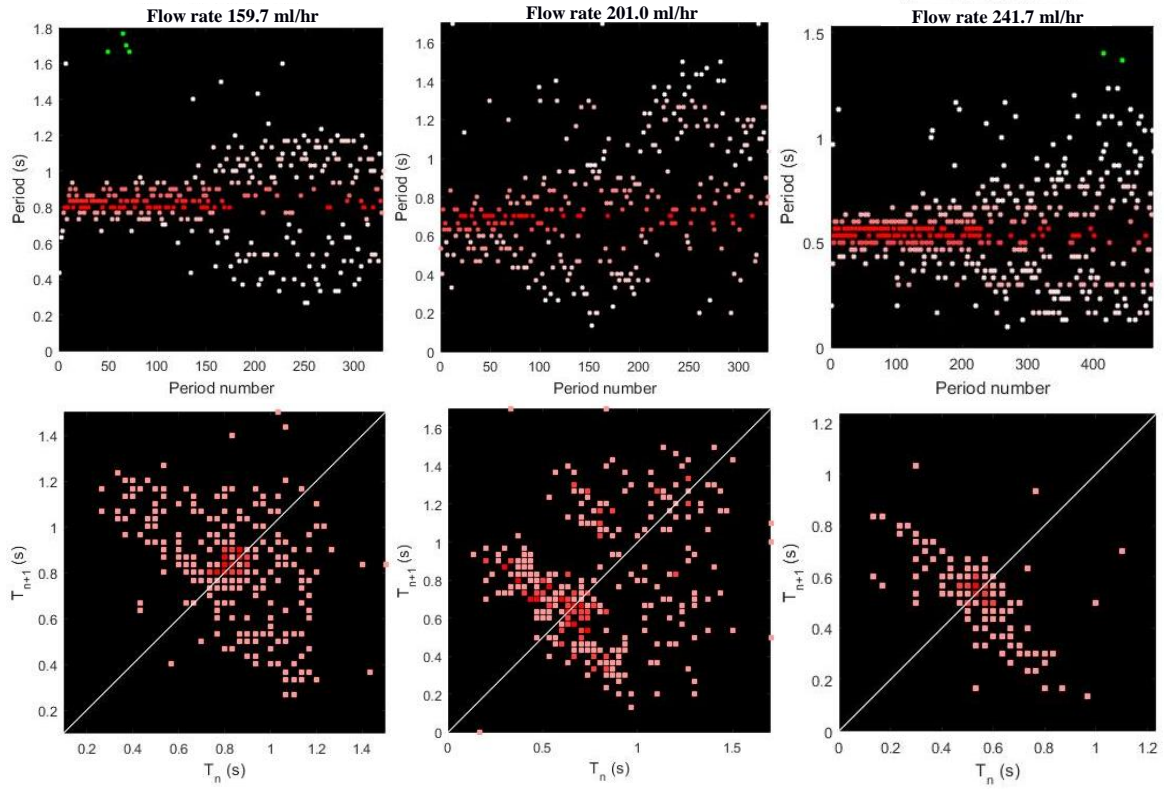


Figure 7.2.12: Unstable single region attractor

Shades of Red – considered values; Green – other values; White – axis of symmetry

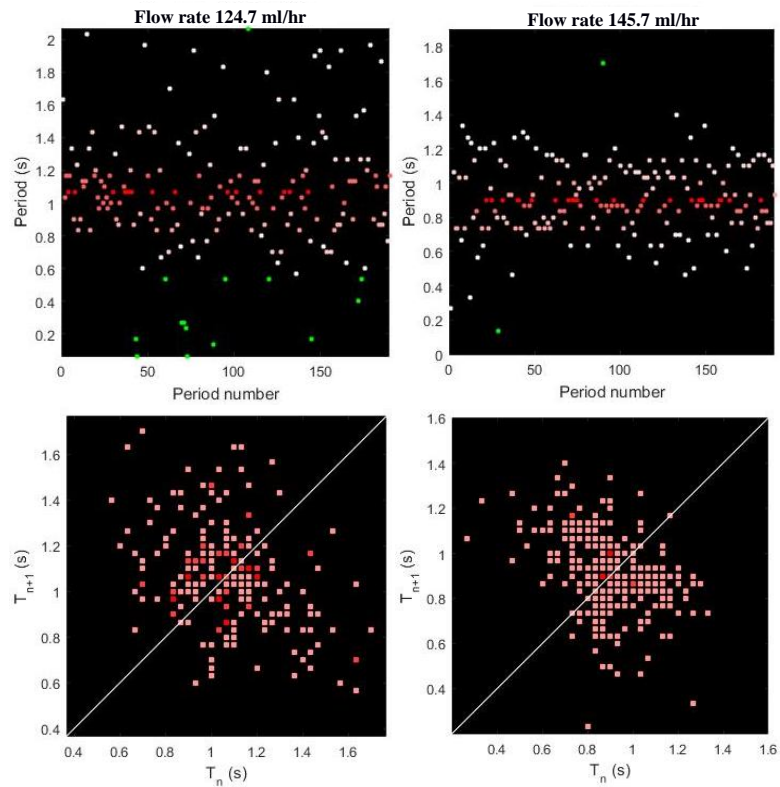


Figure 7.2.13: Weak single region attractor

Shades of Red – considered values; Green – other values; White – axis of symmetry;

In the associated return maps, depending on how close the flow rate number is to a bifurcation point, the attractor weakens. A flow rate of 201 ml/hr is so close to a bifurcation point that the attractor cannot be defined any more as a regional attractor with the location of the most repeating points being well distributed. Similarly, to flow rates which are just past the bifurcation point (Figure 7.2.13).

It is speculated that each bifurcation range develops from a single region attractor, followed by a single region unstable attractor, followed by a single region weak attractor. The speculation here follows from the bifurcation pattern in the mathematical model (Figure 4.3.9 and Figure 4.3.10 – which indicates a single attractor weakening and then leading to bifurcation), as well as the expected development of the attractor with an increase in the flow rate. It is clear that the variations in the period will grow with increasing flow rate, leading to the attractor becoming weaker, which should then lead to a wider attractor region and bigger variations. The next step should be a transition to bifurcation, where the attractor becomes unstable or ceases to exist. After the transition has occurred, the behaviour becomes chaotic and highly irregular. Unfortunately this remains at present only speculation since all of these types of behaviour have never been identified in a single continuous set of flow rates, was although they have been identified at different flow rates in bifurcation plot. The investigation of the unstable single region attractor continued, with a prolonged experiment at a flow rate of 323.7 ml/hr (Figure 7.2.14).

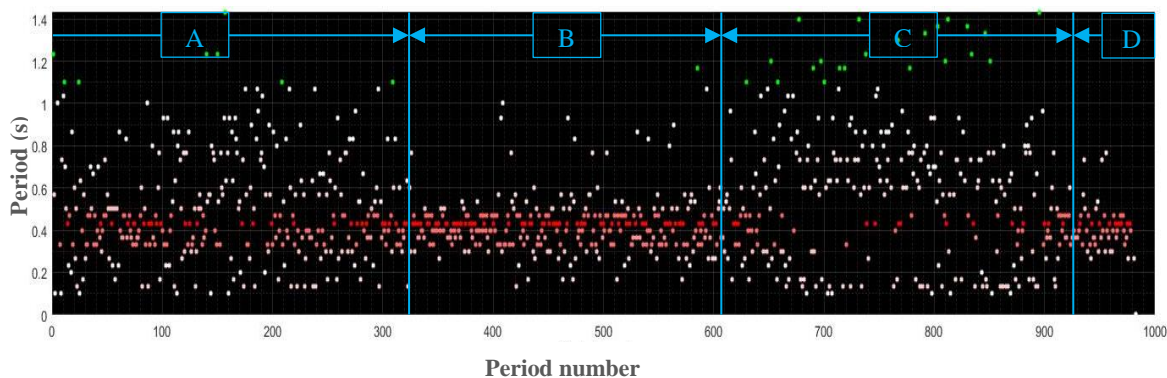


Figure 7.2.14: Sequence map of 323.7 ml/hr
Shades of Red – considered values; *Green* – other values;

Interestingly, the results showed that four different regions can be identified (marked A – D). The first region can be classified as a region of weak single region attractor. As seen from the return map (Figure 7.2.15) for that region it does have similarities with a flow rate of 124 ml/hr in Figure 7.2.13. Region B, on other hand, is quite well defined as a single region attractor with minimal variations (similar to 189 ml/hr in Figure 7.2.11). More interesting are the region that follows. Region C completely bifurcates and has multiple attractors (strange attractors) where no definite trajectory for the following drop detachment period can be identified. Nevertheless, after some time this region collapse and the periods converge back to limit cycle attractors (regional attractors).

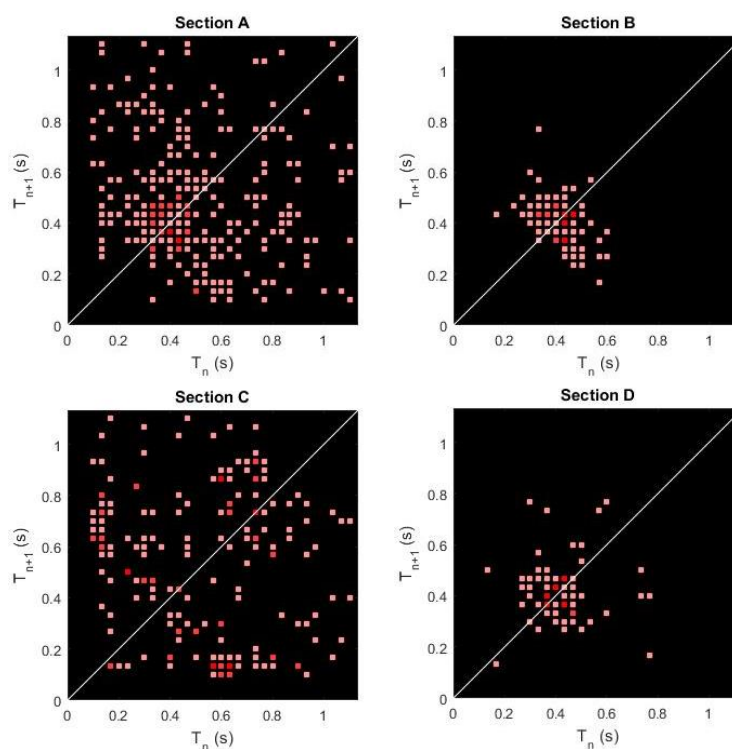


Figure 7.2.15: Return maps a flow rate of 323.7 ml/hr

Shades of Red – considered values; *White* – axis of symmetry

Previously it was noted that in some cases bifurcation leads to the development of period jump, which in simple term is a sudden change in the periodic dripping interval compared to previous flow rates. The chaotic region in the period versus flow rate plot (Figure 7.2.8 and Figure 7.2.9) is no exception to that (Figure 7.2.16).

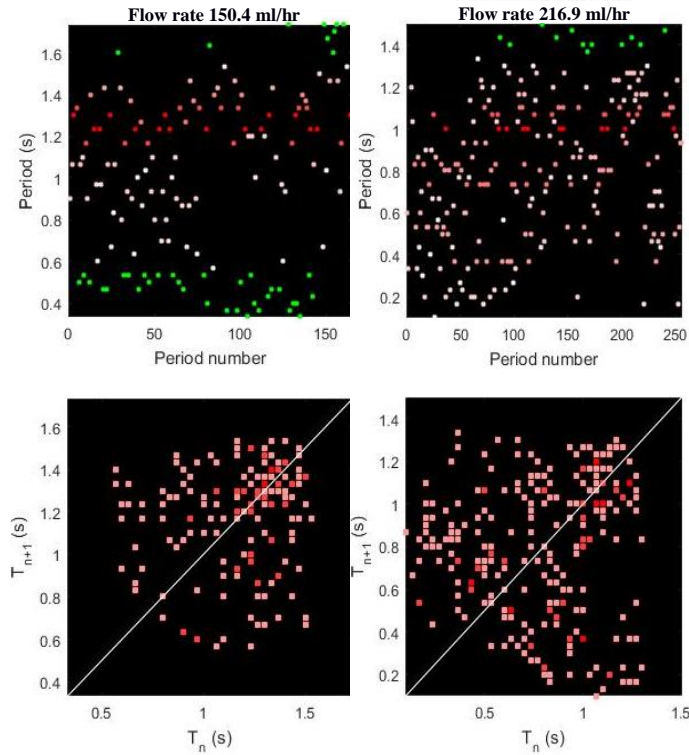


Figure 7.2.16: Period jumps

Shades of Red – considered values; *Green* – other values; *White* – axis of symmetry

In most cases, the period jump is associated with strange attractors, as the behaviour of the drop becomes increasingly unpredictable. This can be identified from the return maps where the concentration of most repeating points is distributed across the plot.

The appearance of the period jump has a complicated nature, which requires additional study. The fact remains that the dripping tap over a large range of data should have an average period value that can be estimated as V_{crit}/\dot{V} (which in the cases of the flow rates above was calculated and confirmed to be equal to 0.97 s and 0.67 s respectively). At the same time the most periods, repeating most often are located around 1.3 s for a flow rate of 150 ml/hr and cannot even be clearly identified for the 216 ml/hr plot. The proposed idea relies on the assumption that the variations in the dripping time are so high that new attractors are created, which can either be limit cycle attractor types (e.g. at a flow rate of 150 ml/hr) or strange attractor types (e.g. for 216 ml/hr). This proposal has some degree of confirmation (Figure 7.2.17).

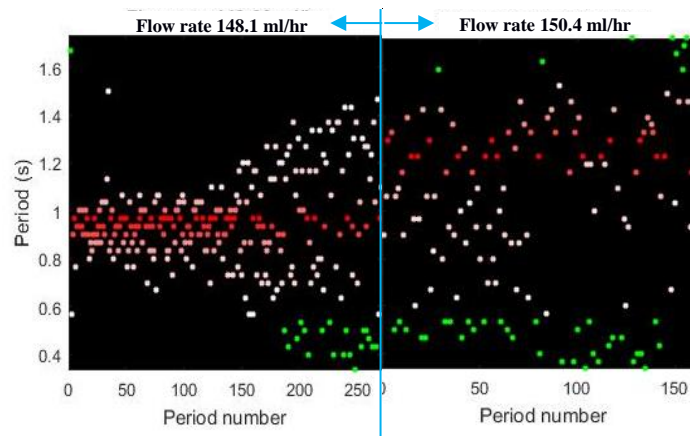


Figure 7.2.17: Period jump development

Shades of Red – considered values; *Green* – other values;

In Figure 7.2.17 two consecutive flow rates are scaled to match the period axis size and merged together. The flow rate on the left of the figure has an unstable regional attractor nature (similar to that shown in Figure 7.2.12) and the flow rate on the right represents the limit cycle attractor of the period jump type. What is observed is that the periods at the flow rate of 150 ml/hr appear as a continuation of the previous flow rate. It already been demonstrated (Figure 7.2.14) that the unstable regional attractor does jump between several types of limit cycle attractors, and the concept proposed here is that if the disturbance of the unstable regional attractor is increased by increasing the flow rate this will lead to a completely different type of attractor (either a weak regional attractor – Figure 7.2.15 section A, or a strange attractor – Figure 7.2.15 section C).

Another form of limit cycle attractor is the periodic attractor, where the periods repeat in a specific order (Figure 7.2.18). These attractors can be identified as data points concentrations in phase space (i.e. the return maps). The point concentration is highly dependent on the dynamic stability of the system. For example it is notable that a flow rate of 141 ml/hr has two strong regions (the first with approximate coordinates of [0.5, 1.3] and the second with [1.3, 0.5]). The symmetry in those coordinates identifies the consistent repetition of those periods hence the system is of the limit attractor type. Noise in the system is also observable, with many points distributed outside those regions.

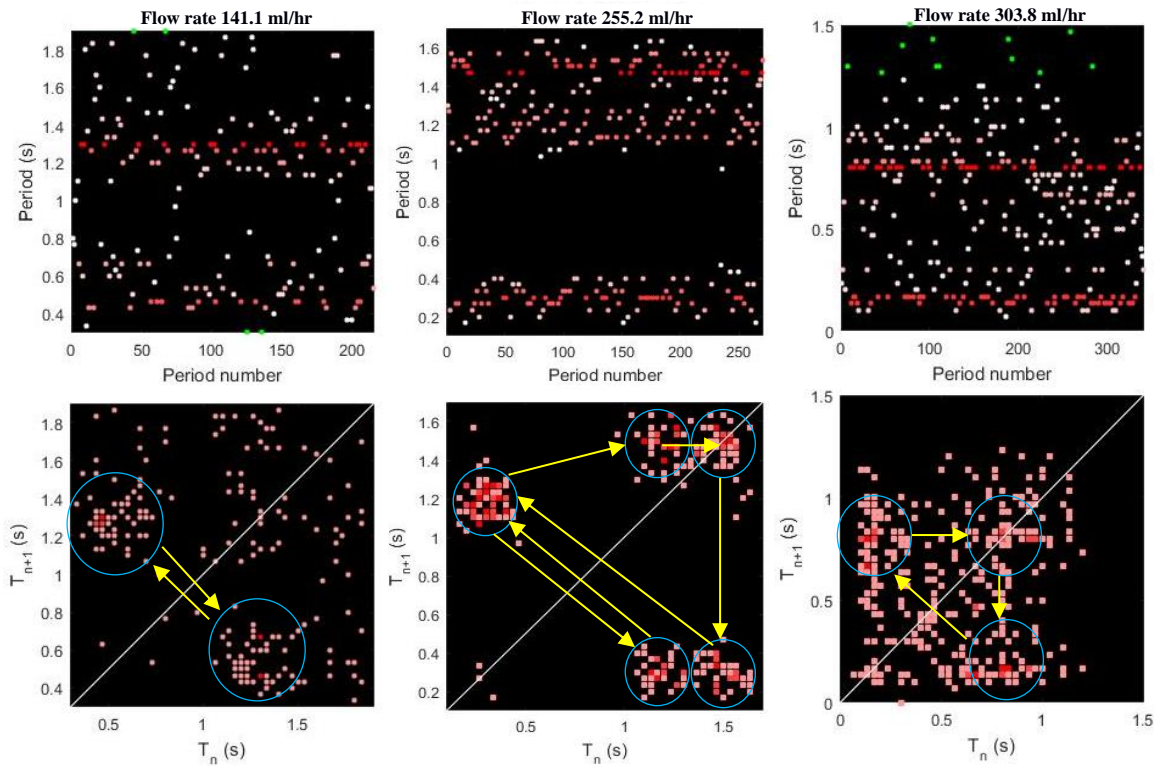


Figure 7.2.18: Limit cycle attractors – periodic attractors

Shades of Red – considered values; *Green* – other values; *White* – axis of symmetry; *Blue* – identified limit cycle attractors; *Yellow* – limit cycle change direction

The system noise can grow (at a flow rate of 303 ml/hr), and can lead to nearly unrecognisable attractor regions. The flow rate of 303 ml/hr has 3 regions (still due to disturbance of the system remains arguable) with coordinates that tend to repeat themselves in the order $[0.2, 0.7] \rightarrow [0.7, 0.7] \rightarrow [0.7, 0.2]$. If the disturbance are reduced, it becomes possible to see a much clearer picture with even more limit cycle attractors (5 for a flow rate 255 ml/hr) with the following repetition cycle $[1.2, 1.5] \rightarrow [1.5, 1.5] \rightarrow [1.5, 0.3] \rightarrow [0.3, 1.2] \rightarrow [1.2, 0.3] \rightarrow [0.3, 1.2]$.

In the strange attractor region (Figure 7.2.19) that was encountered in results shown previously in Figure 7.2.14 section C and in Figure 7.2.16 at a flow rate of 216 ml/hr, it was noted that the sequence map has a high level of variation. The period map shows a wide distribution of data points, with no identifiable pattern.

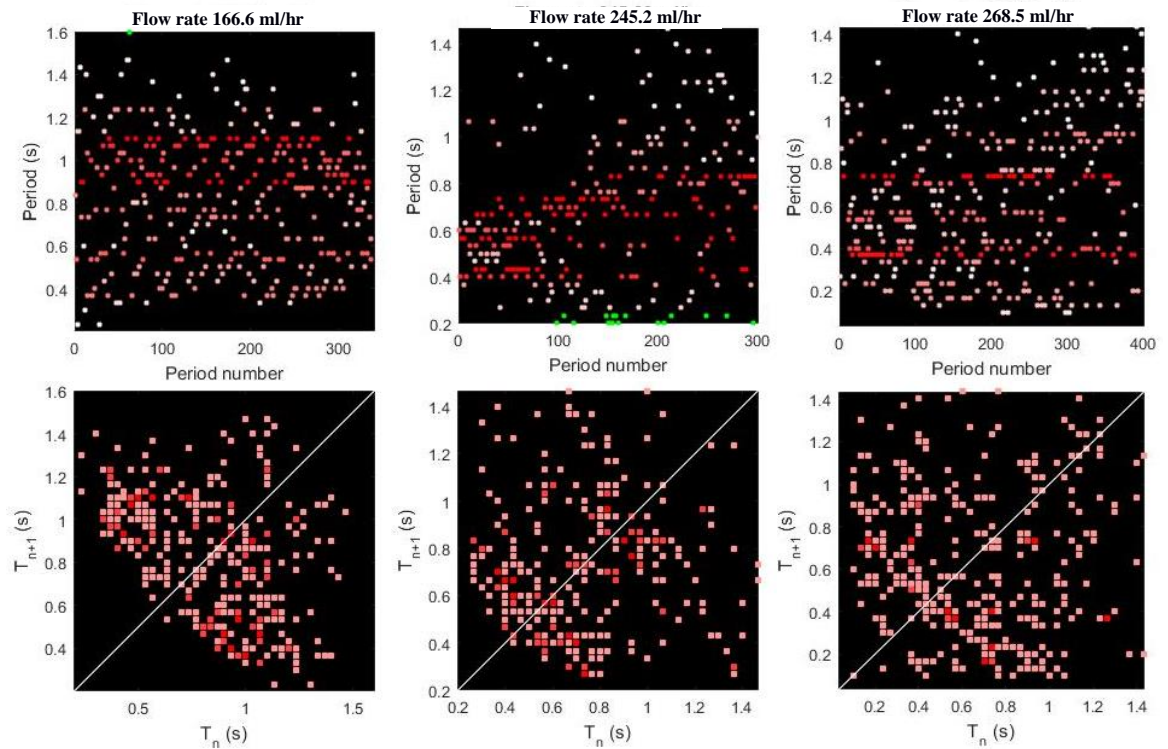


Figure 7.2.19: Strange attractors

Shades of Red – considered values; *Green* – other values; *White* – axis of symmetry;

7.2.3 Summary of experimental results

Previously in sections 6.5.2 and 7.1 the experimental results were presented. Firstly, results associated with the Mass-Spring-Damper model were presented, followed by an analysis of the dripping pattern. In addition to that, in subsection 6.5.2 different types of dripping behaviour were presented. Now it is possible to combine everything together and outline the process based on these experimental results.

The initial flow rate for the investigation was equal to 60.6 ml/hr. At this flow rate, the dripping is periodic with a single point attractor. The experimental set-up was not free from noise, as post-processed results have shown. It was possible to identify that the dripping pattern varies but stays close to the attractor point. In addition, if the drops are perturbed away from the attractor, the periods follow a trajectory that appears itself to be periodic, and this further defines the system as history dependent.

The drop development here goes from steady growth with minor disturbances which are quickly damped if the drop mass is below 20.27 mg. Prior to this point the drop undergoes a shape change from convex to concave. The drop location has a linear dependence on its mass. Beyond this point, the drop starts to exhibit some strong variations in the CoM location if disturbances due to systems noise are present. The system becomes underdamped just beyond this threshold value, until another threshold value of 25.25 mg is reached when the drop behaviour becomes overdamped. When the drop reaches the critical mass of 40.41 mg then necking process begins. The corresponding critical distance, where necking starts is equal to 3.047 mm. In some cases, dripping produces satellite drops that were detected in the experimental results, but the number of these is quite low. Satellite drop formation was predicted by Zhang [18] to form when the parameter $S < 0.0125$, which is defined by Equation 2.2.5 ($S = We \cdot Bo^{0.3921}$). From this relationship, it is possible to calculate the flow velocity at which the satellite drops should form:

$$S = We \cdot Bo^{0.3921} = \left(\frac{\rho d v_o^2}{\sigma} \right) \cdot \left(\frac{\rho g d_o^2}{2\sigma} \right)^{0.19605} \quad \left| \quad 7.2.1 \right.$$

where: $We = \rho d v_o^2 / \sigma$ – Equation 2.1.1

$$Bo = \sqrt{\rho g d_o^2 / (2\sigma)} \text{ – Equation 2.2.2}$$

ρ – density of water (assumed to be 1000 kg/m³ for this calculations)

d – inner diameter of the nozzle (measured to be 0.99 mm)

d_o – outer diameter of the nozzle (measured to be 2.00 mm)

v_o – flow velocity

σ – surface tension (assumed to be 1 mN/m)

g – acceleration due to gravity (assumed to be 9.81 m/s²)

When the equation above is rearranged to find velocity, it becomes:

$$v_o < \sqrt{\frac{0.0125\sigma}{\rho d} \cdot \left(\frac{\rho g d_o^2}{2\sigma} \right)^{-0.19605}} = 2.65 \text{ mm/s} \quad \left| \quad 7.2.2 \right.$$

This can now be converted to volumetric flow rate by multiplying by the inner nozzle area.

Zhang predicted that in our case satellite drops should form at a flow rate below 29.4

ml/hr, which was not confirmed in our experiments, as satellite drops continued to form even beyond this flow rate.

After detachment of the drop in most cases this leads to formation of the residual mass which is around 2.4 mg, but in some cases the drop detaches with a much lower mass left (below 1 mg) which was named as the wetting mass. The property of the wetting mass is different to the residual mass, in that the growth of the wetting mass is delayed. This phenomenon was explained as following detachment the residual inertia pushes the liquid back into the capillary of the nozzle leaving just a little liquid due to liquid-solid interactions. This liquid is forced into any air gaps inside the fluid supply system. The delay in growth is associated with the return of the fluid supply to initial state. For a different flow rate, the amount of the wetting mass residue is different, but it was calculated that there is approximately a 9% chance that detachment will lead to formation of this wetting mass. There does not appear to be any other evident dependence.

With an increase in the flow rate up to 115.3 ml/hr, everything remains largely the same, with some exceptions. Without any specific overall pattern, there appear to be areas where the single point attractor becomes weaker (named here as single region attractors). This was predicted by the MSD model shown on multiple occasions in the bifurcation region before the predicted chaotic region. Unfortunately, it was not possible to identify them as such due to the camera filming speed (30 frames per second – fps). The single region attractor was still considered to be a limit cycle attractor as the periods were followed a fairly predictable pattern.

Beyond the flow rate of 115.3 ml/hr and up to 120 ml/hr is the region where periodic dripping is still observed but in addition the residual mass now becomes higher (around 3.5 mg) and increases as the flow rate increases.

A flow rate of 120 ml/hr produces the first major bifurcation. From the MSD model, the bifurcation point is dependent on disturbances to the flow. This speculation was actually

proven to be correct as verified in these experiments. Importantly, this was identified in the subsection 7.2.2 under the description of the unstable region attractor. What was found is that a sudden perturbation in a system can lead to bifurcation (Figure 7.2.13 and Figure 7.2.14). The bifurcation can persist for some time or can die down. The cause of these transitions remains unknown.

Osborne [5] while summarising the results of a range of research studies has indicated that the beginning of the chaotic region should be located close to a Reynolds number of 50. This experimental investigation has showed that the corresponding Reynolds number is 43, which is close enough.

The first bifurcation gave rise to frequent mid drop formation. The nature of the formation of these drops remains speculative. It was considered that the process of creation of those drops is related to the formation of the wetting mass after detachment. After some liquid is forced back into capillary it takes some time for the system to respond, but when it does this additional volume is pushed out from the system (most likely by air pockets, which had become compressed earlier) at a much faster rate. The flow velocity here is not enough to form a jet but is enough to overcome the surface tension forces, leading to the formation of a fast drop (detachment happens much faster, so the drop period is substantially less).

This flow rate also identified the beginning of the chaotic region, as is clearly identified on the period versus flow rate plots (Figure 7.2.1 and Figure 7.2.2). Additionally, there was a sudden jump in the drop period.

The ensuing flow rates continue to produce chaotic regions, similarly to the mathematical model, having regions of strange attractors followed by the regions of limit cycle attractors. The nature of the appearance of the bifurcation regions as well their disappearance remains unclear (as no flow rate dependence was found). Nor do the bifurcation regions have any fractal nature, and they definitely do not have any similarities in shape (as was speculatively observed in the results of the mathematical model).

Also different flow rates show different types of dripping pattern, with the appearance of mid drops at some flow rates and their disappearance in the following ones. Additional type of dripping mode is introduced when the flow rate reaches 178.1 ml/hr. Then the liquid forced into the capillary after drop detachment is forced out at such a speed that it exceeds the critical Weber number [14] and creates a jetting stream. This stream collapses (as the local flow rate normalises back to the supply rate) forming, after some time, regular drops.

The final flow rate under investigation at 332.1 ml/hr still showed signs of the chaotic region (corresponding to a Reynolds number equal to 119), as was expected, as the Clanet and Lasheras calculations [14] will give a Reynolds number of 560.9 (or 1.552 l/hr).

The horizontal behaviour of the drops was also studied, but in separate experiments where the drops either develop at low flow rates (around 4 ml/hr) or are given time to stabilise with an arbitrary volume. By introducing a perturbation (tapping), it was found that the horizontal drop vibrations exhibit two different types of vibration. The first showed standard damped oscillations, while the second additionally had damped oscillations with amplitude modulation that not always have a specific frequency (but rather it could change during oscillation). The latter vibration also produces much longer oscillations compared to vertical perturbations. Additional experiments are required, as the limited frame rate of current experiments did not allow confirmation of all vibration properties. The impact of horizontal perturbations on dripping also remains unclear.

Dripping dynamics is complex and there is a lot to be considered. For example, Figure 7.2.20 shows the collapse of a jet with a satellite drop detachment. The inertia of the collapsing stream exchanges momentum with a satellite drop that is directed upwards.

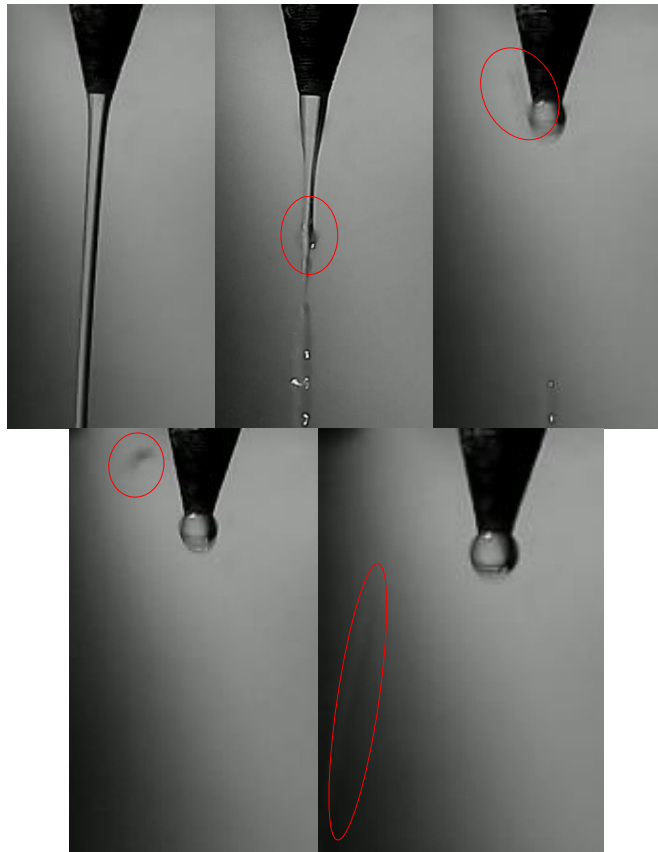


Figure 7.2.20: Strange satellite drop detachment

Quite a lot was dependent on the experimental procedure and its operation. The experimental set-up should account for many unwanted errors in the results. It was noticed that the supply system contains a lot of unnecessary vibrations, which does affect the performance of the experiment. To limit this vibration rubber mats between the experimental module structural components were introduced, as well as TYGON® tubing was used to smooth the pulsation of the liquid due to the syringe pump. Here for future experimental work, it is advised to improve the experimental set-up by adopting strategies to allow multiple levels of isolation across a wide range of frequencies.

The future strategy for the experimental work should first concentrate on the analysis of possible vibrations and identify these sources and their frequencies.

- When the source and frequencies are identified additional implementations of passive isolators should be implemented, such as: use of elastomers and/or cork pads of different properties to minimise the vibration at different frequencies in the module structure

- use of a flow controller to minimise disturbances in the flow. It should be installed just before the nozzle for precise identification of the flow as well as to control the flow fluctuation

Future work should investigate the drop behaviour in the chaotic region using phase plane plots. This should be done by looking at the drop development with time for similar initial states within the same flow rate and tracking down the position and velocity components. Due to the different types of residual mass, as observed in the experiments, additional precautions should be taken and only those with a similar state (within adequate limits) should be included in the study.

Those analyses should allow one to clearly identify graphically the existence of limit cycle attractors [23]. Also, it would be interesting to show the development of the system close to the bifurcation point. Close to the bifurcation point, the system becomes highly unstable (as shown in Figure 7.2.1), but the limit cycle attractors can show that even within this system when the stable point is reached the drops would continue to 'spiral' around the same cycle. The application to phase plane plots is not limited to this. The phase plane plots should provide an additional visual aid where the strange attractors or period jumps were observed.

7.3 Future models

Based on the experimental results it was found that the Mass-Spring-Damper (MSD) model should be updated. The following is a list of findings, which was acquired through experiment:

- The drop Centre of Mass (CoM) location in a non-oscillatory state is linearly dependent on the drop mass
- Beyond this threshold value the spring and damping constants are mass dependent variables
- Detachment occurs when the drop CoM reaches a specific critical distance

- The detachment creates either wetting mass or a residual mass randomly with a formation ratio of approximately 1 to 11
- The residual mass is flow rate dependent
- The wetting mass is followed by an increase in the flow rate

The spring and damping coefficients were found to be mass dependent but these dependences disagree with the Kiyono and Fuchikami model [6]. The first contradiction appears to be the spring approximation. The experiments showed that there is a minimum mass beyond which the spring constant does not exist. In this range, the drop does not appear to have any oscillations. Beyond this threshold value, the oscillation becomes more noticeable. Secondly, the damper constant is also mass dependent, instead of being a constant value.

Any future model should include additional parameters that actually force the drop into instabilities. Firstly, this would include forced vibrations, which could be identified as arising from system noise. Secondly, there are local flow rate variations, due to detachment of the drop.

The z-coordinate of the CoM is a mass dependent variable, which vibrates linearly with a rate of change described by Equation 7.1.7. In addition, to allow for local flow rate variations, the mass should be randomly set to zero in 1 out of every 11 drops on average. In the remaining cases, the residual mass should also be set as a flow rate dependent variable and not as it currently is (dependent only on the detached drop mass). The detachment mass should be defined when the drop CoM has reached a critical distance.

One of the possible approaches for future modelling of the system includes the development of a Mass-Spring-Damper network, which consists of multiple layers of interconnected drop volumes as nodes linked by Spring-Damper connections. In the work of Galvao et. all. [72] this shows a similar network model which is based on an RLC circuit network (a network that consists of R – resistors, L – inductors and C – capacitors). The generalised similarities of those two models become obvious when one considers the

differential equations that describe the system. In the descriptive representation of the new model, based on the referenced work [72], it is possible to start with showing that the 'mass' effects on a system can be linked to 'inductor' properties. Similarly, the 'damper' properties are linked to the 'resistors' and 'springs' to 'capacitors'.

The solution to this model will require the use of fractional calculus, which should lead to a more accurate level of approximation and as a result higher precision. The statement above is made based on an understanding that fractional order differential equations are more suited for this application where the analyses require solving problems of a fractal nature and chaotic behaviour [73].

Here it should be mentioned that additional future work should be performed to adapt the MSD model differential equation. Initially to fit the descriptive model, secondly to allow the development of fractional order differential equations.

Cyrille Henry's work [74] can be used as the cornerstone for establishing the algorithm of the new model. The work describes possible variations, which should be implemented to the MSD network set-up. Different descriptive set-ups within the network can allow variation of the behaviour of the nodes to model differently the drop internal and external interactions.

Drop residues and the local flow rate variation (variation of the flow rate at the nozzle tip) can be modelled using an autoregressive (AR) model or AR with moving average (ARMA). Both of the models consist of linear inputs (the results shown in Figure 7.1.11) with the addition of a random term. Again, here the use of the fractional order calculus becomes beneficial.

Drop shape deformation, when more comprehensively considering intermolecular forces, will lead to a change in the spring constant. Due to this, in future models, it is proposed here to consider the springs behaving non-linearly. It is becoming clear that the spring constant is not a good approximation of stretched liquids, as the stretched liquid behaves

non-linearly and even non-monotonically in some cases. For example, work by Augousti [75], highlights this non-linearity of the forces in liquids at a microscopic level, which demonstrates that the model will still be oversimplified. This limits the validity of these models used in the thesis and this should be acknowledged.

7.4 Future application of the research results

To advance current research several options are considered. One is targeting the microgravity research facility, while the second one targets future research into dripping tap dynamics.

The drop tower future resides on the future investment of additional funds and work hours. The former will require exploring possibilities with potential investors from research organisations and universities. It is proposed to approach the following organisations: the UK Space Agency or National Physical Laboratory. Additional investment opportunities, as well as the size of the funds required, should also be investigated. To continue the commissioning progress additional students should be involved. This can be incorporated into final year project work or a summer internship.

The research into dripping dynamics should expand and include additional experimental studies of drop behaviour in normal gravity as well microgravity. The ground-based research should require performing experiments with cameras of much higher resolution and what is more important with higher frame rates. The microgravity research should advance the knowledge of drop behaviour in the weightless environment. This will lead to an improvement in our understanding of capillary fluid behaviour under microgravity conditions. As a result, this could be potentially used in improved 3-D printing in space or laser-based asteroid mining for example. The case of potential improvement can be used in acquiring additional research funds from such organisations as the European Space Agency or the Netherlands Institute for Space Research. The outcome of drop behaviour in

microgravity can lead to technology development and its commercialization which is associated with liquid handling.

Although the proposed future results are obscure, nevertheless it is believed that the research work should continue with possible discoveries outlining future applications.

CHAPTER 8

CONCLUSION

This chapter will summarise the work carried out during this research. The research targets were set in first chapter and throughout this work it has been shown how those targets were achieved and what the outcomes are. The research work can be separated into three main areas with four targets identified:

1. Drop Tower work
 - a. Assemble of the Drop Tower microgravity facility, and initiating the commissioning process
2. Mathematical modelling
 - b. Complete a study of the non-periodic behaviour of a dripping tap, with the aid of study of a Mass-Spring-Damper (MSD) model
3. Experimental work
 - c. Complete the study of the non-periodic behaviour of a dripping tap, with the aid of an experimental set-up that should be constructed
 - d. Analyse and summarise the observed results and provide ideas for future mathematical models

8.1 Drop Tower work

The Drop Tower project is considered to be one of the most complicated research engineering projects undertaken at Kingston University. The design was conceived by

Kingston University academic staff, who left at the time that the assembly work was carried out. Project management tools were utilised in this project due to its complexity and scale, such as detailed project planning, budget planning, and arrangements for contracting work.

The Drop Tower assembly work was completed. Some stages of the assembly work required manufacturing some components, which was carried out in house, such as structural components of the drag shield, structural components of the surroundings, connectors for the guide rails, etc.

In some cases, the assembly work required high precision. This includes the installation of the drive system and its alignment, which was done to a high standard with a maximal offset including uncertainty of 0.226 mm over a distance of approximately 8 m. The alignment was confirmed by different types of test (static – where the set of measurements were taken at a constant height, and dynamic – where the measurements were taken while the trolley was moving along the track). The alignment was confirmed a year after the initial check and no difference was found compared to the first tests.

The selection of electronic components was proposed by the control system design company ‘Micromech Ltd’. The installation, on the other hand, was completed using our own means and was confirmed to be of a high standards following inspection by the commissioning company – (Micromech).

The Drop Tower’s design targets a wide range of users (from academia to school students). The design can allow for a wide range of experiments to be taken on-board, with the size limited to a 418.6 mm-sided cube and a mass of 20 kg. The facility was proposed to allow for a wide range of gravity levels to be simulated, from a microgravity environment ($10^{-5}g$) to low gravity ($<1g$). It also has high potential for application in Kingston University outreach programmes as the design involved installation of a transparent enclosure.

With this in mind, extra safety measures were taken to make sure that the system is safe to use. In the case of failure detected by the control system, the system will enter a pre-programmed emergency cycle, which will safely return the drag shield to ground level.

The safety monitoring includes:

- Emergency cut-off switches positioned at different locations within the Drop Tower area
- High voltage power monitoring
- Low voltage power monitoring, including installing an Uninterruptable Power Supply (UPS), which allows normal operating for more than 1.5 hours (even though the emergency cycle only lasts a few minutes)
- Limit switches along the guide rails to indicate that ground level is reached and to check that the velocity is in the right region at the upper level
- Thermosensors are installed on both motors to detect overheating
- There are also limit switches and door locks installed monitoring the status of the doors, and the control system would not allow the test to begin (even cutting off the power supply) in the event that the doors are open
- In case of failure the guide rails are equipped with brackets (at the top and the bottom of the Drop Tower) that can limit the motion of the drag shield
- A damper system and soft flooring is available at the bottom to limit damage in the unlikely case of uncontrolled descent
- Finally, the area outside the Drop Tower is protected from flying debris by highly durable acrylic sheets from which the surroundings of the Drop Tower are fabricated.

Safety operation documents were developed for future operation. The work procedure, risk assessment, operational assessment and all other documentation was collected and made available in a single folder available in the Drop Tower laboratory area.

Finally future work suggestions were provided at the end of the chapter, which included the installation of new wiring, separation of the power lines and the signal lines via different cable trunking and using dedicated connectors. This should all be done to decrease the electrical noise in the signal lines.

8.2 Mathematical modelling results

The mathematical model, which was used in this work, is based on the Mass-Spring-Damper (MSD) model, which was first introduced by Shaw [3] and later used, improved and studied by many others. This study differs to previous ones as it has taken quite a wide range of data with equally high precision, provided an analysis of its behaviour and furthermore compared it to experimental results.

The mathematical model has investigated the range of flow rates corresponds to Reynolds numbers from 4 to 175 with a step size of 0.4. The mathematical model was created in “MATLAB®” software and used the ODE-45 (ordinary differential equations) built in solver to solve the relevant second order differential equations. The code created was explained explicitly with pseudo-code displays in the main body of the thesis and actual code included in the Appendix H.

In post-processing the results, it was found that the model shows bifurcation regions all along the selected region, which was unexpected. The existing literature has on multiple occasions [5] predicted that the chaotic region (and hence bifurcation) should appear only past the region of Reynolds number of 50. Interestingly enough, the experimental results also provided similar results. Below a Reynolds number of 50, it was possible to identify weak attractors (limit cycle attractors). The bifurcation plot showed that there exist multiple regions, which are separated by single point attractors (single period dripping). This was later confirmed by experimental results, which showed that even in chaotic regions there are areas where stability can exist. Also, the bifurcation plot has produced bifurcation regions which are quite similar visually, and which with an increase in the flow rate also increase in size (a persistent effect over a wide range of flow rates and with a wider periodic variation). This raised a question about the possible existence of a fractal nature (power law scaling) in the mathematical model. Several options were considered in the search for fractal patterns in the bifurcation regions:

- A one dimensional scaling between the start and end flow rates of bifurcation regions
- A one dimensional scaling between the maximal and minimal periods of the bifurcation regions
- A two dimensional scaling between the area enclosed by the minimum and maximum periods of the bifurcation regions

None of these approaches has demonstrated that the bifurcation plots for the mathematical model are fractal in nature.

The investigation of the results continued with an analysis of the mathematical development of the bifurcation process. The initial conditions of the mathematical model were pre-set, and renewed after each drop detachment. The position of the CoM and the flow velocity were reset to constant values, while the mass (residual mass) was calculated based on the mass of the drop before detachment. The calculation starting mass was chosen to have an arbitrary value, which actually became the cause of perturbations in the mathematical model. This mathematical perturbation demonstrated the propagation from an initially relatively stable system to period doubling and beyond. Now we know that before period doubling (the starting point of bifurcation) the system's stability weakens with an initially applied perturbation. This means that the system requires a longer time (more drops) to reach a point where each drop period start to repeats (becomes periodic). With increasing flow velocity the attractor point becomes weaker, until it breaks down, creating two point attractors (a limit cycle attractor). At this point, the model showed that the system is highly unstable and takes a long time to reach a quasi-periodic dripping state. Depending on the resolution of the simulation, it is expected that at a specific flow rate the period difference in quasi-periodic dripping should be equal to the time resolution. The flow rate continues to increase and the system's limit cycle attractors become stronger which allows the system with an initial perturbation to stabilise much more quickly with the period values becoming further apart. This process continues, with the system spontaneously breaking into more periods. Here we speculated that the system's

bifurcation point is highly dependent on the perturbations to the system or the initial conditions.

Similarly, a discussion was presented on the period jump identified by the mathematical model. Well before the period jump, the system's response due to the initial disturbance is quick and the system ends up at a single attractor point. With flow rate increase the time required for stabilisation grows. At some point (at some particular flow rate) depending on the initial conditions and/or system perturbations, the stabilisation time becomes so long that the system creates a different attractor point. Beyond this point, the strength of the attractor continues to grow, but not for too long as the instabilities will progress which eventually will lead to a bifurcation point.

8.3 Experimental results

To provide an explicit analysis of the mathematical model and to identify the parameters required to improve the existing model it was essential to conduct the experimental studies of the dripping tap. This stage involved the development of an experimental module. This included setting up the design requirements and constraints, selecting components, assembling the module and finally identifying the performance limitations. The main area of interest lay in the study of the Centre of Mass (CoM) in the 3-dimensional space. With this in mind, the experimental operation required to have two cameras filming the drop simultaneously. The cameras were synchronised via on-board computers with the operational software written in the Python language. The operation initially conceived to have a high level of autonomy, with limited interaction via a wireless internet connection.

The experimental operation was tested, and based on the performance of the cameras; the result processing and post-processing code was developed in "MATLAB®" software. The processing code was used to process the video: to identify the nozzle and the drop on both cameras and to confirm (or adjust if needed) synchronisation of the videos. The post-

processing code allowed conversion of the coordinates of the drop edge from each camera and calculation of the drop CoM position.

The results were analysed in two ways. Firstly, for drop behaviour based on the Mass-Spring-Damper (MSD) model, and secondly by consideration of dripping behaviour. The drop studies have identified that the drop necking process starts when the drop reaches a specific critical mass or a critical distance (both of these values in the non-vibrating drop are proportional to one another). The spring constant and the damping constants are mass dependent properties, while the previous model has assumed the damping to be constant. The residual mass was found to be of two types (labelled as residual and wetting mass respectively). In one case, following detachment, the drop has a low mass (usually below 1 mg) and is associated with a delay in the development of the drop. In the other case, the residual mass is a flow rate dependent property starting from a flow rate of 115 ml/hr, and it is constant below this threshold value. The reason for the formation of either of these types of residual mass remains unclear, but it was found that the wetting mass has a 9% possibility of occurring.

The horizontal behaviour of the drop was also studied, but due to the camera speed limitations, it has not provided conclusive results. What was found is that the horizontal vibrations exist in two modes: a natural decay vibration or a natural decay vibration with amplitude modulation. The properties of the modulation as well as its nature require additional studies.

The dripping behaviour studies concentrated on an analysis of the plot of the period versus the flow rate. The studied flow rate region has shown that there were regions of periodic dripping and regions of chaotic dripping. The periodic region consists of limit cycle attractors either characterized by a single period (a strong single period attractor) or by a pattern of successive, repeating periods (a regional attractor). It was speculated that the regional attractors are actually local bifurcations (as predicted by the mathematical model)

but this could not be confirmed due to camera speed limitations. The chaotic region was found to start at a flow rate of 120 ml/hr flow rate consisting of regions of limit cycle attractors (single period attractors, area attractors or quasi-periodic) and strange attractors. The existence of period jumps was also verified.

The chaotic region showed that there is the possibility of the development of different types of dripping process, which includes standard drops, mid-size drops, and jetting.

The starting point of the chaotic region was found to be in slight disagreement, while the start of the jetting region was not identified at all in these experiments, as it was expected.

Finally, the results from both the mathematical model and the experiments were combined to summarise the findings and outline proposal for future development.

REFERENCES

- [1] T. L. Heath, *The works of Archimedes*, Cambridge: Cambridge University Press, 1897.
- [2] L. Rayleigh, “On the instability of jets” in *Proceedings of the London mathematical society*, London, 1878.
- [3] R. Shaw, *Dripping faucet as a model chaotic system*, 1st ed., Santa Cruz: Aerial, 1984.
- [4] K. Kiyono and N. Fuchikami, “Dripping faucet dynamics by an improved mass-spring model”, *Journal of the Physical Society of Japan*, vol. 68, pp. 32-59, 1999.
- [5] B. Osborne, *Liquid Jet Breakup in Reduced Gravity*, PhD thesis, Queensland: University of Queensland, 2008.
- [6] K. Kiyono and N. Fuchikami, “Bifurcation Induced by periodic Forcing and Taming Chaos in Dripping Faucets”, *Journal of the Physical Society of Japan*, vol. 71, no. 1, pp. 49-55, 2002.
- [7] J. Plateau, *Statique expérimentale et théorique des liquides soumis aux seules forces moléculaires*, vol. I, Leipzig: F Clemm, 1873.
- [8] S. Tomotika, “On the Instability of a Cylindrical Thread of a Viscous Liquid Surrounded by Another Viscous Fluid” in *Proceedings of the Royal Society A*, London, 1935.
- [9] S. J. Leib and M. E. Goldstein, “The generation of capillary instabilities on a liquid jet”, *Journal of Fluid Mechanics*, vol. 168, pp. 479-500,

1986.

- [10] S. P. Lin and Z. W. Lian, “Absolute instability of a liquid jet in a gas”, *Physics of fluid A*, vol. 1, no. 3, pp. 490-493, 1989.
- [11] M. L. Cordero, F. Gallaire and C. N. Baroud, “Quantitative analysis of the dripping and jetting regimes in co-flowing capillary jets”, *Physics of Fluids*, vol. 23, no. 9, pp. 094-111, 2010.
- [12] T. Funada and D. D. Joseph, “Viscoelastic potential flow analysis of capillary instability”, *Journal of Non-Newtonian Fluid Mechanics*, vol. 111, pp. 87-105, 2003.
- [13] T. Funada, D. D. Joseph and S. Yamashita, “Stability of a liquid jet into incompressible gases and liquids”, *International Journal of Multiphase Flow*, vol. 30, pp. 1279-1310, 2004.
- [14] C. Clanet and J. C. Lasheras, “Transition from dripping to jetting”, *Journal of Fluid Mechanics*, vol. 383, pp. 307-326, 1999.
- [15] G. I. Taylor, “The dynamics of thin sheets of fluid. III. Disintegration of fluid sheets”, *Proceedings of the Royal Society of London A*, vol. 253, pp. 313-321, 1959.
- [16] J. Eggers and T. F. Dupont, “Drop formation in a one-dimensional approximation of the Navier-Stokes equation”, *Journal of Fluid Mechanics*, vol. 262, pp. 205-221, 1994.
- [17] J. Eggers, “Post-breakup solution of Navier-Stokes and Stokes threads,” *Physics of Fluids*, vol. 26, pp. 072-104, 2014.
- [18] X. Zhang, “Dynamics of Growth and Breakup of Viscous Pendant Drops into Air”, *Journal of Colloid and Interface Science*, vol. 212, pp. 107-122, 1999.
- [19] R. Gunde, A. Kumar, S. Lehnert-Batar, R. Made and E. J. Windhab, “Measurements of the Surface and Interfacial Tension from Maximum Volume of a Pendant Drop”, *Journal of Colloid and Interface Science*, vol. 244, pp. 113-122, 2001.
- [20] Z.-Q. Zhang and Y. H. Mori, “Formulation of the Harkins-Brown

Correction Factor for Drop-Volume Description”, *Industrial and Engineering Chemistry Research*, vol. 32, pp. 2950-2952, 1993.

- [21] E. N. Lorenz, “Deterministic Nonperiodic Flow”, *Journal of the Atmospheric Sciences*, vol. 20, pp. 130-141, 1963.
- [22] B. Osborne and C. Welch, “Two Degree of Freedom Model of Chaotic Dripping in Reduced Gravity”, *Journal of British Interplanetary Society*, vol. 65, pp. 77-86, 2012.
- [23] T. Szirtes, *Applied Dimensional Analysis and Modeling*, Oxford: Elsevier, 2006.
- [24] R. C. Weast, *Handbook of Chemistry & Physics*, Boca Raton: Chemical Rubber CO, 1963.
- [25] A. Akram and A. Ismail, “Comparison of Edgfe Detectors”, *Interantional Journal of Computer Science and Information Technology Research*, vol. 1, no. 1, pp. 16-24, 2013.
- [26] L. G. Roberts, “Machine Perception Of Three-Dimensional Solids”, Massachusetts Institued of Technology, Cambridge, 1963.
- [27] J. M. S. Prewitt, “Object Enhancement and Extraction”, in *Picture Processing and Psychopictorics*, Maryland, Academic Press Inc., 1970, pp. 75-150.
- [28] I. Sobel, “History and Definition of the Sobel Operator”, 12 August 2014. [Online]. Available: <http://www.researchgate.net>. [Accessed 27 April 2016].
- [29] J. Canny, “A Computational Approach to Edge Detection”, *IEEE Transactions on Pattern Analysis and Machine Intelligence*, Vols. PAMI-8, no. 6, pp. 679-697, November 1986.
- [30] V. A. Thomas, N. S. Prasad and C. A. M. Reddy, “Microgravity research platorms - A study”, *Current Science*, vol. 79, no. 3, pp. 336-340, 2000.
- [31] B. Osborne and C. Welch, “Short Duration Reduced Gravity Drop Tower Design and Development”, *JBIS*, vol. 65, pp. 71-76, 2012.

- [32] MGLAB, “Micro-Gravity Drop Experiment Facility, User's guide”, Micro-Gravity Laboratory of Japan, Toki city, 2009, [Online]. Available: <http://www.mglab.co.jp>. [Accessed 24 April 2016].
- [33] National Aeronautics and Space Administration, “Zero Gravity Research Facility at NASA Glenn Research Center, User's guide”, NASA, Cleveland, 2014, [Online]. Available: <http://www1.grc.nasa.gov>. [Accessed 24 April 2016].
- [34] ZARM FABmbH, “ZARM Drop Tower Bremen, User's guide”, ZARM FABmbH, Bremen, 2012, [Online]. Available: <http://zarm.uni-bremen.de/en/>. [Accessed 24 April 2016].
- [35] J. Meseguer, A. Sanz-Andres, I. Perez-Grande, S. Pindado, S. Franchini and D. Alonso, “Surface Tension and microgravity”, *European Journal of Physics*, vol. 35, no. 5, p. 055010 (20), September 2014.
- [36] T. Steinberg, “Reduced gravity testing and research capabilities at new 2.0 second drop tower”, *Journal of Achievements in Materials and Manufacturing Engineering*, vol. 31, no. 2, pp. 822-826, December 2008.
- [37] Canadian Space Agency, “Parabolic Flights”, Canadian Space Agency, 27 November 2008. [Online]. Available: <http://www.asc-csa.gc.ca>. [Accessed 22 April 2016].
- [38] European Space Agency, “Education: Fly Your Thesis”, Space Agency, [Online]. Available: <http://www.esa.int/Education>. [Accessed 24 April 2016].
- [39] H. Binnenbruck and R. Kuhl, “The German Microgravity Research Program”, *Advances in Space Research*, vol. 13, no. 7, pp. 37-45, 1993.
- [40] EuroLaunch, “BEXUS User Manual”, 3 February 2016. [Online]. Available: <http://www.rexusbexus.net>. [Accessed 26 April 2016].
- [41] EuroLaunch, “REXUS User Manual”, 15 December 2014. [Online]. Available: <http://www.rexusbexus.net>. [Accessed 26 04 2016].
- [42] A. Kuh, “UK in ELIPS-4”, UK Space Agency, Swindon, 2013, [Online].

Available: <http://www.physics.open.ac.uk>. [Accessed 26 April 2016].

- [43] I. Macdonald, “Examples of bed rest studies - practical challenges and benefits, presentation”, University of Nottingham, Nottingham, [Online]. Available: http://www.easa.int/Our_Activities/Human_Spaceflight/Bedrest_studies. [Accessed 26 April 2016].
- [44] Parker Hannifin Corporation, Electromechanical Automation Division, “Linear Motors I-Force Ironless and RIPPED Ironcore Series”, 13 December 2010. [Online]. Available: <http://www.parkermotion.com>. [Accessed 5 March 2016].
- [45] Parker Hannifin Corporation, Electromechanical Automation Division, “High power devices, Compax3H Installation Manual”, 7 June 2013. [Online]. Available: <http://www.parker.com/eme>. [Accessed 23 March 2016].
- [46] RLS d.o.o, “LM10 linear magnetic encoder system, Data sheet”, 5 May 2011. [Online]. Available: <http://www.rls.si>. [Accessed 23 March 2016].
- [47] SKF Group, “Product information, Speedi-Roll, LLEHS 25 Speedi-Roll”, 2007. [Online]. Available: <http://www.uk.rs-online.com>. [Accessed 7 March 2016].
- [48] R. Timings and T. May, Newnes Mechanical Engineer's pocket book, Oxford: Clays Ltd, St Ives plc, 1995.
- [49] Rexroth, Bosch Group, “Aluminum Structural Framing System”, September 2014. [Online]. Available: <http://www.boschrexroth-us.com/framing>. [Accessed 10 March 2016].
- [50] PAR Group Ltd, “Polycarbonate Sheet - Lexan(TM) 9030, Technical Data Sheet”, [Online]. Available: <http://www.par-group.co.uk>. [Accessed 13 March 2016].
- [51] National Instruments, “Bus-Powered M Series Multifunction DAQ for USB - 16-Bit”, 6 November 2014. [Online]. Available: <http://www.ni.com>. [Accessed 15 January 2016].

- [52] Artisan Technology Group, "Safety Switches, Guard Locking Switches, TLS-GD2", 5 March 2010. [Online]. Available: <http://www.artisanng.com>. [Accessed 27 March 2016].
- [53] Couzet Control, "DIN Rail Mount 17.5 mm Multifunction MWUA", 2 November 2015. [Online]. Available: <http://www.crouzet.com>. [Accessed 28 March 2016].
- [54] Phoenix Contact, "Uninterruptible power supply - TRIO-UPS/1AC/24DC/ 5 - 28266611", 18 March 2016. [Online]. Available: <http://www.phoenixcontact.com>. [Accessed 18 March 2016].
- [55] Honeywell, "Installation Instructions for the MICRO SWITCH Heavy Duty Limit Switch Series, PK 81116", May 2013. [Online]. Available: <http://www.honeywell.com>. [Accessed 18 March 2016].
- [56] Weforma, "Heavy-Duty Shock Absorbers, LDS 32", 2016. [Online]. Available: <http://www.weforma.partcommunity.com>. [Accessed 16 March 2016].
- [57] Rawlplug Ltd, "RAWL Fixing, RAWL Specification Design Guide", August 2007. [Online]. Available: <http://www.frscott.co.uk>. [Accessed 16 March 2016].
- [58] Koelner group, "Technical Handbook, Introduction to Anchoring", February 2013. [Online]. Available: <http://www.rawplug.com>. [Accessed 17 March 2016].
- [59] Baumer, "Photoelectric sensors, Distance sensors, OADM 20I4460/S14C", 12 May 2012. [Online]. Available: <http://pfinder.baumer.com>. [Accessed 15 January 2016].
- [60] AIM & Thurlby Thandar Instruments, "EL-R & EX-R Series, Linear regulated precision laboratory power supplies", [Online]. Available: <http://www.aimtti.co.uk>. [Accessed 15 January 2016].
- [61] J. W. P. Schmelzer, E. D. Zanotto and V. M. Fokin, "Pressure dependancy of viscosity", *The Journal of Chemical Physics*, vol. 122, pp. 074511-1 - 074511-11, 2005.

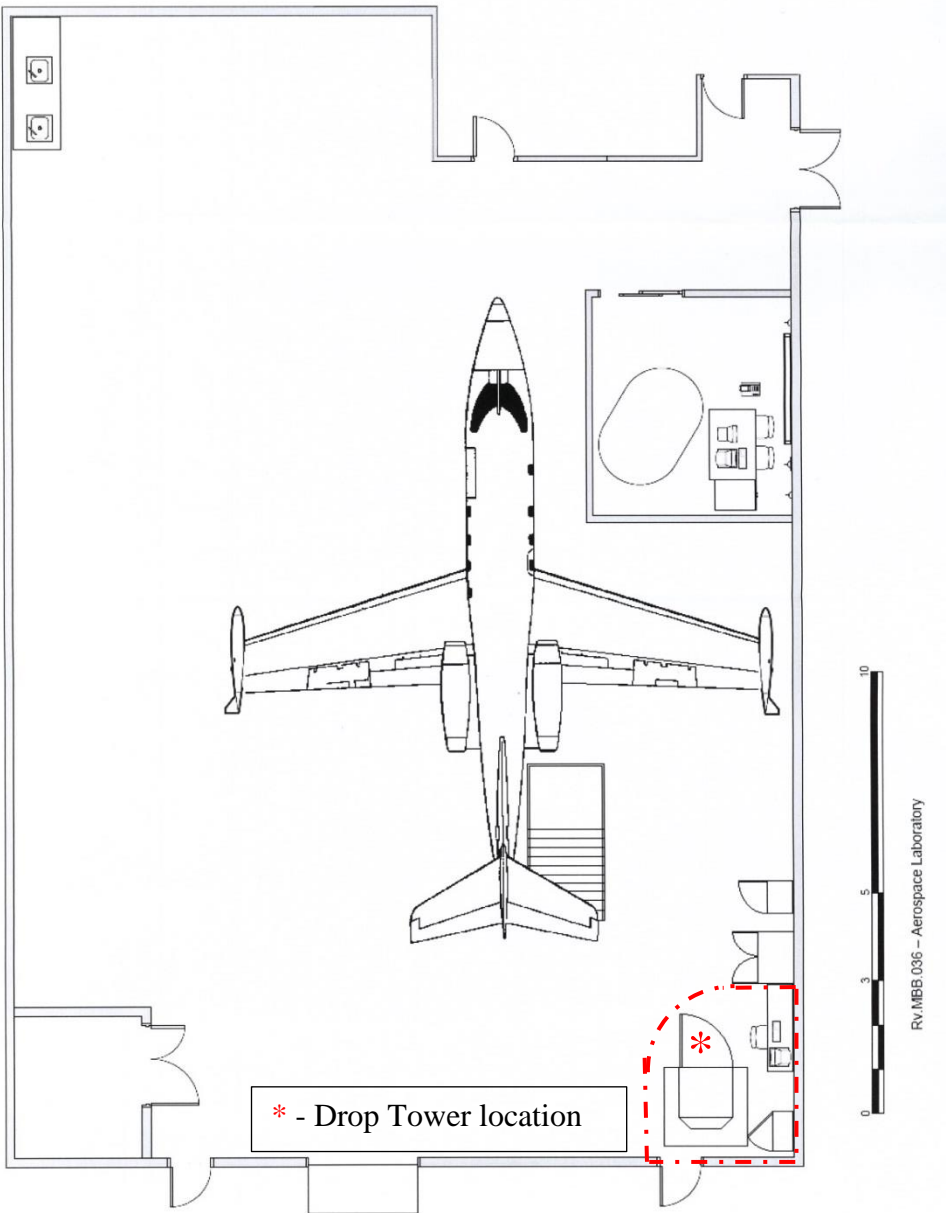
- [62] Cardinal Health, “IVAC(R) Syringe Pumps; Models P7000, P6000, TIVA, TCI & TIVA” November 2006. [Online]. Available: <http://www.franshospitalworkshop.com>. [Accessed 23 May 2016].
- [63] Natural Resources Management and Environment Department, “3. Review of Pumps and Water Lifting Techniques”, 25 May 2007. [Online]. Available: <ftp://ftp.fao.org/docrep/fao/010/ah810e>. [Accessed 24 May 2016].
- [64] Saint-Goban Performance Plastic Corporation, “TYGON S3 E-3603,” 2013. [Online]. Available: <http://www.docs-europe.electrocomponents.com>. [Accessed 24 May 2016].
- [65] Cole-Parmer (R), “Reducing Pulsation in Peristaltic Pumping System”, Cole-Parmer United Kingdom, 25 August 2006. [Online]. Available: <http://www.coleparmer.com>. [Accessed 24 May 2016].
- [66] ACCU DYNE TEST TM, “Critical Surface Tension and Contact Angle with Water for Various Polymers”, Diversified Enterprises, 2016. [Online]. Available: <http://www.accudynetest.com>. [Accessed 24 May 2016].
- [67] Adafruit Learning System, “Adafruit 1-Wire Thermocouple Amplifier - MAX31850K”, 4 September 2015. [Online]. Available: <http://cdn-learn.adafruit.com>. [Accessed 2 June 2016].
- [68] Analog Devices, “ADXL335”, 2010. [Online]. Available: <http://analog.com>. [Accessed 3 June 2016].
- [69] National Instruments, “NI CompactRIO High-Performance Real-Time Controllers, NI cRIO-9012, NI cRIO-9014”, 6 November 2014. [Online]. Available: <http://www.ni.com>. [Accessed 9 June 2016].
- [70] RS Components , “Raspberry Pi 2, Model B”, [Online]. Available: <http://www.uk.rs-online.com>. [Accessed 9 June 2016].
- [71] RS Components, “Raspberry Pi Camera Module”, [Online]. Available: <http://www.uk.rs-online.com>. [Accessed 14 June 2016].
- [72] R. K. H. Galvao, K. H. Kienitz and S. Hadjiloucas, “Conversion of descriptor representations to state-space form: an extension of the

- shuffle algorithm”, *International Journal of Control*, pp. 1-15, 2017.
- [73] R. E. Gutierrez, J. M. Rosario and J. T. Machado, “Fractional Order Calculus: Basic Concepts and Engineering Applications”, *Mathematical Problems in Engineering*, vol. 2010, pp. 1-19, 2010.
- [74] C. Henry, “Mass-Spring-System model for real time expressive behaviour synthesis”, [Online]. Available: <http://www.chnry.net/ch/IMG/pdf/-2.pdf>. [Accessed 4 January 2017].
- [75] A. T. Augousti and G. Rickayzen, “Solvation Forces in a Model Fluid Mixture of Ions and Dipoles”, *Journal of the Chemical Society, Faraday Transactions*, vol. 80, no. 2, pp. 141-156, 1984.
- [76] P. Couillet, L. Mahadevan and C. S. Riera, “Hydro-dynamical models for the chaotic dripping faucet”, *Journal of Fluid Mechanics*, vol. 526, pp. 1-17, 2005.

© Jevgenijs Trunins, 2018

APPENDICES

Appendix A. Learjet laboratory floor plan



Appendix B. Drop Tower experiment procedure checklist

Normal test procedure checklist

CHECK PREVIOUS LOG FOR NO USE NOTES

Test procedure	Checked
1. Check cabinet doors to be locked	
2. Check emergency power cut-off is released	
3. Switch on 415VAC power supply	
4. Power key enabled	
5. Switch on PC	
a. Wait for LabView and Motion Perfect software to be launched (at start-up)	
b. Enter test log data (Motion Perfect)	
6. Position payload	
7. Lock drop tower doors	
8. Start test	
a. Emergency cycle button is released	
b. Press start button	
9. Reset experiment (if needed)	
10. End of test day campaign	
a. Print test log	
b. Switch power off (both)	
c. Lock facility (DO NOT LEAVE KEYS!!!)	

IN CASE OF EMERGENCY CONTACT LAB STAFF OR SUPERVISORY TEAM

Appendix C. Operational profile calculations “MATLAB®” code

```
%Drop Tower operational profile calculation code
%%
%Version: 2.0
%Date: 23/03/2016
%by: Jevgenijs Trunins
%%

clear all; clc;

%Set default limitations
F_max=1170; % (N) - max force motor can take
n=2; % - number of motors in use
M=46.5; % (kg) - mass of drag shield and trolley
v_max=10.40; % (m/s) - maximal allowable velocity
h_s=0.365; % (m) - position of the sensor from drag shield centre
h_d=0.970; % (m) - drag shield height
H=6.827; % (m) - working height of the position sensor
dx=0.02*10^(-3); % (m) - sensor step size

%% Set adjustable limitations
nu=0.95; % - efficiency of the motor
g=9.81; % (m/s^2) - gravitational constant
a_max=5; % g's - maximal allowable acceleration

%% Input parameters
m=input('Mass of payload (kg): ');
b=input('Height of payload (m): ');
mu=input('Gravity quality (m/s^2): ');
mu_max=g-(v_max^2)/(2*H); %calculating max allowable gravity level
while mu>=mu_max %checking if the selected value is below max
    mu=input(['Gravity quality should be below(' num2str(mu_max) ') ']);
end

%% Creating arrays
s=0.5*(h_d-b); % (m) - find the height what payload move in 0g simulation
if mu==0 %If microgravity
    d_pl=zeros(round((H+s)/dx),3); %distance profile for payload
    d_ds=d_pl; %distance profile for drag shield
else %if low gravity
    d_pl=zeros(round((H)/dx),3); %distance profile for payload
    d_ds=d_pl; %distance profile for drag shield
end

%% Calculations
if mu==0 %Finding right acceleration value based on limitations
    a=min([F_max*n*nu/(m+M)+g,a_max*g,(v_max^2)/(2*(H+s-(v_max^2)/...
        (2*g)))]);
else
    a=min([F_max*n*nu/(m+M)+g,a_max*g,(v_max^2)/(2*(H-(v_max^2)/...
        (2*(g-mu)))]);
end
a_dec=min([F_max*n*nu/(m+M)-g,a_max*g]); %calculating max drag shield
%deceleration
d_pl(1,1)=-s-h_s; %setting initial position for payload
if mu==0 %in case of microgravity
    for t=2:round((H+s)/dx)
        %Payload
        d_pl(t,1)=d_pl(t-1,1)+dx; % (m) - position of payload
    end
end
```

```

if d_pl(t,1)<=g*(H+s)/(a+g)-s-h_s %if it is accelerating
    d_pl(t,2)=sqrt(d_pl(t-1,2)^2+2*a*dx); % (m/s) - velocity
    d_pl(t,3)=d_pl(t-1,3)+(d_pl(t,2)-d_pl(t-1,2))/a; % (s) time
else
    d_pl(t,2)=sqrt(d_pl(t-1,2)^2-2*g*dx); % (m/s) - velocity
    d_pl(t,3)=d_pl(t-1,3)+(d_pl(t-1,2)-d_pl(t,2))/g; % (s) - time
end
end
for t=2:round((H+s)/dx)
    %Drag shield
    d_ds(t,1)=d_ds(t-1,1)+dx; % (m) - position of drag shield
    if d_ds(t,1)<=g*(H+s)/(a+g) %if it is accelerating
        d_ds(t,2)=sqrt(d_ds(t-1,2)^2+2*a*dx); % (m/s) - velocity
        d_ds(t,3)=d_ds(t-1,3)+(d_ds(t,2)-d_ds(t-1,2))/a; % (s) time
    elseif d_ds(t,1)<=g*(H+s)/(a+g)+g*s/(a_dec-g) %payload detaches
        %here
        d_ds(t,2)=sqrt(d_ds(t-1,2)^2-2*a_dec*dx); % (m/s) - velocity
        d_ds(t,3)=d_ds(t-1,3)+(d_ds(t-1,2)-d_ds(t,2))/a_dec; % (s)
        % - time
    else %if it is free-fall
        d_ds(t,2)=sqrt(d_ds(t-1,2)^2-2*g*dx); % (m/s) - velocity
        d_ds(t,3)=d_ds(t-1,3)+(d_ds(t-1,2)-d_ds(t,2))/g; % (s) time
    end
end
else %in case of low gravity
    for t=2:round(H/dx)
        %Drag shield
        d_ds(t,1)=d_ds(t-1,1)+dx; % (m) - position
        d_pl(t,1)=d_pl(t-1,1)+dx; % (m) - position of payload
        if d_ds(t,1)<=H*(g-mu)/(a+g-mu) %if it is accelerating
            d_ds(t,2)=sqrt(d_ds(t-1,2)^2+2*a*dx); % (m/s) - velocity
            d_ds(t,3)=d_ds(t-1,3)+(d_ds(t,2)-d_ds(t-1,2))/a; % (s) - time
        else %if it is in low gravity
            d_ds(t,2)=sqrt(d_ds(t-1,2)^2-2*(g-mu)*dx); % (m/s) - velocity
            d_ds(t,3)=d_ds(t-1,3)+(d_ds(t-1,2)-d_ds(t,2))/(g-mu); % (s)
            % - time
        end
    end
    d_pl(:,2)=d_ds(:,2); % (m/s) - velocity of the payload
    d_pl(:,3)=d_ds(:,3); % (s) - time of the payload
end

%% Post processing
d_ds(imag(d_ds)~=0)=NaN; d_pl(imag(d_pl)~=0)=NaN; %remove complex numbers

%% Output plots
subplot(2,2,2)
plot(d_ds(:,1),d_ds(:,2)); hold on; plot(d_pl(:,1),d_pl(:,2),'r')
title('Velocity vs Height'); xlabel('Height (m)'); ylabel('Velocity (m/s)')
grid on; hold off

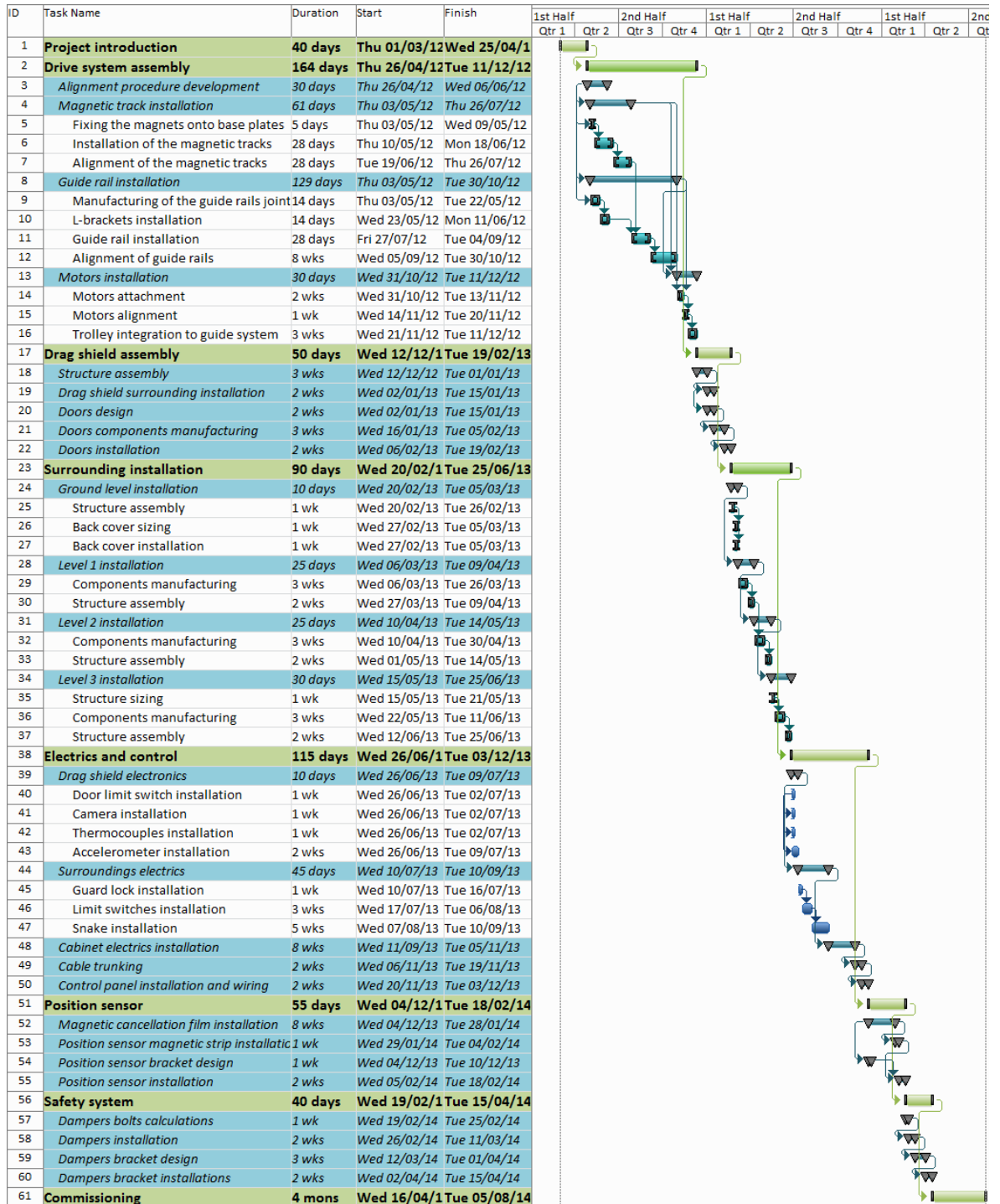
subplot(2,2,1)
plot(d_ds(:,3),d_ds(:,1)); hold on; plot(d_pl(:,3),d_pl(:,1),'r');
title('Height vs Time'); xlabel('Time (s)'); ylabel('Height (m)')
grid on; hold off

subplot(2,2,3)
plot(d_ds(:,3),d_ds(:,2)); hold on; plot(d_pl(:,3),d_pl(:,2),'r');
title('Velocity vs Time'); xlabel('Time (s)'); ylabel('Velocity (m/s)')
grid on; hold off

subplot(2,2,4)
plot(1,1,'r',2,2,'b'); axis off; legend('Payload','Drag Shield'); hold off

```


Appendix D. Drop Tower project Gantt chart (extended)



Appendix E. Drop Tower work budget (extended)

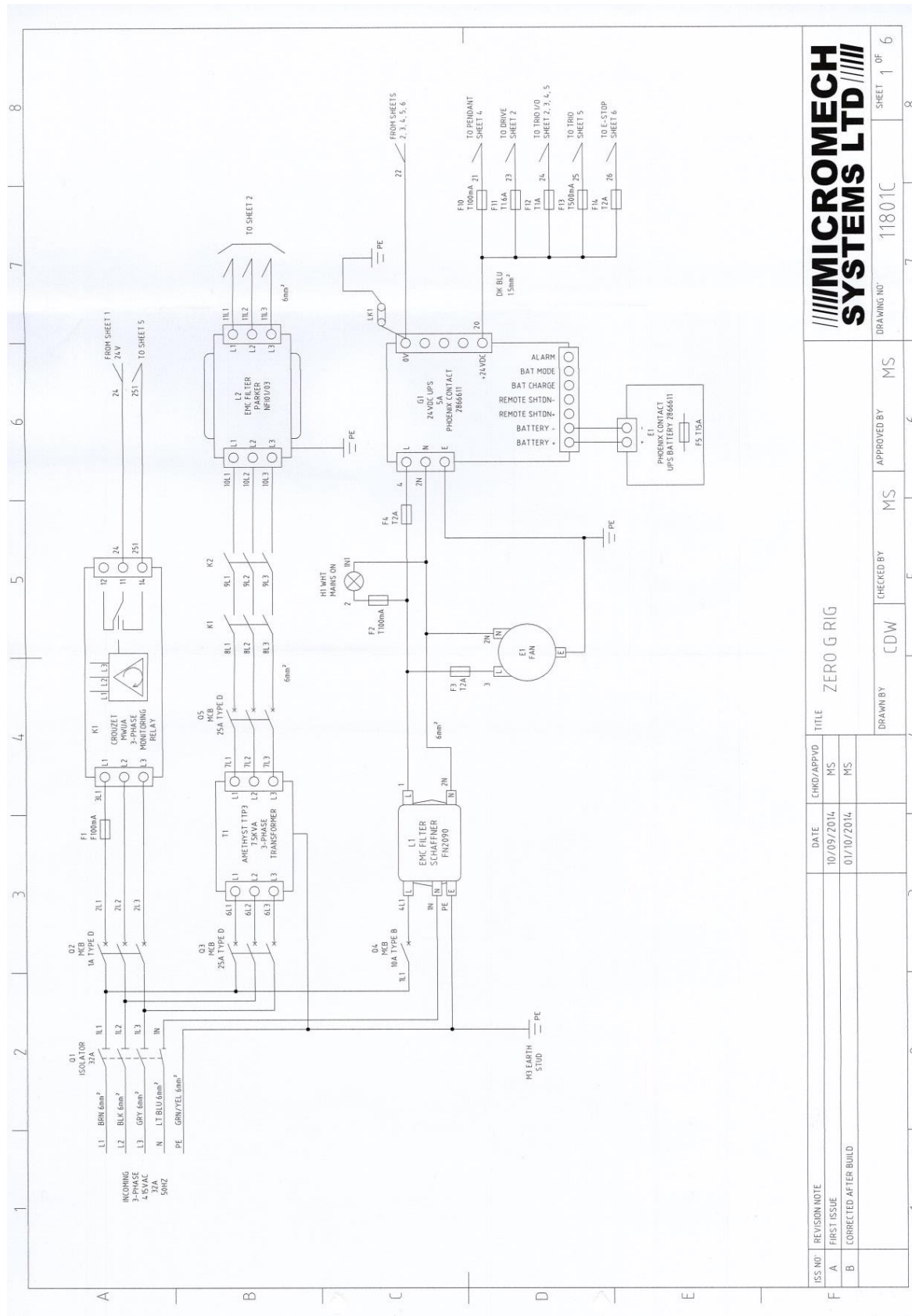
Syst.	Provider	Name	Qty	Price per one (£)	Total Price (£)	Order Date
Control						
	Magnetic shielding	Mumetal 8000x101.6x0.254mm	2	1207.15	2414.30	Aug-15
Magnetic shielding Total					2539.30	
	Micromech	Magnetic scale 8m	1	381.15	381.15	Sep-13
		Linear encoder read head	1	213.22	213.22	Dec-14
		Magnetic scale 8m	1	539.74	539.74	Dec-14
Micromech Total					1134.11	
	National Instruments	SignalExpress license	1	223.74	223.74	Aug-13
National Instruments Total					223.74	
	RS	Microcontroller	1	14.25	14.25	Nov-12
		Heat sink	1	34.89	34.89	Jul-13
		USB cable	4	21.94	87.76	Jul-13
		VGA cable	1	16.33	16.33	Jul-13
		Solid state relay	1	77.39	77.39	Jul-13
		USB cable 5m	2	7.00	14.00	Aug-13
		9-pin D-sub, m-m	1	6.39	6.39	Mar-14
		9-pin D-sub connector female	5	2.31	11.55	Nov-14
		9-pin D-sub connector male	5	2.31	11.55	Nov-14
		D-sub hood, 9pin	8	2.29	18.32	Nov-14
		USB plug A-type male	5	3.24	16.20	Nov-14
		USB plug A-type female chassis	5	0.64	3.20	Nov-14
RS Total					311.83	
Control Total					4208.98	
Electrics						
	Amethyst Design	Transformer repair	1	175.00	175.00	Dec-13
		Delivery charge	1	41.00	41.00	Dec-13
Amethyst Design Total					216.00	
	KUSCO	63A power supply installation	1	984.22	984.22	May-14
KUSCO Total					984.22	
	Micromech	Electrical control cabinet build	1	8562.00	8562.00	Nov-14

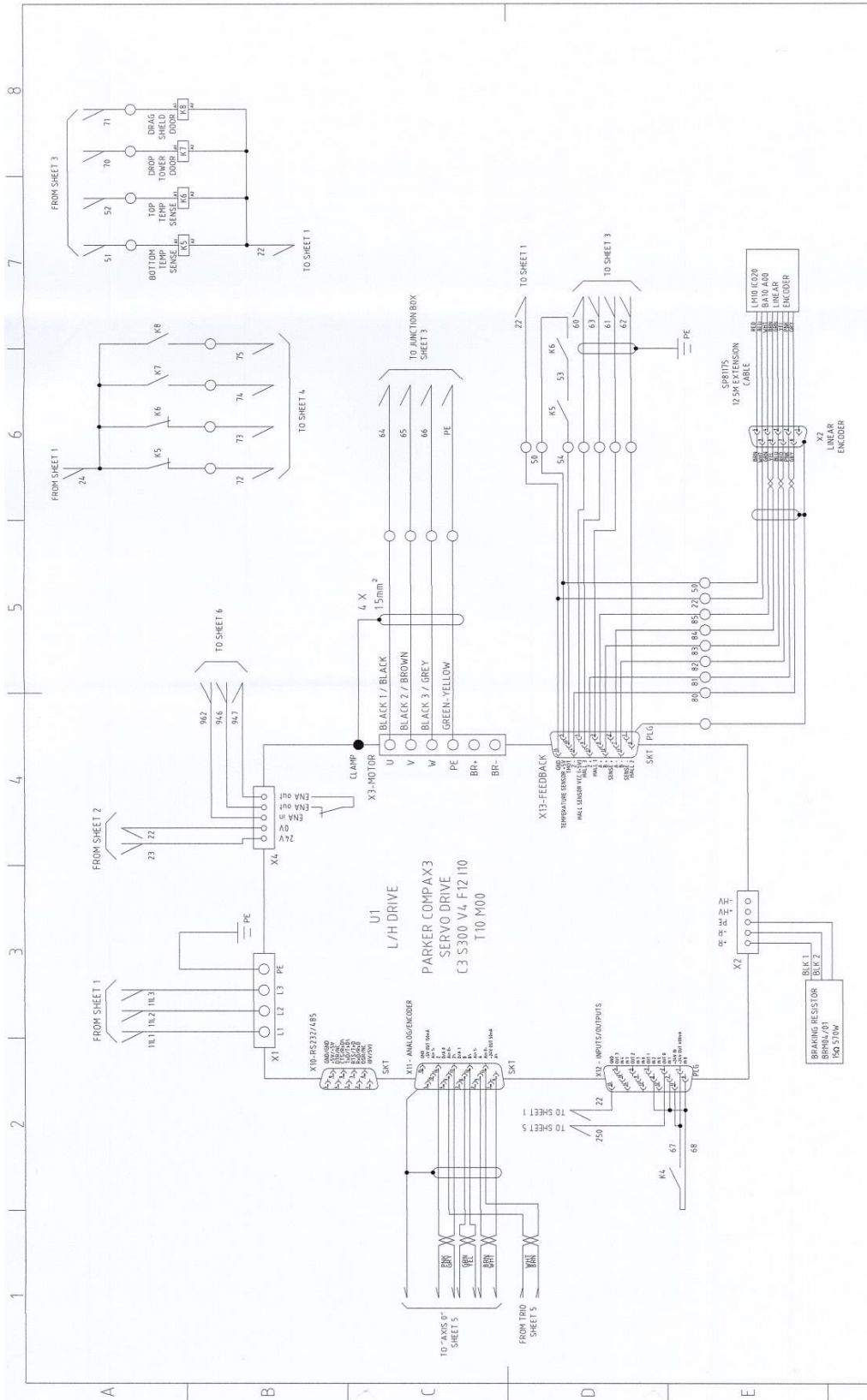
Syst.	Provider	Name	Qty	Price per one (£)	Total Price (£)	Order Date
Micromech Total					8562.00	
RS		Cable gland M20	2	0.69	1.38	Nov-12
		Cable gland M32	2	1.42	2.84	Nov-12
		Spiral cable gland	2	2.37	4.74	Nov-12
		Emergency stop	1	21.60	21.60	Jul-13
		Cable ties	1	20.28	20.28	Jul-13
		Cable trunking	2	17.91	35.82	Aug-13
		AWG28 cable	1	85.08	85.08	Aug-13
		Connector 10pin Male	4	16.78	67.12	Aug-13
		Connector 10pin Female	4	6.60	26.40	Aug-13
		Emergency stop	1	21.60	21.60	Aug-13
		Shielding enclosure	8	6.59	52.72	Mar-14
RS Total					339.58	
Electric Total					10101.80	
Other						
RS		Labcoat	1	6.69	6.69	Nov-12
RS Total					6.69	
Micromech		Delivery charge	1	15.00	15.00	Sep-13
		Delivery charge	1	15.00	15.00	Dec-14
Micromech Total					30.00	
Magnetic shielding		Delivery charge	1	20.00	20.00	Feb-15
		Delivery charge	1	20.00	20.00	Aug-15
Magnetic shielding Total					40.00	
Other Total					76.69	
Safety						
RS		Hazard sticky tape	1	11.82	11.82	Nov-12
RS Total					11.82	
AnyFoam		Foam sheet, 2000x1000x20mm	1	35.56	35.56	Nov-12
AnyFoam Total					35.56	
Simply Foam Products		Closed cell poly sheet	2	109.48	218.96	Aug-13
Simply Foam Products Total					218.96	
Safety Total					266.34	

Syst.	Provider	Name	Qty	Price per one (£)	Total Price (£)	Order Date
Structure						
	Direct Plastic	Lexan poly sheet, 2x2050x1250	4	46.09	184.36	Aug-13
Direct Plastic Total					184.36	
RS		Mounting Rim Profile 8mm	1	12.92	12.92	Nov-12
		Mounting rim profile 10mm	4	16.45	65.80	Nov-12
		End cap for strut profile	1	5.83	5.83	Nov-12
		T-head bolts	22	5.74	126.28	Nov-12
		T-slot M5 nuts	3	3.80	11.40	Nov-12
		M5 screws	1	8.57	8.57	Nov-12
		M12x60 hex bolts	1	19.21	19.21	Nov-12
		M12 nuts	1	20.98	20.98	Nov-12
		PVC cover strip	2	18.43	36.86	Nov-12
		Rubber sealing tape	1	2.54	2.54	Nov-12
		45deg connector	4	10.48	41.92	Nov-12
		End connector	9	9.28	83.52	Nov-12
		Angle bracket 45prof	25	3.13	78.25	Nov-12
		Angle bracket 30prof	1	20.90	20.90	Nov-12
		Mounting rim profile 10mm	2	19.74	39.48	Apr-13
		Strut profile 45x45mm	2	41.86	83.72	Jul-13
		PVC cover strip 10mm	2	22.11	44.22	Jul-13
		PVC cover strip 10mm	2	4.52	9.04	Jul-13
		PVC cover strip 8mm	2	17.67	35.34	Jul-13
		PVC cover strip 6mm	2	4.55	9.10	Jul-13
		45deg connector, 10mm	2	12.57	25.14	Jul-13
		Angle bracket, 45mm	20	4.13	82.60	Jul-13
		PVC cover strip 10mm	1	22.88	22.88	Aug-13
		Angle brackets 30x60x60	1	4.54	4.54	Mar-14
		Angle brackets 30x30x30	2	3.22	6.44	Mar-14
		Strut profile 45x45mm	1	44.80	44.80	Nov-14
		T-head bolts	3	7.25	21.75	Nov-14
RS Total					964.03	
Structure Total					1148.39	
Tools						
RS		Hotmelt adhesive	1	5.33	5.33	Nov-12
		Threading tap	2	10.09	20.18	Nov-12
RS Total					25.51	
Already Hire		Cherry picker hire	2	640.00	1280.00	Jan-16
Already Hire Total					1280.00	
Tools Total					1305.51	

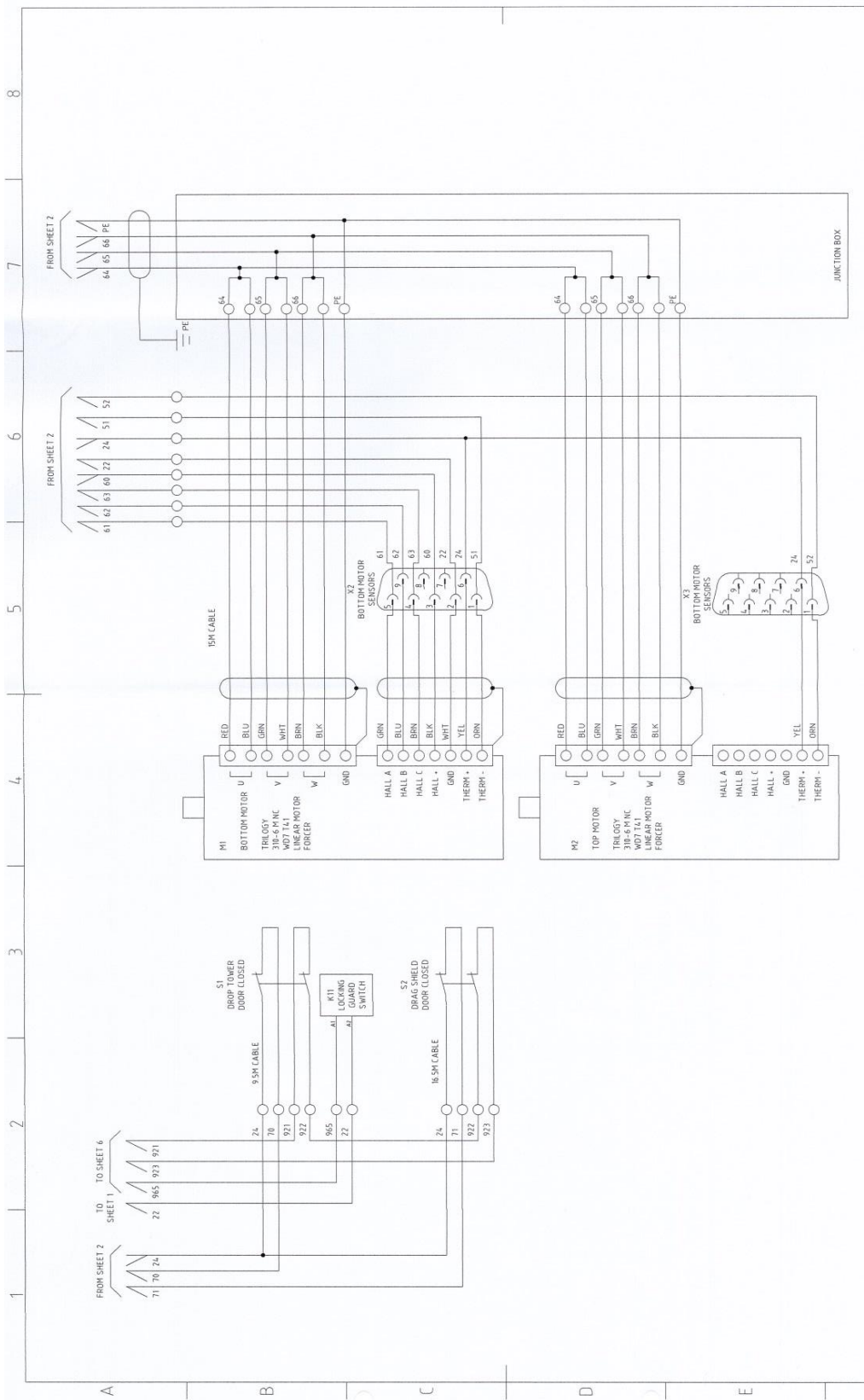
Syst.	Provider	Name	Qty	Price per one (£)	Total Price (£)	Order Date
Sub Total					17107.71	
VAT					3421.54	
Grand Total					20529.25	

Appendix F. Circuit diagram (by “Micromech Systems Ltd”)





ISS NO	REVISION NOTE	DATE	CHKD/APPVD	TITLE	DRAWN BY	CHECKED BY	APPROVED BY	DRAWING NO	SHEET	DF
F				ZERO G RIG				11801C	2	6
A	FIRST ISSUE	10/09/2014	MS				MS			
B	CORRECTED AFTER BUILD	01/10/2014	MS				MS			

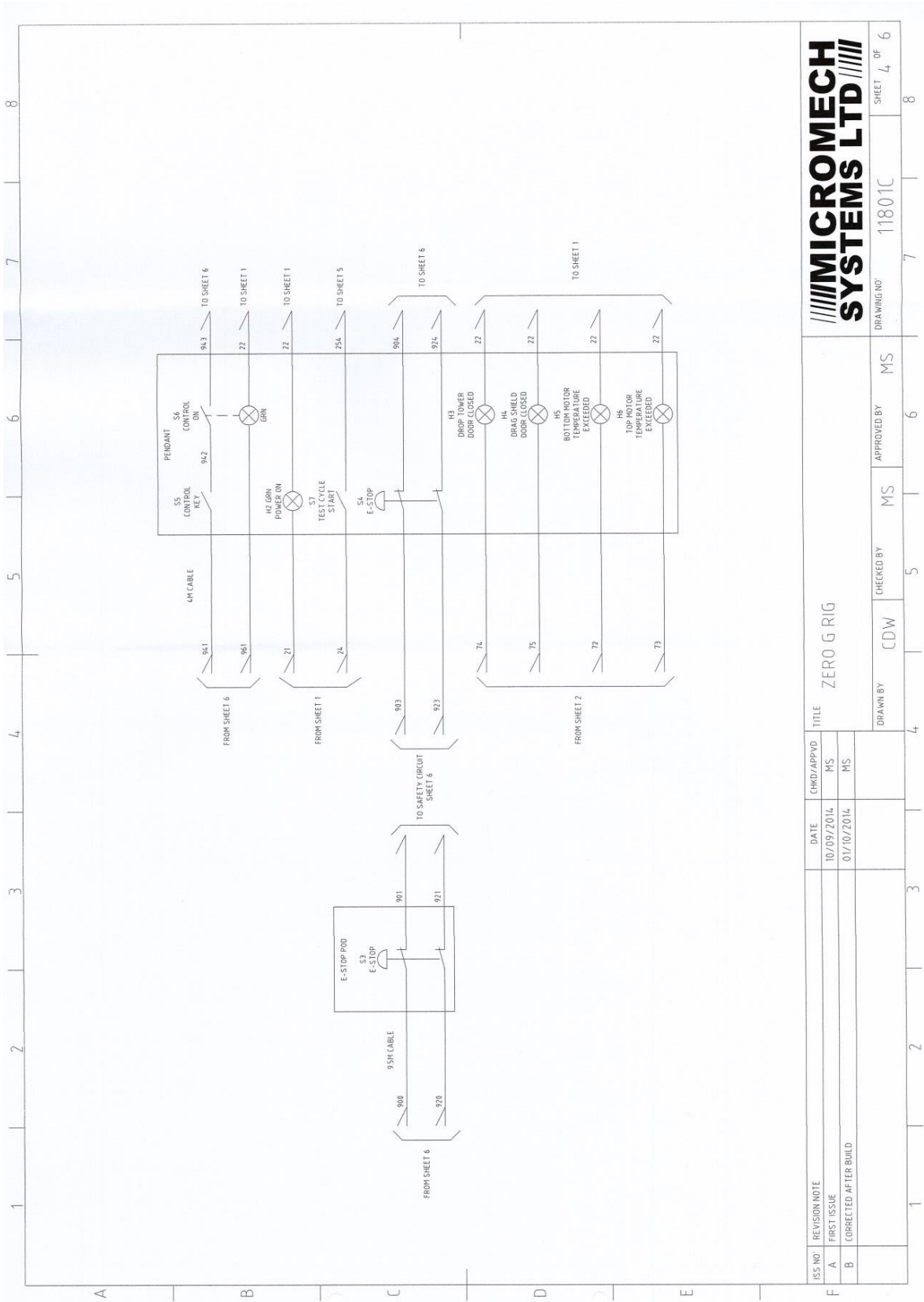


MICROMECH SYSTEMS LTD

DRAWING NO: 11801C SHEET 3 OF 6

ISS NO	REVISION NOTE	DATE	CHKD/APPVD	TITLE
A	FIRST ISSUE	10/09/2014	MS	ZERO G RIG
B	CORRECTED AFTER BUILD	01/10/2014	MS	

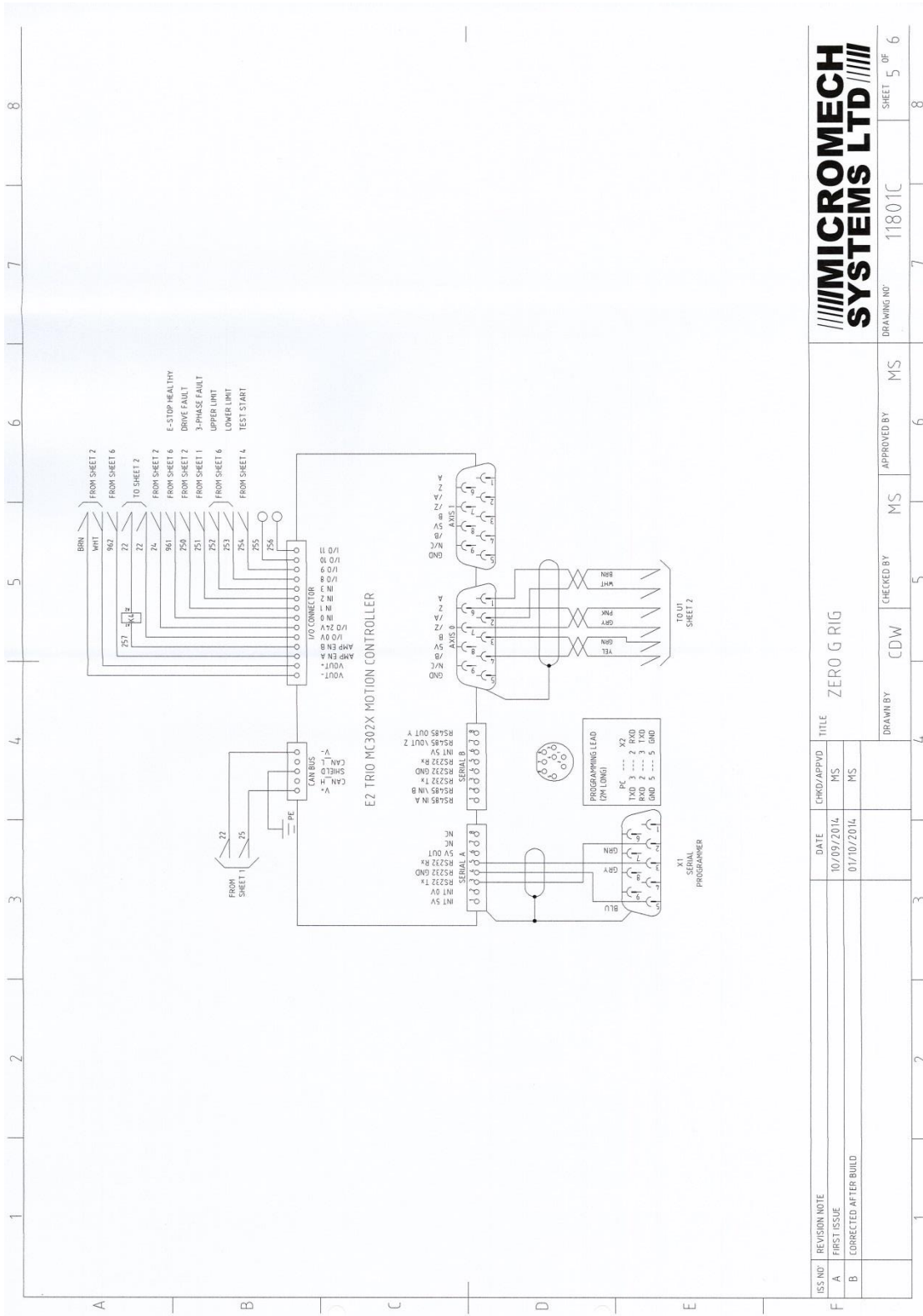
DRAWN BY	CDW	CHECKED BY	MS	APPROVED BY	MS
			DRAWING NO: 11801C		
			SHEET 3 OF 6		



**//////MICROMECH
SYSTEMS LTD//////**

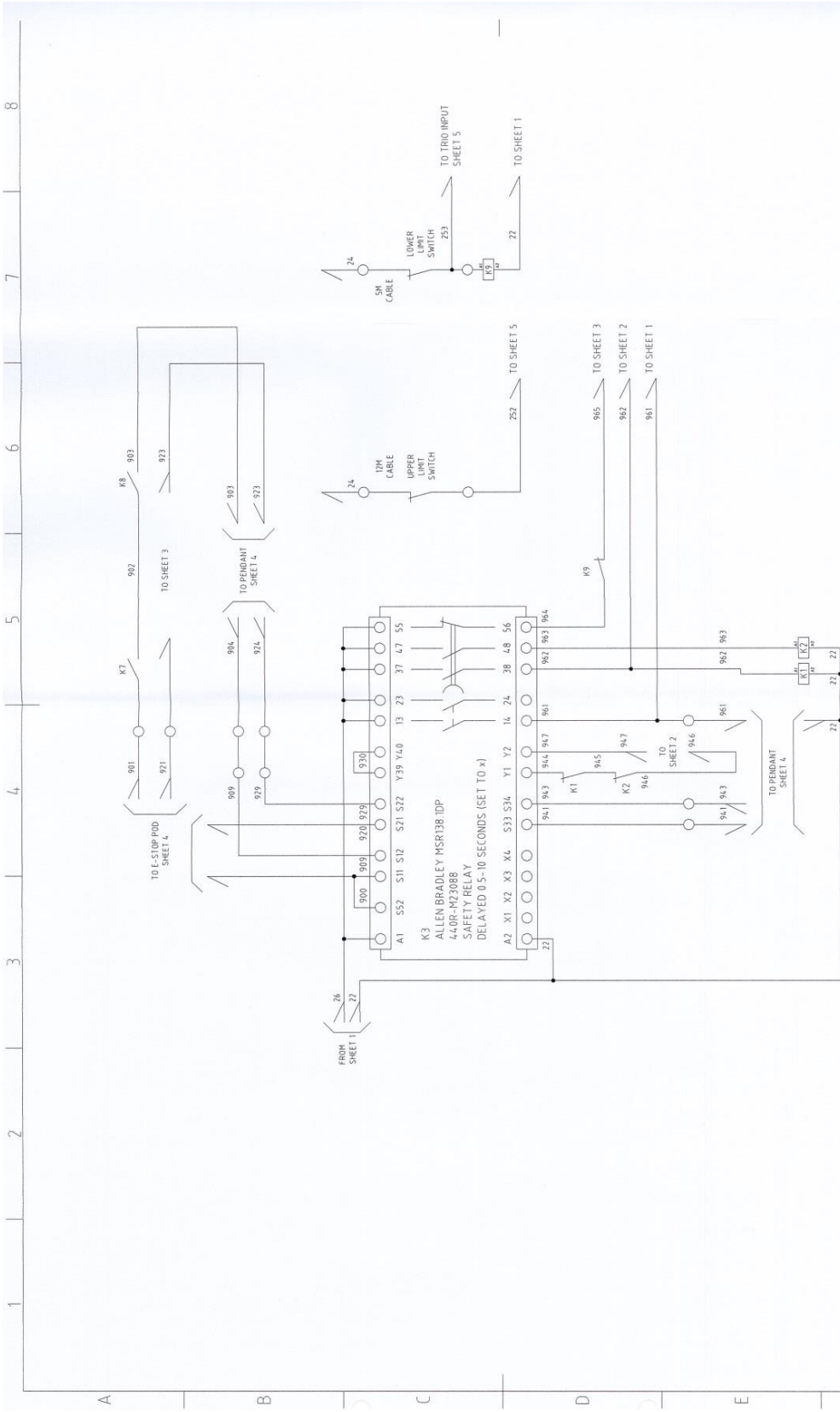
ISS NO	REVISION NOTE	DATE	CHKD/APPVD	TITLE	DRAWING NO	SHEET	OF
A	FIRST ISSUE	10/09/2014	MS	ZERO G RIG	11801C	4	6
B	CORRECTED AFTER BUILD	01/10/2014	MS				

APPROVED BY	MS	CHECKED BY	MS	DRAWN BY	CDW
-------------	----	------------	----	----------	-----



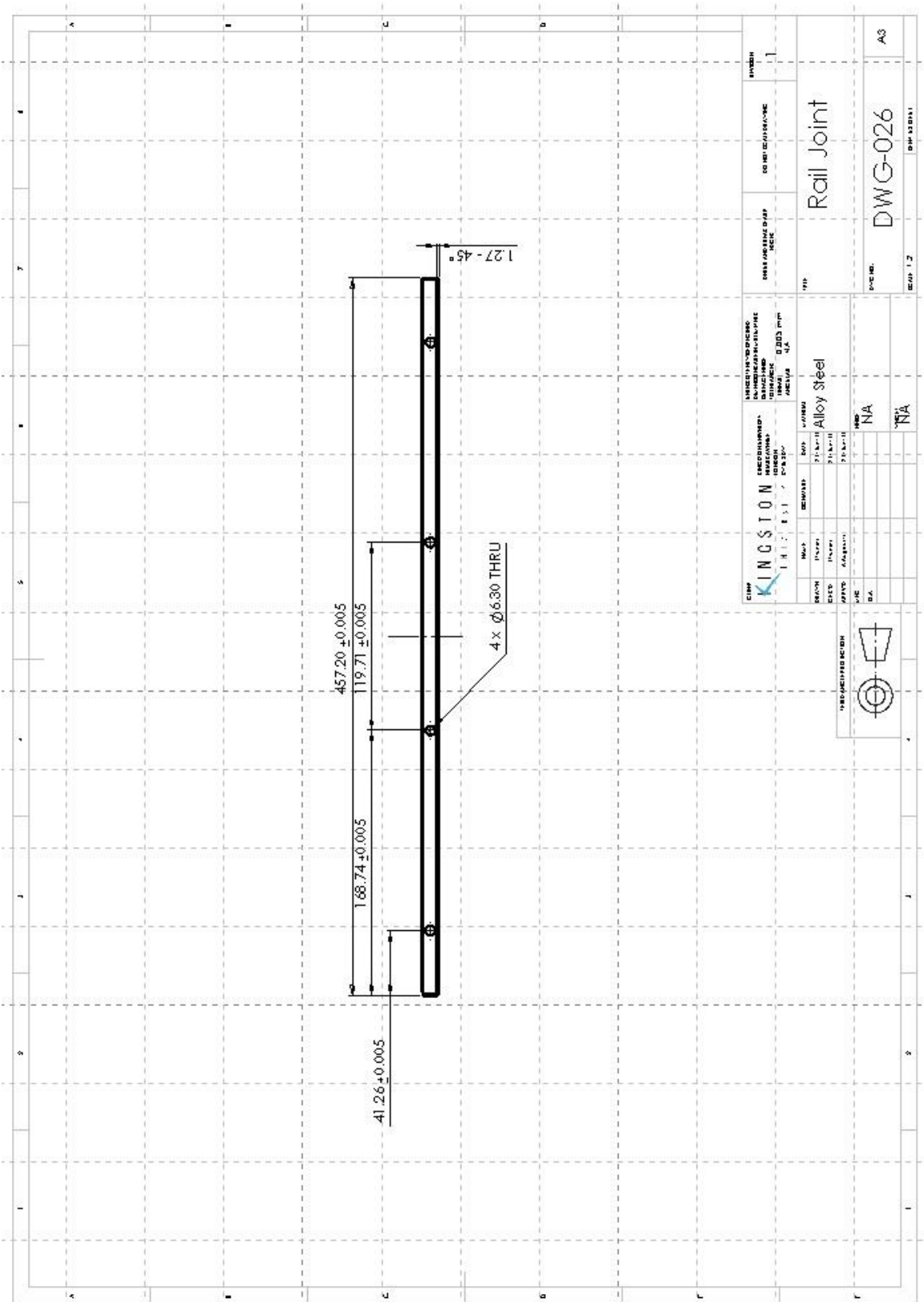
ISS NO	REVISION NOTE	DATE	CHKD/APVD	TITLE
A	FIRST ISSUE	10/09/2014	MS	ZERO G RIG
B	CORRECTED AFTER BUILD	07/10/2016	MS	

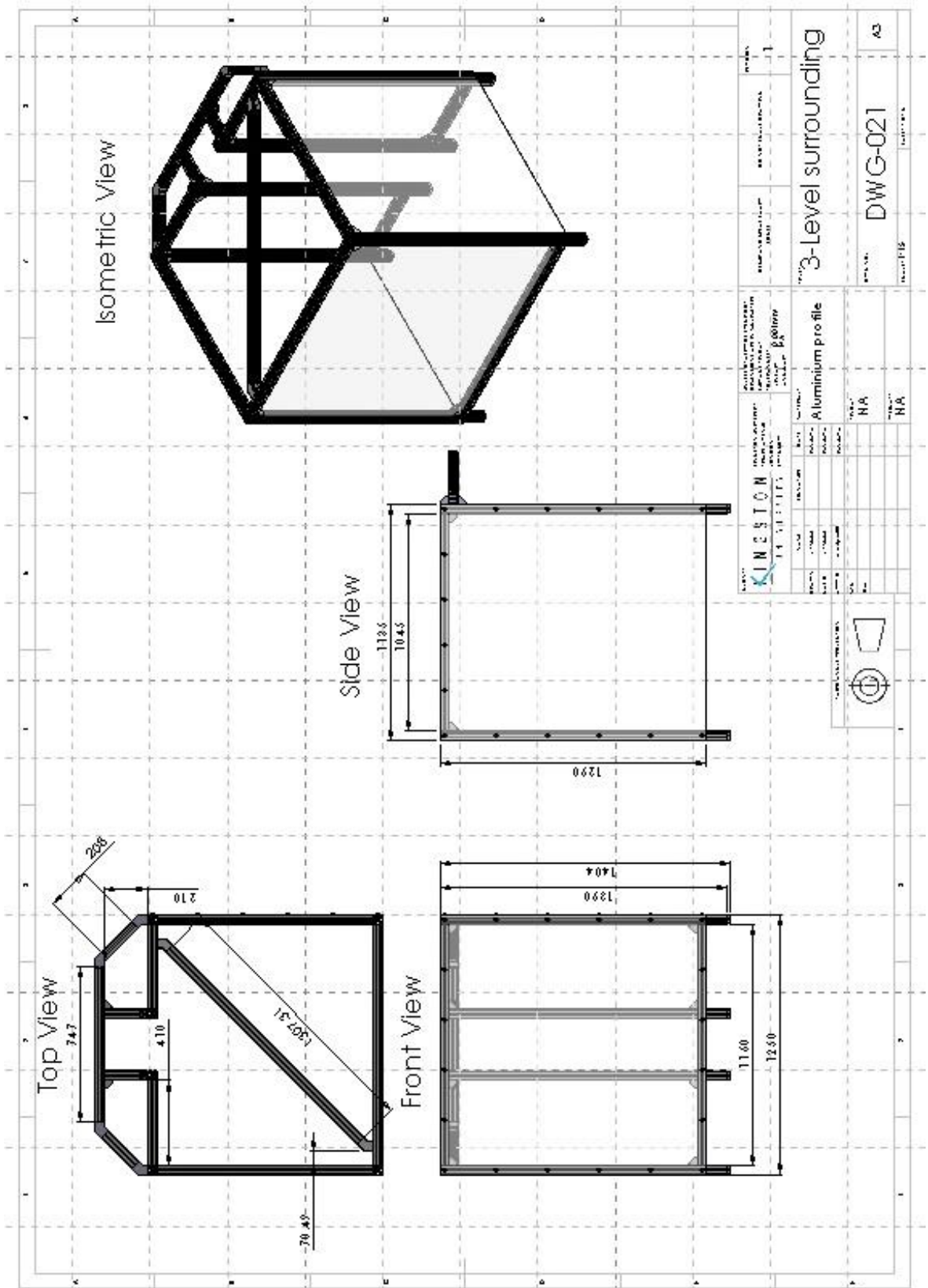
DRAWN BY	CDW	CHECKED BY	MS	APPROVED BY	MS
DRAWING NO			11801C		
SHEET			5 OF 6		

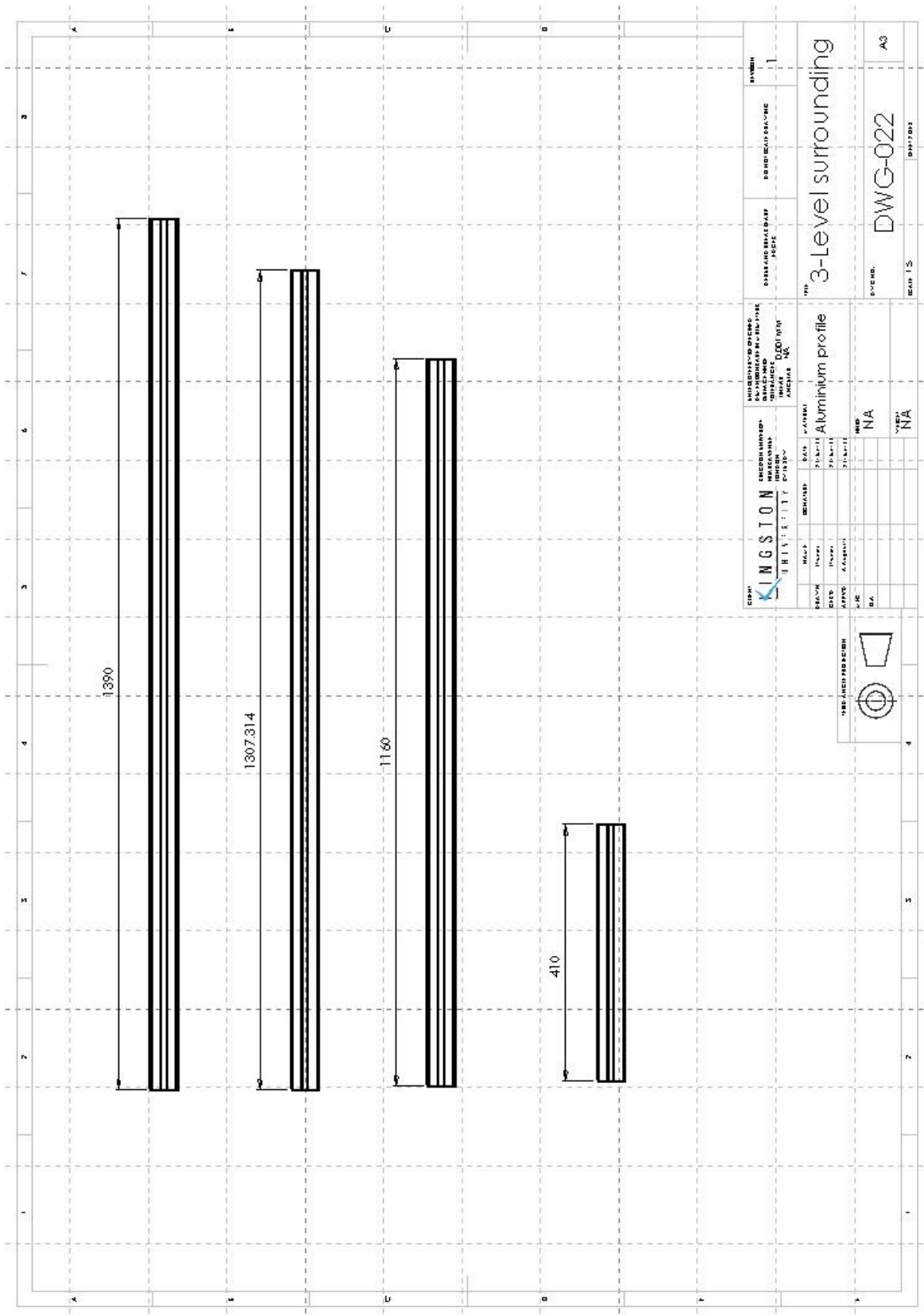


ISS NO	REVISION NOTE	DATE	CHKD/APPVD	TITLE	DRAWN BY	CHECKED BY	APPROVED BY	DRAWING NO	SHEET OF
A	FIRST ISSUE	10/09/2014	MS	ZERO G RIG	CDW	MS	MS	11801C	6 OF 6
B	CORRECTED AFTER BUILD	01/10/2014	MS						

Appendix G. Drop Tower manufacturing components (CAD files)



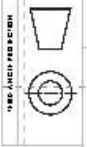


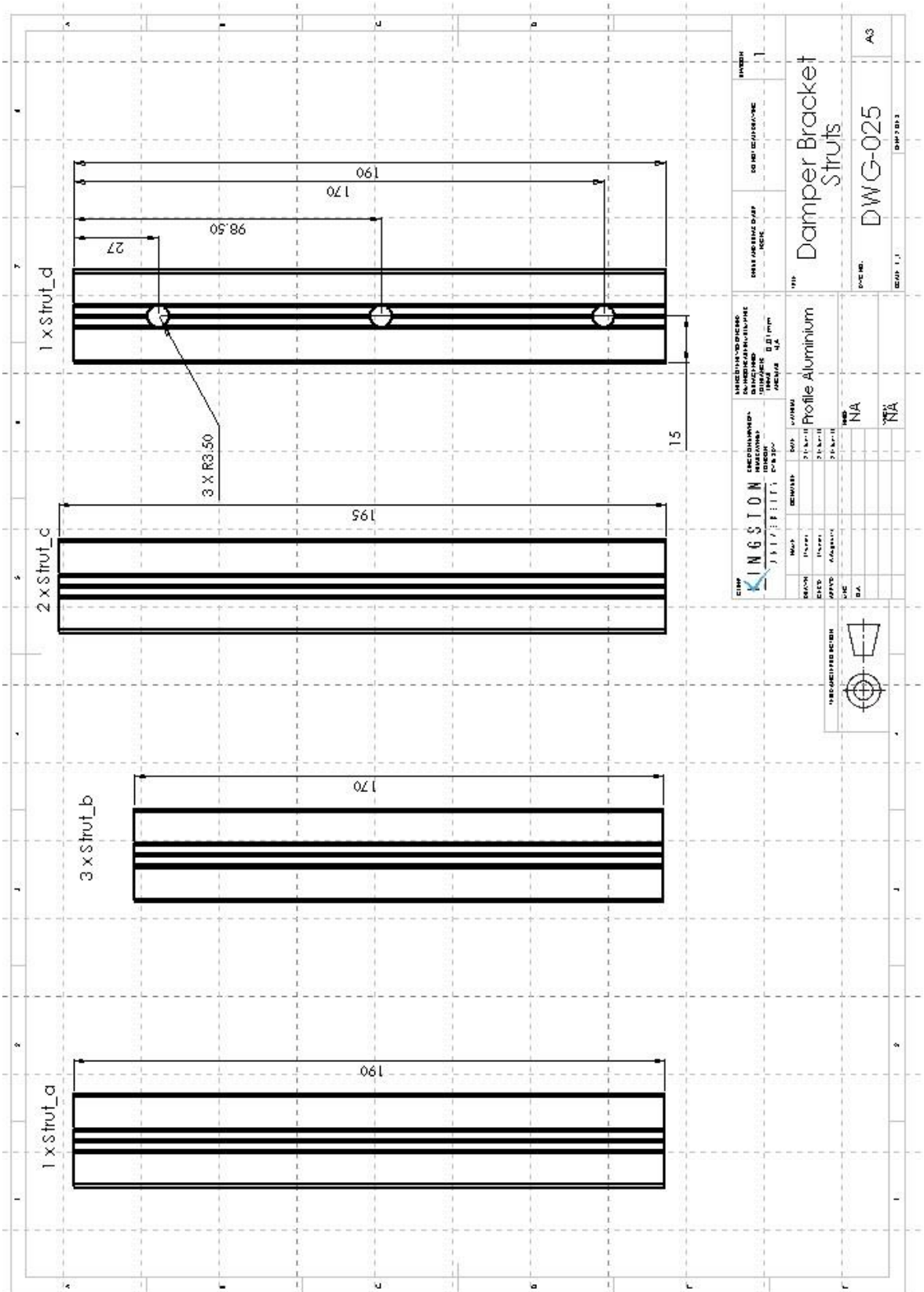


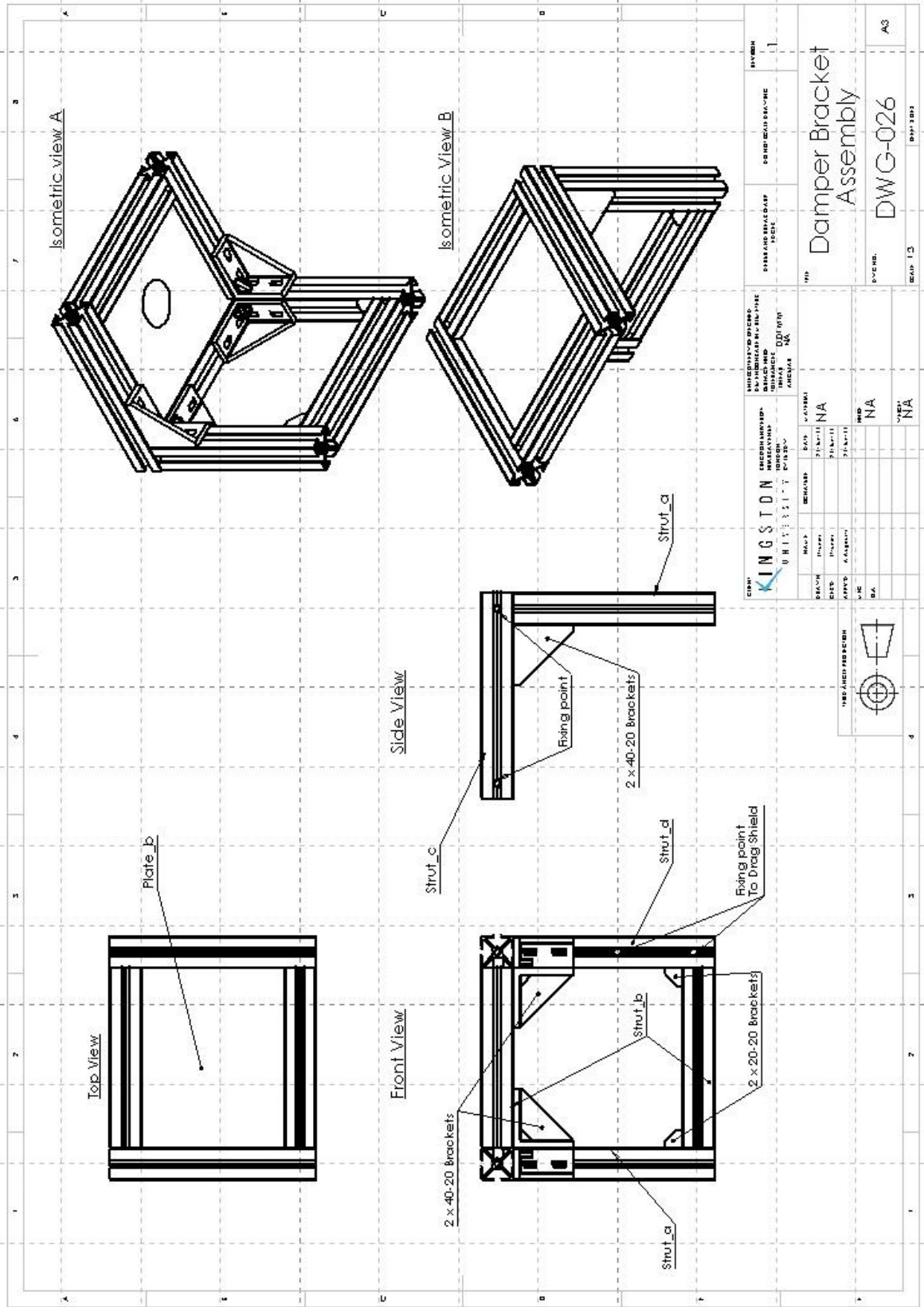
		MATERIALS DIMENSIONS WEIGHT AREA	SECTION AREA PERIMETER WEIGHT AREA	DISTANCE BETWEEN CENTERS (mm)	NUMBER OF PROFILES PER UNIT LENGTH
SECTION NAME (mm)	SECTION AREA (mm ²)	PERIMETER (mm)	WEIGHT (kg/m)	AREA (mm ²)	DISTANCE BETWEEN CENTERS (mm)
SECTION NAME (mm)	SECTION AREA (mm ²)	PERIMETER (mm)	WEIGHT (kg/m)	AREA (mm ²)	DISTANCE BETWEEN CENTERS (mm)
SECTION NAME (mm)	SECTION AREA (mm ²)	PERIMETER (mm)	WEIGHT (kg/m)	AREA (mm ²)	DISTANCE BETWEEN CENTERS (mm)
SECTION NAME (mm)	SECTION AREA (mm ²)	PERIMETER (mm)	WEIGHT (kg/m)	AREA (mm ²)	DISTANCE BETWEEN CENTERS (mm)

3-Level surrounding

OVERNO. DWG-022	SHEET NO. 01/01
DATE 2023	DRAWN BY [Name]
CHECKED BY [Name]	APPROVED BY [Name]
SCALE 1:1	MATERIAL Aluminum profile
UNIT mm	FINISH NA
TOLERANCE NA	STANDARD NA







Appendix H. MSD model “MATLAB®” codes

Appendix H.A. 1-D model simulation running code

```
%Mass spring model running code
%V2
%Jevgenijs Trunins
%15/07/16
%
%
clear all;
clc;

%%Set the simulation limits
v_s=1.1805; %Test start v_0
v_f=1.6835; %Test finish v_0
v_0=v_f;

%%Set the simulation constants
N_T=100; %maximum periods
dv_0=0.0005; %Test step;
d_t=0.001; %Delta t
t_f=3000; %Test time

%%Main simulation loop
while v_0>=v_s;
    %Simulation label
    display('Simulation is Running');
    fprintf('Simulation of velocities: v_0=%.4f-%.4f\n',v_s,v_f);
    fprintf('Done: %.0f%%\n',100-100*((v_0-v_s)/(v_f-v_s)));

    run('MS_model_Kiyono'); %Run

    figure('visible','off'); %Save plot T vs z
    f=plot(t,-z,'k');
    title(['Time vs CoM position (v=' num2str(v_0) ')']);
    xlabel('Time');
    ylabel('CoM position');
    xlim([sum(T_n)-2.5*T_n(2),sum(T_n)]);
    grid on;
    saveas(f,sprintf('%.4fTime-CoM_postion.jpg',v_0));

    n=1; %Save results for T vs z
    fid2=fopen(sprintf('%.4fTime-CoM_position.txt',v_0),'a+');
    while n~=N
        fprintf(fid2,'%.3f\t',t(n));
        fprintf(fid2,'%.5f\r\n',z(n));
        n=n+1;
    end
    fclose(fid2);

    fid=fopen(sprintf('%.4fPeriod.txt',v_0),'a+'); %Save results for T_n
    fprintf(fid,'%.5f\r\n',T_n);
    fclose(fid);

    %Ploting T_n vs n
```

```

d=zeros(1,a-2);
Dump=T_n; %Create dump file
T_n=zeros(1,a-2); %Resize T_n for plot
for n=1:a-2
    d(n)=n;
    T_n(n)=Dump(n+1);
end
f=plot(d,T_n, '.');
title(['T_n vs n (v=' num2str(v_0) ')']);
xlabel('n');
ylabel('T_n');
saveas(f,sprintf('%.4fT_n-n.jpg',v_0));

%Plotting T_n vs T_n+1
T_n_1=zeros(1,a-3); %Create T_n+1 matrix
T_n=zeros(1,numel(T_n_1)); %Resize T_n for plot
for n=1:numel(T_n) %Rearrange T_n and T_n+1
    T_n_1(n)=Dump(n+2);
    T_n(n)=Dump(n+1);
end
f=plot(T_n_1,T_n, 'k*'); %Save plot T_n+1 vs T_n
title(['T_n+1 vs T_n (v=' num2str(v_0) ')']);
xlabel('T_n+1');
ylabel('T_n');
saveas(f,sprintf('%.4fT_n_1-T_n.jpg',v_0));

v_0=v_0-dv_0; %Next step
end

```

Appendix H.B. 1-D dripping dynamics modelling

```

%Mass spring model by Kiyono and Fuchikami 2008
%V3.2
%Jevgenijs Trunins
%15/07/16
%


---


%% Identifying global parameters
global g;
global gamma;
global Q;
global m_i;
global m_c;
global t_crit;

%% Input physical parameters
g=1; %Gravitational parameter
gamma=0.05; %Surface tension parameter
R=0.1842; %Radius of nozzle
m_c=4.61; %Critical mass

%% Define initial conditions
z_0=2; %Drop centre position after brake-up
z_crit=5.5; %Drop centre critical position before break-up
m_i=0.02; %Starting mass
t_i=0; %time set
v_n=0; %dz/dt values set
t_crit=0; %Time after last step

%% Set initial state

```

```

%Calculate initial set-up
Q=pi*R^2*v_0; %flow rate
N=t_f/d_t+1; %Number of total steps set
d_m=Q*d_t; %Mass increase set
%Set domains
t=(t_i:d_t:t_f); %time matrix set
z=zeros(1,N); %z matrix set
m=zeros(1,N-1); %m matrix set
T_n=zeros(1,N_T); %T_n matrix set

%% First step set up
z(1)=z_0; %Initial position
m(1)=m_i; %Initial mass set
n=2; %setting initial steps || Time step #
a=1; %Period time #
True=0; %Compare the period logic || 0 or 1

%%Calculation domain
while n~=N && True==0
    if z(n-1)>=z_crit
        t_crit_old=t_crit;
        t_crit=t(n-1); %Update t_critical

        if a==1
            T_n(a)=t_crit;
            a=a+1;
        else
            T_n(a)=t_crit-t_crit_old;
            a=a+1;
        end

        z(n)=z_0; %Update z value
        v_n=0; %Update dz/dt value

        m_i=0.2*m(n-1)+0.3; %Update mass
        m(n)=m_i;
        if a>=5 %Period comparison
            c=2; %Set initial comparison period
            while c~=a-2 && True==0
                if abs((T_n(a-1)-T_n(c))*10^3)<0.5
                    if abs((T_n(a-2)-T_n(c-1))*10^3)<0.5
                        True=1; %Change logic statement
                    else
                        c=c+1; %Next step
                    end
                else
                    c=c+1; %Next step
                end
            end
        end
    else
        m(n)=m(n-1)+d_m; %Update mass
    end
    T=(t(n):d_t/2:t(n+1)); %Creating time domain for calculations
    [T,Z]=ode45(@MS_solver,T,[z(n),v_n]); %Solving differential
                                        %equation

    z(n+1)=Z(end,1); %Update z value
    v_n=Z(end,2); %Update dz/dt value
    n=n+1; %Next step || If needed
end

%%Resize the matrixes:
%Resize T_n matrix
Dump=zeros(1,a-1); %Create dump matrix

```

```

for n=1:a-1 %Reshape T_n matrix
    Dump(n)=T_n(n);
end
T_n=Dump;

%Resize t and z matrixes
aa=0; %Counter value set
n=N; %Step set
k=z(n); %Set the first value
while k==0
    aa=aa+1; %Counter added
    n=n-1; %Next step
    k=z(n); %Set the value of k
end
Dump=zeros(N,2);
Dump(:,1)=t;
Dump(:,2)=z;
t=zeros(N-aa,1);
z=zeros(N-aa,1);
for n=1:N-aa
    t(n)=Dump(n,1);
    z(n)=Dump(n,2);
end
N=size(t); N=N(1,1);

```

Appendix H.C. ODE45 MS solver

```

%ODE45 solver for the MSD model
%V1.2
%Jevgenijs Trunins
%15/07/16
%


---


%Solving second order M-S equation
function dz_dt=MS_solver(T,z)
    global gamma; %enquire global parameters
    global Q;
    global g;
    global m_i;
    global m_c;
    global t_crit;

    dz_dt_1=z(2);
    dz_dt_2=- (Q+gamma)/(Q*(T-t_crit)+m_i)*z(2)-...
        z(1)*((-11.4*(Q*(T-t_crit)+m_i)+52.5)/(Q*(T-t_crit)+...
            +m_i))*((T-t_crit)<(m_c-m_i)/Q)+g;
    dz_dt=[dz_dt_1;dz_dt_2];
end

```

Appendix H.D. Power law investigation code

```

%Investigating the Power law in bifurcation diagram
%Version 1.2
%Jevgenijs Trunins
%02/12/16
%


---


%%
clear all; clc

```

```

%% Set the simulation limits and constants
v_i=0.6280; v_f=2; dv=0.0005; %Simulation limits and step size
k=1; lgc=0; m=1; A_dump=0; %User constants
A=zeros(2,6); %Generate the initial solution matrix
T=zeros(round((v_f-v_i)/dv)+1,3); %Generate the Period matrix

%% Solver
for v=v_i:dv:v_f
    dump=load(sprintf('%0.4fPeriod.txt',v)); %Read a file
    dump(1,:)=[]; %Remove first value (non-stable value)
    for n=1:length(dump)-2 %Find periodicity
        %Only if two consecutive values are the same
        if dump(length(dump)-n)==dump(length(dump)) %Find first similar
            %value
            if dump(length(dump)-n-1)==dump(length(dump)-1) %Find second
                break %Finish counter
            end
        end
    end
    dump(1:length(dump)-n)=[]; %Based on the counter value delete others
    %numbers
    %Fill period matrix; First column - velocity; Second - max value;
    %Third - min value
    T(k,1)=v; T(k,2)=max(dump); T(k,3)=min(dump);
    if T(k,2)==T(k,3) %Plot min and max value in blue if one period exist
        plot(v,dump,'.r','markersize',12); hold on
    else %Plot in black if more than one
        plot(v,dump,'.k','markersize',12); hold on
    end
    k=k+1; %Next step counter
end

%% Area calculations
for n=1:length(T)
    %Sum areas if there is difference between min and max
    if lgc==1 %Logic gate for summation of areas
        %Sum current value to previous total
        A_dump=A_dump+0.5*dv*(T(n-1,2)+T(n,2)-(T(n-1,3)+T(n,3)));
        if T(n,2)==T(n,3) %In case it diverged to single period
            lgc=0; %Change the gate
            %Record Area value as zero dump file
            A(m,3)=A_dump; A_dump=0; A(m,2)=T(n,1);
            m=m+1; %Next area number
        end
    else %If previously it was single period
        if T(n,2)~=T(n,3) %Check if it changed
            %Calculate the area
            A_dump=A_dump+0.5*dv*(T(n-1,2)+T(n,2)-(T(n-1,3)+T(n,3)));
            lgc=1; %Change the logic
            A(m,1)=T(n,1); %Record the velocity at which it started
        end
    end
end

%Some areas are too small to be considered and are enclosed in between
%single period region. Consider only large values of areas
A(A(:,3)<0.01,:)=[];

%% Finding for the period jump
%Usually associated with big jump of value T
A(1,4)=v_i; m=2; %Record first value
for n=1:length(T)-1 %Search from the records
    if T(n,2)==T(n,3) %Only when there is one period
        if T(n+1,2)-T(n,2)>1 %Here approximated the jump difference as 1
            %Display the line associated with that

```

```

        line([T(n,1) T(n,1)], [10 60], 'Color', [0 1 0], 'LineStyle', ':')
        A(m,4)=T(n,1); m=m+1; %Record the value and next step
    end
end
end

%% Displaying start and end of bifurcation areas
for n=1:length(A)
    line([A(n,1) A(n,1)], [10 60], 'Color', [0 0 1], 'LineStyle', '--') %Start
    line([A(n,2) A(n,2)], [10 60], 'Color', [1 0 1], 'LineStyle', '--') %End
end

%% Calculating the power values
for n=1:length(A)-3
    A(n,5)=log(A(n+1,3))/log(A(n,3)); %1D area change results
    A(n,7)=log(A(n+1,2)-A(n+1,1))/log(A(n,2)-A(n,1)); %Bifurcation
                                                %start-end

    %2D area change
    F=[log(A(n+2,3))-log(A(n+3,4)-A(n+2,4)), log(A(n+3,4)-A(n+2,4)); ...
        log(A(n+1,3))-log(A(n+2,4)-A(n+1,4)), log(A(n+2,4)-A(n+1,4))];
    B=[log(A(n+1,3)); log(A(n,3))];
    alpha(:,n)=F\B;
end
%Plot bifurcation diagram
ylim([25 55]); xlim([v_i v_f])
xlabel('Flow velocity: v_o [normalised units]');
ylabel('Period time: T_n [normalised units]')
set(gcf, 'PaperUnits', 'inches', 'PaperPosition', [0 0 6 3])
print('Area_stud', '-djpeg', '-r450')
hold off
%Plot the area investigation results
figure
%1D area change results
set(gcf, 'PaperUnits', 'inches', 'PaperPosition', [0 0 9 12])
subplot(4,1,1); grid on; plot(T(:,1),T(:,2), '-bx');
title('1D area change results'); y=ylabel('\varsigma', 'rot', 0);
set(y, 'Units', 'Normalized', 'Position', [-0.075,0.6,0], 'FontSize', 15);
grid on; hold on; P1=polyfit(T(1:9,1),T(1:9,2),1);
plot(T(1:9,1),P1(1)*T(1:9,1)+P1(2), '--r', 'LineWidth', 1.5); xlim([0 10]);
%Bifurcation start-end results
subplot(4,1,2)
plot(T(:,1),T(:,3), '-bx'); title('Bifurcation start-end results');
y=ylabel('\varsigma', 'rot', 0);
set(y, 'Units', 'Normalized', 'Position', [-0.075,0.6,0], 'FontSize', 15)
P2=polyfit(T(1:9,1),T(1:9,3),1); grid on; hold on
plot(T(1:9,1),P2(1)*T(1:9,1)+P2(2), '--r', 'LineWidth', 1.5); hold off;
xlim([0 10])
%2D area change results
subplot(4,1,3)
plot(T(1:8,1),T(1:8,4), '-bx'); title('2D area change results')
y=ylabel('\varsigma', 'rot', 0);
set(y, 'Units', 'Normalized', 'Position', [-0.075,0.6,0], 'FontSize', 15)
P3=polyfit(T(1:8,1),T(1:8,4),1); grid on; hold on
plot(T(1:8,1),P3(1)*T(1:8,1)+P3(2), '--r', 'LineWidth', 1.5); hold off;
xlim([0 10])
subplot(4,1,4)
plot(T(1:8,1),T(1:8,5), '-bx'); y=ylabel('\tau', 'rot', 0);
set(y, 'Units', 'Normalized', 'Position', [-0.075,0.6,0], 'FontSize', 15)
P4=polyfit(T(1:8,1),T(1:8,5),1); grid on; hold on
plot(T(1:8,1),P4(1)*T(1:8,1)+P4(2), '--r', 'LineWidth', 1.5); hold off;
xlim([0 10]); xlabel('Bifurcation number (i)');
print('Area_stud_results', '-djpeg', '-r600')

```


Appendix H.E. Results presentation code

```
%Video compiling for T_n vs T_n+_1
%Version 2.0
%Jevgenijs Trunins
%15/12/16
%
%


---


clear all;
%Set constants
v_i=0.035; v_f=2.1915; dv=0.0005; Tn=zeros(100,1);

%% Fit a curve
curve=zeros(round(1+(v_f-v_i)/dv),5); %Set the matrix array for the curve
set                                                                    %points

i=1; v_0=v_i;
while v_0<v_f
    clc; disp('Simulation is Running'); %Sim display notation
    fprintf('%.2f%% - Part 1 Completed', 100*(v_0-v_i)/(v_f-v_i));
    fprintf('\n'); disp('0.00% - Part 2 Completed');
    dump1=load(sprintf('%.4fPeriod.txt',v_0)); %Load the file
    n=size(dump1); n=n(1,1); %Determining size of the loaded file
    dump2=zeros(n-2,1);
    for k=1:n-2 %Deleting first two results, as they are with error
        dump2(k)=dump1(k+2);
    end
    curve(i,1)=v_0; curve(i,2)=mean(dump2); curve(i,3)=min(dump2);
    curve(i,4)=max(dump2);
    v_0=v_0+dv; i=i+1; %Next step
end
fit_curve=fit(curve(:,1),curve(:,2),'fourier8'); %Actual fitting
aw=confint(fit_curve,0.95); %Produce array of coefficients
curve_div_dump=0; %Looking for max divergence
%Calculating mean curve for the video, which result in adapting y-axis
for k=1:i-1
    curve(k,5)=(mean(aw(:,1))+mean(aw(:,2))*cos(curve(k,1)...
        *mean(aw(:,18)))+mean(aw(:,3))*sin(curve(k,1)*mean(aw(:,18)))+...
        mean(aw(:,4))*cos(2*curve(k,1)*mean(aw(:,18)))+mean(aw(:,5))...
        *sin(2*curve(k,1)*mean(aw(:,18)))+mean(aw(:,6))*cos(3*...
        curve(k,1)*mean(aw(:,18)))+mean(aw(:,7))*sin(3*curve(k,1)*mean(a
        w(:,18)))...
        +mean(aw(:,8))*cos(4*curve(k,1)*mean(aw(:,18)))+mean(aw(:,9))*...
        sin(4*curve(k,1)*mean(aw(:,18)))+mean(aw(:,10))*cos(5*curve(k,1)...
        *mean(aw(:,18)))+mean(aw(:,11))*sin(5*curve(k,1)*mean(aw(:,18)))...
        +mean(aw(:,12))*cos(6*curve(k,1)*mean(aw(:,18)))+mean(aw(:,13))...
        *sin(6*curve(k,1)*mean(aw(:,18)))+mean(aw(:,14))*cos(7*...
        curve(k,1)*mean(aw(:,18)))+mean(aw(:,15))*sin(7*curve(k,1)*...
        mean(aw(:,18)))+mean(aw(:,16))*cos(8*curve(k,1)*mean(aw(:,18)))...
        +mean(aw(:,17))*sin(8*curve(k,1)*mean(aw(:,18))));
end

%% Create video objects
vid1=VideoWriter('Tn_VS_n.mp4'); vid1.FrameRate=25; open(vid1);
vid2=VideoWriter('Tn_VS_Tn1.mp4'); vid2.FrameRate=25; open(vid2);
vid3=VideoWriter('Return_map.mp4'); vid3.FrameRate=25; open(vid3);

%% Video recording
```

```

v_0=v_i;
while v_0<=v_f
    clc; disp('Simulation is RUNNING'); %Sim display notation
    disp('100.00% - Part 1 Completed');
    fprintf('%.2f%% - Part 2 Completed', 100*(v_0-v_i)/(v_f-v_i));
    %Create new Tn matrix
    Tn=zeros(100,1);
    dump=load(sprintf('%.4fPeriod.txt',v(m))); %Load file
    dump(1,:)=[]; %Remove first value (non-stable value)
    for t=1:length(dump) %Fill initial values
        Tn(t)=dump(t);
    end
    for n=1:length(dump)-2 %Find periodicity
        %Only if two consequent values are the same
        if dump(length(dump)-n)==dump(length(dump)) %Find first similar
            %value
            if dump(length(dump)-n-1)==dump(length(dump)-1) %Find second
                break %Finish counter
            end
        end
    end
    dump(1:length(dump)-n)=[]; %Based on the counter value delete others
    %numbers
    k=1; %set counter
    for n=t+1:length(Tn) %Fill rest with periodic numbers
        Tn(n)=dump(k); %Fill number
        k=k+1; %Next periodic number
        if k>length(dump) %Check if it is not outside the periodic matrix
            k=1; %Reset if it is
        end
    end
end

%%Plot the figures and save in a video
%Set figure #1
fig1=figure('visible','on'); plot(Tn,'.k');
title(['T_n VS n (v = ' num2str(v_0, '%.4f') ')']);
xlabel('n'); ylabel('T_n'); xlim([0 100]);
ylim([curve(round((v_0-v_i)/dv+1),5)-7 curve(round((v_0-v_i)/dv+1)...
,5)+7]);
writeVideo(vid1,getframe(fig1)); fig1=close;
%Set figure #2
fig2=figure('visible','on');
plot(Tn(2:length(Tn)),Tn(1:length(Tn)-1),'*k');
title(['T_n VS T_n+1 (v = ' num2str(v_0, '%.4f') ')']);
xlabel('T_n+1'); ylabel('T_n'); grid on;
xlim([curve(round((v_0-v_i)/dv+1),5)-7 curve(round((v_0-v_i)/dv+1)...
,5)+7]);
ylim([curve(round((v_0-v_i)/dv+1),5)-7 curve(round((v_0-v_i)/dv+1)...
,5)+7]);
writeVideo(vid2,getframe(fig2)); fig2=close;
%Set figure #3
fig3=figure('visible','on','position',[10,10,1.5*1049,695]);
set(gcf,'Color','White');
nCol=2; nRow=1; %Set # of rows and columns
rowH=0.65; colW=0.42; %Set dimensions
%Set position of lower-left corners
colX=0.06+linspace(0,0.96,nCol+1); colX=colX(1:end-1);
rowY=0.1+linspace(0.9,0,nRow+1); rowY=rowY(2:end);
%Build subplots axes and plot data
rowId=ceil(1/nCol); colId=1-(rowId-1)*nCol;
axes('Position',[colX(colId),rowY,colW,rowH]);
plot(Tn,'.k');
title('T_n VS n'); xlabel('n'); ylabel('T_n'); grid off;
xlim([0 100]);
ylim([curve(round((v_0-v_i)/dv+1),5)-7 curve(round((v_0-v_i)/dv+1)...

```

```

        ,5)+7]);
rowId=ceil(2/nCol); colId=2-(rowId-1)*nCol;
axes('Position',[colX(colId),rowY,colW,rowH]);
plot(Tn(2:length(Tn)),Tn(1:length(Tn)-1),'*k');
title('T_n VS T_{n+1}');
xlabel('T_{n+1}'); ylabel('T_n'); grid on;
xlim([curve(round((v_0-v_i)/dv+1),5)-7 curve(round((v_0-v_i)/dv+1)...
,5)+7]);
ylim([curve(round((v_0-v_i)/dv+1),5)-7 curve(round((v_0-v_i)/dv+1)...
,5)+7]);
axes('Position',[0,0.90,1,0.05]); %Set the title
text(0.5,0,['Return Maps: v = ' num2str(v_0,'%4f')],'FontSize',...
14,'FontWeight','Bold','HorizontalAlignment','Center',...
'VerticalAlignment','Bottom');
set(gca,'Color','None','XColor','White','YColor','White');
writeVideo(vid3,getframe(fig3)); fig3=close; %Take the frame for
%video

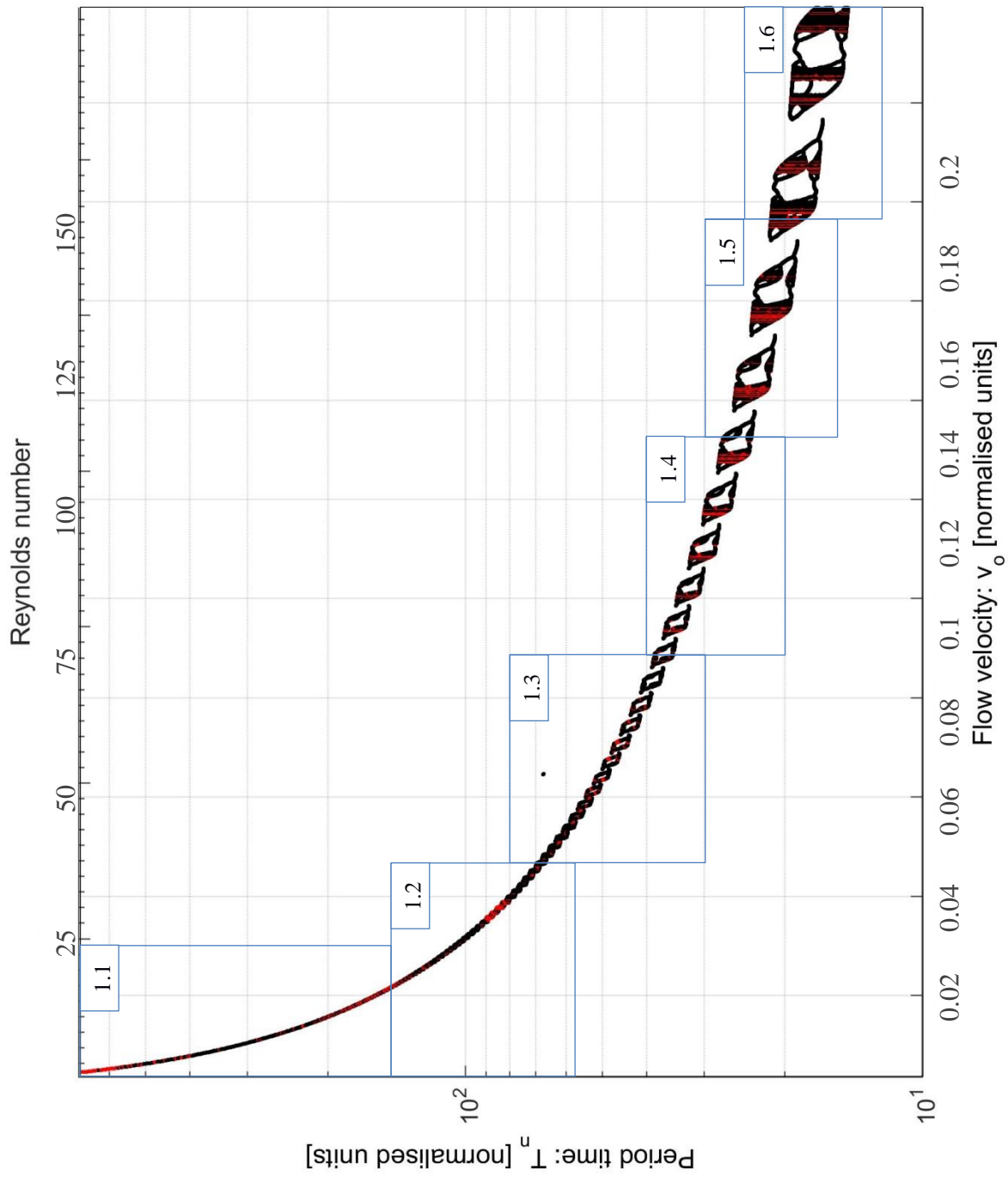
v_0=v_0+dv; %Next step
end

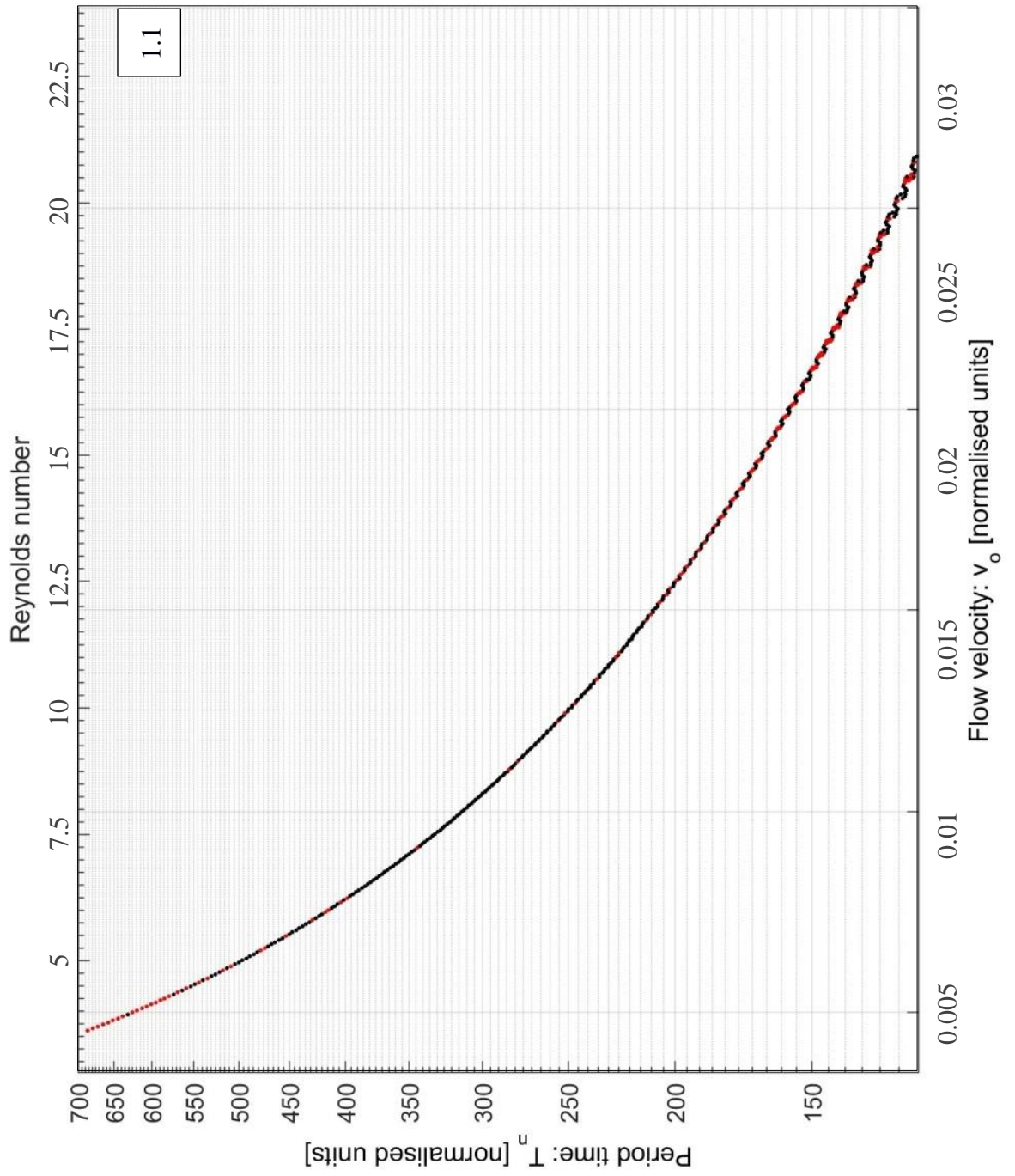
%% Close the videos
close(vid1); close(vid2); close(vid3); %Close and save all videos

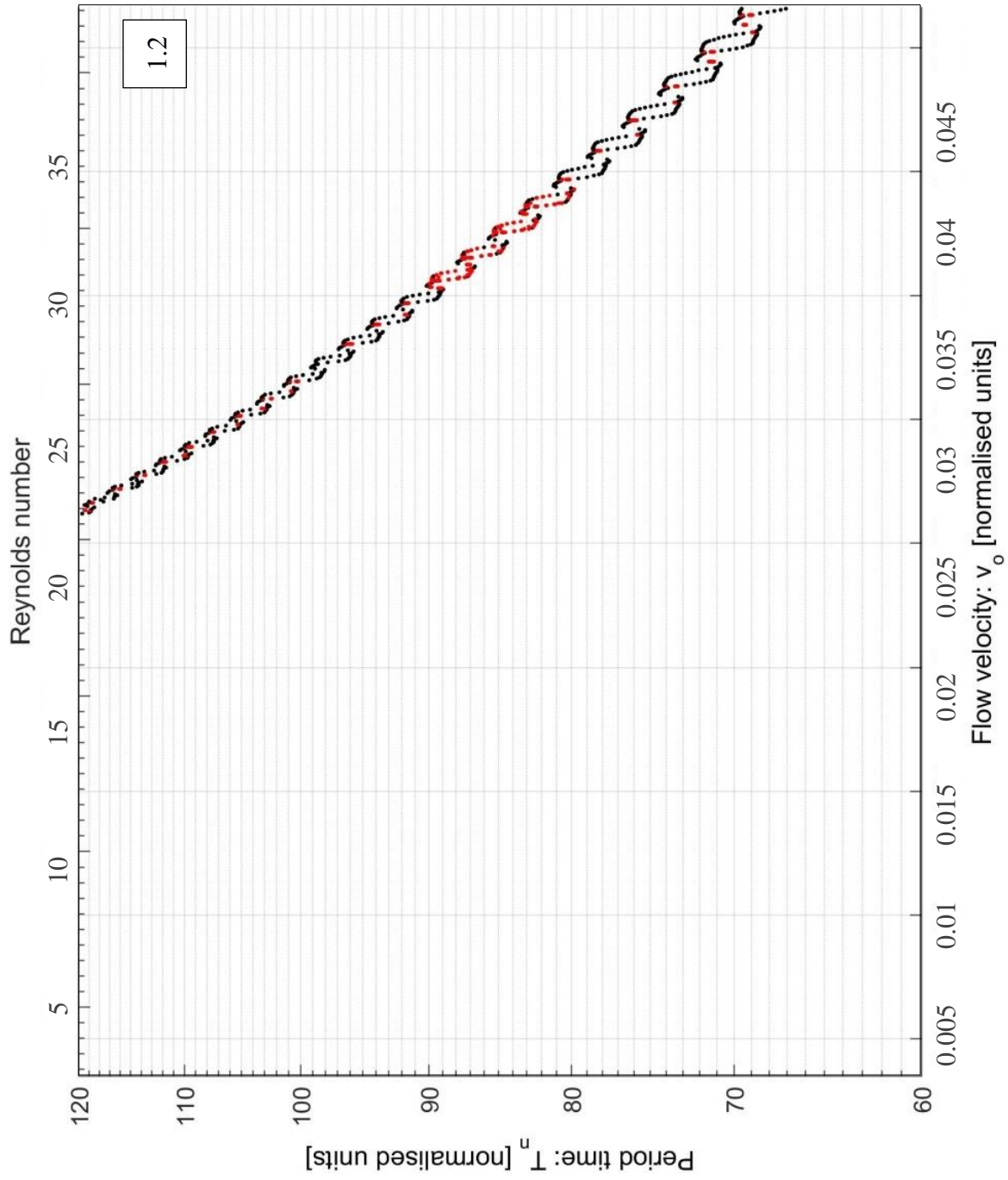
```

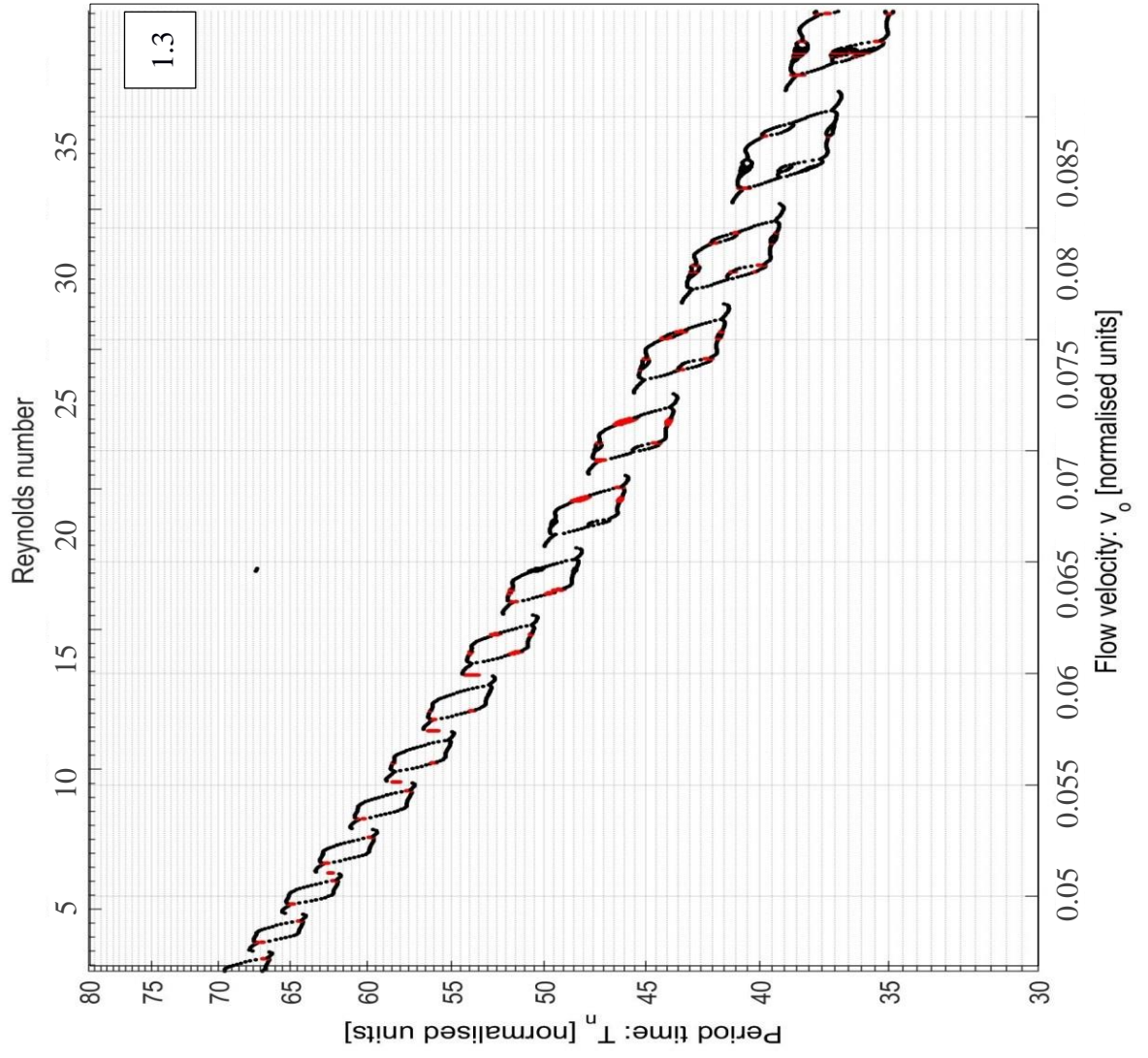
Appendix I. 1-D model results

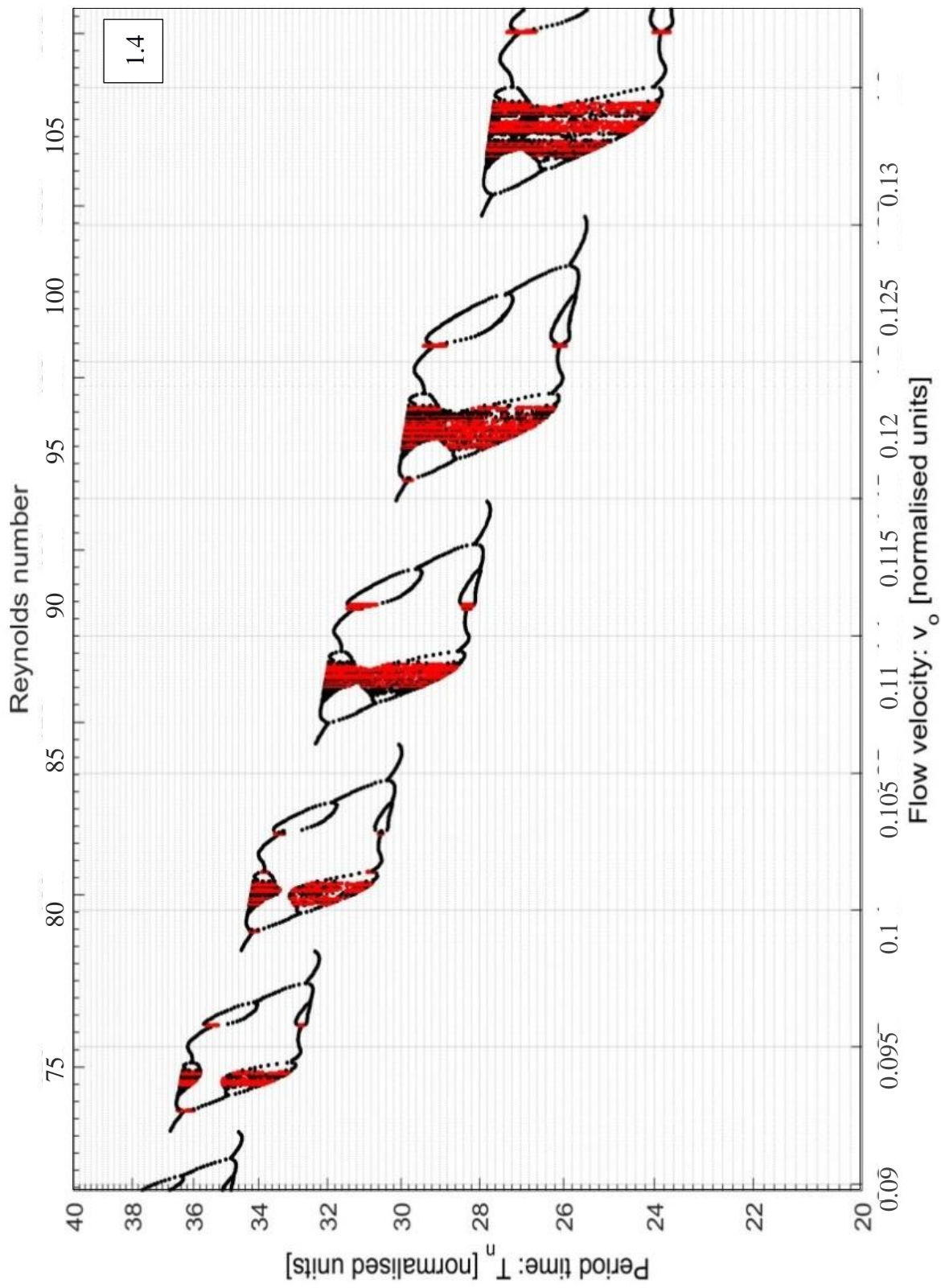
- Bifurcation results graphs

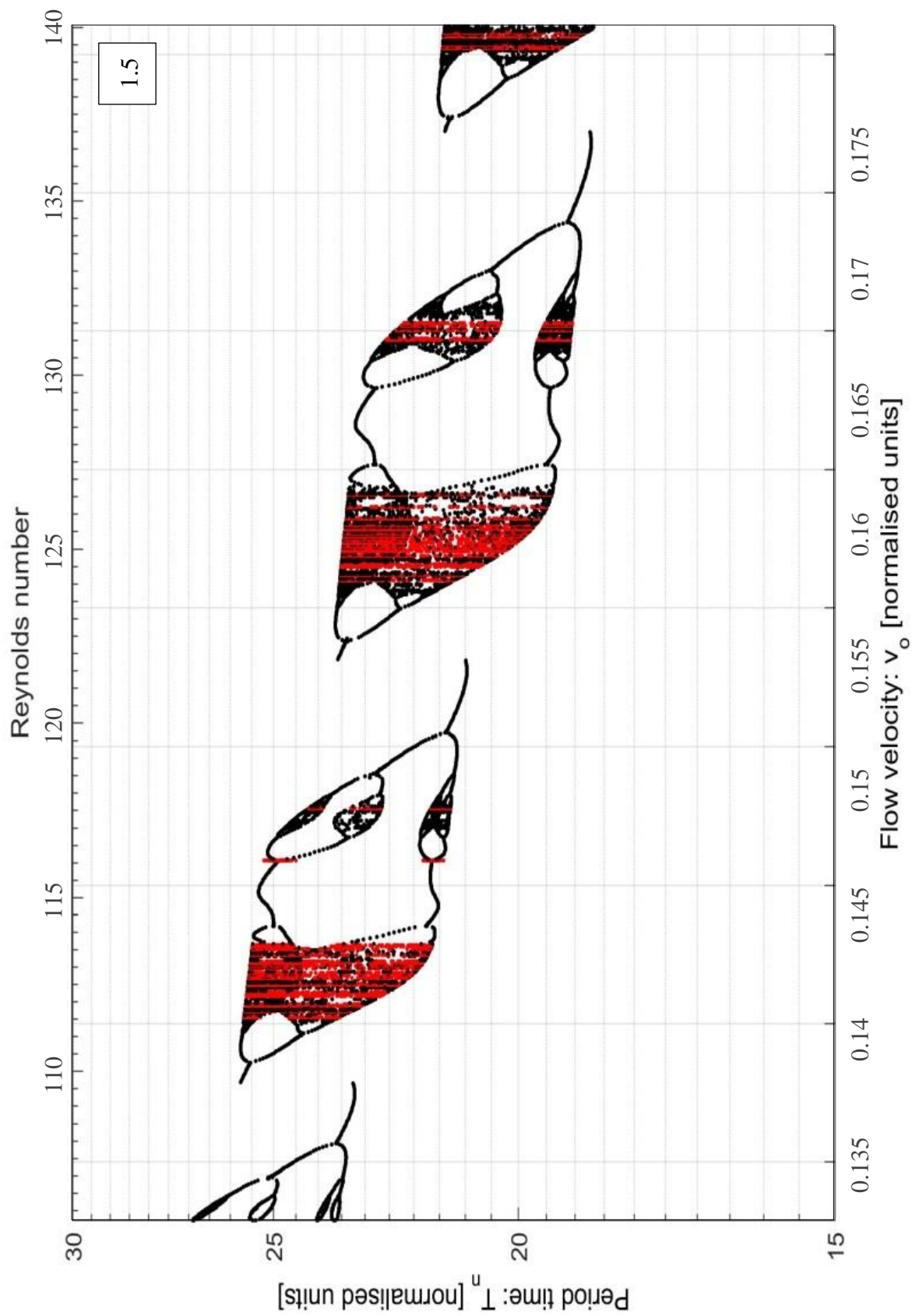


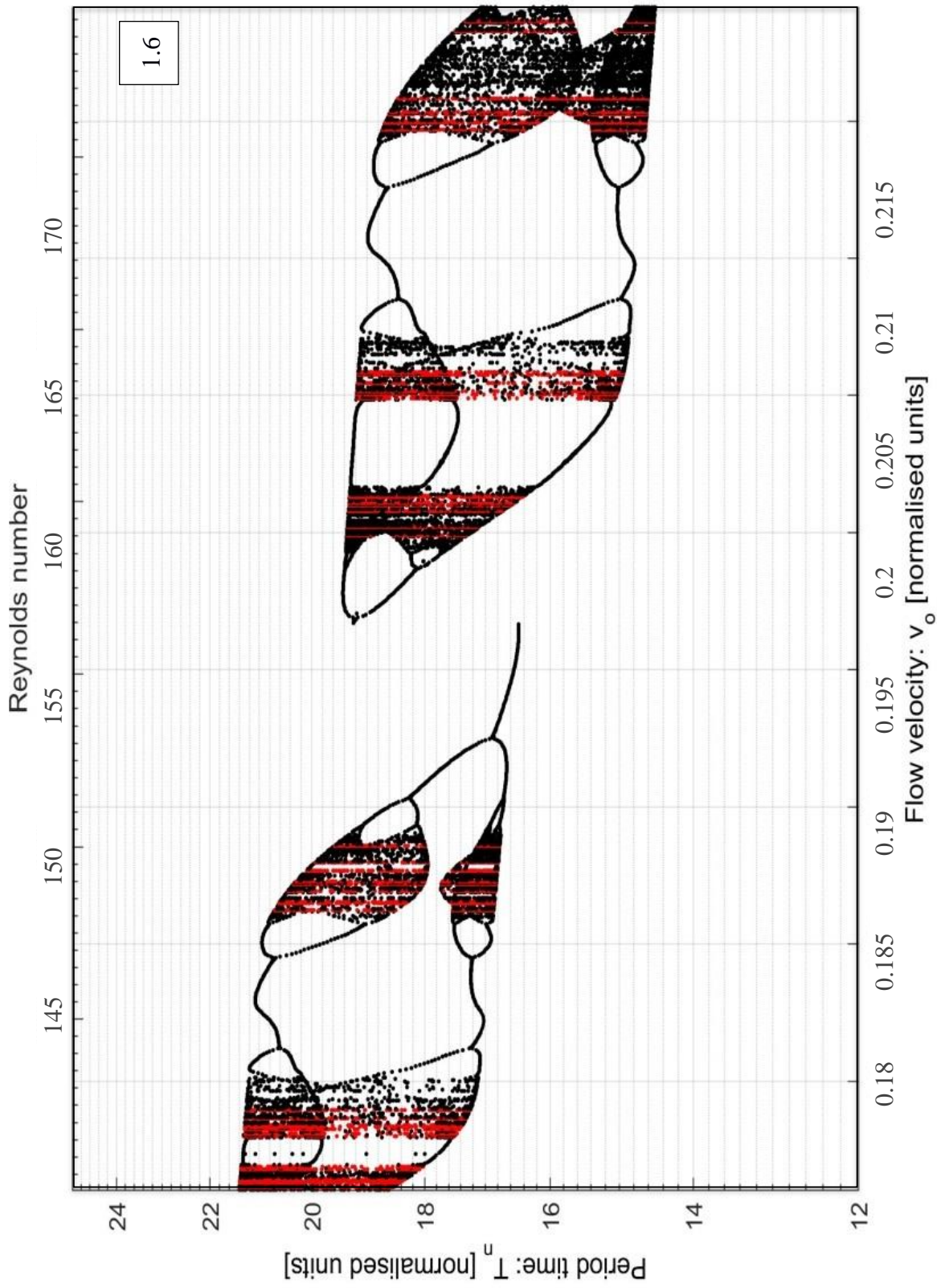




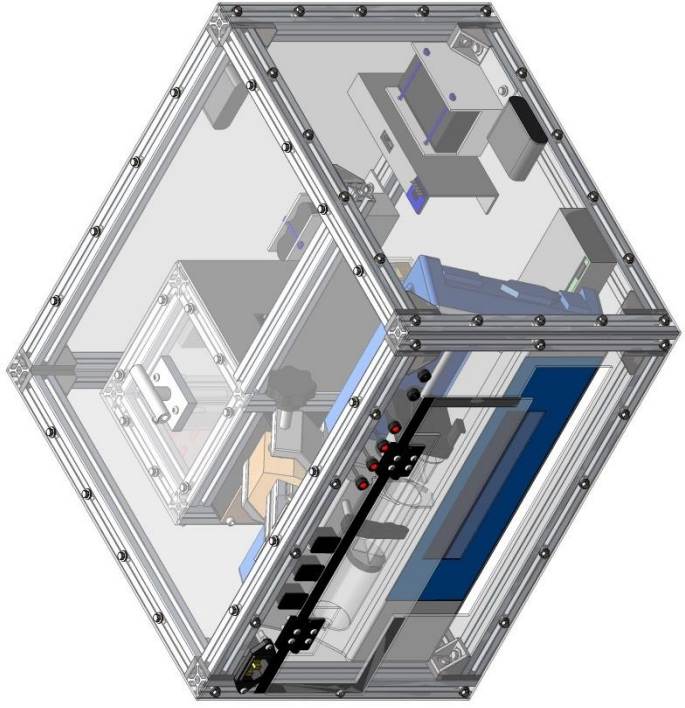




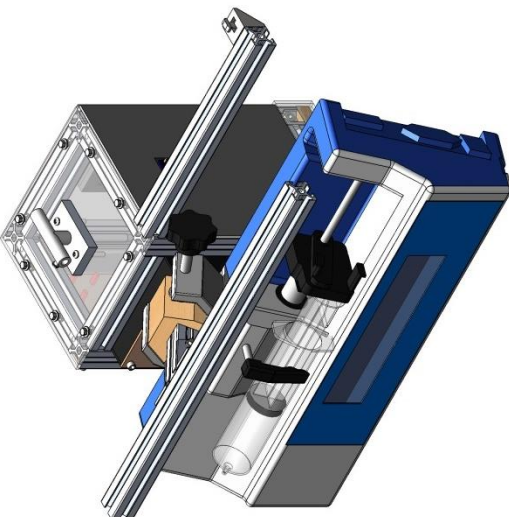




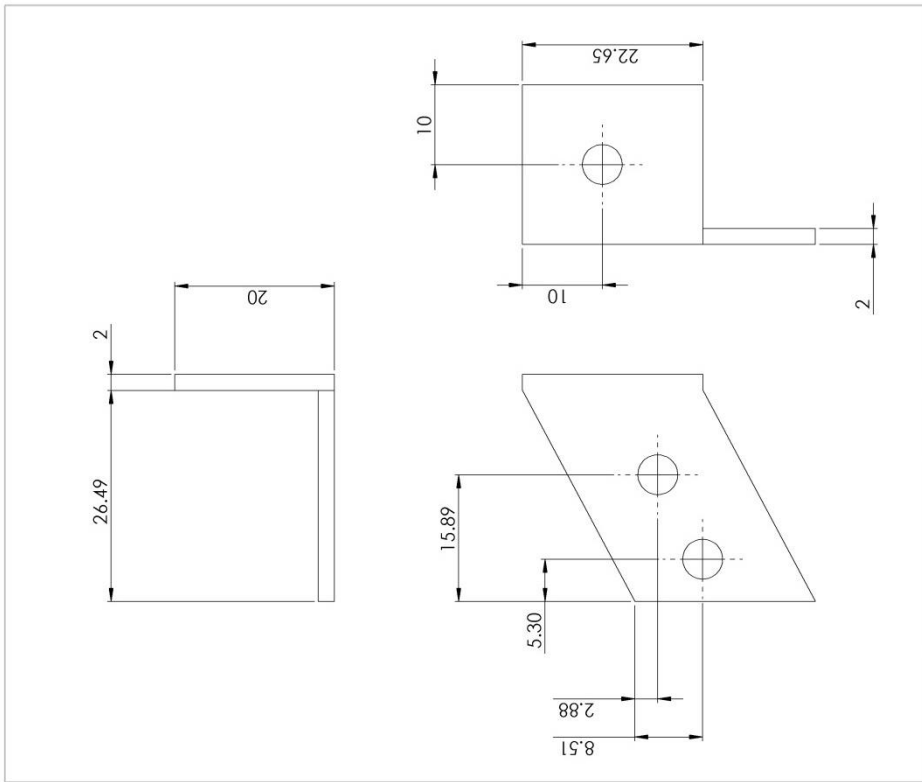
Appendix J. Experimental module technical drawings



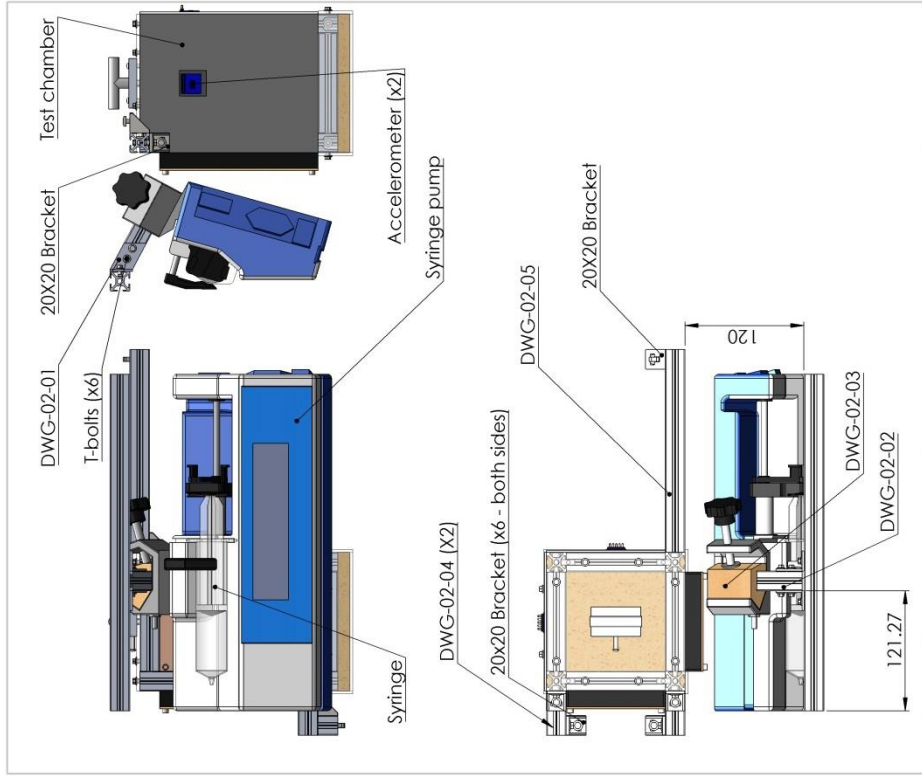
UNLESS OTHERWISE SPECIFIED: DIMENSIONS ARE IN MILLIMETERS TOLERANCES: SURFACE FINISH: RA ANGLE: N/A		FINISH:		DO NOT SCALE DRAWING		REVISION	V4
DRAWN: J. Heath		SIGNATURE:		N/A		Kingston University	
CHECKED: A. Angouill	DATE: 01/05/16	DATE: 01/05/16		TITLE:		Main Assembly	
APPROVED:	DATE: 01/05/16	DATE: 01/05/16		DWG. NO.:		DWG-01	
MFG:		MATERIAL:		SCALE:		A4	
D.A.		WEIGHT:		SHEET:		1 OF 28	



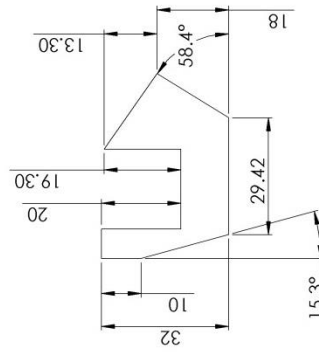
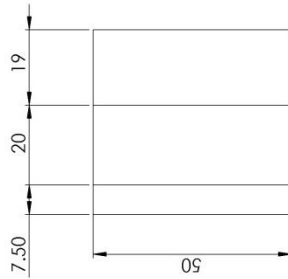
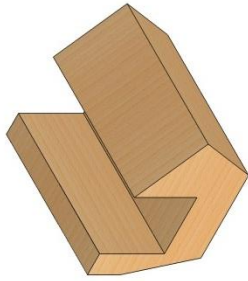
UNLESS OTHERWISE SPECIFIED: DIMENSIONS ARE IN MILLIMETERS TOLERANCES: SURFACE FINISH: RA ANGLE: N/A		FINISH:		DO NOT SCALE DRAWING		REVISION	V4
DRAWN: J. Heath		SIGNATURE:		N/A		Kingston University	
CHECKED: A. Angouill	DATE: 01/05/16	DATE: 01/05/16		TITLE:		Fluid System Assembly	
APPROVED:	DATE: 01/05/16	DATE: 01/05/16		DWG. NO.:		DWG-02(A)	
MFG:		MATERIAL:		SCALE:		A4	
D.A.		WEIGHT:		SHEET:		2 OF 28	



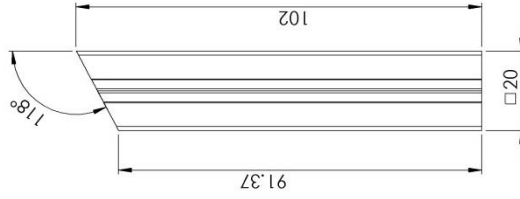
UNLESS OTHERWISE SPECIFIED: DIMENSIONS ARE IN MILLIMETERS TOLERANCES: FRACTIONS DECIMALS		FINISH: N/A	DO NOT SCALE DRAWING	REVISION	V4
DRAWN J. Hanks		DATE 01/05/16	Kingston University		
CHECKED A. Aspinall		DATE 01/05/16	Pump bracket		
APPROVED			DWG NO. DWG-02-01		
MFG.			SCALE: 2:1		
D.A.			SHEET 4 OF 28		
MATERIAL: SS1 D60		WEIGHT: N/A	A4		



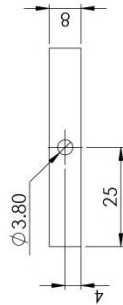
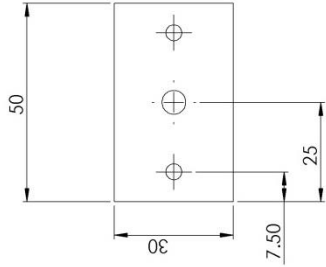
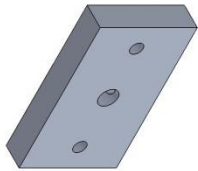
UNLESS OTHERWISE SPECIFIED: DIMENSIONS ARE IN MILLIMETERS TOLERANCES: FRACTIONS DECIMALS		FINISH: N/A	DO NOT SCALE DRAWING	REVISION	V4
DRAWN J. Hanks		DATE 01/05/16	Kingston University		
CHECKED A. Aspinall		DATE 01/05/16	Fluid System Assembly		
APPROVED			DWG NO. DWG-02(B)		
MFG.			SCALE: 1		
D.A.			SHEET 3 OF 28		
MATERIAL: N/A		WEIGHT: N/A	A4		



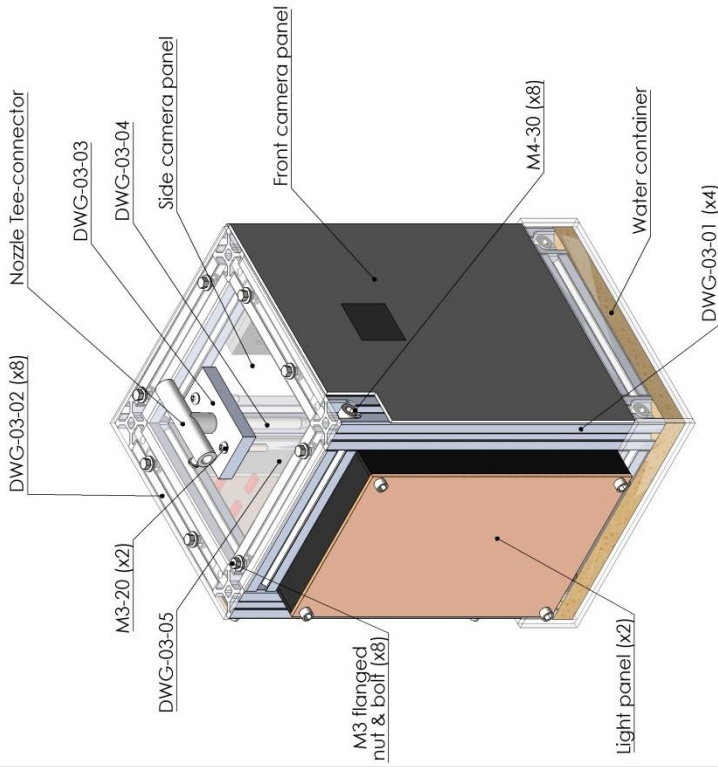
UNLESS OTHERWISE SPECIFIED: DIMENSIONS ARE IN MILLIMETERS SURFACE FINISH: N/A TOLERANCES: ANGULAR: 0.1°		FINISH:	DO NOT SCALE DRAWING		REVISION	V4
N/A		Kingston University		TITLE:		
N/A		Pump strut fixing block		DWG NO. DWG-02-03		
N/A		Aluminum		SCALE: 1:1		
N/A		N/A		SHEET 6 OF 26		
DRAWN	NAME	SIGNATURE	DATE	TITLE:		
CHECKED	J. Inchausti		01/06/16	DWG NO. DWG-02-03		
APPROVED	A. Agostini		01/06/16	MATERIAL: Plywood		
DATE				WEIGHT: N/A		
				A4		



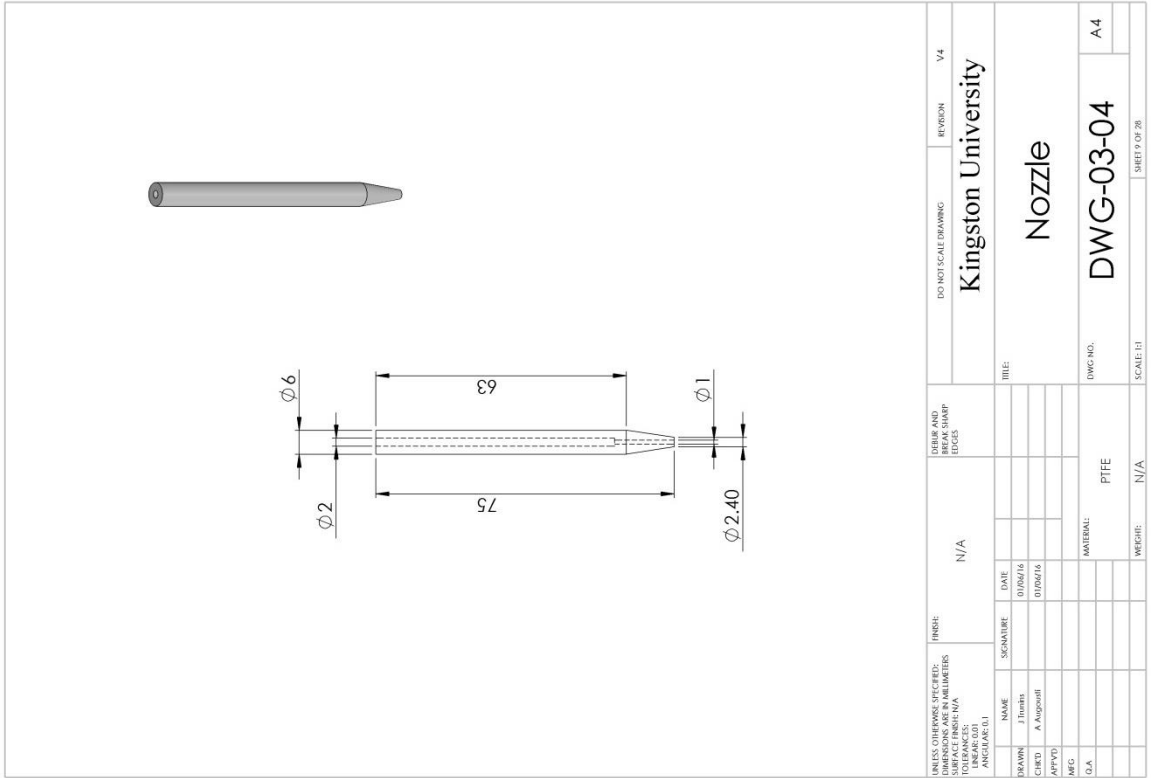
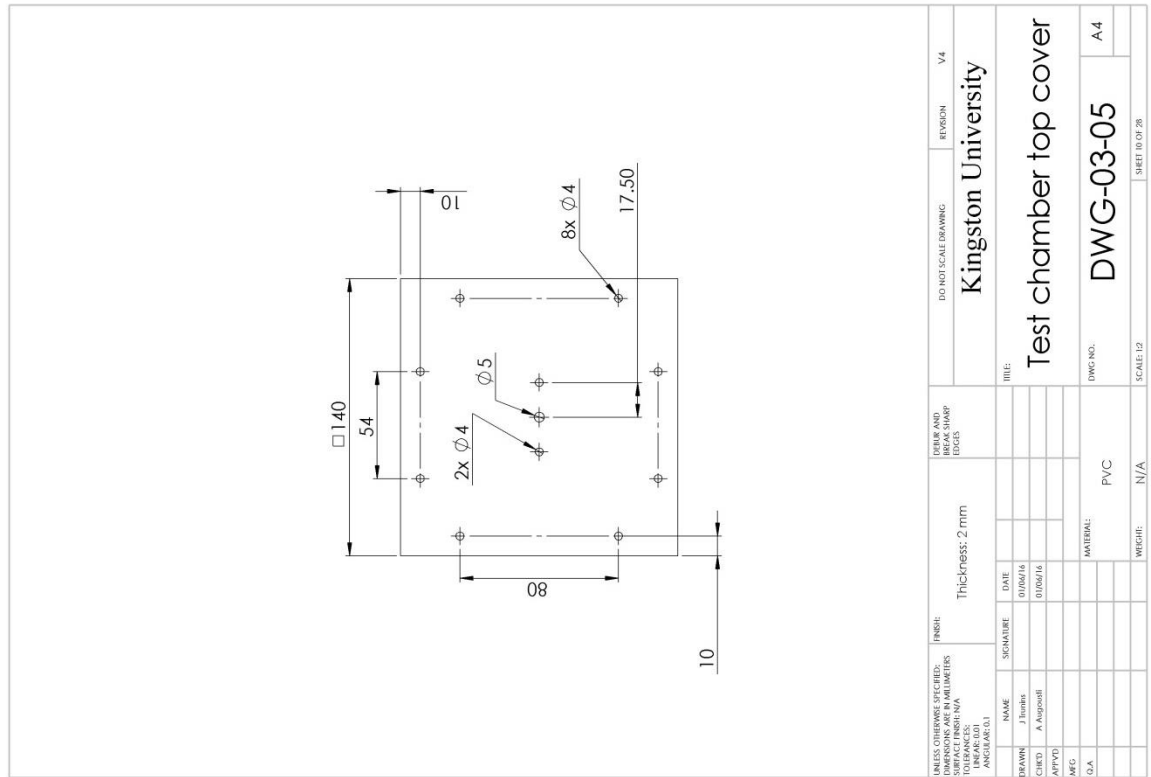
UNLESS OTHERWISE SPECIFIED: DIMENSIONS ARE IN MILLIMETERS SURFACE FINISH: N/A TOLERANCES: ANGULAR: 0.1°		FINISH:	DO NOT SCALE DRAWING		REVISION	V4
N/A		Kingston University		TITLE:		
N/A		Pump fixing strut		DWG NO. DWG-02-02		
N/A		Aluminum		SCALE: 1:1		
N/A		N/A		SHEET 5 OF 26		
DRAWN	NAME	SIGNATURE	DATE	TITLE:		
CHECKED	J. Inchausti		01/06/16	DWG NO. DWG-02-02		
APPROVED	A. Agostini		01/06/16	MATERIAL: Aluminum		
DATE				WEIGHT: N/A		
				A4		

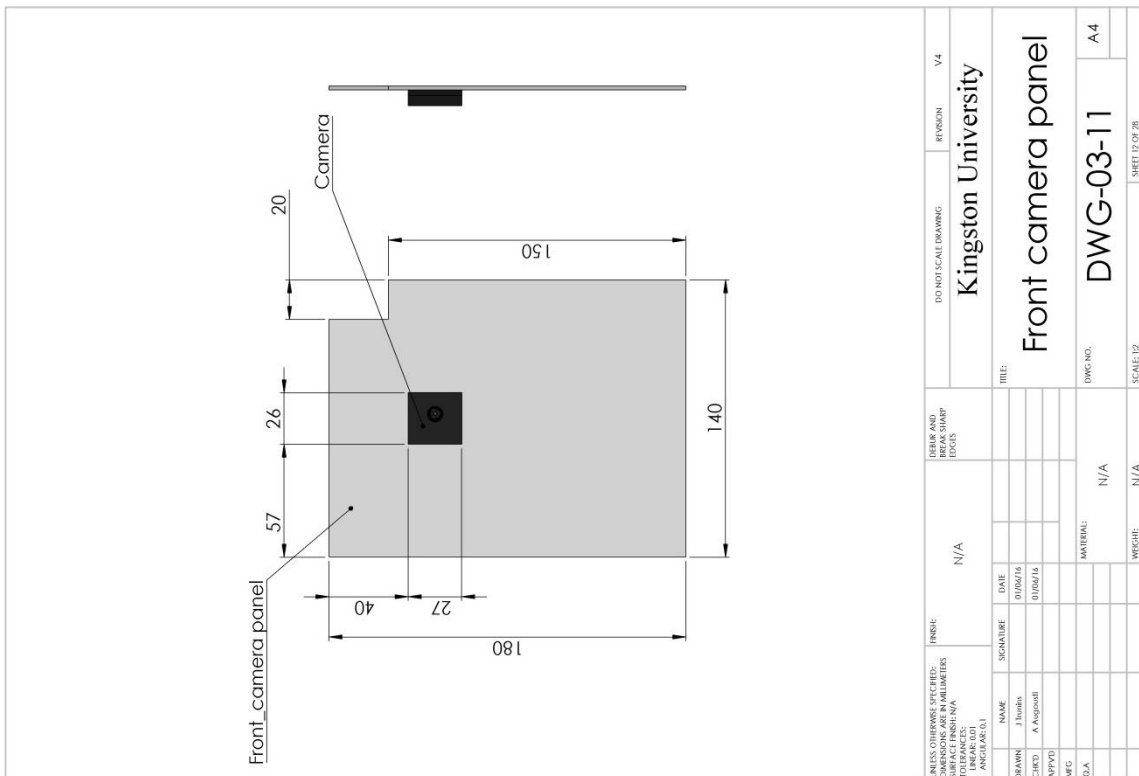
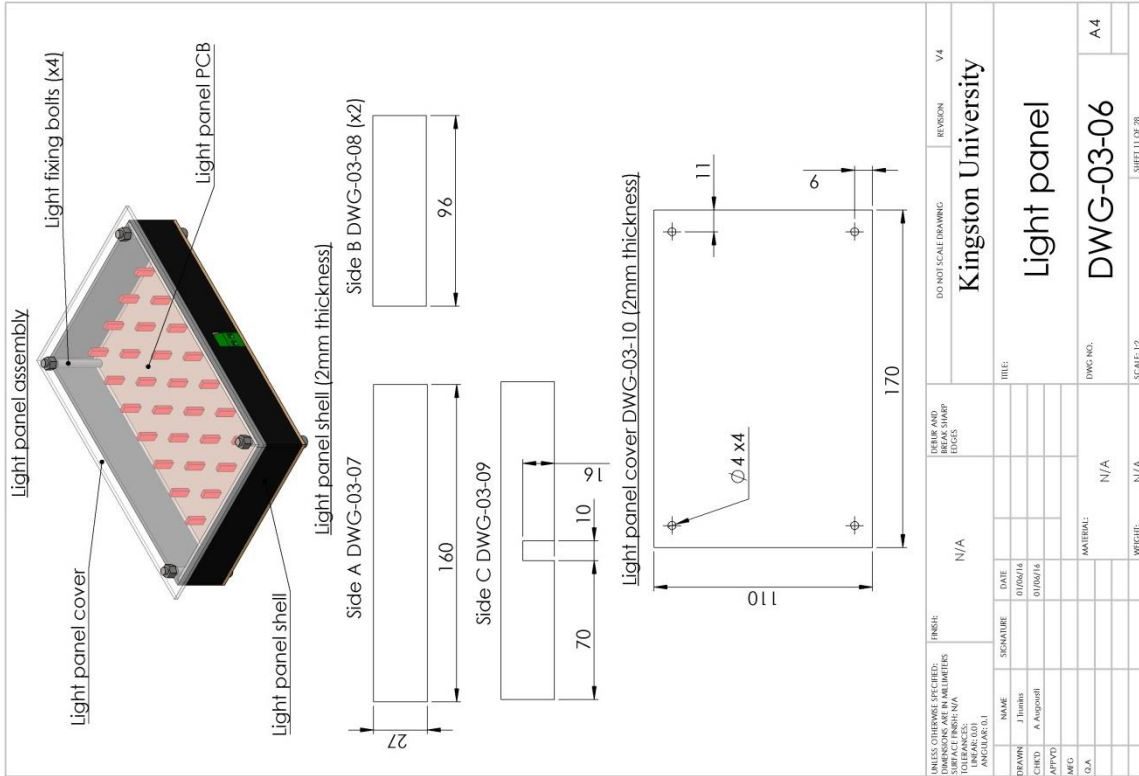


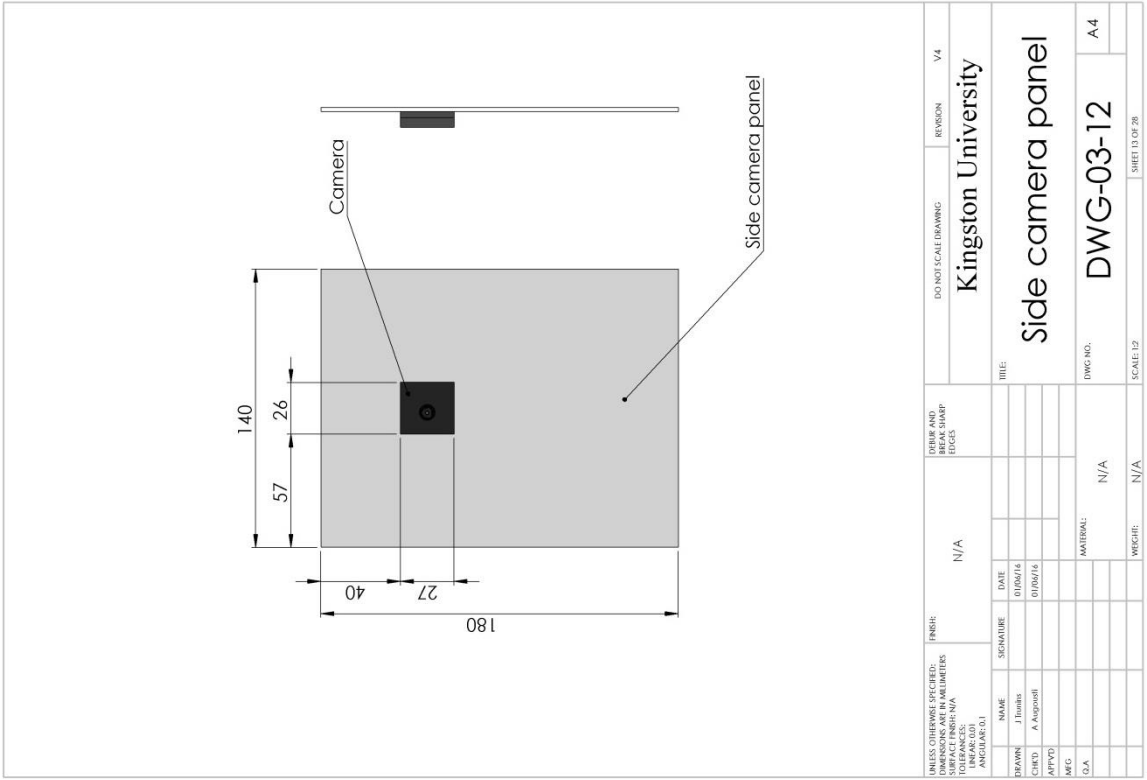
UNLESS OTHERWISE SPECIFIED: DIMENSIONS ARE IN MILLIMETERS TOLERANCES: ANGULAR (S.I.)		FINISH:	DO NOT SCALE DRAWING		REVISION	V4
DRAWN		J. Harris	Kingston University		TITLE:	
CHECKED		A. Asghari	Nozzle fixing block		DWG NO.:	
APPROVED			Aluminium		DWG-03-03	
MFG.			MATERIAL:		A4	
D.A.			WEIGHT:		SCALE: 1:1	
			N/A		SHEET 8 OF 28	



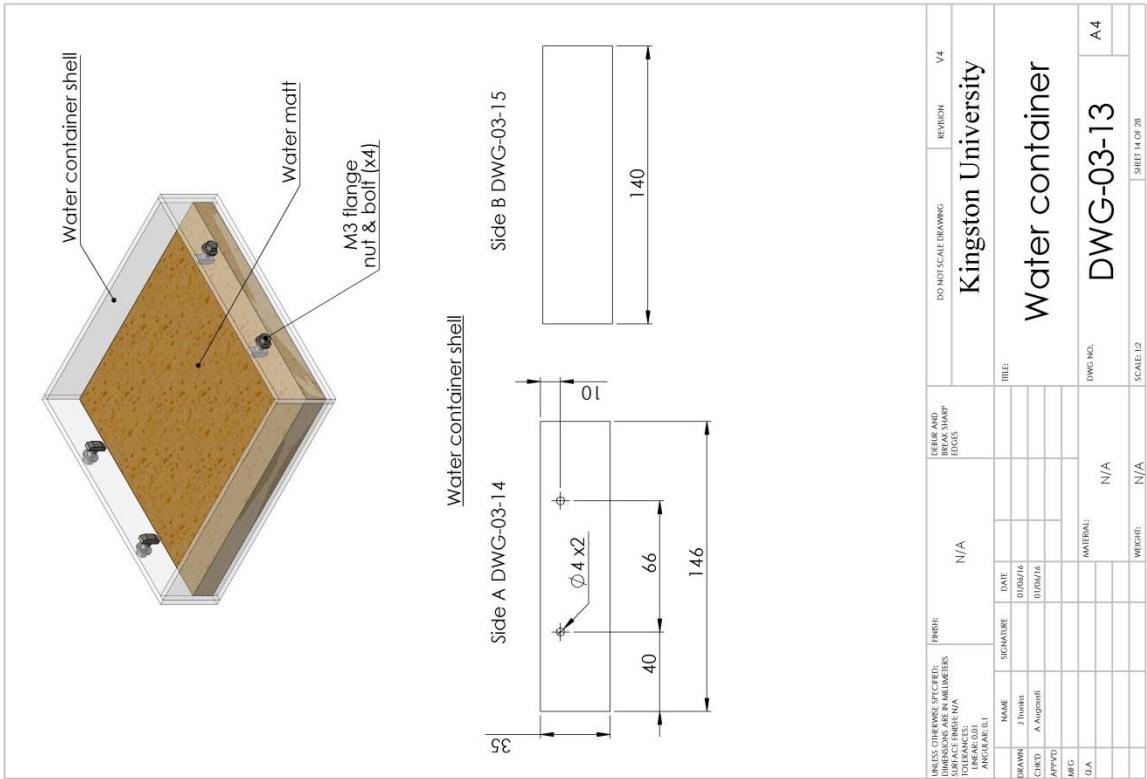
UNLESS OTHERWISE SPECIFIED: DIMENSIONS ARE IN MILLIMETERS TOLERANCES: ANGULAR (S.I.)		FINISH:	DO NOT SCALE DRAWING		REVISION	V4
DRAWN		J. Harris	Kingston University		TITLE:	
CHECKED		A. Asghari	Test chamber		DWG NO.:	
APPROVED			N/A		DWG-03	
MFG.			MATERIAL:		A4	
D.A.			WEIGHT:		SCALE: 1:2	
			N/A		SHEET 7 OF 28	





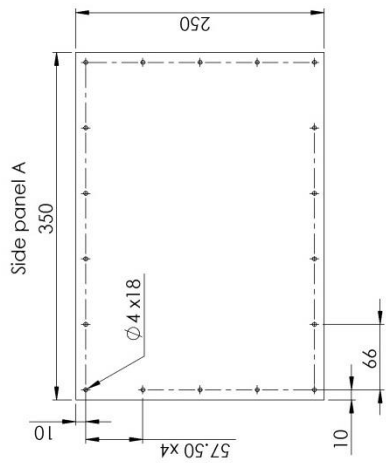


UNLESS OTHERWISE SPECIFIED: DIMENSIONS ARE IN MILLIMETERS		FINISH:		DO NOT SCALE DRAWING		REGION: V4	
TOLERANCES: ANGULAR: 0.1		N/A		Kingston University		DWG NO.: DWG-03-12	
DRAWN: J. Thompson		SIGNATURE:		DATE:		SCALE: 1:2	
CHECKED: A. Asgouli		DATE:		DATE:		SCALE: 1:2	
APPROVED:		DATE:		DATE:		SCALE: 1:2	
MFG:		DATE:		DATE:		SCALE: 1:2	
QA:		DATE:		DATE:		SCALE: 1:2	
MATERIAL: N/A		DATE:		DATE:		SCALE: 1:2	
WEIGHT: N/A		DATE:		DATE:		SCALE: 1:2	

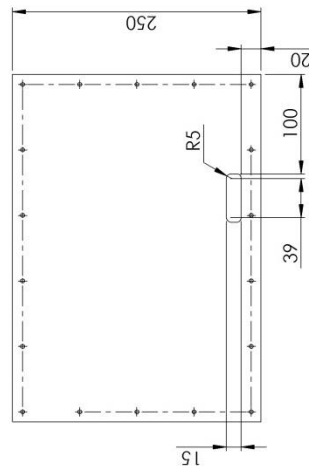


UNLESS OTHERWISE SPECIFIED: DIMENSIONS ARE IN MILLIMETERS		FINISH:		DO NOT SCALE DRAWING		REGION: V4	
TOLERANCES: ANGULAR: 0.1		N/A		Kingston University		DWG NO.: DWG-03-13	
DRAWN: J. Thompson		SIGNATURE:		DATE:		SCALE: 1:2	
CHECKED: A. Asgouli		DATE:		DATE:		SCALE: 1:2	
APPROVED:		DATE:		DATE:		SCALE: 1:2	
MFG:		DATE:		DATE:		SCALE: 1:2	
QA:		DATE:		DATE:		SCALE: 1:2	
MATERIAL: N/A		DATE:		DATE:		SCALE: 1:2	
WEIGHT: N/A		DATE:		DATE:		SCALE: 1:2	

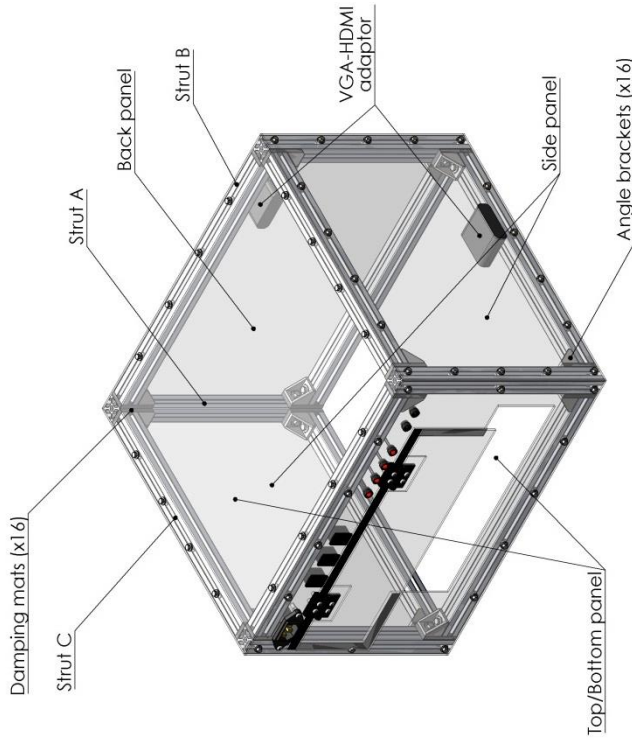
Side Panels



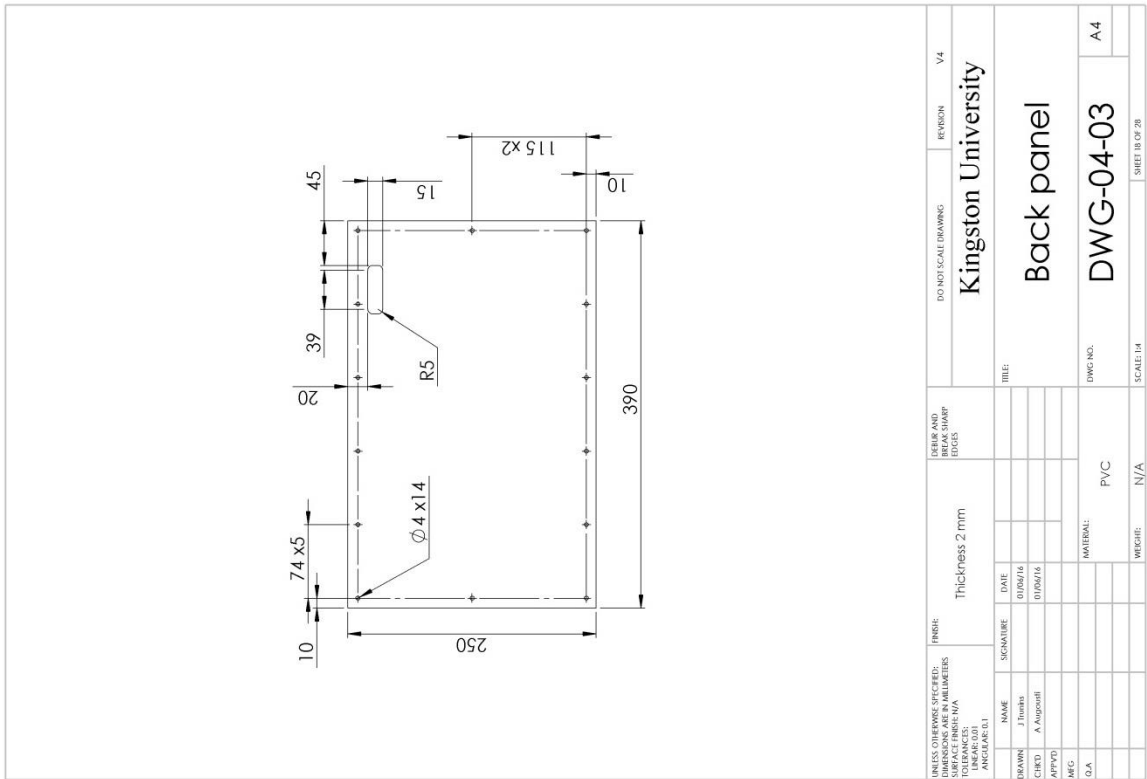
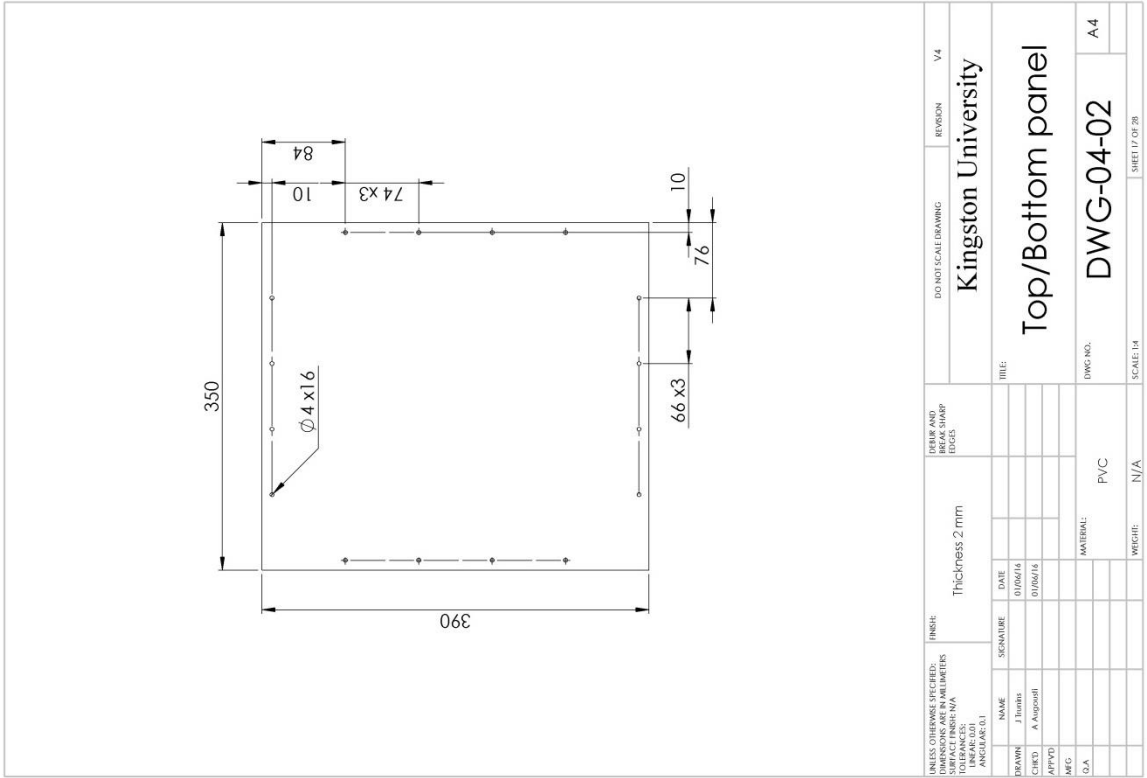
Side panel B

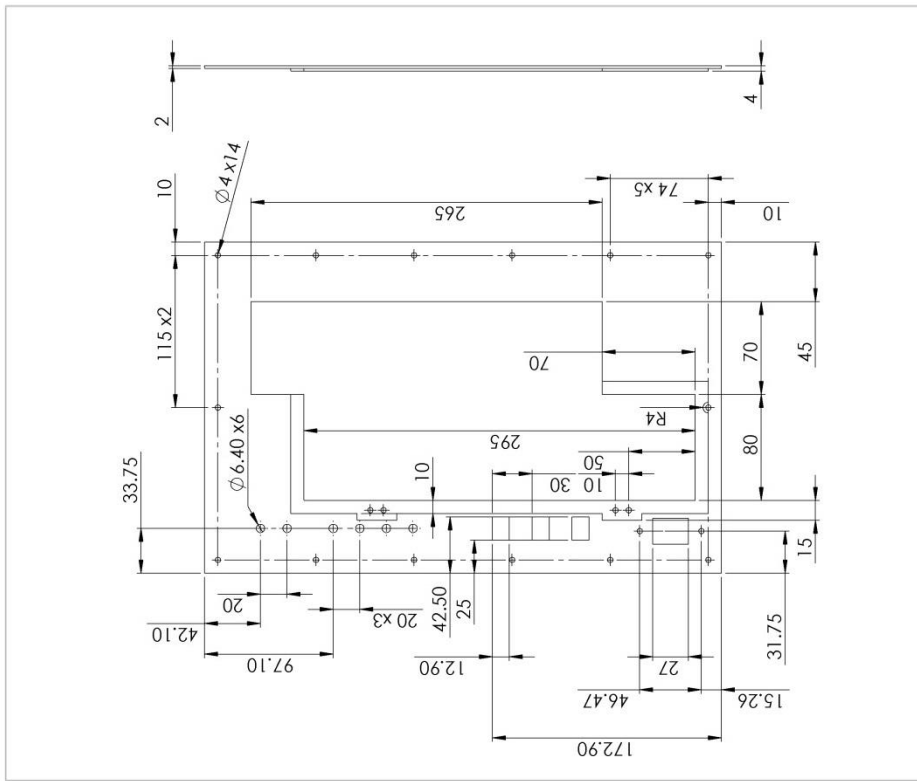


UNLESS OTHERWISE SPECIFIED: DIMENSIONS ARE IN MILLIMETERS TOLERANCES: ±0.10 ANGLES: 90°		PINS:		DIBUR AND BREAK SHAMP (LOGS)		DO NOT SCALE DRAWING		REGION		V4	
NAME		SIGNATURE		DATE		TITLE		Kingston University		V4	
SKW	J. Smith			01/05/16		Side panel					
CHKD	A. Aspinall			01/05/16		Side panel					
APPVD						Side panel					
MEG						Side panel					
QA						Side panel					
MATERIAL:		PVC		DWG NO.:		DWG-04-01		SCALE 1:4		SHEET 16 OF 28	
WEIGHT:		N/A		DWG NO.:		DWG-04-01		SCALE 1:4		SHEET 16 OF 28	

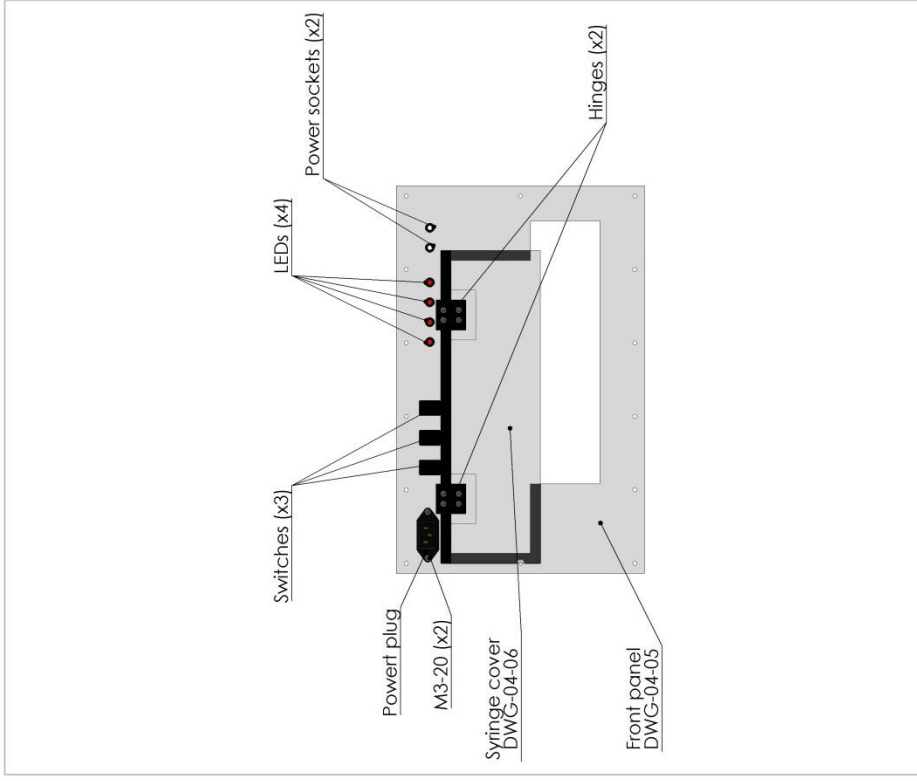


UNLESS OTHERWISE SPECIFIED: DIMENSIONS ARE IN MILLIMETERS TOLERANCES: ±0.10 ANGLES: 90°		PINS:		DIBUR AND BREAK SHAMP (LOGS)		DO NOT SCALE DRAWING		REGION		V4	
NAME		SIGNATURE		DATE		TITLE		Kingston University		V4	
SKW	J. Smith			01/05/16		Structure					
CHKD	A. Aspinall			01/05/16		Structure					
APPVD						Structure					
MEG						Structure					
QA						Structure					
MATERIAL:		N/A		DWG NO.:		DWG-04		SCALE 1:4		SHEET 16 OF 28	
WEIGHT:		N/A		DWG NO.:		DWG-04		SCALE 1:4		SHEET 16 OF 28	

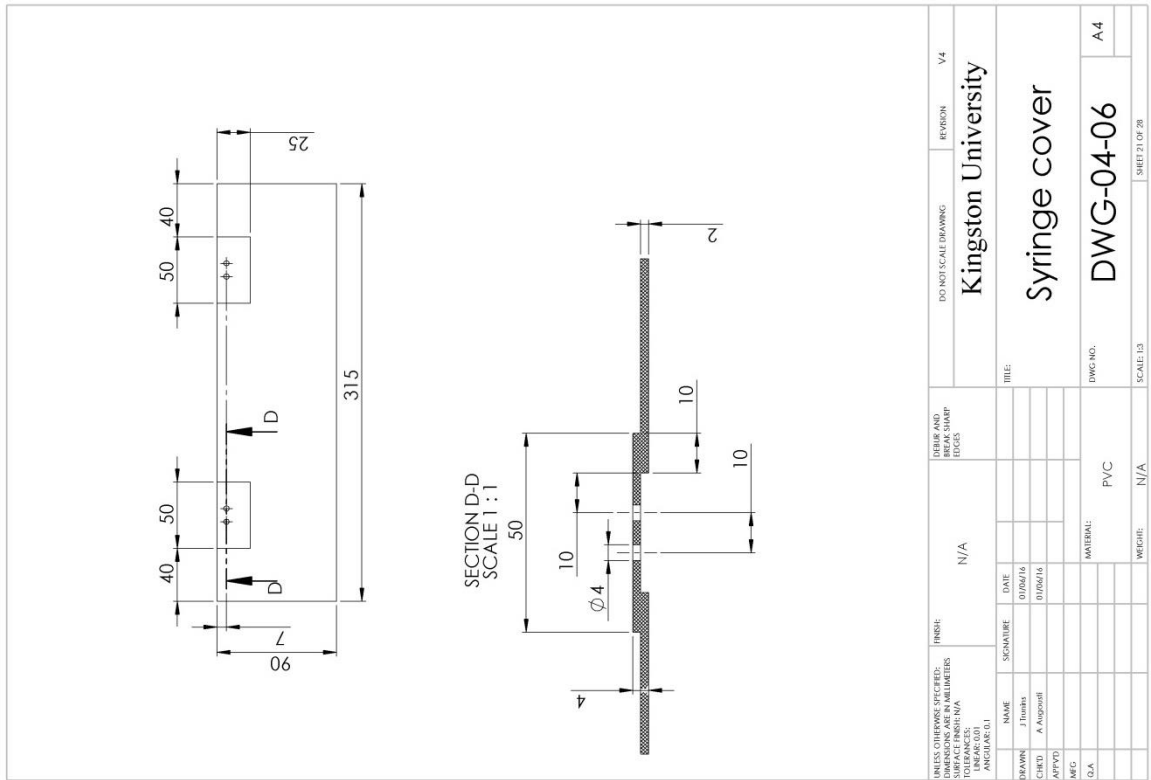




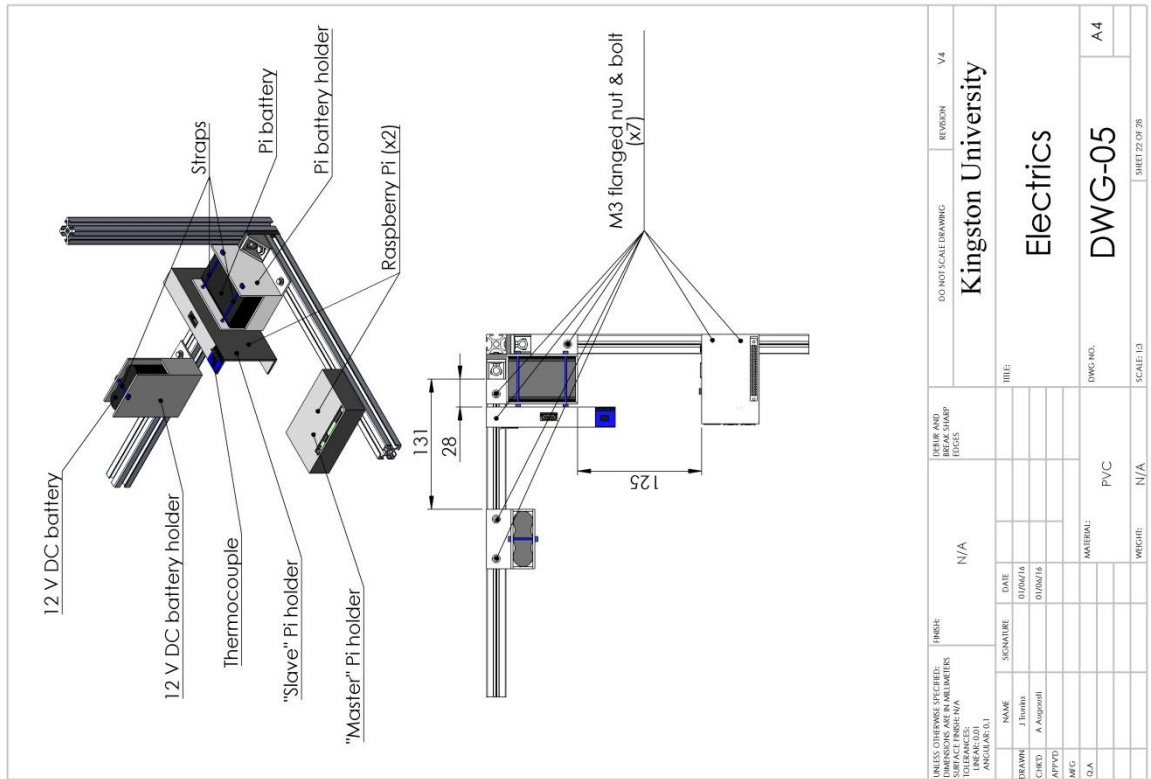
UNLESS OTHERWISE SPECIFIED: DIMENSIONS ARE IN MILLIMETERS FINISH: N/A		DO NOT SCALE DRAWING		REGION	V4
DEBUR AND BREAK SHARP EDGES		N/A		Kingston University	
TOLERANCES: ANGULAR ± 0.1		N/A		Front panel	
NAME	SIGNATURE	DATE	TITLE		
DESIGNER	J. Timms	01/06/16	Front panel assembly		
CHECKED	A. Aspinall	01/06/16	DWG NO. DWG-04-05		
APP'D			SCALE: 1:3		
MFG.			MATERIAL: PVC		
D.A.			WEIGHT: N/A		
			SHEET 20 OF 28		



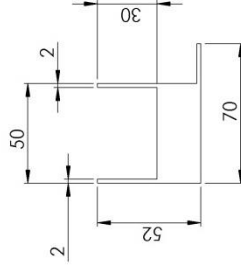
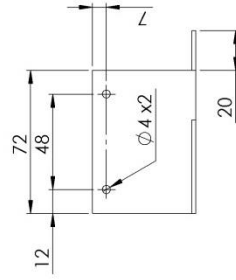
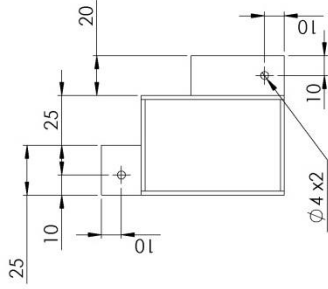
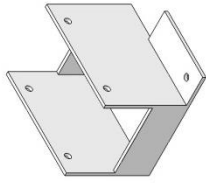
UNLESS OTHERWISE SPECIFIED: DIMENSIONS ARE IN MILLIMETERS FINISH: N/A		DO NOT SCALE DRAWING		REGION	V4
DEBUR AND BREAK SHARP EDGES		N/A		Kingston University	
TOLERANCES: ANGULAR ± 0.1		N/A		Front panel assembly	
NAME	SIGNATURE	DATE	TITLE		
DESIGNER	J. Timms	01/06/16	Front panel assembly		
CHECKED	A. Aspinall	01/06/16	DWG NO. DWG-04-04		
APP'D			SCALE: 1:4		
MFG.			MATERIAL: PVC		
D.A.			WEIGHT: N/A		
			SHEET 16 OF 28		



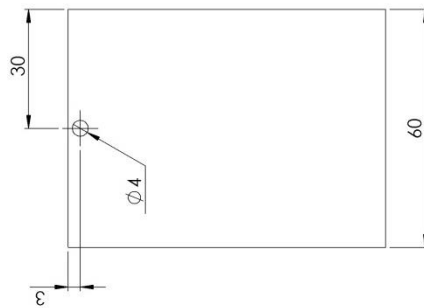
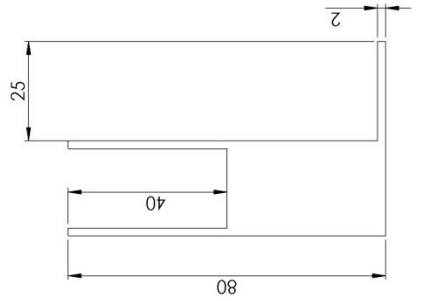
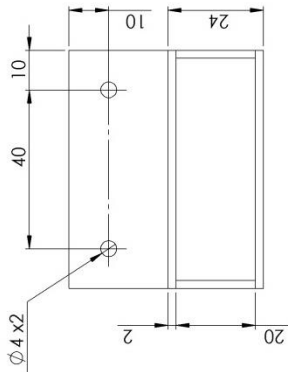
UNLESS OTHERWISE SPECIFIED: DIMENSIONS IN MILLIMETERS SURFACE FINISH: RA TOLERANCES: FRACTIONAL DECIMAL ANGULAR (D)		FINISH:	N/A	DEBurr AND REMOVE SHARP EDGES	REVISION	V4
DO NOT SCALE DRAWING		Kingston University		TITLE:		
DRAWN: J. Thomas		DATE: 01/06/16		SYRINGE COVER		
CHECKED: A. Aspinall		DATE: 01/06/16		SYRINGE COVER		
APPROVED:				MATERIAL: PVC		
MFG:				WEIGHT: N/A		
QA:				SCALE: 1:3		
				DWG NO.: DWG-04-06		
				SHEET 21 OF 28		



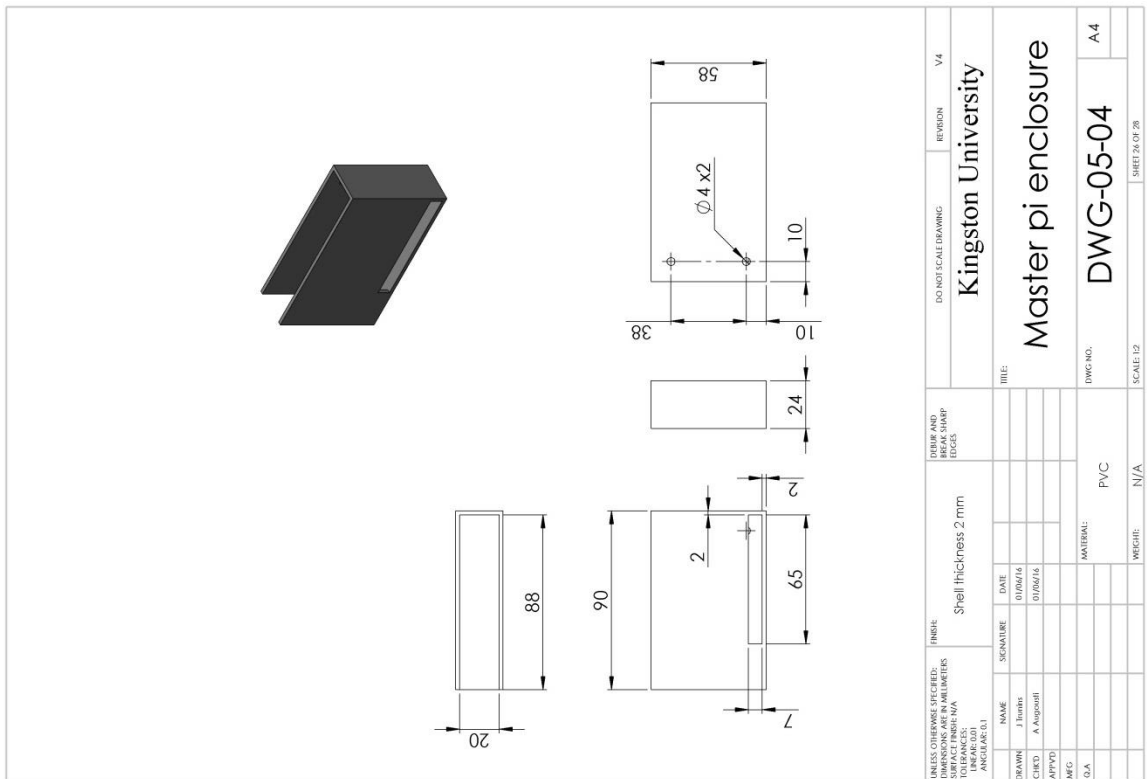
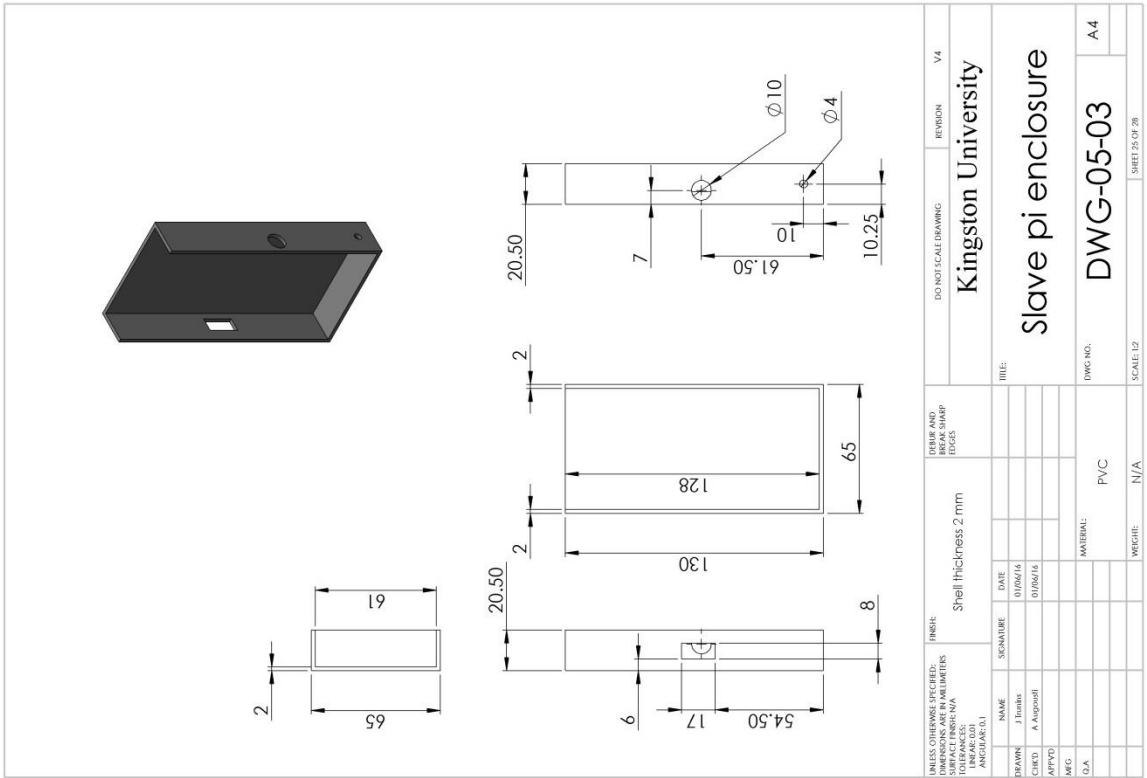
UNLESS OTHERWISE SPECIFIED: DIMENSIONS IN MILLIMETERS SURFACE FINISH: RA TOLERANCES: FRACTIONAL DECIMAL ANGULAR (D)		FINISH:	N/A	DEBurr AND REMOVE SHARP EDGES	REVISION	V4
DO NOT SCALE DRAWING		Kingston University		TITLE:		
DRAWN: J. Thomas		DATE: 01/06/16		ELECTRICS		
CHECKED: A. Aspinall		DATE: 01/06/16		ELECTRICS		
APPROVED:				MATERIAL: PVC		
MFG:				WEIGHT: N/A		
QA:				SCALE: 1:3		
				DWG NO.: DWG-05		
				SHEET 22 OF 28		



UNLESS OTHERWISE SPECIFIED: DIMENSIONS ARE IN MILLIMETERS SURFACE FINISH: RA TOLERANCES: ANGULAR: 0.1°		FINISH: Shell thickness 2 mm		DEBUR AND BREAK SHARP EDGES		DO NOT SCALE DRAWING		REVISION		V4	
DRAWN: J. Ibrahim		SIGNATURE:		DATE:		Kingston University		TITLE:		Pi battery holder	
CHECKED: A. Asghar		DATE:		DATE:		DWG NO.:		DWG NO.:		A4	
APPROVED:		DATE:		DATE:		MATERIAL:		MATERIAL:		DWG NO.:	
MFG:		DATE:		DATE:		PVC		PVC		DWG NO.:	
D/A:		DATE:		DATE:		N/A		N/A		SCALE: 1:2	



UNLESS OTHERWISE SPECIFIED: DIMENSIONS ARE IN MILLIMETERS SURFACE FINISH: RA TOLERANCES: ANGULAR: 0.1°		FINISH: Shell thickness 2 mm		DEBUR AND BREAK SHARP EDGES		DO NOT SCALE DRAWING		REVISION		V4	
DRAWN: J. Ibrahim		SIGNATURE:		DATE:		Kingston University		TITLE:		12 V DC battery holder	
CHECKED: A. Asghar		DATE:		DATE:		DWG NO.:		DWG NO.:		A4	
APPROVED:		DATE:		DATE:		MATERIAL:		MATERIAL:		DWG NO.:	
MFG:		DATE:		DATE:		PVC		PVC		DWG NO.:	
D/A:		DATE:		DATE:		N/A		N/A		SCALE: 1:1	



No.	Name	Drawing No.	Quantity	Comments
052	Straps	DWG-05	3	
053	PI battery	DWG-05	1	
054	12 V DC battery	DWG-05	1	
055	Raspberry Pi	DWG-05	2	
056	PI battery holder	DWG-05-01	1	
057	12 V DC battery holder	DWG-05-02	1	
058	Slave pi holder	DWG-05-03	1	
059	Master pi holder	DWG-05-04	1	

No.	Name	Drawing No.	Quantity	Comments
001	Syringe	DWG-02	1	
002	Syringe pump	DWG-02	1	
003	Accelerometer	DWG-02	1	
004	20x20 Brackets	DWG-02	8	
005	M3 Flanged nut & bolt	DWG-02	8	
006	Pump bracket	DWG-02-01	2	
007	Pump strut fixing strut	DWG-02-02	1	
008	Pump strut fixing block	DWG-02-03	1	
009	Test chamber support	DWG-02-04	2	45 mm
010	Test chamber support	DWG-02-05	1	205 mm
011	M3 Flanged nut & bolt	DWG-03	8	
012	M4-30	DWG-03	8	
013	M3-20	DWG-03	2	
014	Nozzle tee-connector	DWG-03-01	4	200 mm
015	Test chamber structure	DWG-03-02	8	100 mm
016	Test chamber structure	DWG-03-02	8	
017	Nozzle fixing block	DWG-03-03	1	
018	Nozzle	DWG-03-04	1	
019	Test chamber top cover	DWG-03-05	1	140 x 140 x 2 mm
020	Light panel PCB	DWG-03-06	2	
021	Light fixing bolts	DWG-03-06	4	M3-35 mm
022	Light panel shell side A	DWG-03-07	1	27 x 160 x 2 mm
023	Light panel shell side B	DWG-03-08	2	M3-35 mm
024	Light panel shell side C	DWG-03-09	1	27 x 160 x 2 mm
025	Light panel cover	DWG-03-10	1	110 x 170 x 2 mm
026	Front camera panel	DWG-03-11	1	180 x 140 x 2 mm
027	Camera	DWG-03-11(12)	2	
028	Side camera panel	DWG-03-12	2	180 x 140 x 2 mm
029	M3 Flanged nut & bolt	DWG-03-13	4	
030	Water matt	DWG-03-13	1	140 x 140 x 12 mm
031	Water container shell side A	DWG-03-14	2	146 x 35 x 2 mm
032	Water container shell side B	DWG-03-15	2	140 x 35 x 2 mm
033	M3-20	DWG-04	2	
034	M3 Flanged nut & bolt	DWG-04	236	
035	Strut A	DWG-04	4	250 mm
036	Strut B	DWG-04	4	340 mm
037	Strut C	DWG-04	4	300 mm
038	VGA-HDMI adaptor	DWG-04	2	
039	20x20 Brackets	DWG-04	16	
040	Side panel A	DWG-04-01	1	250 x 320 x 2 mm
041	Side panel B	DWG-04-01	1	250 x 320 x 2 mm
042	Top/Bottom panel	DWG-04-02	2	350 x 390 x 2 mm
043	Back panel	DWG-04-03	1	250 x 390 x 2 mm
044	Power sockets	DWG-04-04	2	
045	LEDs	DWG-04-04	4	
046	Switches	DWG-04-04	3	
047	Power plug	DWG-04-04	1	
048	Hinges	DWG-04-04	2	
049	Front panel	DWG-04-05	1	250 x 390 x 4 mm
050	Syringe cover	DWG-04-06	1	90 x 315 x 4 mm
051	M3 Flanged nut & bolt	DWG-05	7	

UNLESS OTHERWISE SPECIFIED: DIMENSIONS IN MILLIMETERS TOLERANCES: FRACTIONS: ±0.10 DECIMALS: ±0.15 ANGLES: ±0.5°		FINISH: N/A		DIBUR AND FINISH STAMP BLOCKS		DO NOT SCALE DRAWING		REVISION V4	
DRAWN: J. Thurn		DATE: 01/04/16		SIGNATURE:		N/A		Kingston University	
CHECKED: A. Aspinall		DATE: 01/04/16		SIGNATURE:		N/A		Kingston University	
APPROVED:		DATE:		SIGNATURE:		N/A		Kingston University	
SCALE: A4		MATERIAL: N/A		WEIGHT: N/A		SCALE: N/A		SHEET 26 OF 28	

UNLESS OTHERWISE SPECIFIED: DIMENSIONS IN MILLIMETERS TOLERANCES: FRACTIONS: ±0.10 DECIMALS: ±0.15 ANGLES: ±0.5°		FINISH: N/A		DIBUR AND FINISH STAMP BLOCKS		DO NOT SCALE DRAWING		REVISION V4	
DRAWN: J. Thurn		DATE: 01/04/16		SIGNATURE:		N/A		Kingston University	
CHECKED: A. Aspinall		DATE: 01/04/16		SIGNATURE:		N/A		Kingston University	
APPROVED:		DATE:		SIGNATURE:		N/A		Kingston University	
SCALE: A4		MATERIAL: N/A		WEIGHT: N/A		SCALE: N/A		SHEET 27 OF 28	

Appendix K. Raspberry PI software installation

SSH set up

```
$ sudo raspi-config
>>Advance options ||>>[RETURN]
>>SSH ||>> [RETURN]
>>enable ||>> [RETURN] ||>> [RETURN]
>>Finish
```

Install i2c-tools

```
$ sudo apt-get install python-smbus
$ sudo apt-get install i2c-tools
```

Installing Kernel support

```
$ sudo raspi-config
>>Advance options
>>I2C
>>Yes
>>OK
>>Yes
>>OK
$ OK
>>Finish
>>Yes
```

Update raspian OS modules

```
$ sudo nano etc/modules #Add following lines at the end:
$ snd-bcm2835
$ i2c-bcm2708
$ i2c-dev
||>> [CTRL]+[x] ||>>[y] ||>> [RETURN]
```

Update raspi-blacklist.conf

```
$ sudo nano etc/modprobe.d/raspi-blacklist.conf #Comment following lines
$ #blacklist spi and i2c by default
$ #blacklist spi-bcm2708
$ #blacklist i2c-bcm2708
||>> [CTRL]+[x] ||>> [y] ||>> [RETURN]
```

Update boot config

```
$ sudo nano boot/config.txt #Add at the end
$ dtparam=i2c1=on
```

```
$ dtparam=i2c_arm=on
||>> [CTRL]+[x] ||>> [y] ||>> [RETURN]
```

Update version of base

```
$ sudo rpi-update
$ sudo apt-get update
$ sudo apt-get dist-upgrade
$ sudo reboot #Reboot
```

VNC installation

```
$ sudo apt-get install tightvncserver
$ tightvncserver #Run VNC server
# Set password
$ microgravity ||>> [ENTER]
# Repeat password
$ [microgravity ||>> [ENTER]
# Would you like to set view-only password
||>> [n] ||>> [RETURN]
```

Setting up the VNC at boot start

```
# Create a file containing the following shell script:
$ #!/bin/sh vncserver
$ :0 -geometry 1920x1080 -depth 24 -dpi 96
# Save this as vnc.sh (for example)
$ chmod +x vnc.sh #Make the file executable
```

To run VNC at boot:

```
$ sudo su #Log into a terminal on the Pi as root
# Create a new file here containing the following script:
$ #!/bin/sh
$ #/etc/init.d/vncboot
$ ### Begin init info
$ # Provides: vncboot
$ # Required-Start: $remote_fs $syslog
$ # Required-Stop: $remote_fs $syslog
$ # Default-Start: 2 3 4 5
$ # Default-Stop: 0 1 6
$ # Short-Description: Start VNC Server at boot time
$ # Description: Start VNC Server at boot time.
$ ### End init info
$ USER=pi
$ HOME=/home/pi
$ export USER HOME
$ case "$1" in
```

```

$         start)
$             echo "Starting VNC Server"
$             #Insert your favoured settings for a VNC session
$             su - pi -c "/usr/bin/vncserver :0 -geometry 1280x800 -depth
16 -pixelformat rgb565"
$             ;;
$         stop)
$             echo "Stopping VNC Server"
$             /usr/bin/vncserver -kill :0
$             ;;
$         *)
$             echo "Usage: /etc/init.d/vncboot {start|stop}"
$             exit 1
$             ;;
$ esac
$ exit 0
# Save this file as vncboot (for example)
$ chmod 755 vncboot #Make this file executable
$ update-rc.d /etc/init.d/vncboot defaults #Enable dependency-based boot sequencing
$ reboot

```

Static IP set-up

```

$ sudo nano /etc/network/interfaces
$ auto lo
$ iface lo inet loopback
$ allow-hotplug wlan0 eth0
$ iface wlan0 inet static
$ address 10.42.43.15
$ netmask 255.255.255.0
$ network 10.42.43.1
$ gateway 10.42.43.1
$ wpa-passphrase Password
$ wpa-ssid MyWifi
$ #iface eth0 inet dhcp
$ iface eth0 inet static
$ address 10.42.43.14
$ netmask 255.255.255.0
$ network 10.42.43.1
$ gateway 10.42.43.1
$ metric 100
$ #wpa-roam /etc/wpa_supplicant/wpa_supplicant.conf
$ iface default inet dhcp
||>> [CTRL+x] ||>> [y] ||>> [ENTER]

```

```
$ sudo nano /etc/wpa_supplicant/wpa_supplicant.conf
Ctrl_interface=DIR=/var/run/wpa_supplicant GROUP=netdev
$ update_config=1
$ network={
$ ssid="TRENDnet"
$ scan_ssid=1
$ psk="passphrase"
$ proto=RSN
$ key_mgmt=WPA-PSK
$ pairwise=TKIP
$ group=TKIP
$ }
```

Running test_2.py script at boot

```
$ sudo nano test.sh
$ #!/etc/bin
$ sleep 10
$ sudo python /home/pi/Documents/test_2.py
||>> [CTRL+x] ||>> [y] ||>> [ENTER]
$ sudo chmod +x /home/pi/Documents/test_2.py
$ sudo nano ~/.config/lxsession/LXDE/autostart
$ @lxterminal -e ~/test.sh #add following line
||>> [CTRL+x] ||>> [y] ||>> [ENTER]
```

Appendix L. Experimental module operational code

Appendix L.A. ADXL345.py – Accelerometer code

```
# ADXL345 Python library for Raspberry Pi
#
# author: Jonathan Williamson
# license: BSD, see LICENSE.txt included in this package
#
# This is a Raspberry Pi Python implementation to help you get started
with
# the Adafruit Triple Axis ADXL345 breakout board:
# http://shop.pimoroni.com/products/adafruit-triple-axis-accelerometer

import smbus
from time import sleep

# select the correct i2c bus for this revision of Raspberry Pi
revision = ([l[12:-1] for l in open('/proc/cpuinfo', 'r').readlines() if
l[:8]=="Revision")+['0000'])[0]
bus = smbus.SMBus(1 if int(revision, 16) >= 4 else 0)

# ADXL345 constants
EARTH_GRAVITY_MS2 = 9.81
SCALE_MULTIPLIER = 0.004
DATA_FORMAT = 0x31
BW_RATE = 0x2C
POWER_CTL = 0x2D
BW_RATE_1600HZ = 0x0F
BW_RATE_800HZ = 0x0E
BW_RATE_400HZ = 0x0D
BW_RATE_200HZ = 0x0C
BW_RATE_100HZ = 0x0B
BW_RATE_50HZ = 0x0A
BW_RATE_25HZ = 0x09
RANGE_2G = 0x00
RANGE_4G = 0x01
RANGE_8G = 0x02
RANGE_16G = 0x03
MEASURE = 0x08
AXES_DATA = 0x32

class ADXL345:
    address = None
    def __init__(self, address = 0x53):
        self.address = address
        self.setBandwidthRate(BW_RATE_25HZ)
        self.setRange(RANGE_2G)
        self.enableMeasurement()
    def enableMeasurement(self):
        bus.write_byte_data(self.address, POWER_CTL, MEASURE)
    def setBandwidthRate(self, rate_flag):
        bus.write_byte_data(self.address, BW_RATE, rate_flag)
    # set the measurement range for 10-bit readings
    def setRange(self, range_flag):
        value = bus.read_byte_data(self.address, DATA_FORMAT)
        value &= ~0x0F;
```

```

    value |= range_flag;
    value |= 0x08;
    bus.write_byte_data(self.address, DATA_FORMAT, value)
# returns the current reading from the sensor for each axis
#
# parameter gforce:
#   False (default): result is returned in m/s^2
#   True           : result is returned in gs
def getAxes(self, gforce = False):
    bytes = bus.read_i2c_block_data(self.address, AXES_DATA, 6)
    x = bytes[0] | (bytes[1] << 8)
    if(x & (1 << 16 - 1)):
        x = x - (1<<16)
    y = bytes[2] | (bytes[3] << 8)
    if(y & (1 << 16 - 1)):
        y = y - (1<<16)
    z = bytes[4] | (bytes[5] << 8)
    if(z & (1 << 16 - 1)):
        z = z - (1<<16)
    x = x * SCALE_MULTIPLIER
    y = y * SCALE_MULTIPLIER
    z = z * SCALE_MULTIPLIER
    if gforce == False:
        x = x * EARTH_GRAVITY_MS2
        y = y * EARTH_GRAVITY_MS2
        z = z * EARTH_GRAVITY_MS2
    x = round(x, 4)
    y = round(y, 4)
    z = round(z, 4)
    return {"x": x, "y": y, "z": z}
if __name__ == "__main__":
    # if run directly we'll just create an instance of the class and
    # output the current readings
    adxl345 = ADXL345()
    axes = adxl345.getAxes(True)
    print "ADXL345 on address 0x%x:" % (adxl345.address)
    print "  x = %.3fG" % ( axes['x'] )
    print "  y = %.3fG" % ( axes['y'] )
    print "  z = %.3fG" % ( axes['z'] )

```

Appendix L.B. MAX31855.py – Temperature sensor code

```

# Copyright (c) 2014 Adafruit Industries
# Author: Tony DiCola
#
# Permission is hereby granted, free of charge, to any person obtaining a
# copy of this software and associated documentation files (the
# "Software"), to deal in the Software without restriction, including
# without limitation the rights to use, copy, modify, merge, publish,
# distribute, sublicense, and/or sell copies of the Software, and to
# permit persons to whom the Software is furnished to do so, subject to
# the following conditions:
#
# The above copyright notice and this permission notice shall be included
# in all copies or substantial portions of the Software.
#
# THE SOFTWARE IS PROVIDED "AS IS", WITHOUT WARRANTY OF ANY KIND, EXPRESS
# OR IMPLIED, INCLUDING BUT NOT LIMITED TO THE WARRANTIES OF
# MERCHANTABILITY, # FITNESS FOR A PARTICULAR PURPOSE AND
# NONINFRINGEMENT. IN NO EVENT SHALL THE
#

```

```

# AUTHORS OR COPYRIGHT HOLDERS BE LIABLE FOR ANY CLAIM, DAMAGES OR OTHER
# LIABILITY, WHETHER IN AN ACTION OF CONTRACT, TORT OR OTHERWISE, ARISING
# FROM, OUT OF OR IN CONNECTION WITH THE SOFTWARE OR THE USE OR OTHER
# DEALINGS IN THE SOFTWARE.
import logging
import math
import Adafruit_GPIO as GPIO
import Adafruit_GPIO.SPI as SPI
# Default I2C address for the device.
MCP9808_I2CADDR_DEFAULT      = 0x18
# Register addresses.
MCP9808_REG_CONFIG           = 0x01
MCP9808_REG_UPPER_TEMP       = 0x02
MCP9808_REG_LOWER_TEMP       = 0x03
MCP9808_REG_CRIT_TEMP        = 0x04
MCP9808_REG_AMBIENT_TEMP     = 0x05
MCP9808_REG_MANUF_ID         = 0x06
MCP9808_REG_DEVICE_ID        = 0x07
# Configuration register values.
MCP9808_REG_CONFIG_SHUTDOWN  = 0x0100
MCP9808_REG_CONFIG_CRITLOCKED = 0x0080
MCP9808_REG_CONFIG_WINLOCKED = 0x0040
MCP9808_REG_CONFIG_INTCLR    = 0x0020
MCP9808_REG_CONFIG_ALERTSTAT = 0x0010
MCP9808_REG_CONFIG_ALERTCTRL = 0x0008
MCP9808_REG_CONFIG_ALERTSEL  = 0x0002
MCP9808_REG_CONFIG_ALERTPOL  = 0x0002
MCP9808_REG_CONFIG_ALERTMODE = 0x0001
class MAX31855(object):
    def __init__(self, clk=None, cs=None, do=None, spi=None, gpio=None):
        self._logger = logging.getLogger('Adafruit_MAX31855.MAX31855')
        self._spi = None
        # Handle hardware SPI
        if spi is not None:
            self._logger.debug('Using hardware SPI')
            self._spi = spi
        elif clk is not None and cs is not None and do is not None:
            self._logger.debug('Using software SPI')
            # Default to platform GPIO if not provided.
            if gpio is None:
                gpio = GPIO.get_platform_gpio()
            self._spi = SPI.BitBang(gpio, clk, None, do, cs)
        else:
            raise ValueError('Must specify either spi for hardware
SPI or clk, cs, and do for software SPI!')
        self._spi.set_clock_hz(500000)
        self._spi.set_mode(0)
        self._spi.set_bit_order(SPI.MSBFIRST)

    def readInternalC(self):
        v = self._read32()
        # Ignore bottom 4 bits of thermocouple data.
        v >>= 4
        # Grab bottom 11 bits as internal temperature data.
        internal = v & 0x7FF
        if v & 0x800:
            # Negative value, take 2's compliment. Compute this with
            # subtraction because python is a little odd about handling
            # signed/unsigned.
            internal -= 4096
        # Scale by 0.0625 degrees C per bit and return value.
        return internal * 0.0625
    def readTempC(self):
        v = self._read32()
        # Check for error reading value.

```

```

    if v & 0x7:
        return float('NaN')
    # Check if signed bit is set.
    if v & 0x80000000:
        # Same as above
        v >>= 18
        v -= 16384
    else:
        # Positive value, just shift the bits to get the value.
        v >>= 18
    # Scale by 0.25 degrees C per bit and return value.
    return v * 0.25
def _read32(self):
    # Read 32 bits from the SPI bus.
    raw = self._spi.read(4)
    if raw is None or len(raw) != 4:
        raise RuntimeError('Did not read expected number of bytes
from device!')
    value = raw[0] << 24 | raw[1] << 16 | raw[2] << 8 | raw[3]
    self._logger.debug('Raw value: 0x{0:08X}'.format(value &
0xFFFFFFFF))
    return value

```

Appendix L.C. Test_1.py – Main test code

```

#!/usr/bin/python
# Test Code for Microgravity experiment module
# Author: Jevgenijs Trunins
#
# Additional example codes used:
# ADXL345 Python example
# author: Jonathan Williamson
#
# Last updates on: 01/12/15
#
# Depending on the PI, uncomment required
# Raspberry PI #1

#FOR BOTH PIs
# Import libraries
from adxl345 import ADXL345 #accelerometer sensor lib import
import Adafruit_GPIO.SPI as SPI #Import thermocouple sensor libs
import Adafruit_MAX31855.MAX31855 as MAX31855
import picamera #import camera lib
import time; import datetime #general lib import
from threading import Thread #threading library
import RPi.GPIO as GPIO #GPIO library
import os; import sys #general lib import

#Constants
dt=5 #test time in seconds
contact_A=14 #sending signal to PI
contact_B=15 #receiving signal to PI
contact_C=22 #power for LED pin
contact_D=4 #Pin to power OFF PI#2
contact_E=27 #Pin to identify initialisation
contact_F=17 #Pin to identify PI#2 is out of memory
mem_lim=20 #(%) memory limitations if it is left only 20% stop
vid_ratio=2 #(MB/s) approximate video file size
CLK=25 #Clock pin set
CS=24 #CS pin set

```



```

DO=18 #DO pin set

#Set-up communication for PI
#Set-up the PI GPIO's pins
#FOR BOTH PIs
GPIO.setmode(GPIO.BCM); GPIO.setwarnings(False) #GPIO initial set-up
GPIO.setup(contact_A,GPIO.OUT) #Synchronisation send pin set
GPIO.setup(contact_B,GPIO.IN) #Synchronisation receiving pin set
GPIO.setup(contact_C,GPIO.OUT) #LED power pin set
#FOR PI#1
GPIO.setup(contact_D,GPIO.OUT) #PI power off pin set
GPIO.setup(contact_E,GPIO.IN) #PI#2 is ready signal set
GPIO.setup(contact_F,GPIO.IN) #PI#2 is out of memory signal set
#FOR PI#2
#GPIO.setup(contact_D,GPIO.IN) #PI power off pin set
#GPIO.setup(contact_E,GPIO.OUT) #PI#2 is ready signal set
#GPIO.setup(contact_F,GPIO.OUT) #PI#2 is out of memory signal set

#Initialise line communication
#FOR BOTH PIs
GPIO.output(contact_C,1); time.sleep(1)
today=datetime.datetime.today() #todays day read
#FOR PI#1
print('Raspberry is ready in 5 seconds'); print('Waiting for second PI')
while True:
    if GPIO.input(contact_E)==1:
        break
#FOR PI#2
#GPIO.output(contact_E,1);

#FOR BOTH PIs
time.sleep(5) #wait for five seconds
#FOR PI#1
print today.strftime('Today %a %H:%M:%S %d/%m/%y')

#Main loop started
#FOR BOTH PIs
while True:
#   FOR PI#1
    a=raw_input('Start a test? y/n ') #pick the input
    if a=='y':
        try: #Wait till the ENTER is pressed
            raw_input('Press ENTER when ready')
        except SyntaxError:
            pass
#   FOR PI#2
#   if GPIO.input(contact_D)==0:
#       GPIO.output(contact_E,0);

#Check the memory status
#   FOR BOTH PIs
    status=os.statvfs('/') #read status data
    free_space=(status.f_bavail*status.f_frsize)#check the free space
                                                #available
    total_space=(status.f_blocks*status.f_frsize) #check the total
                                                #space available
    if (100*free_space/total_space)*100<mem_lim: #if the space is
                                                #less than 20% end the programme
#       FOR PI#1
        sys.exit("Not enough memory") #Exit the system
#       FOR PI#2
#       GPIO.output(contact_F,1) #Send the signal to PI#1
#       sys.exit() #Exit the system
#   FOR PI#1
    if free_space*10e-7<vid_ratio*dt: #Check the recording video size

```

```

                                #is too big
#         FOR PI#1
#         sys.exit("Not enough memory") #Exit the system
#         FOR PI#2
#         GPIO.output(contact_F,1) #Send the signal to PI#1
#         sys.exit() #Exit the system
#     FOR PI#1
#     if GPIO.input(contact_F)==True: #Check if memory status is OK of
#         #PI#2
#         sys.exit("Not enough memory") #Exit the system

#Open a log file to read
#     FOR BOTH PIs
#     with open('ex_log_1.txt','r') as f: #open a file
#         f.seek(-2,2) #jump to the second to last byte
#         while f.read(1)!="\n": #Until EOL is found
#             f.seek(-2,1) #jump back the read byte plus one more
#             last=f.readline() #read last line
ex_no=int(last[:5])+1 #find the test number print('Test No.:
#'+str(ex_no))
#         f.close() #close a file

#Record temperature
#     FOR PI#1
#     temp_sensor=MAX31855.MAX31855(CLK, CS, DO)
#     temp=temp_sensor.readTempC() #record temperature
#     time.sleep(5) #wait time, in case second PI didn't launch
#     GPIO.output(contact_A,1) #send a signal to a PI#2

#Start a test
#     print('Test started')

#If the error encountered in PI#1
#     FOR PI#2
#     while True: #wait till the signal received
#         if GPIO.input(contact_B)==1:
#             break
#         if GPIO.input(contact_D)==1:
#             GPIO.output(contact_C,0)
#             os.system("sudo halt"); sys.exit()

#     FOR BOTH PIs
#     start=time.clock() #remember the time of the event
#     time.sleep(1) #time for signal to be send/received

#     global exitFlag #global exit parameter
#     exitFlag=0 #initial flag set-up
#     def timer(): #function timer definition
#         time.sleep(dt) #set the experiment time
#         global exitFlag; exitFlag=1 #change the global flag
#     def accelerometer(): #function accelerometer defined
#         global exitFlag #connect to global flag
#         acc_file=open("%s_Acc_data_1.txt" % str(ex_no).zfill(5), 'w')
#         #create file for recording
#         adxl345=ADXL345() #set the sensor
#         while exitFlag==0: #while timer function is in operation
#             axes=adxl345.getAxes(True) #get accelerometer readings
#             acc_file.write(str(axes['x'])+'\t\t'+str(axes['y'])
#                 +'\t\t'+str(axes['z'])+'\n') #write accelerometer data
#             acc_file.close() #close the file
#     def video(): #function video set
#         with picamera.PiCamera() as camera: #open the camera with
#             #following parameters
#             camera.resolution=(980,1240) #resolution set
#             camera.framerate=30 #framerate set

```

```

        camera.meter_mode='backlit' #metering mode set
        camera.exposure_mode='backlight' #exposure mode set
        camera.sharpness=100 #sharpness set
        camera.contrast=50 #contrast set
        camera.color_effects=(128,128) #colour set
        camera.start_recording('%s_1.h264' % str(ex_no).zfill(5))
            #define the file to write
        camera.wait_recording(dt) #record for the time
        camera.stop_recording() #stop and save
    th1=Thread(target=timer); th2=Thread(target=accelerometer);
    th3=Thread(target=video) #set the threads
    th1.start(); th2.start(); th3.start() #start the threads
    th1.join(); th2.join(); th3.join() #wait for all threads to
    #finish

#Finish test
#   FOR PI#1
    while True: #wait till receiving the signal
        if GPIO.input(contact_B)==1:
            break
    print('Test finished')
#   FOR PI#2
#   GPIO.output(contact_A,1) #send a signal out
#   FOR BOTH PIs
end=time.clock(); time.sleep(1) #remember the time of the event
GPIO.output(contact_A,0) #switch of the sending pin

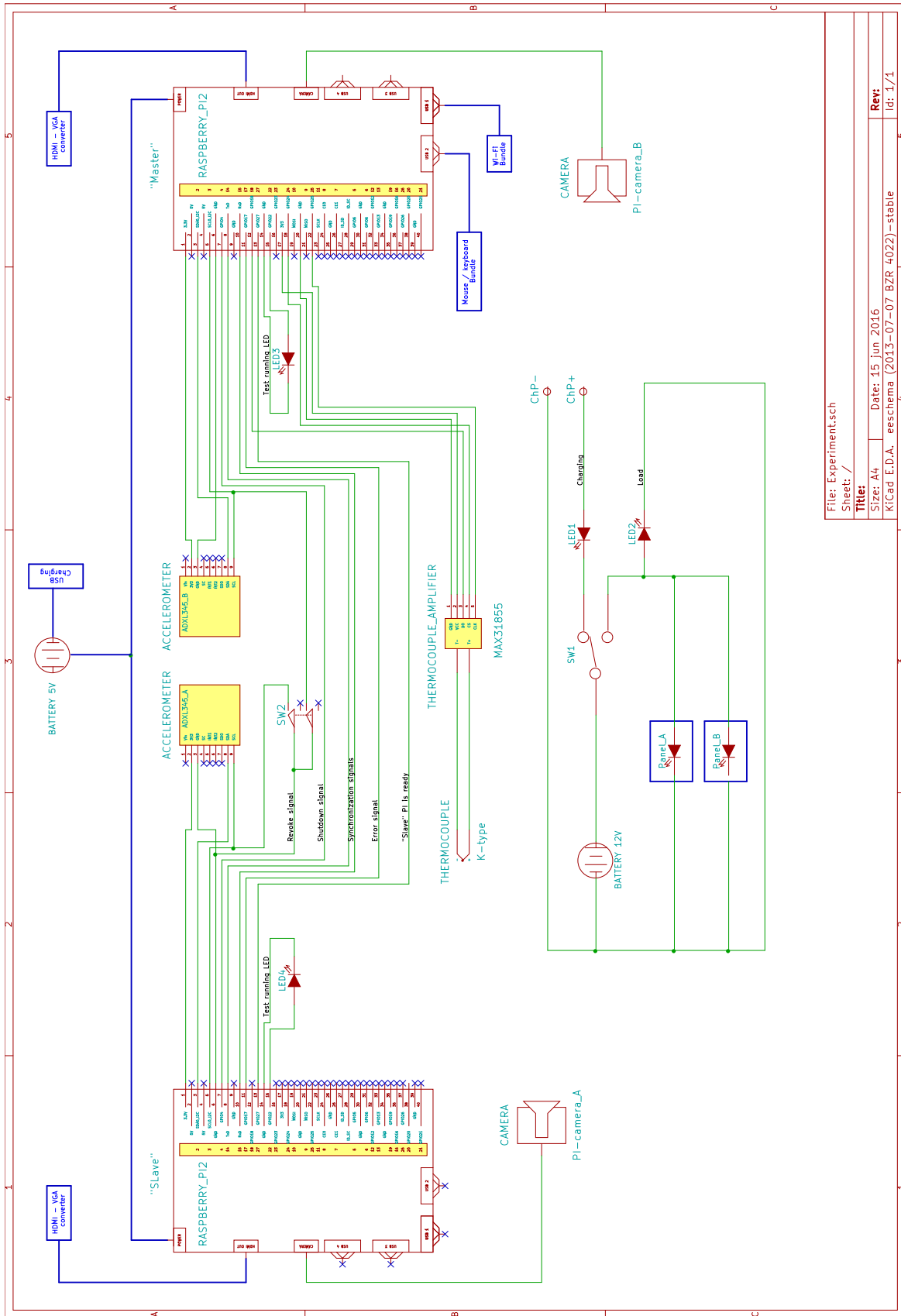
#Open a log file for write
#   FOR BOTH PIs
    with open('ex_log_1.txt','a') as f: #open file
        write=str(ex_no).zfill(5)+today.strftime('%H:%M:%S %d/%m/%y')
            #record data
        f.write(write);
        f.write('\t'+'\t'+str(start)+'\t'+str(end)+'\t'+'\t')
        f.write(str(temp)+'\n')
    f.close() #close the file

#To close the code
#   FOR PI#1
    elif a=='n': #if n
#   FOR PI#2
#   else:
#       FOR BOTH PIs
        GPIO.output(contact_C,0) #Switch off LED
#       FOR PI#1
        GPIO.output(contact_D,1) #Send signal for pi2 to go OFF
        time.sleep(10) #Wait for two seconds
        GPIO.output(contact_D,0) #Switch off signal
#       FOR PI#2
#       os.system("sudo halt") #Switch OFF PI
#       FOR BOTH PIs
        sys.exit() #exit the test

#In case wrong is entered
#   FOR PI#1
    else: #In any other case
        print('Syntax Error')

```

Appendix M. Experimental module circuit diagram



Appendix N. Camera distortion and pixel seizing results

Box #	Top (pixel No.)			Centre (pixel No.)			Bottom (pixel No.)		
	Start	End	Diff	Start	End	Diff	Start	End	Diff
1	23	55	32	20	52	32	17	50	33
2	61	93	32	58	90	32	56	89	33
3	98	131	33	96	129	33	94	127	33
4	137	169	32	135	167	32	133	166	33
5	174	206	32	173	205	32	171	204	33
6	212	244	32	211	242	31	209	242	33
7	249	281	32	248	281	33	247	280	33
8	286	319	33	286	318	32	285	317	32
9	324	356	32	324	356	32	323	355	32
10	362	394	32	361	394	33	360	392	32

Camera 1: Left to Right

Box #	Left (pixel No.)			Centre (pixel No.)			Right (pixel No.)		
	Start	End	Diff	Start	End	Diff	Start	End	Diff
1	155	187	32	157	189	32	157	190	33
2	192	225	33	195	226	31	195	228	33
3	229	262	33	232	264	32	233	265	32
4	267	300	33	269	302	33	270	303	33
5	305	339	34	307	339	32	308	340	32
6	344	377	33	345	377	32	346	378	32

Camera 1: Top to Bottom

Box #	Top (pixel No.)			Centre (pixel No.)			Bottom (pixel No.)		
	Start	End	Diff	Start	End	Diff	Start	End	Diff
1	25	71	46	26	71	45	26	72	46
2	78	123	45	79	123	44	78	123	45
3	131	176	45	130	175	45	131	175	44
4	184	229	45	182	228	46	182	227	45
5	236	281	45	236	282	46	235	281	46
6	289	335	46	288	333	45	288	333	45
7	341	387	46	340	386	46	340	386	46

Camera 2: Left to Right

Box #	Top (pixel No.)			Centre (pixel No.)			Bottom (pixel No.)		
	Start	End	Diff	Start	End	Diff	Start	End	Diff
1	60	107	47	60	105	45	60	106	46
2	113	159	46	113	159	46	114	160	46
3	166	211	45	165	210	45	167	212	45
4	221	267	46	217	263	46	220	265	45
5	276	321	45	271	317	46	273	318	45
6	328	371	46	325	370	45	324	370	46

Camera 2: Top to Bottom

Appendix O. Experimental error calculations

The error propagation method is based on the following differential equation:

$$f = f(x, y, \dots);$$

$$\Delta f^2 = \left(\frac{\partial f}{\partial x} \Delta x\right)^2 + \left(\frac{\partial f}{\partial y} \Delta y\right)^2 + \dots;$$

Critical volume and mass uncertainty calculations (for the data in section 7.1.1)

$$\Delta V = \sqrt{\Delta V_{time}^2 + \Delta V_{video}^2} \text{ (mm}^3\text{)}$$

where: $\Delta V_{video} = \pm 0.053 \text{ mm}^3$, and ΔV_{time} is given by:

$$\Delta V_{time} = \pm (\dot{V} + \dot{V}_{err}) t_{exp} = \pm 5.672 \cdot 10^{-3} \dot{V} \text{ (mm}^3\text{)}$$

Calculating for the maximal flow rate $\dot{V} = 332.064 \text{ ml/hr}$, $\Delta V_{time} = \pm 1.883 \text{ mm}^3$ and $\Delta V = \pm 1.884 \text{ mm}^3$.

$$\Delta m = \sqrt{\Delta m_{time}^2 + \Delta m_{video}^2} \text{ (g)}$$

where: $\Delta m_{video} = \pm 0.053 \cdot 10^{-3} \text{ g}$, and Δm_{time} is given by:

$$\Delta m_{time} = \pm \sqrt{(V \Delta \rho^*)^2 + (V \Delta \rho_{err})^2 + ((\rho^* + \rho_{err}) \Delta V)^2} \text{ (g)}$$

where: $V = 40.450 \text{ mm}^3$, $\rho_{err} = 4.03 \cdot 10^{-6} \text{ g/mm}^3$, $\Delta \rho_{err} = \pm 1.28 \cdot 10^{-5} \text{ g/mm}^3$, and $\Delta \rho^*$, ρ^* are given by:

$$\Delta \rho^* = \pm 3.16 \cdot 10^{-6} \sqrt{1.563 \cdot 10^{-3} T_o^2 + 2.984} \text{ (g/mm}^3\text{)}$$

$$\rho^* = 10^{-3} (0.0005 T_o^2 - 0.0437 T_o + 1.686) \text{ (g/mm}^3\text{)}$$

The T_o term is given by:

$$T_o = T_{mes} - 0.42 = 14.58 \text{ C}^\circ$$

Given that the measured temperature is equal to 15 C° . The values of densities can now be calculated as: $\Delta \rho^* = \pm 5.771 \cdot 10^{-6} \text{ g/mm}^3$ and $\rho^* = 1.143 \cdot 10^{-3} \text{ g/mm}^3$. Finally giving the $\Delta m_{time} = \pm 2.234 \cdot 10^{-3} \text{ g}$ and $\Delta m = \pm 2.235 \cdot 10^{-3} \text{ g}$.

Spring constant and damping constant uncertainty calculations

Spring constant is given by:

$$k = m \omega^2$$

where: k – spring constant (N/m)

m – mass of the drop (kg)

ω – wave frequency (s^{-1}), given by:

$$\omega^2 = \frac{4\pi^2 + \delta^2}{T^2}$$

$$\delta = \frac{1}{N} (\ln z_i - \ln z_f)$$

$$T = \frac{1}{N} (t_n - t_i)$$

where: δ – logarithmic decrement

T – vibration period (s)

N – number of periods

z_i – initial coordinate offset (m)

z_f – final coordinate offset (m)

t_i – initial time (s)

t_n – final time (s)

Putting everything together will give the spring constant to be:

$$k = m \frac{4\pi^2 N^2 + (\ln z_i - \ln z_f)^2}{(t_f - t_i)^2}$$

Values m , z_i , z_f , t_f and t_i all have uncertainty. Using the equation of the error propagation the value of spring constant uncertainty can be found as:

$$\Delta k = \sqrt{\left(\frac{\partial k}{\partial m} \Delta m\right)^2 + \left(\frac{\partial k}{\partial t_n} \Delta t\right)^2 + \left(\frac{\partial k}{\partial t_i} \Delta t\right)^2 + \left(\frac{\partial k}{\partial z_i} \Delta z\right)^2 + \left(\frac{\partial k}{\partial z_f} \Delta z\right)^2}$$

Now finding each squared value separately gives:

$$\frac{\partial k}{\partial m} \Delta m = \frac{4\pi^2 N^2 + (\ln z_i - \ln z_f)^2}{(t_f - t_i)^2} \Delta m$$

$$\frac{\partial k}{\partial t_n} \Delta t = m \left(4\pi^2 N^2 + (\ln z_i - \ln z_f)^2\right) \left(-\frac{2}{(t_f - t_i)^3}\right) \Delta t$$

$$\frac{\partial k}{\partial t_i} \Delta t = m \left(4\pi^2 N^2 + (\ln z_i - \ln z_f)^2\right) \left(-\frac{-2}{(t_f - t_i)^3}\right) \Delta t$$

$$\frac{\partial k}{\partial z_i} \Delta z = 2m (\ln z_i - \ln z_f) \frac{1}{z_i} \Delta z$$

$$\frac{\partial k}{\partial z_f} \Delta z = -2m (\ln z_i - \ln z_f) \frac{1}{z_f} \Delta z$$

Now by approximating values as following:

$$N = 12$$

$$t_f = 1 \text{ s}, t_i = 0 \text{ and } \Delta t = 1/60 \text{ s}$$

$$z_i = 9 \cdot 10^{-5} \text{ m}, z_f = 3 \cdot 10^{-5} \text{ m and } \Delta z = \pm 1.7 \cdot 10^{-5} \text{ m}$$

$$m = 3 \cdot 10^{-5} \text{ kg and } \Delta m = \pm 2.2 \cdot 10^{-6} \text{ kg}$$

It is possible to approximate the values of the partial differentials as:

$$\frac{\partial k}{\partial m} \Delta m \cong \frac{2 \cdot 10^3 + 1}{1} \cdot 2.2 \cdot 10^{-6} \approx 4.4 \cdot 10^{-3}$$

$$\frac{\partial k}{\partial t_n} \Delta t \cong -3 \cdot 10^{-5} (2 \cdot 10^3 + 1) \cdot \left(\frac{2}{1}\right) \cdot \frac{1}{60} \approx -10^{-3}$$

$$\frac{\partial k}{\partial z_i} \Delta z \cong 2 \cdot 3 \cdot 10^{-5} \cdot 1 \cdot \frac{1}{3 \cdot 10^{-5}} \cdot 1.7 \cdot 10^{-5} \approx 3.4 \cdot 10^{-5}$$

And also knowing that:

$$\left(\frac{\partial k}{\partial z_i} \Delta z\right)^2 = \left(\frac{\partial k}{\partial z_f} \Delta z\right)^2$$

$$\left(\frac{\partial k}{\partial t_n} \Delta t\right)^2 = \left(\frac{\partial k}{\partial t_i} \Delta t\right)^2$$

Now the coordinate components of the spring equation can be neglected as they are in order of 100 to the rest of the terms, the spring constant uncertainty can be approximated as:

$$\Delta k \cong \pm \sqrt{(4.4 \cdot 10^{-3})^2 + 2 \cdot (10^{-3})^2} \approx \pm 4.62 \cdot 10^{-3} \text{ N/m}$$

Similarly, the damping constant is expressed as:

$$c = 2\zeta\sqrt{km}$$

where: c – damping constant

ζ – damping coefficient, given by:

$$\zeta = \sqrt{\frac{\delta^2}{4\pi^2 + \delta^2}}$$

Expanding the terms in damping constant equation gives:

$$c^2 = 4 \frac{\delta^2}{4\pi^2 + \delta^2} m^2 \frac{4\pi^2 N^2 + (\ln z_i - \ln z_f)^2}{(t_f - t_i)^2}$$

$$c^2 = 4m^2 \frac{(\ln z_i - \ln z_f)^2}{4\pi^2 N^2 + (\ln z_i - \ln z_f)^2} \cdot \frac{4\pi^2 N^2 + (\ln z_i - \ln z_f)^2}{(t_f - t_i)^2}$$

$$c^2 = 4m^2 \frac{(\ln z_i - \ln z_f)^2}{(t_f - t_i)^2}$$

$$c = 2m \frac{\ln z_i - \ln z_f}{t_f - t_i}$$

$$\Delta c = \pm \sqrt{\left(\frac{\partial c}{\partial m} \Delta m\right)^2 + \left(\frac{\partial c}{\partial t_n} \Delta t\right)^2 + \left(\frac{\partial c}{\partial t_i} \Delta t\right)^2 + \left(\frac{\partial c}{\partial z_i} \Delta z\right)^2 + \left(\frac{\partial c}{\partial z_f} \Delta z\right)^2}$$

Now finding each squared value separately gives:

$$\frac{\partial c}{\partial m} \Delta m = 2 \frac{\ln z_i - \ln z_f}{t_f - t_i} \Delta m$$

$$\frac{\partial c}{\partial t_n} \Delta t = -2m \frac{\ln z_i - \ln z_f}{(t_f - t_i)^2} \Delta t$$

$$\frac{\partial c}{\partial t_i} \Delta t = 2m \frac{\ln z_i - \ln z_f}{(t_f - t_i)^2} \Delta t$$

$$\frac{\partial c}{\partial z_i} \Delta z = 2m \frac{1}{z_i(t_f - t_i)} \Delta z$$

$$\frac{\partial c}{\partial z_f} \Delta z = -2m \frac{1}{z_f(t_f - t_i)} \Delta z$$

It is possible to approximate the values of the partial differentials as:

$$\frac{\partial c}{\partial m} \Delta m \cong 2 \cdot \frac{1}{1} \cdot 2.2 \cdot 10^{-6} = 4.4 \cdot 10^{-6}$$

$$\frac{\partial c}{\partial t_n} \Delta t = -2 \cdot 3 \cdot 10^{-5} \cdot \frac{1}{1} \cdot \frac{1}{60} = -5 \cdot 10^{-7}$$

$$\frac{\partial c}{\partial z_i} \Delta z = 2 \cdot 3 \cdot 10^{-5} \cdot \frac{1.7 \cdot 10^{-5}}{9 \cdot 10^{-5} \cdot 1} \approx 1.13 \cdot 10^{-5}$$

And also knowing that:

$$\left(\frac{\partial k}{\partial z_i} \Delta z \right)^2 = \left(\frac{\partial k}{\partial z_f} \Delta z \right)^2$$

$$\left(\frac{\partial k}{\partial t_n} \Delta t \right)^2 = \left(\frac{\partial k}{\partial t_i} \Delta t \right)^2$$

It is possible to neglect time components as they are in order of hundred in comparison to distance component, giving that the damping constant uncertainty can be approximated as:

$$\Delta c \cong \pm 10^{-5} \sqrt{0.44^2 + 2 \cdot 1.13^2} \approx \pm 1.66 \cdot 10^{-5}$$

Appendix P. Experimental variable recorded data

Day	Test No.	Flow rate (ml/hr)		Pressure (kPa) ± 0.005	Temp. (°C) ± 0.125	Density (g/ml)		Dynamic viscosity (mPa·s)	Surface tension (mN/m)
		Syringe pump	Corrected value			Water	Air		
1	001	50	60.63	102.44	20.25	1.0535	1.2035	0.9989	72.7797
	002	52	63.02	↓	20.25	1.0535	1.2035	0.9989	72.7797
	003	54	65.42		20.50	1.0477	1.2025	0.9989	72.7421
	004	56	67.82	↓	20.50	1.0477	1.2025	0.9989	72.7421
	005	58	70.21		20.50	1.0477	1.2025	0.9989	72.7421
	006	60	72.60	↓	20.50	1.0477	1.2025	0.9989	72.7421
	007	62	74.99		20.75	1.0419	1.2014	0.9988	72.7042
	008	64	77.38	↓	20.75	1.0419	1.2014	0.9988	72.7042
	009	66	79.76		21.00	1.0362	1.2004	0.9988	72.6661
	010	68	82.14	↓	21.00	1.0362	1.2004	0.9988	72.6661
	011	70	84.53		21.00	1.0362	1.2004	0.9988	72.6661
	012	72	86.90	↓	21.00	1.0362	1.2004	0.9988	72.6661
	013	74	89.28		21.00	1.0362	1.2004	0.9988	72.6661
	014	76	91.66	↓	21.00	1.0362	1.2004	0.9988	72.6661
	015	78	94.03		21.00	1.0362	1.2004	0.9988	72.6661
	016	80	96.40	↓	21.50	1.0250	1.1984	0.9987	72.5891
	017	82	98.77		21.50	1.0250	1.1984	0.9987	72.5891
	018	84	101.14	↓	21.50	1.0250	1.1984	0.9987	72.5891
	019	86	103.50		21.75	1.0195	1.1973	0.9986	72.5502
	020	88	105.86	↓	21.75	1.0195	1.1973	0.9986	72.5502
	021	90	108.23		21.75	1.0195	1.1973	0.9986	72.5502
	022	92	110.58	↓	21.50	1.0250	1.1984	0.9987	72.5891
	023	94	112.94		21.50	1.0250	1.1984	0.9987	72.5891
	024	96	115.30	102.28	21.50	1.0250	1.1984	0.9987	72.5891
2	025	98	117.65	102.32	21.00	1.0362	1.2004	0.9988	72.6661
	026	100	120.00	↓	21.00	1.0362	1.2004	0.9988	72.6661
	027	102	122.35		21.00	1.0362	1.2004	0.9988	72.6661
	028	104	124.70	↓	21.00	1.0362	1.2004	0.9988	72.6661
	029	106	127.04		21.00	1.0362	1.2004	0.9988	72.6661
	030	108	129.38	↓	21.00	1.0362	1.2004	0.9988	72.6661
	031	110	131.73		21.00	1.0362	1.2004	0.9988	72.6661
	032	112	134.06	↓	21.25	1.0306	1.1994	0.9987	72.6277
	033	114	136.40		21.25	1.0306	1.1994	0.9987	72.6277
	034	116	138.74	↓	21.25	1.0306	1.1994	0.9987	72.6277
	035	118	141.07		21.25	1.0306	1.1994	0.9987	72.6277
	036	120	143.40	↓	21.25	1.0306	1.1994	0.9987	72.6277
	037	122	145.73		21.25	1.0306	1.1994	0.9987	72.6277
	038	124	148.06	↓	21.50	1.0250	1.1984	0.9987	72.5891
	039	126	150.38		21.50	1.0250	1.1984	0.9987	72.5891

Day	Test No.	Flow rate (ml/hr)		Pressure (kPa) ± 0.005	Temp. (°C) ± 0.125	Density (g/ml)		Dynamic viscosity (mPa·s) ± 0.125	Surface tension (mN/m) ± ??
		Syringe pump	Corrected value ±1.3632			Water ± 0.0392	Air ± 0.0005		
2 Continue	040	128	152.70	↓	21.50	1.0250	1.1984	0.9987	72.5891
	041	130	155.03		21.25	1.0306	1.1994	0.9987	72.6277
	042	134	157.34	↓	21.50	1.0250	1.1984	0.9987	72.5891
	043	136	159.66		21.50	1.0250	1.1984	0.9987	72.5891
	044	138	161.98	↓	21.50	1.0250	1.1984	0.9987	72.5891
	045	140	164.29		21.50	1.0250	1.1984	0.9987	72.5891
	046	142	166.60	↓	21.50	1.0250	1.1984	0.9987	72.5891
	047	144	168.91		21.25	1.0306	1.1994	0.9987	72.6277
	048	146	171.22	101.97	21.25	1.0306	1.1994	0.9987	72.6277
3	049	148	173.52	100.23	22.50	1.0033	1.1943	0.9984	72.4319
	050	150	175.82	↓	22.50	1.0033	1.1943	0.9984	72.4319
	051	152	178.13		22.50	1.0033	1.1943	0.9984	72.4319
	052	154	180.42	↓	22.50	1.0033	1.1943	0.9984	72.4319
	053	156	182.72		22.75	0.9980	1.1932	0.9984	72.3919
	054	158	185.02	↓	22.75	0.9980	1.1932	0.9984	72.3919
	055	160	187.31		22.75	0.9980	1.1932	0.9984	72.3919
	056	162	189.60	↓	22.75	0.9980	1.1932	0.9984	72.3919
	057	164	191.89		23.00	0.9928	1.1922	0.9983	72.3517
	058	166	194.18	↓	23.00	0.9928	1.1922	0.9983	72.3517
	059	168	196.46		23.25	0.9877	1.1912	0.9983	72.3112
	060	170	198.74	↓	23.25	0.9877	1.1912	0.9983	72.3112
	061	172	201.03		23.25	0.9877	1.1912	0.9983	72.3112
	062	174	203.30	↓	23.25	0.9877	1.1912	0.9983	72.3112
	063	176	205.58		23.25	0.9877	1.1912	0.9983	72.3112
	064	178	207.86	↓	23.50	0.9826	1.1902	0.9982	72.2705
	065	180	210.13		23.50	0.9826	1.1902	0.9982	72.2705
	066	182	212.40	↓	23.50	0.9826	1.1902	0.9982	72.2705
	067	184	214.67		23.50	0.9826	1.1902	0.9982	72.2705
	068	186	216.94	↓	23.75	0.9776	1.1891	0.9981	72.2295
	069	188	219.20		23.75	0.9776	1.1891	0.9981	72.2295
	070	190	221.46	↓	23.75	0.9776	1.1891	0.9981	72.2295
	071	192	223.73		23.75	0.9776	1.1891	0.9981	72.2295
	072	194	225.98	↓	24.00	0.9726	1.1881	0.9981	72.1882
	073	196	228.24	100.16	24.00	0.9726	1.1881	0.9981	72.1882
4	074	198	230.50	99.96	22.75	0.9980	1.1932	0.9984	72.3919
	075	200	232.75	↓	22.75	0.9980	1.1932	0.9984	72.3919
	076	202	235.00		22.75	0.9980	1.1932	0.9984	72.3919
	077	204	237.25	↓	23.00	0.9928	1.1922	0.9983	72.3517
	078	206	239.50		23.00	0.9928	1.1922	0.9983	72.3517
	079	208	241.74	↓	23.25	0.9877	1.1912	0.9983	72.3112
	080	210	243.98		23.25	0.9877	1.1912	0.9983	72.3112
	081	212	246.23	↓	23.25	0.9877	1.1912	0.9983	72.3112
	082	214	248.46		23.25	0.9877	1.1912	0.9983	72.3112
	083	216	250.70	↓	23.50	0.9826	1.1902	0.9982	72.2705

Day	Test No.	Flow rate (ml/hr)		Pressure (kPa) ± 0.005	Temp. (°C) ± 0.125	Density (g/ml)		Dynamic viscosity (mPa·s) ± 0.125	Surface tension (mN/m) ± ??
		Syringe pump	Corrected value ±1.3632			Water ± 0.0392	Air ± 0.0005		
4 Continue	084	218	255.17	↓	23.50	0.9826	1.1902	0.9982	72.2705
	085	220	257.40		23.50	0.9826	1.1902	0.9982	72.2705
	086	222	259.63	↓	23.50	0.9826	1.1902	0.9982	72.2705
	087	224	261.86		23.50	0.9826	1.1902	0.9982	72.2705
	088	226	264.08	↓	23.50	0.9826	1.1902	0.9982	72.2705
	089	228	266.30		23.50	0.9826	1.1902	0.9982	72.2705
	090	230	268.53	↓	23.50	0.9826	1.1902	0.9982	72.2705
	091	232	270.74		23.75	0.9776	1.1891	0.9981	72.2295
	092	234	272.96	↓	23.75	0.9776	1.1891	0.9981	72.2295
	093	236	275.18		23.75	0.9776	1.1891	0.9981	72.2295
	094	238	277.39	↓	23.75	0.9776	1.1891	0.9981	72.2295
	095	240	279.60		23.75	0.9776	1.1891	0.9981	72.2295
	096	242	281.81	↓	23.50	0.9826	1.1902	0.9982	72.2705
	097	244	284.02		23.50	0.9826	1.1902	0.9982	72.2705
	098	246	286.22	100.07	23.50	0.9826	1.1902	0.9982	72.2705
5	099	248	288.42	100.12	21.50	1.0250	1.1984	0.9987	72.5891
	100	250	290.63	↓	21.50	1.0250	1.1984	0.9987	72.5891
	101	252	292.82		21.50	1.0250	1.1984	0.9987	72.5891
	102	254	295.02	↓	21.50	1.0250	1.1984	0.9987	72.5891
	103	256	297.22		21.50	1.0250	1.1984	0.9987	72.5891
	104	258	299.41	↓	21.25	1.0306	1.1994	0.9987	72.6277
	105	260	301.60		21.25	1.0306	1.1994	0.9987	72.6277
	106	262	303.79	↓	21.25	1.0306	1.1994	0.9987	72.6277
	107	264	305.98		21.25	1.0306	1.1994	0.9987	72.6277
	108	266	308.16	↓	21.50	1.0250	1.1984	0.9987	72.5891
	109	268	310.34		21.50	1.0250	1.1984	0.9987	72.5891
	110	270	312.53	↓	21.50	1.0250	1.1984	0.9987	72.5891
	111	272	314.70		21.50	1.0250	1.1984	0.9987	72.5891
	112	274	316.88	↓	21.50	1.0250	1.1984	0.9987	72.5891
	113	276	319.06		21.50	1.0250	1.1984	0.9987	72.5891
	114	278	321.23	↓	21.50	1.0250	1.1984	0.9987	72.5891
	115	280	323.40		21.50	1.0250	1.1984	0.9987	72.5891
	116	282	325.57	↓	21.50	1.0250	1.1984	0.9987	72.5891
	117	284	327.74		21.50	1.0250	1.1984	0.9987	72.5891
118	286	329.90	↓	21.50	1.0250	1.1984	0.9987	72.5891	
119	288	332.06	100.77	21.50	1.0250	1.1984	0.9987	72.5891	

Appendix Q. Video processing “MATLAB® code

Appendix Q.A. Run video processing

```
%Experiments processing code
%V4.2
%Evgeny Trunins
%18/04/2017
%
%-----
%% Start simulation
%Simulation flow rate parameters input
clear all;
flowrate_start=input('Simulation starting flow rate = '); %(ml/hr)
flowrate_finish=input('Simulation finish flow rate = '); %(ml/hr)

%% Start processing videos
for flowrate=flowrate_start:2:flowrate_finish
    %Communication message
    clc; disp('Simulation is running');
    disp(sprintf('Processing video flow rate = %d',flowrate));

    %% Constants
    flowrate_true=flowrate+flowrate*(-0.025*flowrate+22.5)/100; %(ml/hr)-
        %recalculate based on correction factor
    Temp=input('Temperature = '); %(deg C) - Set the temperature
    rho=0.0005*Temp^2-0.0437*Temp+1.686; %(g/ml) - Calculate water
        %density
    rho_true=rho+0.00403; %(g/ml) - Adjust based on our measurements
    rho_out=-0.0041*Temp+1.2865; %(kg/m^3) - Calculate air density
    vol=42.33; %(mm^3) - Critical volume set
    Tn_min=0.5*vol*3.6/flowrate_true; %(s) - minimum accepted period time
    Tn_max=2*vol*3.6/flowrate_true; %(s) - maximum accepted period time

    %% Read video
    I_front=VideoReader(sprintf('%d_cam1.mp4',flowrate)); %Read front
        %video file
    I_side=VideoReader(sprintf('%d_cam2.mp4',flowrate)); %Read side video
        %file
    nFrames_front=I_front.NumberOfFrames; %Check value of total frames
        %-> front
    nFrames_side=I_side.NumberOfFrames; %Check value of total frames ->
        %side

    %% Front video
    disp('Processing front camera video'); %Communication message
    frame_no=6;
    Video_processing_nozzle_side_v11 %Define the nozzle
    for frame_no=4:nFrames_front %Process the video
        %Communication message text
        clc; disp('Simulation is running');
        disp(sprintf('Simulation range %d - %d
(ml/hr)',flowrate_start,...
            flowrate_finish));
        disp(sprintf('Current simulation: flow rate = %d',flowrate));
        disp(sprintf('Temperature set = %d',Temp));
        disp(sprintf(...
            'Processing front camera video ----->>>> %.2f%% done',...
            frame_no*100/nFrames_front));
```

```

    try %Try to define nozzle and drop shape
        Video_processing_v0_1_9 %Define the drop shape
    catch %If could not, leave blank value
        B=NaN;
    end
    dlmwrite(sprintf('cam1_%05.f.txt',frame_no),B,'delimiter','\t'...
        , 'precision',4)%Write the results of the drop shape to the
    %file
end

%% Side video
frame_no=6;
disp('Processing side camera video'); %Communication message
Video_processing_nozzle_side_v21 %Define the nozzle
for frame_no=4:nFrames_side %Proces the video
    %Communication message text
    clc; disp('Simulation is running');
    disp(sprintf('Simulation range %d - %d
(ml/hr)',flowrate_start,...
        flowrate_finish));
    disp(sprintf('Current simulation: flow rate = %d',flowrate));
    disp(sprintf('Temperature set = %d',Temp));
    disp('Front camera video is completed');
    disp(sprintf(...
        'Processing side camera video ----->>> %.2f%% done',...
        frame_no*100/nFrames_front));
    try %Try to define nozzle and drop shape
        Video_processing_v0_2_9 %Define the drop shape
    catch %If could not, leave blank value
        B=NaN;
    end
    dlmwrite(sprintf('cam2_%05.f.txt',frame_no),B,'delimiter','\t'...
        , 'precision',4)%Write the results of the drop shape to the
    %file
end

%% Synchronise the video
%Communication message text
clc; disp('Simulation is running');
disp(sprintf('Simulation range %d - %d (ml/hr)',flowrate_start,...
    flowrate_finish));
disp(sprintf('Current simulation: flow rate = %d',flowrate));
disp(sprintf('Temperature set = %d',Temp));
disp('Front camera video is completed');
disp('Side camera video is completed');
disp('Synchronising video ...');
%Front video
B=dlmread(sprintf('cam1_%05.f.txt',4)); %Read first file
B_1=max(B(:,1))-min(B(:,1)); %Calculate the height of the drop
for frame_no=5:nFrames_front %Go through the video results
    B=dlmread(sprintf('cam1_%05.f.txt',frame_no)); %Read the file
    if (max(B(:,1))-min(B(:,1)))/B_1<0.3 %Detect if the height been
        %reduced, and is less than 30% of previous frame
        break %Exit the for loop
    else %If not detected reduction
        B_1=max(B(:,1))-min(B(:,1)); %Update the value of previous
        %height
    end
end
frame_no_start_front=frame_no; %Record the frame number to
    %synchronise
%Communication message
disp(sprintf('Front video first drop detected at
frame %d',frame_no));
%Side video
B=dlmread(sprintf('cam2_%05.f.txt',4)); %Read first file

```

```

B_1=max(B(:,1))-min(B(:,1)); %Calculate the height of the drop
for frame_no=5:nFrames_front %Go through the video results
    B=dlmread(sprintf('cam2_%05.f.txt',frame_no)); %Read the file
    if (max(B(:,1))-min(B(:,1)))/B_1<0.3 %Detect if the height been
        %reduced, and is less than 30% of previous frame
        break %Exit the for loop
    else %If not detected reduction
        B_1=max(B(:,1))-min(B(:,1)); %Update the value of previous
        %height
    end
end
end
frame_no_start_side=frame_no; %Record the frame number to synchronise
%Communication message
disp(sprintf('Side video first drop detected at frame %d',frame_no));
frame_delta=frame_no_start_front-frame_no_start_side; %Difference
if frame_delta>6 %In case there's big difference in synchronised
    %frames
    logic=input(...
        'Frame error encountered, Do you want to continue? (y/n)->
'...
        , 's');
end

%% Manual synchronisation mode
if logic=='n'
    %Displaying frames from two cameras side by side
    figure; subplot(1,2,1); frame_no=frame_no_start_front;
    OF1=([320,800]); %Offset frame read1 - concentrate on specific
    %region
    S1=([400,400]);
    Front_view=zeros(S1(1,1),S1(1,2),3,'uint8');
    Frame=read(I_front,frame_no); %Set the frame to be read
    Frame=imrotate(Frame,-3); %Rotate the frame by 3 degrees
    for k=1:S1(1,1) %Fill the working video array
        for m_1=1:S1(1,2)
            Front_view(k,m_1,:)=Frame(k+OF1(1,1),m_1+OF1(1,2),:);
        end
    end
    imshow(Front_view); %Display front image of the frame detected
    subplot(1,2,2); frame_no=frame_no_start_side;
    OF1=([300,150]); %Offset frame read1 - concentrate on specific
    %region
    Front_view=zeros(S1(1,1),S1(1,2),3,'uint8');
    Frame=read(I_side,frame_no); %Set the frame to be read
    Frame=imrotate(Frame,4); %Rotate the frame by 4 degrees
    for k=1:S1(1,1) %Fill the working video array
        for m_1=1:S1(1,2)
            Front_view(k,m_1,:)=Frame(k+OF1(1,1),m_1+OF1(1,2),:);
        end
    end
    imshow(Front_view); %Display front image of the frame detected
    sub_logic_front=input...
        ('Do you want to keep front frame (y/n)? -> ','s');
    sub_logic_side=input...
        ('Do you want to keep side frame (y/n)? -> ','s');
    while logic=='n' %Entering manual frame identification
        while sub_logic_front~='y' || sub_logic_side~='y'
            if sub_logic_front~='y' %Apply changes to front video
                frame_no=input('Set the new frame for front video =
');
                subplot(1,2,1); OF1=([320,800]); %Operate the frame
                Front_view=zeros(S1(1,1),S1(1,2),3,'uint8');
                Frame=read(I_front,frame_no); Frame=imrotate(Frame,-
                3);
                for k=1:S1(1,1) %Fill the working video array
                    for m_1=1:S1(1,2)

```



```

        Front_view(k,m_1,:)=Frame(k+OF1(1,1),m_1+...
            OF1(1,2),:);
    end
end
imshow(Front_view); %Display frame
%Communication
sub_logic_front=input...
    ('Do you want to keep front frame (y/n)? ->
    ','s');
end
if sub_logic_side~='y' %Apply changes to side viideo
    frame_no=input('Set the new frame for side video =
    ');
    subplot(1,2,2); OF1=([300,150]); %operate the frame
    Front_view=zeros(S1(1,1),S1(1,2),3,'uint8');
    Frame=read(I_side,frame_no); Frame=imrotate(Frame,4);
    for k=1:S1(1,1) %Fill the working video array
        for m_1=1:S1(1,2)
            Front_view(k,m_1,:)=Frame(k+OF1(1,1),m_1+...
                OF1(1,2),:);
        end
    end
    imshow(Front_view); %Display frame
    %Communication
    sub_logic_side=input...
        ('Do you want to keep side frame (y/n)? ->
        ','s');
end
end
end
%One more time confirm the synchronisation
logic=input('Confirm the synchronisation (y/n)? -> ','s');
if logic=='n' %If was wrong, change what is wrong
    sub_logic_front=input...
        ('Do you want to keep front frame (y/n)? -> ','s');
    sub_logic_side=input...
        ('Do you want to keep side frame (y/n)? -> ','s');
end
end
end

%% Back to synchronisation
frame_delta=abs(frame_no_start_front-frame_no_start_side);%Difference
if frame_no_start_front>=frame_no_start_side %Set initial values
    %for frames
    start_front=6; start_side=6+frame_delta;
else
    start_side=6; start_front=6+frame_delta;
end

%% Finding the CoM and Volume for all frames
n=0;
disp('Synchronising video is completed');
disp('Drop shape calculations ...');
for l=0:min(nFrames_front-start_front,nFrames_side-start_side)
    %Read files
    B_front=dlmread(sprintf('cam1_%05.f.txt',start_front+l));
    B_side=dlmread(sprintf('cam2_%05.f.txt',start_side+l));

    try
        %% Scale the drop pictures
        %Update coordinates so that the starting point is in a middle
        %of nozzle
        B_front(:,1)=B_front(:,1)-min(B_front(:,1)); %Update heights
        B_side(:,1)=B_side(:,1)-min(B_side(:,1));
        %Update width
        B_front(:,2)=B_front(:,2)-B_front(1,2)-0.5*(B_front...

```

```

        (length(B_front),2)-B_front(1,2));
B_side(:,2)=B_side(:,2)-B_side(1,2)-0.5*(B_side...
        (length(B_side),2)-B_side(1,2));
%Creating common matrix
B=zeros(max(max(B_side(:,1)),max(B_front(:,1)))*2*10+1,3);
%Set the matrix size depending in which video drop is bigger;
%the main matrix size is the size of the biggest result
%matrix
%(front or side video) with the step of 0.1
for n=2:max(max(B_side(:,1)),max(B_front(:,1)))*10 %Fill the
    %z-component
    B(n,1)=n/10;
    B(length(B)-n,1)=n/10;
end
B(n+1,1)=B(n,1); %Set the first value
%Readjust the front video results so that nozzle diameter is
%the same and the drop height is the same (scale the drop in
%front video)
B_front(:,1)=B_front(:,1)*max(B_side(:,1))/max(B_front(:,1));
B_front(:,2)=B_front(:,2)*B_side(1,2)/B_front(1,2);
B(1,2)=B_side(1,2); %Record firs value in summarised matrix
B(1,3)=B_front(1,2);
k=2; %Set the counter for front results
m=2; %Set the counter for side results
for n=2:length(B)-1 %Go through main results matrix and set
%the points to match the main matrix size
    if B_front(k,1)==B(n,1) %In case if the values of
        %z-coorddinate is the same
        B(n,2)=B_front(k,2); %Just record the value
        k=k+1; %Increase the counter
    elseif B_front(k,1)>B(n,1) && B_front(k,1)>B_front(k-1,1)
        %In case they're not equal but the z-coordinate is
        %increasing
        %Calculate the slope of the front drop profile
        f=(B_front(k,1)-B_front(k-1,1))/(B_front(k,2)-...
            B_front(k-1,2));
        B(n,2)=B(n-1,2)+(B(n,1)-B(n-1,1))/f; %Record value
        if B_front(k,1)<B(n+1,1) %Check if the counter needs
            %to be increased
            k=k+1; %Change counter
        end
    else %In case z-coordinates are not equal but the
        %z-coordinate is decreasing
        %Calculate the slope
        f=(B_front(k,1)-B_front(k-1,1))/(B_front(k,2)- ...
            B_front(k-1,2));
        B(n,2)=B(n-1,2)+(B(n,1)-B(n-1,1))/f; %Record value
        if B_front(k,1)>B(n+1,1) %Check if the counter needs
            %to be increased
            k=k+1; %Change counter
        end
    end
end
if B_side(m,1)==B(n,1) %In case if the values of
    %z-coorddinate is the same
    B(n,3)=B_side(m,2); %Just record the value
    m=m+1; %Increase the counter
elseif B_side(m,1)>B(n,1) && B_side(m,1)>B_side(m-...
    1,1) %In case they're not equal but the z-
    %coordinate is increasing
    %Calculate the slope of the side drop profile
    f=(B_side(m,1)-B_side(m-1,1))/(B_side(m,2)-...
        B_side(m-1,2));
    B(n,3)=B(n-1,3)+(B(n,1)-B(n-1,1))/f; %Record value
    if B_side(m,1)<B(n+1,1) %Check if the counter needs
        %to be increased
        m=m+1; %Change counter
    end
end

```

```

        end
    else %In case z-coordinates are not equal but the
        %z-coordinate is decreasing
        %Calculate the slope
        f=(B_side(m,1)-B_side(m-1,1))/(B_side(m,2)- ...
            B_side(m-1,2));
        B(n,3)=B(n-1,3)+(B(n,1)-B(n-1,1))/f; %Record value
        if B_side(m,1)>B(n+1,1) %Check if the counter needs
            %to be increased
            m=m+1; %Change counter
        end
    end
end

%% Recalculate to include scaling factor
%From now on the distance main units are mm
B=(2/(-2*B(1,2)))*B; % (mm)
B(length(B),:)=[]; %Delete extra line in results

%% Calculate the CoM location && mass
Drop=zeros(max(max(B_side(:,1)),max(B_front(:,1)))*10,7);%Set
%the matrix
for n=1:length(Drop) %Calculate the values of:
    %Drop volume
    Drop(n,1)=(B(n+1,1)-B(n,1))*pi*(B(length(B)+1-n,2)-...
        B(n,2))*(B(length(B)+1-n,3)-B(n,3))/4;
    Drop(n,2)=(B(length(B)+1-n,2)+B(n,2))/2; %X-coordinate of
    %the section
    Drop(n,3)=(B(length(B)+1-n,3)+B(n,3))/2; %Y-coordinate of
    %the section
    Drop(n,4)=0.5*(B(n,1)+B(n+1,1)); %Z-coordinate of the
    %section
    Drop(n,5)=Drop(n,1)*Drop(n,2); %V*x value
    Drop(n,6)=Drop(n,1)*Drop(n,3); %V*y value
    Drop(n,7)=Drop(n,1)*Drop(n,4); %V*z value
end

%% Results
results(l+1,1)=sum(Drop(:,1)); %Record results for drop
%volume
results(l+1,4)=sum(Drop(:,7))/sum(Drop(:,1)); %Record results
%for z-coordinate
results(l+1,2)=sum(Drop(:,5))/sum(Drop(:,1)); %Record results
%for x-coordinate
results(l+1,3)=sum(Drop(:,6))/sum(Drop(:,1)); %Record results
%for y-coordinate
results(l+1,5)=1/30; %Record time of the event
catch %In case there was no drop or nozzle detected
    %Record results
    results(l+1,1)=0; %Volume
    results(l+1,2)=0; %X-coordinate
    results(l+1,3)=0; %Y-coordinate
    results(l+1,4)=0; %Z-coordinate
    results(l+1,5)=1/30; %Time
end
end

%% Axis rotation
%Finding the angles of rotation
alpha_xz=-atan(mean(results(1:60,2))/mean(results(1:60,4)));
alpha_yz=-atan(mean(results(1:60,3))/mean(results(1:60,4)));
%Creating rotation matrixes
rot_xz=[cos(alpha_xz),0,sin(alpha_xz);0,1,0;-sin(alpha_xz),0,...
    cos(alpha_xz)];
rot_yz=[1,0,0;0,cos(alpha_yz),sin(alpha_yz);0,-sin(alpha_yz),...
    cos(alpha_yz)];

```

```

polyfi
rot_yz=0.01706*pi/180
rot=rot_xz*rot_yz;
for n=1:length(results) %Rewrite the results based on rotation
    R=rot*[results(n,2);results(n,3);results(n,4)];
    results(n,2)=R(1,1);
    results(n,3)=R(2,1);
    results(n,4)=R(3,1);
end
for n=1:length(results)
    if abs(results(n,2))>max(abs(results(:,3)))
        results(n,2)=results(n-1,2);
    end
end

%% Results corrections
disp('Drop shape calculations is completed'); %Communication message
disp('Saving the results ...')
results=results(find(results(:,1)>0),:); %Deleting results with mass
    %error
results=results(find(results(:,4)>0),:); %Deleting results with CoM
    %error
%Save file
dlmwrite(sprintf('%d_results1.txt',flowrate),results,'delimiter',...
    '\t','precision',6);
dump2=zeros(length(results)-4,2); %Create matrix to analyse the CoM
    %position
for n=3:length(results)-2 %Go through the results
    dump2(n-1,1)=log(((results(n,4)^2)/(results(n-1,4)*results(n+...
        1,4))));
    %Use log to amplify the pick values
    dump2(n-1,2)=results(n,5); %Record the time
end
dump4=dump2(find(dump2(:,1)>0.75),:); %Remove anything that is not
    %above
[C,ia]=intersect(results(:,5),dump4(:,2));
f_results=results(ia,:);
for n=1:length(f_results)-1
    f_results(n,6)=f_results(n+1,5)-f_results(n,5); %Record Tn
end

%% Results saving
figure('visible','off');
%Plot T_n vs n
plot(f_results(:,6),'.k'); title('T_n vs n'); ylabel('T_n (s)');
xlabel('n'); print(sprintf('%d_Tn-vs-n_all',flowrate),'-djpeg',...
    '-r300');
%Save file
dlmwrite(sprintf('%d_results2.txt',flowrate),f_results,...
    'delimiter','\t','precision',6);
f_results=f_results(find(f_results(:,6)>Tn_min & f_results(:,6)<...
    Tn_max),:); %Removing the results which considered as error
plot(f_results(:,6),'.k'); title('T_n vs n'); ylabel('T_n (s)');
xlabel('n'); print(sprintf('%d_Tn-vs-n',flowrate),'-djpeg','-r300');
%Plot T_{n+1} vs T_n
%Following is done to increase marker size if it was repeated
%value
Tn_dump=zeros(length(f_results)-1,2); %Set the matrix size
Tn_dump=[f_results(1:length(f_results)-1,6),f_results(2:length...
    (f_results),6)]; %Write the dump file
Tn_dump=sortrows(Tn_dump); %Sort the matrix based on first column
Tn(1,1)=Tn_dump(1,1); Tn(1,2)=Tn_dump(1,2); Tn(1,3)=1; k=1;
for n=2:length(Tn_dump) %Go through the matrix and find
    %repetition
    if abs(Tn_dump(n,1)-Tn(k,1))<0.001
        if abs(Tn_dump(n,2)-Tn(k,2))<0.001

```

```

        Tn(k,3)=Tn(k,3)+1; %If found add extra point to
        %marker size
    else
        k=k+1; Tn(k,1)=Tn_dump(n,1); Tn(k,2)=Tn_dump(n,2);
        Tn(k,3)=1;
    end
else
    k=k+1; Tn(k,1)=Tn_dump(n,1); Tn(k,2)=Tn_dump(n,2);
    Tn(k,3)=1;
end
end
for n=1:length(Tn) %Plot with different marker size
    plot(Tn(n,1),Tn(n,2),'.k','markersize',4*Tn(n,3)); hold on
end
title('T_{n+1} vs T_n'); xlabel('T_n (s)'); ylabel('T_{n+1} (s)');
print(sprintf('%d_Tn1-vs-Tn',flowrate),'-djpeg','-r300'); %Save file
%Plot the behaviour results
subplot(3,1,1); %Mass plot description starts here
plot(results(:,5),rho_true*results(:,1),'k');
xlim([round(results(end,5))-10 round(results(end,5))]);
xlabel('Time (s)'); ylabel('Mass (g)'); grid on;
subplot(3,1,2); %Z-coordinate plot description starts here
plot(results(:,5),results(:,4),'b'); ylabel('Z CoM (mm)'); grid on;
xlim([round(results(end,5))-10 round(results(end,5))]); ylim([0 8]);
xlabel('Time (s)');
subplot(3,1,3); %X and Y coordinate plots description starts here
plot(results(:,5),results(:,2),'r'); hold on; grid on; %Plot X
xlim([round(results(end,5))-10 round(results(end,5))]);
plot(results(:,5),results(:,3),'g'); ylabel('X & Y CoM (mm)');%Plot Y
ylim([-1 1]); xlabel('Time (s)');
print(sprintf('%d_behaviour',flowrate),'-djpeg','-r300'); %Save file
hold off
%Plot the displacement at the detachment
figure('visible','off');
f_results(:,2)=f_results(:,2)-mean(f_results(:,2));
f_results(:,3)=f_results(:,3)-mean(f_results(:,3));
plot(f_results(:,5),f_results(:,2),'r'); %X plot
hold on; plot(f_results(:,5),f_results(:,3),'g'); %Y plot
grid minor; xlim([round(results(end,5))-40 round(results(end,5))]);
xlabel('Time (s)'); ylabel('Coordinate (mm)')
print(sprintf('%d_detachment',flowrate),'-djpeg','-r300'); %Save file
hold off
%Save file
dlmwrite(sprintf('%d_results3.txt',flowrate),f_results,...
    'delimiter','\t','precision',6);
end

%% Bifurcation plot
clf; %Clear and prepare the plot
for flowrate=50:2:288 %Go through the results
    drops=[]; drops_dump=[]; %Clear the changing variables
    flowrate_true=flowrate+flowrate*(-0.025*flowrate+22.5)/100; %(ml/hr)
    %recalculate based on correction factor
    work=dlmread(sprintf('%d_results2.txt',flowrate)); %Read results file
    T_dump=work(:,6); %Copy T_n results to work with
    N_total=length(work(work(:,6)~=0,6)); %Calculate total amount of
    %drops in experiment
    T_dump=sort(T_dump); %Sort the file by the period time
    T_dump(1,2)=1; k=1; %Set the counter

    %% Group repeating periodic values and count the amount of them
    for n=2:length(T_dump) %Go through the file
        if T_dump(n,1)==T_dump(k,1) %If the period repeats
            T_dump(k,2)=T_dump(k,2)+1; %Add quantity to how many repeated
        else %If not just consider next one
            k=k+1; T_dump(k,1)=T_dump(n,1); T_dump(k,2)=1;
        end
    end
end

```

```

    end
end
T_dump=T_dump(T_dump(:,2)~=0,:); %Group the values with common period
T_dump=sortrows(T_dump,2); %Sort the array based on repetition
drops=T_dump; %Save result to working array

%% Start with first flow rate
if flowrate==50
    %Here we are removing satellite drops from first flow rate as
    %they are easily identified
    drops=drops(drops(:,1)>1,:);
    %Next step is to remove the error values (the values are well
    %above main region and easily visible
    err_drops=drops(drops(:,1)>3,:); drops=drops(drops(:,1)<=3,:);

    %% Creating attractors
    %Now we start create attractor region(s). It is assumed here that
    %the values with high repetition are main points, in case they
    % are more than one frame time appartmeans that they create two
    %independent attractors. First identify the old attractor
    %location
    drops(:,3:4)=0; %Prepare working array
    for n=1:length(drops) %Go through the matrix
        %Here percentage of the influence by the point is set
        drops(n,3)=drops(n,2)/max(drops(:,2));
        if drops(n,3)>0.75; drops(n,4)=3;
        elseif drops(n,3)>0.5 && drops(n,3)<=0.75; drops(n,4)=2;
        elseif drops(n,3)>0.25 && drops(n,3)<=0.5; drops(n,4)=1;
        else drops(n,4)=0;
        end
        %We set the values of the influence from 3 to 0 which
        %basically says that current flow rate affects 3 to 0 flow
        %rates in front, and acts in horizontal and diagonal
        %direction. Now we going to plot with grey amount of the
%influence it exposes. With addition of overlaping different
%periodic values.

        %Create the zero matrix of influence: "infl" is matrix for
        %next period, and "infl_1" is matrix for period after
        infl=zeros(round((max(drops(:,1))-min(drops(:,1)))*30)+5,2);
        %Fill the matrix with all possible values
        infl(:,1)=(min(drops(:,1))-2/30:1/30:max(drops(:,1))+2/30);
        infl_1=infl; %Keep it the same for now
        for n=1:length(drops) %Filling matrix and calculating sums
            if drops(n,4)==1 %If influence is "1"
                k=1;
                while abs(drops(n,1)-infl(k,1))>1/30; k=k+1; end
                k=k+1; infl(k,2)=infl(k,2)+1;
            elseif drops(n,4)==2 %If influence is "2"
                k=1;
                while abs(drops(n,1)-infl(k,1))>1/30; k=k+1; end
                k=k+1; infl(k,2)=infl(k,2)+1;
                infl(k-1,2)=infl(k-1,2)+1;
                infl(k+1,2)=infl(k+1,2)+1;
            elseif drops(n,4)==3 %If influence is "3"
                k=1;
                while abs(drops(n,1)-infl(k,1))>1/30; k=k+1; end
                k=k+1; infl(k,2)=infl(k,2)+1;
                infl(k-1,2)=infl(k-1,2)+1;
                infl(k+1,2)=infl(k+1,2)+1;
                infl(k-2,2)=infl(k-2,2)+1;
                infl(k+2,2)=infl(k+2,2)+1;
                infl_1(k,2)=infl_1(k,2)+1; %Note only influence "3"
                %affects the flow rate one after
                infl_1(k-1,2)=infl_1(k-1,2)+1;
                infl_1(k+1,2)=infl_1(k+1,2)+1;
            end
        end
    end
end

```

```

        end
    end
end
%% All other flow rates
else %Now there is influence map so we bring the periods based on it
    %Identify how many regions are there???
    infl=infl(infl(:,2)~=0,:);
    drops=T_dump(T_dump(:,1)>min(infl(:,1))-5/30,:); %Read the values
    drops=drops(drops(:,1)<max(infl(:,1))+5/30,:);
    drops(:,3:4)=0;
    for n=1:length(drops) %Here calculate the attractors values
% (peaks)
        drops(n,3)=drops(n,2)/max(drops(:,2));
        if drops(n,3)>0.75; drops(n,4)=3;
        elseif drops(n,3)>0.5 && drops(n,3)<=0.75; drops(n,4)=2;
        elseif drops(n,3)>0.25 && drops(n,3)<=0.5; drops(n,4)=1;
        else drops(n,4)=0;
        end
    end
    drops_dump=sortrows(drops,1); k=1;
    %% Checking side values
    %of the selected region. If the value of max period is high we
    %need to add extra period and see if it is low. The idea here we
    %don't want to miss periodic jump
    while drops_dump(end,3)>0.2 %Check if the value on a side is not
        %repeating 20% of max value. If so influence region should be
        %extended
        drops=[]; %Clear working array and Upload extended values
        drops=T_dump(T_dump(:,1)>min(infl(:,1))-10/30,:);
        drops=drops(drops(:,1)<max(infl(:,1))+(k+15)/30,:);

        drops(:,3:4)=0;
        for n=1:length(drops) %here recalculate the repetition again
            drops(n,3)=drops(n,2)/max(drops(:,2));
            if drops(n,3)>0.75; drops(n,4)=3;
            elseif drops(n,3)>0.5 && drops(n,3)<=0.75; drops(n,4)=2;
            elseif drops(n,3)>0.25 && drops(n,3)<=0.5; drops(n,4)=1;
            else drops(n,4)=0;
            end
        end
        drops_dump=sortrows(drops,1); %and sort values
        k=k+1; %Next step if needed
        %We increase here by one time step each time
    end

    %% To lower the limi at minimum
    %This part is not used but lowers a limit if the lower value
    %repeats to many times (set at "while")
    %%%
    m=k-1; k=1;
    while drops_dump(1,3)>0.15
    drops=[];
    try
        drops=T_dump(T_dump(:,1)>min(infl(:,1))-(k+10)/30,:);
        drops=drops(drops(:,1)<max(infl(:,1))+(m+15)/30,:);
    catch
        break
    end

    drops(:,3:4)=0;
    for n=1:length(drops)
        drops(n,3)=drops(n,2)/max(drops(:,2));
        if drops(n,3)>0.75; drops(n,4)=3;
        elseif drops(n,3)>0.5 && drops(n,3)<=0.75; drops(n,4)=2;
        elseif drops(n,3)>0.25 && drops(n,3)<=0.5; drops(n,4)=1;
        else drops(n,4)=0;

```

```

        end
    end
    drops_dump=sortrows(drops,1);
    k=k+1;
    if drops_dump(1,1)<2/30
        break
    end
end
end
%%%
%% Create new influence map
infl=[];
infl(:,1)=(min(drops(:,1))-2/30:1/30:max(drops(:,1))+2/30);
infl(:,2)=0;
for n=1:length(infl_1)
    try
        if infl_1(n,2)~=0
            k=1;
            while abs(infl_1(n,1)-infl(k,1))>1/30
                k=k+1;
                if k>length(infl); break; end
            end
            k=k+1; infl(k,2)=infl_1(n,2);
        end
    end
end
infl_1=infl; infl_1(:,2)=0;
for n=1:length(drops)
    if drops(n,4)==1
        k=1;
        while abs(drops(n,1)-infl(k,1))>1/30; k=k+1; end
        if k+1>length(infl); break; end
        k=k+1; infl(k,2)=infl(k,2)+1;
    elseif drops(n,4)==2
        k=1;
        while abs(drops(n,1)-infl(k,1))>1/30; k=k+1; end
        if k+2>length(infl); break; end
        k=k+1; infl(k,2)=infl(k,2)+1;
        infl(k-1,2)=infl(k-1,2)+1;
        infl(k+1,2)=infl(k+1,2)+1;
    elseif drops(n,4)==3
        k=1;
        while abs(drops(n,1)-infl(k,1))>1/30; k=k+1; end
        if k+3>length(infl); break; end
        k=k+1; infl(k,2)=infl(k,2)+1;
        infl(k-1,2)=infl(k-1,2)+1;
        infl(k+1,2)=infl(k+1,2)+1;
        infl(k-2,2)=infl(k-2,2)+1;
        infl(k+2,2)=infl(k+2,2)+1;
        infl_1(k,2)=infl_1(k,2)+1;
        infl_1(k-1,2)=infl_1(k-1,2)+1;
        infl_1(k+1,2)=infl_1(k+1,2)+1;
    end
end
end
%%Here the calculations are finished now we displaying the results
%% Calculate the drops type
N_main=sum(drops(:,2)); %Main drop
N_err=work(work(:,6)>=max(drops(:,1)),6);
N_err=length(N_err); %Errors
N_sat=work(work(:,6)<min(drops(:,1)),6); %Satellite and mid drops
    %together
N_sat=N_sat(N_sat~=0); %Satellite seperately
N_sat=length(N_sat(N_sat<=3/30)); %Here is set the value of max sat
    %drop period (right now is 3/30 s)
N_mid=N_total-N_err-N_sat-N_main;

```



```

    if N_mid<0 %Recalculate (this error pops out because in some flow
rates
    %the satellite drops falled down into main region
    N_sat=N_sat+N_mid;
    N_mid=0;
end
QUANT(flowrate,1)=flowrate_true; %Filling the quantity array
QUANT(flowrate,2)=N_total;
QUANT(flowrate,3)=N_main*100/N_total; %main drops (blue)
QUANT(flowrate,6)=N_err*100/N_total; %error drops (red)
QUANT(flowrate,4)=N_sat*100/N_total; %Satellite drops (green)
QUANT(flowrate,5)=N_mid*100/N_total;

%% Peak identity
%This part of the code is not used. Purpose of it is to identify the
%peaks within one flow rate and smooth the curvature between the
%peaks. Providing that the peaks now become 1 and everything else <1
%%%
%Peak identification script
%
% drops_dump=sortrows(drops,1); %Get the values
% [pks,locs]=findpeaks(drops_dump(:,2),drops_dump(:,1));
% %Identify peaks
% peak=[pks,locs];
% [C,i]=intersect(drops_dump(:,1),peak(:,2)); %Find interseption
% peak_dump=peak; peak=zeros(length(i)+2,3); %Create matrixes
% peak(2:length(i)+1,1)=peak_dump(:,1);
% peak(2:length(i)+1,2)=peak_dump(:,2);
% peak(1,1:2)=flip(drops_dump(1,1:2));
% peak(end,1:2)=flip(drops_dump(end,1:2));
% drops_dump(:,3)=0;
% %Zero already existing values, prepare for overwrite
% %Fill the peak values with maximal values, but only if it is above
% %75% above the max peak value
% for n=1:length(i)
%     if drops_dump(i(n),2)/max(drops_dump(:,2))>0.75
%         drops_dump(i(n),3)=1;
%     end
% end
% %Fill begining and end before peak values
% for n=1:i(1)-1
%     drops_dump(n,3)=drops_dump(n,2)/drops_dump(i(1),2);
% end
% for n=length(drops_dump):-1:i(end)+1
%     drops_dump(n,3)=drops_dump(n,2)/drops_dump(i(end),2);
% end
% %Now go throughout the rest of the results, using only min values
% %to desice what is minimum influence
% for n=1:length(i)-1 %Go through peak matrix
%     if drops_dump(i(n),2)<=drops_dump(i(n+1),2)
%         for k=1:find(drops_dump(i(n):i(n+1),2)==...
%             min(drops_dump(i(n):i(n+1),2)))-1
%             drops_dump(i(n)+k,3)=drops_dump(i(n)+k,2)/...
%                 drops_dump(i(n),2);
%         end
%         k=k+1;
%         if drops_dump(i(n)+k,3)==0
%             while drops_dump(i(n+1),2)~=drops_dump(i(n)+k,2)
%                 drops_dump(i(n)+k,3)=drops_dump(i(n)+k,2)/...
%                     drops_dump(i(n+1),2);
%             end
%             k=k+1;
%         end
%     end
% else
%     for k=1:find(drops_dump(i(n):i(n+1),2)==...
%         min(drops_dump(i(n):i(n+1),2)))-1
%         drops_dump(i(n)+k,3)=drops_dump(i(n)+k,2)/...

```

```

%           drops_dump(i(n),2);
%       end
%   end
% end
% %Make sure that all time steps are represented
% drops=drops_dump;
% if round((max(drops(:,1))-min(drops(:,1)))*30)+1~=length(drops)
%     drops_dump=zeros(round((max(drops(:,1))-...
%         min(drops(:,1)))*30)+1,4);
%     drops_dump(1,1)=drops(1,1);
%     for n=2:length(drops_dump)
%         drops_dump(n,1)=drops_dump(n-1,1)+1/30;
%     end
%     k=1;
%     for n=1:length(drops_dump)
%         if round(drops(k,1),3)==round(drops_dump(n,1),3)
%             drops_dump(n,2:4)=drops(k,2:4);
%             k=k+1;
%         else
%             drops_dump(n,2)=0; drops_dump(n,3)=0.1;
%             drops_dump(n,4)=0;
%         end
%     end
% end
% if drops_dump(end,3)>0.2
%     drops_dump(end+1,1)=drops_dump(end,1)+1/30;
%     drops_dump(end,2)=0; drops_dump(end,3)=0.1;
%     drops_dump(end,4)=0;
% end
% drops=drops_dump; %Provide output
%%
%% Bifurcation plot creation
drops=sortrows(drops,2); %Sort by repetition
dim=5; %Set the dimension of the marker
for n=1:length(drops) %Plot each point with different colour
    colour=[1 1-drops(n,3)^1.5 1-drops(n,3)^1.5]; %Set the colour of
    %the marker
    if drops(n,3)>0.1 %Plot only those which values of repetition is
        %above threshold value
        plot(flowrate_true,drops(n,1),'s','Color',...
colour, 'MarkerSize',...
        dim, 'MarkerFaceColor', colour, 'MarkerEdgeColor', colour)
        hold on %Plot and hold on
    end
end
end
%Stop plotting and Set the axis parameters. First plot bifurcation
hold off ; xlim([60 333.5]); xlabel('Flow rate (ml/hr)');
ylabel('Period (s)'); set(gca, 'Color', 'k')
%Now plot quantity bar chart
QUANT=QUANT(QUANT(:,1)~=0,:); %Delete the values of zero flow rate (just
    %a filling error as the flow rate was set with step of 2)
b=bar(QUANT(:,1),QUANT(:,3:6), 'stacked'); b(1).FaceColor='blue';
b(1).EdgeColor='blue'; b(4).FaceColor='red'; b(4).EdgeColor='red';
b(2).FaceColor='green'; b(2).EdgeColor='green'; b(3).FaceColor='yellow';
b(3).EdgeColor='yellow';
legend('Main drops', 'Satellite drops', 'Mid drops', 'Error reads');
xlim([60 333.5]); ylim([0 100]); legend('Location', 'best');
xlabel('Flow rate (ml/hr)'); ylabel('% of total drops');
set(gca, 'Color', 'b')

```

Appendix Q.B. Nozzle identification code

- For “Master” Pi camera file name is: Video_processing_nozzle_v1.m
- For “Slave” Pi camera file name is: Video_processing_nozzle_v2.m

```
%Video processing code - nozzle identification
%V0.1.6
%Jevgenijs Trunins
%15/05/16
%


---


%% Constants
S1=[400,400]; %Size of the front view region
Front_view=zeros(S1(1,1),S1(1,2),3,'uint8'); %Set the size of the video
%matrix
%Offset frame read1 - concentrate on specific region
OF1=[400,675]; %For “Master” Pi
%OF1=[350,0]; %For “Slave” Pi

%% Video to process
Frame=read(I,frame_no); %Set the frame to be read
Frame=imrotate(Frame,-3); %Rotate by -3 deg. for “Master” Pi
%Frame=imrotate(Frame,4); %Rotate by 4 deg. for “Slave” Pi
for k=1:S1(1,1) %Fill the working video array
    for m_1=1:S1(1,2)
        Front_view(k,m_1,:)=Frame(k+OF1(1,1),m_1+OF1(1,2),:);
    end
end
Front_view=rgb2gray(Front_view); %Change colour to grey scale only
%Identify edges
Front_view=edge(Front_view,'Canny',0.15,2); %For “Master” Pi
%Front_view=edge(Front_view,'Canny',0.1,2.5); %For “Slave” Pi

%% Nozzle identification
%Set constants
A=zeros(2,3); %Set nozzle array
k=2; %Set vertical coordinates
%Set left side minimal coordinates
m_1=130; %For “Master” Pi
%m_1=120; %For “Slave” Pi
%Set right side maximal coordinates
m_r=320; %For “Master” Pi
%m_r=290; %For “Slave” Pi

%Identify the starting points
while Front_view(k,m_1)==0 %Look for starting point on left
    m_1=m_1+1;
end %End when the pixel is white
while Front_view(k,m_r)==0 %Looking for starting point on right
    m_r=m_r-1;
end %End when the pixel is white
A(1,1)=k; A(1,2)=m_1; A(1,3)=m_r; %Record coordinates
%Continue to outline the left edge
n=2; logic=0; %Set the logic values
k=k+1; %Set next vertical coordinate
while logic==0 %Nozzle is required to go either down or down and right
    if Front_view(k,m_1)==1 %If the pixel is an edge
        A(n,1)=k; A(n,2)=m_1; %Record the pixel
    else %If the pixel is not an edge
        m_1=m_1+1; %Check the right bottom pixel
        if Front_view(k,m_1)==1 %If the pixel is an edge
            A(n,1)=k; A(n,2)=m_1; %Record the pixel
        else %If the pixel is not an edge
```

```

        logic=1; %Exit the loop
    end
end
n=n+1; k=k+1; %Check next bottom coordinate
end
k_l=k-1; logic=0; n=2; k=n+1; %Update initial coordinates
while logic==0 %Nozzle is required to go either down or down and left
    if Front_view(k,m_r)==1 %If the pixel is an edge
        A(n,3)=m_r; %Record the pixel
    else %If the pixel is not an edge
        m_r=m_r-1; %Check the right bottom pixel
        if Front_view(k,m_r)==1 %If the pixel is an edge
            A(n,3)=m_r; %Record the pixel
        else %If the pixel is not an edge
            logic=1; %Exit the loop
        end
    end
end
n=n+1; k=k+1; %Check next bottom coordinate
end
%Rearrange and combine the matrix to be in form of (x,y)
k=max(A(:,1)); A_dump=A(:,3); A_dump=flipud(A_dump); A(:,3)=[];
for n=k:2*(k-1)
    A(n,1)=k-(n-k); A(n,2)=A_dump(n-k+1);
end

```

Appendix Q.C. Drop identification code

- For “Master” Pi camera file name is: Video_processing_v0_1_8.m
- For “Slave” Pi camera file name is: Video_processing_v0_2_8.m

```

%Video processing code
%V0.1.8
%Jevgenijs Trunins
%03/03/16
%

```

```

%% Constants
S1=[400,400]; %Size of the front view region
Front_view=zeros(S1(1,1),S1(1,2),3,'uint8'); %Set the size of the video
                                             %matrix
%Offset frame read1 - concentrate on specific region
OF1=[200,300]; %For “Master” Pi
%OF1=[170,180]; %For “Slave” Pi

%% Video to process
Frame=read(I,frame_no); %Set the frame to be read
for k=1:S1(1,1) %Fill the working video array
    for m_l=1:S1(1,2)
        Front_view(k,m_l,:)=Frame(k+OF1(1,1),m_l+OF1(1,2),:);
    end
end
Front_view=rgb2gray(Front_view); %Change colour to grey scale only
%Identify edges
Front_view=edge(Front_view,'Canny',0.2,0.5); %For “Master” Pi
%Front_view=edge(Front_view,'Canny',0.05,0.5); %For “Slave” Pi

%%
%Set constants
m_l=70; m_r=200; m=m_l; k=max(A(:,1)); %For “Master” Pi
m_l=120; m_r=200; m=m_l; k=max(A(:,1)); %For “Slave” Pi

```

```

while m~=m_r %Find the bottom of the drop
    m=m_l; bottom=k-1;
    while Front_view(k,m)==0 && m~=m_r %Check the line is not empty
        m=m+1; %Next point
    end
    k=k+1; %Next line checked
end

k=max(A(:,1)); m=m_l; m_min_dump=m_r; m_max_dump=m_l;
while k~=bottom %Go through each row and colour in between the edges
    while Front_view(k,m)==0; m=m+1; end %Find the right edge
    m_min=m; m=m_r; %Record the values
    if m_min<m_min_dump; m_min_dump=m_min; end %Change threshold value
    while Front_view(k,m)==0 m=m-1; end %Find the left edge
    m_max=m; %Record the value
    if m_max>m_max_dump m_max_dump=m_max; end %Change threshold value
    for n=m_min:m_max; Front_view(k,n)=1; end %Colour in between edges
    k=k+1; m=m_l; %Next row
end
m=m_min_dump; k=max(A(:,1)); %Reset parameters
while m~=m_max_dump %Go through each column and colour in between the
    %edges. Similar process as above
    while k~=bottom && Front_view(k,m)==0 k=k+1; end
    k_min=k; k=bottom;
    while Front_view(k,m)==0; k=k-1; end
    k_max=k;
    for n=k_min:k_max; Front_view(n,m)=1; end
    k=max(A(:,1)); m=m+1;
end
%Identify the left curvature of the drop
B_left=zeros(2,2);
for n=max(A(:,1))+1:bottom
    B_left(n-max(A(:,1)),1)=n; m=m_l;
    while Front_view(n,m)==0
        m=m+1;
    end
    B_left(n-max(A(:,1)),2)=m;
end
%Remove the data points if they are same
n=size(B_left); n=n(1,1); n=n-2; t=1;
while t~=n
    if B_left(t,2)==B_left(t+1,2) && B_left(t,2)==B_left(t+2,2)
        B_left(t+1,:)=[]; n=n-1;
    else
        t=t+1;
    end
end
%Smooth the curvature using the moving average method
b=(1/4)*ones(1,4); B_dump=B_left; B_left=filter(b,1,B_left);
t_left=size(B_left); t_left=t_left(1,1); B=zeros(2,2);
for n=1:t_left-1
    if n<3
        B(n,:)=B_dump(n,:);
    elseif n==t_left-1
        B(n,:)=B_dump(n+1,:);
    else
        B(n,:)=B_left(n+2,:);
    end
end
%Identify right curvature of the drop
B_right=zeros(2,2);
for n=max(A(:,1))+1:bottom
    B_right(n-max(A(:,1)),1)=n; m=m_r;
    while Front_view(n,m)==0
        m=m-1;
    end
end

```

```

    B_right(n-max(A(:,1)),2)=m;
end
%Remove the data points if they are same
n=size(B_right); n=n(1,1); n=n-2; t=1;
while t~n
    if B_right(t,2)==B_right(t+1,2) && B_right(t,2)==B_right(t+2,2)
        B_right(t+1,:)=[]; n=n-1;
    else
        t=t+1;
    end
end
%Smooth the curvature using the moving average method
b=(1/4)*ones(1,4); B_dump=flipud(B_right);
B_right=flipud(filter(b,1,B_right));
t_right=size(B_right); t_right=t_right(1,1);
for n=t_left:t_left+t_right-2
    if n==t_left
        B(n,:)=B_dump(n-t_left+1,:);
    elseif n==t_left+t_right-2
        B(n,:)=B_dump(n-t_left+2,:);
    else
        B(n,:)=B_right(n-t_left,:);
    end
end
end

```

Appendix Q.D. Spring & damper constants investigation

```

i=5; %Recording test number
dump=results(13442:13499,:); %Take the first vibration test
m=mean(dump(:,1))*(10^-9)*997; %(kg) Mean drop mass
dump(:,2:4)=dump(:,2:4)/1000; %(m) Convert units

P=polyfit(dump(:,5),dump(:,4),1);%Fit the linear curve
dump(:,4)=dump(:,4)-(P(1)*dump(:,5)+P(2)); %Readjust to be linear and go
    %around zero
dump(:,5)=dump(:,5)-min(dump(:,5)); %Readjust time
[pks,locs]=findpeaks(dump(:,4),dump(:,5)); %Find peaks
f=fit(locs,pks,'exp1'); %Fit the exponential curve
c_f=coeffvalues(f);
plot(dump(:,5),dump(:,4),'k'); hold on; plot(f,'m');

t_0=input('t_0='); %Input the values from the graph of initial
z_0=input('z_0='); %Initial off-set
t_n=input('t_n='); %Final time
z_n=input('z_f='); %Final off-set
N=input('N='); %Period number
plot(t_0,z_0,'*r'); plot(t_n,z_n,'*r'); hold off
T=(t_n-t_0)/N; %Calculate period
delta=(1/N)*log(z_0/z_n); %Logarithmic decrement
zeta=sqrt((delta^2)/(4*(pi^2)+(delta^2))); %Calculate lambda
omega=sqrt((4*(pi^2)+delta^2)/T^2); %Calculate gamma
err=-c_f(1,2)/(zeta*omega)*100-100; %Calculate error in percentage
if abs(err)>5; disp('Error to high'); end
k=m*omega^2; %Calculate the spring constant
lambda=2*zeta*sqrt(k*m); %Calculate damping value

kcm(i,1)=k; %(N/m) Recording k value
kcm(i,2)=lambda; %Recording c value
kcm(i,3)=m; %(kg) Recording m value

```

NOTES